PACIFIC EARTHQUAKE ENGINEERING

The Fifth U.S.-Japan Workshop on Performance-Based Earthquake Engineering Methodology for Reinforced Concrete Building Structures

10–11 September 2003

Sponsors:

Japan Ministry of Education, Science, Sports and Culture
Pacific Earthquake Engineering Research Center

PEER 2003/11
FEB. 2004

The Fifth U.S.-Japan Workshop on Performance-Based Earthquake Engineering Methodology for Reinforced Concrete Building Structures

10–11 September 2003
Hakone, Japan

Organizers

Toshimi Kabeyasawa
Earthquake Research Institute
University of Tokyo

Jack P. Moehle
Pacific Earthquake Engineering Research Center
University of California, Berkeley

Sponsors
Japan Ministry of Education, Science, Sports and Culture
Pacific Earthquake Engineering Research Center
U.S. National Science Foundation

Research Report

PEER Report 2003/11
Pacific Earthquake Engineering Research Center
College of Engineering
University of California, Berkeley

February 2004

PREFACE

Considerable research is under way throughout the world to establish performance-based assessment and design methodology for buildings. Japan and the United States are at the forefront of this research effort, as well as efforts to implement the research results. The U.S.-Japan Cooperative Research in Urban Earthquake Disaster Mitigation, sponsored in Japan by the Ministry of Education, Science, Sports and Culture, and in the U.S. by the National Science Foundation, is funding collaborative research in Japan and the U.S. The Pacific Earthquake Engineering Research Center in the U.S. has established the development of performance-based earthquake engineering methodology as its primary mission. Because of the importance of this topic, it is timely for researchers and practitioners from the U.S. and Japan to meet to exchange technical data and ideas as well as to identify issues of mutual concern and opportunities for cooperative study.

The Fifth Workshop on Performance-Based Earthquake Engineering Methodology for Reinforced Concrete Building Structures was organized to meet the needs and opportunities for research and practice in performance-based engineering. The objectives of the workshop were threefold: (1) to discuss different perspectives on performance-based engineering as it is applied to new and existing concrete buildings in Japan and the United States; (2) to exchange the latest findings related to the same subject; and (3) to enhance communications and promote opportunities for new and continuing collaboration.

The Fifth Workshop was held 10 to 11 September 2003 in Hakone, Japan. It was attended by 14 Japanese and 17 U.S. participants. The participants are identified on the following page.

JAPAN SIDE	U.S. SIDE
Toshimi Kabeyasawa, ERI, U Tokyo Toshikatsu Ichinose, Nagoya IT Daisuke Kato, Niigata U Kazuhiro Kitayama, Tokyo Metropolitan U Tetsuo Kubo, Nagoya IT Masaki Maeda, Tohoku U Shinsuke Nakata, Kochi UT Hiroshi Noguchi, Chiba U Shinsuke Otani, U Tokyo Akenori Shibata, Tohoku Bunka Gakuen U Hitoshi Shiohara, U Tokyo Sunsuke Sugano, Hiroshima U Akira Tasai, Yokohama National U Manabu Yoshimura, Tokyo Metropolitan U	Jack Moehle, UC Berkeley Mark Aschheim, U Illinois—Urbana-Champaign Sarah Billington, Cornell U Craig Comartin, Comartin-Reis Marc Eberhard, U Washington Catherine French, U Minnesota—Twin Cities Mary Beth Hueste, Texas A&M U James Jirsa, U Texas—Austin Stephen Mahin, UC Berkeley Mete Sozen, Purdue U Helmut Krawinkler, Stanford U Michael Kreger, U Texas, Austin Chris Pantelides, U Utah Jose Restrepo, UC San Diego Mason Walters, Forell-Elsesser Engineers, Inc. James Wight, U Michigan Eric Williamson, U Texas—Austin

Front Row: Cathy French, Hiroshi Noguchi, Tetsuo Kubo, Toshimi Kabeyasawa. *Middle Row*: Masaki Maeda, Mete Sozen, Helmut Krawinkler, Jack Moehle, Kazuhiro Kitayama, Mary Beth Hueste, Chris Pantelides, Marc Eberhard, Hitoshi Shiohara, Sarah Billington, Toshikatsu Ichinose, Shinsuke Nakata, Shunsuke Otani. *Back Row:* Daisuke Kato, Akira Tasai, Akenori Shibata, James Jirsa, Mark Aschheim, Michael Kreger, James Wight, Eric Williamson, Mason Walters, Troy Morgan, Manabu Yoshimura, Michael Fardis. Not shown: Shunsuke Sugano.

HOST ORGANIZATIONS AND SPONSORS

The workshop was organized under the auspices of the U.S.-Japan Cooperative Research in Earthquake Disaster Mitigation, with funding in Japan by the Ministry of Education, Science, Sports and Culture, and in the U.S. by the National Science Foundation, the Pacific Earthquake Engineering Research Center, and the State of California.

The technical program was developed by Professor Toshimi Kabeyasawa, Division of Disaster Mitigation Science, Earthquake Research Institute, University of Tokyo, and Professor Jack P. Moehle, Director of the Pacific Earthquake Engineering Research Center, University of California, Berkeley.

ACKNOWLEDGMENTS

This work was supported in part by the Pacific Earthquake Engineering Research Center through the Earthquake Engineering Research Centers Program of the National Science Foundation under award number EEC-9701568.

On the Japan side, this work was supported as part of the Development of Performance-Based Design Methodologies, subtheme (2-1) of the U.S.-Japan Cooperative Research in Earthquake Disaster Mitigation program under grant number 11209203, a grant-in-aid for Scientific Research on Priority Area, Category B, by the Ministry of Education, Science, Sports and Culture.

CONTENTS

SESSION 2-A: EVALUATION OF SEISMIC DEMANDS ♦ Chaired by Eric Williamson and Akenori Shibata

SESSION 2-B: PERFORMANCE OF COLUMN MEMBERS ♦ Chaired by Michael Kreger and Hiroshi Noguchi

SESSION 3-A: PREDICTION OF SEISMIC PERFORMANCE TO COLLAPSE ♦ Chaired by Mark Aschheim and Shinsuke Nakata

PLENARY SESSION 1: KEYNOTE LECTURES

Chaired by

♦ James Jirsa and Toshikatsu Ichinose ♦

DAWN OF EARTHQUAKE ENGINEERING

Shunsuke OTANI[1]

ABSTRACT

This paper briefly reviews the development of earthquake engineering before the measurement of ground acceleration started in the early 1930s and the response calculation was made possible in the early 1940s. The first effort was to estimate the maximum ground acceleration to formulate the design seismic forces, which the engineers and researchers tried to formulate without the knowledge of the measurement of ground acceleration signals. A mechanical analyzer was used to calculate the response of simple systems to ground motion.

DEVELOPMENT OF SEISMOLOGY AND GEOPHYSICS

It is necessary to briefly review the development of seismology before discussing the earthquake engineering. Earthquake phenomena must have attracted the curiosity of scientists in the past. Ancient Greek sophists hypothesized different causes of earthquakes. Aristotle (383-322 B.C.), for example, related atmospheric events such as wind, thunder and lightning, and subterranean events, and explained that the dry and smoky vapors caused the earthquakes under the earth, and wind, thunder, lightning in the atmosphere. Aristotle's theory was believed through middle ages in Europe. The 1755 Lisbon, Portugal, Earthquake (M8.7), which killed 70,000 partially due to Tsunami tidal wave, and a series of earthquakes in London in 1749 and 1750 attracted the interest of European scientists who dealt with the phenomena in a scientific manner.

The first scientific investigation about earthquake phenomena is believed to be carried out by Robert Mallet (1810-1881) who considered the earthquake phenomena as the propagation of vibration waves; he measured the velocity of waves in the earth using explosions of gunpowder. He investigated the earthquake phenomena of the 1857 Naples Earthquake (Mallet, 1862). Such technical terms as "seismology," "hypocenter," "isoseismal," and "wave path" were introduced by him.

The measurement of earthquake ground vibration must have been a challenge for scientists. Chan Heng, in 132 A.D. in China, developed an instrument to detect an earthquake and point out the direction of the epicenter. Mallet also invented an instrument to record the intensity of ground

[1] *Department of Design and Architecture, Faculty of Engineering, Chiba University.*

motion by measuring the direction and distance of a particle moved by the ground motion; the ground motion, however, could not be measured and recorded by these instruments. Many attempts were made to develop seismometers (seismograph) which could record the ground movement (displacement) during an earthquake. An electromagnetic seismograph was developed by Luigi Palmieri (1807-1896) in 1855. This device must have been the state of the art because the Palmieri-type seismometers were formally adopted in a far-eastern developing country of Japan in 1875.

The first seismological society in the world, Seismological Society of Japan, was founded in 1880 when European and U.S. engineering professors, invited to the Imperial College of Engineering in Tokyo, became interested in the 1880 Yokohama earthquake (M5.5), which caused minor damage to buildings, but collapsed a chimney. John Milne (1850-1913), professor of Geology and Mining was the leader in scientific and engineering research. Milne, together with James A. Ewing (1855-1935) and Thomas Gray (1850-1908), developed a modern three-directional seismometer in 1881. Significant contributions to seismology were published in the transactions; e.g., Milne introduced Mallet's work on seismology in the first transactions, and Ewing reported the primary and secondary waves observed in the recorded ground motion.

The University of Tokyo was renamed as the Imperial University in 1886, and the Imperial College of Engineering became a part of the university. Eleven Japanese professors were appointed for the first time at the university; Kiyokage Sekiya (1854-1896), who worked closely with Ewing and Milne, became the first professor in seismology chair in Faculty of Science. Fusakichi Omori (1868-1923), who contributed to significant progress in earthquake engineering and seismology, succeeded the chair in 1897.

The relation of fault movement and earthquake was noted by Grove K. Gilbert (1843-1918), U.S. geologist, who reported in 1872 that earthquakes usually centered around a fault line. Clear relative movement was observed across the fault in the 1906 San Francisco Earthquake (Ms 8.3) which was caused by the fracture of San Andreas Fault over 400 km. The earthquake caused 700 to 800 deaths and destroyed 28,188 buildings. Main source of the disaster was fire. Harry F. Reid (1859-1944), professor at Johns Hopkins University, proposed "Elastic Rebound Theory" to describe the process of an earthquake mechanism in 1908; "... external forces must have produced an elastic strain in the region about the fault-line, and the stresses thus induced were the forces which caused the sudden displacements, or elastic rebounds, when the rupture occurred...." Reid did not explain a mechanism to develop such forces acting about fault-lines.

Alfred Wegener (1880-1930) discussed the theory of continent drift (Wegener, 1915). It is important that he presented the theory with extensive supporting evidence such as geological formations, fossils, animals and climatology. He claimed that a single mass, called Pangaea, drifted and split to form current continents. However, Wegener had no convincing mechanism to explain the continent drift. From the 1950s, the exploration data of the earth's crust, notably the ocean floor, increased; e.g., American physicists Maurice Ewing (1906-1974) and Bruce Heezen (1924-1977) discovered the great global rift (the Mid-Ocean Ridge in Atlantic Ocean). On the basis of these exploration data, Harry Hess (1906-1969), professor of Geology at Princeton University, proposed the theory of sea-floor spreading in 1960, which gave a mechanism to support the Wegener's continent drift. The plate tectonics can describe the accumulation of strains at the boundaries of adjacent plates or within a plate due to the plate movement on the earth surface.

STRUCTURAL DYNAMICS

Galileo Galilei (1564-1642) demonstrated by experiment in 1638 that the distance a particle traveled under gravitational environment was proportional to the square of time it traveled. Sir Isaac Newton (1642-1727) published "Philosophia Naturalis Principia Mathematica" in 1687, in which he proposed the Law of Motion; i.e., when a force acts on a particle, the resultant acceleration of the particle is directly proportional to the force. The equation was introduced to calculate the motion of stars in the universe. The law could not be used in engineering for a long time.

Jean le Rond d'Alembert (1717-1783) published "Traite de Dynamique" in 1743, and described D'Alembert's Principle; i.e., a fictitious inertia force, proportional to the acceleration and mass of a particle but acting in the direction opposite to the acceleration, was introduced to formulate the equilibrium of forces in a dynamic problem.

Structural mechanics developed rapidly in the middle of 19th century. John William Strut, also known as Load Rayleigh (1842-1919), published "Theory of Sound" in 1877, in which he discussed the vibration of a single-degree-of-freedom system with viscous damping under harmonic excitation, longitudinal, torsional and lateral vibration of bars, and vibration of membranes, plates and shells. He was interested in structural dynamics of mechanical systems, but did not relate the knowledge of structural dynamics with earthquake engineering problems.

Such knowledge in structural dynamics could not be used in earthquake engineering for many years because the ground acceleration signal of an earthquake was not known and because the equation of motion could not be solved for an arbitrary excitation function. This paper reviews the progress in earthquake engineering before the dynamic response analysis of a simply system was made possible under earthquake motions.

INTENSITY OF EARTHQUAKE GROUND MOTION

Early earthquake engineers and seismologists must have known the importance of ground acceleration to estimate the intensity of inertia forces acting on structures during an earthquake. The seismograph, however, was not capable of measuring ground acceleration which was more important for engineering purposes. E. S. Holden (1888), Director of the Lick Observatory in California, reported that "The researches of the Japanese seismologists have abundantly shown that the destruction of buildings, etc., is proportional to the acceleration produced by the earthquake shock itself in a mass connected with the earth's surface."

Indeed, in Japan, some efforts were made to estimate the maximum ground acceleration during an earthquake. John Milne and his student Kiyokage Sekiya estimated maximum ground acceleration amplitudes from the measured seismometer (displacement) records by assuming harmonic motions in 1884. Because the dominant frequencies in displacement and acceleration signals were different, this method tended to underestimate the maximum acceleration. Milne (1885) also introduced the West's equation, which was used to estimate maximum ground acceleration α necessary to overturn a rigid body of width b and height h attached on the ground if the inertia force of the ground motion was replaced by the equivalent static force using dynamic equilibrium;

$$\alpha > \frac{b}{h} \tag{1}$$

where acceleration α is expressed as the ratio to gravitational acceleration. This method was extensively used in Japan to estimate the intensity of ground motions from the dimensions of overturned tomb stones after an earthquake, but this method was crude because a peak ground acceleration did not act on the rigid body at rest. It should be noted that the inertia force was replaced by an equivalent static force in these efforts.

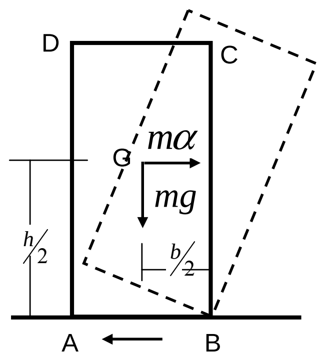

Fig. 1: West's equation to estimate maximum ground acceleration from an overturning rigid body

There were limitations to estimate the ground acceleration intensity during an earthquake without having accelerograph in the late 19th century and early 20th century.

SEISMIC DESIGN FORCES

The 1891 Nohbi Earthquake (M 8.0) caused significant damage to then modern brick and masonry construction in Nagoya City. This was a largest-class near-field earthquake occurring in the Japanese islands. 7,273 were killed in sparsely populated areas, 142,177 houses were destroyed. John Milne and W. K. Burton (1891) reported the disaster. Milne, after noting the effect of surface geology on the damage rate, pointed out that "we must construct, not simply to resist vertically applied stresses, but carefully consider effects due to movements applied more or less in horizontal directions." He could not define the intensity of lateral forces to be used in design. Japanese Government established Earthquake Disaster Prevention Investigation Council in 1892 for the promotion of research in earthquake engineering and seismology, and implementing the research findings in practice. The Seismological Society of Japan was absorbed into the council.

The first quantitative seismic design recommendations were made after the 1908 Messina Earthquake, Italy, which killed more than 83,000 people. Dr. George Housner (1984) stated in his keynote address at the Eighth World Conference on Earthquake Engineering in San Francisco that "The government of Italy responded to the Messina earthquake by appointing a special committee composed of nine practicing engineers and five professors of engineering ... M. Panetti, Professor of Applied Mechanics in Turin ... recommended that the first story be designed for a horizontal force equal to 1/12 the weight above and the second and third stories to be designed for 1/8 of the building weight above." The height of buildings was limited to three stories at the time. Technical background is not clear for this quantification, but it is interesting to note that design seismic forces were initially defined in terms of a story shear coefficient, a ratio of story shear to the weight above, rather than a seismic coefficient, a ratio of the horizontal force of a floor to the weight of the floor.

Riki (Toshikata) Sano (1880-1956) proposed the use of seismic coefficients in earthquake resistant building design (Sano, 1915 and 1916). He assumed a building to be rigid and directly connected to the ground surface, and suggested a seismic coefficient to be equal to the maximum ground acceleration normalized to the gravity acceleration and also uniform along the entire height of the structure. Although he noted that lateral deformation of the structure might amplify response acceleration amplitudes, he ignored the effect in the proposal. The idea of the seismic coefficient was not new, but was used by Milne and Sekiya in the late 19th century. Sano's originality lied in his quantification of the seismic coefficient for a given site. He estimated the maximum ground acceleration in Honjo and Fukagawa areas on alluvial soft soil to be 0.30 G on the basis of the damage of houses in the 1855 Ansei-Edo (Tokyo) Earthquake and in Yamanote area on diluvial hard soil to be 0.15 G. Sano introduced the types of earthquake damages and discussed the earthquake resistance of brick masonry, steel, reinforced concrete and timber houses and buildings.

STRUCTURAL ANALYSIS METHODS

Once design earthquake forces were defined, the stresses in a building must be calculated under the earthquake forces. Building structures are highly statically indeterminate, and practical methods are necessary for seismic design. Fundamental studies of structures were developed in the middle of nineteenth century. James Clerk Maxwell (1831-1879) in 1864 and Otto Mohr (1835-1918) in 1874, separately, found the unit load method to find deflection of elastic trusses and flexibility method to find redundant forces in statically indeterminate trusses. Louis Marie Henri Navier (1785-1836) in 1826 was the first to use the stiffness method of analysis in the problem of two-degree-of-kinematic indeterminacy. Well-known Castigliano's (Carlo Alberto Pio Castigliano, 1847-1884) theorems were presented in 1879.

The slope deflection method was used by W. Wilson and G. A. Maney (1915); a set of linear equations had to be solved before the moment distribution could be determined. The theoretical but practical moment-distribution method was presented by Hardy Cross (1885-1959) in 1930.

Tachu (Tanaka) Naito (1886-1970) of Waseda University introduced the slope-deflection method to Japan in 1922 (Naito, 1924). He analyzed a series of rectangular frames under horizontal forces, and noted that the story shear must be distributed to columns in accordance with their lateral stiffness. Naito proposed lateral force distribution ratios (D-value) for interior (1.0) and exterior (0.5) columns, and for flexible frames (1.0) and shear walls (8 to 20). Simple rules were introduced to estimate the height of inflection points in columns to calculate bending moment from known shear. In the design of the Industrial Bank of Japan Building (8-story steel reinforced concrete building completed just before the 1923 Kanto Earthquake), he adopted reinforced concrete shear walls as earthquake resisting elements. The effectiveness of structural walls was demonstrated by the building during the 1923 Kanto Earthquake.

Naito's D-value method of structural calculation for frame buildings was further extended by Kiyoshi Muto (1903-1989), Imperial University of Tokyo (Architectural Institute of Japan, 1933). Lateral stiffness of a column was theoretically evaluated taking into account (a) flexural stiffness of the column, (b) stiffness of adjacent girders immediately above and below the column, and (c) support conditions at column base. Story shear was distributed to each column in accordance with its lateral stiffness. The moment distribution of the column was determined by the column shear and the height of inflection point, which was evaluated taking into account (a) relative location of story, (b) stiffness of adjacent girders immediately above and below the column, (c) change in stiffness of the adjacent girders, and (d) difference in inter-story height immediately above and below the column. The sum of column end moments at a joint was distributed to girder ends in proportion to the girder stiffness. Various factors were prepared in table format for practical design use.

SEISMIC DESIGN IN CODES

The first Japanese building code, Urban Building Law, was promulgated in April 1919, to regulate buildings and city planning six major cities. Structural design was specified in Building Law Enforcement Regulations; i.e., quality of materials, allowable stresses of materials, connections, reinforcement detailing, dead and live loads, and method of calculating stresses were specified, but earthquake and wind forces were not. The allowable (working) stress design was common procedures at this time in the world; in which the safety factor for uncertainties was considered in the ratio of the strength to the allowable stress of the material.

The 1923 Kanto Earthquake (M 7.9) caused significant damage in Tokyo and Yokohama areas, killing more than 140,000, damaging more than 250,000 houses, burning more than 450,000 houses. More than 90 percent of the loss in lives and buildings was caused by fire. The damage to reinforced concrete buildings was relatively low although there was no seismic design regulations. The damage was observed in reinforced concrete buildings provided with (a) brick partition walls, (b) little shear walls, or constructed with (c) poor reinforcement detailing, (d) short lap splice length, (e) poor beam-column connections, (f) poor construction, or designed with (g) irregular configuration, and (h) poor foundation. Buildings using deformed bars were severely damaged in this earthquake, and the deformed bars were not used until after the late 1960s.

The Building Law Enforcement Regulations were revised in June 1924 to require seismic design using seismic coefficients of 0.10 for the first time in the world. From the incomplete measurement of ground displacement at the University of Tokyo, the maximum ground acceleration was estimated to be 0.3 G, in which G is the gravitational acceleration. The allowable stress in design was one-third to one-half of the material strength. Therefore, the design seismic coefficient 0.1 was determined by dividing estimated maximum ground acceleration of 0.3 G by the safety factor of 3 of the allowable stresses. The regulations further required (a) minimum splice length of 25 times the bar diameter for lap splice, (b) use of top and bottom reinforcement in girders, (c) minimum dimensions of 1/15 times clear height for columns, and (d) minimum longitudinal reinforcement ratio of 1/80 for columns.

The first edition of Uniform Building Code in 1927, a model code in the United States published by Pacific Coast Building Officials Conference, adopted the seismic coefficient method for structural design in seismic regions based on the experience from the 1925 Santa Barbara Earthquake, California. The seismic coefficient was varied for soil conditions between 0.075 and 0.10; this was the first time to recognize the amplification of ground motion by soft soil. After the 1933 Long Beach, California, Earthquake, seismic design became mandatory in California using seismic coefficients of 0.02 by the Riley Act and higher seismic safety, using seismic coefficients of 0.10, was required for school buildings in the Field Act. The 1935 Uniform Building Code adopted the variation of design seismic forces in three seismic zones recognizing the different levels of seismic risk from a region to another.

Building Standard Law, applicable to all buildings in Japan, was proclaimed in May 1950. The Law did not prescribe technical issues, but it referred to the Building Standard Law Enforcement Order (Cabinet Order). The seismic design requirements are outlined below.

Horizontal earthquake force F_i at floor level i was calculated as

$$F_i = Z\ G\ K\ W_i \tag{2}$$

where Z: seismic zone coefficient (0.8 to 1.0), G: soil-structure coefficient (0.6 to 1.0), K: seismic coefficient (0.20 to height of 16 m and below, increased by 0.01 for every 4.0 m above), W_i: weight of story i including live load for earthquake inertia part. The soil-structure coefficient G was varied for soil conditions and for construction materials; e.g., for reinforced concrete construction, the coefficient was 0.8 for rock or stiff soil, 0.9 for intermediate soil, and

1.0 for soft soil. Seismic zone coefficient was based on the seismic hazard map prepared by Hiroshi Kawasumi, professor at Earthquake Research Institute, published in 1946.

At this stage, researchers and engineers discussed the earthquake resistant building design without knowing the probable intensity and characteristics of design earthquake motions.

MEASUREMENT OF GROUND ACCLERATION

Earthquake Research Institute was established at the University of Tokyo in 1925, and replaced the role of the Earthquake Disaster Prevention Investigation Council. Many new efforts were made to understand earthquake phenomena and also to develop technology to reduce earthquake disaster. M. Ishimoto (1893-1940) developed an accelerograph in 1931; the record was used to study the dominant period of ground motion at different sites, but not for the response calculation of a structure.

Kyoji Suyehiro (1877-1932), the first director of Earthquake Research Institute, was invited by American Society of Civil Engineers (ASCE) to give a series of lectures on engineering seismology at U.S. universities in 1931 (Suyehiro, 1932). He pointed out the lack of information about ground acceleration of earthquakes and emphasized the importance of developing accelerograph to record ground acceleration signals during an earthquake.

At the U.S. Seismological Field Survey (later known as U.S. Coast and Geodetic Survey), established in 1932, F. Wenner and H. E. McComb worked on the development of the first strong motion accelerograph (Montana model) in the same year. A accelerograph at Mt. Vernon station measured the motion during the 1933 Long Beach Earthquake, but the amplitude exceeded the limit of the instrument.

Acceleration records of strong earthquake motions were recorded during the 1935 Helena, Montana, earthquake and the 1938 Ferndale, California, earthquake with peak amplitudes of 0.16 to 0.18 G. The well-known El Centro records were obtained in 1940 during the Imperial Valley earthquake. The El Centro records have been studied extensively and considered as the standard acceleration records for a long time. An earthquake acceleration signal is not harmonic, but is quite random in nature containing high-frequency components. The acceleration signal is much different from the displacement signal in terms of frequency content.

RESPONSE ANALYZER

Maurice A. Biot (1905-1985), California Institute of Technology, suggested that earthquake response amplitude of simple systems to transient impulses should vary with their natural periods in 1933, introducing the concept of a response spectrum. He suggested the use of an electric analyzer. Biot, later at Colombia University, developed a manually driven mechanical analyzer (torsional pendulum) to calculate the response of linearly elastic systems to an arbitrary exciting function; the 1935 Helena, Montana, earthquake, the 1938 Ferndale, California earthquake records were used to develop the first earthquake response spectra. No damping was used in the calculation. The undamped response spectrum peaked at 0.2 sec with maximum amplitude of 1.0 G, and the response spectrum decayed inversely proportional to the period of systems as shown in Eq. (3). He pointed out that the response amplitudes could be reduced by the effect of hysteretic energy dissipation of a structure or damping associated with the radiation of kinetic energy to the foundation (K. Sezawa and K. Kanai, 1935).

$$
\begin{aligned}
S_A &= (4T + 0.2)G \qquad && T < 0.2 \text{ sec} \\
S_A &= \frac{0.2}{T} G && T \geq 0.2 \text{ sec}
\end{aligned}
\tag{3}
$$

The lateral force distribution varies with the height due to dynamic effect. The effect was first recognized in the City of Los Angeles Building Code in 1943; i.e., the design seismic coefficient C_i at floor i was defined as

$$C_i = \frac{0.60}{N + 4.5} \tag{4}$$

where N: the number of stories above the story under consideration, but the maximum number of stories was limited to 13. In this requirement, the seismic coefficient increased with height from the ground and also with the number of stories of the building. The 1949 edition of UBC specified similar design seismic forces as follows;

$$F_i = Z \frac{0.15}{N_i + 4.5} W_i \tag{5}$$

where, N : number of stories above, and Z: seismic zone factor.

The joint committee of the San Francisco section of the American Society of Civil Engineers (ASCE) and the Structural Engineers Association of Northern California (SEAOC) recommended a model code in which the base shear coefficient C was inversely proportional to the estimated fundamental period, as shown in Eq. (6) of the structure (Joint Committee, 1951) and the lateral force was distributed linearly from the base to the top.

$$C = \frac{0.015}{T} \qquad 0.02 \le C \le 0.06 \tag{6}$$

The Structural Engineers Association of California (SEAOC) (Seismological Committee, 1957) published a seismic design model code in 1957, which was formally adopted in 1959. The minimum design base shear V for buildings was expressed as

$$V = KCW \tag{7}$$

where horizontal force factor K represents the type of structural systems, and W is the weight of a building. The seismic coefficient C varies inversely proportional to cubic root of the fundamental period T of structures, but limited to 0.10;

$$C = \frac{0.05}{\sqrt[3]{T}} \tag{8}$$

The commentary to the SEAOC Code states that “Requirements containing in such codes are intended to safeguard against major structural failures and to provide protection against loss of life and personal injury. ... The code does not assure protection against nonstructural damage.”

Building Standard Law Enforcement in Japan did not consider the period effect on the amplitude of seismic design forces until the 1981 revision.

SUMMARY AND FUTURE

Although researchers recognized that the building should be designed against horizontal inertia forces developed by earthquake ground motion at the end of nineteenth century, it took them a long time to quantify the design earthquake forces on the basis of observed ground acceleration. Many efforts were made to estimate the maximum ground acceleration amplitudes. Simple structural analysis methods had to be developed before the seismic design could be realized in practice.

Earthquake engineering was further developed by the use of digital computers in response calculation of simple as well as complex nonlinear systems, the use of static as well as dynamic experimental data of structural members and sub-assemblages to failure, the development of vibration control technologies, the observation of damaged structures by earthquakes, and the development of engineering seismology. The objectives of earthquake engineering was the protection of human lives in engineered construction, but this objective can be nearly achieved if the state of art and practice is applied to a new construction. The current objective is directed toward the performance-based engineering; the performance requirements of a given building defined by an owner should be satisfied during and immediately after an earthquake. Some buildings need to function immediately after an earthquake event. For this purpose, the protection of non-structural elements in addition to structural members needs more attention in design. Although non-structural elements are ignored for structural resistance, but are essential for structural function.

REFERENCES

Architectural Institute of Japan (1933). *AIJ standard for structural calculation of reinforced concrete structures* (in Japanese).

Biot, M.A. (1933). Theory of elastic systems vibrating under transient impulses with an application to earthquake-proof buildings, *Proceedings, National academy of science*, Vol. 19, No.2, pp. 262-268.

Biot, M.A. (1941). A mechanical analyzer for the prediction of earthquake stresses, *Bulletin, Seismological society of America*, Vol. 31, No. 2, pp. 151-171.

Cross, H. (1930). Analysis of continuous frames by distributing fixed end moments, *Proceedings, American society of civil engineers*.

Galileo Galilei, (1638). *Discourses concerning two new sciences.*

Holden, E. S. (1888). Note on earthquake-intensity in San Francisco, *The American journal of science*, Third Series, Vol. 35, No. 210, pp. 427-431.

Housner, G.W. (1984). Historical view of earthquake engineering, Conference Lecture, *Proceedings, Eighth world conference on earthquake engineering*, San Francisco, Post-conference Volume, pp. 25-39.

Joint Committee of San Francisco, California section, ASCE, and the structural engineers association of northern California. (1951). Lateral forces of earthquake and wind, *Proceedings, American society of civil engineers*, 77, Separate 66, 38.

Mallet, R. (1862). *The great Napolitan earthquake of 1857: The first principles of observational seismology*, Two volumes, Chapman & Hall, London.

Milne, J. (1885). Seismic Experiment, *Transaction, Seismological society of Japan*, Vol. VIII.

Milne, J., and W.K. Burton (1891). *The great earthquake of Japan 1891*, Lane, Crawford & Co., Yokohama, Japan.

Naito, T. (1924). *Earthquake resistant structure of frame buildings* (in Japanese), Waseda University Press, June 1924.

Sano, T. (1915, 1916). Earthquake resisting structure of houses (in Japanese), *Report, Earthquake disaster prevention investigation council*, No. 83, Volume A, 142 pp. and Volume B, 137 pp.

Seismological Committee (1957). *Recommended lateral force requirements*, Structural engineers association of California.

Sezawa, K. and K. Kanai (1938). Decay in the seismic vibration on a simple or tall structure by dissipation of their energy into the ground, *Bulletin, Earthquake research institute*, Tokyo, 13, 68.

Suyehiro, K. (1932). Engineering seismology: Notes on American lectures, *Proceedings, American society of civil engineers*, No. 4, Part II.

Wegener, A. (1915). *Die Entstehung der Kontinente und Ozeane*, umgearbeitete Auflage.

Wilson, W.M. and G.A. Maney (1915). Wind stresses in the steel frames of office building, *Bulletin, Engineering experimental station*, University of Illinois at Urbana-Champaign, No. 80.

The Theory of Almost Nothing

M. A. SOZEN[1], S. PUJOL[2] and J. RAMIREZ[3]

ABSTRACT

Use of theory in reinforced concrete is good as long as the user does not believe in it. An exact analysis of an approximate model is not necessarily an approximate analysis of the exact model.

This is an essay on the application of theory to simulate the effect of displacement history on the drift capacity of reinforced concrete elements. In this sense, theory is understood to be a vehicle that will help predict as well as explain the response considered.

Wight [Wight 1973] observed that drift capacity of reinforced concrete elements was affected by loading history only if strains in the transverse reinforcement increased cumulatively. He concluded that cumulative strain could be controlled by increasing the amount of transverse reinforcement and suggested that the use of truss analogy in its original form, assigning all the shear to transverse reinforcement, would ameliorate the conditions in most cases. This pragmatic approach is still used in the ACI Building Code [ACI 2002] with compromises made for elements with axial load.

The question addressed in this essay is a very simple one and it might as well be expressed in its narrowest sense. Let us assume that the drift capacity is identified by N, the number of displacement reversals a reinforced concrete member can sustain at a drift ratio of 3% without losing more than 20% of its stiffness. Is N reduced if the element is first subjected to seven displacement-reversal cycles at a drift ratio of 1%? Is N reduced if the element is first subjected to seven displacement-reversal cycles at a drift ratio of 2%?

Pujol made a series of tests [Pujol 2002] aimed at determining the effect of displacement history on N. The details of the tests are described in Appendix A with the experimental

[1] Purdue University, West Lafayette, IN
[2] Wiss Janney Elstner Associates Inc.
[3] Purdue University, West Lafayette, IN

variables and results summarized in Table A1. Figures 1 and 2, showing the variation of mean stiffness with number of cycles, capture the main outcome. (Mean stiffness is the slope of the line joining the forces at maximum and minimum displacements of a cycle.) The results from three similar specimens are shown in Fig. 1. Specimen 10-3-2¼ was cycled at a drift ratio, γ, of 3%. The ability of this specimen to sustain its stiffness was comparable to that for specimen 10-1-2¼ which was first subjected to seven cycles with γ=1%. For both these specimens, perceptible stiffness reduction started at cycle 16. However, perceptible reduction of stiffness for specimen 10-2-2¼, which was first subjected to seven cycles at γ=2%, started at cycle 11 indicating that N was sensitive to displacement history. Figure 2 contains similar results for specimens with a smaller amount of transverse reinforcement. In this case, the specimen that was subjected to seven cycles of γ=2% before being subjected to cycles at γ=3% started losing stiffness at cycle 4 while the one that was cycled at γ=3% started losing stiffness precipitously at cycle 6. A theoretical construct of the observed phenomenon, no matter how limited its domain, might allow us to understand the reasons for the reduction in N and make it possible to project the experimental information.

In order to keep the principles of geometry intact and make an exact analysis, we create an approximate model. We assume that all rotation that produces the drift ratio occurs at two "cracks" as shown in Fig. 3: an inclined crack, making an angle of ϕ with the horizontal and having a rotation ϑ_1, and a vertical crack with rotation ϑ_2. The total rotation (which is equal to the drift ratio, γ) is the sum of the rotations assumed to be concentrated at these two cracks.

$$\gamma = \vartheta_1 + \vartheta_2 \tag{1}$$

A peremptory inspection of the approximate model in Fig. 3 suggests that an increase in the amount of transverse reinforcement crossing the inclined crack will increase the ratio ϑ_2/ϑ_1. And if γ approaches ϑ_2, the transverse reinforcement will tend to maintain its length.

To quantify the trend, we take a few liberties with the forces. The moment resisted by the longitudinal tensile reinforcement at section 2 (internal lever arm assumed to be d) is set equal to the moment resisted on section 1 by the longitudinal and transverse reinforcement, with the centroid of the vertical force assumed to be at βd/2.

$$T_2 - T_1 = \frac{1}{2} A_w \cdot \frac{d}{s} \cdot f_{yw} \cdot \beta \qquad (2)$$

T_2 : force in longitudinal tensile reinforcement at its intersection with idealized crack 2
T_1: force in longitudinal tensile reinforcement at its intersection with idealized crack 1
A_w : cross-sectional area of transverse reinforcement at spacing s
d : effective depth of reinforced concrete element
s: spacing of transverse reinforcement
f_{yw}: yield stress of transverse reinforcement
β : coefficient defining horizontal projection of inclined crack

Equation 2 may be rewritten assuming that the stress-strain relationship of the longitudinal reinforcement is known and expressing the reinforcement amounts as ratios.

$$\rho_t \cdot (f(\varepsilon_2) - f(\varepsilon_1)) = \frac{1}{2} \rho_w \cdot f_{yw} \cdot \beta \qquad (3)$$

ρ_t = longitudinal tensile reinforcement ratio , A_s/bd
A_s = cross-sectional area of tensile longitudinal reinforcement
f(ε) = function describing the complete stress-strain relationship for the longitudinal reinforcement
ρ_w = transverse reinforcement ratio, A_w/bs
b = width of rectangular section

We consider the geometry of the reinforcement strains at sections 1 and 2 and we add three more approximations. We assume φ to be 45^o and β to be 4/5. We also assume the extension at crack 1 to be distributed over 3d/4 and the extension at crack 2 to be distributed over d. This leads to expressions for strain:

$$\varepsilon_1 = \frac{\theta_1 \cdot \beta d}{\frac{3}{4} \cdot d \cdot \cos(\phi) \cdot \sin(\phi)} = \frac{32}{15} \cdot \theta_1 \tag{4}$$

$$\varepsilon_2 = \frac{\theta_2 \cdot \beta \cdot d \cdot \tan(\phi)}{d} \frac{4}{5} = \frac{4}{5} \cdot \theta_2 \tag{5}$$

Combining Eq. 1, 3, 4, and 5

$$\rho_t \left[f\left[\frac{4}{5} \cdot (\gamma - \theta_1)\right] - f\left(\frac{32}{15} \cdot \theta_1\right)\right] = \frac{2}{5} \cdot \rho \cdot f_{yw} \tag{6}$$

Equation 6 can be solved for θ_1. The corresponding extension of transverse reinforcement can be written as

$$\delta_{\max} = \frac{\theta_1 \cdot \beta \cdot d}{2 \cdot (\cos(\phi))^2} = \frac{4}{5} \cdot \theta_1 \cdot d \tag{7}$$

with the nominal strain defined as

$$\varepsilon_{\max} = \frac{\delta_{\max}}{\beta \cdot d} = \theta_1 \tag{8}$$

Now we make one further assumption inspired by observation. We assume that the ratio of the reduction drift to the maximum drift is the same as the ratio of the contraction of the transverse reinforcement to the maximum extension in a cycle.

$$\frac{\delta_r}{\delta_{\max}} = \frac{\gamma_r}{\gamma_{\max}} \tag{9}$$

δ_r = contraction of transverse reinforcement during unloading
δ_{max} = maximum extension of transverse reinforcement in one cycle
γ_r = reduction in drift ratio related to unloading in one cycle
γ_{max} = maximum drift in one cycle

Rearranging and recognizing the cumulative effect of successive displacement cycles

$$\delta_n = \sum_{i-1}^{n} 2 \cdot \delta_{\max i} \left(1 - \frac{\gamma_{ri}}{\gamma_{\max i}} \right) \tag{10}$$

δ_n = extension of transverse reinforcement after n cycles

There are many uses of the theoretical construct developed. Space permits only one example. We ask a simple question: In a specific case[4], how efficient is the transverse reinforcement for different maximum drift ratios. Solving Eq. 6 and 8, we obtain the results shown in Fig. 4. From the figure we conclude that, as would be expected, the required transverse reinforcement to maintain the strain at a given level increases with drift ratio. More importantly, we note that above a certain limit the addition of transverse reinforcement is not efficient and that this limit changes with the maximum drift ratio.

Concluding Remarks

Admittedly, the "theory" presented, although apparently based on the two main anchors of applied mechanics (strain geometry and force equilibrium), dealt with a material removed far from reinforced concrete because of the assumptions. It was, in effect, a theory of almost nothing. Nevertheless, it can be used to organize experience and ask the

[4] f_y=60 ksi, ρ_t=0.015

right questions for further investigation. Theory applied to reinforced concrete is good as long as one does not believe in it.

We conclude with a quote from an Islamic scholar:

He who is in possession of truth must not expose his person, his relatives or his reputation to the blindness, the folly, the perversity of those whom it has pleased God to place and maintain in error.

References

ACI 2002 American Concrete Institute, “Building Code Requirements for Structural Concrete,” ACI, P.O. Box 9094, Farmington Hills, MI.

Pujol 2002 Pujol, Santiago, “Drift Capacity of Reinforced Concrete Columns Subjected to Displacement Reversals,” A Thesis submitted to the faculty of Purdue University in partial fulfillment of the requirements for the degree of Doctor of Philosophy, W. Lafayette

Wight 1973 Wight, J. K., “Shear Strength Decay in Reinforced Concrete Columns Subjected to Large Deflection Reversals,” Ph.D. Thesis submitted to the Graduate College, University of Illinois, Urbana, IL.

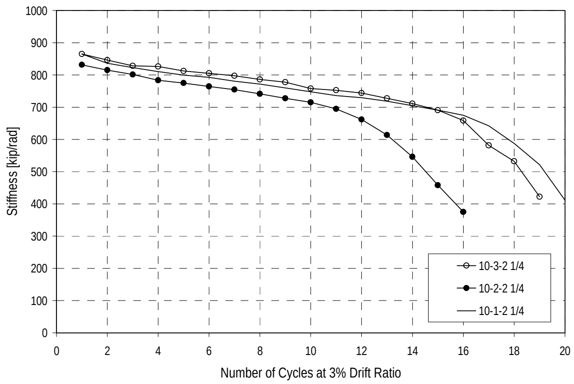

Figure 1 Average stiffness during cycles at 3% drift ratio for specimens 10-3-2¼ North,10-2-2¼ North, and 10-1-2¼ South

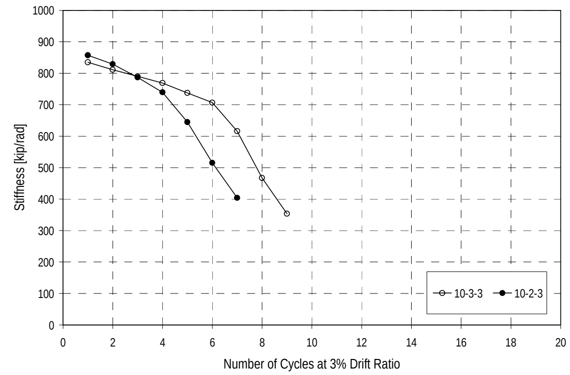

. Figure 2 Average stiffness during cycles at 3% drift ratio for specimens 10-3-3 North, And10-2-3North**.**

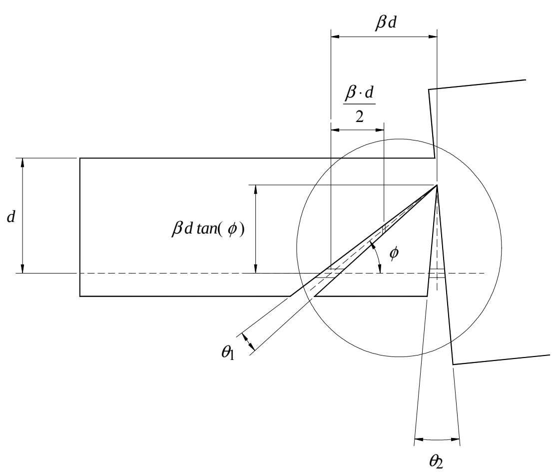

Figure 3 Idealized Cracks

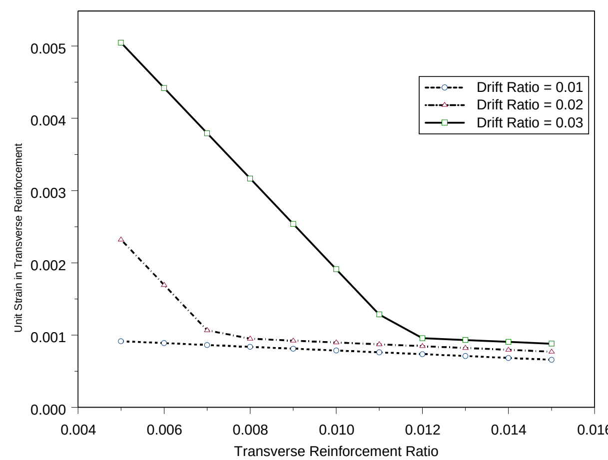

Figure 4 An Example of the Variation with Strain in Transverse Reinforcement with Amount of Transverse Reinforcement

APPENDIX A

Specimen Geometry, Test Setup, and Displacement History

The experimental program included eight test assemblies (Table A1) each of which comprised two individual specimens joined by a center stub. Each specimen represented a cantilever column under constant axial load and a concentrated transverse load applied at its end. The center stub was intended to act as the base of the cantilever columns. All assemblies were tested with simple supports at the free ends of the specimens. Transverse load was applied through the middle stub. As shown in Fig. A1, the axial load was applied through external post-tensioning rods. The intentional variables in the experiments were (1) the spacing of the hoops outside the center stub, (2) the axial load (constant in each test), and (3) the displacement history. Figure A2 shows the dimensions of a typical test assembly. The ranges of the variables in the tests were:

Maximum nominal unit shear stress $V/(b\,d\sqrt{f'_c})$	:	6 to 8 ($\sqrt{f'_c}$ in psi)
Maximum core unit shear stress, $V/(A_c\sqrt{f'_c})$	:	10 to 13 ($\sqrt{f'_c}$ in psi)
Axial load, P	:	0.08 or 0.21 $f'_c A_g$ (30 or 60 kips)
Transverse reinforcement ratio, $A_w/(b\,s)$	:	0.6 % to 1.1 %
Nominal unit transverse stress, $A_w f_{yw}/(b_c\,s)$	:	500 to 1000 psi
Maximum drift ratio, γ_{max}	:	3 % to 4 %

Where V is maximum shear force, b is cross-sectional width, d is effective depth, A_w is total cross-sectional area of transverse reinforcement at spacing s, f_{yw} is transverse reinforcement unit yield stress, b_c is concrete core cross-sectional width (center-to-center of exterior transverse reinforcement), A_c is concrete core cross-sectional area (center-to-center of exterior transverse reinforcement), and s is hoop spacing.

The constants in the experiments were: concrete compressive strength (f'_c , which did vary from 4.1 to 5.2 ksi), longitudinal reinforcement unit yield stress (f_y=65.7 ksi), longitudinal reinforcement ratio (ρ=2.4%), ratio of shear span a, to effective depth (d=2.7), and ratio of gross cross-sectional area to core area (A_g/A_c=2.0). The experimental variables, including the displacement history for each test assembly described in terms of maximum drift ratio, are presented in Table A1. Relative rotation, or drift ratio, is defined in Fig. A3. The rotation of only one of the two specimens per test assembly could be controlled throughout the test. As the tests progressed, damage, stiffness reduction, and rotation concentrated in one of the two cantilevers in each test assembly. The displacement at mid-span was controlled so that the larger of the two rotations did not exceed the target maximum drift ratio. Relative-rotation targets were 1%, 2%, 3%, and 4%. All assemblies were designated using three numerals: the first numeral indicates the level of axial load as a percentage of the product $f'_c A_g$ (where f'_c is the compressive strength of the concrete and A_g is the gross cross-sectional area), the second numeral indicates the maximum drift ratio reached during the initial displacement cycles, and the last numeral is the hoop spacing in inches. Tests were continued until a reduction in mean lateral stiffness of 50% or more was observed. Mean stiffness is defined as the slope of the line joining the peaks of the shear-drift curve for a given cycle.

Materials

All test assemblies were fabricated using normalweight concrete (3/4 in. maximum aggregate size). Table A2 lists relevant mechanical properties of the concrete used. No.6 (3/4 in. diameter) A706 reinforcing bars were used as longitudinal reinforcement. Transverse reinforcement in each specimen was cut from No.2 (1/4 in. diameter) plain steel bars. Transverse reinforcement in the center stub was made with standard Grade 60 No. 3 (3/8" diameter) deformed bars. Table A3 shows the main properties of the reinforcement. Unit strain values in Table A3 include measurements made by two means: Measurements Group type EA-06-250BF-350 electrical strain gages and an MTS 634.25E-54 extensometer with a 2-in. gage length.

Data Collection

Measurements taken during the tests included: transverse and axial load, deflections, rotations, unit strains in the transverse and longitudinal reinforcement, deformations of the concrete surface, and crack widths. Electronic Whittemore gages were used to measure the changes in the distance between steel discs epoxy-glued to the concrete surface on one side of each test assembly. The mesh of reference points attached to the concrete is shown in Fig. A4.

Results

Two series of experiments were carried out to investigate the effect of displacement history on drift capacity (specimens 10-2-3 and 10-3-3, and specimens 10-1-2¼, 10-2-2¼, and 10-3-2¼). In each series, similar specimens were subjected to different displacement histories. Figures A3 to A show shear-drift ratio V vs γ curves recorded.

All specimens developed inclined cracks (cracks with their projections along the column axis not less than their projections on a plane perpendicular to the column axis) before yielding of the longitudinal reinforcement. All specimens reached flexural capacity and developed inelastic deformations. Yielding was observed at a drift ratio of approximately 1%. Maximum nominal shear stresses ranged from 6 to $8\sqrt{f_c'}$ (f'_c in psi).

Table A1 Experimental program.

Test Assembly	Hoop Spacing [in.]	Axial Load [kip]	No. of Cycles at Drift Ratio 1%	2%	3%	4%
10-2-3	3	30	0	7	7	0
10-3-1½	1½	30	0	0	7	11
10-3-3	3	30	0	0	9	0
10-3-2¼	2¼	30	0	0	19	0
20-3-1½	1½	60	0	0	7	10
20-3-3	3	60	0	0	9	0
10-2-2¼	2¼	30	0	7	16	0
10-1-2¼	2¼	30	7	0	20	0

Table A2 Mechanical properties of the concrete.

Assembly	Age	Compressive Strength (6x12in Cylinders) Samples	Compressive Strength (6x12in Cylinders) Average	Compressive Strength (4x8in Cylinders) Samples	Compressive Strength (4x8in Cylinders) Average	Tensile Strength (Split Cylinders) Samples	Tensile Strength (Split Cylinders) Average	Tensile Strength (Flexure Beam) Samples	Tensile Strength (Flexure Beam) Average	Modulus of Elasticity
	[days]		[psi]		[psi]		[psi]		[psi]	[psi]
10-2-3	285	3	4890	2	4470	3	460	3	820	4.15E+06
10-3-1½	334	3	4660	0	---	3	480	3	820	3.88E+06
Rounded Average			4800				470		820	4.02E+06
10-3-3	72	3	4340	0	---	3	440	2	800	3.78E+06
10-3-2¼	152	3	3970	3	3670	3	410	3	780	3.48E+06
20-3-1½	212	3	3980	0	---	3	440	2	800	3.41E+06
Rounded Average			4100				430		790	3.56E+06
20-3-3	54	3	5280	0	---	3	530	3	800	4.35E+06
10-2-2¼	80	3	5060	0	---	3	530	3	860	4.27E+06
10-1-2¼	106	3	5290	0	---	3	510	3	830	4.35E+06
Rounded Average			5200				520		830	4.32E+06

Note: All stresses calculated using nominal areas

Table A3 Mechanical properties of the steel.

		Modulus of Elasticity Based on Readings from		Yield Stress	Start of Strain Hardening Strain		Ultimate Stress
		Gage	Extensometer		Gage	Extensometer	
Bar Diameter	Coupon	ksi	ksi	ksi	Strain x 1E-6	Strain x 1E-6	ksi
3/4 in.	1	---	28,850	65.6	---	7,400	93.0
	2	27,600	28,350	66.0	10,000	7,500	93.6
	4	26,560	28,680	65.6	10,000	7,600	93.0
Rounded Average		27,100	28,600	65.7	10,000	7,500	93.2
1/4 in.*	1	---	31,110	60.2	---	14,900	76.6
	2	---	32,940	57.0	---	16,200	75.2
	3	30,170	32,420	60.0	---	17,000	76.4
	4	31,430	31,180	61.0	17,500	16,400	77.4
Rounded Average		30,800	31,900	59.6	17,500	16,100	76.4

All stresses calculated based on nominal areas.
* Maximum measured deviations from nominal diameter: ±0.005 in.

Table A4 Experimental results.

Test Assembly	Cycle # at 20 % or Larger Stiffness Decrease	Cycle # at 1/4-in. or Larger Transverse Deformation
10-2-3	12	11
10-3-1½	17	>10
10-3-3	7	6
10-3-2¼	15	15
20-3-1½	>16	>16
20-3-3	8	7
10-2-2¼	19	16
10-1-2¼	22	21

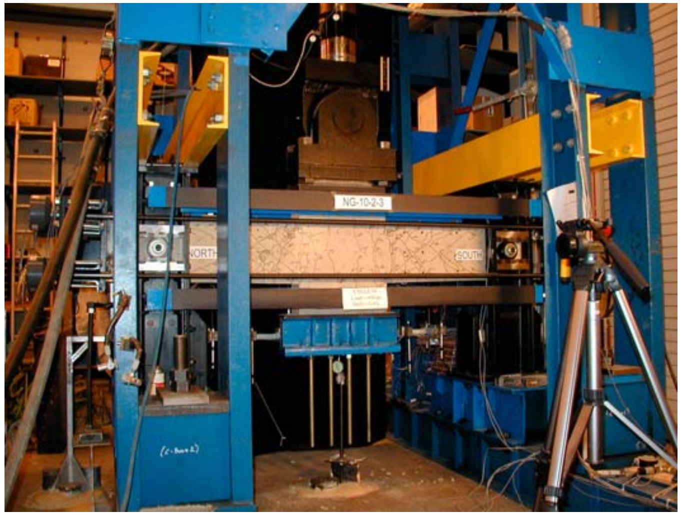

Figure A1 Test setup.

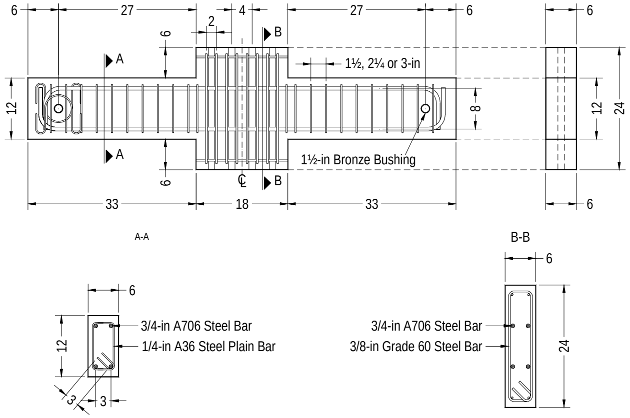

Figure A2 Test Assembly: nominal dimensions (in inches) and reinforcement details.

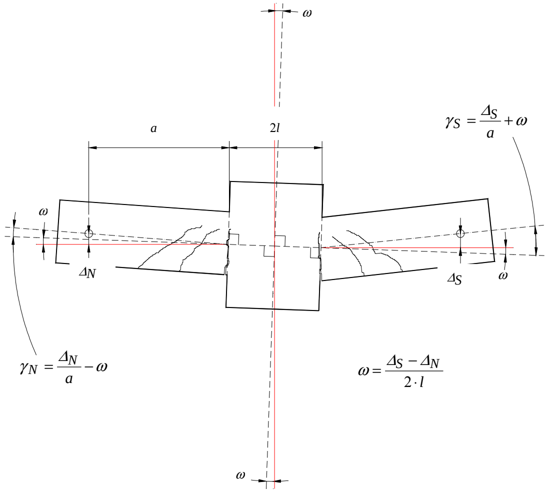

Figure A3 Definition of relative rotation or drift ratio

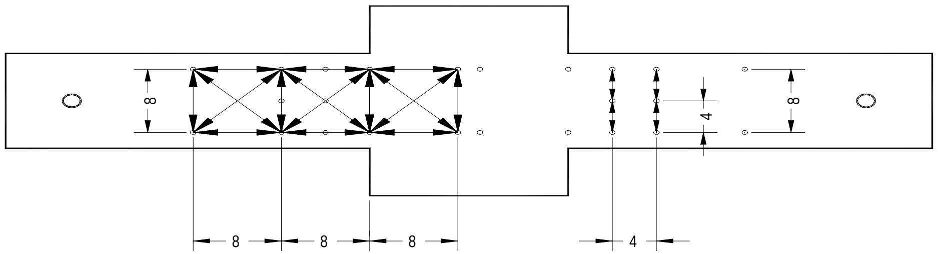

Figure A4 Mesh of Whittemore reference points (dimensions in inches).

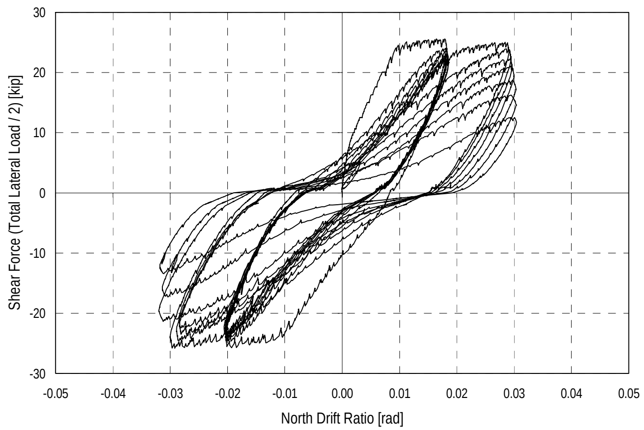

Figure A5 Shear-drift ratio response, specimen 10-2-3 North.

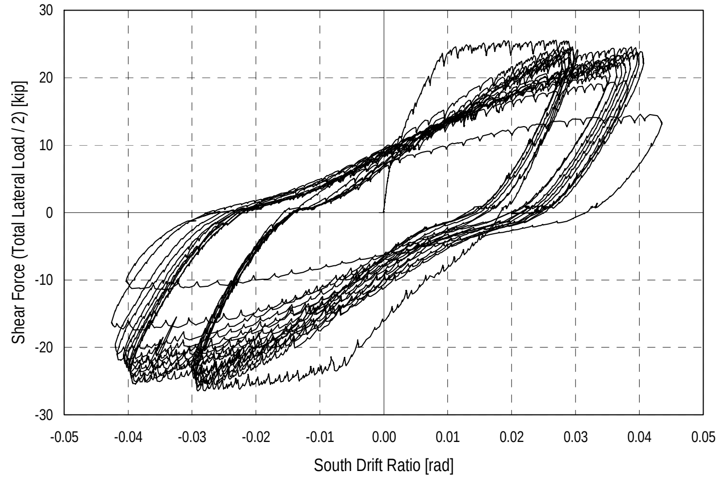

Figure A6 Shear-drift ratio response, specimen 10-3-1½ South.

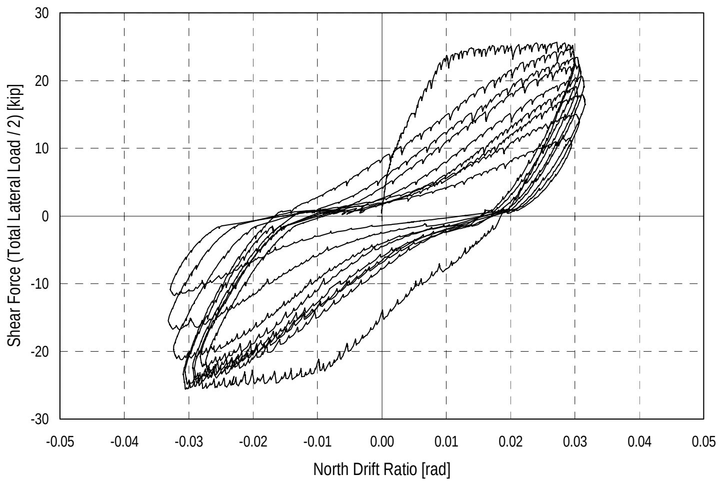

Figure A7 Shear-drift ratio response, specimen 10-3-3 North.

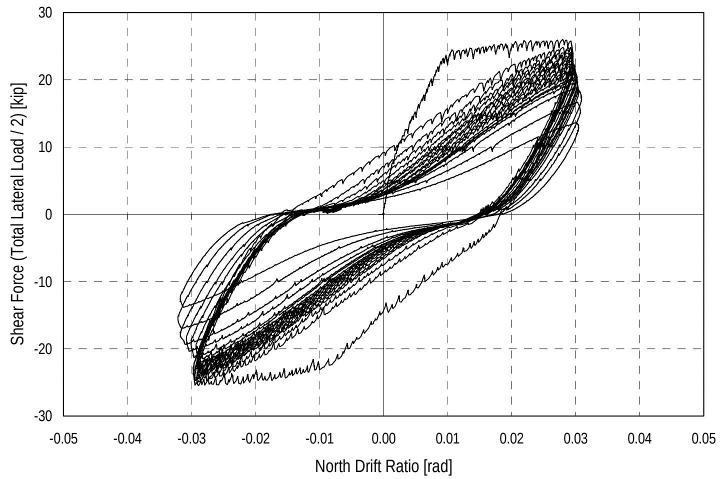

Figure A8 Shear-drift ratio response, specimen 10-3-2¼ North.

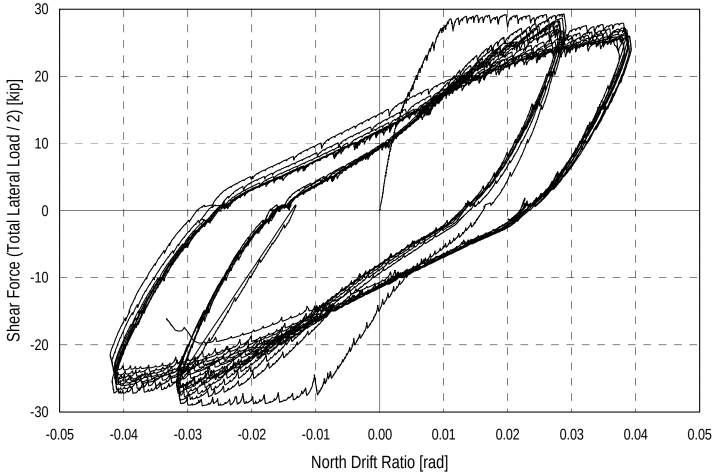

Figure A9 Shear-drift ratio response, specimen 20-3-1½ North.

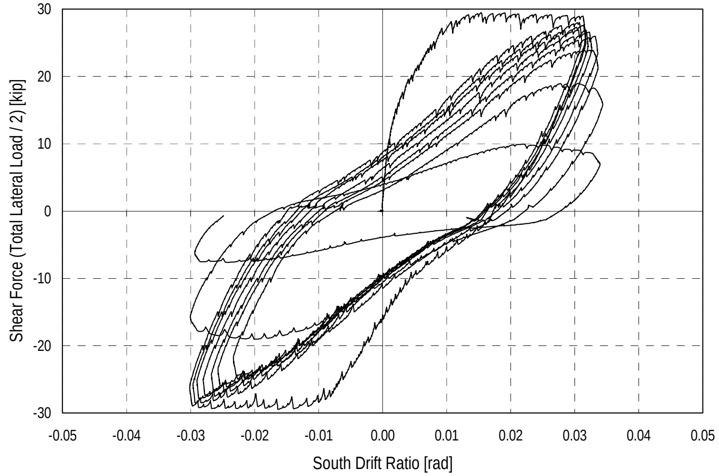

Figure A10 Shear-drift ratio response, specimen 20-3-3 South.

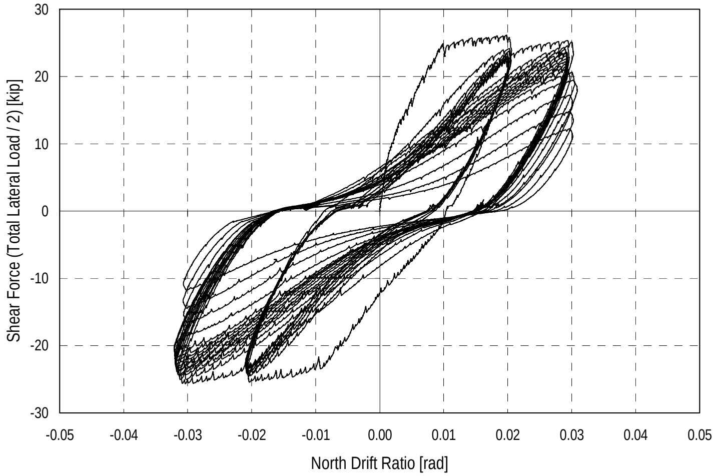

Figure A11 Shear-drift ratio response, specimen 10-2-2¼ North.

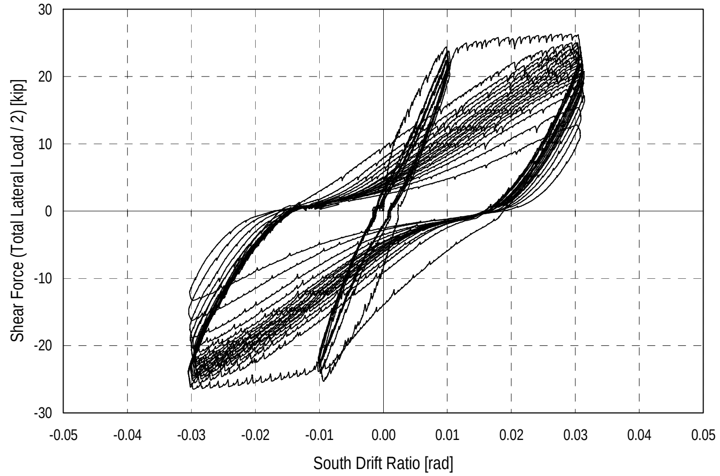

Figure A12 Shear-drift ratio response, specimen 10-1-2¼ South.

PREDICTION OF EARTHQUAKE DAMAGE AND SAFETY IN URBAN LIFE

AKENORI SHIBATA[1]

ABSTRACT

Estimating quantitatively the level and the amount of various urban disasters caused by strong earthquakes is one of the very important problems in considering the strategies for disaster-proof urban planning and emergency response. Problems in the process of damage estimation are discussed through the results of damage prediction in Sendai City.

1. INTRODUCTION

The Hanshin-Awaji great disaster in 1995 has forced us to reconsider the problems of urban disaster prevention and emergency response from a number of different points of view. The new and effective measures of urban disaster mitigation have to be sought based on the tragic experience from this event.

Looking back the history of policies for disaster prevention in Japan after World War II, the Building Standard Law was enforced in 1950 after the Fukui earthquake in 1948, in which the principles of earthquake resistant building design were given. The Basic Act for Disaster Countermeasures was enforced in 1961 after the experience of great disaster by 1959 Ise-wan Typhoon, which has become the basis of disaster countermeasures in Japan. By this act, it is determined that each local government has to have its own local plan for disaster prevention.

In 1978, the Large-Scale Earthquake Countermeasure Act was enforced, accelerated by the social impact of the theory of anticipated Tokai earthquake by Ishibashi in 1976 and also by the 1978 Izu-Oshima Kinkai earthquake. In Shizuoka prefecture where the possibility of expected damage was highest, many countermeasures for the future earthquake were strongly promoted.

The 1978 Miyagi-ken Oki earthquake caused heavy damage to structures and urban functions in Sendai city. After this earthquake, works on the prediction for urban earthquake damage were widely conducted in many local governments in Japan. Miyagi prefecture made investigation on the local soil condition and earthquake hazard map which was published in 1980, and also made the earthquake damage prediction in 1982 based on the published hazard map.

After the 1995 Hanshin-Awaji great disaster, the government enforced the Earthquake Disaster Prevention Special Act, based on which the Five-Year Plan for Emergency Earthquake Disaster Prevention Project was promoted by each local government. Also, the Headquarters for

[1]*Department of Science and Technology, Tohoku Bunka Gakuen University, Sendai, Japan*
Email: shibata@ept.tbgu.ac.jp

Earthquake Research Promotion was established for promoting the earthquake research to strengthen the disaster prevention measures, particularly the reduction of damage and casualties from earthquakes.

The works of earthquake damage prediction were again promoted in many local governments all over Japan, which constituted the basis of new local plans for disaster prevention and emergency response system. Miyagi prefecture and Sendai city also publicized the results of new earthquake damage prediction in 1997 based on the information from the Hanshin-Awaji disaster.

In 2000, a shocking report was issued by the Earthquake Research Committee in the Headquarters for Earthquake Research Promotion. It said that the probability of the next Miyagi-ken Oki earthquake would be about 80% in the coming 20 years. In response to this issue, Sendai city published the new earthquake damage prediction in 2002, taking account of the recent research results. Miyagi prefecture is also working on the new damage prediction. Regarding the Kii-Hanto Oki (Nankai trough) where the 1944 Tonankai earthquake and the 1946 Nankai earthquake occurred, Earthquake Research Committee gave the issue that the probability of the next big earthquake in Nankai trough would be 40 – 50% in the coming 30 years.

In this paper, problems in the prediction method of urban damages are discussed, referring to the results of earthquake prediction for Sendai city.

2. SELECTION OF SCENARIO EARTHQUAKE

Strong earthquakes which will cause damage to a certain area can be inferred on the basis of information about the past earthquakes and earthquake mechanism in the area concerned.

As for Sendai city, two types of strong earthquake have to be considered. The one is the ocean-type (inter-plate) earthquake occurring in Miyagi-ken Oki like the 1978 Miyagi-ken Oki earthquake. This type of earthquake occurs by the subduction of Pacific plate under Ohotsuku plate on which the Tohoku and Hokkaido districts are located. The other is the inland type (intra-plate) earthquake caused by the Nagamachi-Rifu fault crossing under Sendai city. This type of earthquake occurs due to the accumulation of stress within the crust.

The return periods of the above two types of earthquake differ greatly. Miyagi-ken Oki earthquake occurs regularly about every 40 years, while Nagamachi-Rifu fault earthquake has no historical record and its interval is considered to be the order of several thousand years.

The long-term evaluation of Miyagi-ken Oki earthquake was issued in 2000 by Earthquake Research Committee, which was based on the data of 6 large earthquakes occurred in Miyagi-ken Oki during these about 200 years. The occurrence probability is 81% within 20 years and 98% within 30 years, and this fact should be reflected on the preparation of countermeasures for urban earthquake disaster.

The Nagamachi-Rifu fault earthquake will give great damage to Sendai city, like the 1995 Hanshin-Awaji great disaster, though the occurrence probability is low, and should also be

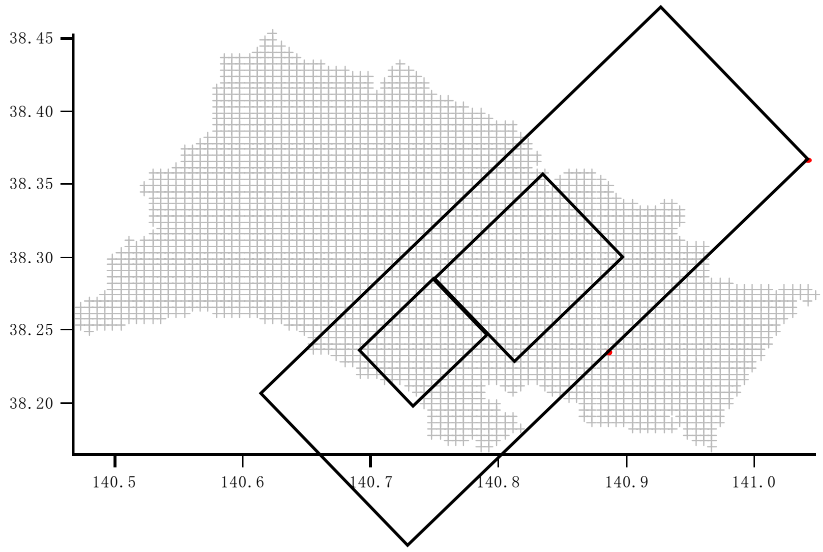

Fig.1 Nagamachi-Rifu fault earthquake model

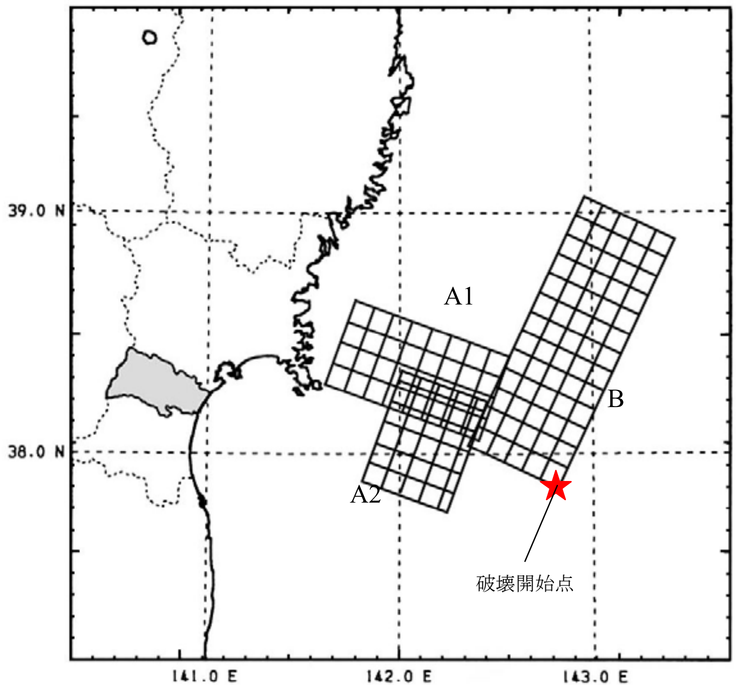

Fig.2 Miyagi-ken Oki Earthquake Model (Single, Multiple)

considered in the disaster prevention plan.

The assumed earthquake model to be used in urban disaster prediction is called scenario earthquake. The two scenario earthquakes were adopted in Sendai disaster prediction in 2002, Miyagi-ken Oki earthquake model and Nagamachi-Rifu fault earthquake model, which are shown in Figs.1and 2. Assumption of scenario earthquake requires the determination of parameters for the fault model as follows: magnitude, position fault, length and width of fault, direction and inclination of fault, S wave velocity, rupture velocity, point of rupture initiation and type of propagation, seismic moment, average slip (total, asperity, background). Up to now the point source model which requires only magnitude and position has often been used. With the development of analysis methods, however, the rectangular fault model is now widely used.

The Nagamachi-Rifu fault model has the magnitude of 7.5, the length and width of 40km x 20km, and two asperity areas in the fault (Fig.1). Asperity is the area of which the slip value is greater than the background fault area and radiates larger element earthquake waves.

As for the Miyagi-ken Oki fault model, two kinds of fault model, single model and multiple model, were used. Single model corresponds to A1 fault in Fig. 2 which has the magnitude of 7.5 and the length and width of 40km x 80km. Multiple model considers the simultaneous action of A1, A2 and B faults in Fig.2. A2 fault has the magnitude of 7.4, the length and width of 55km x 45km, and B fault has the magnitude of 7.8, the length and width of 130km x 50km. Overlapped zones are neglected. These three faults were determined from the estimation of fault models for the past large earthquakes. The A1 fault corresponds to the 1978 Miyagi-ken Oki earthquake.

3. ESTIMATION OF STRONG GROUND MOTION

Various methods have been used for determining the intensity of ground motion by assumed earthquake model. The attenuation equation method for the point source model have long been used which estimate the maximum ground motion (maximum acceleration, maximum velocity, response spectrum) from the magnitude and the focal distance. Recently the empirical Green's function method (the wave superposition method) is widely used for the fault model to predict ground motion.

In the wave superposition method, the fault plane of a large earthquake is divided into several small zones, and the ground motion at a site is estimated by the superposition of small element earthquake waves generated at small zones considering the time delay due to rupture sequence and propagation time. Though the observed records of small earthquakes were originally utilized as the element wave (Hartzell, 1978), the artificial earthquake wave considering the statistical spectral property of the site is now frequently used as the element wave (Boore, 1983). This is called the statistical wave superposition method. In the work of damage prediction for Sendai city in 2002, the modified attenuation equation method for response spectrum using equivalent focal distance considering the fault area was used for Nagamachi-Rifu fault model (Ohno et., 2001),

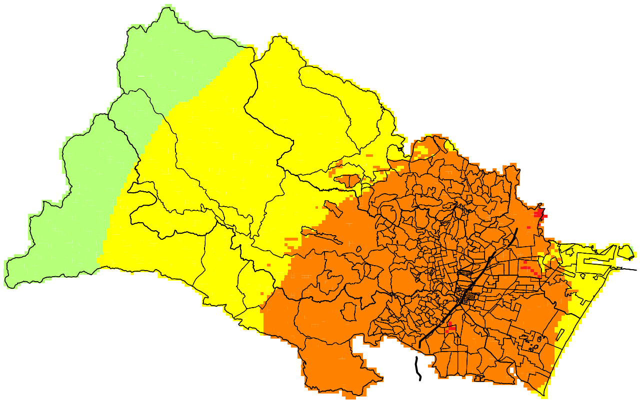

(a)Nagamachi-Rifu fault earthquake

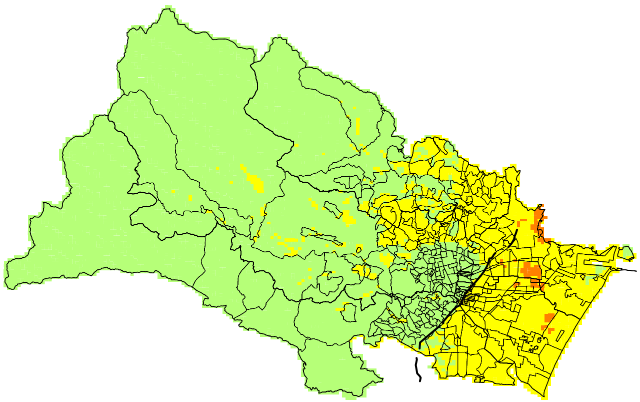

(b) Miyagi-ken Oki earthquake (single)

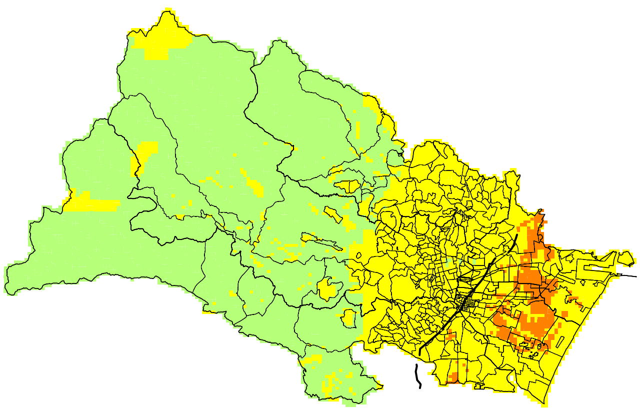

(c) Miyagi-ken Oki earthquake (multiple)

JMA Intensity Scale

Fig.3 Distribution of Ground Motion Intensity and the statistical wave superposition method was used for Miyagi-ken-Oki fault model.

Evaluation of strong ground motion consists of the following two steps. The first step is the estimation of bedrock motion which is generated by fault rupture and propagates in the hard rock (seismic bedrock). The second step is the estimation of surface ground motion considering the amplification of soft soil layers under the site. The amplification characteristics are usually obtained by modeling the soil property of the site as the horizontal soil layers and by calculating the transfer function considering the nonlinearity of the soil. The property of surface ground motion is estimated by multiplying the transfer function of the soil layers to the property of bedrock motion.

Fig. 3(a) shows the intensity distribution of surface ground motion for Nagamachi-Rifu fault model as expressed by the intensity scale of Japan Meteorological Agency (JMA). Fig.3(b) and Fig.3(c) are the intensity distributions for Miyagi-ken Oki single fault model and multiple fault model, respectively. The intensity distribution is evaluated for the unit of 250m x 250m mesh. The expected JMA intensity at the central part of Sendai is 6(strong) for Nagamachi-Rifu model, 5(strong) for Miyagi-ken Oki single model and 6(weak) for Miyagi-ken Oki multiple model.

The surface ground structure of Sendai city differs greatly along the Nagamachi-Rifu fault line appearing on the ground surface. The surface soil condition of the east side of the fault line is the soft alluvium ground while that of the west side is the hard diluvium ground, which affects greatly the intensity distribution of ground motion.

Also, liquefaction of sandy soil gives large effect on the damage to structures and urban functions. Prediction of liquefaction potential was made using PL index at each mesh point in Sendai damage prediction.

4. PREDICTION OF EARTHQUAKE DAMAGE

4.1 Damage to buildings

Damage to buildings by earthquakes closely relates to the safety of citizen’s life and is important in that it gives the basis for predicting fire damage, casualties and refugees. Prediction of damage to buildings is made according to the type of structures (wood, reinforced concrete, steel), considering the characteristics of structural behavior and the construction period.

Basic concept of building damage prediction is the fragility curve which shows the relation between the ground motion intensity and the damage rate (the number of damaged buildings / the total number of buildings) for building groups of different structural types (wooden, RC, S etc.).

There have been many researches on the fragility curve of wooden houses in Japan. Mononobe was the first to give the relation between the damage rate of wooden houses and the ground motion intensity estimated from the overturning of tomb stones (Fig.4)(Mononobe, 1933).

In Sendai damage prediction, the fragility curve obtained from the damage in the 1995 Hanshin-Awaji disaster was used considering the corrections due to the difference in the ground

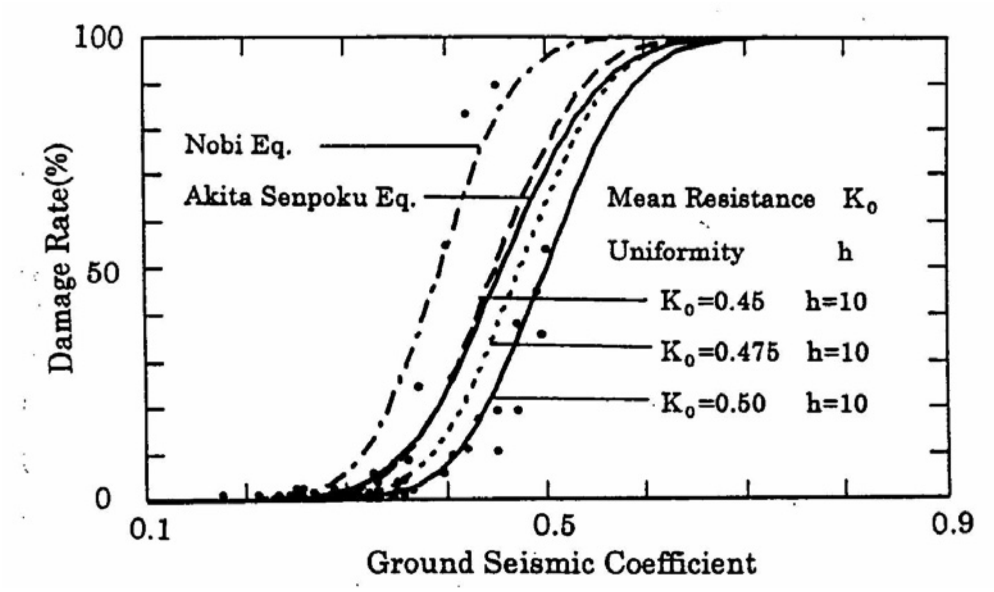

Fig.4 Fragility Curves for Wooden Houses by Mononobe

motion property between Hanshin-Awaji and Sendai and the difference in the resistance capacity of houses which is related to the locality in construction work. Figs. 5 (a), (b) and (c) show the predicted distribution of damage for wooden houses in Sendai city.

In 1995 Hanshin-Awaji disaster, the numbers of damaged wooden houses were about 55 thousand for total collapse and 31 thousand for partial collapse in Kobe city, 92 thousand for total collapse and 79 thousand for partial collapse in total. The damage was severe especially in old wooden houses.

As for the present status of buildings in Sendai city, the total number of existing buildings in Sendai city is about 32 thousand, and the number of wooden houses is 24 thousand which is 75 % of total buildings. The number of buildings constructed before 1981, the year of revision in earthquake resistant design regulation, is about 15 thousand which is 60 % of total wooden houses and 45 % of total buildings.

According to the damage prediction in Sendai city, the numbers of damaged wooden houses (totally/partially) are estimated as 45 thousands (damage rate 20 %) in case of Nagamachi-Rifu fault earthquake, 13 thousands (damage rate 5 %) in case of Miyagi-ken Oki earthquake (single), and 26 thousands (damage rate 10 %) in case of Miyagi-ken Oki earthquake (multiple).

The damage rate of totally and partially collapsed wooden houses was 16 % in the 1995 Hanshin-Awaji earthquake. Predicted damage rate in Sendai city in case of Nagamachi-Rifu fault earthquake is a little larger than that in Hanshin-Awaji earthquake.

Observing in detail the distribution of estimated damage in Sendai city, we notice that, in case of Nagamachi-Rifu fault earthquake for example, the damage rate of wooden houses is about 10 % in Aoba ward or Izumi ward, while greater than 30 % in Wakabayashi ward. It indicates that

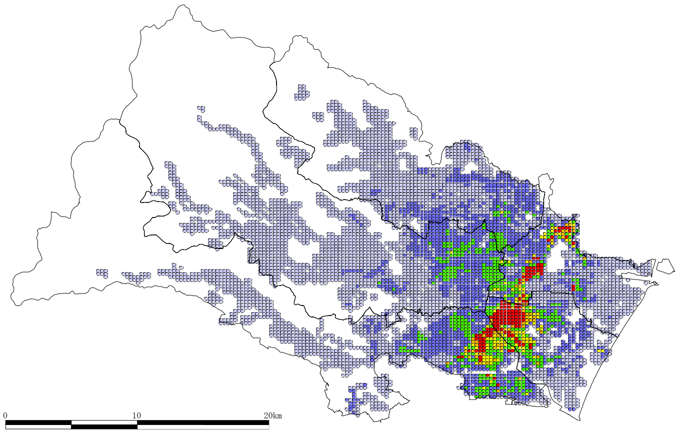

20km

(a) Nagamachi-Rifu fault earthquake

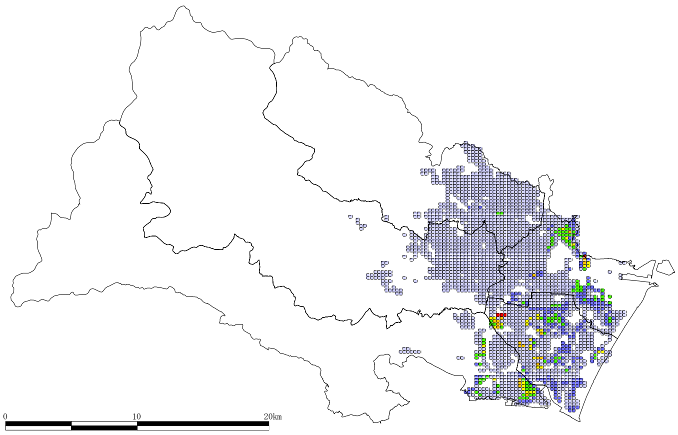

20km

(b) Miyagi-ken Oki earthquake (single)

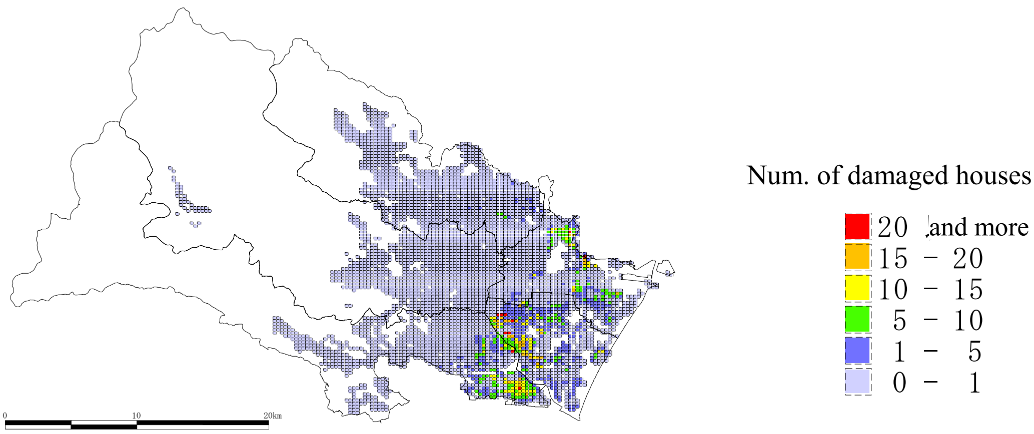

20km

(c) Miyagi-ken Oki earthquake (multiple)

Fig.5 Distribution of Totally and Partially Damaged Wooden Houses the difference in damage is significant according to the areas, which is due to the amplification effect by the surface soil condition. This fact has to be incorporated in the disaster prevention countermeasures in the future.

As for reinforced concrete and steel buildings, the predicted number of damage is about 7100 (damage rate 11 %) in case of Nagamachi-Rifu fault earthquake, 1700 (2.5 %) in case of Miyagi-ken Oki earthquake (single), 2500 (3.7 %) in case of Miyagi-ken Oki earthquake (multiple). The damage rate for reinforced concrete and steel buildings is also greater in Wakabayashi ward where the soil condition is alluvial.

4.2 Damage to concrete block walls

In the 1978 Miyagi-ken Oki earthquake, 9 out of 13 deaths in Sendai city were caused by the falling of block walls. Falling down of concrete block and stone walls causes casualties and also gives great difficulty to various urgent activities as obstacles just after the earthquake.

According to the result of prediction, the number of existing block walls in Sendai city is about 56 thousand, and the numbers of damaged walls (collapsed walls) are estimated as 24000 (12000) in case of Nagamachi-Rifu fault earthquake, 6000 (2100) in case of Miyagi-ken Oki earthquake (single), and 8200 (3000) in case of Miyagi-ken Oki earthquake (multiple).

It is quite necessary to take actions of improving the earthquake safety of block walls and replacing block walls to hedges.

4.3 Damage by outbreak and spread of fires

In the 1995 Hanshin-Awaji disaster, the outbreak of fires in Kobe city on the day of earthquake amounted to 109, the number of burnt houses was more than 7000 and the 444 deaths by fire were reported.

In predicting the damage by fire caused by earthquake, the conditions such as the season and the time influence the results greatly. Two cases were considered in the Sendai earthquake damage prediction, the summer daytime (12:00) with wind speed 4.5 m/s and the winter evening (18:00) with wind speed 6.0 m/s. The former corresponds to the condition of the less possibility of fire outbreak, while the latter corresponds to the larger possibility.

The process of predicting fire damage is as follows. First, the number of outbreak of fire from fire origins is estimated from the number of damaged houses considering the season and the time. Next, the possibility of extinction of fires is examined considering the power of fire-fighting. For the fire outbreak points where fire extinction is impossible, the spread of fire of is considered. The area of spreading is predicted taking account of wind effect, and the number of burnt houses is estimated.

The number of burnt houses in Sendai city after 6 hours of earthquake occurrence is estimated as about 2000 for the summer daytime and about 10000 for the winter evening in case of Nagamachi-Rifu fault earthquake, 500 for the summer daytime and 4700 for the winter evening in case of Miyagi-ken Oki earthquake (single), 900 for the summer daytime and 5800 for the winter evening in case of Miyagi-ken Oki earthquake (multiple).

4.4 Casualties

More than 6000 were killed and 38 thousands were wounded in 1995 Hanshin-Awaji earthquake disaster. Refugees amounted to 230 thousands just after the earthquake.

It is very important to predict the number of casualties and refugees when considering the emergency response after earthquake. In the Sendai earthquake damage prediction, the number of deaths caused by building collapse (deaths by fallen furniture included) and caused by fires is predicted.

The number of the deaths in Sendai city is predicted as 751 for the summer daytime and 1032 for the winter evening in case of Nagamachi-Rifu fault earthquake, 16 for the summer daytime and 27 for the winter evening in case of Miyagi-ken Oki earthquake (single), and 57 for the summer daytime and 87 for the winter evening in case of Miyagi-ken Oki earthquake (multiple).

The number of the wounded is predicted as about 13 thousand for the winter evening in case of Nagamachi-Rifu fault earthquake, and 1900 for the winter daytime in case of Miyagi-ken Oki earthquake (single).

4.5 Damage to lifelines

Lifelines such as waterworks, sewerage, gas and electric power are indispensable functions to urban life and the prediction of damage to lifelines by earthquake and of its recovery is very important for planning emergency response and recovery strategies.

For the prediction of damage to water supply, sewerage and gas systems, the following steps are considered. First, the standard damage rate (number of damaged points per km) is calculated based on the standard fragility curves based on the information of lifeline damage by the past strong earthquakes including 1995 Hanshin-Awaji disaster, Next, the correction factors are considered according to the kinds of soil condition, the liquefaction potential, the kinds of pipes, the diameters of pipes, etc., and finally the damage rate and the number of damaged points in piping systems are estimated.

(a) Water supply

The total length of water pipes in Sendai city is about 3000 km, and the number of damaged points is about 2600 (0.83 points / km) in case of Nagamachi-Rifu fault earthquake, and about 900 (o.28 points / km) in case of Miyagi-ken Oki earthquake (single).

(b) Sewerage

The total lengths of pipes for sewage and for rainwater are about 3000 km and 2000 km, respectively, and the numbers of damaged points for sewage pipes and for rainwater pipes are about 10000 and 2000, respectively.

(c) Gas

The gas department of Sendai city supplies gas to 345 thousand houses in Sendai city and in neighboring three cities and three towns. The total length of gas main pipes is about 400 km for middle pressure and about 3000 km for low pressure, and the number of supply pipes is about 190 thousands. The number of damaged points is about 3800 for low pressure main pipes and 5500 for supply pipes in case of Nagamachi-Rifu fault earthquake, 2200 for low pressure pipes and 1800 for supply pipes in case of Miyagi-ken Oki earthquake (single).

The percentage of gas stop is estimated as 100 % in case of Nagamachi-Rifu fault earthquake and 56 % in case of Miyagi-ken Oki earthquake (single). Time to recovery is expected as 30 days in case of Nagamachi-Rifu fault earthquake and 14 days in case of Miyagi-ken Oki earthquake (single).

(d) Electric Power

Facilities for generation and transmission of electric power are considered to have enough earthquake resistance capacity to avoid serious damage by earthquake.

As for the distribution system (electric wires and poles) to supply electricity in wide areas, serious trouble will not occur for the intensity scale of 5 and below, but for the intensity scale of 6 and more, damage by strong shaking will occur to wires and poles, and also building collapse, fire and damage to loads will cause damage to electricity distribution systems. The number of electric wire cut is estimated as about 13000 in case of Nagamachi-Rifu fault earthquake and 8000 in case of Niyagi-ken Oki earthquake (single). The failure of electric supply is estimated to occur in 72 thousand houses in case of Nagamachi-Rifu fault earthquake and 40 thousand houses in case of Miyagi-ken Oki earthquake (single). Time to retrieval of electricity is expected to be about 2 days and a half for all cases.

(e) Information

Communication in disaster situation has become more and more important for the sake of faster response to emergency and maintaining urban functions. Tools for communication include telephone, cellular phone, public exclusive line, amateur wireless, taxi wireless, internet and so on, and the situation for information transfer has been changing drastically.

As for the telephone circuit, the number of circuit troubles is estimated as 166 thousands and the time to recovery is expected as 10 days in case of Nagamachi-Rifu fault earthquake, while 34 thousands and 3 days in case of Miyagi-ken Oki earthquake (single).

5. SOCIAL SYSTEMS FOR SAFE CITIES

For the earthquake safety of cities, the following two measures are important. The one is to promote the countermeasures for structural and functional safety of cities against severe earthquakes based on the results of earthquake damage prediction. The other is to prepare the systems of emergency response just after the earthquake at national and local government level as well as private NPO/citizens level and to maintain the systems by constant checking and exercise so as to function effectively in the event of earthquake.

Earthquake resistance capacity of buildings in Japan has been changed owing to the revision of building standard law and the enforcement of new earthquake resistant design code in 1981, which was proofed by the 1995 Hanshin-Awaji disaster. The law for seismic retrofit was enforced in 1995 and the seismic diagnosis as well as reinforcement of old buildings has been promoted.

As for public buildings, especially school buildings, there has been considerable progress regarding seismic diagnosis and retrofit all over Japan. As for private buildings, especially wooden private houses, however, little progress has been seen up to now, in spite of its urgent necessity. Several hopeful movements are now emerging such as the financial aid to diagnosis retrofit of private houses by national and local governments.

Constant brush up of emergency response system should be done by each local government. Up-to-date technologies such as real-time damage prediction have to be examined. Close cooperation of local governments, NPO/citizen groups and private enterprises - disaster prevention networks - should be constructed in the future community aiming at earthquake safety.

6. CONCLUSIONS

Outline of the process of selecting scenario earthquakes and predicting earthquake damages in cities is discussed in this paper based on the earthquake disaster prediction of Sendai city in 2002. Continual level-up of the precision in damage prediction methodologies as well as constant renewal of basic data should be considered. Disaster education in schools is the principal basis of disaster prevention and further research and practice are strongly expected in this field.

The contents of this paper are based on the work by Sendai city (Sendai city, 2002). Deep thanks are to Sendai city and to Tohoku Electric Power Company for allowing the usage of data and the quotation.

REFERENCES

Boore, D. M. (1983), Stochastic simulation of high-frequency ground motions based on seismological models of the radiated spectra, BSSA, Vol.73, No.6:1865-1894

Hartzell, S. H. (1978), Earthquake aftershocks as Green’s functions, Geophysical Research Letters, Vol.5, No.1:1-4

Mononobe, N (1933), Theory of earthquake resistant civil engineering structures (in Japanese)

Ohno, S., Takahashi, K. and Motasaka, M. (2001), Empirical estimation of horizontal and vertical motions based on California earthquake records and its application to Japan inland earthquakes, J. Struct. Constr. Eng., AIJ, No.544, 39-46

Sendai city (2002), Report on the earthquake damage prediction in Sendai city (in Japanese)

Shibata A.(2003), Earthquake damage prediction of cities and safety of social systems, Electric Power Civil Engineering, No.303:6 – 11 (in Japanese)

ASSESSMENT OF THE COLLAPSE OF A CONCRETE FRAME INTENDED TO MEET U.S. SEISMIC REQUIREMENTS

Jack P. MOEHLE[1]

ABSTRACT

The Royal Palm Resort building was a 220-unit hotel and condominium complex comprising three main 12-story blocks separated from one another by seismic joints. The design of the special-moment-resisting concrete frame structure was based on requirements for seismic zone 3 of the 1988 Uniform Building Code. The building sustained damage ranging from light to partial collapse during the 8 August 1993 Guam earthquake. Examination of the structural drawings and the structure following the earthquake revealed apparent violations of the building code requirements. Analyses and tests were carried out to identify the effect of various deficiencies on the observed performance. The study concludes that failure of short columns restrained by architectural elements was the primary cause of collapse.

INTRODUCTION

The Royal Palm Resort was a twelve-story hotel and condominium complex constructed shortly before the Guam earthquake of 8 August 1993. The building was intended to satisfy requirements of the 1988 Uniform Building Code [UBC 1988]. The structural framing comprised reinforced concrete moment-resisting frames founded on a reinforced concrete mat. The building sustained significant damage leading to partial collapse during the earthquake. Given the recent design code and the poor performance, the building became the subject of considerable interest among structural engineers.

Detailed analyses of the building have been conducted since the earthquake. These include estimates of the ground shaking, study of the structural design and construction, examination of damage patterns, tests of scaled models of building components, and static and dynamic analyses considering linear and nonlinear response. In light of the detailed studies, some significant differences of opinion exist regarding the causes of the failure. The following text provides one interpretation of the collapse of this building.

[1] *Pacific Earthquake Engineering Research Center, University of California, Berkeley*
Email: moehle@peer.berkeley.edu

BUILDING DESCRIPTION

The Royal Palm Resort was a 220-unit hotel and condominium complex with adjoining parking building located at Tumon, Guam. The complex comprised two 12-story tall reinforced concrete structures (A-Block and B-Block) with an interconnecting 12-story elevator/stair tower (C-Block). Seismic joints separated the three blocks. Figure 1 presents an elevation and Figure 2 presents the plan of A-Block.

A-Block was a twelve-story, reinforced concrete space frame structure with beams framing between columns in two orthogonal directions. B-Block had similar framing and was twelve stories tall from grid line A to D and one or two stories tall from grid line D to G. Story heights are shown in Figure 1. The floor slab typically was 150 mm thick except at grade where it was 130 mm thick. A 0.9-m thick reinforced concrete mat supported the superstructure on lean concrete supported on sand underlain by coralline limestone. In addition to the primary beam-column framing elements, the structure included other secondary structural and nonstructural elements such as reinforced concrete walls enclosing elevator shafts and CMU infills.

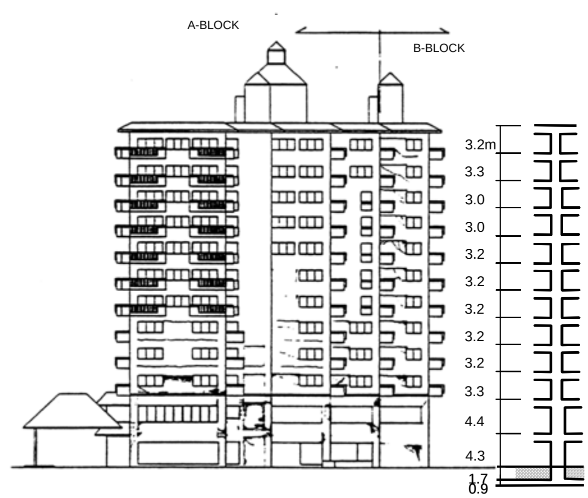

Figure 1 – Elevation.

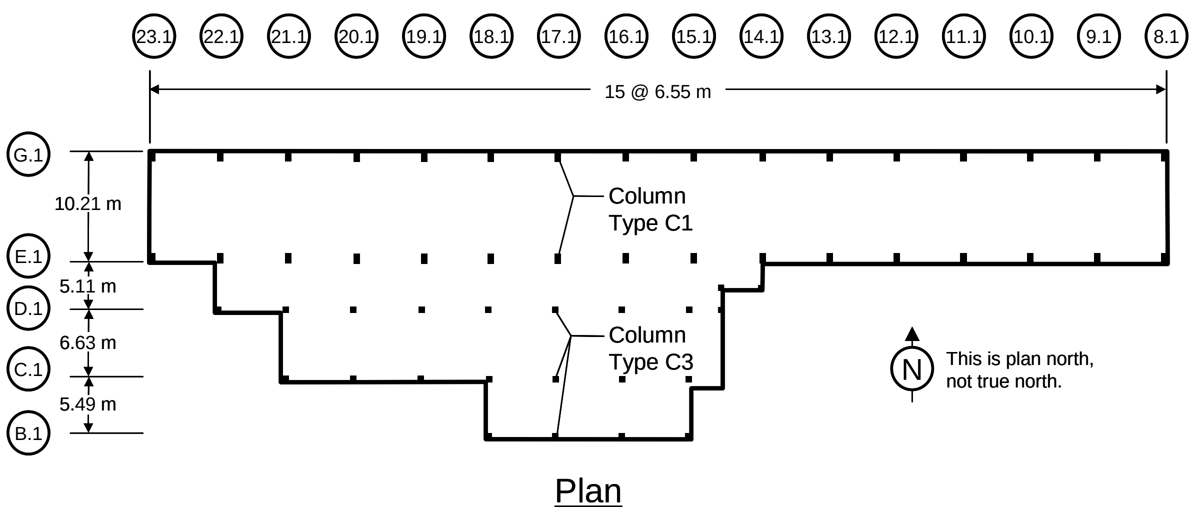

Figure 2 – Plan of A-Block.

The structural drawings note that the design was according to the Uniform Building Code [UBC 1988], and project specifications stipulate the work to be according to the ACI Standard Building Code Requirements for Reinforced Concrete [ACI 1989]. At the time of the design, Guam was designated seismic zone 3. Construction of the complex commenced on 1 April 1991 and was substantially completed by 30 April 1993.

Specified compressive strength of concrete was 27.6 MPa and reinforcement was A615 Grade 60 for No. 6 (19 mm) and larger diameter bars and Grade 40 for No. 5 (16 mm) and smaller diameter bars. The concrete masonry infill units (CMU) were specified as ASTM C90 Grade N-I, f_m' = 9.3 MPa. Shop drawings showed CMU cells to be not grouted with the exception of cells with rebar, freestanding walls, and ground floor walls; grout strength was specified to be 13.4 MPa. Measured mean yield and ultimate stresses were 462 MPa and 690 MPa for No. 9 (27 mm) bars; for No. 4 (13 mm) bars yield stress ranged from 331 MPa to 469 MPa and ultimate stress ranged from 483 MPa to 703 MPa. Concrete strengths ranged from a low of 24.1 MPa (at one location on the eighth floor) to 45.5 MPa.

The columns in A-Block along grid lines E.1 and G.1 (Figure 2) were designated type C1 and had rectangular cross section of 0.61 m by 1.06 m at the ground floor level (Figure 3). The columns along grid lines B.1, C.1, and D.1 were designated type C3 and had square cross section of 0.61 m by 0.61 m. Two smaller columns were located near the elevator between grid lines 14.1-15.1 and D.1-E.1. Type C1 columns reduced to 0.61 m by 0.91 m at the third floor level, and to 0.61 m by 0.76 m at the tenth floor level. The structural drawings show notable differences in the detailing of type C1 and C3 columns. In type C1 columns in the lower stories, the hoops are shown as No. 5 (16 mm) bars spaced at 102 mm on centers at the column ends (notation t_a in Figure 3) and 127 mm on centers along the midheight. In type C3 columns, the hoops are shown as No. 4 (13 mm) bars at 102 mm on centers at the

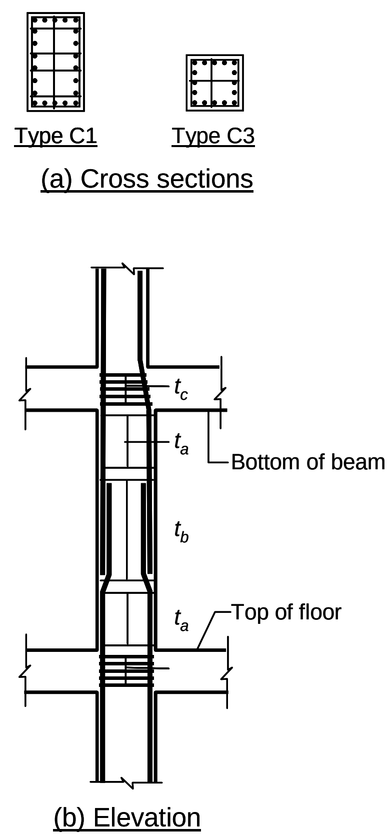

Figure 3 – Typical column details.

column ends and 305 mm on centers along the midheight. Column longitudinal reinforcement lap splices are shown near the midheight of the columns. Maximum hoop spacing according to prevailing codes was 102 mm at column ends, 102 mm along laps, and 152 mm elsewhere.

An important difference between A-Block and B-Block is that B-Block had no type C3 columns in the high-rise section. In the high-rise section of B-Block, all columns were either type C1 or C2. Type C2 columns had cross section measuring 0.61 m by 0.76 m with No. 5 (16 mm) hoops and cross ties at maximum spacing of 178 mm.

Beams framing along grid lines B.1, C.1, D.1, E.1, and G.1 typically had width of 0.61 m and depth of 0.76 m. Those framing in the orthogonal direction in the second floor had variable depth, typically being 0.61 m by 1.42 m between grid lines E.1 and G.1 and 0.61 m by 0.91 m elsewhere. Sizes varied on different floors. Single-hoop stirrups were spaced at 100 mm to 150 mm near the column face. The as-built condition had a reinforced concrete drop wall at the southwest perimeter of the building at the second and third floor levels. These drop walls were cast monolithically with the beams and columns, with continuous reinforcement into each. Slabs were cast monolithically with the beams. A typical detail is in Figure 4.

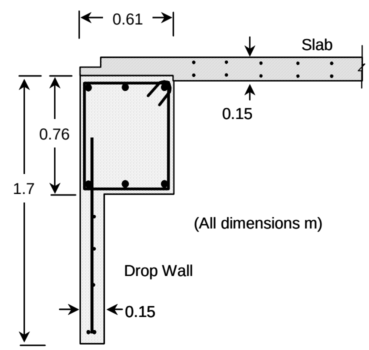

Figure 4 – Cross section of typical beam with drop wall.

The structural drawings show beam-column joints reinforced with transverse reinforcement similar to that provided in the end regions of the columns that frame into the joints (Figure 3). Post-earthquake studies showed that the joint reinforcement in many joints, especially in the lower floors, was not according to the drawings. In some cases, the joints appeared to have no transverse reinforcement. In other cases reinforcement was widely spaced, or was provided by overlapped U-bars in place of continuous perimeter hoops.

Concrete masonry unit (CMU) walls were used for all exterior walls (0.20 m thick), for main corridor walls, around stairways, around toilet rooms, and around flue spaces at kitchens. In addition, at several locations in the first and second stories a double-wall CMU construction was used to form a planter box, the space between the walls being used for landscaping. Coupled with the drop walls, this resulted in an apparent captive column condition for second-story columns at the southwest perimeter of the building (Figure 5). The structural drawings specify that full-height CMU walls have a 25 mm gap at the top, with steel angles snug tight against the CMU and anchored into the bottom of the beams to provide out-of-plane stability. The structural drawings also specify a 13 mm joint between the CMU walls and the columns, filled with pre-molded expansion joint filler. The as-built condition had CMU walls constructed directly against columns with Hilti-nailed dovetail connections to the columns at 0.61 m on centers and a solid mortar connection with No. 4 (13 mm) dowels epoxy-anchored into the beams. Grouting was inconsistent with the drawings and inconsistent throughout the building.

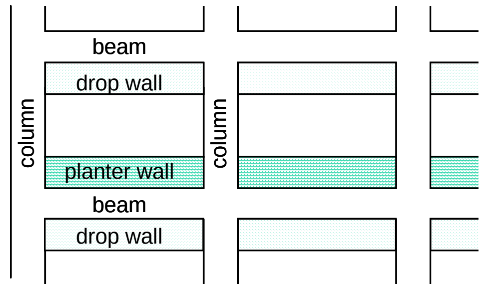

Figure 5 – Framing constrained by concrete drop walls and planter walls.

Reinforced concrete walls (150 mm thick) enclosed elevator shafts at grid lines 14.1-15.1 and grid lines D.1-E.1 in A-Block. The structural drawings specify a single curtain of wall reinforcement, anchored into adjacent columns.

THE EARTHQUAKE

The earthquake occurred at 6:34 P.M. local time, Sunday, 8 August 1993. The estimated M8 event had epicenter approximately 60 km to the southeast of Tumon in the Mariana Trench. The earthquake caused damage to many buildings on Guam. It is reported that 50 percent of the hotel rooms in the Tumon area were out of use following the earthquake. A general description of the event is provided in [EERI 1995].

There were no functioning strong motion instruments near the site of the Royal Palm Resort. Therefore, ground motions had to be estimated using attenuation relations and simulations. Somerville [1997] examined worldwide instrumentation and

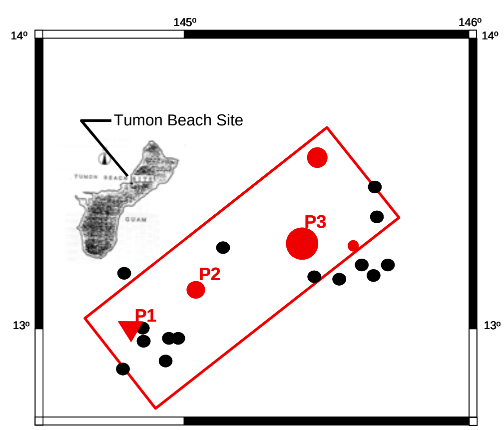

Figure 6 – Location of main events and aftershocks, and inferred rectangular rupture plane.

identified three main events shown as P1, P2, and P3 in Figure 6. Overall estimated rupture time was 32 sec. Somerville estimated peak ground acceleration at the site had a median value around 0.15g with 84th percentile motion as high as 0.36g. Hamburger [1998] summarizes response spectra estimated by various means (Figure 7).

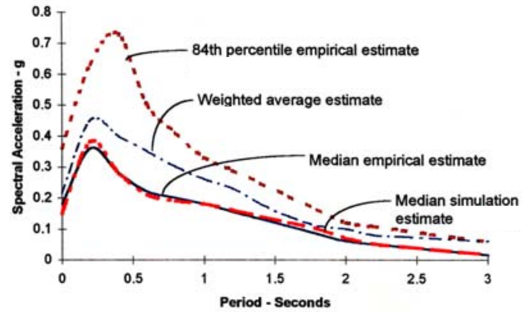

Figure 7 – Estimated response spectra.

EARTHQUAKE PERFORMANCE OBSERVATIONS

The Royal Palm Resort experienced damage ranging from light to extensive in various portions of the structure. The heaviest damage occurred in A-Block, where failures of columns, joints, beams, and CMU infills resulted in partial collapse primarily in the southwest portion of the block in the first and second stories, causing the block to drop as much as about 1.5 m at these locations and lean toward the south starting around the second story, with total residual roof displacement of about 2.7 m to the south (Figure 8). Lateral offset at the collapsed floor was relatively small. Damage to B-Block was light to moderate.

Figure 8 – View of A-Block (C.1-21.1 shown center).

CMU wall damage was heaviest in the first two stories of A-Block, but was visible throughout the building, ranging from minor cracking to complete failure and collapse from the surrounding frame. Essentially complete column, beam, and beam-column joint failures occurred at several locations around the southwest perimeter of A-Block. Failures also occurred at several interior columns. Damage decreased toward the northeast, consistent with the final building position.

Figure 9 depicts the variety of failure observed around the southwest perimeter. Damage around the joint led to shortening of the second and third stories at E.1-23.1 (Figure 9a). Corner joint failures occurred in type C3 columns at D.1-22.1, B.1-18.1, and B.1-15.1 (Figure 9b). Corner column failure occurred at C.1-21.1 (Figure 9d). Figure 9(e) shows type C3 edge column failure, typical of columns at the southwest perimeter except for corner columns at E.1-23.1, D.1-22.1, B.1-18.1, and B.1-15.1.

(a) Frame at grid line 23.1

(b) Column B.1-18.1

(c) Upper-story C3 column

(d) Column C.1-21.1

(e) Edge column along grid line B.1

Figure 9 – Details of column and joint failures.

Though not shown, columns toward the interior of the building failed along their clear height at or adjacent to the second story and shortened as might be anticipated given the shortening of the second story as the building leaned toward the south. Above the third story, structural damage was relatively light, though several exterior type C3 columns on the south side of the building showed significant inclined cracking (Figure 9c).

CALCULATED BUILDING CHARACTERISTICS

Various analyses have been conducted on the subject building, with emphasis on A-Block. This section presents results of strength calculations for beams and columns to gain a sense of the likely failure modes. The focus is on columns along the southwest perimeter of the building.

Figure 4 depicts a typical cross section for a beam along the southwest portion of the building, showing the beam, drop wall, and floor slab. Figure 10 presents calculated moment-curvature relations for different cross sections assuming presence or absence of various components of the composite beam. Section A, considering the beam without drop wall or slab, indicates relatively ductile response. Addition of the drop wall and slab adds considerable moment strength.

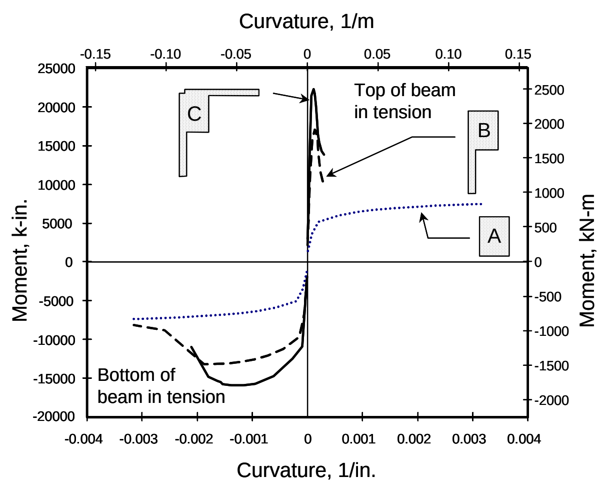

Figure 10 – Calculated moment-curvature relations.

Demands on type C3 columns can be estimated by comparing relative strengths of the beams in flexure, the column in flexure, and the column in shear. Beam moment strength was taken as the moment strength calculated for the beam considering contribution of the drop panel and participating slab; calculations show that the planter walls would increase beam stiffness but not strength if cells were not grouted (photographs indicate some cells were not grouted). Column moment strength was calculated on the basis of moment-curvature analyses for varying axial loads. Column shear strength was computed according to the shear strength formula proposed in [Moehle 2001]. Assuming inflection points at the midheight of the column above and below a joint, equilibrium can be used to identify the maximum shear demands on the column. Figure 11 shows results of the analysis. The shear corresponding to development of beam flexural hinging (flexural strength as shown in Figure 10) is 1100 kN. The shear corresponding to hinging in the columns varies with axial load and with the assumption for location of column plastic hinges. For this analysis, the plastic hinge is taken at the top of the CMU planter walls and bottom of the drop wall; this results in a high estimate of the shear force because yielding may penetrate beneath the top of the planter walls and above the bottom of the drop walls. As shown, there is a close balance between flexural strengths of the columns and beams, with column strength being the larger of the two. Calculated shear strength [Moehle 2001] depends on whether the column is yielding in flexure with "significant" flexural ductility. Two shear strengths are shown, one assuming the column does not yield in flexure and the other assuming it does. By these analyses, the column shear strength is less than the demand corresponding to flexural hinging of either the beam or column.

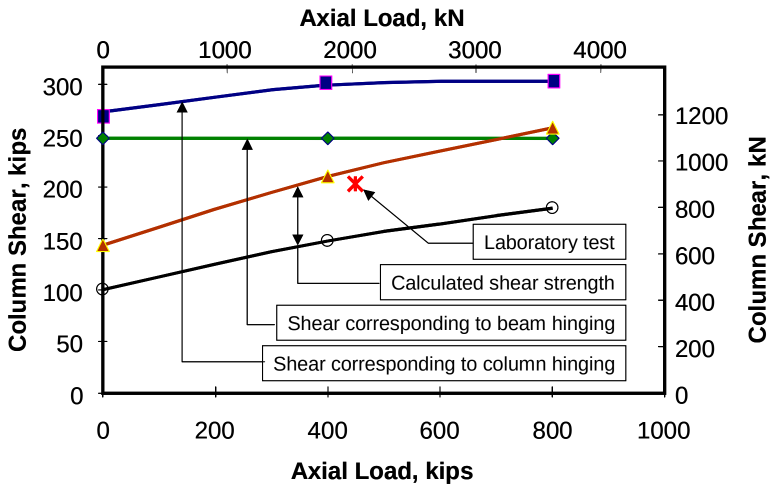

Figure 11 – Shear demands and capacities of Type C3 columns.

Joint strengths were calculated according to ATC 40 [1996]. Demands on edge joints were well below capacities for loading parallel or perpendicular to the edge. Nominal strength for corner joints based on design concrete compressive strength of 27.6 MPa is $V_j = 0.5\sqrt{f_c^{'}}A_j$ (N, mm units) = 974 kN. For loading in any direction, joint demands (assuming joints do not fail) are limited by beam flexural strengths. For loading to the north or the east, the column would bear against the CMU planter walls, leading to a nominal joint shear demand of 1410 kN. For loading to the south or west, the columns would pull away from the planter walls, with nominal joint shear demand of 1130 kN. Note that for this latter case, the column would be much more flexible than adjacent edge columns that are restrained by the planter walls, so that reaching critical joint shear before failing the edge columns in shear seems unlikely.

EXPERIMENTS ON CRITICAL COMPONENTS

Sozen [1997] reports results of tests on scaled models of the type C3 columns (Figure 12). Axial load was constant and lateral load was in the plane of the drop walls and planter walls. Test results demonstrate that the columns were vulnerable to shear failure at relatively small lateral drift. Measured shear strength, scaled to full scale, is close to the calculated strength (Figure 11). Tests were stopped before loss of axial load capacity.

Priestley and Hart [1994] conducted tests on a model of a type C3 column corner connection, but without the planter walls or floor slab. Lateral loads were cycled in two horizontal directions, both independently and simultaneously. Axial load started at $0.15f'_cA_g$ and was cycled in proportion with lateral loads, reaching a minimum value of $-0.07f'_cA_g$ and maximum value of $0.39f'_cA_g$. Nominal joint shear stresses reached $0.52\sqrt{f'_c}A_j$ (N, mm units) in the longitudinal

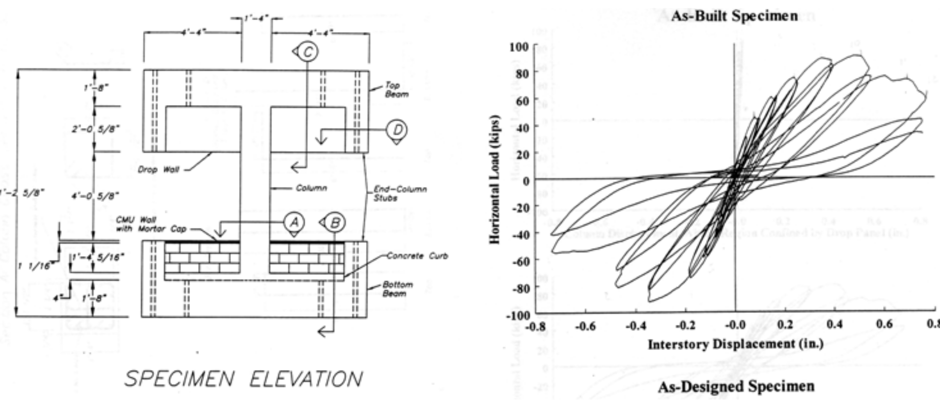

(a) Specimen configuration (b) Measured response

Figure 12 – Test of type C3 column model.

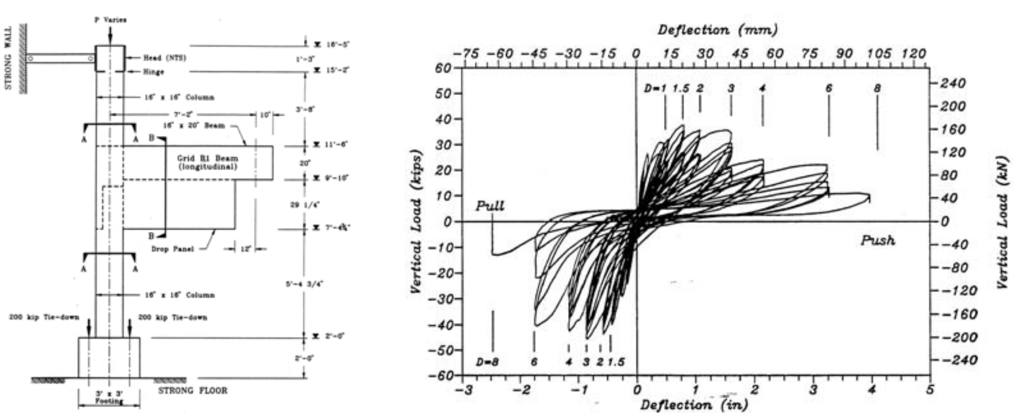

(a) Specimen configuration (b) Measured response

Figure 13 Test of type C3 corner beam-column joint model.

direction and $0.69\sqrt{f_c^{'}}A_j$ in the transverse direction. For both directions of loading, beam longitudinal reinforcement strain was more than three times the yield value when maximum joint forces were reached, suggesting prior flexural yielding controlled the joint strength. Maximum drift ratio in the longitudinal pull direction (top of beam in tension) was approximately 0.029, while that in the longitudinal push direction was approximately 0.044. The joint began to lose axial load during the pull cycle in the diagonal direction to vector drift ratio of about 0.036; while attempting to reapply the axial dead load of $0.15f^{'}_cA_g$ the joint began to fail axially. This observation and the appearance of the crushed joint and buckled column bars suggest that the joint had reached the drift corresponding to axial collapse.

FAILURE ANALYSES

Figure 14 compares load-deformation relations obtained from the tests on models of the edge column and corner beam-column joints. Column shears are normalized to the maximum value measured in that test. Drift ratios are modified from test values; for edge columns, beam flexibility was added analytically, and for corner connections, minor adjustments were made to account for beam flexibility and boundary conditions. For longitudinal response, the data suggest the edge columns would fail well before the corner joints. For transverse response, deformation capacity of joints is about double that of the restrained columns (note that the re-entrant corner columns are restrained by CMU planters for loading in this direction).

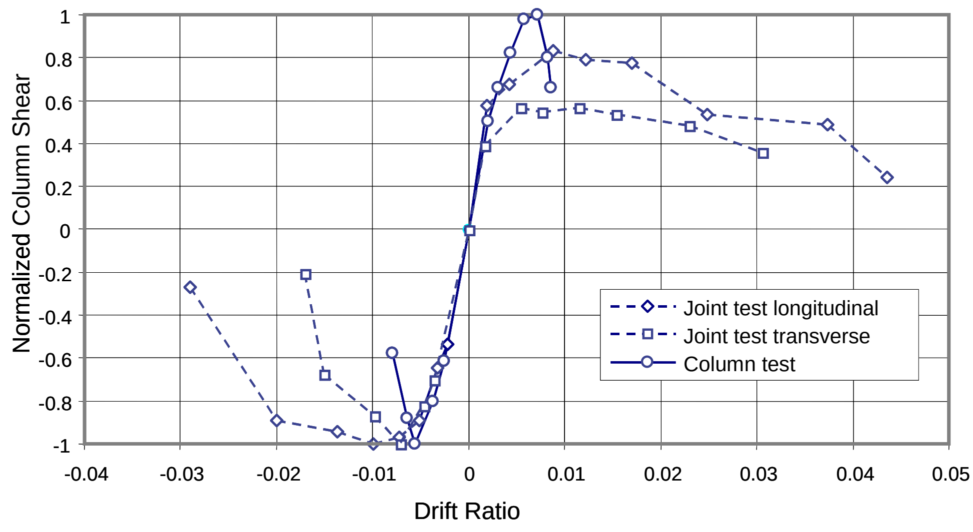

Figure 14 Load-deformation relations of edge columns and corner joints.

It is noteworthy that the columns were loaded with constant axial load and two lateral displacement cycles at each displacement amplitude, while the corner beam-column connections were loaded by variable axial load and two longitudinal, two transverse, and two diagonal lateral displacement cycles at each displacement amplitude. The more severe loading regime for the corner beam-column connections is likely to have reduced the apparent deformation capacity of those components.

The column tests were terminated before columns lost axial-load-carrying capacity. Drift at axial collapse can be estimated using the model presented in [Moehle 2001]. Analyses of the structure indicate that axial load in edge columns may have reached around 5000 kN due to gravity and overturning effects. The interstory drift ratio at axial collapse for this axial load, estimated using the analytical model and considering flexibility of adjacent framing, is 0.009. This value seems credible given the trend of the measured load-deformation relation of the column (Figure 14).

Plastic collapse analyses also provide insight into the likely collapse scenario. Figure 15 shows two collapse modes considered. Figure 15(a) considers the case where the corner beam-column joint or column at B.1-18.1 (Figure 2) loses axial capacity and earthquake loading is toward the southwest. For this loading, the maximum column axial load is at B.1-17.1 (Figure 2). Assuming all beams develop moment capacities (calculated using measured mean yield strength of 462 MPa and slab contribution equal to half the compression flange width of ACI 318), the column axial load is 11,300 kN, which is less than the calculated compression capacity of 13,300 kN. Figure 15(b) considers the case where the edge columns including the captive column at the re-entrant corner C.1-18.1 fail. Using the same assumptions, the calculated column axial load for interior columns is as high as 14,800 kN, which exceeds the axial capacity of the column.

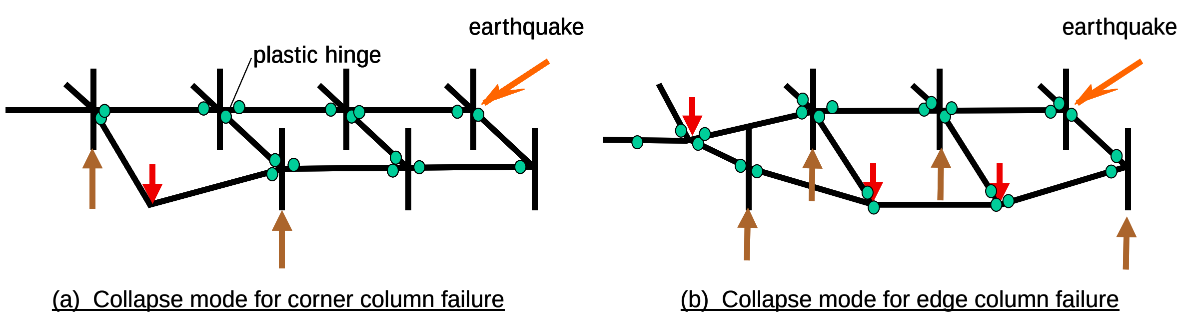

Figure 15 – Collapse modes.

The preceding calculations assume the axial capacity of a column is equal to the value calculated for monotonic axial compression loading. Combined axial load and moment may reduce the axial capacity, as concrete crushing initiates in the concrete cover and progresses toward the core. With low amounts of transverse reinforcement, crushing can continue into the core, leading to compression failure at reduced axial load. With code-required transverse reinforcement to confine the core concrete, crushing would be arrested in the core and the column should be able to sustain the full axial capacity.

Damage due to cyclic shear also can reduce axial capacity of shear-critical columns with insufficient transverse reinforcement [Tasai, 2000].

In light of the preceding discussion and test data, it is plausible that a corner column failure could result in edge column failure if that edge column already was damaged in shear and did not have sufficient transverse reinforcement to confine the core concrete. A more plausible scenario, considering all the evidence, is that shear damage reduced the axial capacity of the edge columns, leading to collapse as overturning actions exceeded reduced column capacities.

Nonlinear static analyses reported by Hamburger [1998] incorporated the test results in a three-dimensional model of the building. Where the test specimens lacked a component (beams in the case of the column tests and planter walls in the case of the joint tests), these were added analytically. Longitudinal and transverse periods were calculated to be 0.8 sec and 1.2 sec, respectively. Response spectra (Figure 7) indicate the transverse accelerations would be approximately 1.5 times the longitudinal accelerations for linear response. Therefore, lateral loads were applied in the proportion 1.5:1. Under loading to the southwest, nonlinear response began when lateral load corresponded to approximately 0.15g and 0.1g for transverse and longitudinal directions, respectively. Edge column failures were calculated for global response acceleration levels of 0.28/0.19g. Removal of the failed columns led to collapse of the second story. Results were similar for loading to the northeast.

SUMMARY AND CONCLUSIONS

The Royal Palm Resort sustained partial collapse during the 1993 Guam earthquake. Failures occurred in both columns and beam-column joints. Study of the collapse leads to the following conclusions:

- Both analyses and tests show that both the columns and the corner beam-column joints were susceptible to failures under certain loading conditions.

- Deformation capacities defined by tests indicate that the edge columns would sustain critical shear failures well before the corner beam-column joints would sustain similar failures.

- Collapse analyses indicate that edge column failure could result in progressive collapse, while corner beam-column joint failures could not. This conclusion is based on the assumption that the axial capacity of a column is equal to the monotonic axial compression capacity. Axial capacity of a lightly confined column may be reduced owing to interaction with flexure and shear. This observation suggests the possibility that overturning action on shear damaged edge columns may have triggered collapse. Axial capacity would not be as adversely affected if the columns had adequate transverse reinforcement.

- Nonlinear static analyses demonstrate that failure of the edge columns would precede that of the corner beam-column connections, and would lead to progressive collapse. These analyses also show that this failure mode would be expected for acceleration levels that are credible at the building site.

It is concluded that collapse of the Royal Palm Resort was triggered by failure of the second-story edge columns along the south edge of the building. Shear distress in the captive columns likely reduced their axial-load-carrying capacity, resulting in axial compression failure, leading to progressive collapse.

ACKNOWLEDGMENT

Eduardo Fierro of Wiss Janney Elstner Associates, Inc, provided photographs of building damage. Views presented in this paper are those of the author, and do not necessarily represent those of other individuals or organizations cited.

REFERENCES

[ACI 1989] - *Building Code Requirements for Reinforced Concrete (ACI 318-89) and Commentary (ACI 318R-89)*, Farmington Hills, Michigan.

[ATC 40 1996] – "Recommended Methodology for the Seismic Evaluation and Retrofit of Existing Concrete Buildings," Seismic Safety Commission, State of California, *Report No. SSC-96-01*, Sacramento, California. Also available as Applied Technology Council report no. ATC-40.

[EERI 1995] - *Guam Earthquake Reconnaissance Report*, Earthquake Engineering Research Institute, Oakland California, April 1995.

[Hamburger 1998] – Hamburger, R. O., "Supplemental Report: Failure Investigation, Beach Wing, Royal Palm Resort, Tumon, Guam, EQE International Report, June 2004.

[Moehle 1997] – Moehle, J. P., "Royal Palm Resort, Guam – An evaluation of the causes of the failure in the earthquake of 8 August 1993," Engineering Report, March 1997.

[Moehle 2001] - Moehle, J., K. Elwood, and H. Sezen (2001), "Gravity Load Collapse of Building Frames during Earthquakes," *ACI SP-197, Behavior and Design of Concrete Structures for Seismic Performance*, American Concrete Institute.

[Priestley and Hart 1994] - Priestley, M., and G. Hart (1994), "Seismic Behavior of "As-Built" and "As-Designed" Corner Joints," SEQAD Report to Hart Consultant Group, *Report #94-09*, 93 pp. plus appendices.

[Somerville 1997] – P. Somerville, "Earthquake Ground Motion at the Site of the Royal Palm Resort during the August 8, 1993 Guam Earthquake," Woodward-Clyde Federal Services, Pasadena, CA, March 18, 1997.

[Sozen 1997] – Sozen, M. A., "On the Cause of the Structural Failure of Block A Building, Royal Palm Resort, Guam, in the August 1993 Earthquake," Engineering Report, June, 1997.

[Tasai 2000] - Tasai, A., "Residual Axial Capacity of Reinforced Concrete Columns during Shear Deterioration," Proceedings, The Second US-Japan Workshop on Performance-Based Earthquake Engineering Methodology for Reinforced Concrete Building Structures, Sapporo, Japan, 11-13 September 2000, *Report No. PEER-2000/10*, Pacific Earthquake Engineering Research Center, University of California, Berkeley, pp.257-267.

[UBC 1988] – *Uniform Building Code*, International Conference of Building Officials, Whittier, CA, 1988.

SESSION 1-A: DESIGN AND CONSTRUCTION PRACTICE

Chaired by

♦ Helmut Krawinkler and Manabu Yoshimura ♦

PERFORMANCE OF RC FRAME BUILDINGS DESIGNED FOR ALTERNATIVE DUCTILITY CLASSES ACCORDING TO EUROCODE 8 (FINAL VERSION, 2003)

T.B. PANAGIOTAKOS & M.N. FARDIS[1]

ABSTRACT

For the first time after the finalization of the European Norm for seismic design of buildings (Eurocode 8 - EC8), the performance of RC buildings designed with this code is evaluated through systematic nonlinear analyses. RC frames with 4, 8 or 12 stories are designed for a PGA of 0.2g or 0.4g and to one of the three alternative ductility classes in EC8. The performance of the alternative designs under the life-safety (475 year) and the damage limitation (95 year) earthquakes is evaluated through nonlinear seismic response analyses. The large difference in material quantities and detailing of the alternative designs does not translate into large differences in performance. Design for either Ductility Class High (H) or Medium (M) of EC8 is much more cost-effective than for Ductility Class Low (L), even in moderate seismicity.

1. INTRODUCTION

In the 2003 version of the European Norm for seismic design (Eurocode 8, EC8) design of RC buildings may be according to one of three alternative Ductility Classes: High (H), Medium (M) or Low (L). For DC M and H frames EC8 requires: (a) strong column-weak beam design (via capacity design of columns with an overstrength factor of 1.4 on beam strengths); (b) capacity design of all members against pre-emptive shear failure; and (c) detailing of all members for ductility. Detailing rules in DC H are more stringent than in DC M. Proportioning and detailing for DC L is that of structures not designed for earthquake resistance. The force-reduction factors for DC H, M or L are equal to $4.5a_R$, $3a_R$ and 1.5, respectively, (where a_R accounts for system redundancy and overstrength and in multistory frames may be taken equal to a default value of 1.3) and are much lower than the R-factors of US codes for Special, Intermediate or Ordinary RC frames, respectively, although detailing and proportioning requirements are similar. In this paper frames designed for a PGA of 0.2g or 0.4g according to the 3 alternative Ductility Classes of EC8 are evaluated via nonlinear time-history analyses at the collapse-prevention and the damage-limitation performance levels under the 475-year and the 95-year earthquakes, respectively.

[1] *Structures Laboratory, Department of Civil Engineering University of Patras, Patras, GREECE*

2. DESIGN OF FRAMES TO EUROCODE 8 (DC L, M, H)

RC frames with 4, 8, or 12 stories of 3m height are designed to the final (2003) versions of the European structural design standards (Eurocode 2 for concrete buildings and Eurocode 8 for earthquake resistant buildings), for one of the three alternative Ductility Classes (DC H, M or L), a 475yr PGA of either 0.2g or 0.4g and an elastic response spectrum with an amplification factor of 2.5 on PGA up to a period of 0.6sec, falling as 1/T thereafter. Each frame has three 5m bays in both horizontal directions. The slab is 0.15 m thick and in design contributes to the beam moment of inertia with an effective flange width according to Eurocode 2. In addition to self-weight, a distributed dead load of 2 kN/m^2 for floor-finishes and partitions and a live load with nominal value of 1.5 kN/m^2 is considered. In the combination of gravity loads, nominal dead and live loads are multiplied with load factors of 1.35 and 1.5, respectively. In the seismic load combination, dead and live loads enter with the nominal value or 30% of the nominal value, respectively. Concrete with nominal cylindrical strength f_{ck} = 30MPa and fairly ductile Tempcore steel with nominal yield stress f_{yk} = 500MPa, are used. Columns are square with the same side length h_c in all stories, but are smaller in the two exterior columns so that their uncracked gross-section stiffness is about half that of the interior ones (so that elastic seismic chord rotation demands at the two beam ends of exterior bays are about equal). Beams have the same web width (b_w = 0.3m for the 0.2g design PGA, b_w = 0.35m for the 0.4g PGA) in all stories, but different depth, h_b.

Design is based on the results of linear static analysis for heightwise linearly distributed lateral forces. As such a procedure systematically overestimates the results of a modal response spectrum analysis, EC8 allows multiplying analysis results by 0.85. Lateral forces are derived from the design spectrum at the fundamental period of the building estimated on the basis of the Rayleigh quotient and 50% of uncracked gross section stiffness. Torsion due to accidental eccentricity and simultaneous horizontal components of the earthquake (according to the 0.3:1 rule) are neglected in design, as the seismic response analyses for the evaluation of the performance in Sections 3 and 4 take place in 2D, under one horizontal component and without accidental eccentricity. The columns of the bottom story are assumed fixed at grade level. The finite size of beam-column joints is considered, but joints are assumed to be rigid. P-Δ effects are

Email: fardis@upatras.gr

neglected. Beam gravity loads are computed on the basis of beam tributary areas in the two-way square slab system.

At a preliminary design stage the uniform column depths h_c and the beam depths h_{bi} at each story are tailored to the interstorey drift ratio limitation of 0.5% (for brittle non-structural infills) for the 95-year damage limitation earthquake, taken as 50% of the 475-year one. Small initial member sizes are assumed; then the (constant throughout the building) column depth h_c is chosen to fulfil the 0.5% drift limit at the story with the smallest interstorey drift among those violating the limit. In other stories beam depth is increased until the 0.5% drift limitation in the story is fulfilled. In proportioning afterwards the beam reinforcement for the ULS for bending on the basis of the linear analysis results of the so-sized frame, beam depths in a few stories may increase further, to avoid violation of the maximum top steel ratio at the supports. The analysis is repeated for conformity of the fundamental period and of other results to the final member sizes.

Table 1 lists the column sizes and the axial load ratio, $\nu_d = N/A_c f_{cd}$, at the base of the column under the gravity loads acting simultaneously with the design earthquake. Final beam depths, h_b, top and bottom beam reinforcement ratios, ρ and ρ' (average at the two ends) and column total steel ratio ρ_c for each story, are given in Figures 1 to 3. In 8- or 12-story frames designed for a PGA of 0.4g, it was not feasible to have the same column size for DC L as for DC M or H. In the 12-story frames with design PGA of 0.2g, keeping column size the same for DC L as in M and H, gives oversized columns for DC M and H and excessive beam reinforcement ratios for DC L.

Table 1: Column sizes and normalized axial load: $\nu_d = N/A_c f_{cd}$ at base due to gravity loads

Building	Design	Design PGA : 0.20g				Design PGA : 0.40g			
		Exterior columns		Interior columns		Exterior columns		Interior columns	
		h_c (m)	ν_d	h_c (m)	ν_d	h_c (m)	ν_d	h_c (m)	ν_d
4-story	All designs	0.45	0.051	0.55	0.078	0.55	0.077	0.65	0.122
8-story	DC L	0.55	0.075	0.65	0.115	0.75	0.098	0.90	0.138
	DC M or H	0.55	0.075	0.65	0.115	0.55	0.153	0.65	0.240
12-story	DC L	0.85	0.065	1.00	0.086	1.00	0.110	1.20	0.138
	DC M or H	0.85	0.065	1.00	0.086	0.60	0.198	0.70	0.314

Table 2 lists the material quantities required for one frame in the 18 designs. It is clear from the required beam depths in the frames designed for a PGA of 0.4g, or from the required beam reinforcement in those designed for a PGA of 0.2g, that design for strength alone (for DC L) is much less cost-effective than design for ductility (for DC M or H) and is not a viable option for medium-high rise frames, even for moderate seismicity (PGA of 0.2g) and/or low-rise frames.

Table 2: Concrete volume (m^3) and steel weight (t) per frame, including transverse beams

Building and DC		Design PGA : 0.20g						Design PGA : 0.40g					
		Beams		Columns		Total		Beams		Columns		Total	
		concrete	steel	concrete	steel	concrete	steel	concrete	steel	concrete	steel	concrete	steel
4-story	L	16.76	2.81	12.12	1.75	28.88	4.56	22.64	2.24	17.40	2.76	40.04	5.00
	M	17.64	1.22	12.12	1.63	29.76	2.85	20.58	1.86	17.40	2.43	37.98	4.29
	H	16.76	1.17	12.12	1.79	28.88	2.95	22.64	1.39	17.40	2.47	40.04	3.86
8-story	L	44.54	9.25	34.80	5.55	79.34	14.80	57.11	8.08	65.88	7.78	122.99	15.86
	M	37.49	4.91	34.80	4.31	72.29	9.23	45.28	6.13	34.80	5.20	80.08	11.32
	H	37.04	3.68	34.80	4.83	71.84	8.52	41.67	4.50	34.80	4.73	76.47	9.24
12-story	L	75.41	21.01	124.02	7.86	199.43	28.87	94.15	22.11	175.68	18.67	269.83	40.78
	M	74.09	10.01	124.02	6.63	198.11	16.64	66.37	11.56	61.39	9.56	127.76	21.12
	H	75.41	6.66	124.02	8.39	199.43	15.04	67.40	8.73	61.20	8.84	128.60	17.58

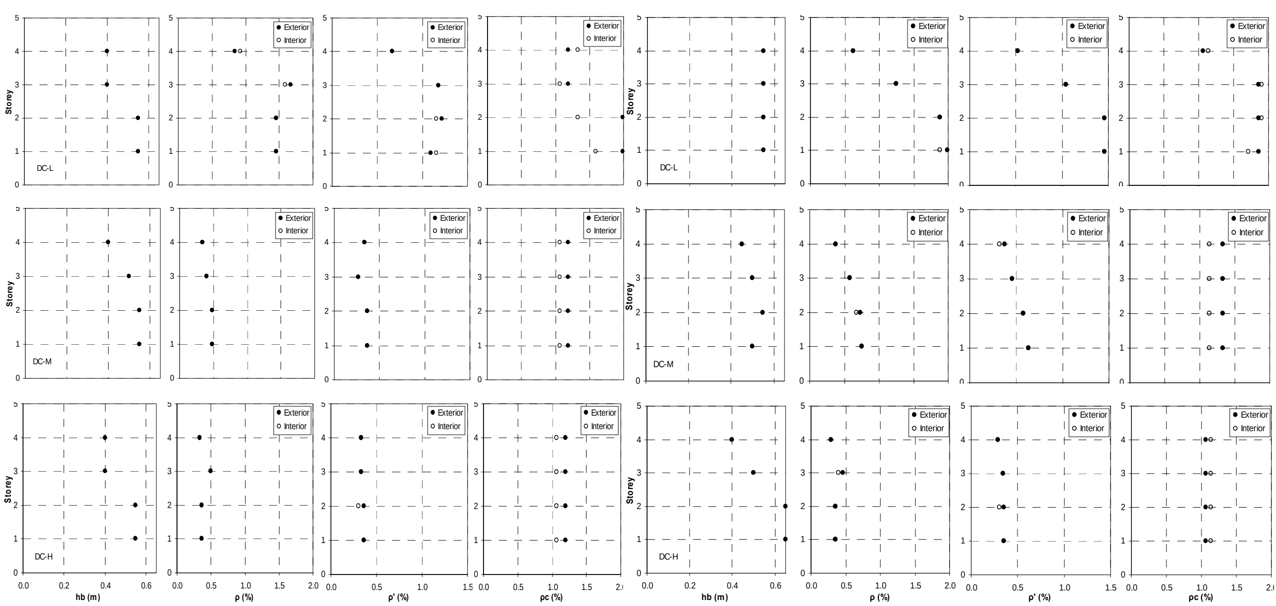

(a) (b)

Figure 1: Beam depth (h_b), beam top (ρ) and bottom (ρ') reinforcement ratio and column total reinforcement ratio (ρ_c) in 4-story frames for DC L (top), M (middle) or H (bottom). Design PGA: (a) 0.2g; (b) 0.4g. Closed circles: exterior and open circles: interior members.

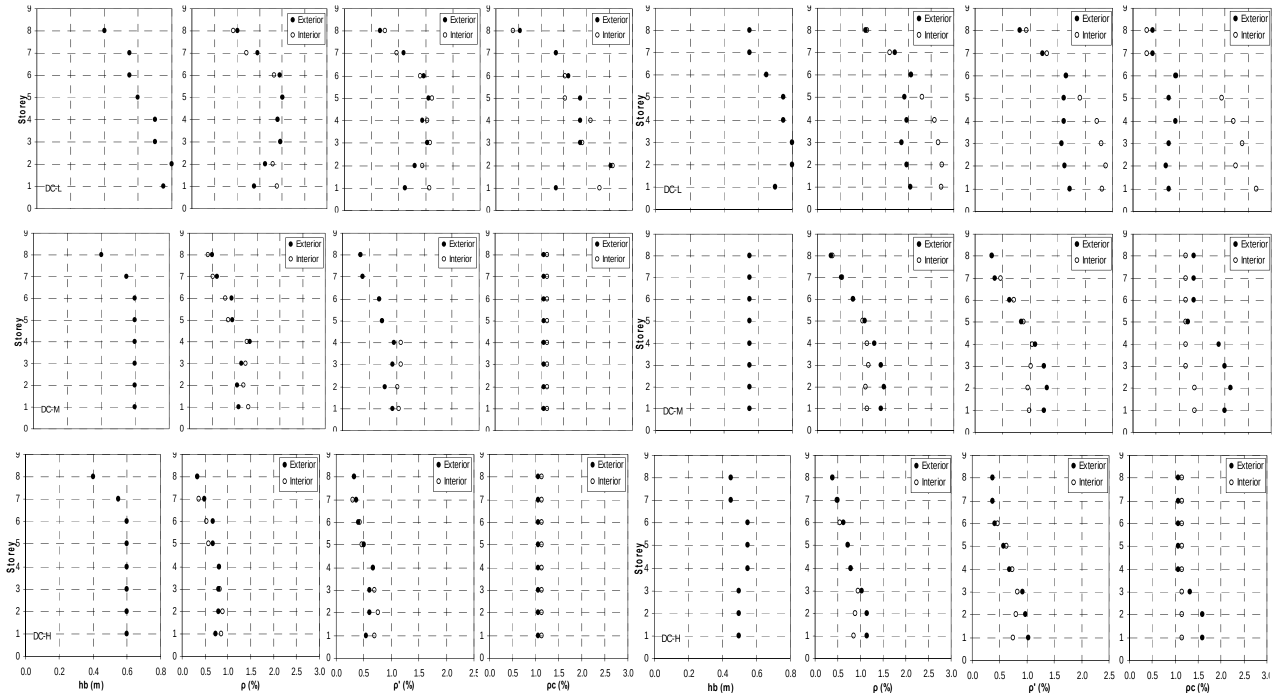

(a) (b)

Figure 2: Beam depth (h_b), beam top (ρ) and bottom (ρ') reinforcement ratio and column total reinforcement ratio (ρ_c) in 8-story frames for DC L (top), M (middle) or H (bottom). Design PGA: (a) 0.2g; (b) 0.4g. Closed circles: exterior and open circles: interior members.

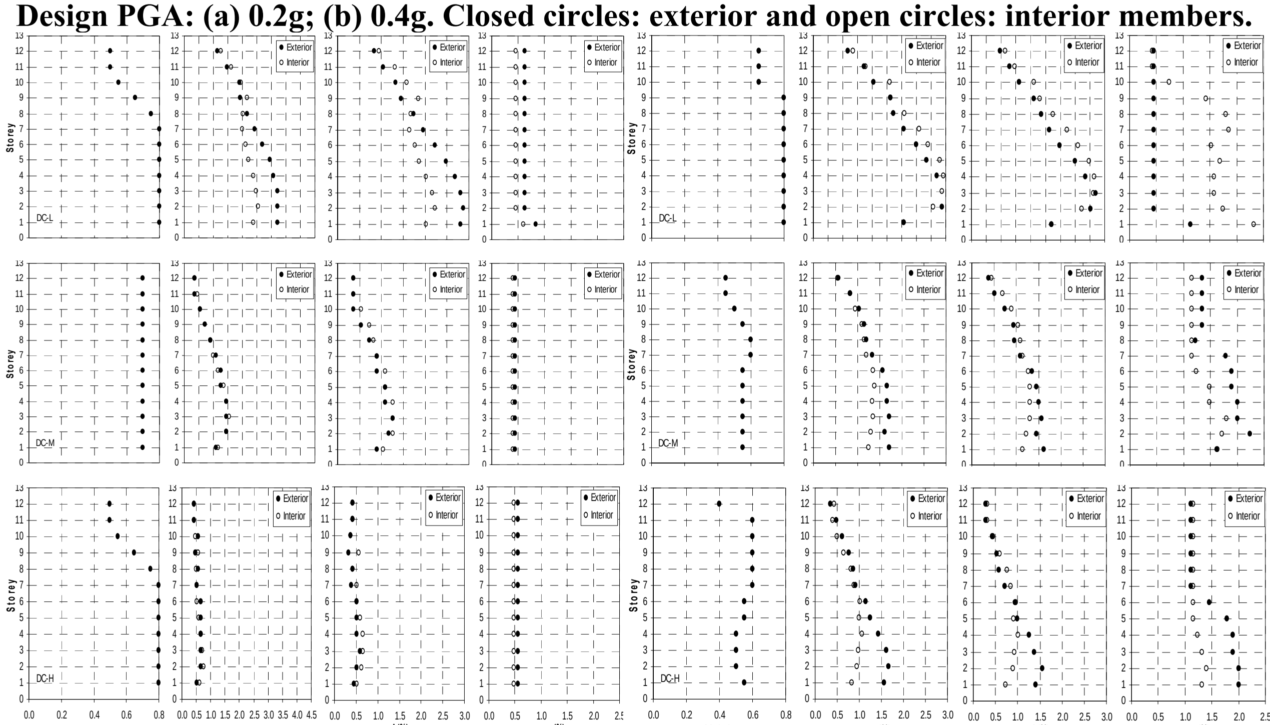

(a) (b)

Figure 3: Beam depth (h_b), beam top (ρ) and bottom (ρ') reinforcement ratio and column total reinforcement ratio (ρ_c) in 12-story frames for DC L (top), M (middle) or H (bottom). Design PGA: (a) 0.2g; (b) 0.4g. Closed circles: exterior and open circles: interior members.

3. PERFORMANCE EVALUATION UNDER THE DESIGN (475-YR) EARTHQUAKE

Member deformation demands due to the design (475 yr.) earthquake are estimated via nonlinear dynamic analysis of the response to a set of seven motions emulating historic records from Southern Europe or California, scaled to the design PGA of 0.2g or 0.4g. These motions are modified to conform to the 5%-damped elastic response spectrum used for the design.

Mean values of material strengths: $f_{ym} = 1.15f_{yk} = 575$MPa, $f_{cm} = f_{ck}+8 = 38$MPa are used in the nonlinear analysis and in the evaluation of member performance from it. A point-hinge model is used for members. The yield moment of the point-hinge is equal to the ultimate moment of the section, for the instantaneous value of the axial force, as this changes during the time-history analysis. A simplified Takeda model is used for the moment-plastic hinge rotation hysteresis law. It has: (a) a bilinear skeleton curve (for monotonic loading) with post-yield hardening ratio equal to 5%, (b) unloading to a residual plastic hinge rotation at zero moment equal to 70% of that for unloading at the stiffness of the elastic branch, and (c) reloading thereafter towards the extreme previous point on the skeleton curve in the direction of reloading. Rayleigh damping is considered, with viscous damping ratio of 5% at the fundamental period of the elastic frame and at twice that period. The elastic stiffness of members is taken equal to their secant stiffness at yielding of both ends in antisymmetric bending: $EI_{eff}= M_yL_s/3\theta_y$, with M_y the yield moment of the member end section (equal to the ultimate moment for the initial value of the axial force), L_s the shear span (taken equal to half the member clear length) and θ_y the chord-rotation of the shear span at yielding, estimated according to Panagiotakos and Fardis (2001) and *fib* (2003). On average, the so-calculated EI_{eff} is in agreement with over 1500 test results, but is only 25% of the EI-value of the uncracked gross section. P-Δ effects are considered in columns.

Columns are assumed fixed at grade level; beam gravity loads are based on beam tributary areas in the two-way square slab system; the finite size of beam-column joints is considered; joints are assumed rigid but the contribution of bar pull-out from joints to the fixed-end rotation at member ends is considered via the value of θ_y used in calculating EI_{eff}. On each side of a beam the width of the slab considered as effective in tension and contributing to the top reinforcement of the beam end sections with the slab bars that are parallel to the beam, is taken as 25% of the beam span.

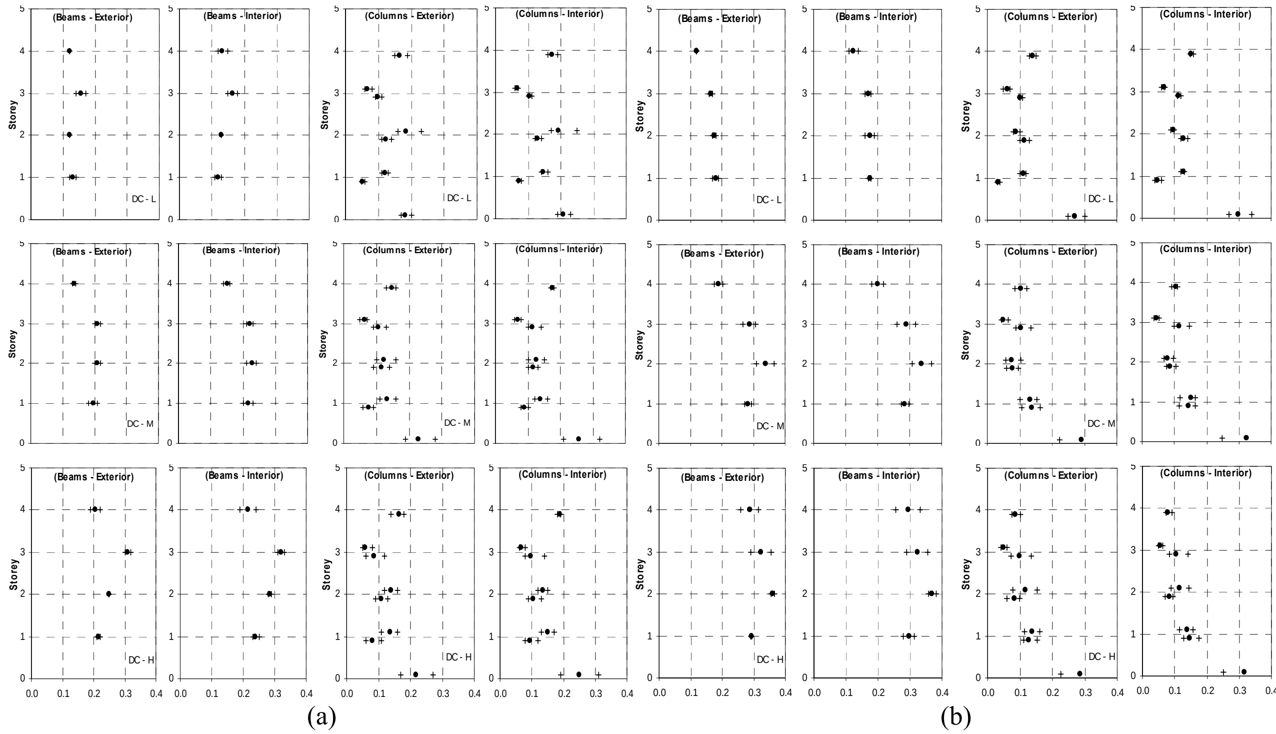

Figure 4: Minimum-maximum range and mean member chord-rotation demand-to-supply ratio from 7 time-history analyses of 4-story frames with design PGA: (a) 0.2g; or (b) 0.4g.

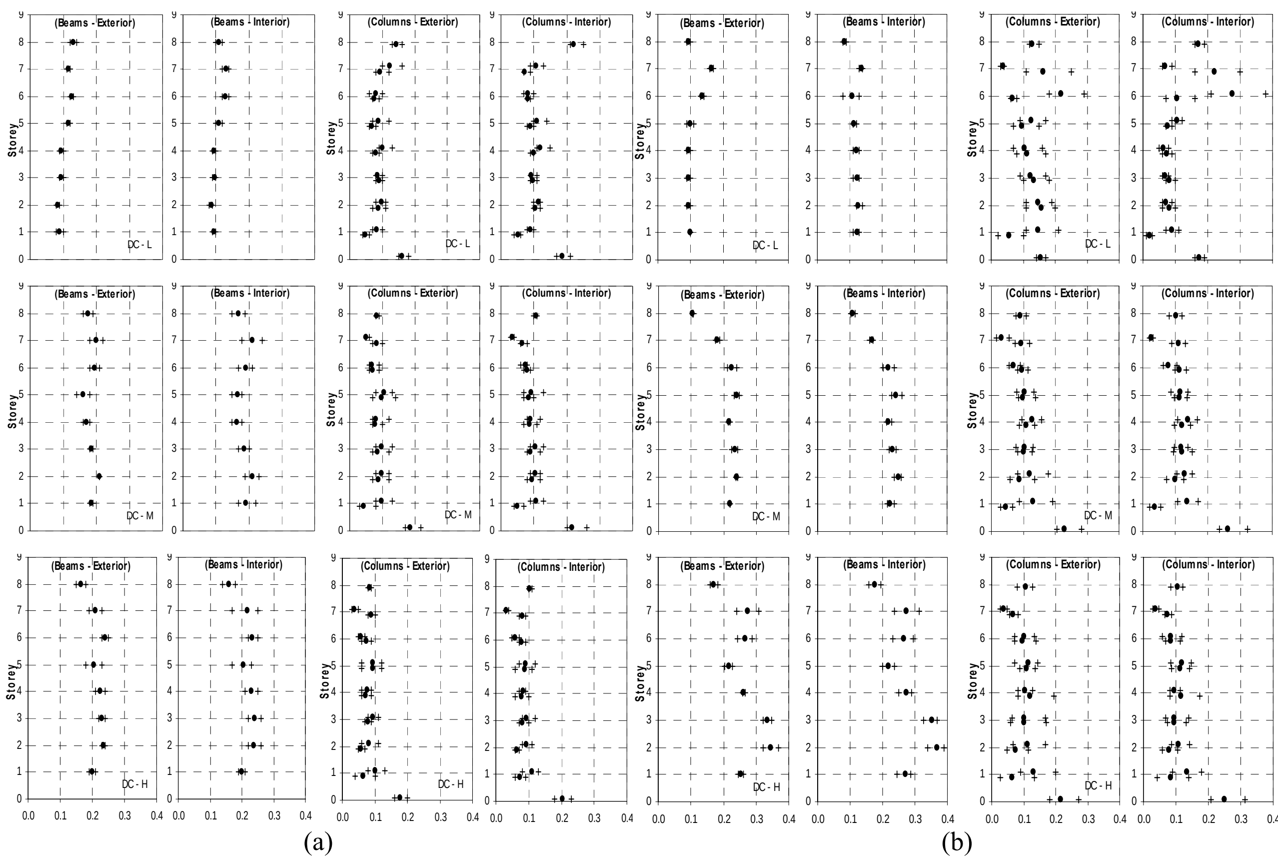

Figure 5: Minimum-maximum range and mean member chord-rotation demand-to-supply ratio from 7 time-history analyses of 8-story frames with design PGA: (a) 0.2g; or (b) 0.4g.

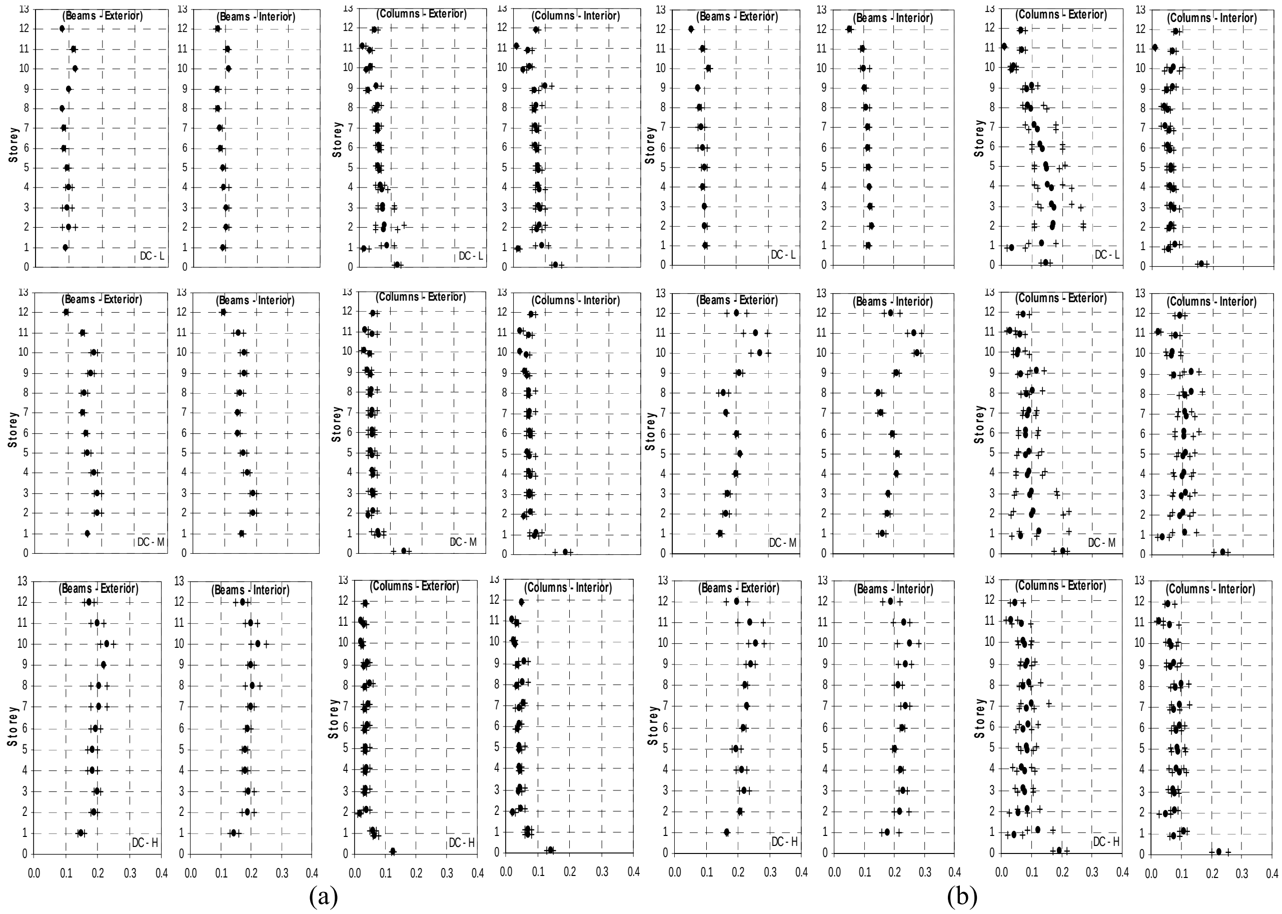

Figure 6: Minimum-maximum range and mean member chord-rotation demand-to-supply ratio from 7 time-history analyses of 12-story frames with design PGA: (a) 0.2g; or (b) 0.4g.

Frame performance under the 475-yr earthquake is evaluated on the basis of the ratio of chord rotation demand at member ends to the corresponding supply or capacity. Member capacity is taken equal to the chord rotation at which the member exhibits a drop in peak lateral force resistance during a cycle, above 20% of the maximum previous lateral resistance during the test ("loss of lateral load capacity", considered as a "near-collapse" condition at the member level). This member chord rotation capacity is computed via an empirical expression fitted to the results of over 1000 cyclic tests to failure (Panagiotakos and Fardis 2001, *fib* 2003).

The member chord rotation demand-to-supply ratio is considered as a "damage ratio" against loss of lateral load capacity ("collapse") of the member. Figures 4 to 6 give the range (minimum and maximum) and the mean of this "damage ratio" for the beams and the columns of the frames for the seven ground motions, each considered to act in the positive and in the negative direction.

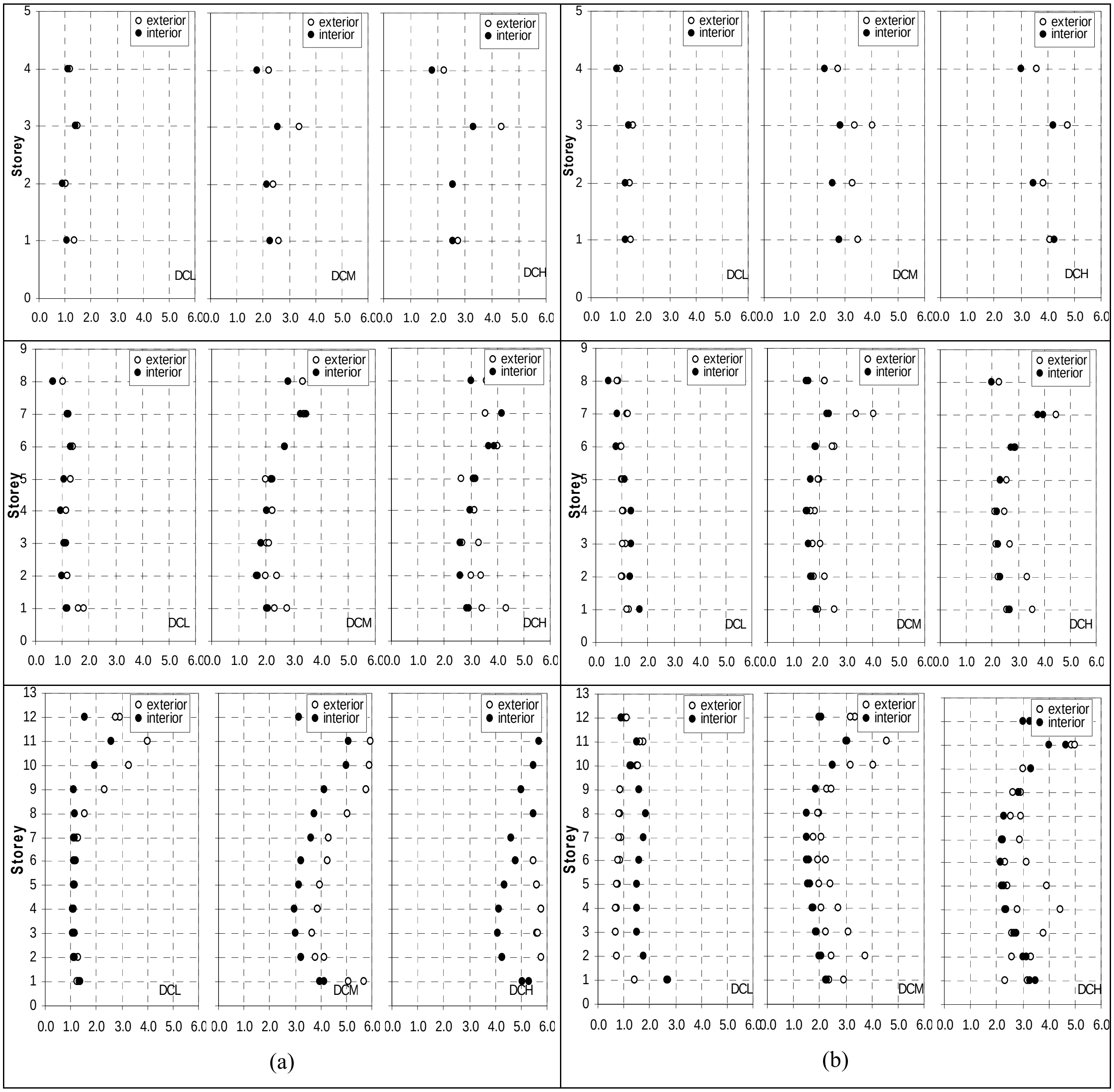

Figure 7: Ratio of sum of column flexural capacities to sum of beam flexural capacities around joints in frames of: DC L (left), M (middle) or H (right). Design PGA: (a) 0.2g; (b) 0.4g. Closed circles: exterior joints; open circles: interior joints.

To assist in the interpretation of the concentration of inelastic deformation and damage in beams or columns, Figure 7 presents the values of the ratio of the sum of column flexural capacities around joints to the sum of beam flexural capacities around the same joint, separately for interior or exterior joints and for each sense of moments around the joint. The effect of the fluctuation of axial load on column capacity, which is taken into account during the seismic response analysis, is neglected in the calculation of column flexural capacity. Beam negative moment capacities are much larger that in design calculations, due to the large contribution of slab reinforcement parallel to the beam considered in the nonlinear response analysis but neglected in design. Despite of that, in DC M and H frames the sum of column capacities exceeds that of beams by a factor much greater than the factor of used in design. In DC L frames, which do not have a strong column - weak beam design, the column-to-beam flexural capacity ratio is around 1.0, often falling behind that value and suggesting plastic hinging in columns.

The main conclusion from Figures 4 to 6 is that, despite their large differences in member cross-sections and amount and detailing of reinforcement, frames with the same number of stories designed for the same PGA but for different DC have similar performance under the 475-yr earthquake. “Damage ratios” are very consistent between interior and exterior members and fairly similar in frames with different number of stories. This means that the application of Eurocode 8, with its three alternative ductility options, results in fairly uniform and consistent performance under the 475-yr earthquake. It is noteworthy that the maximum values of the demand-to-supply ratio are always less than the threshold of about 0.4 corresponding to the 5%-fractile of member chord-rotation capacity; providing a safety margin against the inherent uncertainty of ultimate deformation capacity. More specifically, the following conclusions are drawn from Figures 4 to 6.

In the frames designed for ductility (i.e. for DC M or H), the chord rotation demand-to-supply ratio (“damage ratio”) assumes very similar values at all intended plastic hinge locations – i.e. at ends of beams and at the base of columns at grade level: in general between 0.2 and 0.3 (or 0.1 to 0.15 at the base of columns of 12-story frames designed to 0.2g). The value of the “damage ratio” is much lower over the rest of the column height (around 0.1, or 0.05 in the 12-story frames designed to 0.2g) than at grade level, consistent with the high column-to-beam flexural capacity ratios shown in Figure 7 for the DC M and H frames. Beam “damage ratios” decrease slightly when going from DC H to DC M. Above the base of the columns, the “damage ratio” is not significantly affected by design to either DC M or DC H. Although differences in performance of the DC M and H frames under the 475-yr earthquake are hard to identify, design for DC H seems to give slightly better overall performance only in the 12-story frame designed for a PGA of 0.4g. In that particular case the DC H frame has lower and more consistent “damage ratios” in the columns above the ground story and overall similar beam performance. In all other cases, design for DC M consistently gives slightly superior performance in the beams than design for DC H. As far as the columns are concerned, performance is about the same in all DC M or H frames other than the 12-story ones designed for 0.4g.

Frames designed to DC L (i.e. for strength alone rather than for controlled inelastic response and ductility) have always lower beam “damage ratios” than DC M or H frames, despite (a) the less confining reinforcement and the lower minimum compression reinforcement ratio of DC L beams and (b) the reduction in beam deformation capacity effected by the smaller shear span ratio, L_s/h, of DC L beams which are deeper than their DC H and M counterparts. This is attributed to: (a) the large flexural capacity of these beams, which promotes plastic hinging and inelastic deformations in columns instead of beams (cf. Figure 7); and (b) the increase in beam deformation capacity due to the heavy bottom reinforcement owing to proportioning of the end sections of these beams for the large positive seismic moments of the analysis for the design seismic action. The columns of all DC L frames designed for a PGA of 0.2g, as well as those of the 4-story frames designed for a PGA of 0.4g, have similar “damage ratios” as in the frames designed to DC M or H. This is despite the apparent occurrence of inelastic deformations at several levels of DC L columns and the effect of the lower confining reinforcement on their deformation capacity, and is attributed to the reduction in deformation demands owing to the larger overall effective stiffness of DC L frames, due to their heavier reinforcement. Given that DC L frames designed for a PGA of 0.2g, as well as DC L 4-story frames designed for a PGA of 0.4g have also slightly superior beam performance, their overall performance under the 475-yr earthquake is equal or slightly better than that of the DC M or H designs.

The columns of 8- or 12-story DC L frames designed for a PGA of 0.4g do not show a clear concentration of plastic hinge rotations at the base. This is not surprising, in view of the column-to-beam capacity ratios in Figure 7. Moreover, they show a very large scatter of the “damage ratio” in the upper stories, indicative of erratic column hinging due to higher-mode response.

“Damage ratios” are large in the upper story columns of these designs, despite: (a) the reduced deformation demands due to the larger overall effective stiffness of these frames, effected by the large cross-section and the heavy reinforcement of their members; and (b) the increase in column chord-rotation capacity due to the lower column axial load ratio, ν_d, effected by the larger column size (cf. Table 1). It is concluded, therefore, that for a PGA of 0.4g, in addition to being not cost-effective, DC L gives also inferior overall performance under the 475-yr earthquake.

4. DAMAGE LIMITATION PERFORMANCE UNDER THE 95-YEAR EARTHQUAKE

Frame members were sized so that story drift ratio under the 95-yr earthquake, computed via elastic analysis with 50% of the uncracked gross section stiffness, nowhere exceeds the damage limitation threshold of 0.5%. Frame performance under this earthquake is evaluated via nonlinear dynamic analysis of the response to the same set of seven motions used in the analyses for the 475-yr earthquake, scaled this time to the PGA of the 95-yr earthquake (taken as 50% that of the 475-yr one). The same modeling was used as in the response analyses for the 475-yr event.

Figure 8 shows the range (minimum and maximum) and the mean value of the computed story drift ratios over the seven input ground motions. DC L frames, with their higher overall effective stiffness due to the large cross-section and the heavier reinforcement of their members, have lower drifts than DC M or H ones. With few exceptions, the drifts of DC M and H frames exceed the damage limitation threshold of 0.5%. The main reason is that in the analysis member elastic stiffness is, on average, half of the conventional value of 50% of that of the uncracked gross section used in design. Plastic hinging and P-Δ effects increase computed drifts further. Given all these sources of deviation, the magnitude of the violation of the 0.5% threshold is still small.

5. CONCLUSIONS: COST EFFECTIVENESS OF ALTERNATIVE DESIGN OPTIONS

The performance of all frames (even of those not designed for ductility) is satisfactory under the

475yr earthquake and acceptable under the 95yr one. Differences in seismic performance of the three alternative designs are limited, in view of their large difference in material quantities. DC L has a disadvantage under the 475-yr earthquake for medium-high rise frames in high seismicity and an advantage over DC M or H at the damage limitation earthquake. In view of the different material quantities and of the fairly similar performance of the 3 alternative designs, design for strength alone (DC L) is much less cost-effective than design for ductility (DC M or H) and not a viable option for medium-high rise frames even in moderate seismicity (PGA of 0.2g). Design for DC L is less cost-effective than for M or H even in low-rise frames in moderate seismicity.

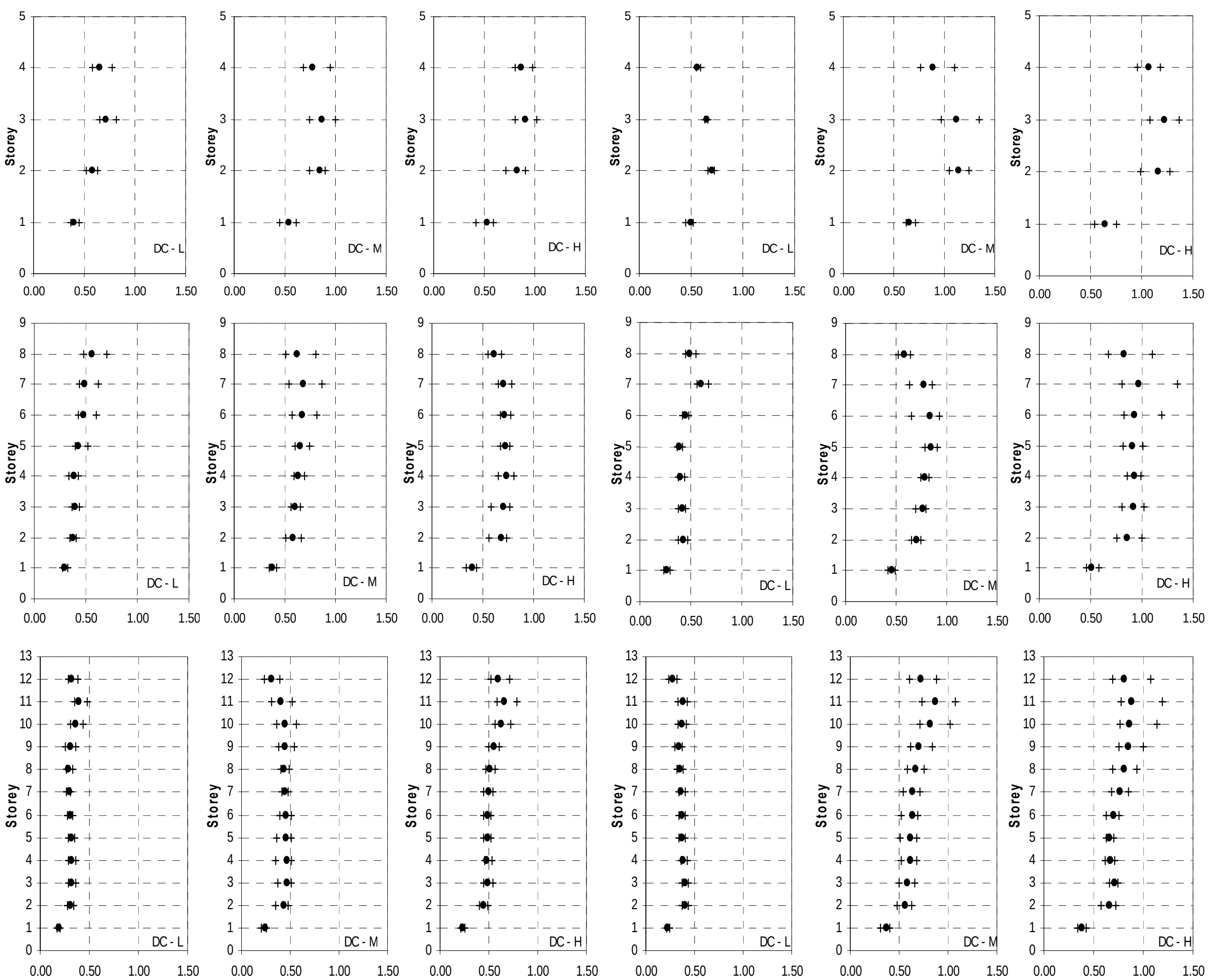

(a) (b)

Figure 8: Minimum-maximum range and mean story drift ratio from 7 time-history analyses under damage limitation (95-yr) earthquake for design PGA: (a) 0.2g; or (b) 0.4g. Top: 4-story frames; middle: 8-story frames; bottom: 12-story frames.

6. REFERENCES

CEN (2003). prEN1998-1: Eurocode 8: Design of structures for earthquake resistance. Part 1: General rules, seismic actions and rules for buildings. Formal Vote version, October 2003.

fib-Fédération internationale du béton (2003). *Seismic assessment and retrofit of RC buildings*. Chapter 4: *fib* Bulletin No. 24, Lausanne.

Panagiotakos T., and M.N. Fardis (2001). Deformations of RC members at yielding and ultimate. ACI Structural Journal, 98, 2: 135-148.

THE DAMAGE CONTROL AND CONSTRUCTION COST OF REINFORCED CONCRETE BUILDING

Shinsuke NAKATA[1]

ABSTRACT

This report is the discussion of seismic device example of reinforced concrete important buildings which can keep enough serviceability of the buildings against giant earthquake. Such criteria of the serviceability is defined that the response story drift angle R which is less than 1/200. Within the limited response story drift, the remaining flexural crack width can be less than 0.2 mm.. In this report two cases are analyzed in this paper as follows

1)Total cost evaluation of buttress strengthening type of existing six story reinforced concrete building which was constructed in 1964

2)Case study on seismic design of seven story reinforced concrete building based on the response drift for serviceability and the cost performance

These two cases are discussed about total cost evaluation ; construction cost and repair cost after giant earthquake. Existing six story reinforced building was constructed forty years ago and It was designed based on the old seismic design standard. Basing on the new seismic index, the seismic performance of this building was judged as unsuitable. After setting buttress to existing building, the elasto-plastic frame analysis and the non-linear dynamic response analysis showed less than the target story drift angle. The buttress strengthening is the most effective and the most economic device. The base isolation system to existing building is also effective on seismic improvement. However the total cost is the most economic in the buttress system from the cost analysis. This paper tries to control damage level by changing structural members due to earthquake input. Considering construction cost and cost of repair works after giant earthquake, the total cost of the building is tried to be clearly evaluated in the life of the building. This research results show the new concept on the damage risk management against giant earthquake. Especially the important buildings e.g. hospitals, governmental offices and firehouses should be designed in higher grade design criteria as shown in this paper.

1 Introduction:

In Japan many important buildings such as governmental offices, police stations, fire stations and hospitals etc are constructed by reinforced concrete. However these old buildings are designed based on the old seismic codes and their seismic performance is not enough.

[1] *Department of Infrastructure Systems Engineering, Kochi University of Technology, Kochi, Japan*

Reinforced concrete buildings which were constructed before 1971 were designed so that their shear failure strength of member is smaller than their flexural strength in many cases. Recent earthquake damages showed their shear failure touching off their collapse. In the Japanese old type reinforced concrete columns will show such shear failure at the story drift angle ; less than 1/200.

So called important buildings can not be opened their inside space during seismic strengthening works. The conventional strengthening works disturb daily business work in the building with noise, soot and smoke. If the working staff in the building try to move another rental building and work daily jobs during strengthening work, it takes much additional cost. Considering these conditions, the buttress strengthening was proposed as the most reasonable method. If this method can be controlled required seismic shear capacity within the limit story drift angle, this will be the most inexpensive method. However this requires extra space for buttress setting. Installation of base-isolation system to existing building takes much cost.

In this paper, the first phase is introduced such buttress strengthening.

In the second phase, damage control of new building is discussed. Reinforced concrete buildings will cover the seismic regulations in each country based on the design seismic force. However such designed buildings will suffer expected damage due to giant earthquakes. In Japan, the philosophy of seismic design criteria is that designed buildings is allowed to be severe damage due to giant earthquake, however they never collapse. Recently there are so many cases that buildings should have good enough performance to keep serviceable functions even if giant earthquakes occur. In this case study, the controlling of severe earthquake damage was focused. Therefore the target of this study is to find out the reasonable design method for the building which remain slight damage due to giant earthquake. Finally comparison of the total construction costs including repair cost after damage among several levels of seismic design criteria. Considering construction cost and cost of repair works after building damage, as the main objective of this research work, the total cost of the building is tried to be clearly evaluated in the life of the building.

2. Buttress Strengthening

a) Details of Target Building

In this analytical work, the governmental office building was selected. This reinforced concrete building has 19 spans in ridge direction and 3 spans in span direction and constructed in 1969 when the old seismic code was used. The required amount of hoop reinforcement was smaller than that in new code. The static elasto-plastic frame analysis for this building showed that 72 columns of total 480 columns were fragile shear failure. Here we adopted buttress strengthening and at the same time the response story drift angle was to be controlled not to occur shear failure.

b) Details of Buttress Strengthening

The outlines of buttress system is shown in Fig.1. The height of the buttress is 21.5 meters, same as the height of existing building and its thickness is 1.0 meter. The required width of the buttress depends on the evaluated subsidence of the foundation of the buttress so that response story drift should remain within the story drift less than shear failure story drift. Considering soil condition, the width of the buttress was designed as 11.0 meters. Connecting buttress system to existing building , the going up of the foundation should be carefully checked . Because this going-up also much effected to the rotation of the buttress system.

The connecting surface between existing building and buttress is fixed with anchor bolts and post-casted concrete mortar. the pedestal foundation piles at the most exterior part of existing building can be one factor for the resistance of uplifting of buttress system against earthquake load. And pile foundation of buttress system is adopted as reinforced concrete pile. Its diameter is 2.4 meters and its length is 15.0 meters. At the base of piles the reinforced concrete mat is set to keep enough protection of settlement of foundation. Fig.2 shows two cases of foundations, case 1 is regular pile system and the case 2 is devised as low depth foundation system. In the real soil condition at the existing building. N-value of soil at 15 meters level was 26 and that at 30 meters level was 40 .

To control uplift of buttress system, case 2 contains reinforced concrete mat was set at the bottom of foundation as counter weight. General dimensions were shown in Fig.2

c) Discussion of Subsidence of Buttress

The allowable story drift of existing building was set up 1.0 cm which is less than the story drift of shear failure of column in existing building. From the dynamic and static response analysis based on the tri-linear restoring force model for reinforced concrete members, the required shear capacity of each story can be calculated so that this building never occur shear failure at this story drift.

Next the subsidence deformation is calculated in the case 1as shown in Fig.2 .In this design buttress itself can be considered as rigid body. Its foundation's rotation is so large and the required shear force causes rotation moment for buttress as 38716 ton・m. This overturning moment is covered by four buttress. Then one buttress will bear the moment, 9750 ton・m. The width of each buttress is 11.0 meters ,then the charged axial force of pile system becomes 886 ton. For such axial force , the amount of subsidence of piles shall be calculated. If the story drift is allowed as 1.0 cm in each story, the subsidence of buttress can be allowed 3.07 cm from geometric relationship. Considering soil condition, the real results of calculated subsidence deformation was 2.85 cm which is less than 3.07 cm. This means the target design subsidence was satisfactory.

d) Discussion of Withdrawal Resistance

From the calculation results , the pull-out force of pile due to the rotation of buttress was 886 ton. Already the subsidence of buttress was solved The factors of counter weight resistance for withdrawal of buttress are listed as shown in Table 1. Uplifting force is 886 ton and the resistance factors are shown in Fig.2 (hatched parts) . The total counter weight becomes 1429 ton which is enough larger than withdrawing force . This means that uplifting of buttress does not occur.

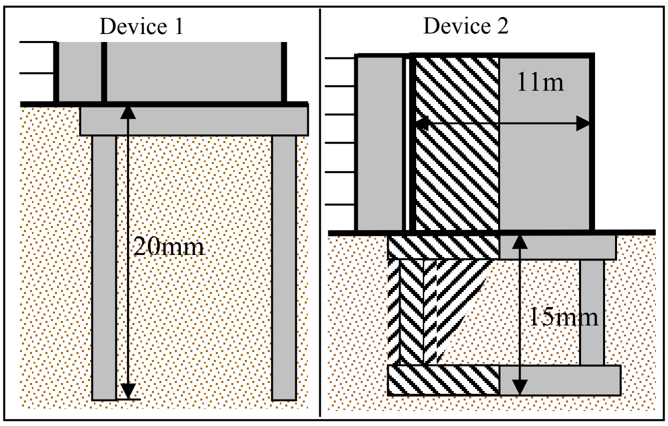

Fig. 1 Buttress Strengthening

Table 1　Counterweight for Withdraw of Buttress

Buttress	283.80
Footing Foundation	31.20
Piles	119.43
Inside Concrete Matt	195.78
Soil	798.79
Total	1429.00

Table 2　Outlines of Cost Evaluation for Each Seismic Improvement (this building)

Type of seismic improvement	Cost (million yen)
Retrofit base isolation	1000～1200
Usual seismic strengthening	200～300
Buttress strengthening	50～100

e) Comparison of Cost to Other Seismic Improvement

The total estimated cost of buttress strengthening is calculated as fifty four million yen included 4sets of buttress which is required for the design .　This estimation is based on the magazine “cost information for construction” (in Japanese)　Table 2 shows the cost comparison of other seismic improvement devices. The buttress strengthening is very inexpensive and setting base isolation is so expensive. Because this work is required very precise level of foundation works during setting base isolation systems. The function of the business works in the building never stops during this foundation works. That is to say, this device has the merit that the business space is secured during this seismic device work. The usual seismic strengthening contains seismic strengthening of existing columns and installation of steel framed brace . The strengthening cost of each column is 0,5 million yen so that shear failure does not occur before reaching flexural failure. Setting steel framed brace into open frame costs 2 million yen. Further the business space can not be available during this strengthening work. They have to move and work another space . This extra cost becomes huge sum which is not included in Table 2.

The buttress strengthening does not disturb business space during this work. Because the buttress is installed outside of the building. Therefore the buttress strengthening will be the most effective and reasonable seismic device if such building has the space for setting buttress.

3. Case Study of Damage Control Due to Giant Earthquakes

a) Analytical Process

The judgment of response story drift and damage grade is based on the elasto-plastic analysis and dynamic response analysis of the non-linear mathematical models of reinforced concrete building. The target original building is the reinforced concrete 7 story building which is designed by existing Japanese seismic design criteria. Changing dimensions of members section (beams, columns and shear walls) and their amount of reinforcements, the response story drifts were compared. In the Japanese seismic design code, severe damage is allowed due to giant earthquakes. However this research target is to find out the possibility to keep in the slight damage which remains within the story drift of the serviceability limit. Finally the cost evaluation is discussed for each combination of structural members. In this case , the cost of repair works after estimated damage was also included.

Fig.2 shows the target building which was constructed as the test building for U.S.-Japan Cooperative Research Program. [1)] This building was used for a series of pseudo dynamic response tests. Therefore the detailed damage situation was recorded in detail for each response story drift. The test building has 3 spans, 6 m, 5 m and 6 m for testing direction and the cross direction has two spans, 6 m and 6 m. The floor slab is 17 m by 12 m. The total height of this building is 21.75 m, the story height of first story is 3.75 m other story 3.0 m. In the central planar the continuous shear wall is arranged for testing direction. The detailed dimensions are listed in Table 3.

Damage controlling was evaluated by damage grade ; response deformation and cracks. In Japan, it is recommended that if the response story drift angle R is less than 1/200, repair works is not necessary. ($R \fallingdotseq \delta / H$, δ: response story drift (cm) H: story height) Further following items are confirmed that the flexural yield does not occur and crack width is less than 0.2 mm and shear failure is never caused. In the dynamic response analysis for the evaluation of such damage grade, seven earthquake input motions were selected. They are all normalized, as maximum velocity is 50 kines.

The integration of cost calculation for constructing structural elements includes expected repair works after damage due to such input earthquakes. The real cost for repair works was based on the data of existing examples. Estimated damage , crack patterns and crack length are derived from the test results.

Table 3 .Structural Members List :mm

	beam		column		Shear wall	
	ends	center	B x D	500x500	thickness	200
B x D	300 x 500		Top	8-D22	Length	500
Top	3-D19	2-D19	Bottom	8-D22	arrangement	Vertical & hor. 2-D10@200
Bottom	2-D19	3-D19	Hoop 2-D10@100			
stirrup	2-D10 @100	2-D10 @100			Connec. Column	500 x 500 8-D22

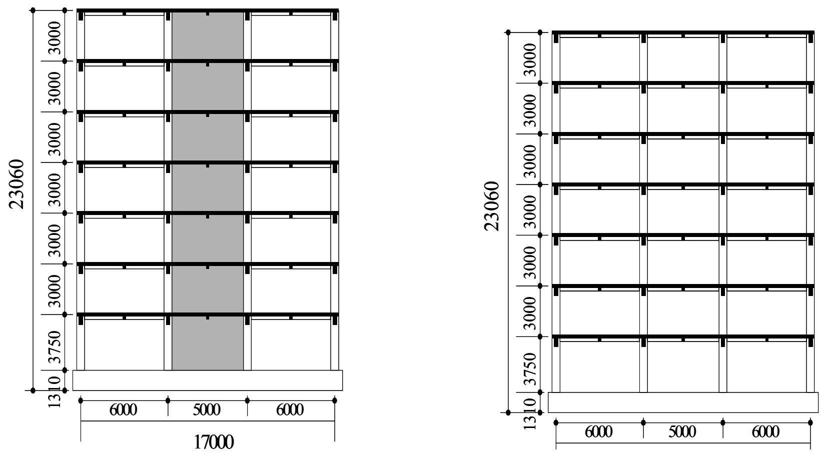

Fig.2 Original Test Building

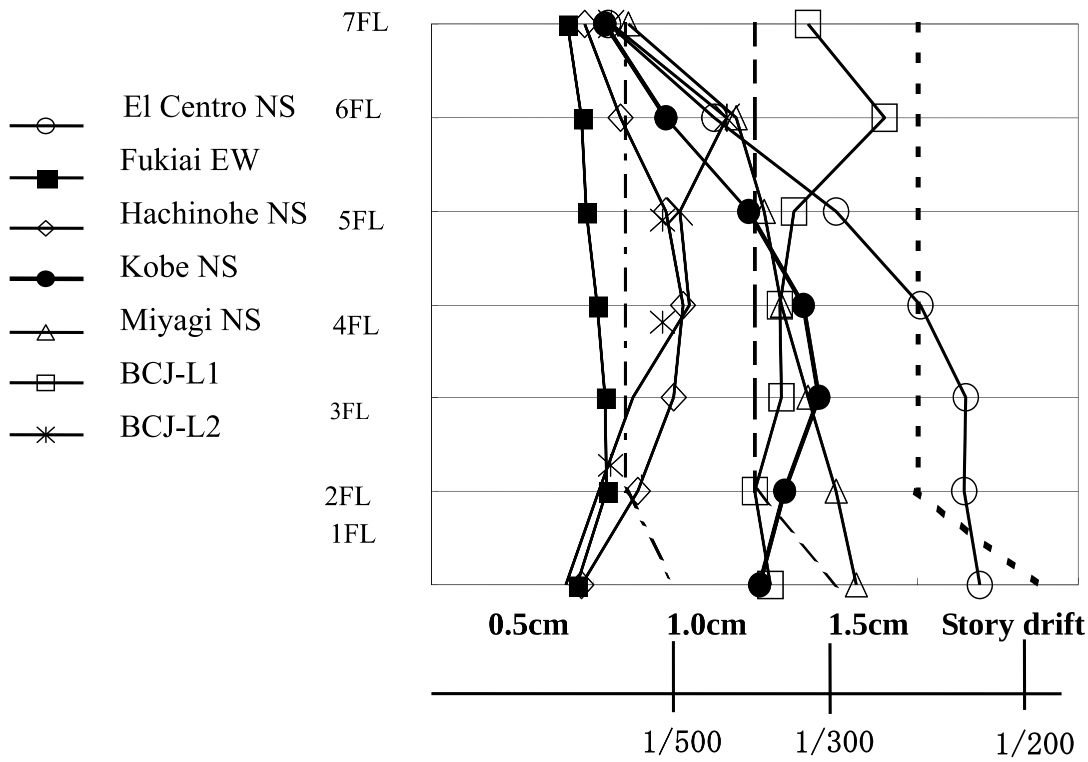

Fig.3 Dynamic Response Story Drift in Case 3

Table 4 Cost Evaluation (unit: 10^4yen)

	Material cost	Constr. cost	Damage grade	Repair cost	Total
Original Bldg.	1877	2488	Severe	9050	11538
CASE 1	2066	2677	Medium	8568	11245
CASE 2	2183	2794	Medium	8568	11362
CASE 3	2538	3148	Slight	1428	4576

b) Analytical Results

Changing dimensions of members section (beams, columns and shear walls) and amount of reinforcements, three cases of building structures are analyzed; CASE 1, CASE2 and CASE3. In CASE 1, the dimension of section of beam was changed to 40cm x 60cm and its reinforcements are 4-D22 (D22; deformed bar ,nominal diameter ;22mm) . Thickness of floor slab is also increased to 18 cm. The calculated shear capacity of CASE 1 building is larger than the original building by around 100 tons (36 % larger). However ,for the strengthening only beam elements, the margin factor of the strength of column to that of beam was smaller then the analytical response showed that some of columns had flexural yield preceding beam yielding. In CASE2, the thickness of shear wall increased to 50 cm from 20 cm and its reinforcements were increased to 2-D16@100mm in vertical and horizontal directions adding CASE 1. The response story drift in CASE 2 exceeded 1/200 and it was not satisfactory with serviceable damage criteria.

In CASE 3 , dimensions of columns were enlarged (column;70cm x70cm) and amount of longitudinal reinforcement of column and beam is also increased (column; 16-D29, beam;4-D29) in addition to CASE 1 and 2. Fig.2 shows the maximum dynamic response story drift in each story. Among them, the third story showed maximum response ratio 1/188 in the El Centro earthquake input. There was no result to exceed the criteria ; 1/200 in other six input earthquakes .the maximum remaining crack width was evaluated 0.05 mm in beams. It was judged that this response results did not reach to the limit of serviceability.

Table 5 Comparison of Material Cost in Each Case ( ): ratio to original

	Original Building	Case 1	Case 2	Case 3
Concrete	358	456(1.27)	485(1.36)	550(1.54)
Casting Form	2864	2832(0.99)	2819(0.98)	3023(1.06)
Reinforcement	33	38(1.15)	47(1.41)	67(2.01)

c) Construction Cost and Cost of Repair Works

The amount of concrete volume and amount of reinforcements were calculated and construction cost was calculated based on the magazine (Japanese) , "Kensetu Bukka (Construction Prices Dec. 2002). This cost is composed of soil treatment, foundation, temporary construction and construction of structural members. And the cost of building equipment and finishing works is not included.

The increased amount of concrete and reinforcements are listed in Table 5. In CASE 3, concrete is 1.5 times and reinforcement is around two times of those in the original building.

From the test results of full scale seven story reinforced concrete building and the case studies of dynamic response analysis, the damage grade was evaluated in each case. The setting up of the repair cost is as follows; 10000 yen / m^2 in case slight damage, 29000yen / m^2 in case small damage and 60000yen / m^2 in case medium level of damage. (refer [3]) The total cost including repair cost is listed in Table 2.

Looking at both construction cost and the evaluated repair cost, those in CASE 1 is smaller damage than that of the original building, however the total cost in CASE 1 become higher than that in the original building. Because both cases showed similar damage grade. The building in CASE 3 which was satisfactory to the damage control criteria showed the most economic result. This analysis is mainly judged by the response story drift angle, 1/200 . If this criteria is focused to the remaining crack width, CASE 1 and CASE 2 showed crack width is larger than 0.2 mm. In the structural member of flexural failure type, the remaining flexural crack width is less than 0.2 mm even if such members experienced flexural failure. That is to say, as long as the structural members don't occur their fragile shear failure, the seismic improvement design for serviceability keeping against giant earthquake will be easier. Through this analytical process, careful design arrangement will be the effective device for the damage controlling of reinforced concrete buildings.

7. CONCLUSIONS

1) The existing six story reinforced concrete building was successfully designed the seismic improvement by adding buttress system. In moderate cost, the buttress system was designed that buttress never occur pull-out and subsidence. From the cost evaluation, the buttress strengthening shows the most inexpensive device.

This type of strengthening can be controlled response story drift against giant earthquakes. This means that this type of seismic device can be easily selected by the owners of buildings. Because the owner can pick up the menu of expected building damage due to giant earthquake.

2) Damage controlling design of reinforced concrete buildings was realized in this case study considering the total cost including expected repair cost at giant earthquake damage. It is suggested that two types of costs consideration from seismic design level and repair works

level should be taken care, if the designer has to expect giant earthquake during their life cycle. Especially when the very important building is tried to be designed, such damage controlling design will be required considering use period of the building.

References

1) Seismic Index Guidelines for Existing Reinforced Concrete Buildings Building Disaster Prevention Association (Japanese) 2001

2) Recommendations for Design of Building Foundations, Architectural Institute of Japan,1991

3) "Cost Information for Construction" (in Japanese) winter 2002

4): Earthquake Effects on Reinforced Concrete Structures U.S.-Japan Research ACI SP-84

5) "Accumulated effect of earthquake damage to life cycle seismic improvement of reinforced concrete buildings" AIJ proceedings, 2002

5) "A Survey Report on Seismic Risk Evaluation for Existing Buildings Based on the Damage Example Database of in Hyougo-ken Nanbu Earthquake " AIJ Technical Report No12,pp 41-46,2001

INNOVATIVE APPROACHES TO PERFORMANCE-BASED SEISMIC REHABILITATION OF CONCRETE BUILDINGS

Troy A. MORGAN and Mason T. WALTERS[1]

ABSTRACT

Current approaches to seismic rehabilitation of concrete buildings now recognize the need to satisfy specific performance objectives. While these performance objectives have been implied in the past, modern rehabilitation guidelines are more explicit in quantifying demand and capacity parameters that must be met to satisfy particular performance goals. This performance-based approach requires rigorous analytical tools, and at the same time provides a means to implement innovative rehabilitation strategies. Specifically, displacement-based evaluation of buildings gives the engineer more flexibility in devising an upgrade that balances stiffness, strength, and ductility to limit displacements to an acceptable level. This paper a) describes current methodologies for rehabilitation of concrete buildings in the context of performance-based engineering, b) outlines the analytical tools commonly used, and comments on their applicability, and c) presents two innovative concrete rehabilitation projects, one buckling-restrained brace and ductile shear wall retrofit, and one seismic isolation retrofit. The applicability of various rehabilitation approaches is discussed, particularly in light of the individual building owner's objectives.

1. INTRODUCTION

Since the inception of prescriptive codes for the seismic design of new buildings, design practices and the provisions that govern them have steadily evolved as the engineering community has come to more thoroughly understand how structures of all types respond to earthquake ground motion. Building codes now recognize the need for controlled yielding in structural elements during an earthquake, and require detailing of the lateral system to develop the anticipated yielding mechanism. As the inelastic response of structures has been studied, the role of displacement capacity has taken on greater significance as a design parameter for structures as a whole, specifically in reinforced concrete construction. The assessment of building seismic performance has come to rely on ground motion demands not considered in the design of a vast majority of existing concrete construction in the United States. Consequently, building officials have long been concerned with the ability of these structures to meet the inherent life-safety performance goals of modern construction. In addition, some building owners require enhanced seismic performance of their facilities, and for a variety

[1] *Forell/Elsesser Engineers, Inc., San Francisco, CA, USA, E-mail: troy@forell.com, Fax: (415) 837-0800*

of reasons are interested in preserving the building's architectural fabric in the process. This has led to the development of numerous strategies for the seismic rehabilitation of existing concrete buildings. As estimates of seismic demand have improved and nonlinear structural analysis techniques have become more robust, so too has the ability to achieve a desired seismic performance goal for an existing structure through innovative means. An innovative approach to seismic rehabilitation often leads to a reliable, cost-effective solution, and sometimes can even create the opportunity for a feasible rehabilitation scheme where traditional strengthening may not be practical.

The purpose of this paper is to describe various innovative approaches to seismic rehabilitation of concrete buildings, focusing on the application of each in achieving specific performance criteria. Two concrete rehabilitation projects are presented to further illustrate the performance-based approaches outlined herein. The first is a university laboratory retrofitted with buckling-restrained (unbonded) braces and ductile shear walls, and the second is an architecturally significant state capitol building to be retrofitted with seismic isolation.

2. OVERVIEW OF INNOVATIVE APPOACHES TO REHABILITATION

2.1. Component-Level Retrofit

An evaluation of an existing concrete building for seismic vulnerabilities may reveal that the seismic system possesses adequate stiffness and strength to limit ductility demands to acceptable levels. However, other critical components of the structure may not be detailed to remain stable under the induced displacements. In the case of slabs, bearings walls, and columns, such a deficiency is a potential life-safety hazard. The identification of this type of deficiency requires analysis beyond the traditional static approach. A more appropriate analysis is a displacement-based demand assessment that estimates maximum inelastic deformations in the primary gravity-resisting elements, then designing an upgrade that permits these elements to remain stable under expected deformations. The displacement demands are often determined through either response spectrum analysis or pushover analysis. These analyses are treated in subsequent sections.

Strategies for remediation of component-level deficiencies include:

- Augmenting column or wall *displacement* capacities through fiber-wrap, steel jacketing, added confining steel/cover concrete.

- Adding reinforcement to slab-column and beam-column joints where negative flexural capacity is often inadequate.
- Providing back-up gravity-resisting elements that become active in the case of a local element failure.

It should be noted that the above-described approaches do not significantly alter the global seismic response of the structure, as very little stiffness, strength, or damping is added as a result. Such retrofit strategies are appropriate where life-safety is the target performance goal at the design earthquake, and project-specific requirements limit the scope of work that can be done.

2.2. Augmenting System Stiffness

Oftentimes, a seismic evaluation will reveal that displacement demands for a structure exceed the acceptance criteria for the building's structural components. This is often the case for antiquated lateral systems designed and detailed using force-based provisions. Since elastic spectral displacements are a function of natural period and damping, one method for reducing displacements is to reduce the period, or increase the stiffness of the structure. This has been a popular approach in the past, but it has several drawbacks. As stiffness of a structure increases, the strength often increases as well, leading to larger mechanism-level forces in the diaphragms, collectors, and foundations. As more components need remediation, construction costs increase dramatically, especially where access is difficult. The increase in stiffness also translates to non-structural anchorage requirements, as floor accelerations will also increase. It has also been demonstrated that significant increases in building stiffness can change the inelastic behavior of the structure, such that there may be amplification of drifts at moderate- to high-levels of ductility demand [Newmark, 1982, Miranda, 2000.] Stiffness is often added to a lateral system in the form of concrete shearwalls, concrete moment frames, or steel braces. Case Study 1 presented herein describes a concrete building rehabilitated through an increase in system stiffness and system ductility capacity.

2.3. Enhancing System Ductility Capacity

In the case where an adequately stiff lateral system is accompanied by brittle hysteretic behavior, an increase in ductility capacity is often warranted. An increase in displacement capacity is tantamount to an increase in ductility capacity where the overall system strength is left unaltered. Techniques for such an increase in displacement capacity are similar to those presented above in Sec. 2.1, applied to elements of the lateral system. It is advantageous to take such an approach since the increase in strength can typically be small, thus limiting the expected demands in diaphragm, collector, and foundation elements.

2.4. Adding Viscous Damping to System

Another effective method of reducing seismic displacements is the addition of viscous damping. This relatively modern technique for rehabilitation generally consists of adding viscous damping hardware to an existing frame through steel braced frames. The frames act as a rigid support against which the damper may react. This technique is only applicable to relatively flexible lateral systems (moment frames), and provides an alternative to increasing the system stiffness. Added viscous damping is advantageous because component displacement demands are reduced without a commensurate increase in forces delivered to the structure. This comes about because of the phase difference between force response in structural elements (which are proportional to displacement) and force response is the damping devices (which are proportional to velocity.)

2.5. Seismic Isolation

In cases where a building owner has exceptional seismic performance goals, the only viable rehabilitation strategy may be seismic isolation. A seismic isolation building retrofit includes the separation of the structure from the foundation system, and the replacement of this rigid plane with a flexible one consisting of isolation hardware. This addition of a flexible plane significantly lengthens the structural period, effectively decoupling the seismic response from the most severe ground motion input. The effect of such a retrofit is that virtually all earthquake-induced deformation occur at the isolation level, and both superstructure inter-story drifts *and* floor accelerations are greatly reduced from their fixed-base condition. Here, a classic dilemma is avoided, namely that while energy dissipation is proportional to displacement, so too is expected structural damage. For an isolated building, there need not be large structural deformations to effectively dissipate the input energy from the ground motion.

Common attributes of isolated existing concrete buildings include the following:

- Possess an Important Function
- Deemed Architecturally Noteworthy
- Enjoy Popularity Among the Public
- Listed on the National Historic Register

Case Study 2 presented herein describes a building possessing all of the above attributes, which is proceeding toward rehabilitation using seismic isolation.

3. ANALYSIS TECHNIQUES

In order to effectively evaluate potential seismic deficiencies in a concrete building, an appropriate analysis must be executed. The analysis should be sufficiently complex to capture the desired performance metrics, but no more complex than necessary. The analyses presented below are routinely performed for a variety of rehabilitation projects, and the process for each is briefly described along with its appropriate usage.

3.1. Linear Static Analysis

The most rudimentary analysis procedure is linear static analysis, a procedure whereby the nonlinear dynamic response is represented by a set of equivalent linear static forces. Current guidelines for seismic rehabilitation [FEMA, 2000] implement a pseudostatic procedure for calculating earthquake response. In this procedure, the lateral seismic loads applied to a structural model represent unreduced elastic demands determined from a 5%-damped response spectrum. These "elastic-level" forces are used for computation of deformations in the structure, a reasonable approach given the general insensitivity of seismic deformations to material nonlinearities. Component acceptance criteria are determined by comparing the elastic demands to a capacity that is increased by a prescriptive factor that accounts for the expected ductility capacity of the element.

This linear static approach is generally sufficient to identify many of the possible deficiencies in a concrete building. Its relative simplicity is its obvious advantage, and the static approach should be one of the first steps in any seismic evaluation. Reliance solely on a static evaluation should generally be avoided where there are mass or stiffness irregularities in the building, velocity-dependent response is expected (i.e. viscous damper retrofit), or a more refined estimate of seismic response parameters is desired. In fact, the benefit of many innovative rehabilitation strategies may not be fully appreciated when viewed through a static analysis due either to the complex characterization of response modification devices, or because the potential cost savings in expected earthquake losses may be underestimated by the conservatism of static results.

3.2. Response Spectrum Analysis

Response spectrum analysis (RSA) provides an improvement over static analysis where significant irregularities exist because the actual linear modes of vibration are considered in computing seismic response. Where the fundamental mode is essentially linear over the buildings height, mass participation is typically substantial in this mode, and the results of RSA do not differ appreciably from those of the static analysis. However, particularly for concrete buildings with soft-story mechanisms, RSA is a valuable tool for evaluating the resulting increased seismic demands, as it weighs the response in various modes based on the spectral shape. RSA does not capture either velocity-dependent response or nonlinear response.

3.3. Pushover Analysis

Nonlinear static (pushover) analysis is often used in the seismic evaluation and rehabilitation of concrete buildings. In this type of analysis, the lateral system of the structure is modeled with nonlinear hinges in components where inelastic behavior is possible. These hinges are generally bilinear with an unloading branch, and are assigned to axial, shear, and flexural degrees-of-freedom. Once the model is complete, a various distributions of static deformations are applied to the structure. These deformations are monotonically increased, and at each displacement step, equilibrium is solved for iteratively, and converged steps are recorded. The results of the analysis are a family of pushover curves, which plot a deformation index (typically roof displacement) against a force/acceleration index (typically base shear.) This relationship is particularly useful in drift-based evaluations since the displacement limits of individual components are apparent from the pushover curve. In addition, the computation of element demands depends on the nonlinear behavior of adjacent structural elements, an important feature of capacity-based design. It is important that an appropriate method is chosen for estimating inelastic displacement demands from a pushover analysis and a response spectrum. The results of the various methods can vary considerably, so it is prudent to apply multiple approaches.

A description of methods for estimating inelastic displacements in multi-story buildings can be found in (Miranda, 2002).

3.4. Nonlinear Response History Analysis

In cases where the expected structural response during an earthquake cannot be adequately captured by one of the above analysis techniques, a nonlinear response history analysis (NRHA) may be employed. Such an analysis is typically in order where response includes gap behavior (foundation rocking or pounding), hook behavior (tension-only elements), velocity-dependent behavior (viscous dampers), and virtually all types of seismic isolation hardware. Such an analysis requires the generation of a suite of acceleration histories, typically selected or scaled to be compatible with a target response spectrum. One important feature of NRHA with respect to performance-based engineering is the incorporation of ground-motion variability into the estimation of structural demands. Modern analytical tools make it possible to evaluate demands under a variety of ground motions and assess the level of reliability of these demand estimates. Since performance-based engineering is inherently a probabilistic framework, it is becoming more important for engineers to assess performance metrics appropriately. NRHA is a useful tool in advancing toward this goal.

4. CASE STUDY 1: UNIVERSITY LABORATORY

4.1. Building Description

This laboratory building was constructed circa 1963 and is comprised of a three-story tower structure atop an expanded two-story basement. The tower portion has a rectangular plan configuration and measures approximately 100 ft (30.8 m) by 160 ft (49.2 m.) The basement portion extends to several adjacent buildings, and has overall plan dimensions of approximately 172 ft (52.9 m) by 215 ft (66.2 m.) Story heights are 15 ft (4.6 m) and 17 ft (5.2 m) for the first two basement levels, 18 ft (5.5 m) for the first (plaza) level, and 12 ft (3.7 m) for the upper two levels. A photograph of the exterior building is shown in Figure 1.

The tower structure roof and floor framing systems are post-tensioned lightweight concrete slabs supported directly on concrete columns and bearing walls. There are no beams, column capitals, or drop panels beneath the slab. The second- and third-floor perimeter slab edges are supported by a cantilevered roof slab by means of high-strength steel tension rods along the north and south ends of the building, and by pre-cast, pre-stressed concrete cladding elements along the east and west ends.

The lateral force resisting system is comprised of the floor slabs, which act as diaphragms, and transfer loads to the stair and elevator core concrete walls, and four large concrete box columns located at the corners of the structure. The walls are typically 10 in. (25.4 cm) thick and act as shear walls, transferring lateral forces down the structure to their foundations. The columns and slabs do not appear to be detailed to act in frame-action, and therefore provide negligible lateral strength.

4.2. Seismic Hazard

The seismic hazard on the University of California, Berkeley campus has been studied and quantified through probabilistic site hazard analysis. The major source of seismic activity on the Berkeley campus is the Hayward Fault, passing directly across the eastern side of campus. A family of ground motion spectra have been developed for earthquake levels EQ-I (72-yr return period), EQ-II (475-yr return period), and EQ-III (970-yr return period.) The acceleration spectra for EQ-II and EQ-III events (the levels of hazard considered for the project) are shown in Figure 2.

The seismic evaluation of the building was conducted in accordance with the University Seismic and Structural Engineering Guidelines. For existing buildings, the criteria prescribes two minimum seismic performance objectives as follows:

1. Life safety performance level for the seismic hazard level EQ-II, where EQ-II corresponds to an earthquake ground motion representation having a 10% chance of being exceeded in 50 years, or an event with a recurrence interval of 475 years; and
2. Collapse prevention performance level for seismic hazard level EQ-III, where EQ-III corresponds to an earthquake ground motion representation having a 10% chance of being exceeded in 100 years, or an event with a recurrence interval of 970 years.

The acceptance criteria for the existing building structure were based on the deformation limits set forth in ATC-40 (Applied technology Council, 1996.) Table 1 lists the key limits that are used for the building evaluation.

Figure 1: Laboratory building prior to commencement of retrofit construction

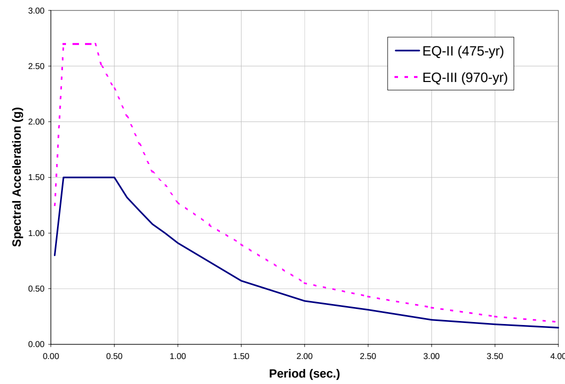

Figure 2: Site-specific ground motion spectra (5% damped)

Table 1: Deformation limits

	ITEM	LIFE SAFETY	COLLAPSE PREVENTION
GLOBAL LIMITS	Maximum total drift	0.02	0.33 x Vi/Pi
INDIVIDUAL ELEMENT LIMITS	Reinforced concrete two-way slabs and slab-column connections, in radians	0.001	0.002
	Reinforced concrete walls controlled by flexure, in radians	0.01	0.015
	Reinforced concrete walls controlled by shear, in radians	0.006	0.0075

4.3. Seismic Deficiencies

A nonlinear static (pushover) analysis of the building was conducted to identify failure mechanisms and to determine maximum inelastic deformations in the existing building components. This required the development of a capacity curve, relating overall lateral strength to lateral displacement, and a demand spectrum, relating spectral acceleration to spectral displacement.

The capacity curves for the building's longitudinal and transverse direction are shown on Figure 3. The behavior of the individual concrete core elements is generally characterized by flexural yielding at the bases of the walls, followed shortly by the onset of rapid shear degradation. Some of the core elements are shear-critical and consequently have limited ductility capacity. The negative slope on capacity curves represents the rapid loss of shear strength in the global structure. Figure 3 indicates that the capacity curves fall significantly short of the demand curves, which can be interpreted as potential for overall structural failure. Other serious seismic vulnerabilities have been identified, including (a) lack of adequate punching shear strength in slab-to-column joints; and (b) lack of seismic drift provisions in the precast cladding hangar connections along the east and west faces of the building.

The slab-to-column joints will be subjected to high moment demands due to seismic loading. These joints, already highly stressed under gravity loads alone, do not have the reserve capacity to accommodate the shear stresses corresponding to the seismic moment demands. A brief analysis indicates that the slabs are expected to reach their ultimate shear capacity at a story drift of approximately 0.5 in (1.3 cm), or .0035 times the story height. This is a drift level that is expected in a moderate earthquake. There is some mild steel passing through the joints, which could mitigate the potential for collapse of a slab section; however, failure of a sufficient number of slab sections may lead to a complete “pancake-type” structural collapse.

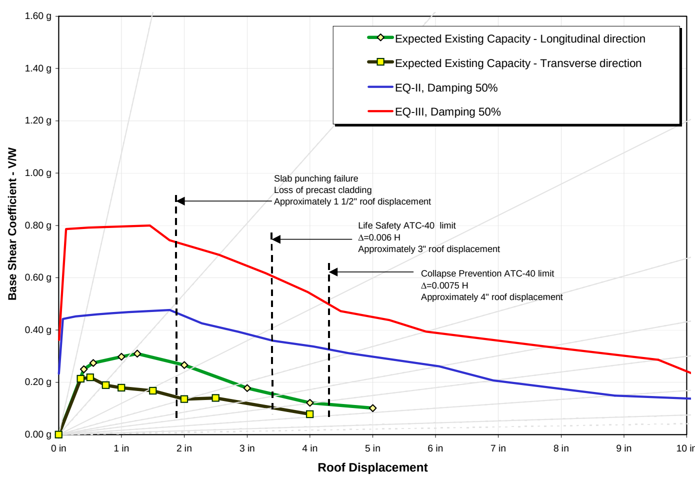

Figure 3: Demand-capacity spectrum for existing building

The precast concrete cladding elements along the east and west walls are stiff and will attract high seismic forces. The cladding provides vertical support of the second and third floors slab edges, and the connections between the precast cladding and slab edges do not have tolerances for interstory movements. At relatively low seismic drift levels, on the order of 0.25 to 0.5 in (0.64 to 1.3 cm), the panels are expected to crack and spall, and the welded panel connections to the slabs are expected to fracture. The panels could ultimately fall off the building on to the plaza level, with the resulting potential for collapse of the perimeter floor slabs.

4.4. Rehabilitation Scheme

The primary objective of the rehabilitation is to maintain life safety under the EQ-II event and collapse prevention under the EQ-III event, and this objective formed the basis for selection of a retrofit scheme. The controlling limits on roof displacement are approximately 3 to 4 in. (7.6 to 10.2 cm) for life safety, and 4 to 5 in. (10.2 to 12.7 cm) for collapse prevention. Other major objectives of the retrofit design include the development of strengthening measures to provide protection to vulnerable slab-to-column joints and precast concrete cladding elements.

A number of seismic upgrade alternatives were studied. The retrofit solutions typically included the introduction of new steel braced frames in the transverse direction and concrete shear walls in the longitudinal direction. The scheme eventually chosen included buckling-restrained braced frames at the north and south ends of the building. The braces are characterized by large deformation capacity and significant energy dissipation that shows little degradation over numerous cycles. The frames are detailed such that the columns do not pass through the slabs so as not to disrupt the existing post-tensioning tendons. The existing concrete box columns adjacent to the steel braces are thickened to provide the frames with continuous chord action for seismic overturning considerations. The capacity curve for the braced frame direction is shown in Figure 4. Concrete shear walls are placed in the east and west ends of the building, and measure approximately 20 ft (6.2 m) long by 20 in. (51 cm) thick. The wall thickness is driven in part by the placement of reinforcing steel that is designed to pass through the slabs without disrupting the existing tendons. The walls are interconnected with steel angle collector elements placed beneath the existing slabs. The walls are founded on mat footings. The capacity curve for the shear wall direction is shown in Figure 5. In addition to the upgrade of the lateral system, special steel collars and ledgers were designed to be placed at all gravity columns and bearing walls to provide a backup system in case of punching shear failure. These supplemental supports act as a way of increasing the slabs deformation capacity without adding stiffness or strength to the overall system.

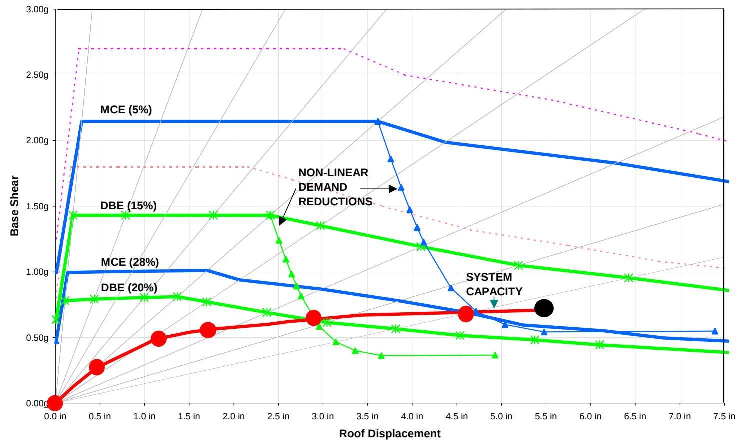

Figure 4: Demand-capacity spectrum for buckling-restrained brace frame retrofit direction

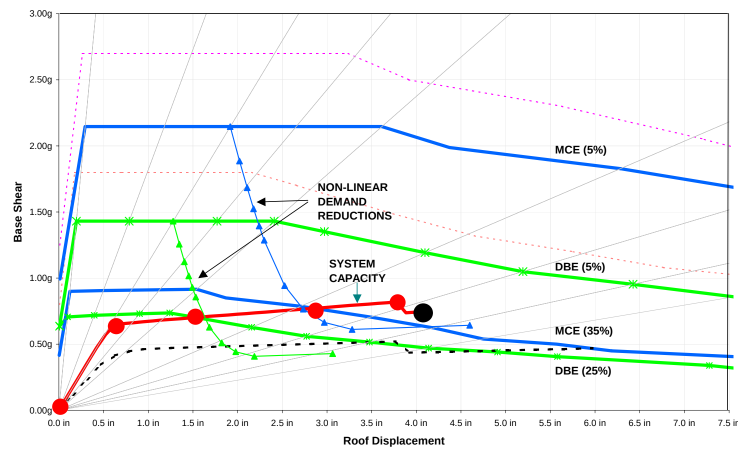

Figure 5: Demand-capacity spectrum for shear wall retrofit direction

5. CASE STUDY 2: STATE CAPITOL BUILDING

5.1. Building Description

The Utah State Capitol building, completed in 1916, is of Beaux Arts style architecture and represents one of the states most recognizable landmarks. The main building measures 404 ft (124.3 m) longitudinally and 240 ft (73.8 m) transversely. The height from the base level to the peak of the dome is 286 ft (88 m.) The building's structural system consists of reinforced concrete floor slabs, beams and columns. The foundation system consists of reinforced concrete spread footings. The drum and dome are concrete shells founded on four large piers that extend to a mat foundation. An exterior elevation of the building is shown in Figure 6.

5.2. Seismic Hazard

The building is located within 50 km of numerous known active faults, all of which have the capability to induce seismic events greater than moment magnitude (M_w) of 5. The most significant of these faults is the 370-km Wasatch fault zone, a normal fault capable of severe ground shaking. At its closest proximity, traces of the Wasatch fault are within 0.5 km of the building site. Based on all known source characteristics, both probabilistic and deterministic seismic hazard analyses were carried out. The probabilistic seismic hazard analysis (PSHA) was used to generate response spectra for various earthquake recurrence intervals. Plots of these spectra are shown in Figure 7.

Since the analysis of isolation systems frequently requires a nonlinear response history analysis, a suite of acceleration histories was developed for the project. Very few historical normal-faulting earthquakes have been recorded by strong motion instruments, and even fewer by instruments close to the source. Consequently, synthetic seismograms were generated using a model based on the physics of fault rupture known as the Composite Source Model (CSM.) The specifics of the CSM are described by (Keaton, 2000.)

Figure 6: South view of state capitol building

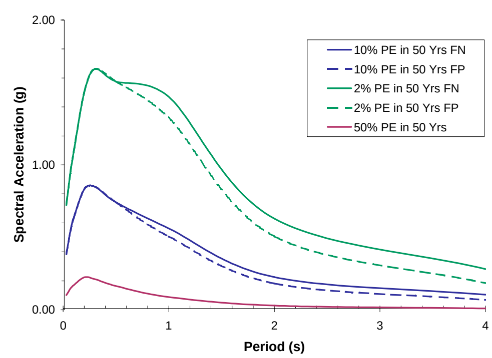

Figure 7: Site-specific response spectra for three recurrence intervals, with directional effects

It can be seen from Figure 7 that the 2%/50 yr. event is significantly larger than the 10%/50 yr. event. This is typical of seismic demands in many of the moderate seismic zones in the U.S. The performance criteria for the building was a minimum of Life Safety in the 10%/50 yr event, and Collapse Prevention in the 2%/50 yr event.

5.3. Seismic Deficiencies

The seismic evaluation of the state capitol building was per the 1991 Uniform Building Code (Seismic Zone 3), and it revealed numerous seismic deficiencies. The building is heavy and is of non-ductile concrete construction. Infill walls are unreinforced masonry and stone, and have very little deformation capacity. As these walls are also quite stiff in comparison to the concrete frame, they tend to attract large seismic demands. The concrete floor and column framing was designed for gravity only, and the strength and detailing do not indicate that it can sustain the large expected displacements following the expected loss of the infill walls. Most columns are tied with 1/4 in. dia. smooth bars at 12 in. spacing. Most beams are not detailed with stirrups and therefore are not confined in a way that permits significant inelastic deformations. The diaphragms, masonry parapets, stone cladding, and dome drum all exhibited poor seismic performance for all levels of earthquake considered. In light of the expected seismic performance, the State decided to proceed with developing options for seismic rehabilitation. This rehabilitation is also part of a larger preservation effort slated for the entire State Capitol including historic preservation and facility upgrade.

5.4. Rehabilitation Scheme

The historic nature of the State Capitol building leads to a complex treatment of seismic demand. The structural elements are brittle, and therefore deformation-sensitive, while the historic fabric, including stone, marble, and masonry, is not well-anchored, and therefore acceleration-sensitive. The majority of even the most modern techniques for seismic retrofit can reliably limit only one of these two damage indices. In addition, the architectural preservation requirements of the project made intrusive structural work complex and potentially impossible. Retrofit options considered included a) new perimeter shear walls and diaphragm/collector strengthening and b) seismic isolation. Seismic isolation was chosen for the enhanced seismic performance and the significantly reduced disruption to the buildings architectural fabric.

The design of the isolation system considers three types of isolation hardware: a) lead rubber bearings, b) high-damping rubber bearings, and c) friction pendulum bearings. The final isolation system will be chosen through a competitive bid process. The behavior of the building after isolation is expected to be essentially elastic in the 10%/50 yr earthquake, and show minimal cracking and nonstructural damage in the 2%/50 yr event. This is a significant improvement of the original minimum performance objective. New concrete shear walls will be added at the interior of the building to add stiffness and reduce diaphragm demands. Some perimeter shotcrete will be added to improve the deformation capacity of the concrete pier-spandrel framing at the exterior windows. The dome drum will also have shotcrete added around the window openings to improve overall shear capacity. Maximum isolator displacements are 8 in. (20.3 cm) and 21 in. (53.3 cm) for the 10%/50 yr and 2%/50 yr events, respectively. The corresponding acceleration profiles for each level are shown in Figures 8 and 9, and for each of the three types of isolation hardware. The most significant modification to the building will be the addition of an isolation plane at the base of the building, including alterations to the foundations and mechanical/plumbing systems. This project is currently in design, and the contract document phase commenced as of the time of this writing.

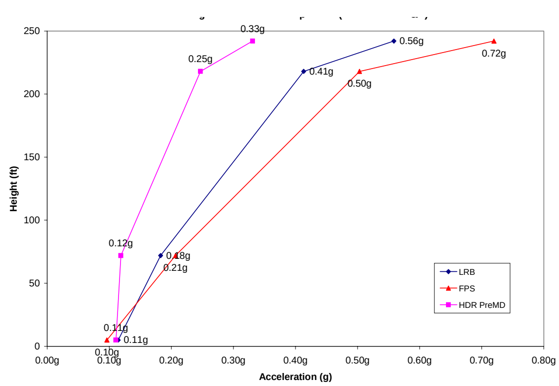

Figure 8: 10%/50 yr acceleration profile

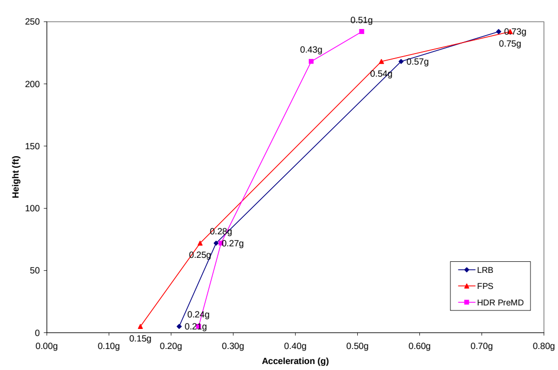

Figure 9: 10%/50 yr acceleration profile

6. CONCLUSIONS

This paper has the purpose of outlining how concrete buildings are now being evaluated and rehabilitated using performance-based engineering. This new methodology has given the engineer greater flexibility in developing a seismic solution best tailored to the specific building and corresponding performance objectives. Rigorous analytical tools have also made creative and innovative approaches to rehabilitation possible. Two projects have been briefly presented to highlight the ways performance-based engineering has been applied to existing concrete buildings, and to contrast the features of each building that lead to different rehabilitation approaches. As performance-based engineering continues to become increasingly accepted as a useful methodology for seismic evaluation and rehabilitation, solutions which limit the hazards posed by existing buildings will become more efficient, reliable, and economical.

7. REFERENCES

Applied Technology Council. (1996). *ATC 40: The Seismic Evaluation and Retrofit of Concrete Buildings*, 2 Volumes, Redwood City, CA.

FEMA 356: Prestandard and Commentary for the Seismic Rehabilitation of Existing Buildings (2000). Federal Emergency Management Agency, Washington, D.C.

Keaton, J. R. (2000). Synthetic Seismograms for Normal Faulting Earthquakes Using the Composite Source Model, Earthquake Engineering Research Institute Professional Fellowship Report for 1999, Oakland, CA.

Miranda, E. and V. V. Bertero. (1994). Evaluation of Strength Reduction Factors for Earthquake-Resistant Design, *Earthquake Spectra*, vol. 10, no. 2, Oakland, CA.

Miranda, E. and J. Ruiz-Garcia,. (2002). Evaluation of approximate methods to estimate maximum inelastic displacement demands. *Earthquake Engineering & Structural Dynamics*, 31, 3.

Newmark, N.M. and W.J. Hall. (1982). *Earthquake Spectra and Design,* Earthquake Engineering Research Inst., Oakland, CA.

KEYWORDS

Seismic evaluation, rehabilitation, base isolation, unbonded brace, pushover analysis

SESSION 1-B: EVALUATION OF STRUCTURAL PERFORMANCE

Chaired by

♦ Marc Eberhard and Hitoshi Shiohara ♦

SUBJECTS OF ANALYTICAL RESEARCH TOWARD PERFORMANCE EVALUATION DESIGN OF RC STRUCTURES

H. NOGUCHI[1]

ABSTRACT

The seismic design provisions for a beam-column joint in the AIJ Guidelines are based mainly on earlier experimental studies. However, it is necessary to establish a more rational performance evaluation design especially for joints subjected to two directional seismic forces. This can be accomplished by the analytical study of stress transfer mechanisms of joints. In order to understand the damages of concrete in the joint, accumulated absorbed strain energy of concrete and reinforcement elements was calculated from the FEM analytical results. It is very important to discuss the stress transfer mechanisms and evaluate the damages of concrete and reinforcement in the joint toward the establishing of a more rational performance evaluation design of RC structures.

1. INTRODUCTION

Beam-column joints in reinforced concrete (RC) buildings are generally subjected to forces in two orthogonal directions during an earthquake. The structural performance of the joint under such seismic forces has not been understood clearly and rationally in previous studies. The stress transfer mechanisms of the joint are 3-D problems, and the joint is confined by its lateral reinforcement, transverse beams, slabs and a column axial force. It is necessary to understand the structural performance of the joint subjected to two directional seismic forces, not only by experimental studies but also by using 3-D analytical techniques.

Design Guidelines for Earthquake Resistant RC Buildings Based on Ultimate Strength Concept, published by Architectural Institute of Japan (AIJ Guidelines), suggests that 3-D interior beam-column joints should be independently designed for two principal directions. The seismic design provisions for joints in AIJ Guidelines are based on earlier experimental studies. However, it is necessary to establish a more rational performance evaluation design for joints under two directional seismic forces. This can be accomplished by the analytical study of stress transfer

[1] *Department of Design and Architecture, Faculty of Engineering, Chiba University, Chiba, Japan*
Email: noguchi@faculty.chiba-u.jp

mechanisms of joints. In order to understand quantitatively the damages of concrete and reinforcement in a joint, moreover, accumulated absorbed strain energy of concrete and reinforcement elements in FEM analysis was calculated. It is very important to discuss the stress transfer mechanisms and the damages of concrete and reinforcement in a joint to develop a more rational performance evaluation design of RC structures.

2. THREE-DIMENSIONAL FEM ANALYSIS OF RC BEAM-COLUMN JOINTS SUBJECTED TO TWO DIRECTIONAL LOADINGS

In this research, the beam-column joint having lateral beams and slabs was considered. The specimens receive two directional loadings. For evaluating the influence of two directional loadings, lateral beams and slabs in the analysis, three-dimensional nonlinear FEM analysis was carried out.

The investigation was done for obtaining fundamental data regarding the influence of lateral beams, slabs and two directional loadings (forty five degree directional loadings). In addition, the purpose of the investigation is to research the earthquake-proof efficiency of the joint. This section is the report regarding experimental and analytical summary.

2.1 Outline of FEM Analysis

2.1.1 Reference specimens

Specimen BJ-3D-0, beam-column joint with lateral beams was tested by Nakano and Tachibana (Tachibana,1998), and the Specimen J-12, beam-column joint with lateral beams and slabs was tested by Shiohara (Shiohara, 1993). And this paper reports the influence of two directional loadings, lateral beams and slabs in the analysis. Dimension and reinforcement arrangement of the Specimen BJ-3D-0 and the Specimen J-12 are shown in Fig. 1. In addition, the property of the used materials is shown in Table 1. The Specimen BJ-3D-0 is a 1/2.5 scaled three-dimensional

Table 1 Character of the Material

Specimen		J-12	BJ-3D-0
(a)Beam	Section	24cm ×32cm	24cm ×36cm
	Upper Bars	10-D13	4-D19+4-D16
	Bottom Bars	10-D13	4-D19+2-D16
	Shear Reinforcement	2-D6@50	2-ϕ10@75
(b)Column	Section	30cm ×30cm	34cm ×34cm
	Main Reinforcement	20-D16	24-D19
	Shear Reinforcement	3-D6@50	2-ϕ10@65
(c)Joint	Shear Reinforcement	2-D6×5 @50	2-ϕ10@55
(d)Slab	Type of Reinforcement	SD35	
	Bar Arrangement	D6@150S	

Specimen	Reinforcement		Yield Strength (MPa)	Tensile Strength (MPa)
BJ-3D-0	SD345	D19	464	725
	SD345	D16	487	766
	SD345	D10	410	564
	KSS-785	ϕ10	929	1052
J-12	USD685	D13	711	949
	USD980	D16	973	1058
	USD780	D6	800	950
	SD345	D6	399	501

Compressive Strength of Concrete	BJ-3D-0 σ_b=42(MPa)
	J-12 σ_b=60(MPa)

beam-column joint. The beam span is 2,500mm and interstory height is 1,614mm. The dimensions of the beam and column are 34cm x 34cm and 24cm x 36cm, respectively. The Specimen J-12 is a 1/2.5 scaled three-dimensional slab-beam-column joint. The beam span is 2,700mm and interstory height is 1,400mm. The dimensions of the beam and column are 30cm x 30cm and 24cm x 32cm, respectively. Thickness of slabs is 6cm.

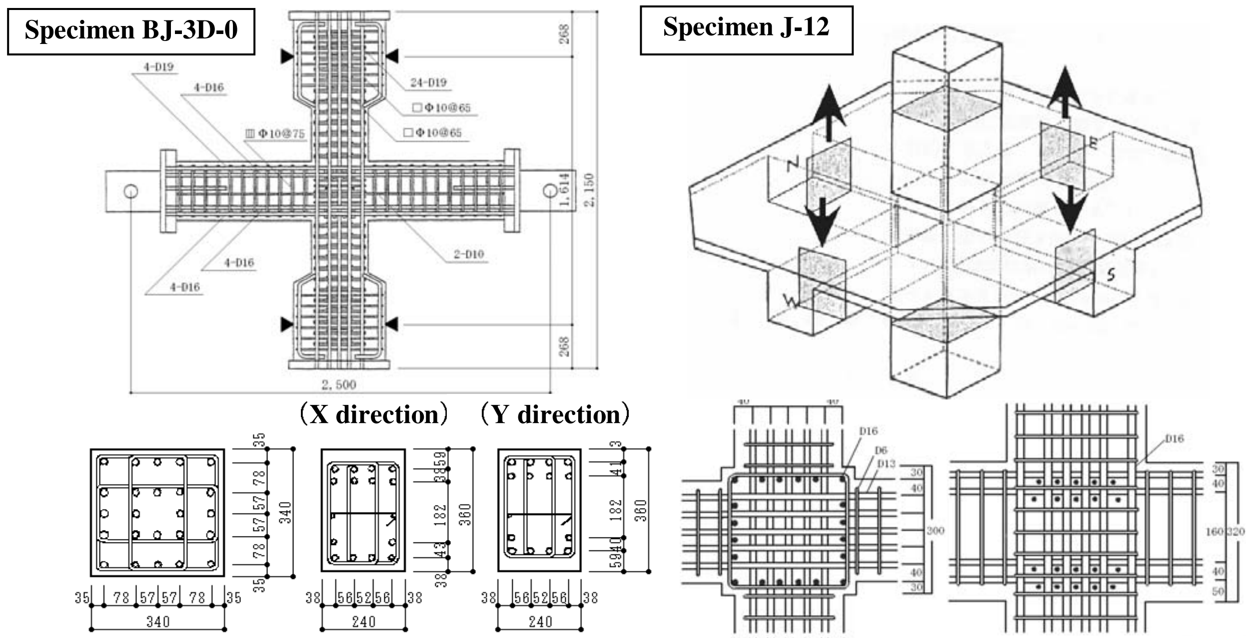

Fig.1 Dimension and Reinforcement Arrangement of Specimens BJ-3D-0 and J-12

2.1.2 Loading method

In the test, reversed cyclic loads were applied to two beam-ends of the Specimen BJ-3D-0, with constant axial force of 2840kN (=0.59 σ_B : σ_B =concrete compressive strength) on the top of a column. Loading patterns of horizontal force are shown in Fig. 2, in both directions with the displacement-controlled drift angle R=1/250, 1/100, 1/50 and 1/25rad. The reversed cyclic loading was done. Finally monotonous loading was done till R=1/15rad on both directions simultaneously. In the test, reversed cyclic loads were applied to two beam-ends of the Specimen J-12, with constant axial

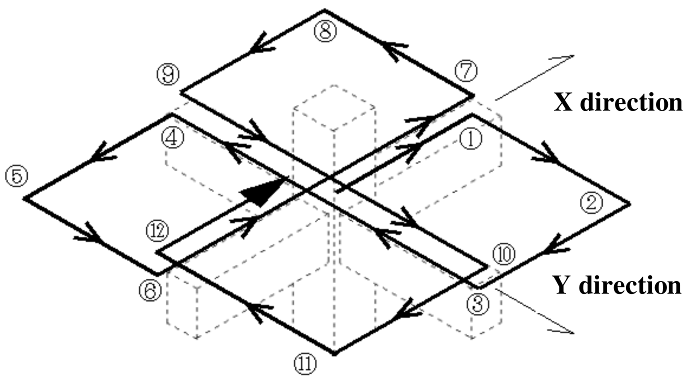

Fig.2 Loading Patterns

force of 1590kN (=0.30σ_B) on the top. Loading patterns of horizontal force are shown in Fig. 2. The drift angle R is 1/200, 1/100, 1/50 and 1/33, 1/25rad.

2.1.3 Experimental results

The beam flexural yielding before joint shear failure was observed in both Specimens BJ-3D-0 (R=1/50rad) and J-12 (R=1/33rad) in the test. Therefore, both specimens were considered as the beam flexural yielding type.

2.1.4 Analytical method and material models

The analysis was carried out by using a three-dimensional nonlinear FEM program developed by Uchida and Noguchi (Uchida and Noguchi, 1998). The boundary conditions for the top and bottom of the column and beam ends were set up according to the experiment. In the analysis, monotonic loads were applied to the ends of beams in specimens. The following materials models were introduced into the FEM program. Concrete was represented by 8-node solid elements. The failure was judged by the five parameter criterion which was added two parameters to the three parameter criterion proposed by Willam and Warnke. The five parameters were decided from the panel experiment by Kupfer et al. The Saenz model (Specimen BJ-3D-0) and the Fafitis-Shah Model (Specimen J-12) were used for the ascending compressive stress-strain relationships of concrete. Confined effect by lateral reinforcement on the compressive descending stress-strain relationships were represented by the Kent-Park model. Longitudinal and lateral reinforcement of columns and beams were modeled by linear elements. The stress-strain relationships of the longitudinal and lateral reinforcement were assumed to be bilinear. The bond between the longitudinal reinforcement and concrete was assumed as perfect. The slippage of beam longitudinal reinforcement through a joint was not considered.

2.2 Outline of FEM Analysis of 3-D Beam-Column Joint with Lateral Beams

2.2.1 Modeling of analysis

The modeling of specimens is shown in Fig. 3. The beam main reinforcement was two layers of bar. But in order for beam flexural yielding moment to become equal, it was changed into one layer of bar. Shear reinforcement was arranged in order for shear reinforcement ratio to become equal. The boundary condition was set up according to the experiment. After the constant axial force loading, the anti-symmetrical vertical directional loads were subjected to the beam ends. This is the same as the experiment. In the experiment the reversed cyclic loading was carried out, but in the analysis one and two directional loading were carried out with monotonic loading. The concrete and reinforced material characteristics were set up according to the experiment.

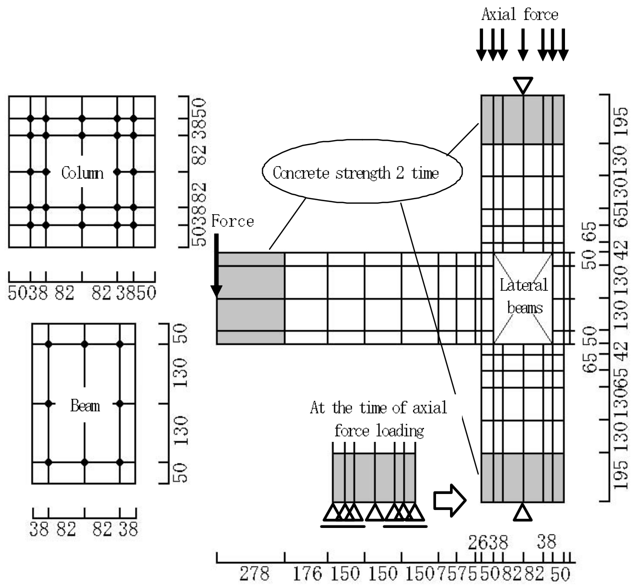

Fig.3 Modeling of Specimens

2.2.2 Analytical results

2.2.2.1 Restoring force characteristics

The analytical story shear force - story displacement relationships and the calculated story shear forces at the beam flexural yielding are shown as compared with the test results in Fig. 4. Although the experimental hysteresis curve is X-direction, the story displacement of X-direction in each cycle was increased by Y-directional loading. The broken line in the figure shows the experimental envelope curves in the state where the story displacement of X-direction increased. This broken line shows the envelope curves at the two directional loading. The analytical initial stiffness was higher than the experimental one. The analytical maximum story shear force (Px = 233.3 kN) of X-directional loading were higher than the test results (Px = 202.9 kN) about 11 percent. The analytical maximum story shear force (Px =180.4 kN) of two directional loading corresponded to the test results (approximately Px = 175 kN). The yielding of beam longitudinal reinforcement was observed in the analysis, and the stress condition of joint concrete elements did not reach strain softening after the peak stress at the maximum story shear force. It was recognized that the analytical failure mode was beam flexural yielding, and it was corresponding to the test result.

The analytical story shear force - story drift angle of the joint and the test result are shown in Fig. 5. In Fig. 5 as well as Fig. 4, the broken line shows the experimental result of two directional loading. The behavior of X-direction loading and two directional loading corresponded to the test results.

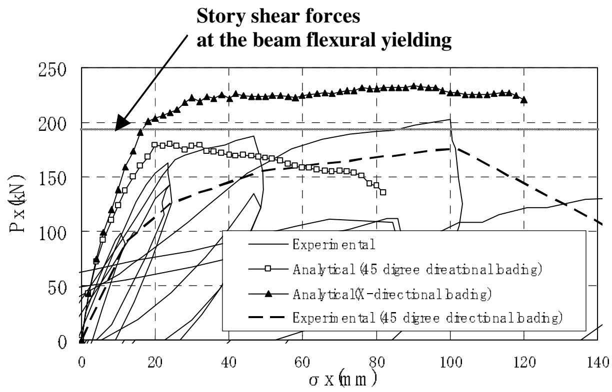

Fig.4 Story Shear Force –
Story Displacement Relationships

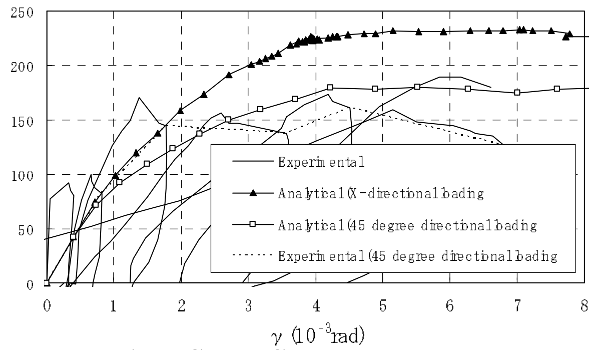

Fig.5 Story Shear Force –
Story Drift Angle of the Joint

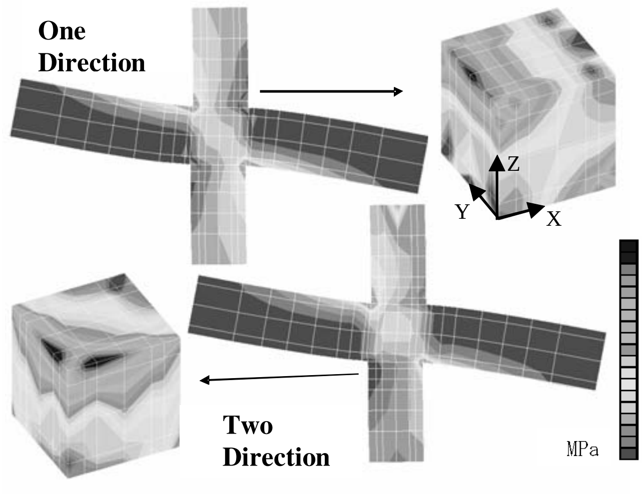

Fig.6 Principal Compressive Stress
Contours of Whole Frames
and Beam-Column Joints
at the Maximum Strength

2.2.2.2 Stress transfer mechanisms

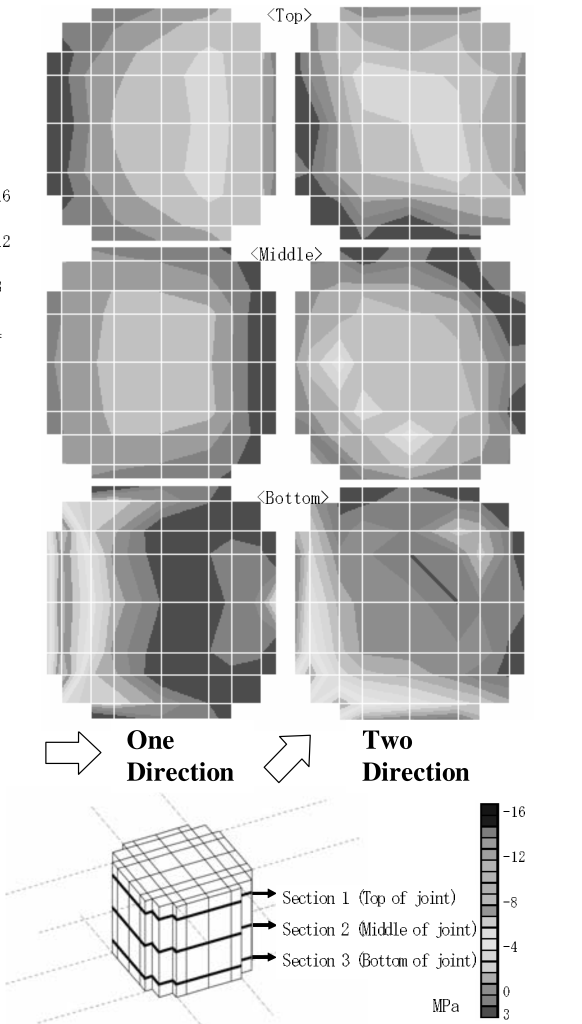

Fig.7 Principal Compressive Stress
Contours on the Joint Horizontal Section
at the Maximum Strength

Figure 6 shows the principal compressive stress contours of whole frames and beam-column joints. Magnification ratio of the deformation is 30 times. Compressive stress flow (compression strut) of the diagonal direction is observed in the joint. Figure 7 shows the principal compressive stress contours on the joint horizontal sections of the joint concrete nearly at the story drift angle of

1/100rad. Though the compressive stress is concentrated at the center of the middle section of the joint, it is concentrated near at the beam critical section (at right side) on the top and bottom section of the joint. From this observation, it is recognized that the inclined compressive struts are formed. In the case under two directional loading, the compressive stresses are transferred uniformly and widely in the joint to two beams. But in the case under one-directional loading, the compressive strut width decreased at the center of the joint from the wide compressive strut width at the area near to the beam.

2.3 Outline of FEM Analysis of 3-D Beam-Column Joint with transverse beams and a slab

2.3.1 Modelling of Analysis

Figure 8 shows the modelling of the Specimen J-12. Two layers of beam main reinforcement in Specimen J-12 were changed to one layer, similar to Specimen BJ-3D-0. The boundary condition was applied in the test. The material characteristics were given according to the experiment. In the experiment the reversed cyclic loading was carried out, but in the analysis one and two directional loadings were carried out with monotonic loading.

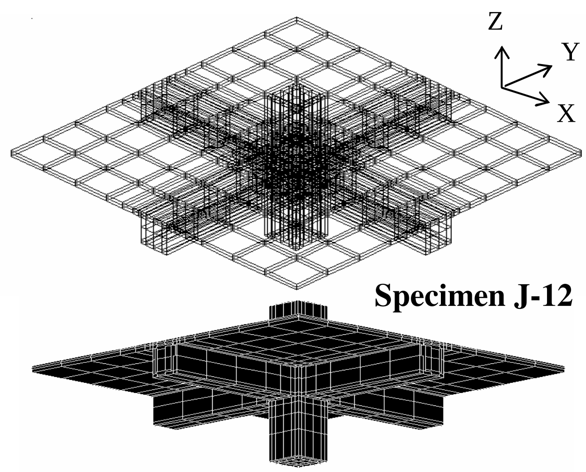

Fig.8 Finite Element Idealization

2.3.2 Analytical results

2.3.2.1 Story shear force-story displacement relationships

The analytical story shear force-story displacement relationships of both one and two directional loadings are shown as compared with the test results in Fig. 9, respectively. The analytical initial stiffness was higher than the experiment.

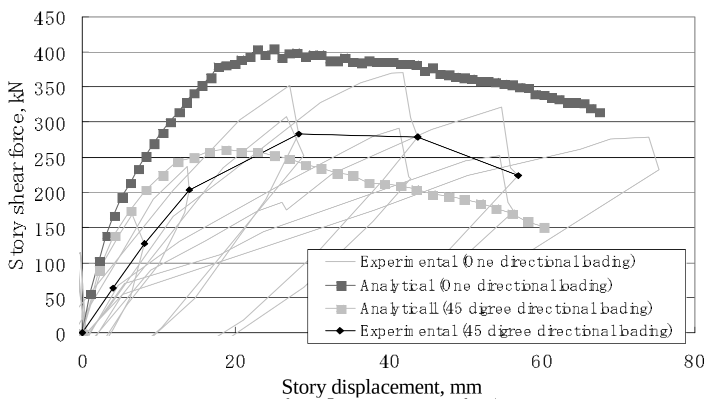

Fig.9 Story Shear Force-Story Displacement Relationships

It is considered that this was due to the local flexural crack on the critical section of the beam and the bond-slippage behaviour between beam longitudinal bars and concrete in a joint, which were not taken into account in the model. The analytical maximum story shear force of 404kN of one directional loading was higher than the test results of 370.7kN about 8.2%. In the analysis as well as the experiment, the beam flexural yielding before joint shear failure were observed both in the case of one and two directional loadings.

2.3.2. Stress transfer mechanisms

At the maximum story shear force with one and two directional loadings, the contour of compressive principal stress at the vertical section of whole frame is shown in Fig. 10, and the contour of compressive principal stress of joints is shown in Fig. 11. In addition, Fig. 12 shows the contour of compressive principal stress at the horizontal section of joints. From Fig. 10, in the case of one directional loading, a wide compressive strut is formed at the joint entrance. But its width becomes narrow in the joint center, and the stress concentrates at the center. It is recognized that compressive stress is transmitted widely to the joint through two beams with two directional loading.

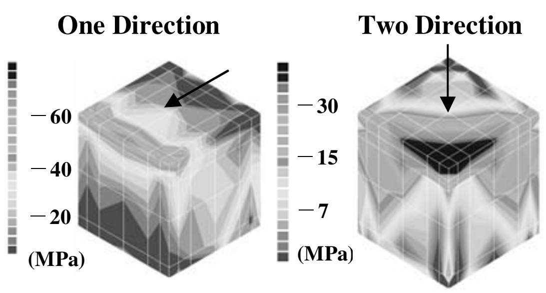

Fig.11 Compressive Principal Stress of Joints at the Maximum Strength

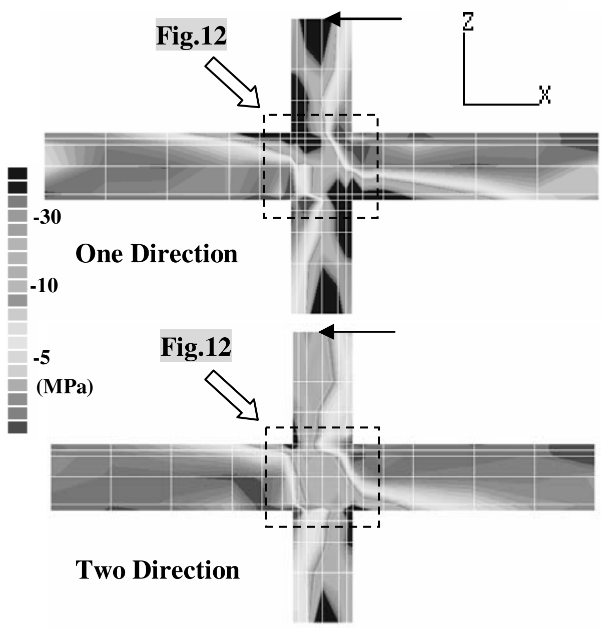

Fig.10 Compressive Principal Stressmum Strength

In Fig. 12 in the joint central part on one directional loading compressive stress is concentrated at the center. Because of the stress concentration near the end surface of the beam at the joint top, it is understood that the diagonal compressive strut is formed in the joint. Figure 13 shows the contour of compressive principal stress of slabs. Stress states showed the mountain shaped and the butterfly shaped distributions with one and two directional loadings, respectively. In the Specimen J-12, the slab effective width of RC standard (AIJ) is 72cm and the thick line in Fig. 13 shows that. As for both one and two directional loadings, it is understood that compressive stress is concentrated within the effective width of a slab.

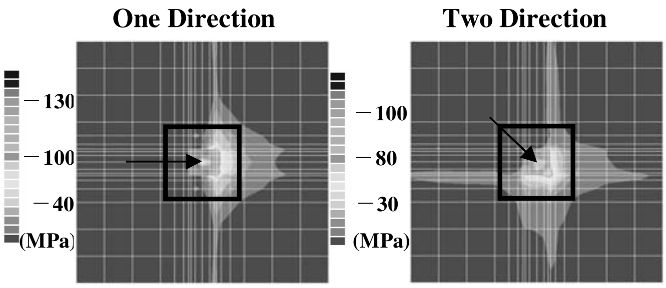

Fig.13 Compressive Principal Stress of Slab at the Maximum Strength

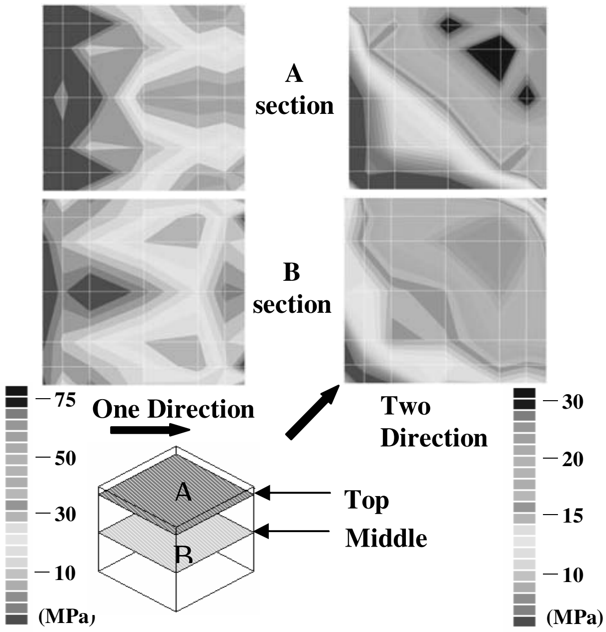

Fig.12 Compressive Principal Stress of Horizontal Section of Joint at the Maximum Strength

2.3.2.3 Accumulated Absorbed Strain Energy of Reinforced Concrete

As for the ductility of RC structures and members, it is known that the ductility changes mainly with the past load history. With the increase of cyclic loading number, even in the loading of fixed displacement, the decrease of stiffness and strength is observed. Then, from the viewpoint of energy, the trial to evaluate the seismic safety of the structure is done recently. In the research by Uomoto et al. (Uomoto et al., 1993), in spite of differences of loading history, flexual failure typed beam specimens failed at the identical value of accumulated absorbed strain energy. As for the same failure mode, the possibility of presuming numbers of the reversed cyclic loads untill the failure by the accumulated absorbed strain energy was shown.

In addition, in the research by Suzuki et al. (Suzuki et al.,1994), the technique for predicting the degree of damage was suggested as an index by the accumulated absorbed strain energy. Furthermore the application was tried to evaluate the level of the reliability of RC structures. In the research, it is indicated that the accumulated absorbed strain energy is the quantity which corresponds to the damage of RC structure. For grasping the detailed damage development analytically until the final state of the RC structure and its performance evaluation. It is important that quantitative evaluation by accumulated absorbed strain energy of concrete element, hoop element and all of element in specimen. The visual evaluation by accumulated absorbed strain energy of concrete element, hoop element is also important. Furthermore by displaying the accumulated absorbed strain energy as the total system of reinforced concrete in the figure of contour, it becomes possible to understand the concentricity of the damage as the total system of reinforced concrete. The definition of the accumulated absorbed strain energy is shown in Fig. 14.

Definition

$$U = \int_V \{\varepsilon\}^T \cdot \{\sigma\} \cdot dV$$

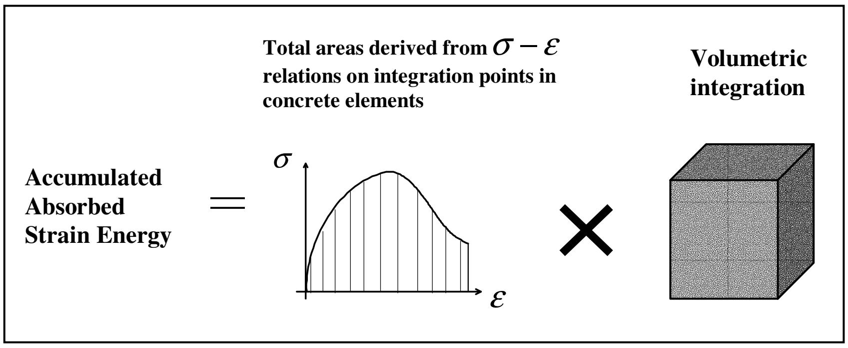

Fig.14 Definition of Accumulated Absorbed Strain Energy

The strain energy distribution as the reinforced concrete sistem at the maximum strength of the Specimen J12 is shown in Fig. 15. In the figure, it is recognized that the tensile energy of concrete is about 1/100 times in comparison with the compressive energy. In addition, the strain energy of tensile reinforcement is recognized from the vertical section of the beam.

It is observed that strain energy distribution of the joint has become asymmetric in the top and bottom. Because of the slab effect, the energy of tensile reinforcement side where the slab is not attached is larger than the energy of tensile reinforcement side where the slab is attached. And the beam main reinforcement of the joint works as a truss mechanism and stores the strain energy there. Therefore, the strain energy of the tensile reinforcement side where the slab is not attached in the joint is higher. The strain energy of compressed side in the joint was observed, but there is a difference of energy of 50 times or more in comparison with the tensile side in the joint.

In the future, it is necessary to consider the performance evaluation method and how to define the degree of damage by making good use of the accumulated absorbed strain energy.

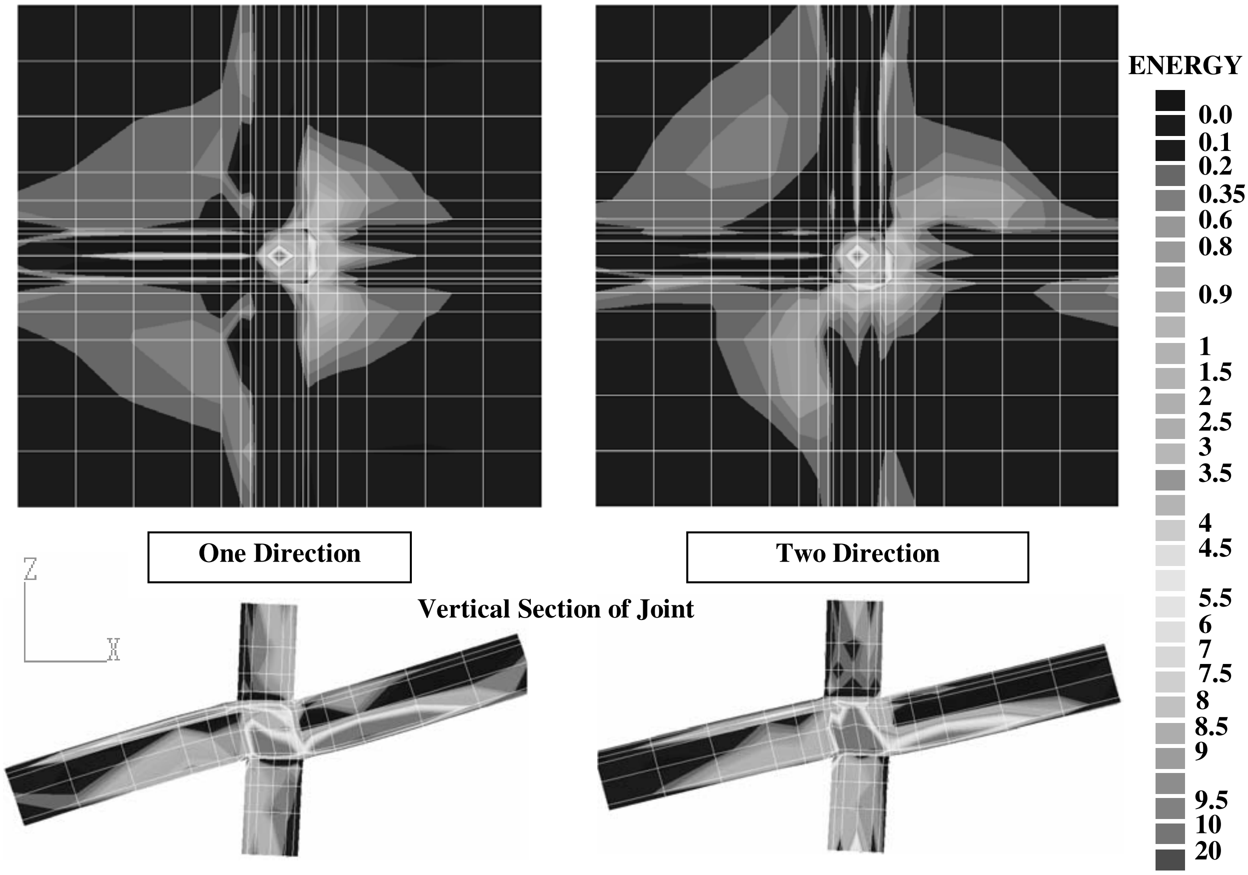

Fig.15 Distribution of Accumulated Absorbed Strain Energy of Specimens

3. CONCLUSIONS

In order to investigate the effect of lateral beams and slabs on the seismic performance of beam-column joints under one and two directional loadings, three-dimensional FEM analysis was carried out (Horibe, Kusakabe, Kashiwazaki and Noguchi, 2003).

The following conclusions can be derived:

(1) Analytical initial stiffness was slightly higher than the experimental one. But comparing with the test results, the ductility showed a satisfactory correspondence.

(2) It was possible to grasp the difference of a principal compressive stress state in the joint and slabs under one and two directional loadings.

(3) It was recognized that the principal compressive stress was concentrated on the effective width of a slab.

(4) It was possible to grasp the differences of the accumulated absorbed strain energy as the RC in a joint and a slab under one and two directional loadings.

4. REFERENCES

Architectural Institute of Japan (1990). Design Guidelines for Earthquake Resistant Reinforced Concrete Buildings Based on Ultimate Strength Concept.

Horibe, A., Kusakabe, M., Kashiwazaki, T. and Noguchi, H. (2003). Three-dimensional FEM Analysis of RC Beam-Column Joints Subjected to Two Directional Loadings, *Summaries of Technical Papers of Annual Meeting of Architectural Institute of Japan, C-2*: 469-474.

Nito, Y., Yoshimura, T., Hukazawa, K., Tachibana, M., and Nakano, K. (1994). Effect of Bi-Directional Loading on Crack Behaviour of Inner R/C Structure under Bi-Directional Earthquake Motions, *Summaries of Technical Papers of Annual Meeting of Architectural Institute of Japan, C-2*: 507-512.

Suzuki, M., Akakura, Y., Adachi, H., and Ozaka, Y. (1994). Evaluation of damage index of reinforced concrete structure, *Summaries of Technical Papers of Annual Meeting of Japan Society of Civil Engineers, No.490/V-23*: 121-129.

Tubosaki, H., Oka, K., Hurukawa, J., and Shiohara, H. (1993). Evalution of slab-beam-column joints subjected to bidirectional loading, *Summaries of Technical Papers of Annual Meeting of Architectural Institute of Japan*: 877-882.

Uchida, K. and Noguchi, H. (1998). Analysis of Two Story, Two Bay Frame Consisting of Reinforced Concrete Columns and Steel Beams with Through-Beam Type Beam-Column Joints, *Journal of Structural and Construction Engineering, No.514*: 207-214, (in Japanese).

Uomoto, T., Yajima, T., and Hongo, K. (1993). Damage evaluation of reinforced concrete beams subjected to cyclic bending moment using dissipated energy, *Summaries of Technical Papers of Annual Meeting of Japan Society of Civil Engineers, No.460/V-18*: 85-91.

DETERMINATION OF CRITICAL SHEAR, MOMENT, AND DEFORMATION INTERACTIONS FOR RC SLAB-COLUMN CONNECTIONS

James O. JIRSA[1]

ABSTRACT

The objective of this project is the determination of critical shear, moment, and deformation interactions at the connections of reinforced concrete slab-column buildings. While considerable research has been conducted to determine shear and moment interactions, little is known about the effect of inelastic deformations due to lateral displacements of the structure on subsequent shear transfer capacity. The consequences of different sequences of load application that produce damage to a level less than failure is generally not understood. For assessment of damaged structures and for design of structures to control damage, the effects of such load sequences must be determined. Buildings that have been subjected to damaging earthquake deformations (even if the damage has not threatened the integrity of the structure during the earthquake) or other disastrous loadings may suffer latent damage that could lead to failure of the connection or progressive collapse of the structure under subsequent post-earthquake loading combinations.

1. BACKGROUND

Flat plate and flat slab floor systems are widely used in residential and commercial buildings. In the United States, flat plate systems have been an economical form for use in buildings that do not have to accommodate large gravity loads. The addition of drop panels permits an increase in the gravity load capacity. In construction, the key feature of these systems is the simplicity of formwork that leads to speed of construction. For the owners and occupants, the space can be easily reconfigured to permit a variety of uses. While slab-column floor systems remain a very economical and popular form for architects and developers, the systems have some inherent problems that must be considered by the structural engineer.

In buildings that must resist lateral wind or earthquake forces, the column-slab connection is a very flexible unit. In order to control lateral deformation, separate lateral load-carrying elements can be provided in the form of perimeter moment-resisting frames, structural walls, or infills. The problem of deformation control is especially critical where these systems are used in seismic zones. Many pre 1970’s slab-column systems are located in regions that were once considered to have “low” seismicity and relied the slab-column connections for providing the necessary lateral

[1] *Department of Civil Engineering, The University of Texas at Austin, Austin, Texas, 78712*
Email: jirsa@uts.cc.utexas.edu

capacity. With the modification of seismic hazard maps in recent years, the required lateral capacity of buildings has increased and deformation control has become an even more critical requirement. This is especially true in cases where ductile moment-resisting perimeter frames have been added or where steel braces have been introduced as a rehabilitation measure to provide added lateral strength and stiffness. Frames or braces added on the exterior faces of the building do not interfere with the interior floor space or reduce the floor to ceiling clearances. The cost of rehabilitation can be reduced if modifications to the interior structural systems are not needed. However, the structures may still experience considerable lateral deformation that results in damage at slab-column connections. Such damage has been reported following the recent Nisqually, Washington earthquake (Bartoletti 2002).

The addition of new "column capitals" (shown in Fig. 1) is one approach to strengthening slab-column connections directly rather than adding new lateral force resisting systems that limit lateral deformation and "protect" the weak slab-column connections.

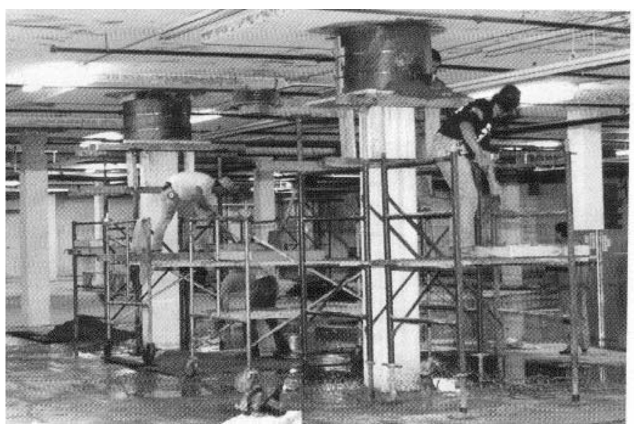

a) Strengthening of slab-column connections

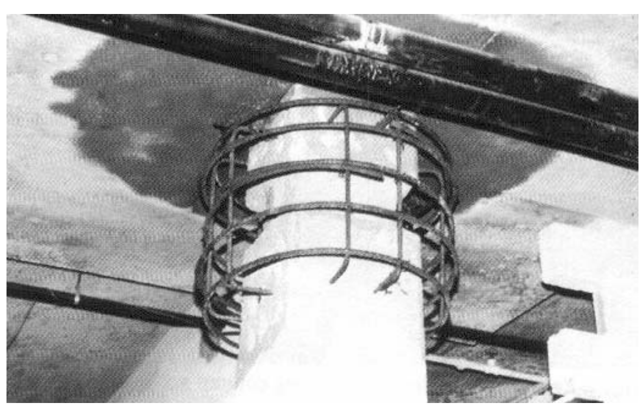

b) Reinforcement in new column capital

Fig. 1 Rehabilitation of slab-column floor system (Popovic and Klein 2002)

The "Achilles' heel" of flat plate and flat slab floors is the transfer of shear from the floor to the columns. Two-way or punching shear capacity is quite low and is a function of the moment transfer that accompanies shear transfer at the slab-column connection. Strength calculations for such connections are complex (ACI 318 2002). Computation of shear and moment strength is further complicated by the amount of inelastic action that occurs at the connection and is the main reason that deformation control is needed. Moehle (Hwang and Moehle 2000; Pan and Moehle 1989 and 1992) and Durrani (Robertson and Durrani 1991 and 1992, Durrani, Du, and Luo 1995; Wey and Durrani 1992) have done extensive research on the interaction of gravity loads and lateral displacements leading to failure. However, their research does not address the situation where failure has not occurred under lateral displacements of the structure but enough damage may have been produced so that subsequent loading with higher gravity loads could be disastrous. The poor performance of slab-column buildings in the 1985 Mexico City and other recent earthquakes can be attributed to the inherent weaknesses of the connections. Flexible floors, connections prone to shear failure, and slender supporting columns create the potential for failure at many locations in such a system. To correct these deficiencies and to control the deformations that could trigger loss of shear transfer at the connections, rehabilitation of such structures usually involves the addition of separate lateral load resisting elements. The cost of rehabilitation is directly related to the level of lateral capacity required or the maximum deformation considered acceptable. Since the designer must make calculations of these response characteristics, accurate simulation of slab-column connection response is critical to the design of the retrofit system and the associated cost to the owner.

2. SEQUENCE OF DAMAGE

In a building that has been damaged, it is necessary to determine if damage (cracking and inelastic strains in the reinforcement at or near the slab-column connection) due to lateral displacements of the structure has reduced the gravity load carrying capacity of the system. Currently, there are no established procedures or experimental data for determining the gravity load carrying capacity of a slab-column connection as a function of the degree of damage that has occurred previously. The lack of technical data is apparent in studying the most recent document available for seismic rehabilitation—FEMA 356 (FEMA 2000). While the interactions between shear and moment are taken into account in the FEMA provisions for analysis and acceptance criteria under earthquake actions, the provisions are not applicable for previous damage or post-earthquake behavior. Likewise, for rehabilitation of existing undamaged structures or for design of new systems, there is insufficient technical data on which to base deformation limits for protecting the gravity load capacity of such connections, for selecting appropriate rehabilitation techniques (the FEMA document is particularly lacking in this area), or for evaluating the effectiveness of techniques such as those shown in Fig. 1. It should be noted that if a structure has large gravity loads on the floors, a punching failure might occur during the earthquake and result in collapse of the entire structure. In a structure that has suffered a "pancake" failure, it is impossible to determine the triggering failure mechanism but punching shear is often theorized. Perhaps the most difficult issue to resolve is the capacity remaining in a complex system when damage has occurred or to determine the lateral force-lateral deformation relationship for a system where complex interactions between several different types of actions occur and the controlling mode of failure cannot be well defined beforehand.

3. ANALOGOUS CASE—COLUMN AXIAL CAPACITY

A comparable situation may help clarify the type of interaction that forms the hypothesis for this project. Many studies have been conducted defining the shear or flexure-axial load interactions for columns. Algorithms have been defined to represent those interactions in analyzing the response of buildings. However, until very recently the effect of lateral column cyclic deformations on the column capacity under gravity loads was not defined (column stability or slenderness, P-Δ effects, can be included relatively easily). Recent work at UC Berkeley (Elwood and Moehle 2001) has provided new insights into column capacity-story drift relationships. Figure 2 is a sketch of an envelope curve for the axial capacity vs drift relationship for a column in a structure subjected to cyclic deformations to increasing peak drift levels. The applied load on the column remains the same but as the lateral deformations (story drift levels) increase, the axial capacity is reduced because of damage to the hinging region of the column. If the unsupported length of the column is small (short or captive columns) and shear response controls, shear damage to the column reduces the axial capacity. At the point where the axial capacity and the applied load intersect, the column would be expected to fail axially. The higher the level of applied load, the lower will be the drift at which axial failure would be expected. Columns at the lower levels of the structure would be more vulnerable than those at upper levels because the applied loads would

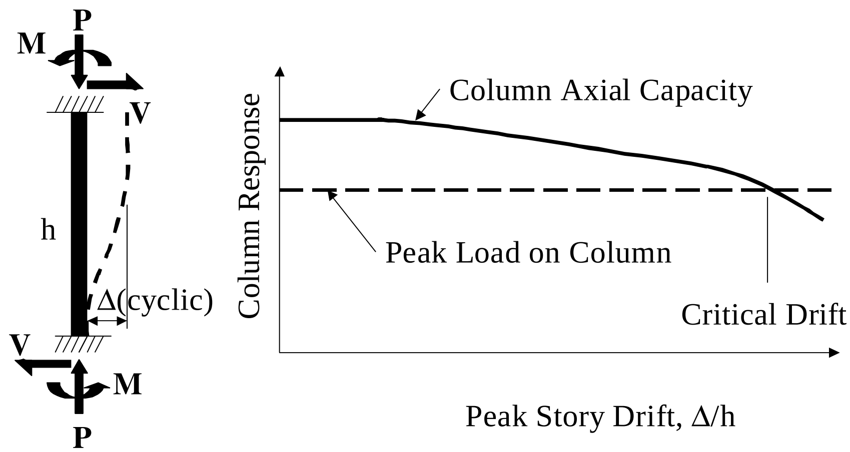

Fig. 2 Axial Capacity-Drift Interaction

generally be a greater fraction of the capacity and the lateral forces (and often drifts) are greater in lower stories of older existing buildings, especially those with soft first stories. (It is assumed in this example that the story drift is an indicator of the damage level for either shear or flexural failure of the column, however, this may not be a satisfactory indicator for use in evaluating a damaged structure because the peak drift that has occurred may not be readily apparent or easily determined.)

4. SLAB-COLUMN CONNECTION FAILURES

For slab-column structures the same types of failures are possible, however, it is likely that punching shear failures will control, especially in flat plates. Figure 3 is a sketch of a slab-column connection region of a floor slab system. In this case, the lateral deformations of the structure produce moment and shear on the connection that is superimposed on the moments and shears from gravity loads on the floors. Flexural cracks will develop on the top surface of the slab across the negative moment section at the face of the column and on the bottom of the slab on the opposite face (Fig. 4). The amount of cracking and the positive moment capacity developed on the opposite face will depend on the amount and location of bottom reinforcement in the slab and the anchorage details of that reinforcement. In older structures, very little bottom reinforcement was required to extend to the column and it was often only extended a short distance into the column. Current design codes (ACI 2002) require that some continuous bottom slab reinforcement be extended through the column to provide a minimum level of structural integrity in the event a punching shear failure occurs. Regardless of the detail, it is likely that under reversed cyclic loading, cracking will extend through the depth of the slab with positive moment cracks joining previously formed negative moment cracks. This region of the slab is also where the critical punching shear section is located.

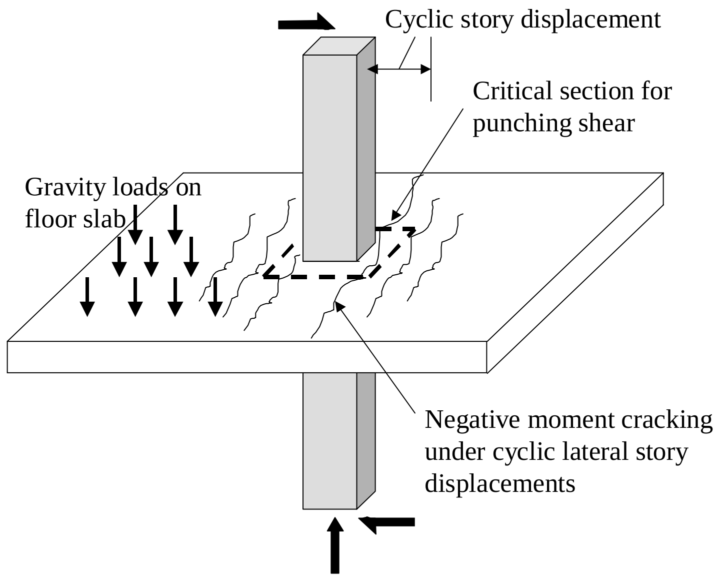

Figure 3. Area around slab-column connection

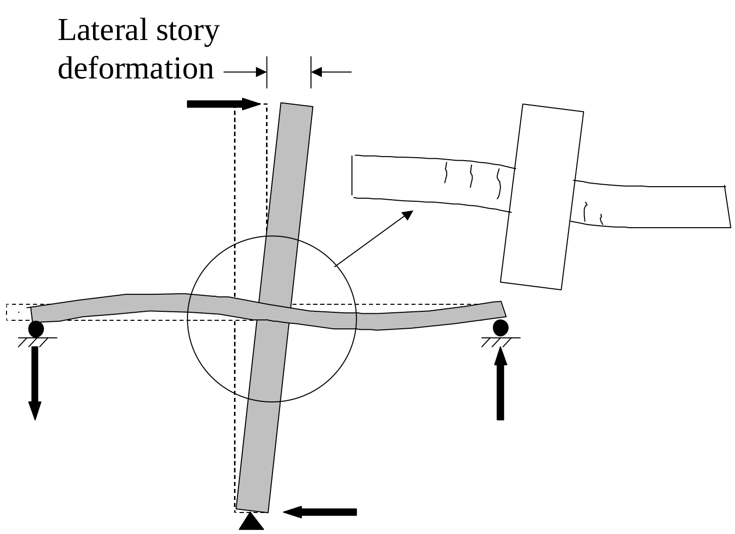

Fig. 4 Flexural crack formation due to lateral story displacement

Typically the punching shear failure starts at the location along the critical section (shown by the dashed line around the perimeter of the column) where shears from the gravity loads add to shears from the portion of the slab moment acting on the connection that is considered to be transferred by shear on the faces of the critical section. Punching shear failure under large gravity loading is shown in Fig. 5. ACI 318 (2002) and ACI 352 (1997) provide guidance for considering the effects of simultaneous application of a specified combination of shear and moment at a slab column connection. However, maximum moment transfer and maximum shear transfer under gravity loading do not occur simultaneously. The sequence of application of loads producing damage that does not lead to failure has not been evaluated. It is essential that such load sequences be considered because buildings that have been subjected to damaging earthquake deformations (even if the damage has not threatened the integrity of the structure during the earthquake) may result in latent damage that could lead to failure under subsequent post-earthquake loading combinations.

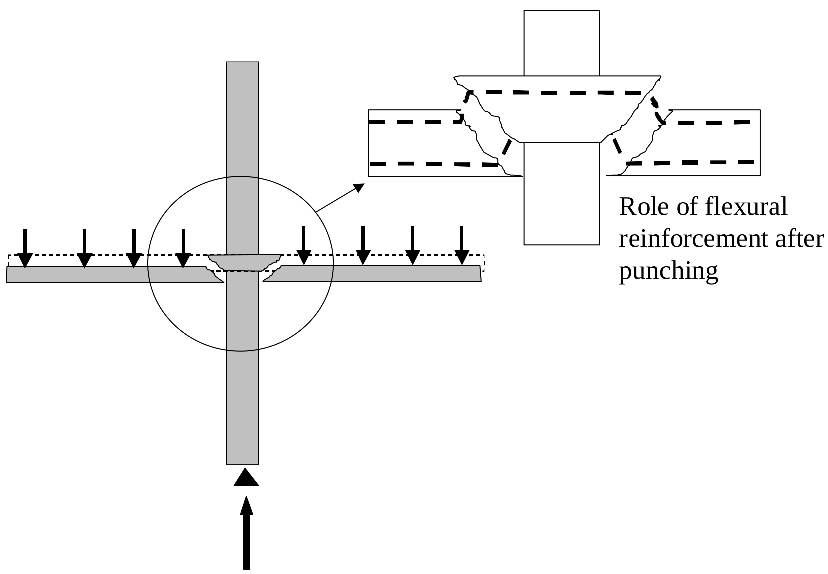

Fig. 5 Punching shear failure under gravity loading

5. RESEARCH OBJECTIVES

The experimental work proposed for this project is based on subjecting specimens to separate loading cases—first producing flexural damage at the slab-column connection due to lateral displacement of the structure (cyclic loading to simulate earthquake effects) and then subjecting the damaged specimen to loading that maximizes the potential for punching shear (gravity loading). Cyclic loading is intended to produce damage to the slab-column connection region, particularly around the critical section for punching shear. The level of damage may be defined in terms of the lateral drift ratio, the amount of cracking and the crack widths, the extent of yielding of the reinforcement in the slab at the connection, or other characteristics that will become apparent during testing. In addition, it is intended to utilize non-destructive techniques to better quantify the level of damage. The gravity loading will be increased incrementally until a punching shear failure occurs. The objective of the test program will be to determine the relationship between punching shear capacity of the slab-column connection as a function of previous damage to the slab by earthquake actions on the structure (Fig. 6). The information will be valuable for the following uses:

1) Determining the likelihood of punching shear failures under gravity loading after damage has occurred due to an earthquake.
2) Development of response characteristics for use in pushover or other seismic analyses of new or existing structures.
3) Establishing reasonable deformation limits for evaluation and design of rehabilitation schemes for existing slab-column structures.
4) Evaluating the feasibility of modifications to the slab-column connections (enlarging column capitals or increasing the shear strength of the slab at critical shear sections) to improve the load transfer capacity of the existing system.

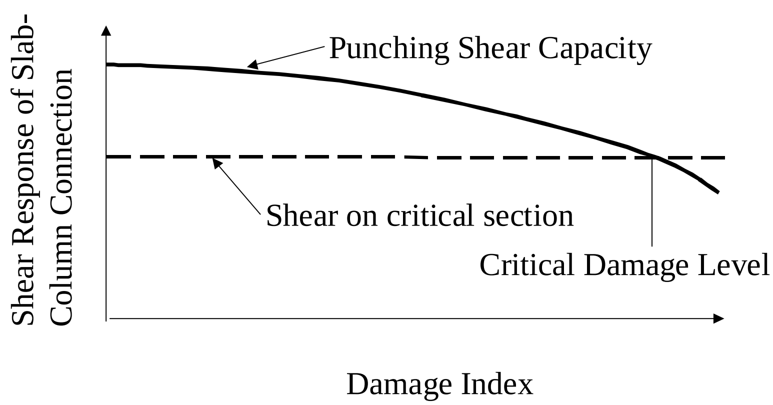

Fig. 6 Punching Shear Capacity-Damage Index Interaction

5.1 Research Program

A series of slab-column specimens will be tested to establish the influence of degree of previous earthquake-related damage on the punching shear capacity of slab-column floor systems under gravity loads. The key elements of the project are as follows:

1. Determine typical floor details of existing structures in consultation with designers working on rehabilitation of slab-column structural systems.
2. Conduct analyses of selected floor slab systems to determine the details of test specimens and to simulate the behavior of the connection region in the complete structural system.
3. Determine--
    a. Degree of damage under earthquake loading as determined through visual observations, measured local or global deformations, and non-destructive techniques.
    b. Influence of moment transfer in combination with gravity loading (it is unlikely that gravity loading will ever occur without any moment transfer because structural systems and loadings are rarely symmetrical)
4. Evaluate effects of--
    a. Slab thickness, column or capital size (defines the critical section for punching shear)
    b. Slab reinforcement details at connection
    c. Strengthening the connection through the use of column capitals to increase the critical shear section at the slab-column joint (providing a capital before or after subjecting the specimen to earthquake loading) or increasing the shear capacity of the slab using either conventional steel or new CFRP reinforcing materials.
5. Define the influence of previous damage to the slab by earthquake actions on the structure on the punching shear capacity of slab-column connections. Crack width, extent and location of cracks, and residual deformations in the connection region after the simulated earthquake loading has been completed will provide some quantifiable measures of response and damage. However, the results of techniques such as SASW testing should provide the most reliable indication of internal damage to the concrete.

6. Develop algorithms for relationships between damage due to lateral deformations and subsequent load transfer capacity under gravity loads suitable for pushover (or other analyses) of new, existing, or rehabilitated structures.

5.2 Non-Destructive Techniques

The use of non-destructive techniques is a critical aspect of damage assessment. In previous research on reinforced concrete shear wall structures under cyclic loads to large deformation levels at the University of Texas, spectral analysis of surface waves (SASW) testing was used to assess damage in the walls. The SASW technique will be used to assess the integrity of the concrete material in the slab-column joint region at various stages of loading and story drift levels. One difficulty that arises with this technique (and other nondestructive techniques) is that under cyclic deformations, cracks open and close. Even though the cracking and damage may be severe at peak deformation in one direction, once the cracks close as loading is reversed, the SASW results may indicate that the damage is not as severe when the cracks are closed. However, various reference locations for reading the seismic waves introduced to the slab (hammer blow to the surface) may permit a more global indication of the total damage to concrete in the connection region. The ultimate goal in studying this technique would be to provide a reliable means of assessing damage conditions in the field so that owners and designers would be able to make rehabilitation or demolition decisions based on quantifiable damage levels.

6. REFERENCES

ACI Committee 318 (2002), "Building Code Requirements for Structural Concrete (318-02), American Concrete Institute.

ACI Committee 352 (1997), "Recommendations for Design of Slab-Column Connections in Monolithic Reinforced Concrete Structures (ACI 352.1R-97)," American Concrete Institute.

Bartoletti, S. (2002), Private Communication regarding damage in flat plate structures in Nisqually earthquake.

Durrani, A. J., Du, Y., and Luo, Y. H. (1995), "Seismic Resistance of Non-Ductile Slab-Column Connections in Existing Flat-Slab Buildings, *ACI Structural Journal,* American Concrete Institute, July-Aug. 1995, pp 478-487

Elwood, K. J., and Moehle, J. P. (2001), "Shake Table Tests on the Gravity Load Collapse of Reinforced Concrete Frames," Paper presented at Third US-Japan Workshop on Performance-Based Earthquake Engineering Methodology for Reinforced Concrete Building Structures," Seattle.

FEMA (2000), "Prestandard and Commentary for the Seismic Rehabilitation of Buildings,", Federal Emergency Management Agency, FEMA 356.

Hwang, S-J, and Moehle, J. P. (2000), "Vertical and Lateral Load Tests of Nine-Panel Flat-Plate Frame," *ACI Structural Journal,* American Concrete Institute, Jan,-Feb. 2000, pp 193-203

Pan, A. D., and Moehle, J. P. (1989), "Lateral Displacement Ductility of Reinforced Concrete Flat Plates," *ACI Structural Journal,* American Concrete Institute, May-June 1989, pp 250-258

Pan, A. D., and Moehle, J. P. (1992), "An Experimental Study of Slab-Column Connections," *ACI Structural Journal,* American Concrete Institute, Nov.-Dec. 1992, pp 627-638

Popovic, P. L., and Klein, G. J. (2002), "Strengthening with Shear Collars," *Concrete International,* American Concrete Institute, Vol. 24, No. 1, pp 32-36.

Robertson, I. N, and Durrani, A. J. (1991), "Gravity Load Effects on Seismic Behavior of Exterior Slab-Column Connections," *ACI Structural Journal,* American Concrete Institute, May-June 1991, pp 255-267

Robertson, I. N, and Durrani, A. J. (1992), "Gravity Load Effects on Seismic Behavior of Interior Slab-Column Connections," *ACI Structural Journal,* American Concrete Institute, Jan.-Feb. 1992, pp 36-45

Wey, E. H., and Durrani, A. J. (1992), Seismic Response of Interior Slab-Column Connections with Shear Capitals," *ACI Structural Journal,* American Concrete Institute, Nov.-Dec. 1992, pp 682-691

7. KEYWORDS

Slab-column connections, shear strength, drift ratio, shear/moment/deformation interaction, damage level, assessment, rehabilitation.

PERFORMANCE OF A FIBER-REINFORCED CONCRETE INFILL PANEL SYSTEM FOR RETROFITTING FRAME STRUCTURES

Sarah L. BILLINGTON[1]

Keith E. KESNER[2]

ABSTRACT

This paper presents the results of an experimental and analytical investigation of an infill wall system developed for retrofitting frame structures. The system is designed for flexibility in application, easy replaceability, and protection of secondary systems. The infill is composed of precast panels made with a ductile fiber-reinforced cementitious material, referred to as engineered cementitious composites (ECC). Pretensioned bolted connections are used both between individual panels and at the connections to the frame structure. Experiments on connection response to compression and shear loading as well as individual panel response to cyclic lateral load were performed. A constitutive model for ECC was applied to simulate panel response. Detailed finite element models were conducted to study to performance of the panels and connections in a steel frame. It was found that the panels fail primarily in a flexure mode and that reinforced ECC panels could reach strengths 45% higher than a reinforced concrete panel. Through numerical simulations, it was determined that various panel arrangements can lead to a range of strength and stiffness increases in a frame without causing premature damage to the frame.

1. INTRODUCTION

A new infill wall system is being investigated for the seismic strengthening and retrofit of frame structures (Figure 1). The infill system is composed of precast panels made with a ductile fiber-reinforced cementitious material, referred to as engineered cementitious composites (ECC). Pretensioned bolted connections are used both between individual panels and at the connections to the frame structure. The system was originally investigated for application in steel frame structures, but the system has been developed such that it can be used in concrete frame structures, if appropriate. The system was also originally intended for application to critical facilities. Therefore, key aspects of this system are rapid installation, flexibility in location of the panels within a frame bay, the ability for the panels to be relocated with changes in facility use, protection of both the structural frame and secondary systems, and ease of replacement after damage from seismic events. This system builds on previous work related to precast concrete infill panels (Frosch et al. 1996) and precast ECC panels (Kanda et al. 1998).

[1] *Department of Civil and Environmental Engineering, Stanford University, Stanford, CA USA, e-mail: billington@stanford.edu*

[2] *School of Civil and Environmental Engineering, Cornell University, Ithaca, NY USA, e-mail: kek11@cornell.edu*

To develop this system, a series of feasible panel sizes and geometries were first determined from preliminary analyses. A set of connection experiments and single panel experiments were then conducted. Using the experimental results, a finite element modeling approach was calibrated and used to predict the performance of a single frame with partial and complete infills. A macro-modeling approach is currently being investigated for predicting the performance of large-scale structures with the proposed infill system. This paper presents selected results from the single panel tests and the finite element modeling used to predict the performance of infills in a single bay of a steel frame. Full details of this research are found in Kesner (2003).

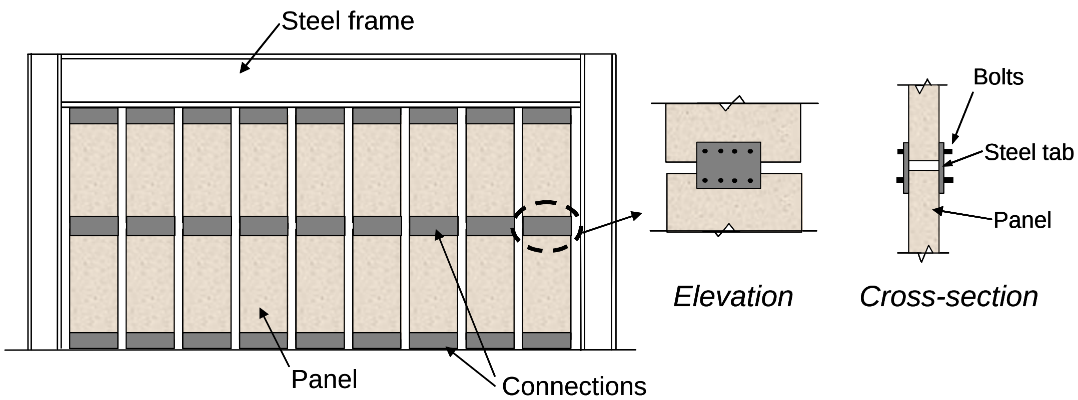

Figure 1: Infill panel system

2. INFILL PANEL SYSTEM

As shown in Figure 1, the infill panels are to be installed in pairs, with connections at the top and bottom of the panels only. With this arrangement, each pair of panels (vertically) acts as a fixed-end beam when the frame experiences lateral loads. Therefore the connection between the panels themselves is a point of inflection. This beam-like arrangement is most appropriate for the ECC material which is extremely tough in both tension and compression. The beam arrangement also allows all panel pairs to resist lateral loads somewhat evenly. If the panels were connected along their sides, a large diagonal strut would form as well as a vertical tensile force, causing some panels to carry considerably more force than others.

The panels are envisioned to be portable and easily installed. They would measure 1200-1500 mm tall, 600-900 mm wide and 75-100 mm thick, depending on the needs of the building to be retrofit. The connections use steel plates and angles with pretensioned bolts at the panels (Figure

1). In the connection to the frame, pretensioned bolts or welding would be used for steel frames, and for concrete frames, bolts would be anchored to the concrete.

The ECC has a Portland cement matrix and roughly 2% volume fraction of short, randomly distributed polymeric fibers. The material was originally developed from micromechanical tailoring of fiber and matrix properties with the resulting composites showing multiple, fine (steady-state) cracking and significantly higher tensile ductility (up to 300x more) than conventional cementitious materials. ECC also exhibits pseudo-strain hardening and therefore energy dissipation (Li 1998) (Figure 2).

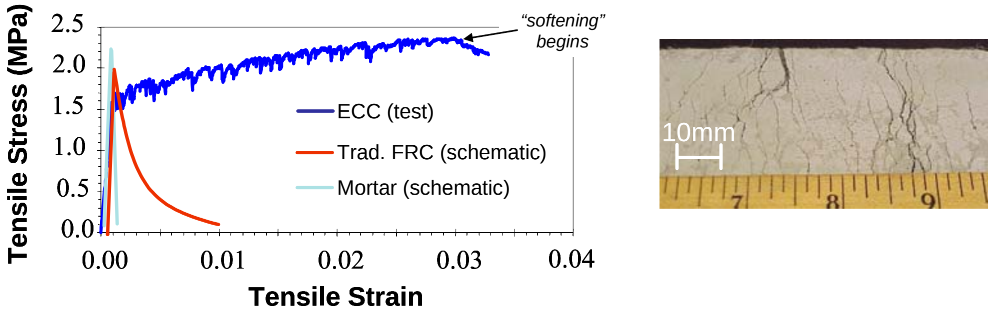

(a) Tensile ductility of ECC *(b) Multiple, fine cracking*

Figure 2: Properties of ECC

ECC is made up of cement, silica fume or fly ash, fine sand, water and fibers. There is no coarse aggregate in the composite. As a result, the cement volume relative to traditional concrete is high and in the proposed system, larger time-dependent volume changes are to be expected, particularly in the connection areas that are pre-tensioned. In terms of fabrication, the material is mixed in a conventional mortar mixer. The roughly ¾-scale panels tested in this research were fabricated without major difficulty. In addition, ECC segments (310mm x 310mm x 930mm) of precast segmental bridge piers for testing were recently cast in a major commercial precasting yard (Rouse and Billington 2003).

3. EXPERIMENTAL PROGRAM

Experimental testing was conducted on the strength of the connections between the ECC infill panels in compression and in shear, the long-term performance of the pretensioned bolt loads in the connections, and a series of single infill panels subjected to cyclic lateral load. The connection strength tests were used to design the connections for the single panel tests. Details of the connection tests are given in Kesner and Billington (2003).

3.1 Single Panel Test Program and Set-up

To evaluate the beam-type infill system a series of single panels were tested. Specific goals of the testing were to: (1) examine panel peak load vs. drift capacity; (2) examine the energy dissipation of the panels; and (3) determine and observe the panel failure mechanisms. The variables in the panel experiments were ECC mix design, panel reinforcement, and panel shape. In addition, a traditional concrete panel was tested.

3.1.1 Panel Geometry and Materials

Table 1 shows a summary of the panels tested in the program. In Table 1, panel material SP is ECC with an ultra-high molecular weight polyethylene fiber (trade name Spectra®) and without any fine aggregate. SP-A is the SP mix with fine aggregate. RECS-A is ECC with a polyvinyl alcohol fiber and with fine aggregate. The rectangular panels were 1220 mm tall, 610 mm wide and 75 mm thick. The tapered panel had a reduced width (305 mm) at the top of the panel, with the tapered section starting 150 mm above the base of the panel. Figure 3 shows a schematic comparison of the different panel geometries. In all panels, a bolt spacing of 75 mm was used with the centerline of the bolts located 75 mm from the top/bottom and side edge of panels. The number of bolts used was based upon the connection testing.

Table 1: Summary of panel specimens

Panel	Geometry	Panel Material	Reinforcement
1	Rectangular	SP	0.44% WWF[1]
2	Rectangular	SP	0.44% WWF with perimeter bar
3	Rectangular	SP-A	0.44% WWF with perimeter bar
4	Rectangular	RECS-A	0.44% WWF with perimeter bar
5	Rectangular	Concrete	0.44% WWF with perimeter bar
6	Tapered	RECS-A	0.44% WWF with perimeter bar

[1] WWF = welded wire fabric (W4 wire, 5.7mm diameter)

The basic reinforcement used in the panel was welded wire fabric (WWF), which was detailed to provide 75 mm spacing between wires. In addition to the WWF reinforcement, a 9.5 mm-diameter reinforcing steel perimeter bar was used in the majority of the panels to provide additional tensile reinforcement. The combination of the perimeter bar and WWF provided sufficient reinforcement distribution in the panel, without creating consolidation problems due to reinforcement congestion. Material tests were performed to determine the properties of both the panel materials and the reinforcing steel prior to panel testing. Table 2 shows a summary of pertinent material properties.

Table 2: Properties of cementitious materials used in panel testing

Material	First Cracking Strength (MPa)	Yield Strength[1] (MPa)	Ultimate Tensile Strength[2] (MPa)	Tensile Strain Capacity[3] (%)	Ultimate Compressive Strength (MPa)	Modulus of Elasticity (GPa)
SP	1.2	n.a.	1.5	2.3	63	13.8
SP-A	1.2	n.a.	1.4	0.8	38	11.2
RECS-A	1.4	n.a.	2.1	0.5	41	12.1
Concrete	3.6[4]	n.a.	n.a.	n.a.	36	28.6
Perimeter bar	n.a.	427	667	n.a.	n.a.	200
W4 wire	n.a.	500	640	n.a.	n.a.	200

1. Stress at 0.2% strain
2. Determined at wire or bar fracture
3. Defined as strain capacity at the onset of softening
4. Determined in a split cylinder test, ASTM C-469

The rectangular panels were cast on their sides (the tapered panel was cast flat) and wet cured for 28 days. The panels were then allowed to dry under laboratory conditions (roughly 21° C. and 50% RH). Prior to testing, the bolt holes were cored in the panels and the connections regions were sandblasted to maximize the connection capacity (Kesner and Billington 2003).

3.1.2 Test Set-up and Loading

The single panel tests represented one half of a beam-type infill section, with the lateral load applied at the top (free end) where the point-of-inflection would be in the beam-type infill (Figure 4). Each panel was subjected to a symmetric cyclic lateral load to increasing drift levels (±0.25%, ±0.5%, ±1%, ±1.5%, ±2%, ±3%) with the measured displacement at the top of the panel used as the control parameter. The panel displacement was determined from the average reading of two LVDTs at the top of the panel. The panel drift (expressed as a percentage) was defined as the average displacement measured at the top of the panel divided by the panel height. With pauses in testing to mark cracks and take measurements and photographs, each panel test took approximately 8 hours to complete.

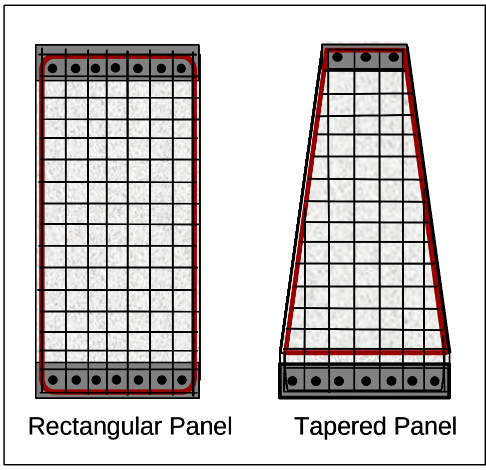

Figure 3: Panel geometries

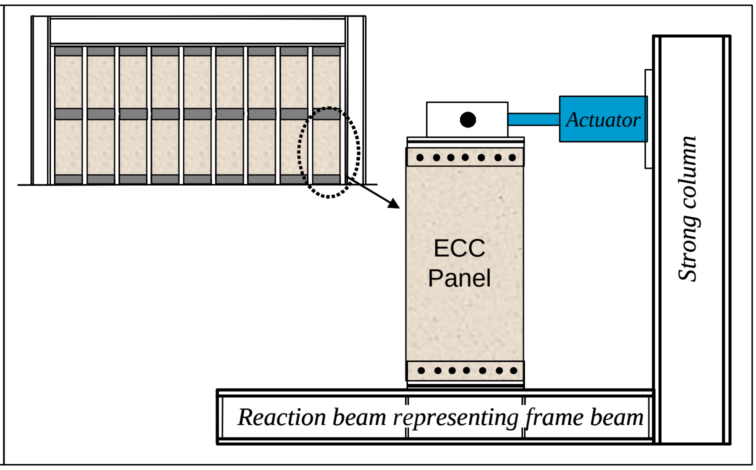

Figure 4: Single panel test set-up

3.2 Selected Experimental Results

3.2.1 Panel Load-Drift Response

Figure 5 shows the load displacement response obtained from Panels 2, 4 and 5. Figure 6 shows a typical cracking pattern on an ECC and concrete panel. The pinching behavior seen in the load-drift response is attributed to the cracks in the ECC (and concrete) gradually closing and at larger drifts (>0.5%) due to slippage of the reinforcement (weld failures were observed in the welded wire fabric in some instances). The panel load increases as the cracks fully close and bear compression. Additionally, some slippage of the panel in the connection region likely contributed to the pinching of the load-drift response.

Panels 2 and 4 carried increasing loads until the peak strain capacity of the ECC was reached. After the peak strain capacity was reached (between 0.75-1.25% drift), a major crack opened towards the base and multiple cracking stopped. With the major crack opening, strength degradation occurred as load was shed from the ECC and was carried predominantly by the steel reinforcement. The significant difference in compressive strength of the ECC in Panel 2 (mix SP, Table 2) relative to Panel 4 (mix RECS-A, Table 2) did not appear to affect the overall panel strength. The combination of ECC and reinforcement led to a 45% increase in peak load-carrying capacity relative to the reinforced concrete panel strength.

The response of the concrete panel (Panel 5) was significantly different from that of the ECC panel. The lack of tensile strain capacity in the concrete resulted in fewer cracks forming in the

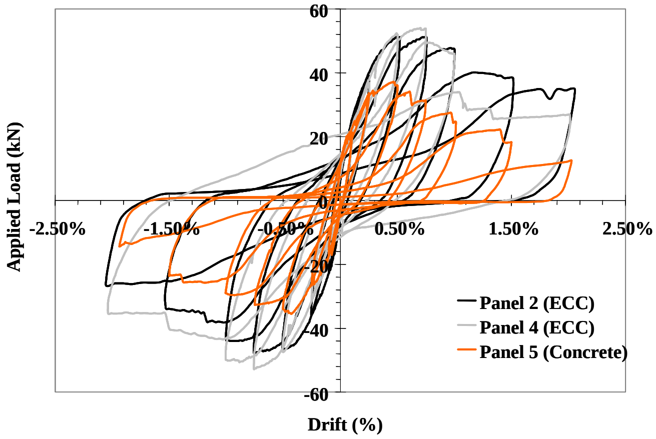

Figure 5: Load-drift response of selected panels

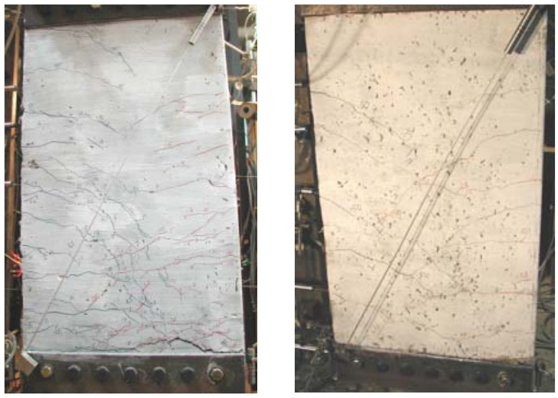

(a) Panel 4 near failure (b) Panel 5 near failure

Figure 6: Panel cracking patterns

panel (Figure 6b). A major (dominant) crack formed at the base of the panel at 0.5% drift, and the peak load reached corresponded with the peak load carrying capacity of the reinforcing steel alone (similar to the residual strength of the ECC panels). In all of the panels a small amount of panel slippage was observed as a result of slippage in the pretensioned connection. Further discussion of this slippage is found in Kesner (2003).

3.2.2 Panel Failure Mechanisms

All of the panels failed in a flexure mode. In all of the panels made with ECC, failure was initiated by softening of the ECC material (that is, the ECC strained beyond its peak strength, Figure 2). After ECC softening began, WWF mesh fracture and bond failures were observed, resulting in sudden drops of load-carrying capacity. The softening of the ECC occurred at the base of the panels in the area immediately above the connection region. The precompression in the connection region by the panel bolts held the material within the connection intact. Damage was only observed at the panel edges in the connection region, where there was less precompression.

The failure of the concrete panel was also initiated by the formation of a single dominant tensile crack at the base, leading to overloads on the steel reinforcement. Fracture and development failure of the WWF then occurred. There was extensive spalling of the concrete in the connection region that was not seen in the ECC panels. Along with the spalling, there was a development failure (bar slippage) of the perimeter bar at the base of the panel. Figure 7 compares the intact connection region of Panel 2 (ECC), relative to the extensive damage in the

(a) Panel 6 (a) Panel 5

Figure 7: Connection regions at failure

connection region of Panel 5 (Concrete). Spalling of the concrete in the connection region resulted in the lower residual strength of Panel 5, relative to the ECC panels with similar reinforcement, because the perimeter bar in Panel 5 was not fully developed.

4. ANALYTICAL PERFORMANCE PREDICTIONS

To understand how the combination of the single panels in an infill system will behave within a frame, numerical modeling was performed. Two levels of modeling detail are necessary to evaluate the infill system. First, detailed finite element models are necessary to study the local effects of the system on the frame (e.g. at connections between the panels and an existing frame) as well as assess the general range of stiffness and strength changes possible with various infill arrangements. Second, larger-scale models are needed to study the impact of the system on multi-story frames. Detailed analyses have been conducted and large-scale analyses with macro-models are underway. Selected results of the detailed analyses (Kesner 2003) are presented here.

4.1 Single Panel Test Simulations

4.1.1 Finite Element Modeling of Single Panel Tests

The single panel experiments were simulated using nonlinear finite element modeling. Two different modeling approaches were taken that varied in the detail of the connection region. Figure 8 shows the finite element model with the detailed modeling of the base. The model was comprised of four-noded plane-stress elements representing the ECC and embedded reinforcement for the WWF and perimeter bar. Bond-slip of the reinforcement was not modeled. The connection region was modeled as a composite of the steel connection and the confined ECC in between. No attempt was made to model the observed slippage of the panel in the connection

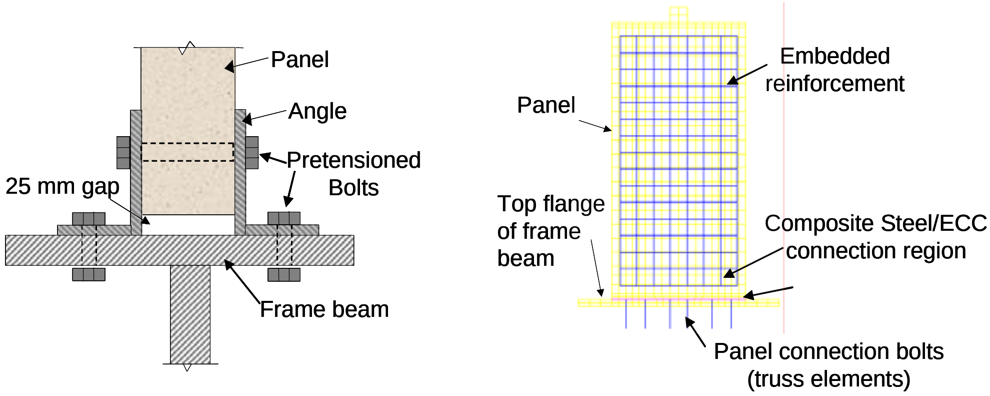

(a) Cross-section through base connection in experiment

(b) Elevation of finite element model

Figure 8: Base connection (a) and model of panel with details of base connection (b)

region. In the simple finite element model, the panel bolts at the base were not explicitly modeled and a fixed connection was modeled rather than using a series of interface elements.

The ECC was modeled using a total-strain based model using a rotating crack model in tension (Han et al. 2003). This model uses uniaxial stress-strain data, which was obtained from uniaxial tension-compression experiments on ECC (Kesner et al. 2003). However, the initial stiffness of the material recorded in the uniaxial material testing was reduced for the simulations by 50-70%. The steel reinforcement was modeled as elastic-plastic using data from tensile experiments. The analyses were displacement controlled to prescribed drifts corresponding to the loading scheme from the experiments. Further details of these simulations are given in Kesner (2003).

4.1.2 Simulation Results for Single Panel Tests

Figure 9 compares the load-drift results obtained from the experiment and simulation of Panel 1. This simulation was conducted to +/- 3% drift. The simulation was able to predict the load capacity reasonably well at various drift levels, and also capture the residual displacement of the panels, up to approximately 2% drift. At higher drift levels, the simulation overestimates the strength of the panel (that is, the residual strength after the load drops from the peak). The overestimation of residual strength is attributed to the perfect bond modeling and the lack of modeling fracture in the reinforcing steel.

The more detailed finite element model was then analyzed to determine the ability of such a model to predict the bolt loads in the connection of the base of the panel to the steel frame beam.

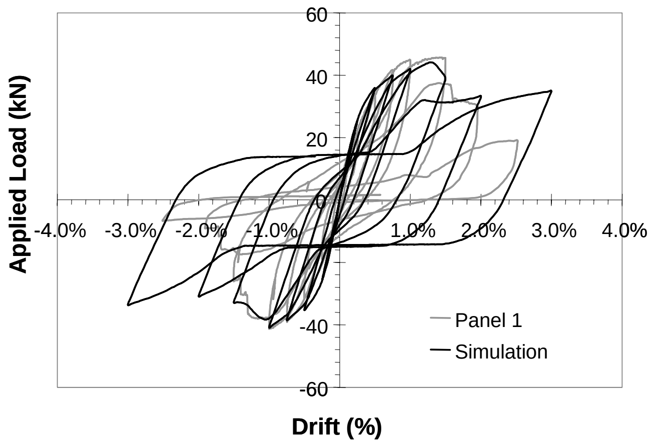

Figure 9: Load-drift response of experiment and simulation

It was found that a reasonable prediction of the bolt forces was made provided that the material at the edge of the panel but within the connection region was allowed to respond nonlinearly (i.e. crack). From this detailed model, it was also found that the steel frame beam did not experience any localized yielding at the bolted connections after the panel had been loaded to ±1% drift. This modeling approach could be used to study the impact of the retrofit on an existing structure.

4.2 Infilled Frame Simulations

4.2.1 Finite Element Modeling of Infilled Frames

To examine further the impact of the retrofit installation on a frame, a series of plane stress models of a single bay frame with infill panels were analyzed. The installation of two, four, and six beam-type infill sections was examined. Figure 10 shows the finite element model of the bare frame with 2 infill panels added. The flange width, flange thickness and web thickness of the columns was 254 mm, 15.2 mm, and 9.4 mm, respectively. The beam flange width, flange thickness and web thickness was 229 mm, 17.8 mm, and 11.2 mm, respectively. The base of

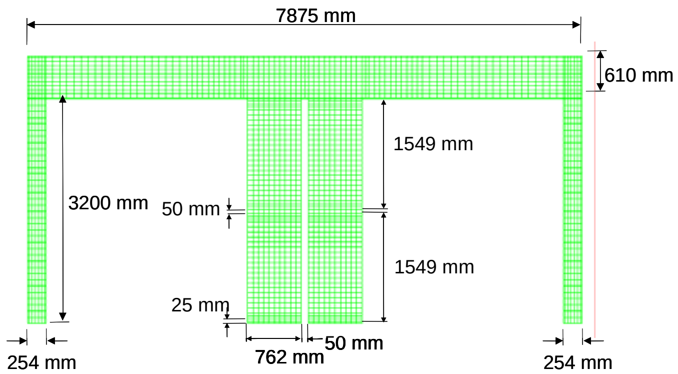

Figure 10: Finite element mesh of a steel frame with two beam-type infills

each frame column was fixed and the beam-column joints were assumed to be full moment connections. Each infill panel was 762 mm wide by 1549 mm tall by 100 mm thick. A gap of 25 mm was used between the top (or bottom) of the panels and the frame, and a 50 mm gap was used between the two infills making up a beam-type infill. The gap between each beam-type infill was 50mm. The material properties used in the analysis are given in Kesner (2003).

The connections were modeled in two ways to simulate bolted and welded connections, respectively, between the bottom flange of the frame beam and the beam-type infill sections. The connection members were 25 mm thick (the equivalent of two 12.7 mm thick connection tabs). The bolted connection was simulated using interface elements between the bottom flange of the beam and the infill connection member. Six pairs of bolts, spaced 75 mm apart were simulated in the connection. In the welded connections, the bottom flange and infill connection elements were connected at a common node. The connection of the infills at the base of the model was fixed. A cyclic displacement to varying drift levels up to ± 1% was simulated. The response of the models with the welded and the bolted connections showed negligible differences and only the response of the bolted frame simulations are shown here.

4.2.2 Simulation Results for Infilled Frames

For the bare frame, yielding was predicted to occur at 0.75% drift. Yielding was concentrated at the beam-column joints up to 1% drift. Figure 11 shows the load-drift results obtained from simulations with two and six beam-type infill section additions. Results obtained from simulations using beam elements for the frame members are also shown in Figure 11. The models with the plane stress elements for the frame had a lower stiffness than the models with beam elements for the frame. The difference in frame element stiffness was due to the effective length of the columns in the beam model being longer (nodes were at the centerline of the beams) than that in the plane stress model.

The beam-type infill additions resulted in significant increases in the stiffness, strength and energy dissipation compared to the bare frame. However, the infill additions also resulted in residual drifts of up to 0.35% as per the simulations. The beam-type infill installation did not result in localized yielding of the frames where the panels were connected. For example, Figure 12 shows principle strain contours at 1% drift obtained from the six beam-type infill additions

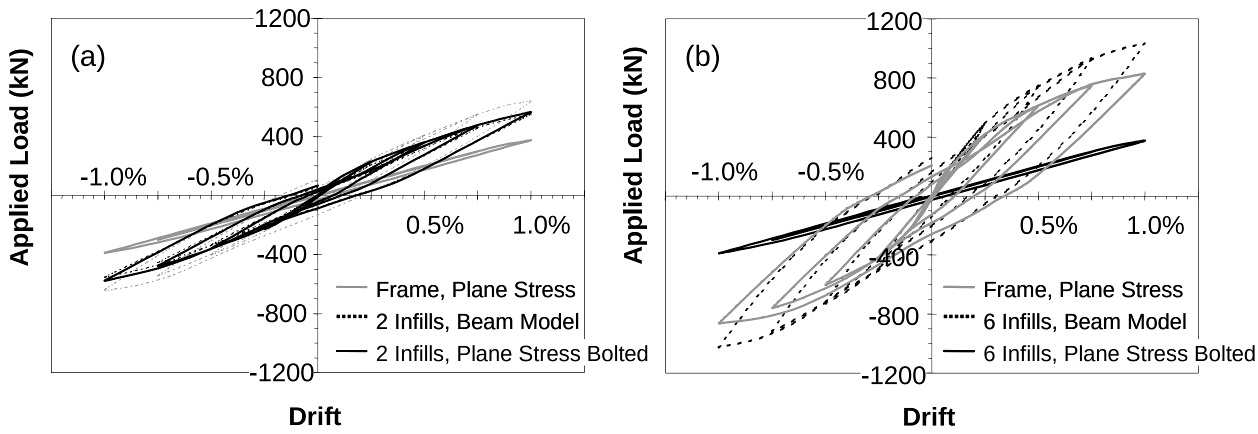

Figure 11: Load Drift Response of bare frame and various numbers of infill sections

with bolted connections. The upper limit in the strain contours is 0.0017, the yield strain of the steel frame members. No localized yielding of the frame members was observed at the infill-to-beam connection regions. Yielding in the frame was concentrated at the beam-column joints, as in the bare frame response, and also at the column bases. Similar to the bare frame response, yielding of the frame with the infill additions began at a drift level of approximately 0.75%.

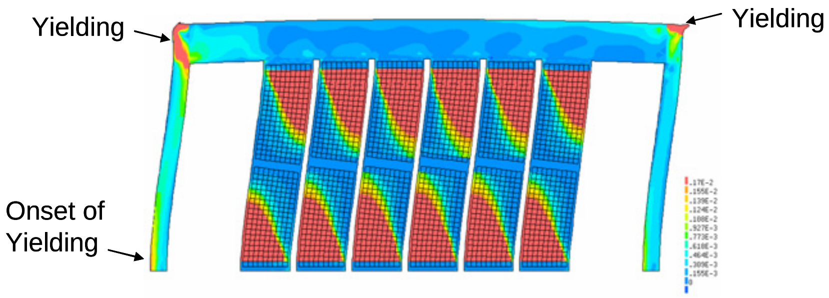

Figure 12: Principle strains at 1% drift

5. FUTURE WORK

One of the intentions of the retrofit system investigated here was that it might protect secondary systems in structures, in particular health care facilities. To be able to assess the system's ability to protect secondary systems, a considerable amount of additional research is necessary. A macro-modeling approach for the infills is necessary to be able to efficiently evaluate the performance of large-scale frames with various arrangements of the retrofit installed. Detailed information on the maximum allowable interstory drift and/or the maximum floor accelerations that various secondary systems can withstand is also needed. A challenge will then be to balance the various requirements of the secondary systems using this retrofit system. Finally, it will be important to conduct large-scale tests of such a system in actual frames that are subjected to cyclic and/or seismic loads to verify system performance and provide data for model calibration. Additional issues that should be addressed with this system are methods to limit bolt tension loss over time (due creep and shrinkage of ECC), and methods of connecting the infill system in concrete frames.

6. CONCLUSIONS

A retrofit system for frame structures is under development and selected results of a set of experiments and simulations evaluating the performance of the system were presented here. The single panel experiments established the load-drift response and failure mechanisms of a variety of single panels. The ECC panels reached higher peak loads, exhibited more distributed, fine cracks and achieved more energy dissipation than a similarly reinforced concrete panel. All panels failed in a flexure mode with a single dominant base crack and reinforcement slippage and fracture.

Using simple constitutive laws based on uniaxial tensile response of the ECC and steel, it was possible to capture the strength, stiffness, residual strength and energy dissipation obtained in the panel tests with reasonable accuracy. In terms of failure mechanisms, the predominantly flexural mode of failure was predicted. However, fracture and debonding of the reinforcement was not modeled, limiting the accuracy of the simulations in predicting residual strength and the full failure mechanism. Using a detailed model of the panel and base connection region, simulations were able to predict approximately the variation in panel connection bolt force under cyclic loading. Such simulations can be used to design connections in the infill system.

In these simulations, the modulus of elasticity of the ECC needed to be reduced by 50-70% to improve the accuracy of the results. While some stiffness reduction may be warranted to account for shrinkage cracking, a more significant amount of stiffness decrease may be caused by slippage of the panel in the connection region. Panel slippage was not modeled in the simulations presented here.

The effect of the addition of ECC infill sections on an existing structure indicated that the ECC infill sections will not result in localized yielding at the connection of the infill section to the frame. Furthermore, the simulations of an infilled frame demonstrated the variety of response in terms of changes in strength, stiffness, energy dissipation and residual drift possible with various panel arrangements. With accurate prediction tools, it is envisioned that this infill system can be implemented in different ways to satisfy performance limits for a variety of frame structures.

7. REFERENCES

Frosch, R.J., W., Li., J.O. Jirsa, and M.E. Kreger. (1996) "Retrofit of Non-Ductile Moment-Resisting Frames Using Precast Infill Wall Panels," *Earthquake Spectra*, **12**(4): 741-760.

Han, T.S., P.H. Feenstra, and S.L. Billington, (2003) "Simulation of Highly Ductile Fiber-Reinforced Cement-based Composites," *ACI Structures Journal,* in press.

Kanda, T., S. Watanbe, and V.C. Li. (1998) "Application of pseudo strain hardening cementitious composites to shear resistant structural elements," *Fracture mechanics in concrete structures,* Proc. Framcos-3, Eds. H. Mihashi and K. Rokugo. Volume III, pp. 1477-1490.

Kesner, K.E. (2003) *Development of Seismic Strengthening and Retrofit Strategies for Critical Facilities Using Engineered Cementitious Composite Materials*, PhD Thesis, Cornell University, 337 pp.

Kesner, K.E. and S.L. Billington, (2003) "Experimental Response of Precast Infill Panel Connections and Panels Made with DFRCC," *J. Advanced Concrete Technology*, in press.

Kesner, K.E., S.L. Billington and K.S. Douglas (2003) "Cyclic Response of Highly Ductile Fiber-reinforced Cement-based Composites," *ACI Materials Journal*, in press.

Li, V.C., (1998) "Engineered Cementitious Composites – Tailored Composites Through Micromechanical Modeling," in *Fiber Reinforced Concrete: Present and the Future* edited by N. Banthia, A. Bentur and A. Muft, Canadian Society for Civil Engineering, Montreal, pp. 64-97.

Rouse, J.M. and S.L. Billington (2003) "Behavior of Bridge Piers with Ductile Fiber Reinforced Hinge Regions and Vertical, Unbonded Post-Tensioning," Proc. *fib* Symposium on Concrete Structures in Seismic Regions, Greece, May.

8. KEYWORDS

Seismic retrofit, fiber-reinforced concrete, precast infill panels, pretensioned bolt connections, cyclic load

SESSION 2-A: EVALUATION OF SEISMIC DEMANDS

Chaired by

♦ Eric Williamson and Akenori Shibata ♦

SEISMIC DEMANDS FOR PERFORMANCE-BASED DESIGN OF FRAME STRUCTURES

Ricardo A. MEDINA [1] and Helmut KRAWINKLER [2]

ABSTRACT

This paper focuses on the presentation of results for engineering demand parameters (EDPs) that are relevant for seismic performance assessment and performance-based design. Addressed are roof and story drifts (for structural damage and drift sensitive non-structural damage), absolute floor accelerations (for acceleration sensitive content damage), and strength demands relevant for the design of columns. The sensitivity of the results to several basic assumptions made in the mathematical models of frames is evaluated. Structure P-delta effects are included and are found to have a predominant effect for long period flexible structures. The results are presented in order to document behavior patterns that are characteristic for regular moment resisting frame structures.

1. INTRODUCTION

This paper presents a summary of salient results obtained from a statistical evaluation of engineering demand parameters (EDPs) for generic frame structures. The emphasis is on the identification of patterns and trends in EDPs, which is intended to facilitate (a) understanding of response behavior, (b) performance assessment, and (c) the decision process in the conceptual design phase of performance-based design. All assumptions, specifics, and details of the study are documented in (Medina, 2003). The emphasis is on documentation, with much of the interpretation left to the reader.

2. STRUCTURES, GROUND MOTIONS, AND REPRESENTATION OF RESULTS

EDP evaluation is carried out using a family of one-bay generic frame models with number of stories, N, equal to 3, 6, 9, 12, 15, and 18, and fundamental periods, T_1, of 0.1N (stiff frames) and 0.2N (flexible frames), see Figure 1. The frames are designed so that the first mode shape is a straight line and simultaneous yielding occurs at all plastic hinge locations under a parabolic load pattern and at a base shear yield strength of V_y. Plastification, which is modeled by nonlinear rotational springs, is permitted only at beam ends and column bases. This model is called “beam hinge”, BH, model see Figure 2. The hysteretic behavior of the rotational springs is defined by a

[1] *Department of Civil and Environmental Engineering, University of Maryland, College Park, MD 20742, USA Email: ramedina@umd.edu*

[2] *Department of Civil and Environmental Engineering, Stanford University, Stanford, CA 94305-4020, USA Email: krawinkler@stanford.edu*

"happy" peak oriented model, see Figure 2, with the term "happy" implying that the springs possess infinite ductility and exhibit no strength deterioration. [The effects of deterioration are evaluated in a separate study (Krawinkler and Ibarra, 2003)]. Strain hardening of 3% is assumed at all plastic hinge locations. Structure P-delta effects are considered, but the effects of gravity load moments are ignored. For the nonlinear time history analyses, 5% Rayleigh damping is assigned to the first mode and the mode at which the cumulative mass participation exceeds 95%.

A set of 40 ordinary ground motions (denoted as LMSR-N) is used to carry out the seismic demand evaluation. The ground motions are from Californian earthquakes of moment magnitude between 6.5 and 6.9 and closest distance to the fault rupture between 13 km and 40 km. Near-fault effects are not considered. These ground motions were recorded on NEHRP site class D.

The analysis approach consists of performing for each structure and each ground motion a series of nonlinear time history analyses. The parameter used to "scale" the ground motion intensity for a given structure strength, or to "scale" the structure strength for a given ground motion intensity, is the parameter $[S_a(T_1)/g]/\gamma$, where $S_a(T_1)$ is the 5% damped spectral acceleration at the fundamental period of the structure, and γ is the base shear coefficient, i.e., $\gamma = V_y/W$. This

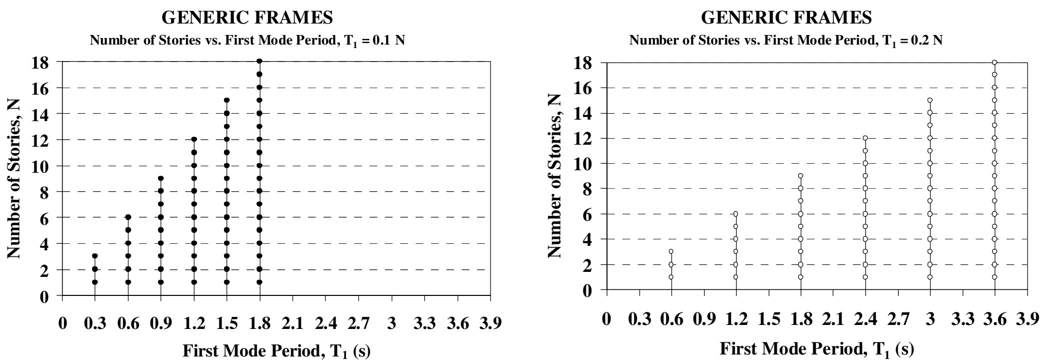

Figure 1. Family of generic frames; (a) stiff frames, T_1 = 0.1N, (b) flexible frames, T_1 = 0.2N

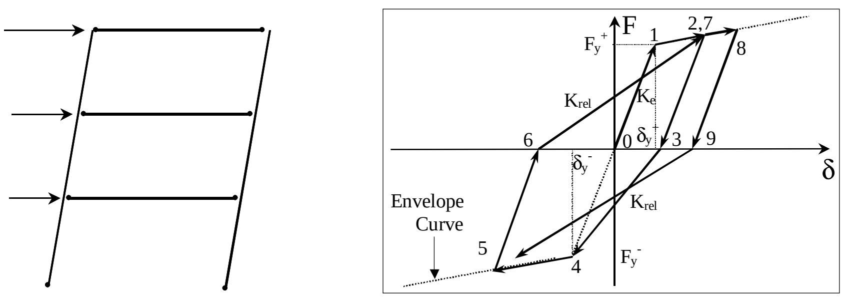

Figure 2. Frame with beam hinge mechanism, and peak-oriented hysteretic model

parameter identifies the intensity of the ground motion (using $S_a(T_1)$ as the ground motion intensity measure) relative to the structure base shear strength. The use of $[S_a(T_1)/g]/\gamma$ as a relative intensity measure can be viewed two ways; either keeping the ground motion intensity constant while decreasing the base shear strength of the structure (in which case the relative intensity represents the ductility-dependent response modification factor [often denoted as R_μ] because no overstrength is present), or keeping the base shear strength constant while increasing the intensity of the ground motion (the Incremental Dynamic Analysis (IDA) perspective).

Relationships between an EDP (which could be a deformation, energy, strength, or acceleration quantity) and the relative intensity usually are represented in a normalized form, see Figure 3a, or can be de-normalized into an IDA by selecting a specific value for γ, see Figure 3b. Statistical measures of EDPs can be obtained for a given value of relative intensity, resulting in median curves and median ± dispersion curves. From here on only median curves will be presented.

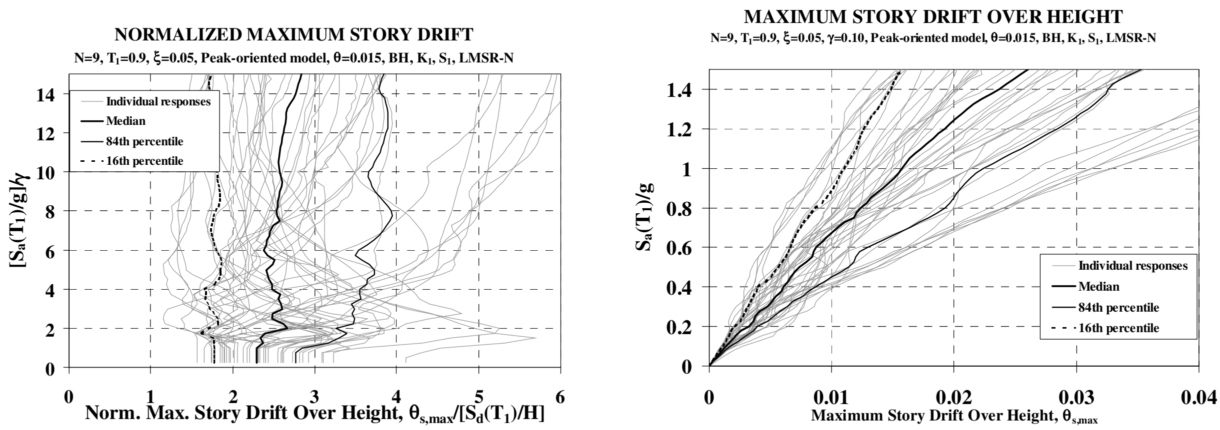

Figure 3. Statistical IM-EDP relationships, N = 9, T_1 = 0.9 s., (a) normalized, (b) IDA for γ = 0.1

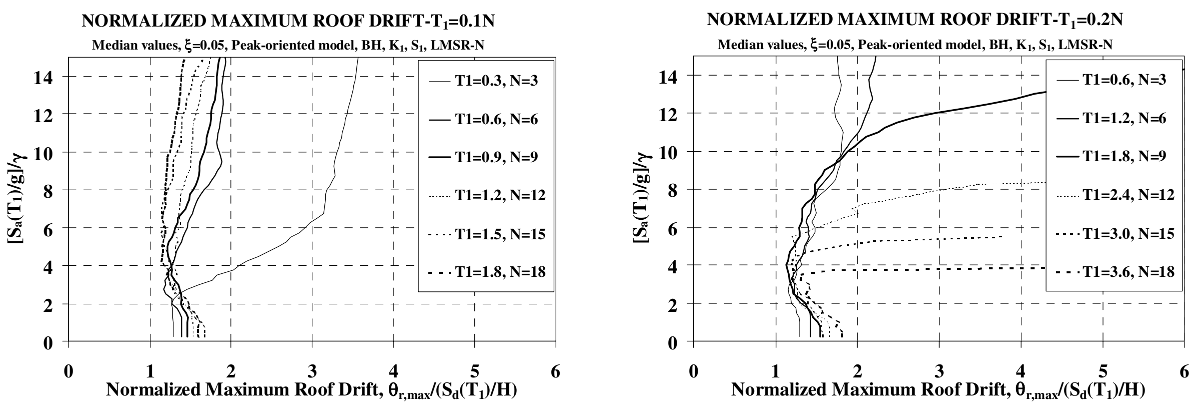

Figure 4. Normalized maximum roof drift; (a) stiff frames, (b) flexible frames

3. ROOF AND STORY DRIFT DEMANDS

The variation of roof drift demands with relative intensity is presented in Figure 4 for stiff and flexible frames. The figure shows that roof drift demand, once normalized to the elastic spectral displacement divided by height, is not sensitive to the relative intensity - except for short period structures (T_1 = 0.3) and flexible long period structures for which P-delta effects cause a negative tangent stiffness (which may lead to collapse, as seen when the slope of a curve becomes zero).

Figures 5 to 9 present quantitative data (median values based on record-to-record variability) on the dependence of drift demands on first mode period and on frame stiffness (stiff vs. flexible frames). The left half of each figure is for small relative intensities ($[S_a(T_1)/g]/\gamma$ from 0.25 (elastic) to 2.0), and the right half for large ones ($[S_a(T_1)/g]/\gamma$ from 4.0 to 8.0). Results are presented for max. roof drift, average of max. story drifts (measure of average damage), and max. story drift over all stories (measure of max. damage), as well as for ratios of average over roof drift and max. over roof drift. There are clear patterns, having to do with short and long period

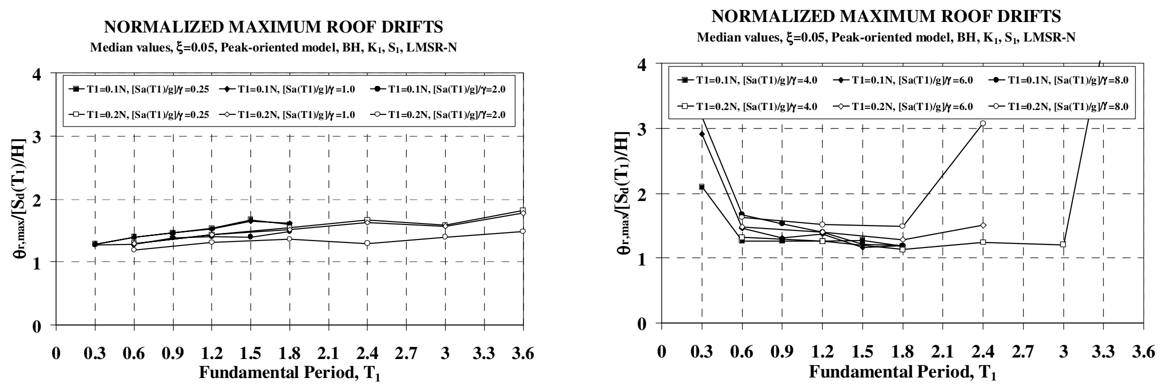

Figure 5. Dependence of norm. max. roof drift on T_1; various relative intensities

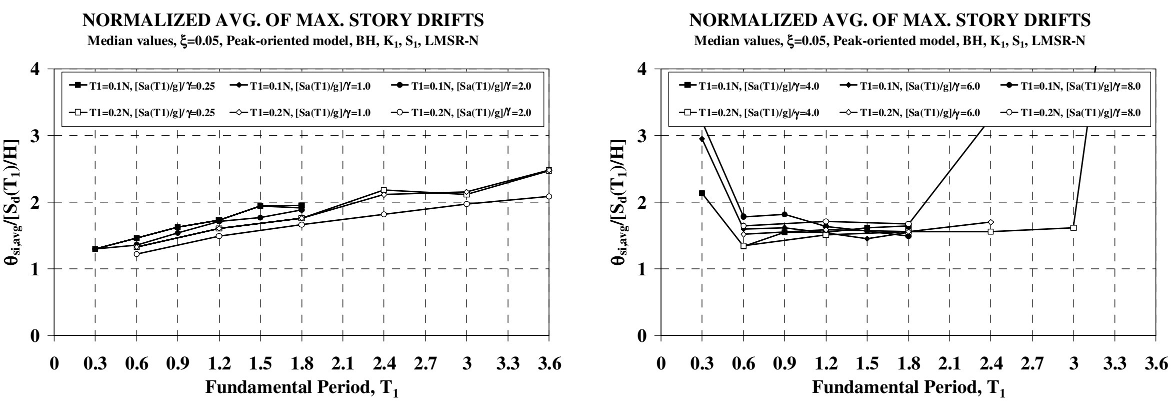

Figure 6. Dependence of norm. average of max. story drifts on T_1; various relative intensities

(P-delta controlled) structures and with the extent of inelastic behavior (relative intensity). Figure 8 shows that the ratio of average of max. story drifts over max. roof drift is clearly larger than 1.0 and increases with period (which has implications on the target displacement of the pushover analysis), and Figure 9 presents detailed results on the ratio of max. story drift over roof drift.

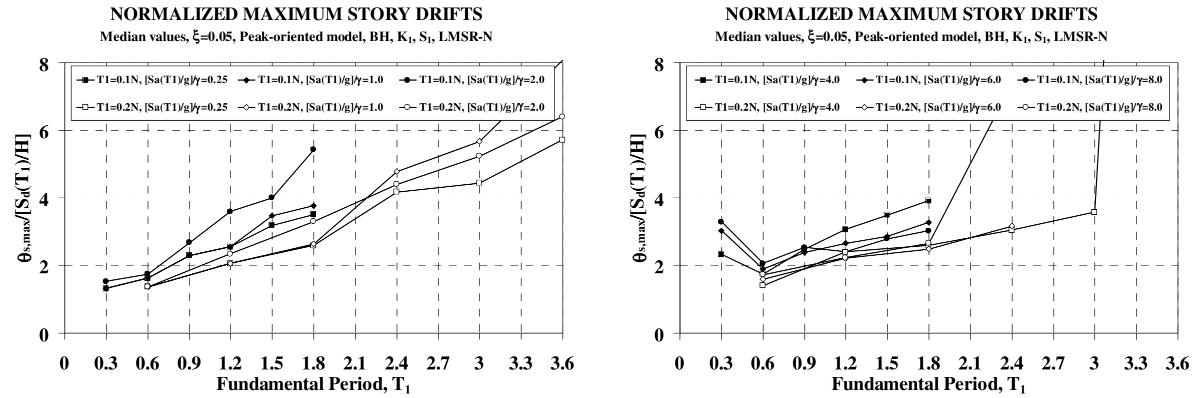

Figure 7. Dependence of norm. max. story drift over height on T_1; various relative intensities

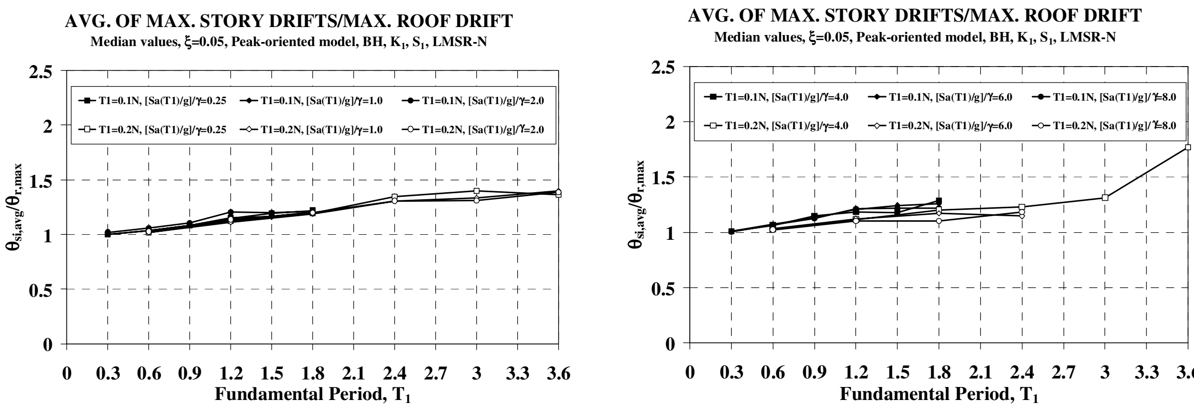

Figure 8. Dependence of ratio of avg. of max. story drifts to max. roof drift on T_1

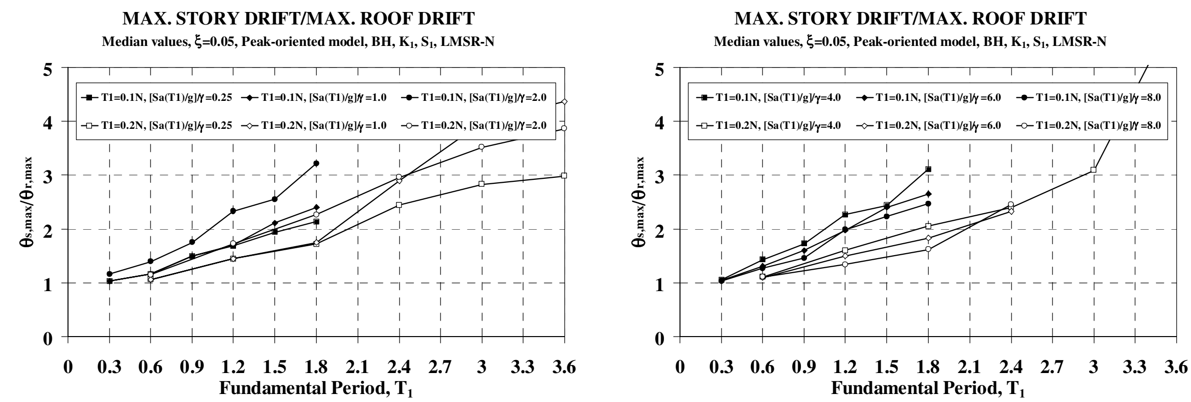

Figure 9. Dependence of ratio of max. story drift over height to max. roof drift on T_1

Figure 10 illustrates how the story drift profile changes with period and extent of inelasticity (relative intensity). The elastic profiles show a clear tendency towards large story drifts at the top for longer period structures. In part, this phenomenon has to do with the decision to tune stiffnesses so that the first mode shape of the structure is a straight line. As the structures become more inelastic, this tendency diminishes and a migration of maximum story drifts towards the base of the structures is observed.

Residual (post-earthquake) drift is often used as a measure of permanent damage. As a comparison of Figure 11b and 10b indicates (both figures have the same normalizing parameter on the EDP axis), the maximum residual story drift at a relative intensity of 4.0 is about a quarter of the maximum story drift. Results not shown here have demonstrated, however, that the dispersion in the residual drifts is very large and that the residual drifts depend strongly on the hysteretic system. For "pinched" hysteretic systems the residual drift grows considerably in the median, but the dispersion becomes even larger. Compared to patterns in most other deformation parameters, the patterns in residual drifts are not very consistent.

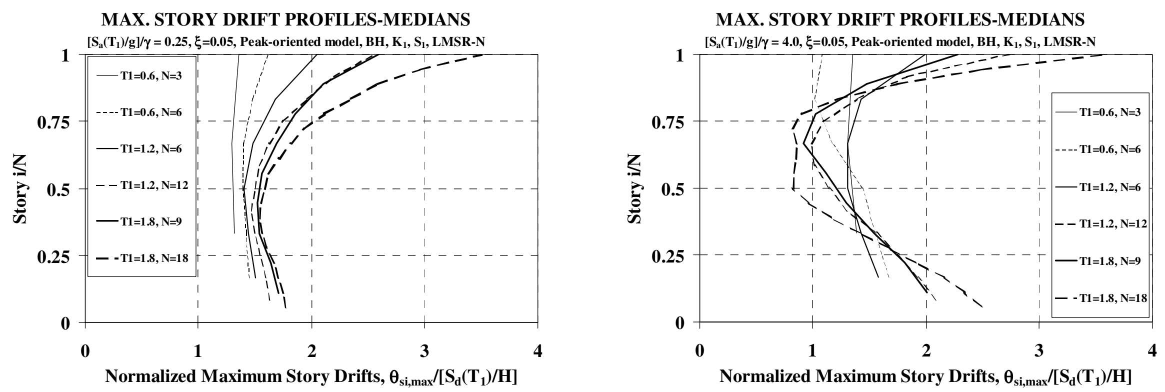

Figure 10. Distribution over height of norm. max. story drifts; $[S_a(T_1)/g]/\gamma = 0.25$ & 4.0

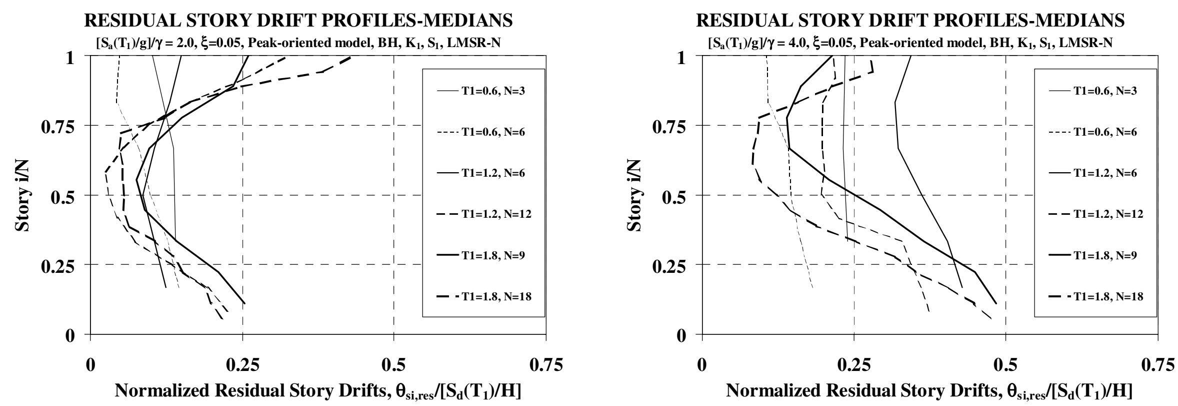

Figure 11. Distribution over height of norm. residual story drifts; $[S_a(T_1)/g]/\gamma = 2.0$ & 4.0

4. FLOOR ACCELERATION DEMANDS

In the context of economic losses, damage to acceleration sensitive building content may become a dominant consideration. The maximum absolute floor acceleration, $a_{f,max,}$ is a necessary, albeit mostly insufficient, measure for acceleration sensitive content damage. Figure 12 illustrates the dependence of floor acceleration (average and max. over height, both normalized w.r.t. PGA) on the relative intensity for a 9-story structure. There are three distinct regions in the plot, which are common to all frames used in this study. The first region defines the elastic range in which the normalized $a_{f,max}$ remains constant regardless of the relative intensity. In the second region, the normalized $a_{f,max}$ decreases rapidly with an increase in relative intensity. The third region corresponds to the stabilization of normalized $a_{f,max}$ values for very large relative intensities. In the third region, higher modes have a significant contribution to the acceleration response of the system, and the first mode does not dominate. Therefore, normalized $a_{f,max}$ values are not inversely proportional to the relative intensity, as is the case for an inelastic SDOF system.

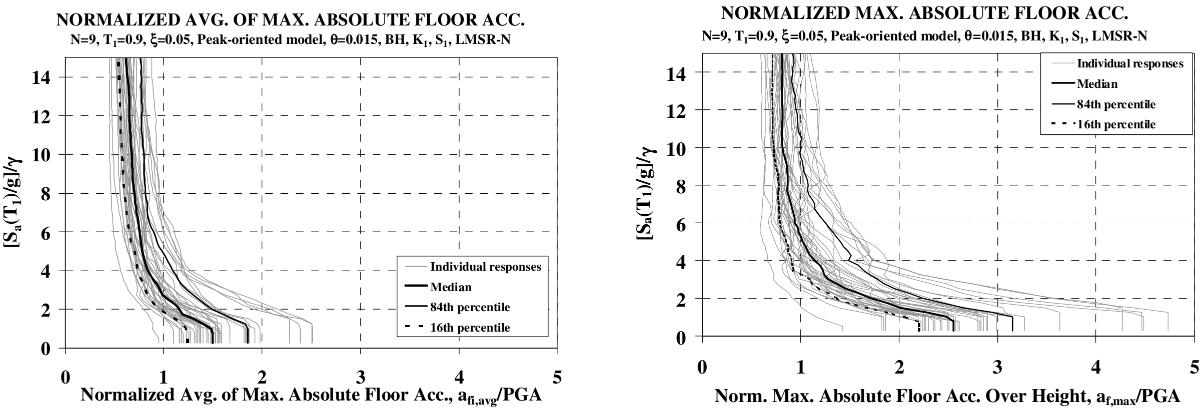

Figure 12. Variation with relative intensity of (a) norm. avg. of max. absolute floor accelerations, and (b)norm. max. absolute floor acceleration; 9-story, T_1 = 0.9 s.

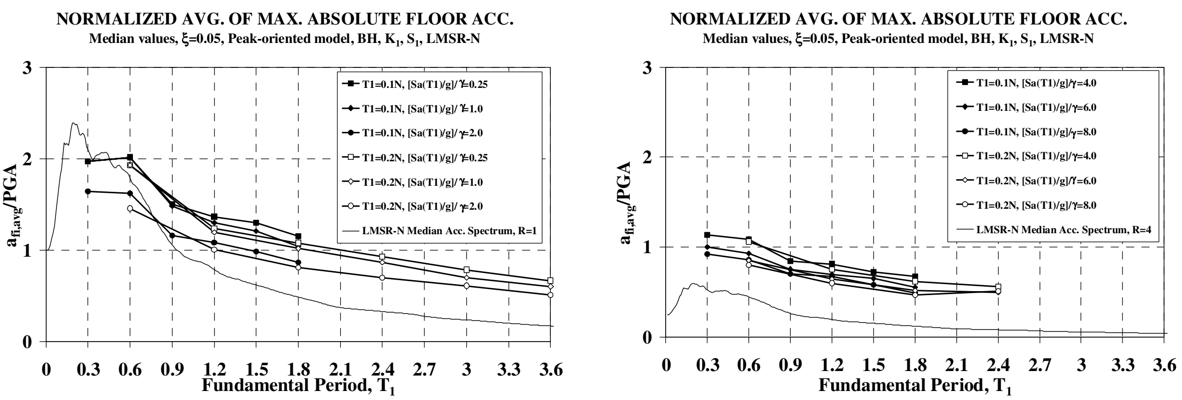

Figure 13. Dependence of norm. average of maximum absolute floor accelerations on T_1

The fact that for the same ground motion intensity floor accelerations do not vary proportionally to the yield strength is evident also from Figures 13 and 14. For large relative intensities (right graphs) the normalized absolute acceleration stabilizes and is only weakly dependent on the level of inelastic behavior. The figures also demonstrate that normalized maximum acceleration demands are not inversely proportional to the R factor, and hence, the level of inelastic behavior. It is noted that for elastic behavior the difference between maximum and average floor accelerations is large, whereas it becomes small for highly inelastic behavior.

Figure 15 shows the normalized floor acceleration profiles for relative intensity levels of 0.25 (elastic) and 4.0. It can be seen that $a_{f,max}$ migrates from the top story for elastic behavior to the bottom stories for highly inelastic systems. Moreover, as the system becomes more inelastic, the maximum floor accelerations stabilize and remain rather constant over the height of the frame. This general pattern has been observed for the complete family of generic frames.

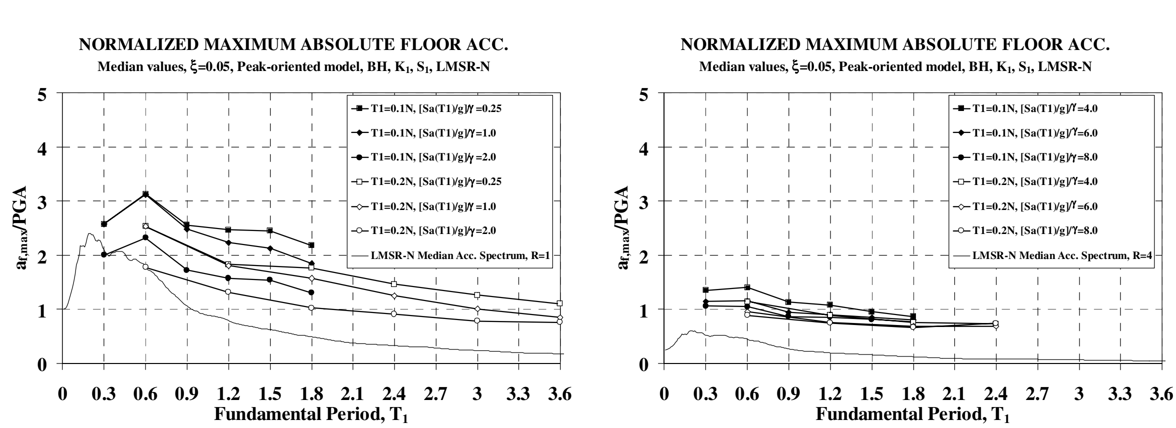

Figure 14. Dependence of norm. max. absolute floor acceleration over the height on T_1

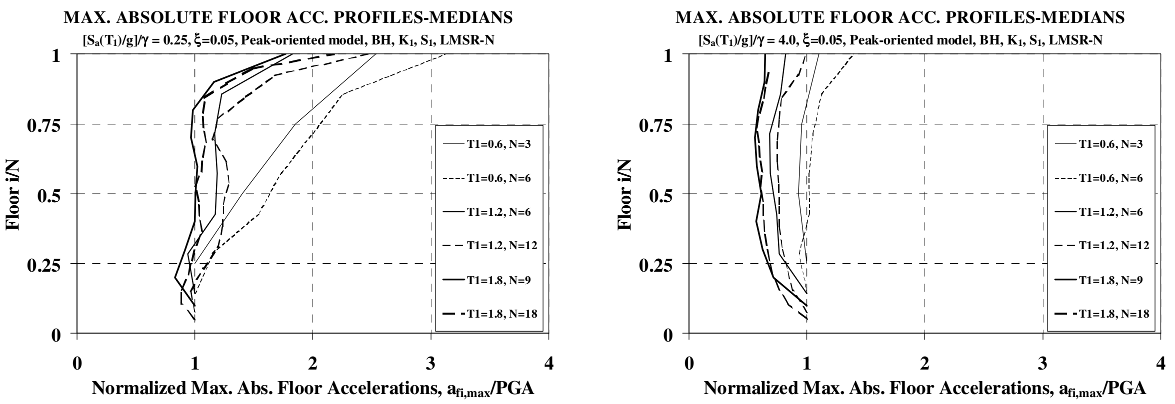

Figure 15. Distribution over height of norm. max. absolute floor acceleration, $[S_a(T_1)/g]/\gamma = 0.25$ (elastic) and 4.0

5. GLOBAL AND LOCAL STRENGTH DEMANDS

Story shear and overturning moment demands. Column shear design may be governed by one of several considerations, one of them being the story shear strength demand predicted from analysis, such as a pushover. As Figure 16 shows, the dynamic story shear demands may be considerably larger than those predicted from a pushover analysis. And so may be the dynamic overturning moment (OTM) demands, which control the axial force design of columns. Figure 17 shows pushover as well as dynamic OTM results for the case of Figure 16. In this example the pushover provides good estimates of OTM demands, but only because all stories yield simultaneously. Many results by others have shown that pushovers often are poor predictors of OTM demands unless all stories yield simultaneously in the pushover. The conclusion is that results from a pushover analysis must be treated with great caution when they are used for strength design of structures with significant higher mode effects.

Strong column – weak beam concept. It is well established that strict adherence to the strong column – weak beam concept is difficult to implement. Present US guidelines recommend that the strong column factor (sum of column bending strength over sum of beam bending strength) be about 1.2. The results of Figure 18 demonstrate that prevention of plastic hinging of columns would require very large strong column factors. The presented results show that the required strong column factor increases almost linearly with the relative intensity, and may exceed a value of 2 at a relative intensity of 4, and a value of 3 at a relative intensity of 8. Figure 19 shows that this factor is relatively uniform over the height of the structure. These large factors would not show up in a pushover analysis, because in part they are caused by higher (primarily second) mode effects. Strict adherence to the strong column concept may not be necessary at every

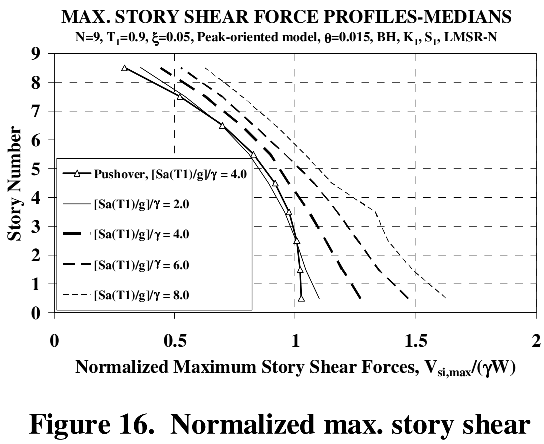

Figure 16. Normalized max. story shear forces, N = 9, T_1 = 0.9 s.

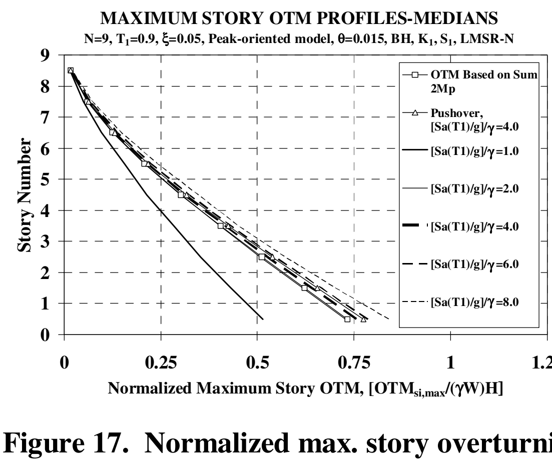

Figure 17. Normalized max. story overturning moments, N = 9, T_1 = 0.9 s.

column, but the very large values of these factors raise questions on the validity of the presently employed approach. A phenomenon associated with the moment redistribution that causes the large strong column factors is the occurrence of large bending moments at midheight of columns, see Figure 20. These large moments may deserve explicit design consideration.

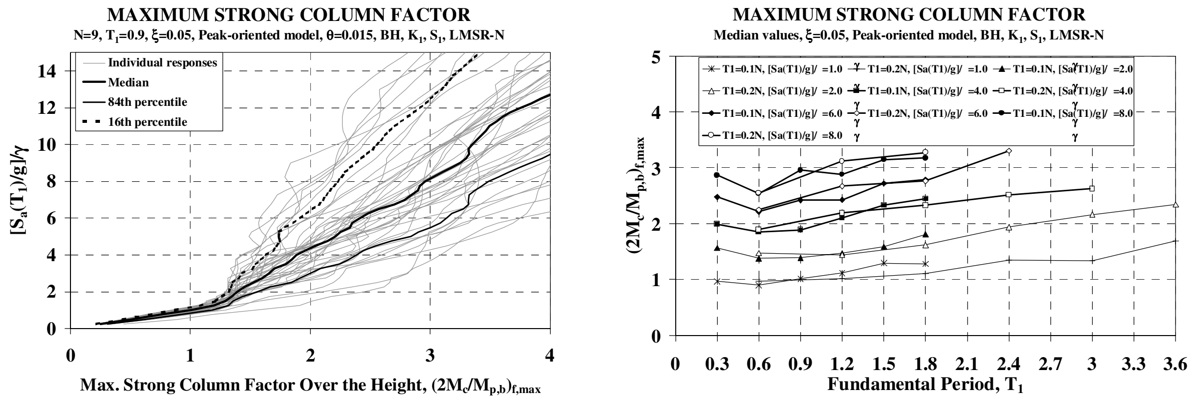

Figure 18. Maximum strong column factor over the height; (a) variation with relative intensity for 9-story, $T_1 = 0.9$ s., (b) dependence on relative intensity and T_1

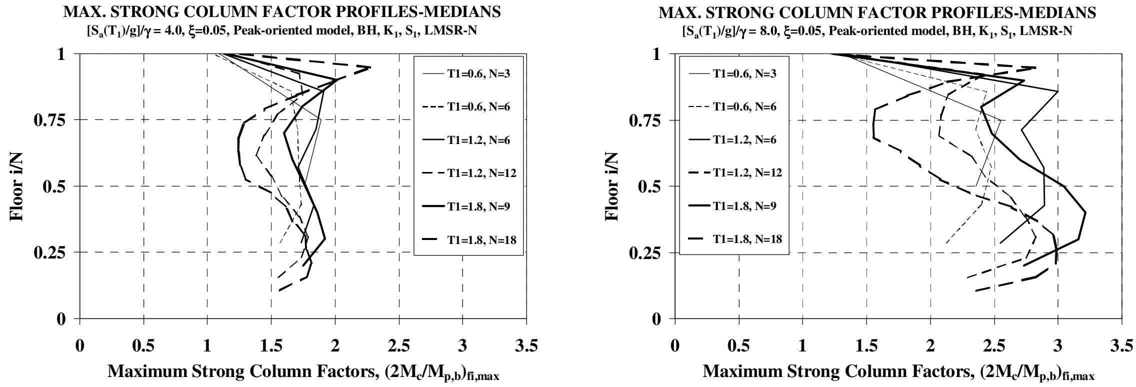

Figure 19. Distribution over height of max. strong column factors; $[S_a(T_1)/g]/\gamma = 4.0$ & 8.0

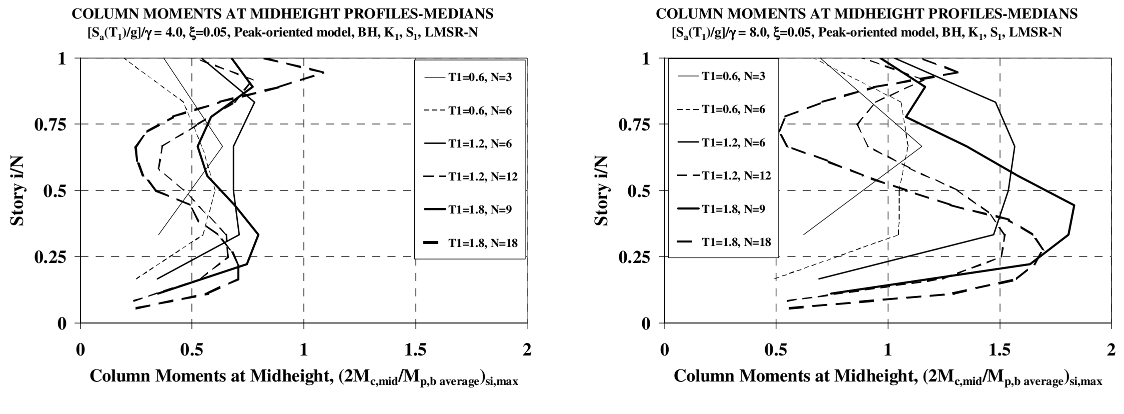

Figure 20. Distrib. over height of norm. max. column moments at midheight, $[S_a(T_1)/g]/\gamma = 4.0$ & 8.0

6. RESPONSE SENSITIVITIES

The results presented in this paper are median values obtained under a great number of assumptions. Some have to do with the selected ground motions, and others with the choices of structural parameters. The effects of a few of the latter are discussed next.

Effect of hysteretic model. All results presented so far are for a peak oriented hysteresis model. Figures 21 to 23 show representative results on the effect of different models on the roof and story drift demands. The general conclusion is that the "pinching" model (severe pinching of hysteresis loops) leads to somewhat greater drift demands than the peak oriented and bilinear model. This pattern is equally valid for roof and maximum story drift demands, as the ratio of the two EDPs is essentially independent of the hysteretic model, see Figure 23. However, this pattern is reversed in the case of flexible structures that are controlled by P-delta effects. In this case the bilinear model gives the largest predictions of EDPs, and pinched models the smallest, because they spend the least time on the envelope of the response curve (results not shown).

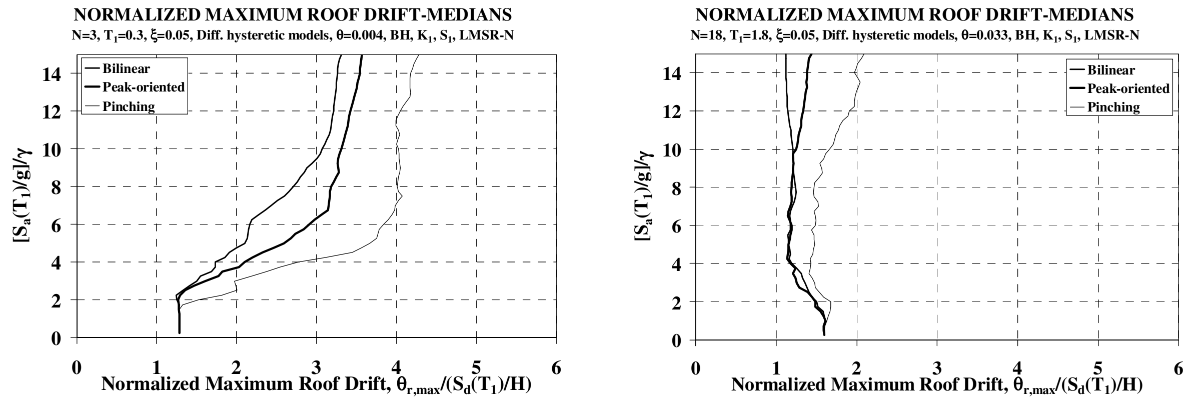

Figure 21. Effect of hysteretic model on norm. max. roof drift, T_1 = 0.3 s. & 1.8 s.

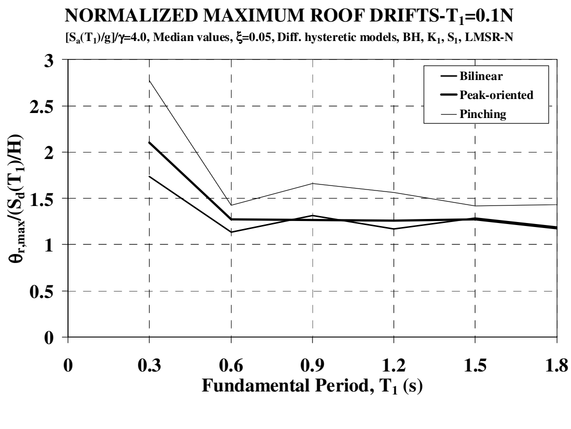

Figure 22. Effect of hyst. model on norm. max. roof drift, dependence on period

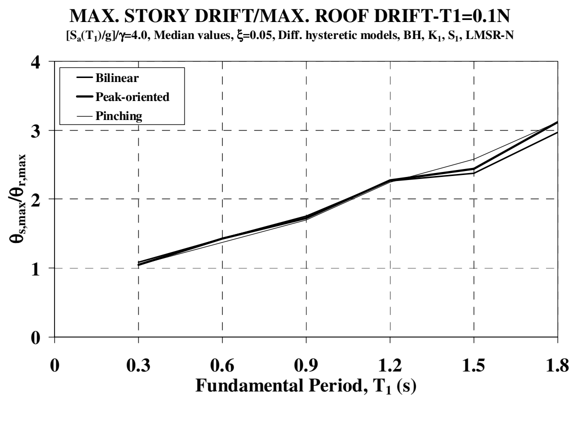

Figure 23. Effect of hyst. model on ratio of max. story drift to max.roof drift, $[S_a(T_1)/g]/\gamma = 4.0$

Effect of material strain hardening. In the results presented so far, 3% strain hardening is assumed in the hysteretic model. In general the sensitivity to small variations in strain hardening is small, except when the extent of inelasticity becomes very large or the structure becomes P-delta sensitive. This is illustrated in Figure 24, which shows relative intensity – roof drift curves for a 9-story frame with strain hardening of 3% and 0%. For the flexible structure (T_1 = 1.8 sec.) the lack of strain hardening leads to P-delta collapse at a relative intensity of about 8.

Effect of P-delta. This effect cannot be separated from the strain hardening effect. If the effective post-yield tangent stiffness (in which strain hardening and second order effects have opposing effects) becomes negative, P-delta sensitive response will be obtained. For instance, the two structures whose response is shown in Figure 25, have the same number of stories and strain hardening, but the flexible one has a first story elastic stability coefficient that is four times as large as that for the stiff one. The flexible structure collapses at a relative intensity of four.

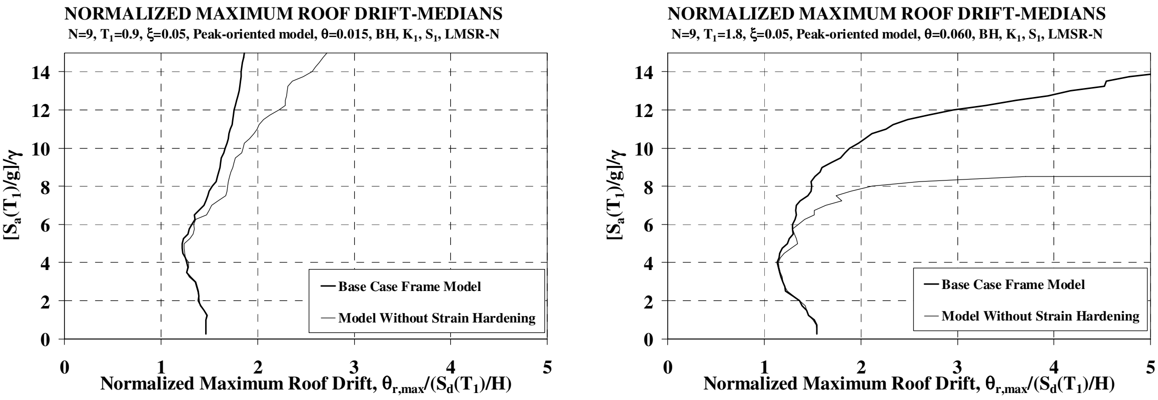

Figure 24. Effect of strain hardening on norm. max. roof drift, 9-story, T_1 = 0.9 & 1.8 s.

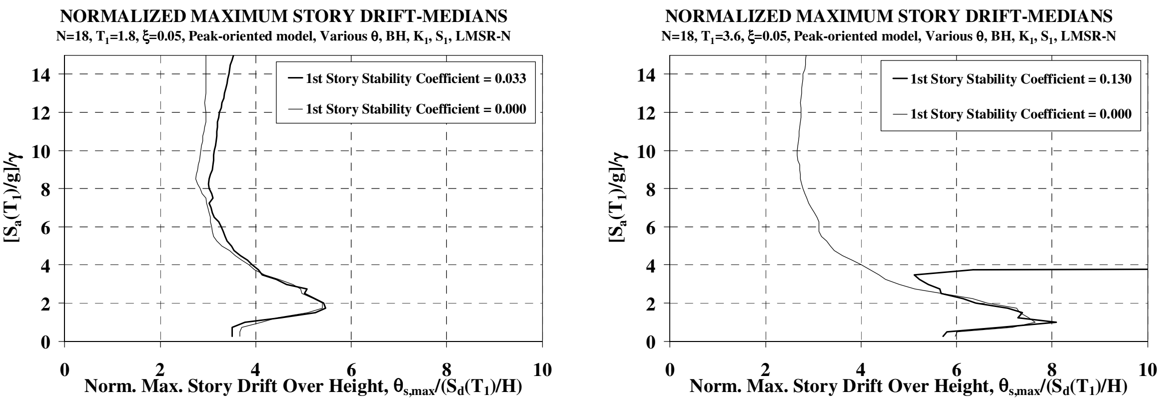

Figure 25. Effect of P-delta on norm. max. story drift over height, 18-story, T_1 = 1.8 & 3.6 s.

Effect of gravity load moments. If significant gravity load moments are present, see Figure 26, the initial inelastic response of the structure will be affected. But this effect is present only for relatively light inelastic response, and fully diminishes at relative intensities that require highly inelastic response, see Figure 27. The reason is that because of shakedown the effect of gravity moments on the element hysteretic response disappears at deformation levels larger than that associated with the second branch of the trilinear pushover curve shown in Figure 26.

Effect of type of mechanism. All results presented so far are for BH models in which plastic hinges are permitted only at beam ends and column bases. If plastic hinges are permitted to occur only in the columns and not in the beams (CH model), individual story mechanism will develop, which are known to have a very detrimental effect. The effect on the maximum story drift over the height is illustrated in Figure 28. The curves between BH and CH models deviate rapidly for relative intensities greater than about one, and in several cases early P-delta triggered collapse is noted for the CH model structures.

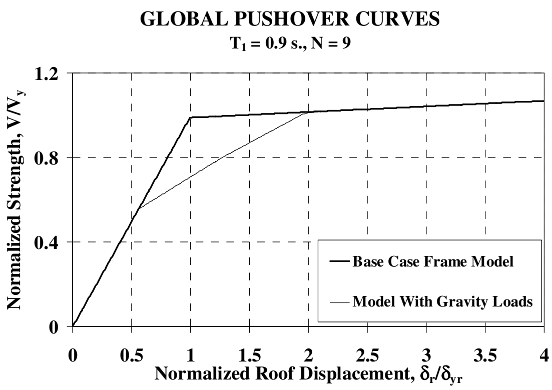

Figure 26. Global pushover curve without and with gravity moment effect, 9-story

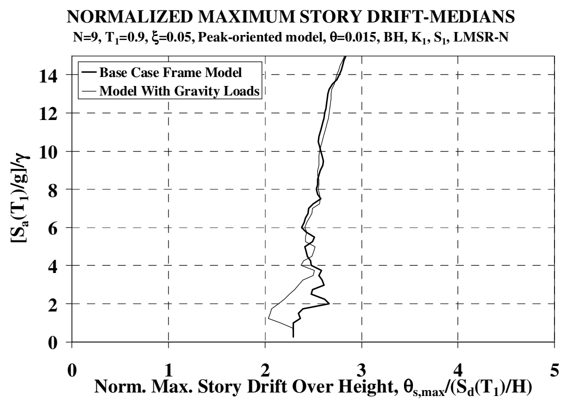

Figure 27. Effect of gravity moments on norm. max. story drift over height, N = 9, T_1 = 0.9 s.

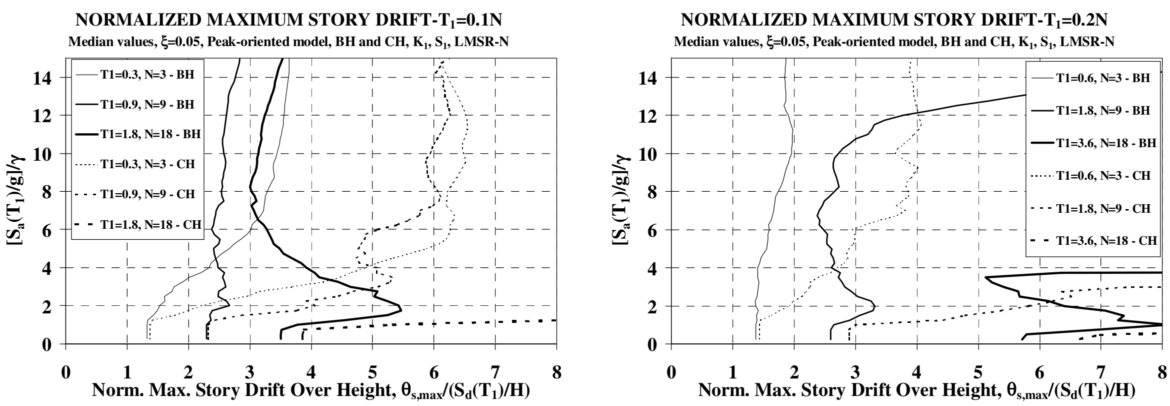

Figure 28. Effect of mechanisms on norm. max. story drift over height, T_1 = 0.1N & 0.2N

7. SUMMARY

Rigorous performance assessment requires comprehensive and rigorous tools and extensive knowledge and data on ground motions, geological and geotechnical conditions, the soil-foundation-structure system, and the distribution and properties of the nonstructural systems and of building contents. This includes data on the randomness/uncertainty of the physical properties describing all these phenomena and subsystems. When the issue is loss estimation, cost data may become an overriding consideration, and when the issue is life safety, we have challenging tasks ahead of us to define the extent of collapse and to relate collapse modes to injuries and fatalities. All these issues deserve much of our attention, so we can make the next big step forward. But in the meantime we should not forget that engineers have to design buildings quickly and efficiently, and that their decisions have to be based mostly on well established concepts of strength, stiffness, and ductility, supplemented by advancing knowledge in detailing, capacity design, and advancements in material and control technologies that provide new and exciting alternatives for performance enhancements.

For this reason, improving the understanding of structural behavior and of response patterns that significantly affect decisions on the engineering parameters on which most design are based, should remain a noble objective of research. This paper provides a short summary of quantitative information on many relevant EDPs for moment-resisting frames, which has been obtained from a rather comprehensive parameter study of generic frame structures.

8. ACKNOWLEDGEMENTS

This research is supported by the Pacific Earthquake Engineering Research (PEER) Center, an Engineering Research Center sponsored by the US National Science Foundation. This support is much appreciated.

9. REFERENCES

Medina, R. A. (2003). Seismic demands for nondeteriorating frame structures and their dependence on ground motions. *Ph.D. dissertation*, Department of Civil and Environmental Engineering, Stanford University, Stanford, CA.

Krawinkler, H. and Ibarra, L. (2003). Collapse probability of frame structures with deteriorating properties. Proceedings of *Performance-Based Engineering for Earthquake Resistant Reinforced Concrete Structures, International Symposium Honoring Prof. Shunsuke Otani*, Tokyo, September 8/9, 2003.

CORRELATION OF INELASTIC RESPONSES WITH DISSIPATED ENERGY OF R/C BUILDINGS

Tetsuo KUBO[1]

ABSTRACT

Correlation of inelastic responses of a reinforced building with energies dissipated within the building during inelastic responses obtain when subjected to strong earthquake ground motion. A SDOF oscillating system is employed in analysis, representing a weak-beam and strong-column design based R/C building. Utilizing four components of real earthquake motion, through a numerical analysis, energies dissipated by the damping mechanisms, the hysteresis mechanisms and the inertia kinematics mechanisms, and the energy applied to the building by seismic excitation are evaluated with variation of the developed inelastic responses of building. Examined and discussed the correlation of the energies evaluated herein with the developed inelastic responses in ductility factors. Substitute damping coefficients are evaluated for the response for an equivalent linear system. Provided that the energy applied to a building can be prescribed during a strong earthquake ground motion as one of design parameters, a proposal to estimate an inelastic response of R/C building based on the energy dissipated within a building is introduced.

1. INTRODUCTION

Correlation of inelastic responses of reinforced concrete building with the energies dissipated by the responses of building is examined (Kubo and others, 2003, and Okuda and others, 2003). Energy dissipated by the building during the responses and that dissipated exclusively by the inelastic hysteretic characteristics are examined. Herein the paper, discussed is the correlation between the peak responses in an inelastic region during intense ground motions and the energies dissipated by the building responses associated with the variation of inelastic responses.

2. ANALYTICAL MODEL FOR SIMULATION

2.1 Building Model for Analysis

[1] *Department of Architecture, University of Tokyo, Tokyo (effective on and from October 16, 2003) and Earthquake Disaster Mitigation Res. Ctr, National Research Institute for Earth Science and Disaster Prevention, Kobe, Japan*

Email: kubo@arch.t.u-tokyo.ac.jp ; kubo@edm.bosai.go.jp

A single-degree-of-freedom oscillating system is examined in the study. The SDOF system will represent a multi-story building, the response mode of which during earthquake excitation remains unchanged. The model of SDOF system will represent a building designed by the concept of "the weak-beam and strong-column design," response mode of which will be well represented by a uniquely prescribed shape.

The mass of the system is assumed to be unity of 1.0×10^3kg. The primary curve for the load-deflection characteristics is specified by the tri-linear model as shown in Figure 1. The coefficient of yielding strength of building is taken 0.3 with 2.94 kN in strength. That of cracking strength is one-third of yielding strength. The ratio of equivalent yielding stiffness compared to that of elastic stiffness is 1/4, and the elastic stiffness is determined prescribing the fundamental period of the system to be 0.4 seconds.

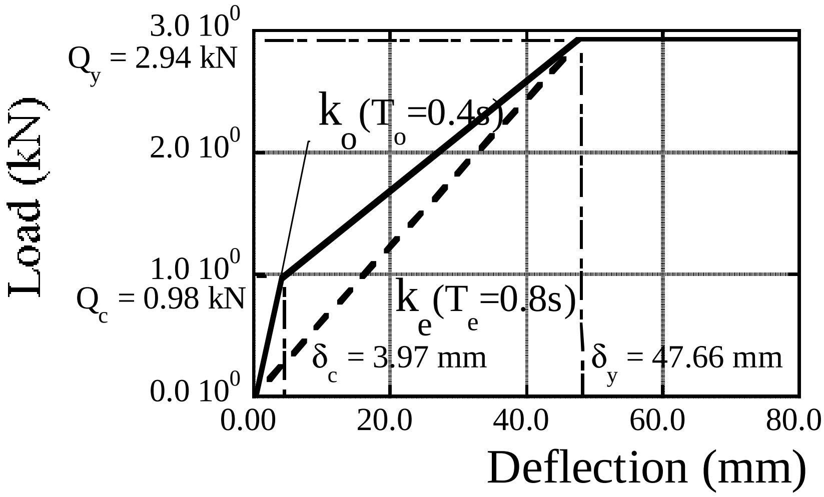

Figure 1 Load-Deflection Characteristics of Building Model in Analysis.

The hysteresis rule employed in the analysis is described by the Takeda model, representing well flexural yielding characteristics.

2.2 Strong Earthquake Ground Motions

Four real earthquake strong ground motions listed in the following are employed in analysis: (1) El Centro S00E Comp., Imperial Valley Earthquake of 1940 (ELC S00E); (2) Taft N69E Comp., Kern County Earthquake of 1952 (TFT N69E); (3) Hachinohe Harbour, East-West Comp., Tokachi-oki Earthquake of 1968 (HCH EW); and (4) Tohoku University, North-South Comp., Miyagi-ken Oki Earthquake of 1978 (THU NS).

The amplitudes of motion are scaled so as the resulting maximum displacement responses to fall in the value of unity, three and five and 10 expressed in terms of the ductility factor μ. The responses of μ equal to three and five correspond to design level, and those equal to unity and/or 10 reveal the lower and upper bound conditions.

3. ENERGY DISSIPATED WITHIN THE SYSTEM

3.1 Equation of Motion for a SDOF Oscillating System

The equation of motion for the SDOF oscillating system is described as in Equation (1).

$$m\ddot{x} + c_i^{i+1}\dot{x} + k_i^{i+1}\,\Delta x + F(t) = -m\ddot{y}_0(t) \qquad (1)$$

in which F(t) denotes the restoring force of the system during inelastic responses.

3.2 Equation of Motion in Dissipating Energy Expression

Multiplying both the right and left hand sides of Equation (1) by (Δx) and integrating them with respect with time t, we obtain the following equation:

$$m\int \ddot{x}\dot{x}dt + \int c_i^{i+1}\dot{x}\dot{x}dt + \int (k_i^{i+1}\Delta x + F(t))\dot{x}dt = -m\int \ddot{y}_0(t)\dot{x}dt \qquad (2)$$

Substituting E_I = $m\int \ddot{x}\dot{x}dt$, E_D = $\int c_i^{i+1}\dot{x}\dot{x}dt$ and E_S = $\int (k_i^{i+1}\Delta x + F(t))\dot{x}dt$ into Equation (2), we find:

$$E_I + E_D + E_S = -m\int \ddot{y}_0(t)\dot{x}dt = E_T \qquad (3)$$

in which E_I, E_D, and E_S denote the energies dissipated by inertia mass kinematics, damping mechanisms and hysteretic mechanisms of inelastic responses, and E_T designates the energy applied to the system during the seismic action. Note that E_I equals zero when the response velocity of the system $\dot{x}$ reaches zero at the end of responses.

In this study herein, the fraction of critical damping in Equation (2) is taken equal to 0.05 for a R/C building.

4. RESPONSES OF THE SYSTEM SUBJECTED TO EARTHQUAKE MOTIONS

4.1 Responses of The Building

Peak displacement responses of the building associated with the variation of ductility factors and input earthquake ground motions are listed in Table 1. Figures in the parentheses indicate the inelastic responses expressed in terms of the ductility factor.

Table 1: Peak displacement responses.

Ductility Factor μ	ELC S00E	TFT N69E	HCH EW	THU NS
1.0	4.88 (1.02)	4.50 (0.94)	5.26 (1.10)	4.79 (1.01)
3.0	14.60 (3.06)	14.82 (3.11)	14.73 (3.09)	15.53 (3.26)
5.0	24.28 (5.09)	23.64 (4.96)	24.27 (5.09)	23.91 (5.02)
10.0	49.23 (10.33)	48.60 (10.20)	48.03 (10.08)	49.23 (10.33)

(in cm)

4.2 Energies Dissipated within The Building

Figures 2 and 3 show the responses of energies dissipated within the system when subjected to the ELC NS and HCH EW motions, producing the inelastic responses of five and three in ductility factor, respectively. Duration of ground motion excitation is 40 seconds with 10 seconds null acceleration follows, generating free vibration for the system to reach the equilibrium condition at the end of excitation.

Table 2 tabulates the total applied energy E_T (Total Energy Applied to Building in kJoule) for responses associated with ductility factors and input earthquake motions. Tables 3 and 4 list the energies dissipated by the building E_S (Dissipated Energy by Hysteresis Mechanisms) and E_D (Dissipated Energy by Damping Mechanisms) with ratios of E_S/E_T and E_D/E_T. Figures in the parentheses indicate the ratios. As is expected, the energy dissipated by the inertia kinematics E_I of building response is almost zero.

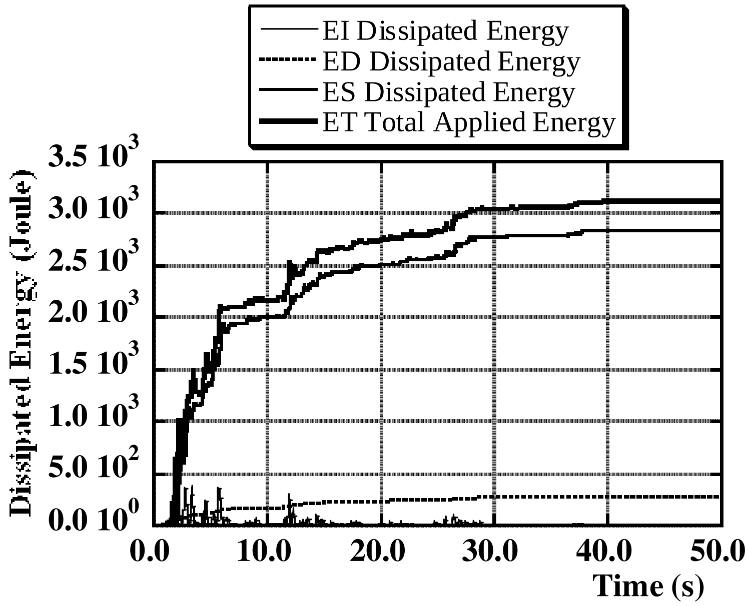

(b) Energy dissipated during building responses.

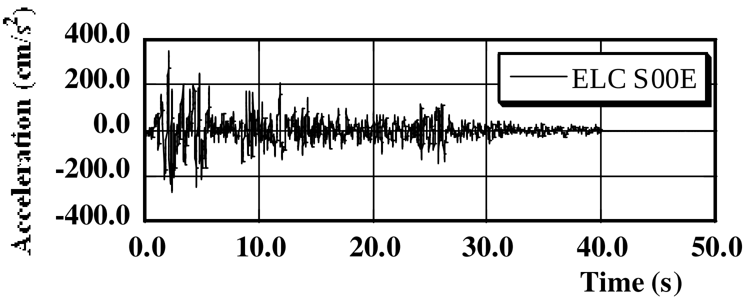

(a) Time trace of the earthquake ground motion applied to the building.

Figure 2: Energies dissipated within the building: El Centro S00E component; and maximum displacement response μ = 5.0.

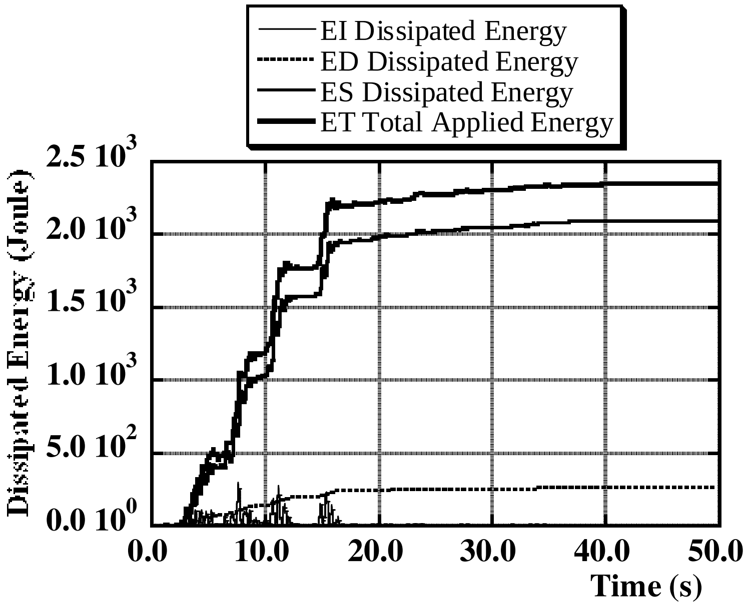

(b) Energy dissipated during building responses.

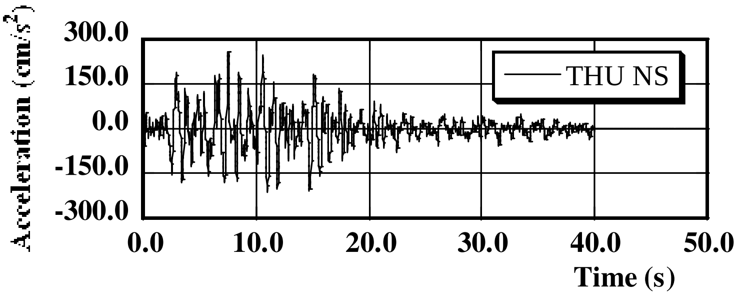

(a) Time trace of the earthquake ground motion applied to the building.

Figure 3: Energies dissipated within the Building: Tohoku University NS component; and maximum displacement response μ = 3.0.

Table 2: Total energy applied to the building during earthquake ground motion: E_T.

Ductility Factor μ	ELC S00E	TFT N69E	HCH EW	THU NS
1.0	0.467	0.461	0.444	0.411
3.0	1.604	2.154	2.020	2.357
5.0	3.125	4.532	2.701	3.605
10.0	5.501	8.786	4.451	5.503

(in k Joule)

Table 3: Energy dissipated by the damping mechanisms: E_D.

Ductility Factor μ	ELC S00E	TFT N69E	HCH EW	THU NS
1.0	0.140 (0.300)	0.165 (0.358)	0.129 (0.291)	0.121 (0.295)
3.0	0.209 (0.130)	0.230 (0.107)	0.194 (0.096)	0.262 (0.111)
5.0	0.284 (0.091)	0.297 (0.066)	0.207 (0.077)	0.276 (0.076)
10.0	0.345 (0.063)	0.480 (0.055)	0.237 (0.053)	0.328 (0.060)

(in k Joule)

Table 4: Energy dissipated by the hysteresis mechanisms: E_S.

Ductility Factor μ	ELC S00E	TFT N69E	HCH EW	THU NS
1.0	0.327 (0.700)	0.296 (0.642)	0.315 (0.709)	0.290 (0.705)
3.0	1.395 (0.870)	1.924 (0.893)	1.826 (0.904)	2.094 (0.889)
5.0	2.841 (0.909)	4.235 (0.934)	2.494 (0.923)	3.329 (0.923)
10.0	5.155 (0.937)	8.305 (0.945)	4.214 (0.947)	5.175 (0.940)

(in k Joule)

5. INELASTIC RESPONSES AND ENERGIES DISSIPATED WITHIN THE BUILDING

5.1 Energies Dissipated by The Hysteresis Mechanisms Associated with Responses

The correlation of the energy dissipated by the hysteresis mechanisms of inelastic responses E_S with the inelastic responses of building is examined. The plot of the dissipated energy E_S associated with the maximum displacement responses experienced is shown in Figures 4(b) and 5(b). The axes x and y denote the maximum displacement responses experienced within the building and the dissipated energy E_S, respectively. When the building develops fresh inelastic responses, one can find a certain amount of E_S dissipated accompanied with increase of potential energy within the building. Within the plots, one can realize that a large amount of E_S is dissipated within hysteresis mechanisms in cyclic responses of building. Observe the plots in Figures 5(b) and 6(b) together with the load-deflection hysteresis responses shown in Figures 5(a) and 6(a).

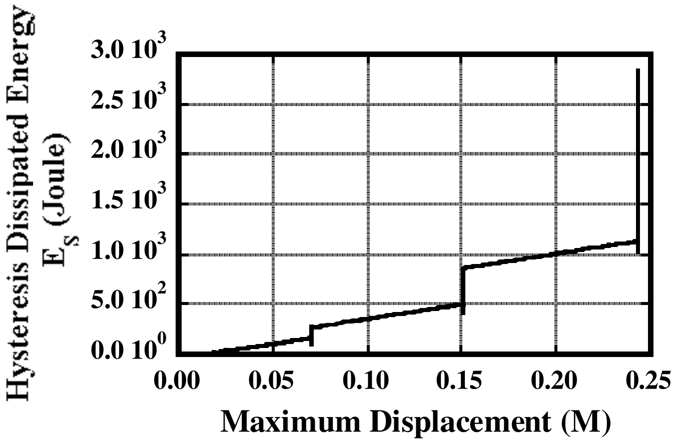

(b) Dissipated energy E_S associated with maximum experienced response.

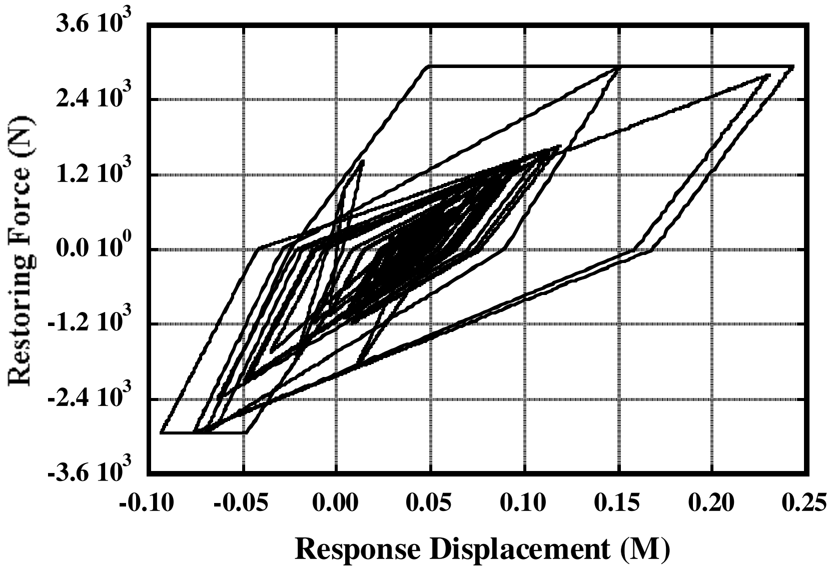

(a) Load-deflection hysteresis of responses.

Figure 4: Energies dissipated by hysteresis mechanisms: El Centro S00E component; and maximum displacement response μ = 5.0.

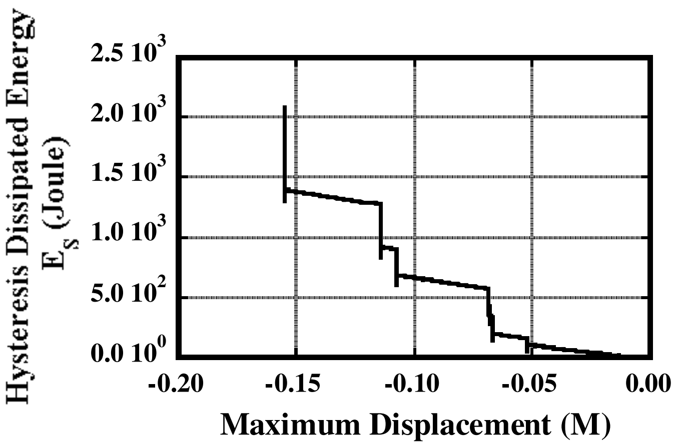

(b) Dissipated energy E_S associated with maximum experienced response.

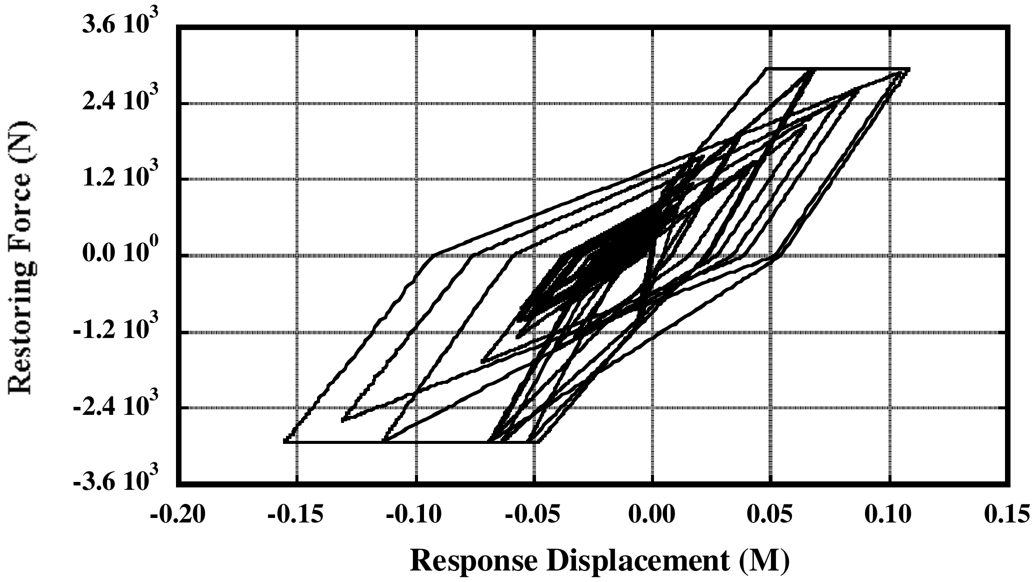

(a) Load-deflection hysteresis of responses.

Figure 5: Energies dissipated by hysteresis mechanisms: Tohoku University NS component; and maximum displacement response μ = 3.0.

5.2 Energies Required to Develop The Peak Inelastic Displacement Response

Herein we define the energy E_P required providing potential energy to develop an inelastic response. With specifying the inelastic responses, we can find out the energy E_P uniquely in Figure 6, and vice versa. The energy E_P obtained when subjected to the strong earthquake motions is tabulated in Table 5. Figures in the parentheses denote the ratios of the energy to that dissipated by the hysteresis mechanisms E_S.

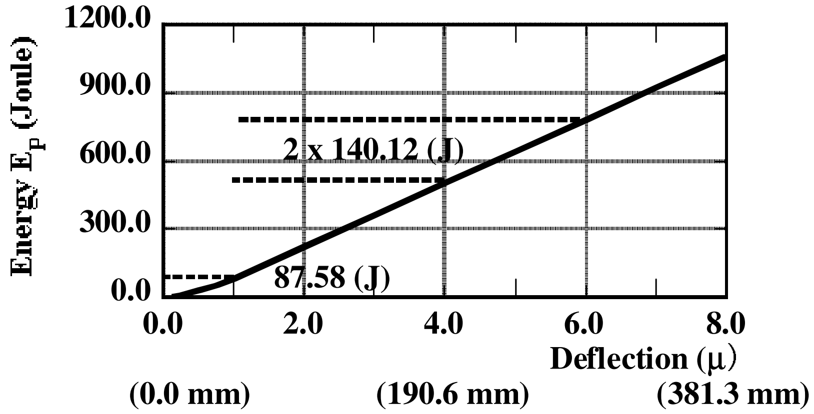

Figure 6: Energies E_P required to develop the specific inelastic deflection responses.

Table 5: Energy E_P evaluated for the responses.

Ductility Factor μ	ELC S00E	TFT N69E	HCH EW	THU NS
1.0	0.091 (0.278)	0.088 (0.297)	0.102 (0.324)	0.088 (0.303)
3.0	0.377 (0.270)	0.383 (0.199)	0.381 (0.209)	0.404 (0.193)
5.0	0.661 (0.233)	0.643 (0.152)	0.661 (0.265)	0.650 (0.195)
10.0	1.395 (0.271)	1.376 (0.166)	1.360 (0.323)	1.395 (0.269)

(in k Joule)

5.3 Correlation of Inelastic Reponses with Energies Dissipated within The Building

Figures 7(a) through (c) show the correlation of displacement responses in ductility factor with the energy dissipated during the building responses of E_T, E_S and E_D, respectively. For reference, the correlation of displacement and energy E_P in the numerical analysis is illustrated in Figure 8.

The energy E_P is uniquely correlated with inelastic responses, and the energy E_S would be closely correlated with inelastic responses of building, since the energy E_S is obtained from inelastic hysteresis energy dissipation during the responses.

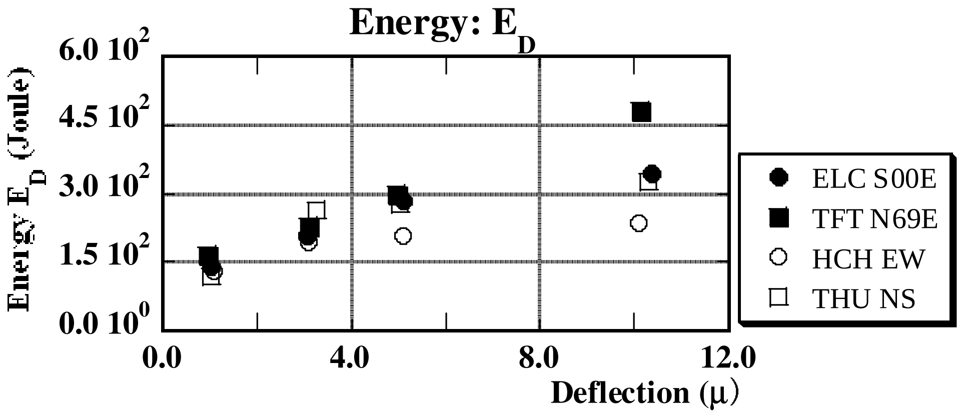

(c) Correlation of inelastic responses with energy E_D.

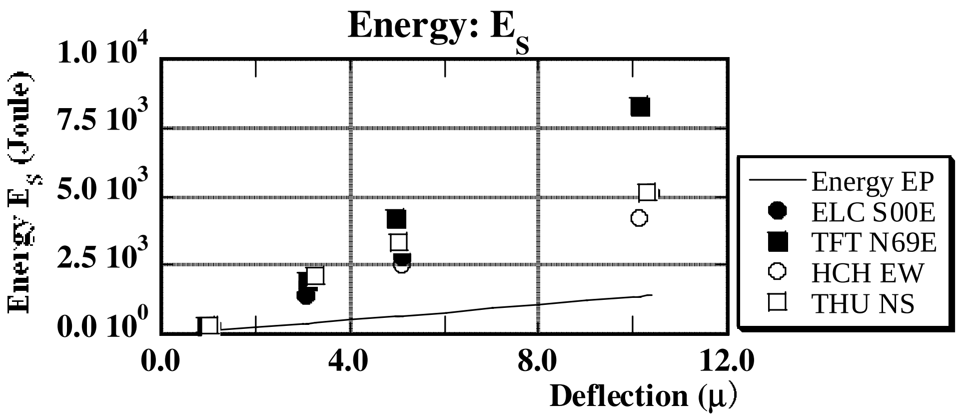

(b) Correlation of inelastic responses with energy E_S.

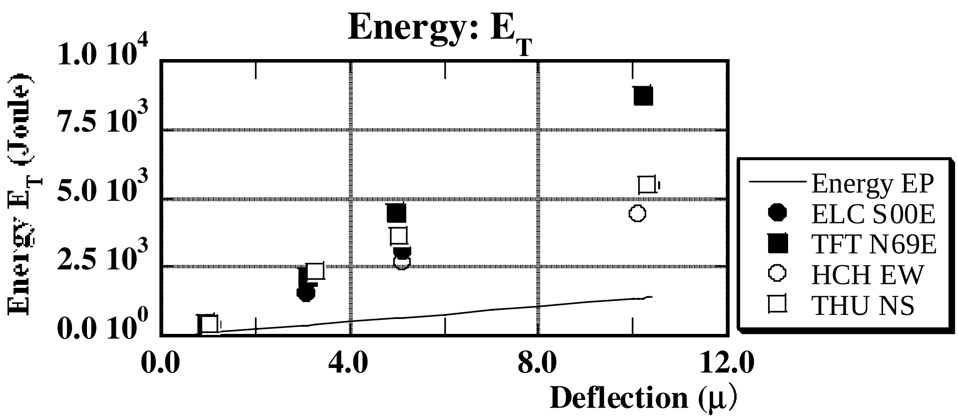

(a) Correlation of inelastic responses with energy E_T.

Figure 7: Correlation of inelastic responses with energies E_T, E_S and E_D.

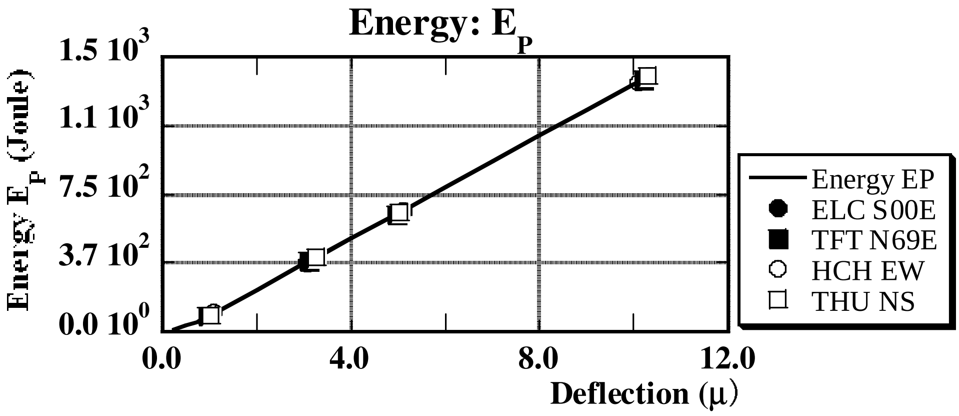

Figure 8: Correlation of inelastic responses with energies E_P in numerical analysis.

5.4 Substitute Damping Coefficient for An Equivalent Linear Oscillating System

The substitute damping coefficients of the building evaluated for responses subjected to the earthquake motions are summarized in Table 6 and Figure 8 (Shibata, 1981). Note that the damping coefficient for the building is set 0.05 fraction of critical damping.

Table 6: Substitute damping coefficient for the responses of building.

Ductility Factor μ	ELC S00E	TFT N69E	HCH EW	THU NS
1.0	0.089	0.078	0.095	0.099
3.0	0.19	0.21	0.22	0.20
5.0	0.24	0.23	0.26	0.23
10.0	0.30	0.27	0.35	0.29

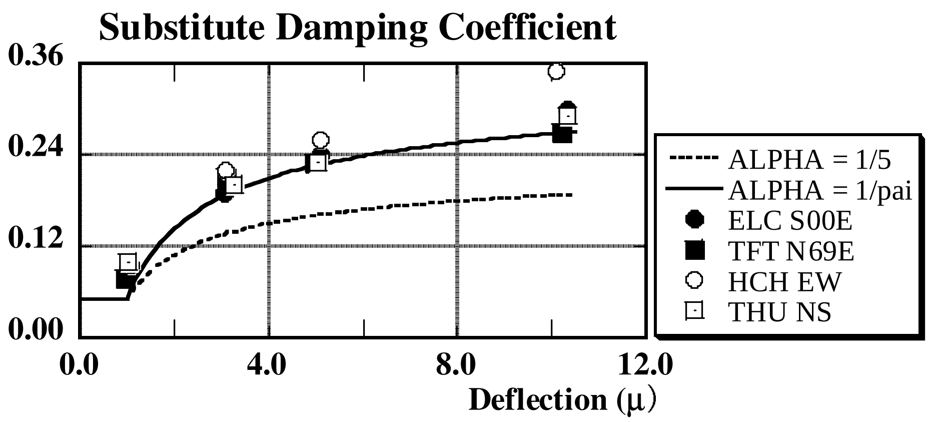

Figure 9: Substitute damping coefficient for an equivalent linear oscillating system for inelastic responses of the building.

6. CONCLUDING REMARKS

Energies dissipated within the building during seismic responses are evaluated, associated with the inelastic deflection. Four real earthquake ground motions are utilized in analysis. Energies dissipated by the hysteresis mechanisms and damping mechanisms, and that applied to the building during seismic action are examined in correlation with the inelastic responses developed.

The results obtained herein can be summarized in the following conclusive statements:

(1) The ratios of energy dissipated by the damping mechanisms E_D to the applied energy E_T, i.e., the ratios E_D/E_T, lie in the range from 0.053 to 0.13, varying with the produced deflection. For inelastic responses with ductility factors 3 and 5, the average ratios E_D/E_T equals about 0.11 and 0.078, respectively.

(2) The conclusive statement in the above Item (1) leads to the second statement that the ratios of E_S to E_T fall in the range of 0.87 and 0.95, varying with the produced inelastic responses. In responses with ductility factor 3 and 5, the average ratios are 0.89 and 0.92, respectively. The greater the ratios are, the greater inelastic responses are produced. We can conclude that the ratios E_S/E_T would be 0.9 for responses developing ductility factor of 3 to 5.

(3) The ratios of E_P/E_S, in which E_P designates the energy to develop the inelastic deflection responses, fall in the values between 0.21 and 0.22 for responses with ductility factors 5 and 3, respectively. For responses with ductility factors unity and 10, they are 0.30 and 0.26, respectively. The energy E_P and the inelastic deflection responses μ correspond uniquely with each other. If we find out the value of E_P, we can determine the maximum inelastic response of the building.

(4) Though the examination herein, we can estimate the inelastic response of a building in correlation with energies applied to the building during seismic excitation as follows:
   (a) Based on a design basis, find and fix the total energy applied to a building E_T;
   (b) The energy E_S dissipated by the hysteresis mechanisms can be determined by 0.9 times as large as the total applied energy E_T;

(c) The energy E_P developing the inelastic responses can be estimated by the value of 0.2 times as large as the dissipated energy E_S; and

(d) The inelastic responses are uniquely evaluated from the energy E_P and vice versa.

6. REFERENCES

Kubo, T., Y. Yamamoto, Y. Okuda and H. Kato, Correlation of Dissipated Energy Within a Building to Inelastic Response during an Intense Ground Motion, Part 1: Analysis with Variation of Damping Characteristics, Transactions of The AIJ Tokai Chapter Architectural Research Meeting, Vol. 41, pp. 365-368, February 2003. (in Japanese)

Okuda, Y. J. Yamamoto and T. Kubo, Correlation of Energy Dissipation within The System to Inelastic Responses during Intense Ground Motions, Part 1: Responses of R/C Buildings Using A Set of Synthetic Motions, Summaries of Technical Papers of Annual Meeting, Architectural Institute of Japan, Vol. Structures II, pp. 399-400, September 2003. (in Japanese)

Shibata, A., *Seismic Structural Analysis*, Morikita-Publishing Co. Ltd., 342 pages, June 1981. (in Japanese)

7. ACKNOWDEGMENT

Numerical analysis herein has been carried out by Mr. Yuki Okuda, Graduate Student, Nagoya Institute of Technology, Nagoya, Japan. The author would like to express sincere thanks and appreciation for his assistance herewith.

KEYWORDS

Reinforced Concrete, Reinforced Concrete Building, Seismic Design, Seismic Response, Inelastic Response, Energy Dissipation, Hysteresis Dissipated Energy, Substitute Damping, Hysteresis Damping, Takeda Model

THE SCALED NDP: A PRACTICAL PROCEDURE FOR OVERCOMING LIMITATIONS OF THE NONLINEAR STATIC PROCEDURE

Mark A. ASCHHEIM[1]

Tjen TJHIN[2]

Mehmet INEL[3]

ABSTRACT

Nonlinear Static Procedures have become widely accepted for use in seismic design and evaluation in recent years. While generally acceptable for peak displacement estimates, the accuracy of the NSP is poor for quantities that are significantly affected by higher modes. In recent work performed for the ATC-55 project, a new approach was identified for determining those quantities that are significantly affected by higher modes. The Scaled Nonlinear Dynamic Procedure (Scaled NDP) is described herein. The Scaled NDP is easily implemented in practice and requires little effort beyond a nonlinear static analysis. Suggestions are made for the use of the NSP and Scaled NDP in Performance-Based Earthquake Engineering.

1. INTRODUCTION

Nonlinear static procedures (NSPs) have become well known in the United States and Japan, with the implementation of procedures based on Capacity Spectrum Method (CSM) in ATC-40 (1996) and the Building Standard Law Enforcement Order (MOC 2000) and the description of the Displacement Coefficient Method (DCM) in FEMA-273 (1997) and FEMA-356 (2000). In these implementations, a nonlinear static (pushover) analysis is used to characterize the response of the structure, which customarily is represented on a plot of base shear versus roof displacement, known as a "capacity curve." The expected peak displacement, or "target displacement," is determined by means of an "equivalent" single-degree-of-freedom oscillator, whose properties are derived from the capacity curve. Values of various response quantities (e.g. story shears, plastic hinge rotations) are determined as the values computed in the nonlinear static (pushover) analysis at the instant in the analysis at which the roof displacement is equal to the estimated (or target) displacement. Although the CSM and DCM can lead to different estimates of the target displacement, modifications being developed in the ongoing ATC-55 project are expected to reduce these differences.

[1] *Civil Engineering Department, Santa Clara University, California, Email: maschheim@scu.edu*

The load pattern used in pushover analyses generally is similar to or equal to a first mode pattern. Many researchers (e.g. Miranda 1991, Collins et al. 1996, Cuesta and Aschheim 2001, Chopra et al. 2003) have shown that such approaches can lead to good estimates of peak displacements. The success of these quasi-first mode pushover approaches can be attributed to the relatively small contribution of higher modes to displacements. This can be understood for elastic response by noting that the vector of peak displacements due to the i^{th} mode, $\mathbf{x}_i$, is given by

$$\mathbf{x}_i = \Gamma_i S_d(T_i)\boldsymbol{\varphi}_i \tag{1}$$

where $S_d(T_i)$ is the spectral displacement associated with the period T_i, Γ_i is the modal participation factor, and $\boldsymbol{\phi}_i$ is the mode shape for the i^{th} mode. Higher mode contributions to displacements typically are minor because both Γ_i and S_d typically are much smaller for the 2nd and higher modes, relative to their 1st mode values.

Higher modes can contribute more significantly to other quantities, such as story shears and interstory drifts. This can be appreciated by noting for elastic response that the vector of lateral forces $\mathbf{F}_i$ associated with developing the peak displacements, $\mathbf{x}_i$, can be expressed as

$$\mathbf{F}_i = \Gamma_i S_a(T_i)\mathbf{M}\boldsymbol{\varphi}_i \tag{2}$$

where $\mathbf{M}$ is the mass matrix and $S_a(T_i)$ is the spectral acceleration associated with the period T_i. This indicates the lateral forces will typically have more substantial contributions from the higher modes, because the shape of the response spectrum will often result in higher mode spectral accelerations that exceed those of the first mode.

Techniques to account for the contributions of higher modes have been proposed to improve the NSP (e.g. ATC-40 1996, Chopra and Goel 2002, Aydinoglu 2003). An alternative is the use of Scaled Nonlinear Dynamic Analysis.

2. ATC-55 MDOF STUDIES

The Scaled NDP developed from the observation of results obtained in the ATC-55 Multi-Degree-of-Freedom studies. These studies were conducted to illustrate the accuracy of several pushover analysis techniques in relation to the results obtained from nonlinear dynamic analysis. Five

---

[2] *Department of Civil and Environmental Engineering, University of Illinois, Email: tjhin@students.uiuc.edu*
[3] *Department of Civil Engineering, Pamukkale University, Denizli, Turkey; minel@pamukkale.edu.tr*

building models were used, consisting of the 3- and 9-story steel frames designed for Los Angeles in the SAC program and an 8-story reinforced concrete wall building used as an example in ATC-40. The ground motions were selected to represent motions that potentially could occur at a given site, characterized by NEHRP Site Class C soil conditions, magnitudes (M_s) between 6.6 and 7.6, and epicentral distances of between 8 and 20 km. To investigate accuracy as a function of drift level, the records were each scaled to achieve a peak roof displacement of 0.5, 2, or 4% of the height for the steel frames and 0.1, 1, and 2% of the height for the concrete wall. Further information will be available in FEMA-440, to be published in 2004.

The pushover techniques consisted of quasi-first mode load vectors (consisting of first mode, inverted triangular, rectangular, and “code” load vectors, an “SRSS” load vector, and an adaptive first mode vector), as well as a variant of the Multimode Pushover Analysis method in which elastic contributions of the 2nd and 3rd modes were combined with the first mode contributions, using an SRSS combination. Assuming that the peak roof displacement could be estimated correctly, the quasi-first mode load vectors were applied until the roof displacement was equal to the pre-determined target displacement. Response quantities were determined at this displacement for the quasi-first mode load vectors, while higher mode contributions were determined based on the mean of the elastic spectra associated with the ground motions for the particular building and drift level, since the ground motions had been scaled individually to obtain the same predetermined peak roof displacement in the nonlinear dynamic analyses. Some results are illustrated in the following.

Figure 1 compares estimates of the interstory drifts (Figure 1a) and story shears (Figure 1b) made using various pushover methods with the range of values computed by nonlinear dynamic analysis, for the SAC 9-story steel frame, at a roof drift of 4% of the height of the building. The bar symbol at each floor (or story) indicates the minimum, maximum, mean, and mean plus and minus one standard deviation results obtained from the 11 dynamic analyses; the “+” indicates the median value. Higher modes are reflected in the results obtained from the nonlinear dynamic analysis of the yielding system, but are absent from the quasi-first mode pushover results. The more complex multiple mode calculation is often an improvement over the quasi-first mode estimates, but the estimates obtained by this approach were not consistently reliable, with significant errors developing for some cases.

Figure 2 compares estimates of story shears (Figure 2a) and overturning moments (Figure 2b) made using various pushover methods with the range of values computed by nonlinear dynamic analysis, for the 8-story reinforced concrete wall building, for the roof displacement equal to a value of 2% of the height of the building. Again, the contribution of higher modes (also described as "MDOF effects" for nonlinear systems) causes the dynamic peaks to be systematically higher than the quasi-first mode estimates.

Also shown in these figures (with circles and triangles) are peak values obtained using two additional ground motions, each scaled to achieve the same predetermined roof drift in the nonlinear dynamic analyses. It can be observed that these results are consistent with the results from the 11 ground motions. Hence, it is observed that for many structures, a single nonlinear dynamic analysis provides results of higher fidelity than those obtained with pushover analyses. This observation is the basis of the Scaled NDP described below.

3. THE SCALED NDP

3.1 Description of the method

Step 1. Estimate the peak displacement of the roof (or more generally, a "control point") using a NSP. An accurate estimate is desirable; improvements to be recommended by ATC-55 may be used.

Step 2. Select n ground motion records that reflect the characteristics of the hazard (e.g. magnitude, distance, site class) and for each record, conduct a nonlinear dynamic analysis, with the record scaled iteratively until the peak displacement of the control point is equal to the estimate determined in Step 1. Extract peak values of the response quantities of interest from the results of each analysis and compute the sample mean, $\bar{x}_n$, of each peak quantity of interest. At least three analyses ($n \geq 3$) are suggested.

Step 3. To address sampling error, arising from the limited number of observations of each quantity, and to estimate peak response quantities at the mean plus κ standard deviation level, multiply the sample mean, $\bar{x}_n$, by $c(1+\kappa\text{COV})$. For large samples (perhaps for $n \geq 7$) the COV may be estimated as the sample COV. For smaller n, it is suggested that a baseline value of 0.25

be assumed for the COV, based on the results of the MDOF studies. The term κ assumes a value of zero where estimates of the true mean are sought. The term c is given by

$$c = \frac{1}{1 - \left(\Phi^{-1}(\alpha)\right)\frac{COV}{\sqrt{n}}}, \tag{3}$$

based on the assumption that the response quantities are normally distributed, with $\Phi^{-1}(\alpha)$ representing the value for which the cumulative standard normal distribution is equal to α. Equation (3) simplifies to c = 1 for a confidence level, α, of 50%, representing that the sample mean is the best estimate of the true mean. For α = 90%, Equation (3) simplifies to

$$c = \frac{1}{1 - 1.28\frac{COV}{\sqrt{n}}}. \tag{4}$$

Thus, using Equation (4), there is a 90% probability that $c(1+\kappa COV)\bar{x}_n$ exceeds the true mean plus κ standard deviations, assuming that the response quantities are normally distributed.

Values of c computed using Equation (4) are provided in Table 1. Table 1 can be used to indicate the number of analyses to run—that is, the point when the benefit of additional analytical data is of negligible benefit. The derivation of Equations (3) and (4) will be presented in FEMA-440, to be published in 2004.

The nonlinear static analysis of Step 1 typically requires the greatest effort, principally with regard to the preparation of the inelastic model. The dynamic analyses of Step 2 are relatively easy to run, and the statistical estimates of Step 3 are easily made. Consequently, the Scaled NDP requires little effort beyond the determination of the NSP displacement estimate.

3.2 Illustration of the method

It is anticipated that the NSP will be used in preliminary design to determine the strength and stiffness required for the structure to satisfy global performance criteria. Once the proportions of the structural members have been established, the Scaled NDP may be used to assess or characterize the performance of the structure, or to determine some quantities required for design, such as the forces in brittle members that are intended to remain elastic. Two examples are used to illustrate the method.

Interstory Drift Estimate: The sample mean of the peak values of interstory drift at the lowest story of the 9-story frame at a predetermined roof drift of 4% is $\bar{x}_n = 6.5\%$ (Figure 1a). The true COV is estimated from the 11 peak dynamic responses to be 0.16. For this COV, Equation 4 results in c = 1.05. The true mean value of peak interstory drift is estimated to not exceed $c\bar{x}_n$ = 1.05(6.5%) = 6.8% at the 90% confidence level. That is, there is a 90% probability that the true mean peak interstory drift at the lowest story is less than 6.8% at the hazard level that produces a roof drift of 4%.

Story Shear Estimate: The sample mean of the peak story shears at the lowest story of the 8-story wall at a predetermined roof drift of 2% is $\bar{x}_n$ = 1070 kips. To guard against the potential for shear failure, an "upper bound" limit on shear demands is desired. Based on the 11 analyses, the true COV of the story shears is estimated to be 0.22. Using Equation 4, c = 1.09. Therefore, there is a 90% probability that the true mean plus one standard deviation peak story shear is less than $(1 + \kappa\text{COV})\,c\bar{x}_n$ = (1 + 0.22)(1.09)(1070 kips) = 1420 kips, for the hazard that produces a roof drift of 2%.

3.3 Observed Coefficients of Variation

The coefficients of variation (COV) of the response quantities determined in the MDOF studies were examined for each response quantity at each floor or story for each of the five building models, for each of the three predetermined drift levels. In general, the COVs differ for each response quantity and are highest at the upper stories and near the base of each model. Approximate upper bounds to the COVs are summarized in Table 2, where "approximate" indicates that the limit was exceeded by a small amount at a limited number of locations. It is suggested that a COV of 0.25 may be used for all quantities in cases where a sufficient number of analyses are not available for establishing a better estimate of the true COV.

3.4 Dependence of sample mean and COV on sample size

Data generated in the ATC-55 studies was re-interpreted in order to observe the influence of n on the sample mean and sample COV. Three sequences of the eleven ground motions used in the original analyses were randomly selected and statistics on the peak response quantities (displacement, interstory drift, story shear, and overturning moment) were computed for the first n records of each sequence, for $2 \leq n \leq 11$. Results are presented in Figure 3 for selected locations in the 9-story steel frame and in Figure 4 for selected locations in the 8-story reinforced concrete wall. Although some scatter is evident, one may interpret the figures as supporting the use of $n \geq 3$ for determination of $\bar{x}_n$ and $n \geq 7$ for determination of the COV.

3.5 Discussion

Among the various analytical methods available today, nonlinear dynamic analysis is generally considered to produce the most accurate results, with accuracy limited only by modelling error. The Scaled NDP inherently accounts for the influence of higher modes and capacity limits on demands, and each analysis conducted contributes positively to the estimation of central tendency and variance. One may consider the load vector used in the Scaled NDP to be a dynamic load vector, which varies with each ground motion, in contrast to the static load vectors used in the various NSPs.

The scaling of ground motions to obtain a peak roof displacement equal to the estimate obtained using a NSP appears to reduce the COVs obtained for each response quantity relative the COVs obtained using traditional spectrum compatible motions (based on elastic response spectra). Effectively, the NSP is being used to map the hazard, represented using elastic spectra at a specified probability of exceedance, to the roof displacement, wherein the roof displacement estimate is made by means of an "equivalent" SDOF system and a relationship between elastic and inelastic response. In addition to being a function of period, the "hazard" can now be viewed as a function of the properties that determine the roof displacement estimate—the yield strength and deformation characteristics of the structure. The relatively low COVs make the design of structures practicable in an environment of probabilistically specified seismic demands. Furthermore, conventional smoothed elastic design spectra may be used as the basis for the NSP estimates of peak roof displacement, and thus site-specific design spectra that have already been developed in many parts of the world can be made use of.

Various researchers, including the authors, have already developed relatively simple procedures for performance-based design based on "equivalent" SDOF systems. Thus, it is feasible to develop a preliminary design based on global performance criteria using an NSP and to use the scaled NDP to characterize the performance of the design and to determine some additional quantities needed for the design, such as the forces to be sustained by brittle members that must remain elastic.

The Scaled NDP is a relatively new procedure. Refinements and improvements potentially may be made in the areas of (1) characterization and selection of site specific ground motions, (2) determination of the confidence levels (α) and numbers of standard deviations above the mean (κ) that should be used for various response quantities, (3) establishment of minimum numbers of analyses required for estimation of the mean and COV, and (4) improvement of precision of the NSP estimates of peak roof displacement. The Scaled NDP was developed for planar models; after sufficient experience is obtained with planar systems, generalizations of the method for structures that require three-dimensional models would be of interest.

4. CONCLUDING REMARKS

Results obtained in the ATC-55 studies illustrate that substantial errors can occur when estimating response quantities such as interstory drift, story shear, and overturning moments using various load vectors that have been proposed for the NSP. These errors are attributed to the presence of significant higher mode contributions, also termed multi-degree-of-freedom effects. In many cases, a single nonlinear dynamic analysis provided a better estimate of these response quantities than could be obtained with a nonlinear static analysis. Based on this observation, a method known as the Scaled Nonlinear Dynamic Procedure was formalized. Two examples illustrated the use of the method.

The Scaled NDP makes use of existing Nonlinear Static Procedures for estimating peak displacement response, and inherently accounts for higher mode contributions and capacity limits associated with inelastic behavior. The Scaled NDP is easy to implement in practice because relatively little effort is required beyond that required for the nonlinear static analysis.

It is feasible to use methods based on NSPs for preliminary determination of the strength and stiffness required for the structure to satisfy global performance objectives in the context of performance-based design. Various proposals for this already have been made, by the authors and others. The preliminary requirements may then be used for the detailed design of the structure. The Scaled NDP may then be used to assess or evaluate the performance of the design, and to determine other quantities required for design, such as the forces that must be resisted elastically.

The Scaled NDP leverages the substantial effort that already has gone into the development of site-specific descriptions of hazard in many countries, in the form of elastic spectra at specified probabilities of exceedance, because the elastic spectra are the basis for the peak displacement estimates of the NSP. The simplicity of the method and the reliance on spectral descriptions of hazard makes the Scaled NDP amenable to specification in codes for the design of buildings.

5. ACKNOWLEDGMENTS

This paper describes work performed under the auspices of the ATC-55 project of the Applied Technology Council, funded by the Federal Emergency Management Agency. Guidance provided by the Project Management Committee is appreciated. In particular, the suggestions of Craig Comartin and Ron Hamburger, the assistance of Professor Y.K. Wen, and the thoughtful consideration given by Professor Helmut Krawinkler are gratefully acknowledged. The views expressed do not necessarily represent those of the above individuals and organizations.

6. REFERENCES

ATC-40 (1996). *Seismic Evaluation and Retrofit of Concrete Buildings*. Report No. SSC 96-01, Applied Technology Council, Redwood City, CA.

Aydinoglu, N. (2003). An incremental response spectrum analysis procedure based on inelastic spectral displacements for multi-mode seismic performance Evaluation. Bulletin of Earthquake Engineering, 1: 3-36.

Chopra A.K. and Goel R.K. (2002) "A modal pushover analysis procedure for estimating seismic demands for buildings," Earthquake Engng. Struct. Dyn., 31, 561-582.

Chopra AK, Goel RK, Chintanapakdee C, (2003). Statistics of single-degree-of-freedom estimate of displacement for pushover analysis of buildings. Journal of Structural Engineering, ASCE, 129 (4): 459-469.

Collins, K. R., Wen, Y. K., and Foutch, D. A. (1996). An alternative seismic design procedure for standard buildings. Eleventh World Conference on Earthquake Engineering, Pergamon, Elsevier Science Ltd.

Cuesta, I., and Aschheim, M., (2001). *Using pulse R-factors to estimate the structural response to earthquake ground motions*, CD Release 01-03, Mid-America Earthquake Center, Mar.

FEMA 273 (1997). *NEHRP Guidelines for the Seismic Rehabilitation of Buildings*. Report No. FEMA 273, Federal Emergency Management Agency, Washington, DC.
FEMA 356 (2000). *Prestandard and Commentary for the Seismic Rehabilitation of Buildings.* Report No. FEMA 356, Federal Emergency Management Agency, Washington, DC.
Ministry of Construction, (2000). *Building Standard Law Enforcement Order* and *Notifications*, June.
Miranda, E. (1991). Seismic evaluation and upgrading of existing buildings. Ph.D. thesis, Univ. of California at Berkeley.

7. KEYWORDS

nonlinear dynamic analysis, nonlinear static procedure, higher mode effects, pushover analysis

Table 1: Values of *c* at the 90% confidence level

	Coefficient of Variation									
n	0.05	0.10	0.15	0.20	0.25	0.30	0.35	0.40	0.45	0.50
3	1.04	1.08	1.12	1.17	1.23	1.29	1.35	1.42	1.50	1.59
5	1.03	1.06	1.09	1.13	1.17	1.21	1.25	1.30	1.35	1.40
7	1.02	1.05	1.08	1.11	1.14	1.17	1.20	1.24	1.28	1.32
10	1.02	1.04	1.06	1.09	1.11	1.14	1.17	1.19	1.22	1.25
20	1.01	1.03	1.04	1.06	1.08	1.09	1.11	1.13	1.15	1.17
100	1.01	1.01	1.02	1.03	1.03	1.04	1.05	1.05	1.06	1.07

Table 2: Approximate upper bounds to the COVs over the height of each building model

Building Model	Interstory Drift	Story Shear	Overturning Moment
3-story steel frame	0.15	0.15	0.15
3-story steel frame (weak story)	0.20	0.15	0.15
8-story reinforced concrete wall	0.10	0.20	0.15
9-story steel frame	0.20	0.20	0.20
9-story steel frame (weak story)	0.30	0.25	0.25

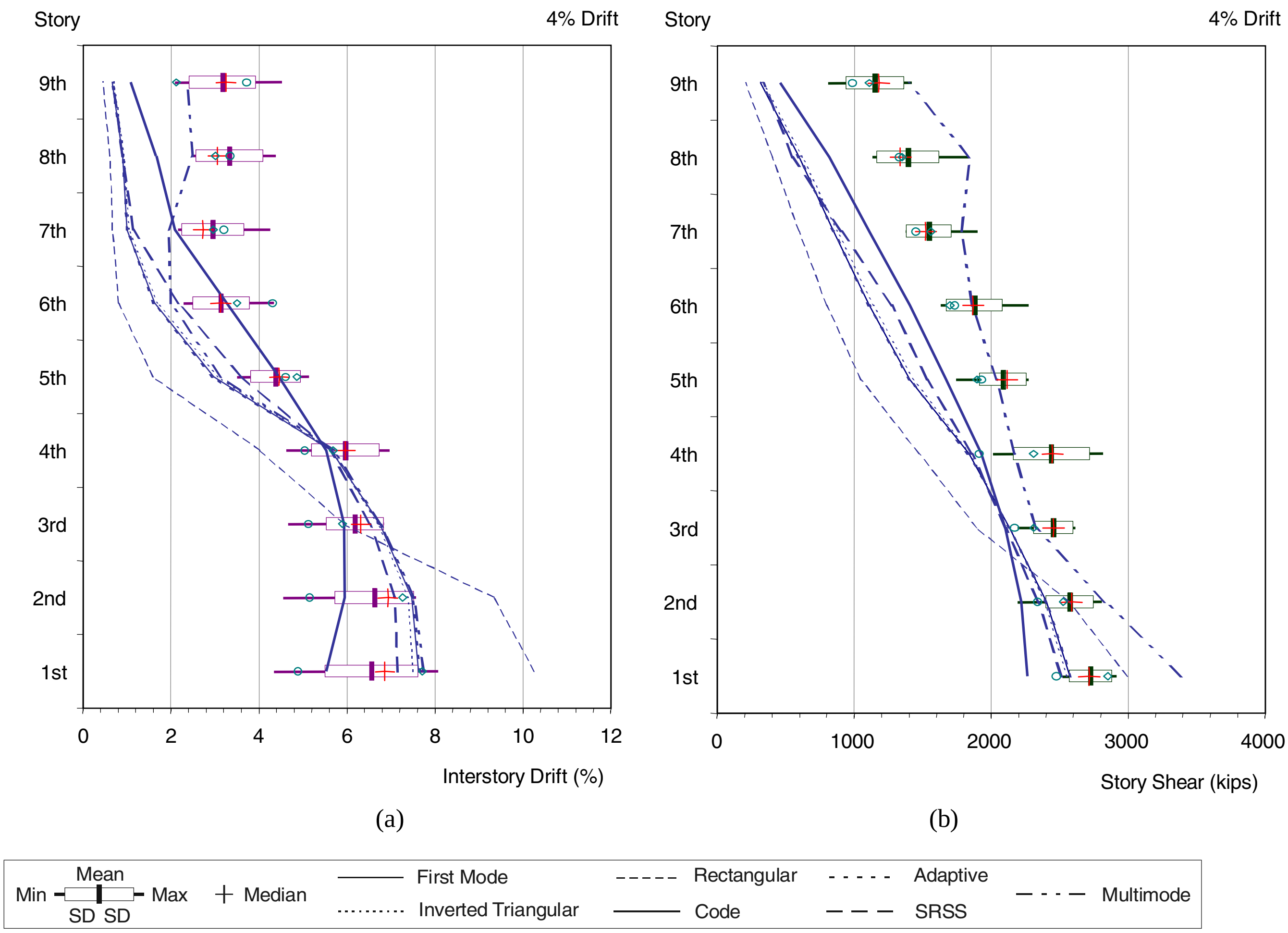

Figure 1. Comparison of NSP estimates and values computed by nonlinear dynamic analysis using 11 ground motion records scaled to achieve a roof drift of 4%, for the 9-story steel frame building: (a) interstory drifts, and (b) story shears.

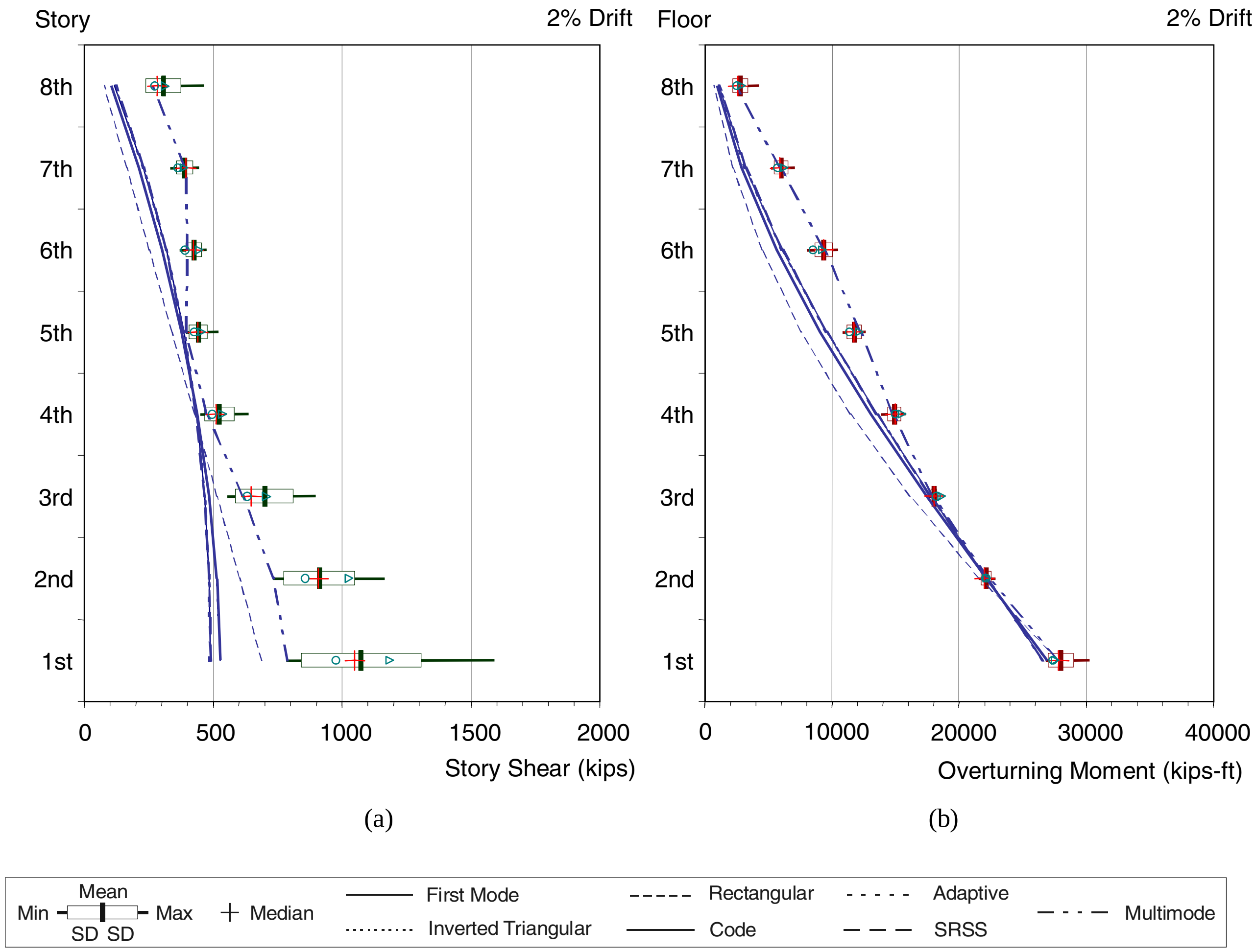

Figure 2. Comparison of NSP estimates and values computed by nonlinear dynamic analysis using 11 ground motion records scaled to achieve a roof drift of 2%, for the 8-story reinforced concrete wall building: (a) story shears, and (b) overturning moments.

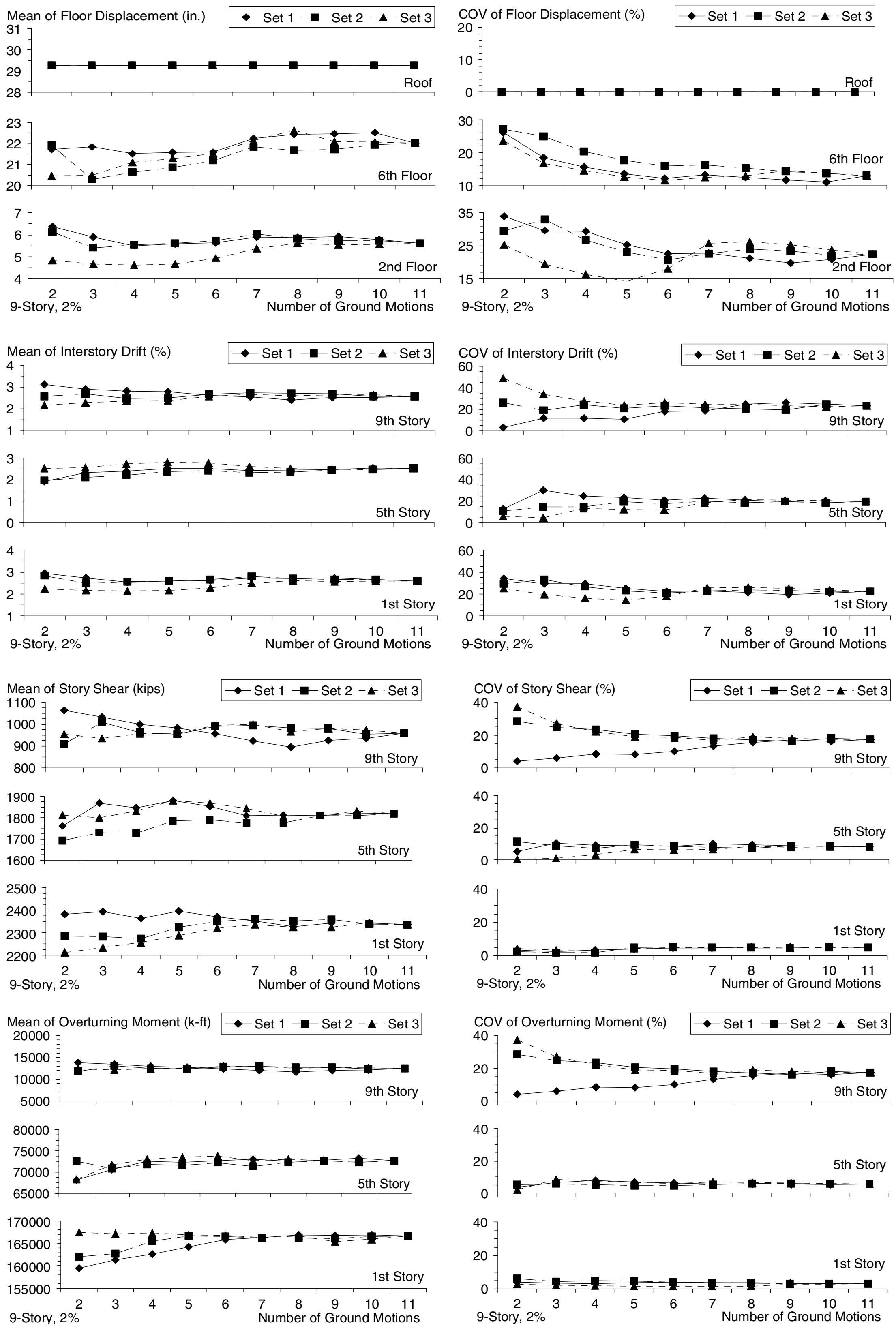

Figure 3. Means and COVs as a function of n for the 9-story frame at 2% drift.

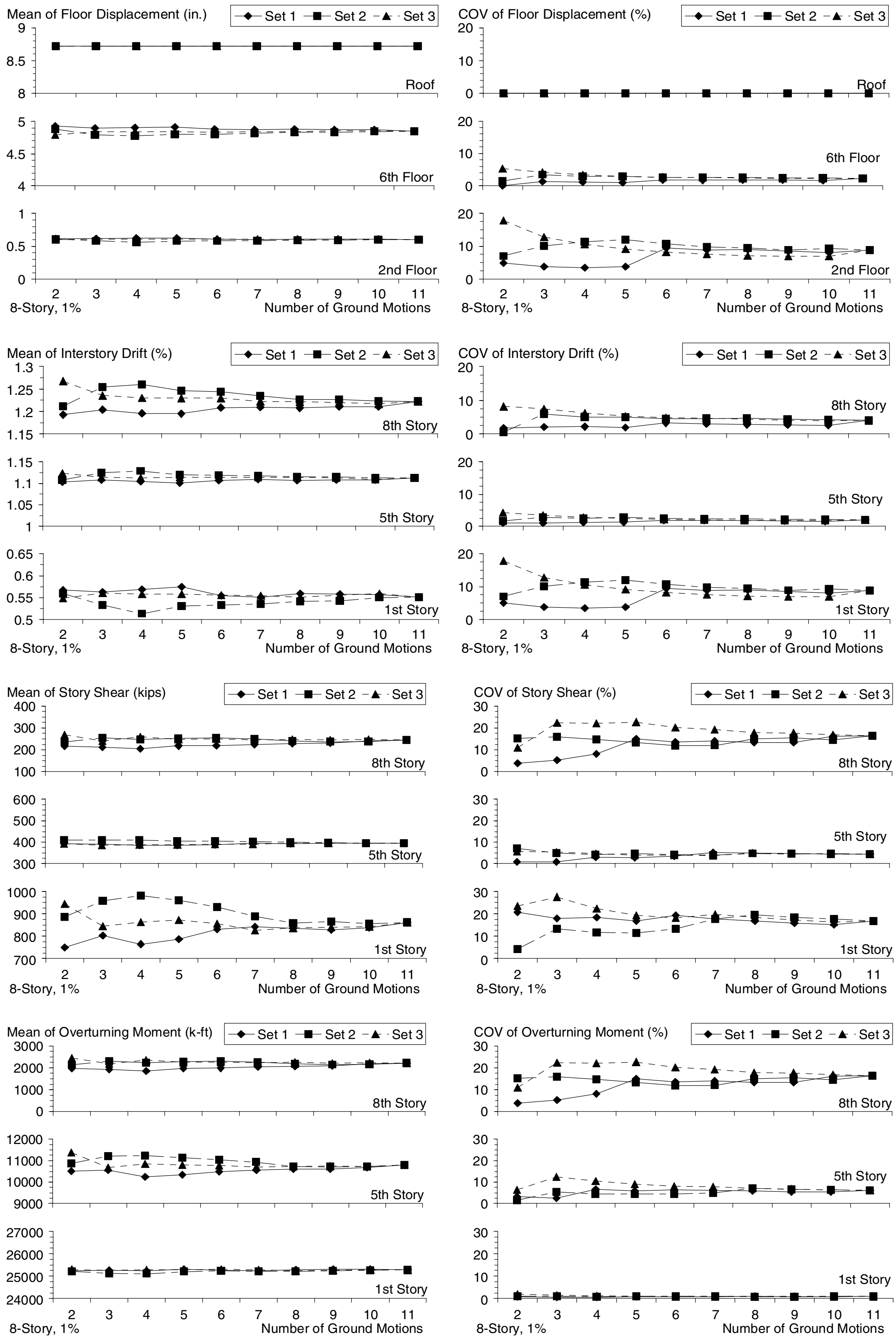

Figure 4. Means and COVs as a function of *n* for the 8-story wall building at 1% drift.

SESSION 2-B: PERFORMANCE OF COLUMN MEMBERS

Chaired by

♦ Michael Kreger and Hiroshi Noguchi ♦

EFFECT OF LOADING HISTORY ON DUCTILITY OF RC COLUMN

Toshikatsu ICHINOSE and Hisashi UMEMURA[1]

ABSTRACT

There have been many proposals for estimating the ductility of reinforced concrete (RC) members failing in shear after inelastic loading. However, the precision of such proposals is generally poor. This paper reviews experimental researches on the effect of loading history on ductility of RC columns and discusses the probable reasons of the poor precision.

1. INTRODUCTION

Shear failure after inelastic cyclic loading is often observed in reinforced concrete (RC) beam or column whose shear strength is only slightly larger than its flexural strength. In the AIJ Design Guidelines (1999), this kind of failure is attributed to the two reasons: (1) the reduction of effective compressive strength of concrete due to intersecting flexural-shear cracks, and (2) the reduction of aggregate interlocking due to wide flexural-shear cracks (Ichinose 1992). Priestley et al (1994) expressed the strength degradation by reducing the contribution of concrete to the shear strength. Pujol et al (2000) described the effect using the Coulomb criterion. Moehle and Elwood (2003) derived an empirical equation to describe directly the deformation capacity. However, the precision of each proposal is not good enough.

One of the reasons for the poor precision may be the effect of loading history. The other reason may be an uncertainty in the shear strength. The objective of this paper is to summarize available experimental works on the topic.

[1] *Nagoya Institute of Technology, Nagoya 466-8555, Japan*
Email: ich@nitech.ac.jp

2. SHEAR FAILURE AT LARGE DUCTILITY --- TESTS AT TOKYO SCIENCE UNIVERSITY

Kinugasa et al (1994) tested ten specimens with identical detailing under different loading excursions. The cross section of the specimens is shown in Fig. 1a. Shear reinforcement ratio, $A_w/(s.b)$ was 0.75 %. Selected results are shown in Figs. 1 and 2. One can have the following observations.

(a) Under the cyclic loading shown in Fig. 1a, the specimen showed large ductility.

(b) Cyclic loadings at an amplitude of 80×10^{-3} rad. shown in Fig. 1b caused large stiffness degradation but small strength degradation.

(c) Cyclic loadings at an amplitude of 120×10^{-3} rad. shown in Fig. 1c caused large stiffness degradation as well as large strength degradation.

(d) Incremental cyclic loadings shown in Fig. 1d caused large strength degradation from an amplitude of 100×10^{-3} rad. which is between the values found in Figs. 1b and 1c.

(e) Cyclic loadings between positive and zero deflections shown in Fig. 2 caused considerable strength degradation. Note that the degradation started when the amplitude of the deflection angle was 100×10^{-3} rad., which is similar to that of Fig. 1d.

In short, a threshold of deflection angle amplitude seems to exist for strength degradation irrespective of loading types.

3. SHEAR FAILURE AT SMALL DUCTILITY --- TESTS AT NAGOYA INSTITUTE OF TECHNOLOGY

Matsuzawa et al (2002) conducted tests of RC members shown in Fig. 3 (without cross ties). The test parameters were the loading conditions: (1) the axial force ratio (0 or 0.062) and (2) the lateral loading excursion. All the specimens were designed identically so that the shear strengths were slightly larger than the flexural strengths. The specimens were then subjected to monotonic loadings, uni-directional cyclic loadings and bi-directional cyclic loadings. Selected load-deflection relations are shown in Fig. 4. The ductility capacity, which is largest for the specimen under monotonic loading (AN3), is strongly influenced by the lateral loading excursions. For the specimen under uni-directional loading (AN4), the ductility capacity is almost the same as the specimen under bi-directional loading (AN5), although the number of cyclic reversals and the cumulative plastic deformation of AN4 are much smaller than those of AN5.

Umemura et al (2003) conducted tests of RC columns shown in Fig. 3. The test parameters were (1) the presence of cross ties and (2) the lateral loading excursions. The axial force ratio was fixed at 0.12. The design of the specimen without cross ties was the same as the specimens of the previous study by Matsuzawa et al. The shear reinforcement ratios, $A_w/(s.b)$, equal to 1.7 %, were identical for all the specimens. The results for the specimens without cross ties are shown in Fig. 5.
In this case, the ductility capacity for the specimen under uni-directional loading (BN2) is larger than that of the specimen under bi-directional loading (BN3) contrary to the previous research. This difference in the results may be because of the dispersion of the shear strength while the shear/flexural strengths of the specimens are small.

The specimens subjected to monotonic and bi-directional cyclic loadings were CT-scanned after the failure tests. The obtained patterns of the widest shear cracks are illustrated in Fig. 6. For the specimen subjected to bi-directional cyclic loading, a couple of thin shear cracks are generated after cyclic loading, localizing the deformed zone, and causing the decrease in shear strength. As a result, the angle of the widest crack is lower than that of the specimen under monotonic loading.

4. SHEAR FAILURE BEFORE FLEXURAL YIELDING --- TESTS AT GIFU UNIVERSITY

Uchida et al (2001) conducted four specimens with identical detailing shown in Fig. 7 under monotonic loading. The right half of the specimens did not have stirrup. The observed crack patterns and the load-deflection relationships are shown in Fig. 8. Three of the specimens failed in shear before flexural yielding but one of them failed after large flexural deformation. We can observe a close relation between the observed strengths and the crack patterns: the inclination of the major crack of the specimen S-4, which showed the smallest strength, propagated from the loading point in about 20 degrees, whereas that of the specimen S-2 with the largest strength and ductility propagated in about 45 degrees. Since the formation of crack may vary randomly, it is natural that the strength and ductility may largely vary.

5. GENERAL TRENDS (CONCLUDING REMARKS)

It is already recognized that loading history does not affect ductility if shear failure occurs before flexural yielding. On the other hand, experiments by Kinugasa et al (1994) indicate that a threshold of deflection angle amplitude seems to exist for strength degradation irrespective of loading types for specimens with large ductility. To integrate these trends, one can imagine a relationship shown in Fig. 9.

We also should pay attention to the uncertainty of shear strength observed by Uchida et al (2001). It means that the graph in Fig. 9 should be factored in the horizontal direction as shown in Fig. 10. Note that the same amount of uncertainty is assumed for the shear strength in each type of loading history. Fig. 10 indicates that the dispersion of ductility under cyclic loading in one side is larger than that under cyclic loading in both sides. The figure also indicates the possibility that the ductility under cyclic loading in both sides can be larger than that in one side as observed by Matsuzawa et al (2002) if the shear/flexural strength ratio is small.

Acknowledgements: Grateful thanks are due to Drs. Kinugasa and Uchida for providing test data.

REFERENCES

Architectural Institute of Japan (1999). *Design Guidelines for Earthquake Resistant Reinforced Concrete Buildings Based on Inelastic Displacement Concept*, Tokyo, Japan. (in Japanese)

Ichinose, T. (1992): 'A shear design equation for ductile RC members,' *Earthquake Engineering and Structural Dynamics*, Vol. 21. No. 2, pp. 197-214.

Ichinose, T. and Hanya, K. (1995): "Three Dimensional Shear Failure of R/C Beams", *Proc.* International Conference on Concrete under Severe Condition, Vol. 2, 1737-1747

Ichinose, T., Imai, M., Okano, T., and Ohashi, K. (2001): “Three-Dimensional Shear Failure of RC Columns after Cyclic Loading,” Modeling of Inelastic Behavior of RC Structures under Seismic Loads, *Committee Report*, ASCE, 546-561

Kinugasa, H. and Nomura, S. (1994): “Failure mechanism under reversed cyclic loading after flexural yielding,” *Concrete research and technology*, 5(2), 85-97, (in Japanese)

Matsuzawa A, Iyoshi M, Umemura H, and Ichinose T. (2002) “Effect of loading history and axial force on strength deterioration of RC members,” *Proc. of the Japan Concrete Institute*, Vol. 24 (CD-ROM)

Moehle, J. and K. Elwood (2003), “Collapse performance prediction for RC frame structures,” Paper No. 154, Proceedings, 2003 Pacific Conference on Earthquake Engineering, Christchurch, New Zealand

Priestley, M. J. N., and Benzoni, G. (1994): “Seismic shear strength of reinforced concrete columns,” J. Struct. Engineering, ASCE, 120 (8), 2310-2329

Pujol, S., Sozen, M., and Ramirez, J. (2000): “Transverse Reinforcement for Columns of RC Frames to Resist Earthquakes.” Journal of Structural Engineering, ASCE, 126 (4), 461-166

Umemura H, Ichinose T , and Matsuzawa A. (2003) “Effect of loading history and cross-ties on restoring-force-characteristics of RC members,” *Proc. of the Japan Concrete Institute*, Vol. 25 (CD-ROM)

Uchida, Y., H. Morimoto, and T. Tsukamoto (2001): Post-peak behavior of RC beams failing in shear, *Proc*. of the 56th annual conference of the JSCE, vol. 443, pp. 886-887 (CD-ROM)

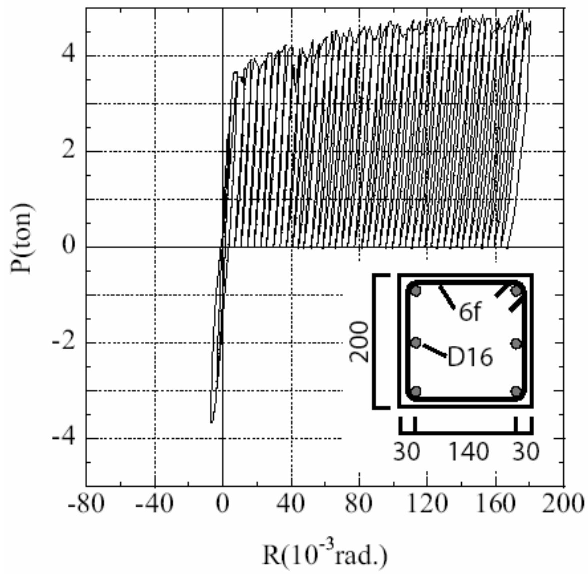

(a) Monotonic loading

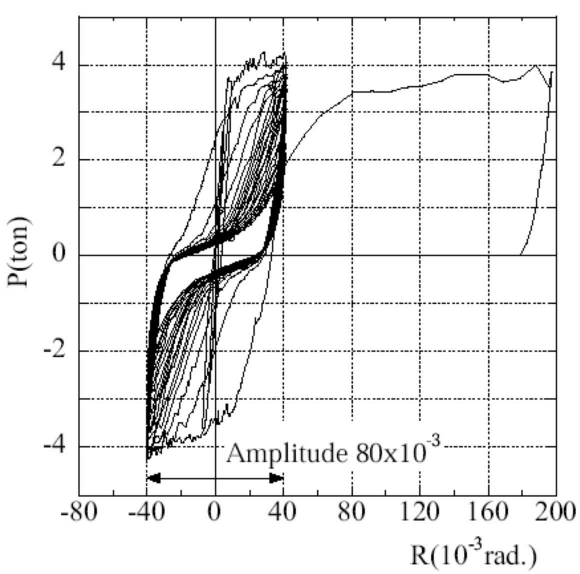

(b) Cyclic loading with small amplitude

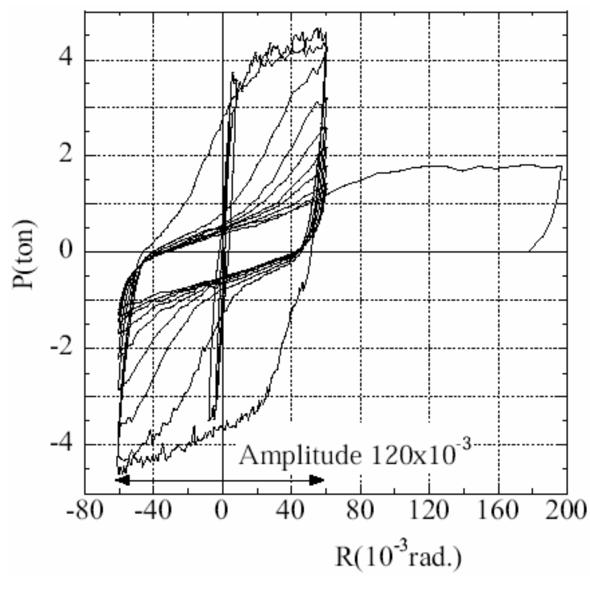

(c) Cyclic loading with large amplitude

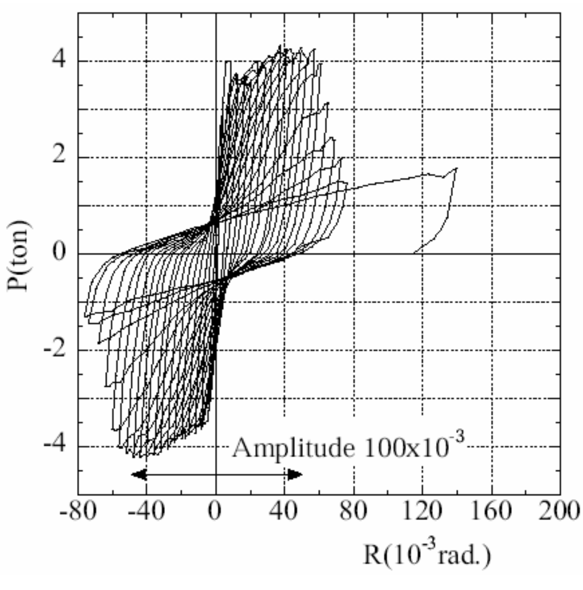

(d) Incremental cyclic loading

Fig. 1 Test results of Kinugasa et al (1994)

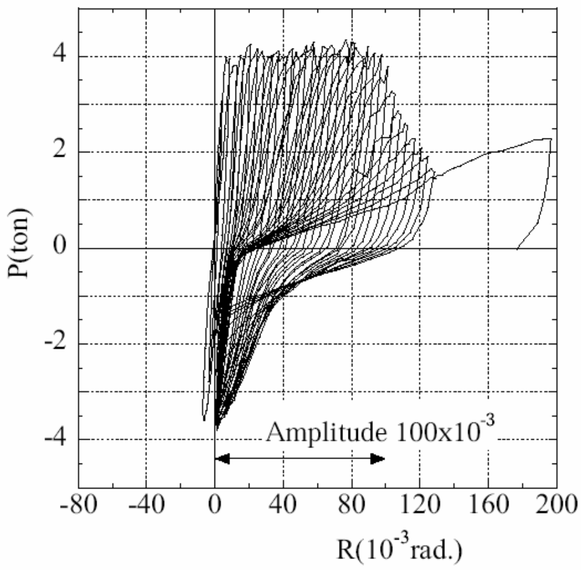

Fig. 2 Test result of Kinugasa et al (1994), one-side cyclic loading

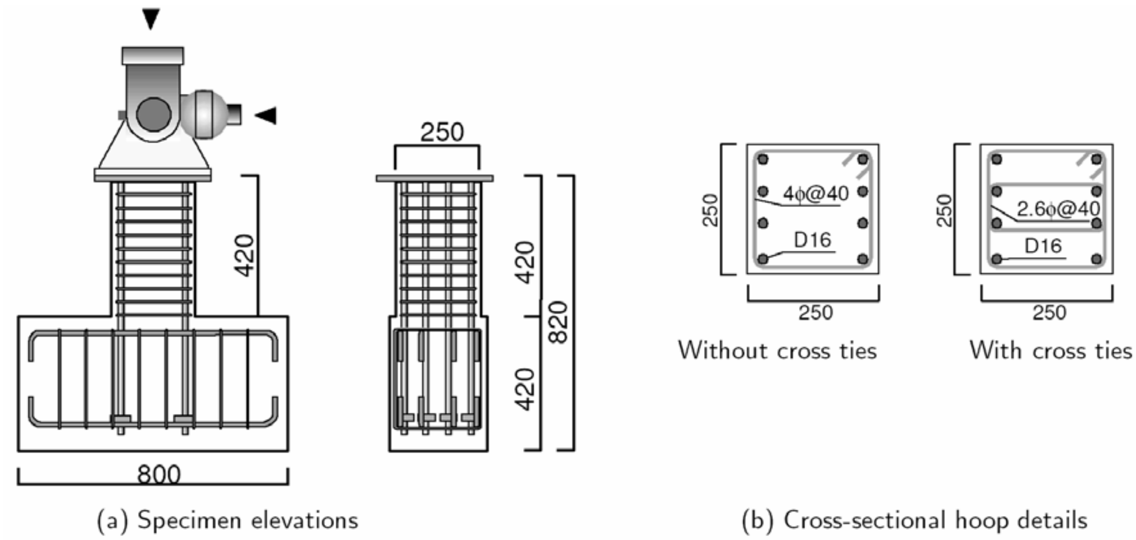

Fig.3 Test specimens of Matsuzawa et al.(2002) and Umemura et al.(2003)

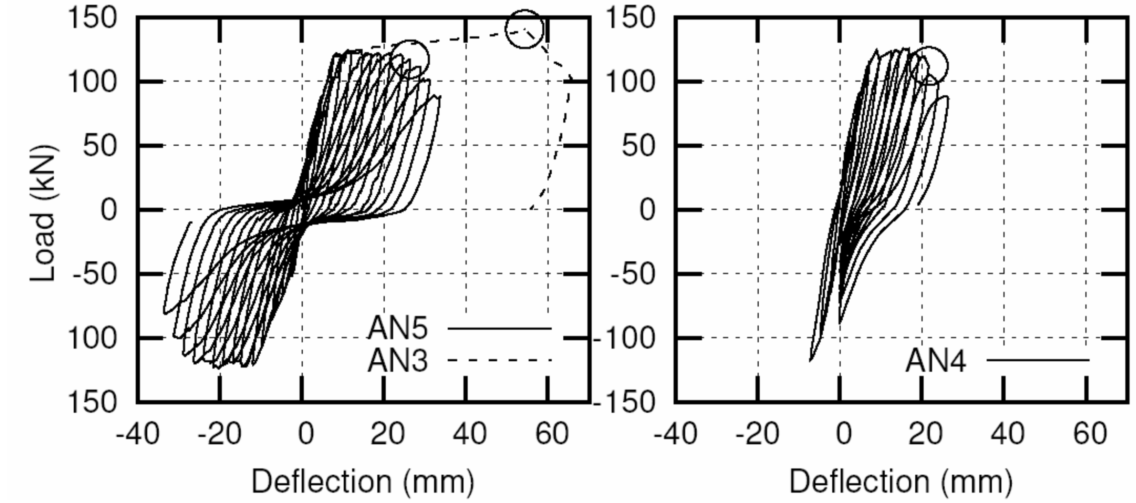

(a) Monotonic and bi-directional cyclic loading (b) Uni-directional cyclic loading

Fig.4 Test results of Matsuzawa et al.(2002

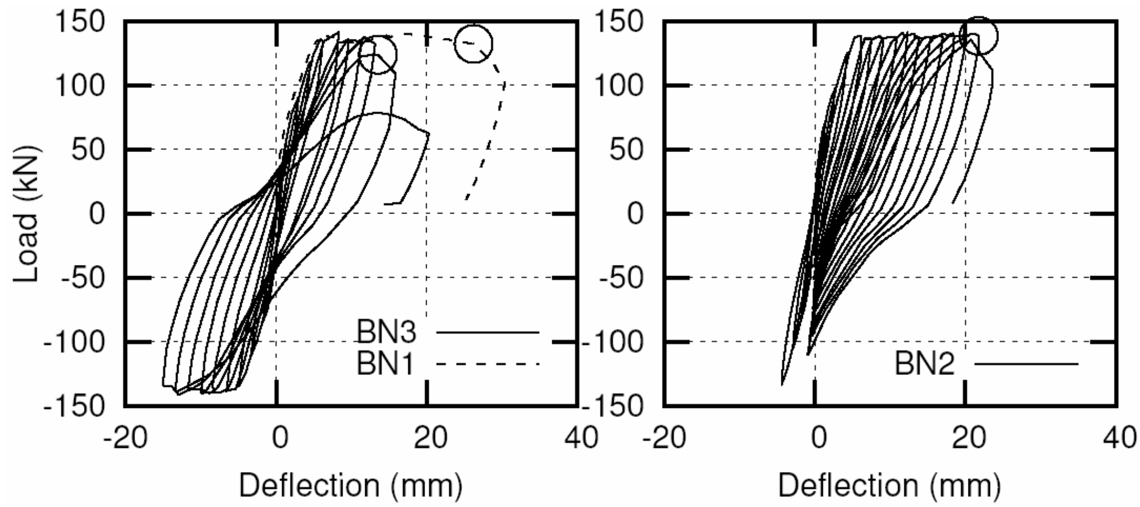

(a) Monotonic and bi-directional cyclic loading (b) Uni-directional cyclic loading

Fig.5 Test results of Umemura et al.(2003)

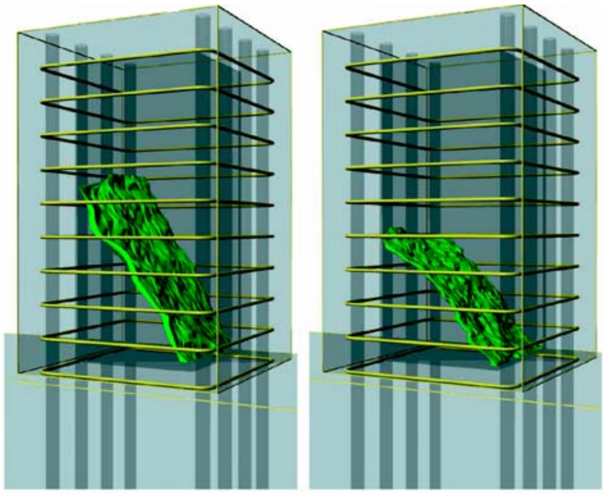

(a) Monotonic loading　　　　　　(b) Bi-directional cyclic loading

Fig.6　Patterns of widest shear crack obtained by ct-scan

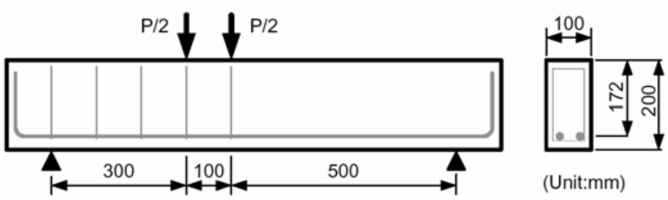

Fig. 7　Test specimen of Uchida et al (2001)

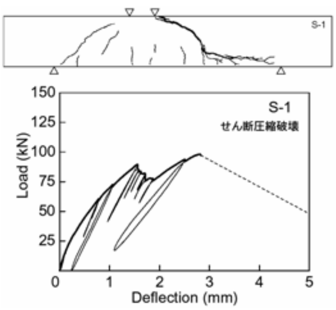

(a) Specimen S-1

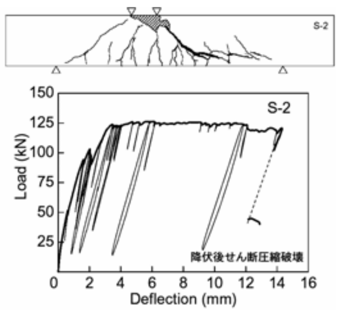

(b) Specimen S-2

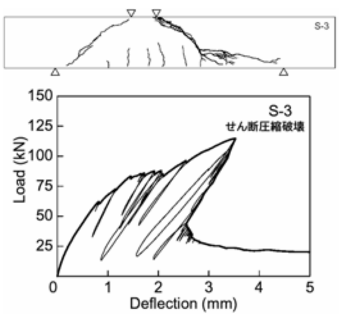

(c) Specimen S-3

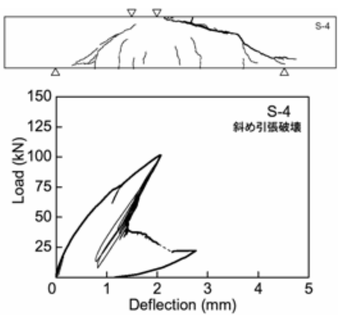

(d) Specimen S-4

Fig. 8　Test results of Uchida et al (2001)

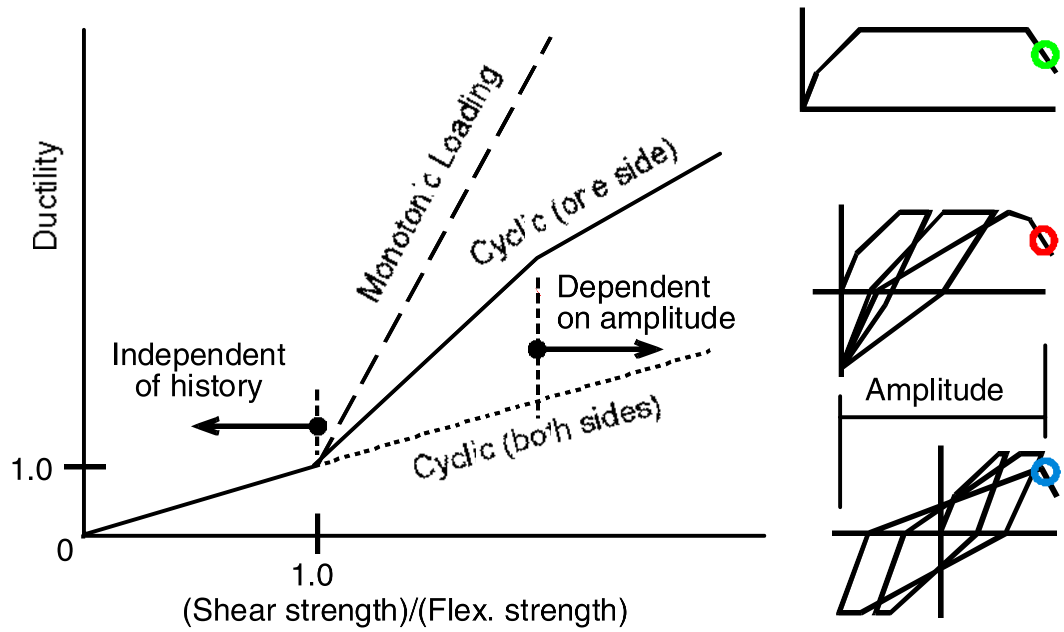

Fig. 9 Expected ductility depending on loading history

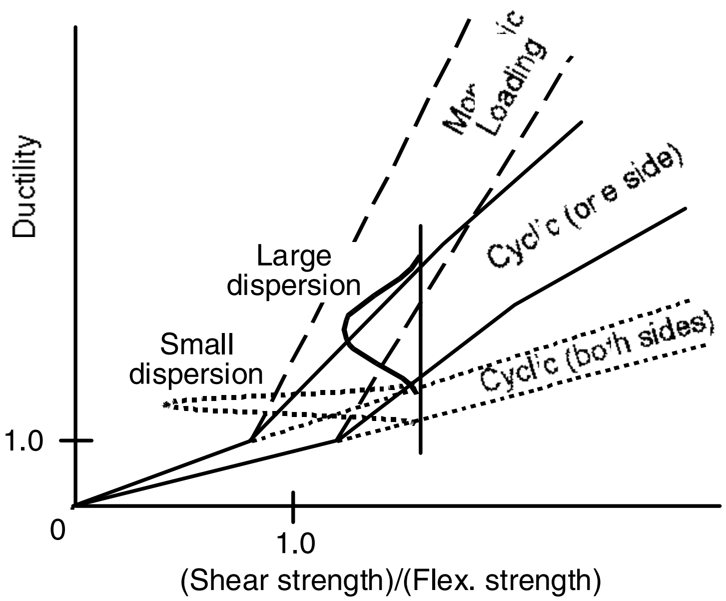

Fig. 10 Expected ductility considering uncertainty

A SIMPLE PERFORMANCE MODEL FOR BAR BUCKLING

M. O. Eberhard[1] and M. P. Berry[2]

ABSTRACT

A practical model has been developed to predict the lateral deformations at which longitudinal bars begin to buckle in reinforced concrete columns. The model is based on theoretically expected trends in drift ratio as a function of the effective-confinement ratio, axial-load ratio and aspect ratio. The model was calibrated and evaluated using 104 documented observations of bar buckling during cyclic tests. For spiral-reinforced concrete columns, the ratios of the measured displacements at bar buckling to the calculated displacements had a mean of 1.0 and a coefficient of variation of 25%. For rectangular-reinforced concrete columns, these ratios had a mean of 1.0 and a coefficient of variation of 26%.

1. INTRODUCTION

To implement performance-based earthquake engineering, it is necessary to relate deformation demands placed on structural members with the likelihood of reaching particular levels of damage. Buckling of longitudinal bars in a column is a particularly important performance state, because such damage can greatly affect the post-earthquake repair costs and the functionality of a structure. This paper provides a link between the level of deformation imposed on a column and the likelihood that a reinforcing bar will have begun to buckle. The proposed model is simple enough to be suitable for earthquake engineering practice.

2. MODEL DEVELOPMENT

A practical model can be developed by combining plastic-hinge analysis with approximations for the column yield displacement, plastic curvature, buckling strain and plastic-hinge length to develop a relationship between the drift ratio imposed on a column and the likelihood that at least one of the longitudinal bars will have begun to buckle.

[1] *Associate Professor, Department of Civil and Environmental Engineering, University of Washington, More Hall, Box 352700, Seattle, WA 98195-2700; PH (206) 543-1075; FAX (206) 543-1543; email: eberhard@u.washington.edu*

[2] *Graduate Research Assistant, Department of Civil and Environmental Engineering, University of Washington. More Hall, Box 352700, Seattle, WA 98195-2700; PH (206) 543-4815; FAX (206) 543-1543; email: mpberry@u.washington.edu*

2.1 Plastic-Hinge Analysis

According to plastic-hinge analysis, the total displacement, Δ, of a reinforced concrete member deformed beyond the yield displacement can be decomposed into two parts, the response up to the yield displacement, Δ_y, and the plastic deformation, Δ_p. The plastic deformation is assumed to result from the rigid-body rotation of the member around the center of a plastic-hinge near the base of the column. For simplicity, the curvature in the plastic-hinge is assumed to be constant ($\phi_p = \phi - \phi_y$) over an equivalent plastic-hinge length, L_p. The plastic rotation, θ_p, can then be expressed as, $\phi_p L_p$, and the total tip deflection is

$$\Delta = \Delta_y + \theta_p \left(L - L_p/2\right) = \Delta_y + \left(\phi_p L_p\right) \left(L - L_p/2\right) \tag{1}$$

where L is the distance from the column base to the point of contraflexure.

If $L_p / 2 << L$, and buckling is assumed to occur after column yielding, the displacement at the onset of buckling can be expressed as

$$\Delta_{bb} = \Delta_y + \phi_{p\_bb} L_p L \tag{2}$$

where ϕ_{p_bb} is the plastic curvature at the onset of bar buckling. The following sections present approximations for Δ_y, ϕ_{p_bb} and L_p.

2.2 Column Yield Displacement

According to Kowalsky (2002), the yield curvature of a reinforced concrete column cross-section can be estimated from the column depth and the yield strain of the tension reinforcement (ε_y).

$$\phi_y \cong \lambda \frac{\varepsilon_y}{D} \tag{3}$$

where λ = 2.45 for spiral-reinforced columns and 2.14 for rectangular-reinforced columns. Assuming that the moment-curvature relationship is linear up to column yield and neglecting the contribution of shear deformations, the approximate yield displacement is

$$\Delta_y \cong \frac{\phi_y L^2}{3} \cong \frac{\lambda}{3}\varepsilon_y \frac{L^2}{D} = \frac{\lambda}{3E_s} f_y \frac{L^2}{D} \tag{4}$$

where E_s and f_y are the elastic modulus and yield stress of the longitudinal reinforcement.

2.3 Plastic Curvature

Based on axial equilibrium requirements for a reinforced concrete cross-sections, the normalized plastic curvature ($\phi_{p\_norm} = \phi_{P\_n} D / \varepsilon_n$) at a given strain ($\varepsilon_n$) can be approximated with the following equation.

$$\frac{\phi_{p\_n} D}{\varepsilon_n} = \frac{G_0}{1 + G_1 \dfrac{P}{A_g f_c'}} \tag{5}$$

where D is the column depth, P is the axial load, A_g is the gross area of the cross section, f_c' is the compressive strength of the concrete. G_0 and G_1 are parameters that depend on the level of strain. For example, at a maximum strain of ε_n = 0.004, G_0 and G_1 can be taken as 5.3 and 9.4 respectively.

The normalized plastic curvatures (computed with moment-curvature analysis) for a compressive strain of ε_n = 0.004 were compared with curvatures calculated with (5) for 288 flexure-dominant columns (*www.u.washington.edu/~peera1*). The ratios of the plastic curvatures calculated with moment-curvature analysis to the plastic curvatures calculated with (5) had a mean of 1.0 with a coefficient of variation of 18%. This equation can also be used to approximate the relationship between the strain at the onset of bar buckling (ε_{bb}) with the curvature at the onset of bar buckling (ϕ_{p_bb}).

The strain ε_{bb} is influenced by the effectiveness of transverse reinforcement in confining the concrete core and longitudinal reinforcement. A common measure of this effectiveness is the effective confinement ratio, which is defined as $\rho_{eff} = \rho_s f_{ys} / f_c'$, where ρ_s is the volumetric transverse reinforcement ratio, f_{ys} is the yield stress of transverse reinforcement, and f_c' is the concrete compressive strength respectively. For simplicity, the critical strain is assumed to vary linearly as a function of the effective confinement ratio, as follows

$$\varepsilon_{bb} = \chi_0(1+\chi_1\rho_{eff}) \tag{6}$$

where χ_1 and χ_2 are constants. The parameter χ_1 is expected to be larger for spiral-reinforced columns than for rectangular-reinforced columns because spiral reinforcement is more effective at confining the longitudinal reinforcement.

By substituting (6) into (5) and combining constants, the plastic curvature at the onset of bar buckling can be expressed as

$$\phi_{p\_bb} \cong \frac{\eta_0}{D}\left(\frac{(1+\eta_1\rho_{eff})}{1+\eta_2\dfrac{P}{A_g f'_c}}\right) \tag{7}$$

where η_0, η_1 and η_2 are constants.

Plastic-Hinge Length

Numerous models have been proposed to estimate the plastic-hinge length of structural members In many of these models, the expression for the plastic-hinge length is proportional to the column length, *L*, column depth, *D*, and the longitudinal reinforcement properties, as in the following equation.

$$L_p = \alpha L + \beta D + \xi f_y d_b \tag{8}$$

where d_b is diameter of the longitudinal bar, f_y is the yield stress of the longitudinal reinforcement, and α, β and ξ are constants whose magnitude varies according to the particular model. The general form of (8) is adopted for the purpose of this paper.

Drift Ratio at Bar Buckling

By substituting the approximations for yield displacement (4), plastic curvature (7) and plastic-hinge length (8), into (2), and dividing by the column length, the drift ratio at bar buckling can be expressed as

$$\frac{\Delta_{bb}}{L} = \frac{\lambda}{3E_s} f_y \frac{L}{D} + C_0 \left(1 + C_1 \rho_{eff}\right) \left(1 + C_2 \frac{P}{A_g f'_c}\right)^{-1} \left(1 + C_3 \frac{L}{D} + C_4 \frac{f_y d_b}{D}\right) \qquad (9)$$

The five constants in (9), $C_0 ... C_4$, are combinations of earlier constants. Their magnitudes can be evaluated from experimental observations of bar buckling. A simpler version of (9) is suitable for design.

$$\frac{\Delta_{bb\_calc}}{L}(\%) = 3.25\ (1 + k_e \rho_{eff} \frac{d_b}{D})\ (1 - \frac{P}{A_g f'_c})\ (1 + \frac{L}{10D}) \qquad (10)$$

where k_e = 150 for spiral-reinforced columns and k_e = 50 for rectangular-reinforced columns.

MODEL EVALUATION

The results of nearly 500 tests of spiral-reinforced and rectangular-reinforced concrete columns were assembled to provide a basis with which to evaluate column performance methodologies. This database provides digital force-displacement histories for columns, as well as key material and geometric properties (Parrish and Eberhard 2001, Berry and Eberhard 2003). It has been posted on the World Wide Web at *http://ce.washington.edu/~peera1* and *http://nisee.berkeley.edu*. The form of (10) is consistent with trends observed from the database for spiral-reinforced concrete columns (Fig. 1) and for rectangular-reinforced columns (Fig. 2). These figures show the variation of the drift ratio at the onset of bar buckling as a function of key column properties. To isolate the effect of each property, the database was organized into families, in which all columns in a family had similar properties except for the property being studied. These families are connected with lines in Figs. 5 and 6. It should be noted that the families do not take into consideration variations in the displacement history imposed on each column.

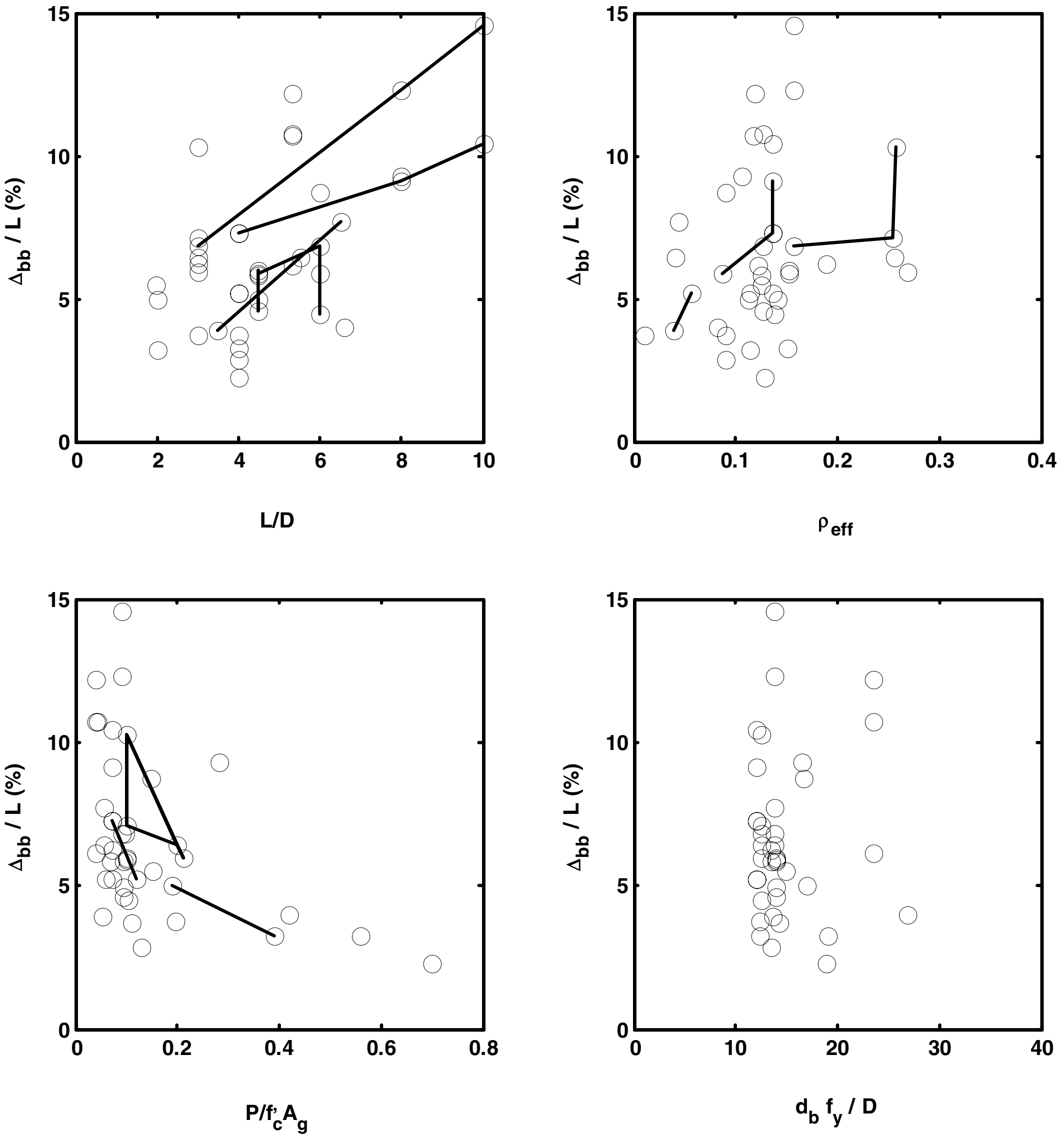

Fig. 1. Trends Observed for Spiral-Reinforced Columns in Database

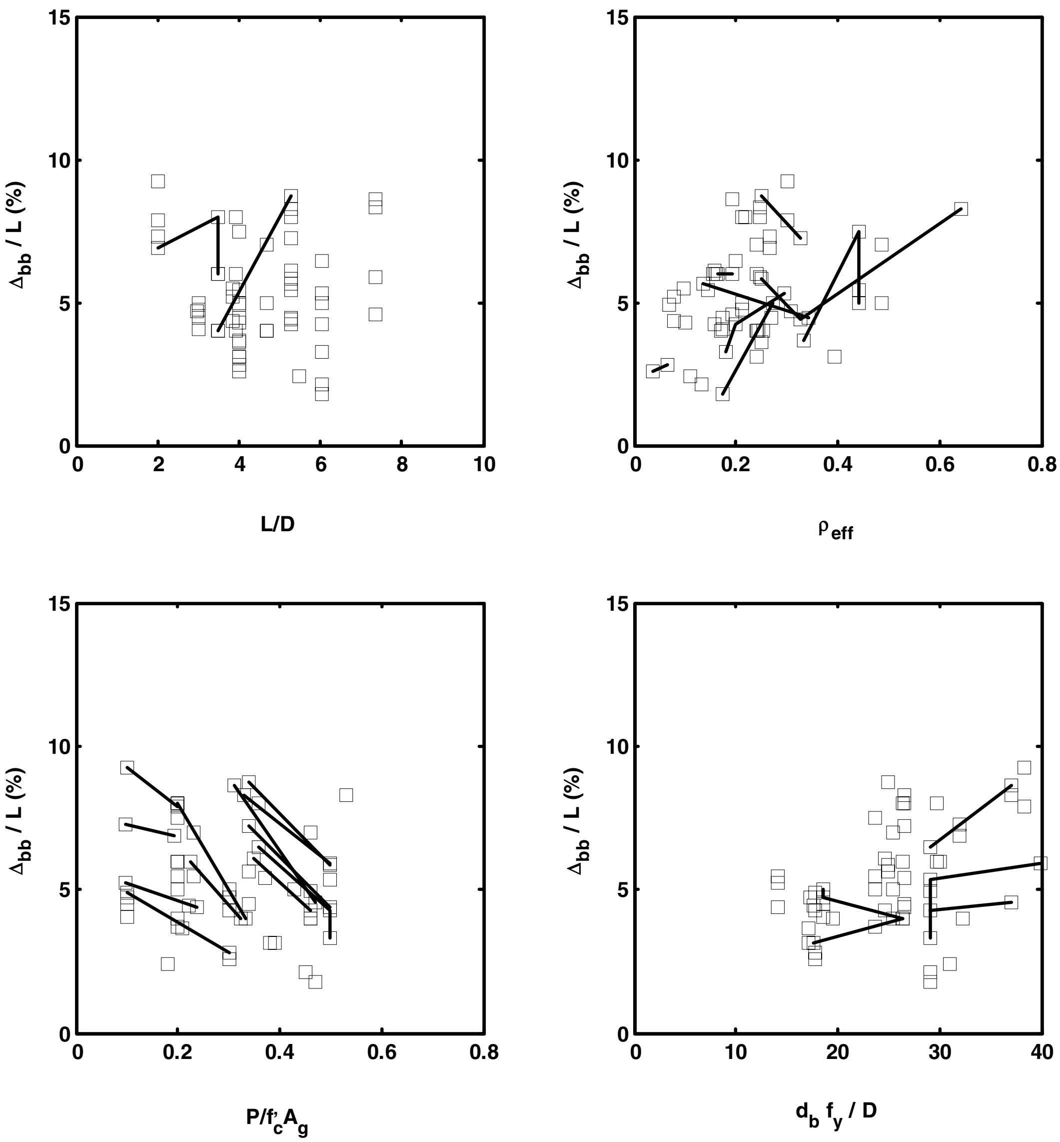

Fig. 2. Trends Observed for Rectangular-Reinforced Columns in Database

The accuracy of (10) was evaluated by comparing measured and predicted displacements for 104 observations of the onset of bar buckling during cyclic tests. The accuracy of the model was similar for spiral-reinforced columns (COV = 25%) as for rectangular-reinforced columns (COV 26%). The accuracy of the model is also illustrated by the statistics in Table 1 and the fragility curves in Figure 3.

Table 1. Accuracy Statistics for Proposed Model

Column Type	Number of Tests	Mean, $\frac{\Delta_{BB}}{\Delta_{calc}}$	Coefficient of Variation
Spiral-Reinforced	42	1.0	25%
Rectangular-Reinforced	62	1.0	26%

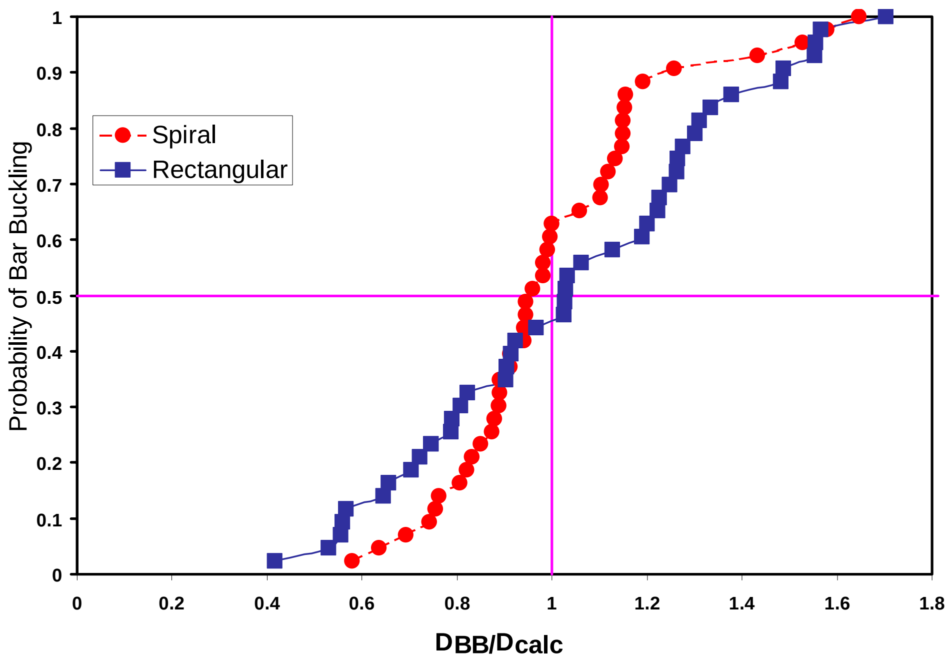

Figure 3. Fragility Curves for Bar Buckling

CONCLUSIONS

A simple performance model for column bar buckling was developed based on approximations of plastic-hinge analysis, moment-curvature analysis, the effect of confinement provided by the transverse reinforcement, and plastic-hinge lengths. The general form of the resulting relationship was simplified for practical applications and calibrated using a database of 104 observations of bar buckling during cyclic tests. The model accounts for the effects of effective-confinement ratio, axial-load ratio and aspect ratio on displacement demand.

ACKNOWLEDGMENTS

Support of this work was provided primarily by the Earthquake Engineering Research Centers Program of the National Science Foundation, under Award Number EEC-9701568 through the Pacific Earthquake Engineering Research Center (PEER).

KEYWORDS

Reinforced concrete, column, performance, damage, buckling

REFERENCES

Berry, M.P. and M.O. Eberhard (2003, in press), Column Deformation Demands at Concrete Spalling and Bar Buckling, Pacific Earthquake Engineering Research Center Report PEER-2003, University of California, Berkeley, September.

Kowalsky, M. J. (2002). A Displacement-Based Approach for the Seismic Design of Continuous Concrete Bridges." *Earthquake Engineering and Structural Dynamics*, 31(3), 719-747.

Parrish, M. and Eberhard, M.O. (2001). Accuracy of Seismic Performance Methodologies for Rectangular Reinforced Concrete Columns, Proceedings, Third US-Japan Workshop on Performance-Based Earthquake Engineering Methodology for Reinforced Concrete Building Structures, Seattle, Washington, August, 11pp.

EFFECT OF HYSTERETIC REVERSALS ON LATERAL AND AXIAL CAPACITIES OF REINFORCED CONCRETE COLUMNS

Hassane OUSALEM, Toshimi KABEYASAWA[1] and Akira TASAI[2]

ABSTRACT

The combination of loading frequency and loading magnitude of lateral load on buildings due to earthquakes are always not constant, but variables within the duration of a single earthquake. This fact is more pronounced and results are more scattered when dealt with different earthquakes. In order to analyze the structural response to such kind of excitations and understand the effect of hysteretic reversals on lateral and axial capacities, seven reinforced concrete column specimens were tested under different lateral loading histories. The experimental results are presented and discussed and finally results of a trial on shear-friction model are summarized.

1. INTRODUCTION

In order to secure societies from earthquake disasters, it is necessary to develop analytical and experimental works to assess the collapse of buildings. Studies showed that the seismic performance of individual structural elements in moderately tall reinforced concrete buildings depends on the mechanical and geometric characteristics of loaded elements, as well as on the type of loadings (Moehle 2000, et al). While effects of different types of axial loading had previously been investigated (Ousalem 2002), this paper presents experimental results of columns subjected to constant axial loading and different types of uni-directional cyclic lateral loading, simulating near and far field earthquake shakings. The testing program included 16 specimens. Seven of them are the subject of this paper while other specimens are oriented to strengthening studies. The experimental results were analyzed to reach conclusions as to the effect of hysteretic reversal type on columns response including deformability, axial stiffness, shear strength degradation, and the limit to sustain the axial load.

1 Earthquake Research Institute, The University of Tokyo, Tokyo 113-0032, Japan, Email: kabe@eri.u-tokyo.ac.jp

2 Dept. of Architecture and Building Science, Faculty of Engineering, Yokohama National University, Yokohama 240-8501, Japan Email: tasai@arc.ynu.ac.jp

2. TESTED SPECIMENS AND EXPERIMENT PROGRAM

The tested specimens were scaled to 1/3 of actual columns, considered representative of those in the first story of moderately tall building systems located in seismic regions. The cross section of all columns was square (300x300mm). Geometric details and material mechanical properties are depicted and listed in **Figure 1** and **Table** 1, respectively. The principal variables of the testing program were, mainly, transverse reinforcement ratio and lateral loading type, while the axial load was constant for all specimens. The presumed axial load ratio based on a concrete strength of 24 MPa was 0.25, which corresponds to a constant axial load of 540 kN actually applied on all specimens, although cylinder concrete tests revealed somewhat higher strength. The columns were tested in a vertical position. Independent axial and lateral loads were applied simultaneously to specimens. Laterally, columns were subjected to an anti-symmetric double curvature bending where the loading path was controlled by displacement. In order to simulate the action of near and far field earthquakes, two types of lateral loading were selected. Until a certain level, the total maximum deflection for both loading types was the same. The difference resided in the number of intermediate hysteretic reversal peaks as shown in **Figure 2**, then Type-2 becomes monotonic.

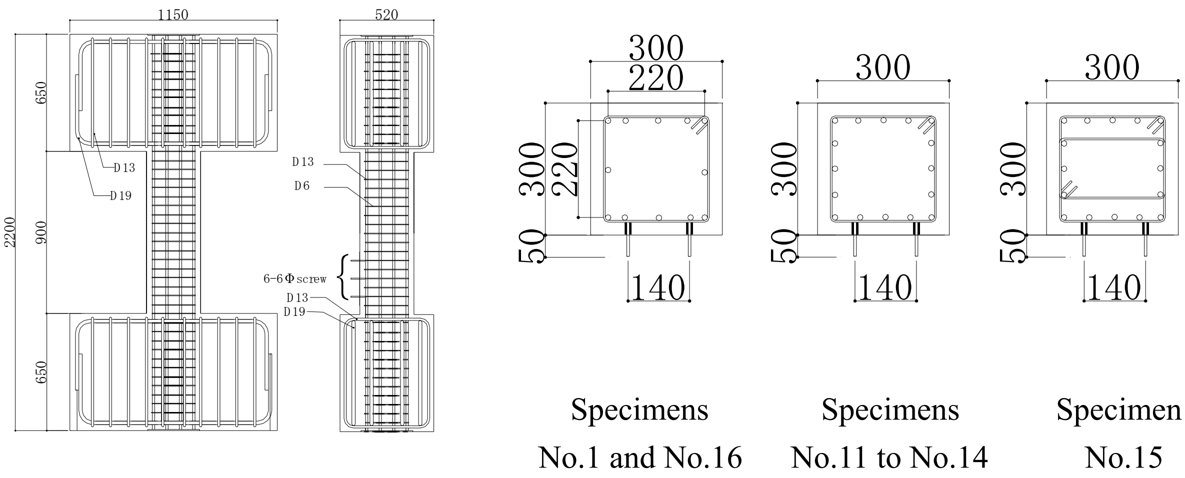

Figure 1: General description - Geometric details of tested specimens

Table 1 Material and characteristics of specimens

Specimen	Height (mm)	Shear span ratio	Concrete strength σ_B (MPa)	Axial load ratio η	Longitudinal reinforcement (MPa)	Transverse reinforcement (MPa)	Lateral loading type
No.1	600	1	27.7	0.22	12-D13 ρ_g=1.69%	2-D6@50 ρ_w=0.43%	Type-1
No.11	900	1.5	28.2	0.21	16-D13 ρ_g=2.26% σ_y=447	2-D6@150 ρ_w=0.14%	Type-1
No.12							Type-2
No.13			26.1	0.23		2-D6@50 ρ_w=0.43% σ_{wy}=398	Type-1
No.14							Type-2
No.15						4-D6@50 ρ_w=0.85%	Type-2
No.16	600	1			12-D13 ρ_g=1.69%	2-D6@50 ρ_w=0.43%	Type-2

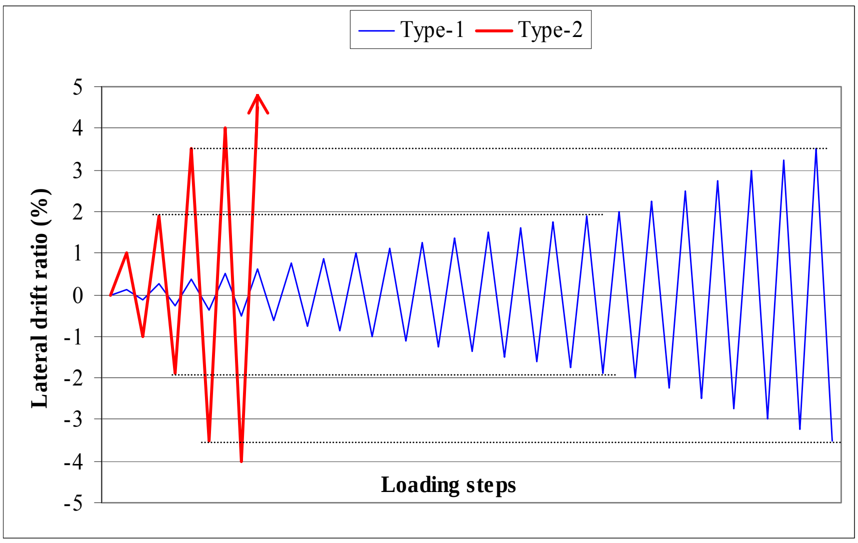

Figure 2: Lateral displacement loading patterns

3. OBSERVED BEHAVIOR, VISIBLE DAMAGE AND FAILURE MODE

In changing lateral loading, the results exhibited some differences among tested specimens, while few differences were noticed among specimens with low transverse steel ratio or low shear span ratio. However, visible damages were more noticed under loading Type-1. Also, collapse of columns was less brittle under loading Type-1 than under lateral loading Type-2. Regardless of the type of loading, all specimens failed as predicted by design: except for specimen No.15, all specimens were designed to fail in shear. Shear cracks characterized the crack patterns development and conditioned the failure mode of columns, except for specimen No.15. While failure in specimens with low transverse steel ratios or low shear span ratio (No.1, No.16, No.11, No.12) was due to clear diagonal tension cracks, failure in other specimens with higher transverse steel ratios and higher shear span ratio (No.13, No.14) was based on truss mechanism. Specimen No.15 experienced the formation of truss mechanism after yielding of longitudinal reinforcement. Bond splitting and spalling of concrete cover were observed on specimens during the last loading cycles. Actually, evolution of cracks and their widths depended closely on the type of lateral loading. Their number was higher and their width was lower under lateral loading Type-1 than under lateral loading Type-2. Finally, collapse was reached when columns were unable to sustain any more the applied axial load, which corresponded at the time when shear strength decay consumed nearly the whole lateral capacity of columns. Also, in good accordance with conclusions of previous experiments on nearly similar columns(Ousalem et al 2002), collapse occurred along inclined planes. For all specimens, plane inclinations were slightly steeper under lateral loading Type-2 than under loading Type-1.

4. COLUMNS RESPONSES

The data analysis of tested specimens indicated the dominance of shear deformation during loading against the flexural one. The lateral drift responses of all specimens, except in specimen No.15, showed a fast increase the lateral deformation due to shear rather than in the curvature. Also, except on specimen No.15, no longitudinal bar yielded before shear failure in all specimens. Yield was reached for almost all stirrups depending on the position of the stirrups to the major cracks. All steel strains, generally, reached slightly higher maximum values under loading Type-1 than under loading Type-2. Buckling of longitudinal bars, which occurred simultaneously when stirrups' hooks opened was one of the conditions that lead to collapse.

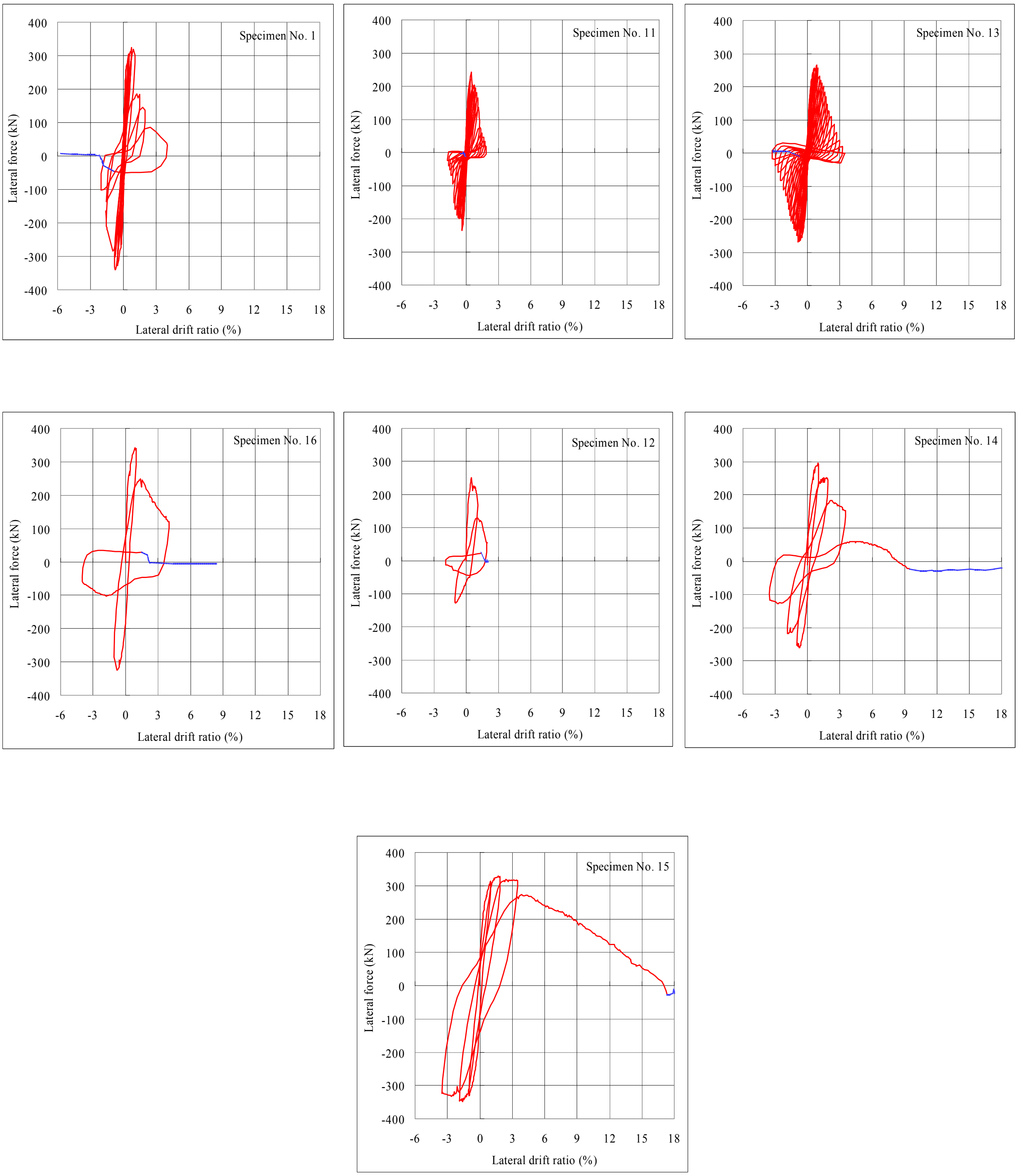

Figure 3: Lateral load-lateral drift responses

4.1 Lateral Load-Lateral Displacement Responses

Tested columns' lateral load-lateral drift ratio responses are depicted in **Figure 3**. As observed on specimens with same shear span ratio, high transverse reinforcement ratio provided high shear resistance and allowed large lateral deformability. Also, shear strength reached high levels for specimens with low shear span ratio, however their lateral deformability was low. Compared to loading Type-1, the application of loading Type-2 resulted in higher shear strength on the first loading direction and in lower shear strength on the opposite direction. Higher values were obtained because of absence of low amplitude reversals, which would induce some damage. Lower values were obtained in the opposite direction because of the cracks imposed by the large amplitude of the first loading direction. Those cracks induced a drop in the shear strength on the first loading direction that influenced the shear strength in the opposite direction. Also, shear strength degradation was more pronounced under loading Type-1 than under loading Type-2, which can be explained by the development of more cracks in the first loading type than in the second one. As for lateral deformability, in specimens No.1 and No.16 or No.13 and No.14 that responded relatively to the different lateral loading type, loading Type-2 induced higher lateral deformability. Specimens No.11 and No.12 did not show any difference toward applied lateral loading type.

4.2 Vertical Displacement Responses

Concerning the vertical deformation responses shown in **Figure 4**, experimental data showed that degradation of column axial stiffness was comparable from a certain level of testing for both lateral loading types, although degradation was faster at the beginning of loading for specimens subjected to loading Type-1. Finally, collapse occurred at the same level of vertical deformation for each pair (No1 and No.16, No11 and No.12, and No.13 and No.14). Furthermore, transverse steel content and shear span ratio influenced differently the evolution of axial stiffness. For columns with the same shear span ratio, providing more stirrups delayed degradation in the axial stiffness, consequently collapse occurred at higher vertical deformation. However, for columns with same transverse steel ratio, difference in shear span ratio resulted in the same limit vertical deformation and collapse.

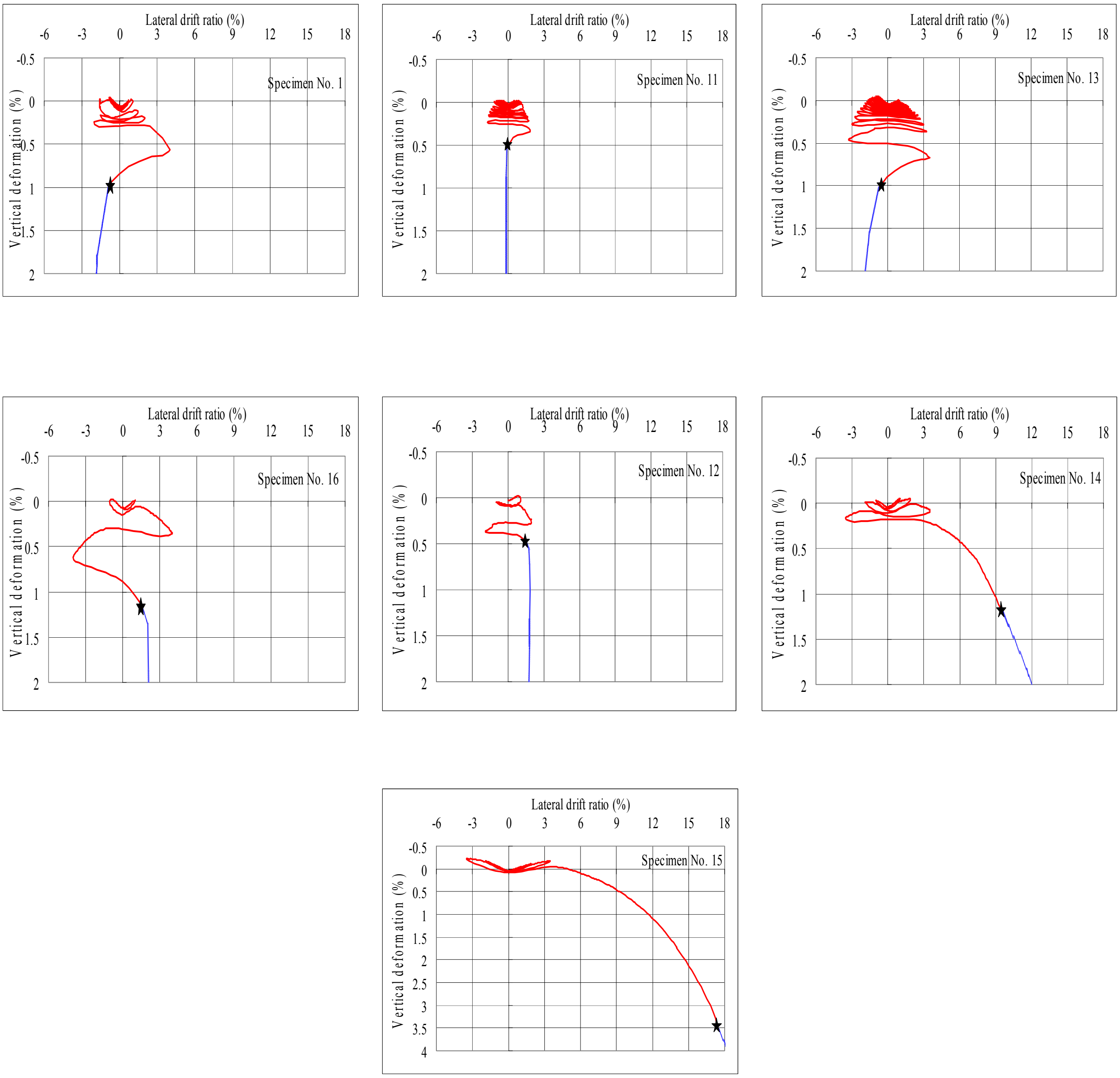

Figure 4: Vertical deformation-lateral deformation responses

4.3 Dissipated Energy

Depending on the loading type and the reinforcement amount, the total dissipated energy, obtained from lateral and vertical loads, as shown in **Figure 5**, varied from one element to another. Higher values were obtained for higher confinements, for higher shear span ratios and also for higher numbers of hysteretic reversals. Loading Type-1 induced higher total dissipated energy than loading Type-2. Also, while not depicted by a figure, a tentative to assess the part of energy dissipated by reinforcements and concrete was carried out. Ramberg-Osgood model was used to assess stresses in the reinforcements and approximate their corresponding amount of dissipated energy. The part of energy dissipated by concrete was deduced from the total one. It was found that during loading concrete dissipated far higher amount of energy in all specimens, compared to steel. This fact calls attention to the effect of friction and its contribution to dissipate energy.

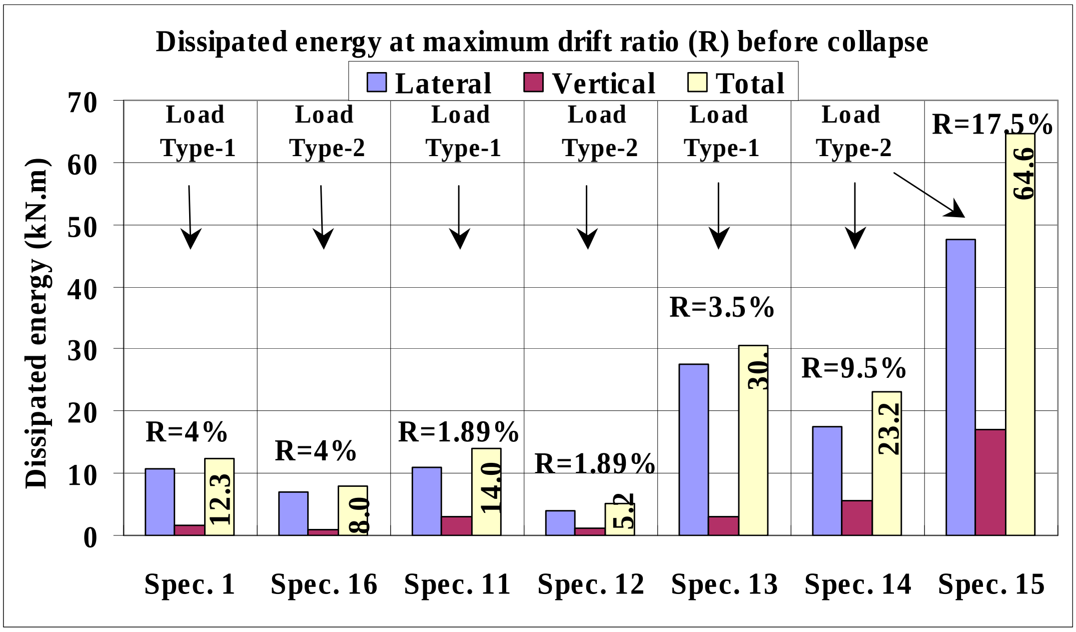

Figure 5: Dissipated energy

5. SHEAR-FRICTION MODEL

The shear-friction model (Moehle 2000) shown in **Figure 6**, based on an assumed diagonal failure plane, was applied to the tested specimens in order to find some convenient relationships that allow assess the ultimate limit of columns failing in shear in terms of the axial load $\boldsymbol{N}$ and its corresponding lateral drift ratio $\boldsymbol{R}$. The ultimate stage is attained when the resulting sliding force $\boldsymbol{S}$ along the failure plane reaches the plane tangent component of the compression force $\boldsymbol{C}$ by means of friction $\boldsymbol{\mu}$. Actually, the inclined plane angle θ is a very crucial parameter that has not a negligible effect on the aimed results. Inclination of observed failure planes during testing, applied axial load and forces developed by stirrups crossing the presumed planes were the basis to express the variation of friction along the presumed plane. **Figure 7**, which includes other experimental results (Moehle 2000 and Ousalem 2002), is a trial to relate the observed failure plane inclination to some main parameters by means of a simple function. The figure shows an assumed variation function of plane inclination where data errors were taking as a half of the calculated standard deviation ($\sigma_{\tan\theta}$=0.282, $\overline{\tan\theta}$=0.753). As to friction variation, considering or neglecting the dowel action of longitudinal reinforcement resulted in differences as to required friction values at columns' ultimate stage. The formulation of the friction, after some trials, was expressed relatively well by combination of different parameters than by a single one, to name the lateral drift ratio ***R***. The friction is shown in **Figure 8** including data of previous experiments and data reported by other authors (Moehle 2000).

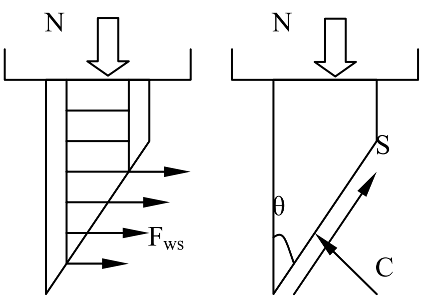

Limit equilibrium:

$$S = \mu.C$$

S: sliding force,

C: Compression force,

N: Applied axial load,

Fws: Stirrups' forces

Figure 6: Shear-friction model

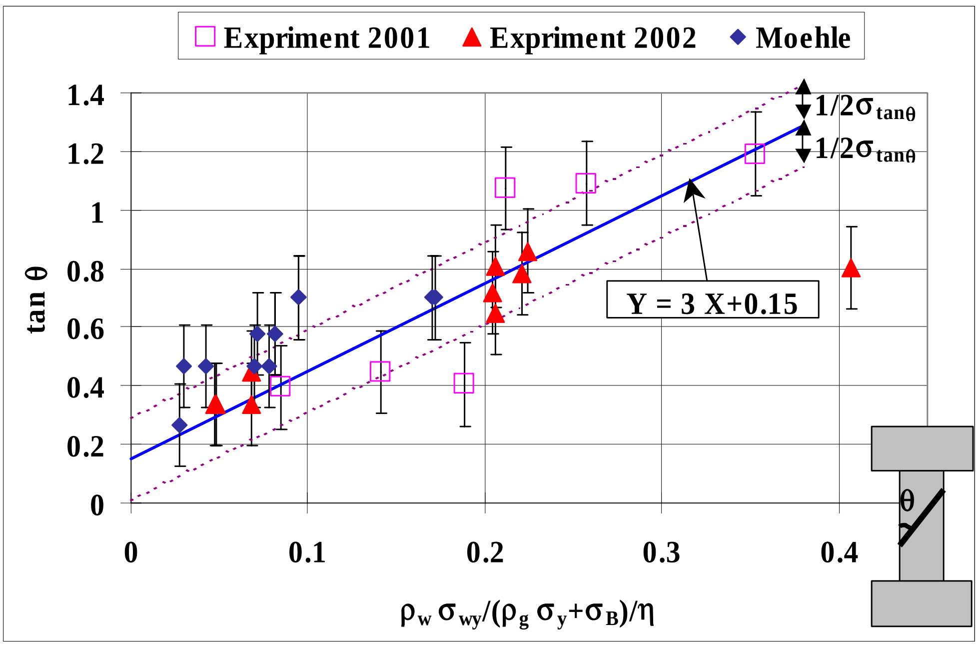

Figure 7: Observed angles of critical cracks

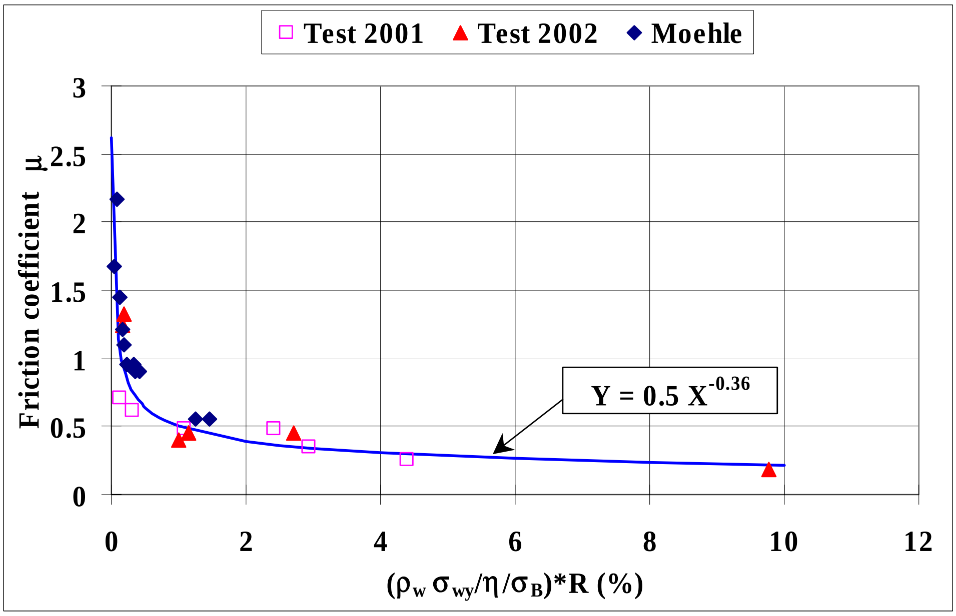

Figure 8: Shear-friction formulation

6. CONCLUSIONS

The lateral loading pattern changed in this RC column testing program. The following conclusions can be drawn:

(1) Evolution of cracks and their widths depends closely on the type of lateral loading. Their number is higher and their width is narrower under Type-1 loading (many hysteretic reversals).

(2) Shear strength degradation is more pronounced under Type-1 loading (many hysteretic reversals).

(3) For low transverse reinforcement ratio, lateral loading type has negligible effect on the attained maximum lateral drift. However, it has an effect on the maximum shear strength in the negative loading direction, where maximum shear strength is higher under loading Type-1 than under Type-2 (few hysteretic reversals)..

(4) For high transverse steel ratio or low shear span ratio, lateral loading Type-2 induces larger lateral deformability than loading Type-1.

(5) Axial stiffness degradations under both loading types are comparable. Limit vertical

deformations are also comparable and collapse of columns occurs at the same level of vertical deformation despite the loading type difference.

(6) Total energy dissipated under loading Type-1 is higher than under loading Type-2.

(7) Friction along failure plane at column's ultimate stage is well formulated by combining different parameters, including lateral drift ratio.

7. KEYWORDS

Reinforced Concrete Columns, Hysteretic Reversals, Axial Load, Lateral capacity, Axial Capacity, Shear Span Ratio, Transverse Reinforcement, Shear Failure, Bond Splitting, Shear-Friction Model, Drift Ratio

REFERENCES

Jin-keun, K., and L. Sang-Soon, The behavior of reinforced concrete columns subjected to axial force and biaxial bending, *Engineering Structures*, Vol. 23, 2000, pp. 1518-1528.

Moehle, J.P., K.J. Elwood, and H. Sezen, Shear failure and axial load collapse of existing reinforced concrete columns, *Proceedings of The 2 nd U.S.-Japan Workshop on Performance-Based Earth. Eng. Methodology for R/C Building Structures*, 2000, Sapporo, Japan, pp. 233-247.

Ousalem, H., T. Kabeyasawa, T., Tasai, A., and Y. Ohsugi, Experimental study on seismic behavior of reinforced concrete columns under constant and variable axial loadings, *Proceedings of The Japan Concrete Institute*, Vol. 24, No. 2, 2002, pp. 229-234.

SESSION 3-A: PREDICTION OF SEISMIC PERFORMANCE TO COLLAPSE

Chaired by

♦ Marc Aschheim and Shinsuke Nakata ♦

Computational Modeling of Structural Collapse

E. B. WILLAMSON[1] and G. KAEWKULCHAI[2]

ABSTRACT

The analysis of planar frame structures for the collapse limit state is presented within the context of performance-based seismic engineering. Unlike previous studies, dynamic load redistribution, including both geometric and material nonlinearities, is considered and has been determined to play a significant role in predicting the onset of structural collapse. This paper provides an overview of the computational framework needed to carry out collapse analyses. Research findings indicate that reliance on component-level failure analysis for predicting the onset of structural collapse may not be reliable when damage-dependent system-wide behavior is considered.

1. INTRODUCTION

Performance-based design for seismic events requires engineers to compute the response of structures so that the behavior corresponding to different performance limit states can be accurately captured. Thus, when designing for collapse prevention, engineers must understand the ways in which structural components fail and how the failure of one or several members affects the response of an entire structural system. Even though a structural component may not experience excessive damage due to a large magnitude earthquake, it can still fail as a result of being overloaded from load redistribution. If a damaged structure cannot adequately resist the redistributed loads, there is a good possibility the structure may collapse progressively.

Consideration of system-wide structural response is an important aspect of the progressive collapse problem. Simply stated, the loss of an important structural component (or components) may not necessarily lead to overall structural failure. For example, observations made after past earthquakes both here and abroad (e.g., Northridge, 1994; Kobe, 1995; Ceyhan, Turkey 1998) have clearly shown that a large number of buildings have sustained significant damage, including individual column failure, without structural collapse (Figure 1).

[1] *Department of Civil Engineering, University of Texas at Austin, Austin, TX 78737, USA*
email: ewilliamson@mail.utexas.edu

[2] *Department of Civil Engineering, University of Texas at Austin, Austin, TX 78737, USA*
email:nguang@mail.utexas.edu

Figure 1: Column failure without structural collapse.

While it is possible for structures to withstand large amounts of damage before failure ensues, there are many cases in which local component failure does lead to collapse. Incidents for structures that are loaded by blast or impact are numerous and include the Ronan Point Apartment Collapse in 1968, the U.S. Embassy failures in Kenya in 1998, the Murrah Building in Oklahoma City in 1995, and, most recently, the World Trade Center in September of 2001. Though perhaps not as well known as these tragic events, other examples exist for structures that are loaded seismically. One such case is that of the Cypress Viaduct near San Francisco following the Loma Prieta earthquake. During the ground shaking, a large portion of the upper deck failed and fell onto the lower deck, killing 40 people. Following the earthquake, the viaduct was scheduled to be demolished, and a wrecking ball was used to impact one of the end columns on the upper level. After several blows with the wrecking ball, the column being struck failed. This failure was immediately followed by the collapse of the remainder of the structure (5 piers supporting 4 spans). According to Booth and Fenwick (1994), the tendency for progressive collapse certainly contributed to the loss of life during the earthquake.

Due in large part to these past incidents, there is growing concern that structures be designed so that overall system behavior is considered and the potential for progressive collapse is minimized. Interest in this topic concerns not only new construction, but it also addresses the retrofit and repair of structures that may not satisfy current code requirements or that may have suffered damage while in service. For example, Moehle et al. (2000) have reported that engineers in California have found that it is not economically feasible to protect all columns from failure when seismically retrofitting an older structure. Consequently, there is a need to develop a better understanding of how load is transferred from a failed member to the remainder of the structure, particularly for cases involving dynamic loads. To date, however, only a limited number of studies have considered analysis for the collapse limit state. Much of the reason for this lack of information is due to the emphasis on individual component response in previous research. Even current performance-based methodologies (FEMA 273, 1997) consider only damage to individual structural elements when evaluating a building for collapse. As discussed earlier, data gathered from past earthquakes have demonstrated that individual elements can experience significant damage or even failure without collapse of the entire structure.

With the growing emphasis on performance-based earthquake engineering, there is an expectation that a structure can be designed to achieve a target performance level for an earthquake of a given intensity. Performance, in this context, is measured in terms of damage accumulation (Vision 2000, 1995). Consequently, models used for analysis should provide a measure of damage sustained under cyclic loads. Furthermore, consideration should be given to structural stability under the dynamic earthquake forces. Characterization of a given performance level cannot be based on arbitrary lateral drift limits (Williamson, 2003; Vian and Bruneau, 2002). Rather, analysis models must be capable of representing the state of a structure at various levels of sustained damage. For the collapse limit state, this notion implies that analysis tools be capable of accounting for the sequence of member failures throughout a given scenario so that collapse can be detected and not inferred by an artificial limit.

In analyzing structures for collapse, modern building codes (IBC, 2000; GSA, 2001) favor a procedure known as the "alternate load path method." With this approach, one, or perhaps several, load-carrying members are assumed to fail and are removed from the structural model for the purposes of analysis. The remaining structure is then analyzed to determine if other member failures result. Because the collapse limit state represents the most severe performance level, the primary focus is on the prevention of widespread failure propagation. Accordingly, unfactored loads are used, and strength reduction factors are ignored. The procedure continues until there are no further member failures or the structure remains capable of supporting its loads despite the loss of various structural components. As a result of using the alternate load path method for progressive collapse analyses, information on static load redistribution for the structure under consideration is obtained. One criticism of this method is that it fails to consider dynamic effects that inevitably result following the failure of one or more load carrying members.

Pretlove et al. (1991) discussed the importance of dynamic load redistribution in their research on the progressive failure of a tension spoke wheel. These researchers demonstrated that a static analysis predicting a damaged structure to be safe from progressive failure may not be conservative if inertial effects are taken into consideration. The authors (Kaewkulchai and Williamson, 2002) also demonstrated the importance of considering inertial effects for frame structures. Although dynamic effects on the response of truss structures during progressive failure have been presented in the research literature (Malla and Nalluri, 1995, 2000), few researchers have considered dynamic load redistribution in the progressive collapse analysis of frame structures. In this paper, we document the development of a computational tool that is capable of performing collapse analyses of planar frame structures in an efficient manner. A description of the model formulation and solution procedure is provided. Example analyses are given at the end of the paper to demonstrate which factors have the greatest impact on the progressive collapse of planar frame structures.

2. ANALYTICAL MODELS OF FRAME STRUCTURES

Various analytical models for analyzing frame structures have been presented in the literature. These models can generally be classified into three main groups according to their complexity: global models, discrete element models and finite element models.

With global models, only a few degrees of freedom are selected to represent the response of a structure. For example, the typical assumptions needed to characterize a frame as a shear building give rise to a model with one degree of freedom per storey. Under these conditions, local member forces and deformations are not obtained directly from the analysis. Thus, global models are primarily useful for preliminary design but not for final design. For the discrete element models, a frame is represented as an assemblage of individual members (i.e., beam-column elements) that describe the behavior of structural members. These discrete elements are generally connected at nodes located at the element ends in which degrees of freedom, corresponding to the nodes, represent the structural response. Local member forces and deformations, as a function of structural degrees of freedom, can be obtained directly from an analysis. Finally, with finite elements models, the members and joints of a frame are divided into a large number of finite elements. Material and element properties are typically described at the stress-strain level. Such models will give the most accurate response of critical regions. Use of such models for an entire frame, however, requires extensive computational resources for the nonlinear dynamic analysis of large structures. Thus, such models are not well suited for design or large-scale parameter studies.

While discrete element models do not provide the same level of resolution of finite element models, they do provide sufficient detail on the response of structural members for conditions being addressed by this research. Furthermore, given the fact that limited data are available to validate computational models of collapse, it is practical to first consider models that can capture the response of individual members yet are not so computationally intensive that parameter studies cannot be conveniently conducted. Accordingly, discrete element models for frame structures are used in the current study.

3. SOFTWARE DEVELOPMENT

In this section, a brief overview of the solution methodology used to develop the computer software for progressive collapse analysis of planar frame structures is given. Additional information can be found in Kaewkulchai and Williamson (in press).

The solution methodology is based upon the conventional direct stiffness method for the analysis of planar frame structures. The governing equations of dynamic equilibrium are solved numerically using the Newmark-beta method (Newmark, 1959). A proportional (Rayleigh) damping matrix is assumed along with the use of a lumped mass matrix. Geometric nonlinearity (P-Δ effect) is taken into account by using a simplified geometric stiffness matrix, and a lumped plasticity model for cubic beam-column elements is employed to account for material nonlinearity. To solve the nonlinear system of equations, the well-known Newton-Raphson method is employed.

A unique feature of the developed software is that the effects of strength and stiffness degradation of members are modeled explicitly by means of a damage index. Thus, rather than using an arbitrary rule to determine the onset of member end failure, the damage index at each member end is updated throughout the response history and is used to quantify when failure occurs. Following failure, a modified member stiffness procedure with releases of end forces is used to track the response of the failed end without the introduction of additional nodes in the main structure. The following sections describe in greater detail particular aspects of the computational software for collapse analysis.

3.1 Beam-column Element

The beam-column element employed in this study is based upon a formulation that was originally developed by Kim (1995) for the analysis of planar frames subjected to earthquake excitation. The element incorporates a lumped plasticity model to capture nonlinear material response. Inelasticity of the element under a combination of axial force and moment is assumed to occur only at element ends or hinges. Currently, the software utilizes multi-linear force-deformation relationships in combination with a modified Mroz's hardening rule (Figure 2), but other constitutive models are possible (e.g., Takeda, et al., 1970). Future research will focus on including material models that can incorporate response features that are specific to reinforced concrete frames such as hysteresis pinching, bar slip, etc.

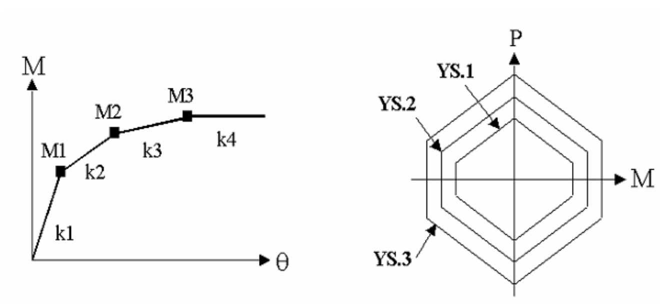

Figure 2: Multi-linear force–deformation relationships and yield surfaces.

Unlike standard stiffness-based methods of analysis, the element utilizes a flexibility-based formulation which relies on force interpolation functions that satisfy the equilibrium of bending moments and axial force along the length of the element. Thus, at the element level, instead of using displacement interpolation functions (i.e., cubic Hermitian shape functions) that may not be appropriate when hinging occurs at member ends to establish the element stiffness matrix, force equilibrium, which requires no assumptions regarding the way a beam-column element deflects, can be used to establish the flexibility matrix for an element. The element flexibility matrix can then be used to compute the element stiffness matrix. Various researchers have demonstrated the usefulness and efficiency of using flexibility-based approaches in determining the response of frame members that respond nonlinearly (e.g., Spacone, et al., 1996; Neuenhofer and Filippou, 1997).

3.2 Damage Model

Traditionally, earthquake-resistant design procedures have considered the effects of damage indirectly by means of a response parameter such as the ductility factor, which is defined as the maximum displacement of a system normalized by the yield displacement (Newmark and Hall, 1982). Such an approach, however, fails to recognize that inelasticity and damage are two distinct phenomena that should be treated independently (Kachanov, 1986; Lemaitre and Chaboche, 1994). Furthermore, use of a single parameter such as the ductility factor as the only indicator of damage has been criticized in the research literature. McCabe and Hall (1989) have shown that the underlying hypotheses of the ductility factor approach lose validity for very stiff or very flexible structures. Ballio and Castiglioni (1994) suggest that the ductility factor method implicitly assumes structural regularity and a global collapse mechanism.

As stated above, damage indices in current earthquake engineering practice play a passive role. They are used to quantify a performance state at the conclusion of an analysis, but they are not used to affect the way structural response evolves. In the present study, however, damage is used to modify the properties of a structure so that the response of a damaged system depends not only upon the previous stress-strain history, but also upon the rate at which damage accumulates. Thus, systems with the same initial properties can reach failure at different stages due to characteristics of the earthquake excitation as well as the way damage accumulates during the response period. While this concept is not new (see, for example, work by Baber and Wen, 1981), it is one that has not been used directly to evaluate structural performance limit states.

To perform collapse analyses, the beam-column element originally developed by Kim (1995) was modified in this research to make its response depend explicitly on the level of damage sustained by the system for the analysis being considered. Several models of damage have been proposed in the literature that depend upon a damage index, *D*, having a value ranging from 0 (no damage) to 1 (total damage). Examples include those of Park and Ang (1985) for concrete members and Krawinkler and Zohrei (1983) for steel members. In the current study, a modified version of the Park and Ang (1985) model is used. Thus, the damage index, *D*, is assumed to be a linear function of the maximum deformation and the accumulated plastic energy such that

$$D = \alpha U(\delta) + \beta W(\delta) \tag{1}$$

where α, β are constant (material) parameters, $U(\delta)$ is a function that depends upon the maximum deformation, and $W(\delta)$ is a function that depends upon the accumulated plastic energy.

In computing the response history of a structure, the damage index is updated at each time step. The values of α and β can be adjusted to account for different rates of damage accumulation and thereby represent a variety of response models that have been proposed in the literature (Williamson, 2003). The effects of damage on the hysteretic response of a tip-loaded cantilever beam under cyclic load are shown in Figure 3 as a function of the damage parameters. Additional details are given in Kaewkulchai and Williamson (in press).

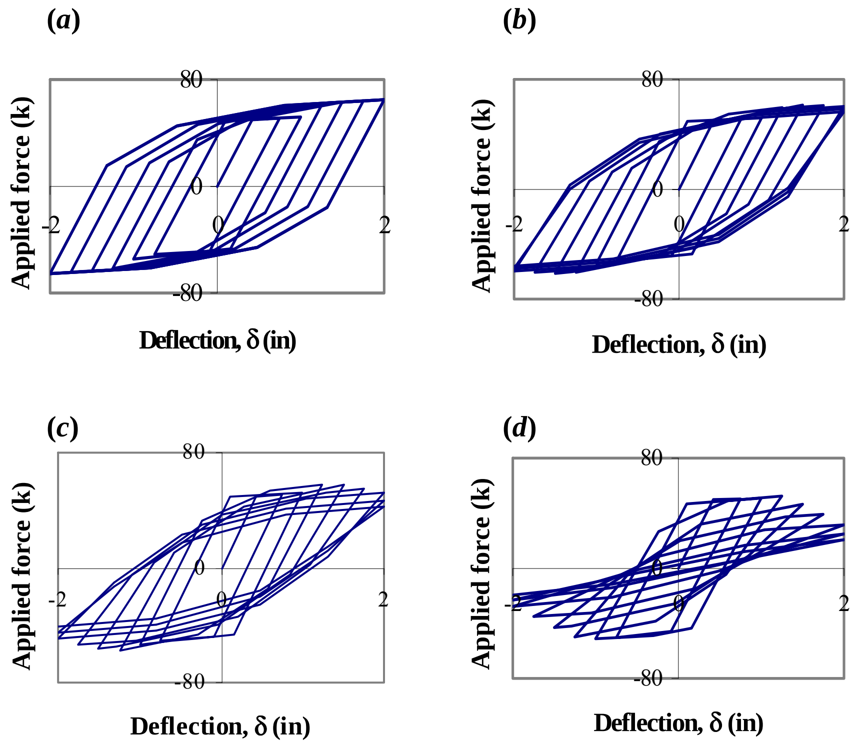

Figure 3: Response of a cantilever beam with different rates of damage (α, β), (*a*) No damage ($\alpha = \beta = 0$), (*b*) Slight damage ($\alpha = \beta = 0.01$), (*c*) Moderate damage ($\alpha = \beta = 0.03$), (*d*) Severe damage ($\alpha = \beta = 0.1$).

3.3 Member End Failure

For each element, a damage index associated with each member end, D_i at hinge i and D_j at hinge j, is used to determine the onset of member end failure. When a damage index of a hinge reaches a value of one, the hinge is assumed to fail and separate completely from the main structure (Figure 4).

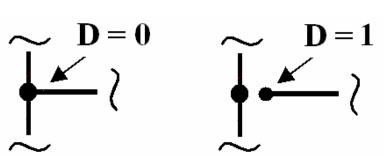

Figure 4: Hinge separation (total damage), *D* = 1.

One alternative for computing the response of a structure with an element that has one end failed is to introduce a new node to the structural model. This approach, however, can be cumbersome, as introducing the new node with corresponding new degrees of freedom requires that the size of the system mass, damping, and stiffness matrices be expanded, and it requires redefining the element connectivity relationships. Throughout a given analysis case, it is possible that many end failures can occur, thus requiring significant efforts to modify the computational parameters defining the problem being considered. Rather than introduce a new node and additional degrees of freedom, we take an alternative approach in the current study. A modified member stiffness procedure with releases of end forces is employed. This procedure is described in the following section.

3.4 Post-Analysis after Member End Failure

One unique aspect of the developed software is the capability of performing an analysis of frame structures after failure of member ends. This aspect involves updating various computational parameters. For example, consider a structural frame in Figure 5 in which a beam member has the internal forces at end *j* before failure equal to F_j, V_j and M_j. To maintain equilibrium at the onset of hinge separation, the internal forces of the failed hinge (end *j*) are released and applied back to the main structural frame. At this point, the externally applied load vector of the frame is modified to include those internal forces resulting from the failed end. At the failed end, equal and opposite internal forces are applied so that the member forces at this end become zero. Within that time step, the mass matrix is modified to represent the loss of mass contributing to the failed end of the beam member. Then, damping and stiffness matrices are modified to represent the current state of the structural configuration. It is also important to recognize that jumps in acceleration at the node connecting to the failed hinge will occur due to suddenly released forces. These jumps in acceleration can be obtained by satisfying the new equilibrium conditions of the node. After updating nodal accelerations, the analysis can then be carried on to the next time step.

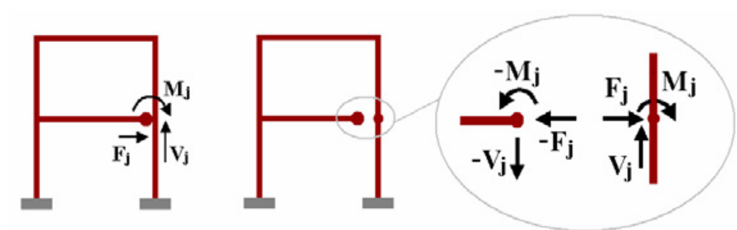

Figure 5: Post analysis after member end failure.

3.5 Impact of Failed Members

When a member fails, whether at one or both ends, the failed ends move independently from the main structure. Therefore, this member may come into contact with another member. When contact occurs, additional mass and impact forces are imposed on the main structure. These impact forces are likely to be one of the key aspects causing progressive collapse of buildings. To approximate the response of frame structures subjected to impact forces, an imaginary node is introduced at the contact point. By conservation of momentum, a new initial velocity of the node can be obtained using the new mass and the impacting velocity. The gravity load due to the impacting mass is also modeled as an externally applied force. Then, by using the modified member stiffness approach and condensing out the imaginary node, an analysis can be continued with little disturbance to the main analysis routine. A detailed discussion of this topic is given in a forthcoming paper by the authors.

4. ANALYSIS AND RESULTS

In this section, analysis results for a three-bay, three-story frame are presented. Analyses are performed in two parts. The first part considers gravity loads only. Static and dynamic solutions for an initial collapse scenario are carried out and compared to emphasize the drawback of using the conventional alternate load path method for computing the collapse limit state. The second part deals with the seismic analysis of the frame subjected to the 1994 Northridge earthquake. The response of the structure under earthquake excitation is compared with the case in which only gravity loads act.

The three-bay, three-story frame shown in Figure 6 consists of three different bay widths of 200, 240 and 280 in, with a constant height of 144 in. Member properties for all beams and columns are shown in the figure. It is further assumed that the frame has a uniform load of 0.5 kips/in acting on all beams.

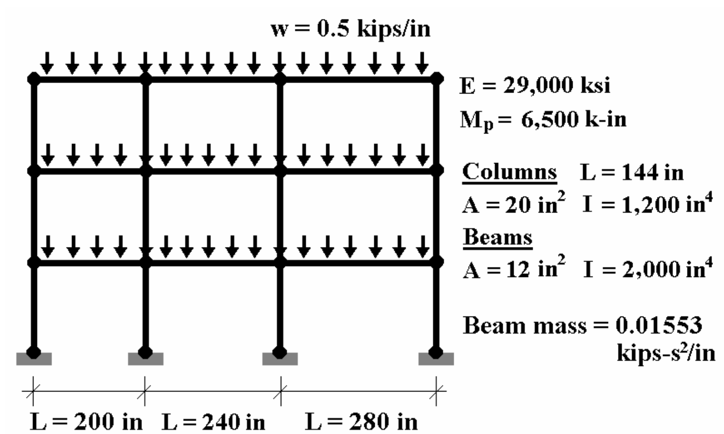

Figure 6: Frame structural configuration and member properties

4.1 Analysis with the Alternate Load Path Method

Using the concept of the alternate load path method, this section details the response of the example frame when subjected to an initiating collapse event. The failure of the first floor column that is second from the right end forms the initial collapse scenario. Both static and dynamic solutions are carried out and compared. The response of the frame is computed with the structure starting from a deformed configuration (i.e., failure of the column occurs after the frame reaches equilibrium under the static loads). For the dynamic analysis, the time step size is set to be 0.02 s, and a beam mass of 0.0155 kips-s^2/in is used for all beam members. In addition, as is typical when using a lumped mass formulation, rotational inertia is ignored. Damping is also ignored due to the fact that material inelasticity tends to dominate energy dissipation for systems in which yielding of the elements occurs.

The results obtained from the static and dynamic analyses are summarized and compared in Figure 7 and Table 1. Figure 7 shows plastic hinge locations obtained from both analyses. As can be seen from the figure, including inertial effects results in a response behavior with a greater number of plastic hinges. In Table 1, the vertical displacement and plastic hinge rotations at various points (see Figure 7) are provided for assessing the level of plasticity and comparing the static and dynamic analyses. In addition, dynamic increase factors (DIF) are determined by computing the ratio of the maximum response for the dynamic case versus the static case.

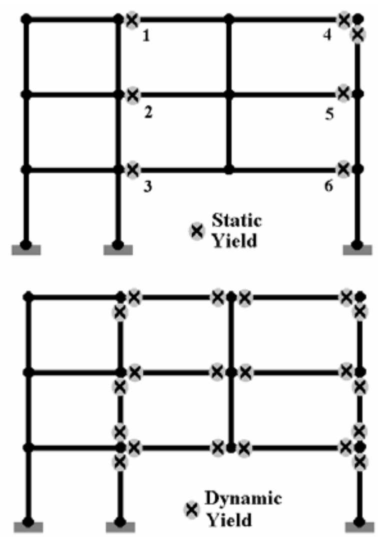

Figure 7: Plastic hinge locations obtained from static and dynamic analyses

Table 1: Comparisons of displacement and plastic rotations

	Static Analysis	Dynamic Analysis	DIF
Vertical Displacement	-28.47	-60.91	2.1
Plastic Rotation (Point 1)	-0.10	-0.24	2.4
Plastic Rotation (Point 2)	-0.072	-0.25	3.4
Plastic Rotation (Point 3)	-0.069	-0.25	3.6
Plastic Rotation (Point 4)	0.023	0.059	2.6
Plastic Rotation (Point 5)	0.064	0.21	3.3
Plastic Rotation (Point 6)	0.064	0.21	3.2

As can be seen in Table 1, the dynamic increase factor (DIF) for the vertical displacement is 2.1, and those for the plastic rotations range from 2.4 to 3.6. These results demonstrate that accounting for dynamic effects leads to considerably greater inelastic deformations throughout the frame in comparison to the static analysis. Thus, accounting for dynamic load redistribution appears to be an important feature in predicting the potential for progressive collapse of frames.

4.2 Seismic Analysis

This section provides details on the seismic analysis of the example frame subjected to the 1994 Northridge earthquake. The ground motion considered was the Sylmar Olive View Hospital record having a maximum acceleration of 0.843g at 4.22 s. In these analyses, the time step size is equal to 0.02 s. The uniform dead load acting on the beams gives values of nodal mass equal to 0.0155 kips-s^2/in for all beam members. Because the self-weight of the columns is small and there are no other dead loads acting on these members, their mass contribution is ignored. Velocity-proportional damping is also neglected.

Analyses are performed for the frame considering the effects of damage on the strength and stiffness degradation of the members. The collapse behavior of the damaged frame subjected to gravity load and earthquake is compared with the one utilizing the alternate load path method subjected to gravity load only. For the earthquake case, the first floor column that is second from the right end is assumed to be more brittle than the other columns. As such, it experiences damage at a greater rate than the other members (i.e., larger values of α and β in the damage model). For the damage parameters selected ($\alpha = 0.02$ and $\beta = 0.01$), this column fails at time = 3.59 s during the 180th step in the analysis. All beams in the model employ these same damage parameters, but the other columns employ $\alpha = 0.02$ and $\beta = 0.0001$. Additional information on the sensitivity of the computed results to the selected values of the damage parameters can be found in Kaewkulchai (2003). For the case where only gravity load is present, the frame is subjected to the initiating collapse event due to the failed column as previously discussed. The collapse progression for the damaged frame due to earthquake and gravity load is presented in Figure 8, while Figure 9 shows the collapse sequence for the damaged frame subjected to gravity load only.

Figures 8 and 9 show similar collapse patterns between the two cases in which the first fracture occurs at 0.436 s after initial failure for the first case, and 0.430 s in the second case. For the analysis with gravity load only, however, the collapse process takes 0.634 s, while for the case considering earthquake and gravity load, the total time from the first to the last member failure is 0.570 s. Furthermore, more members fail simultaneously in the seismic analysis case compared to the gravity case. Note that, for the seismic analysis, most columns experience inelasticity. Large plastic deformations in these columns could lead to another column failure if a faster rate of damage accumulation is employed, and hence possibly a different progressive collapse pattern. Additional research is needed to characterize appropriate values for the damage parameters as a function of member properties and reinforcement detailing.

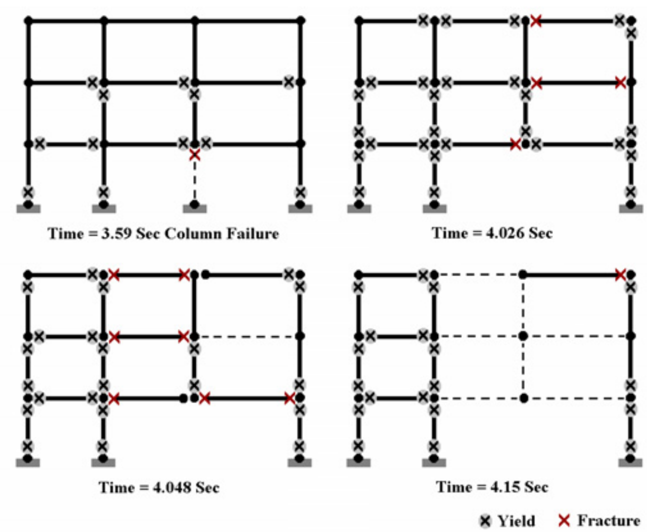

Figure 8: Collapse sequence for the damaged frame due to earthquake and gravity

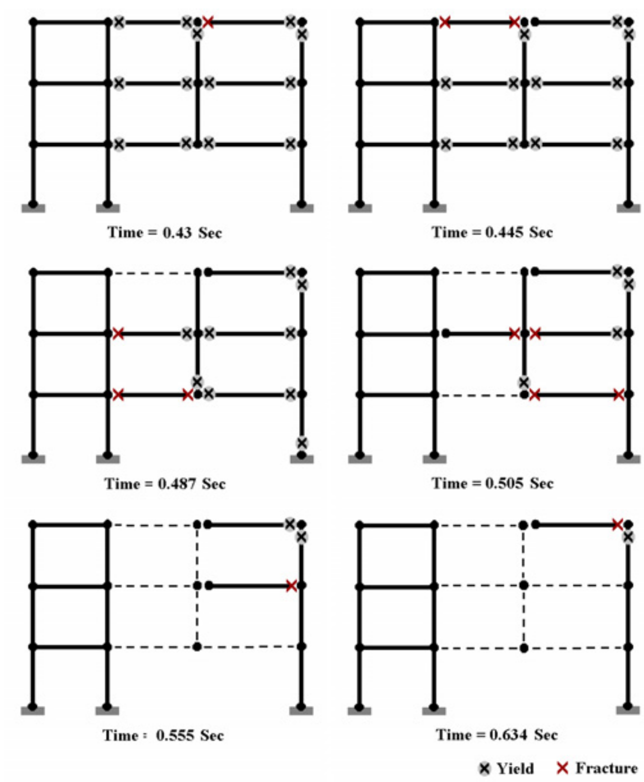

Figure 9: Collapse sequence for the damaged frame subjected to gravity load only (the alternate load path method)

5. SUMMARY AND CONCLUSIONS

Progressive collapse of buildings has been known to be an important design consideration since the 1970s after the Ronan Point Apartment building collapse in London. Current building codes and provisions have addressed the progressive collapse issue indirectly through the use of minimum requirements on structural strength, ductility, redundancy, and continuity. In addition, a direct design procedure, known as the alternate load path method, is recommended by current building codes as a simplified analysis technique for investigating the potential for progressive collapse. Several researchers, however, have shown that the results obtained from this method may not be conservative because inertial effects are neglected. Consequently, the current study focuses on computing the dynamic response of planar frame structures subjected to an initiating collapse event.

In this paper, a description of the solution methodology used to develop computational software for progressive collapse analysis is given. Sample analyses that consider the response of planar frames subjected to an initiating failure event are also presented, and computed results demonstrate that dynamic effects play a significant role. Because of the lack of experimental data available, future research will focus on conducting more parametric studies so that key factors contributing to the progressive collapse of planar frame structures can be identified.

6. REFERENCES

Baber, T. T. and Wen, Y. K. (1981). “Random Vibration of Hysteretic, Degrading Systems.” *Journal of the Engineering Mechanics Division*, ASCE, 107(6), 1069-1087.

Ballio, G. and Castiglioni, C. A. (1994). “An Approach to the Seismic Design of Steel Structures Based on Cumulative Damage Criteria.” *Earthquake Engineering and Structural Dynamics*, 23(9), 969-986.

Booth, E. and Fenwick, R. (1994). *Concrete Structures in Earthquake Regions*. Addison-Wesley Longman Higher Education, London.

FEMA 273 (1997). NEHRP *Guidelines for Seismic Rehabilitation of Buildings*. Federal Emergency Management Agency, Washington D.C., October 1997.

General Services Administration (2001). *Progressive Collapse Analysis and Design Guidelines for New Federal Office Buildings and Major Modernization Projects*. Central Office of the GSA.

IBC (2000), International Building Code, International Code Council, USA.

Kachanov, L. M. (1986). *Introduction to Continuum Damage Mechanics*. Martinus Nijhoff Publishers, Dordrecht, Netherlands.

Kaewkulchai, G., and Williamson, E. B. (2002). “Dynamic Progressive Collapse of Frame Structures.” *The 15th Engineering Mechanics Division Conference*. New York, ASCE.

Kaewkulchai, G. (2003). “Progressive Collapse of Planar Frames” Ph.D. Dissertation. University of Texas at Austin.

Kaewkulchai, G., and Williamson, E. B. (in press). “Beam Element Formulation and Solution Procedure for Dynamic Progressive Collapse Analysis.” *Computers & Structures* (accepted for publication 4 Aug 2003).

Kim, K. D. (1995), Development of Analytical Models for Earthquake Analysis of Steel Moment Frames, Ph.D. Dissertation, University of Texas at Austin.

Krawinkler, H., and Zohrei, M. (1983), "Cumulative Damage in Steel Structures Subjected to Earthquake Ground Motions." *Computers & Structures*, **16**(1-4), 531-541.

Lemaitre, J. and Chaboche, J.-L. (1994). *Mechanics of Solid Materials*. Cambridge University Press, Cambridge.

Malla, R. B., and Nalluri, B. (1995), "Dynamic Effects of Member Failure on Response of Truss-type Space Structures." *Journal of Spacecraft and Rockets*, **32**(3), 545-551.

Malla, R. B., and Nalluri, B. (2000), "Dynamic Nonlinear Member Failure Propagation in Truss Structures." *Structural Engineering and Mechanics*, **9**(2), 111-126.

McCabe, S. L. and Hall, W. J. (1989). "Assessment of Seismic Structural Damage." *Journal of the Structural Division*, ASCE, 115(9), 2166-2183.

Moehle, J. P., Elwood, K. J., and Sezen, H. (2000). "Gravity Load Collapse of Building Frames During Earthquakes." Uzumeri Symposium, ACI Convention, Fall 2000.

Neuenhofer A, and Filippou FC. (1997), "Evaluation of Nonlinear Frame Finite-Element Models." *Journal of Structural Engineering*, ASCE, **123**(7), 958-966.

Newmark, N. M. (1959), "A Method of Computation for Structural Dynamics." *Journal of Engineering Mechanics*, **85**, 67-94.

Newmark, N. M. and Hall, W. J. (1982). *Earthquake Spectra and Design*. Earthquake Engineering Research Institute, Berkeley, CA.

Park, Y. J., and Ang, A. H. S. (1985), "Mechanistic Seismic Damage Model for Reinforced Concrete." *Journal of Structural Engineering*, **111**(4), 722-739.

Pretlove, A. J., and Ramsden, M., Atkins, A. G. (1991), "Dynamic Effects in Progressive Failure of Structures." *International Journal of Impact Engineering*, **11**(4), 539-546.

Spacone, E., Ciampi, V., and Filippou, F. C. (1996), "Mixed Formulation of Nonlinear Beam Finite Element." *Computers & Structures*, **58**(1), 71-83.

Takeda, T., Sozen, M., and Nielson, N. N. (1970). "Reinforced Concrete Response to Simulated Earthquakes." *Journal of the Structural Division*, ASCE, 96(ST12), 2557-2573.

Vian, D. and Bruneau, M. (2002). "Tests to Collapse of Simple Structures and Comparison with Existing Codified Procedures." *Proceedings: 7th U.S. National Conference on Earthquake Engineering*, Boston, MA.

Vision 2000 - A Framework for Performance Based Earthquake Engineering (1995). Structural Engineers Association of California, Sacramento, CA.

Williamson, E. B. (2003). "Evaluation of Damage and P-Δ Effects for Systems under Earthquake Excitation." *Journal of Structural Engineering*, ASCE, Vol. 129, No. 3, pp. 1036-1046.

COLLAPSE DRIFT OF REINFORCED CONCRETE COLUMNS

M. Yoshimura[1], Y. Takaine[2] and T. Nakamura[3]

ABSTRACT

Half-scale specimens with shear or flexure-shear failure modes simulating RC columns designed by the old code were tested until they came to be unable to sustain axial load. Test variables were longitudinal reinforcement, axial load and transverse reinforcement. Using results from this test and the past tests, general nature of column collapse, especially lateral drift associated with collapse was discussed. Some structural indices that were considered to govern the collapse drift were also discussed.

1. INTRODUCTION

The minimum performance that columns are required during severe earthquakes is to support axial load. During past severe earthquakes, a number of RC columns designed by the old code failed in shear (Photo 1(a)) and eventually came to be unable to sustain axial load or collapsed. To evaluate the seismic performance of old columns, it is necessary to grasp how these columns reached the collapse and how much the drift associated with the collapse was. However, researches on these issues are insufficient.

Moehle et al. proposed the equation that predicted the collapse drift (Moehle et al., 2001). Whereas this equation ignored the effect of longitudinal reinforcement on the collapse drift, some test results have revealed the longitudinal reinforcement heightens the collapse drift (Nakamura et al., 2003). This is an interesting issue to be discussed.

At past earthquakes, amongst rather long columns, some failed in shear after flexural yielding (Photo. 1(b)) while others failed in shear without flexural yielding. This paper is intended to study the collapse of rather long columns with $h_0/D=4$ (h_0: column clear height,

[1]*Department of Architecture, Tokyo Metropolitan University, Hachioji, Japan*
Email: myoshim@arch.metro-u.ac.jp

[2]*Department of Architecture, Tokyo Metropolitan University, Hachioji, Japan*
Email: takaine@ecomp.metro-u.ac.jp

[3]*Department of Architecture, Tokyo Metropolitan University, Hachioji, Japan*
Email: takaya@ecomp.metro-u.ac.jp

D: column depth) that may result in either failure mode. Using the results of this test and the past tests for $h_0/D=3$ and 2 (Nakamura et al., 2002 and Nakamura et al., 2003), the combined effect of longitudinal reinforcement and axial load on the collapse drift, the application of the above equation to these tests, and the relations between the ratio of computed shear strength to computed flexural strength that is often used to assess member deformability and the collapse drift are studied.

(a) Shear failure **(b) Flexure-Shear failure**

Photo 1: Real damage (1995 Kobe Earthquake)

2. OUTLINE OF TESTS

Eight half-scale specimens simulating columns designed by the old code are summarized in Table 1 and an example of reinforcement details is shown in Fig. 1. They were designed so that shear failure or shear failure after flexural yielding might result. A column section ($b\times D=300\text{mm}\times 300\text{mm}$), column clear height ($h_0=1200\text{mm}$) were uniform. Test variables were as follows: 1) longitudinal bar ratio, $p_g=2.65\%$, 1.69% and 0.94%, 2) axial stress ratio, η = 0.20, 0.30 and 0.35, and 3) transverse bar ratio, $p_w=0.21\%$, 0.14% and 0.11%. Material properties are listed in Tables 2 and 3.

Test apparatus is shown in Fig. 2, where the pantograph was placed so that the loading beam at the column top did not rotate (double curvature deformation was realized). A loading method was as follows. The specimens were loaded to the lateral direction under constant vertical load. The vertical actuator was controlled by load while the lateral actuator was by displacement. And the test was terminated by the limiter of the vertical actuator that was set to operate when vertical deformation (axial shortening) reached 50mm.

The general rule of loading was that the specimens were displaced to the positive direction until collapse after subjected to a full reversal with drift angle of 0.5%, 1% and 2%. Some specimens collapsed during the reversed loading.

Table 1: Structural properties of specimens

Name	h_0 (mm)	b×D (mm)	h_0/D	p_g (%)	η [1]	p_w (%)
No.1	1200	300×300	4	2.65 (12-D16)	0.20	0.21(2-D6@100)
No.2						0.14(2-D6@150)
No.3						0.11(2-D6@200)
No.4					0.30	0.21(2-D6@100)
No.5					0.35	0.21(2-D6@100)
No.6				1.69 (12-D13)	0.20	0.21(2-D6@100)
No.7						0.14(2-D6@150)
No.8				0.94 (12-D10)		0.14(2-D6@150)

(1) $\eta = N/(bD\sigma_B)$ (N: Axial load, σ_B: Concrete strength)

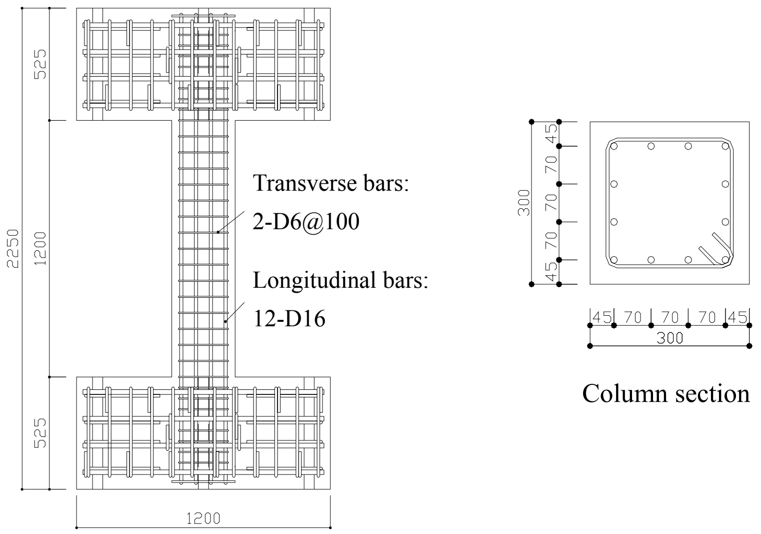

Fig. 1: Reinforcement details of specimen (No. 1)

Table 2: Material properties of steel

	Yield stress (N/mm^2)	Yield strain (%)
D16	402	0.240
D13	409	0.232
D10	388	0.220
D6	392	0.235

Table 3: Material properties of concrete

Max. stress (N/mm^2)	Strain at max. stress (%)
30.7	0.222

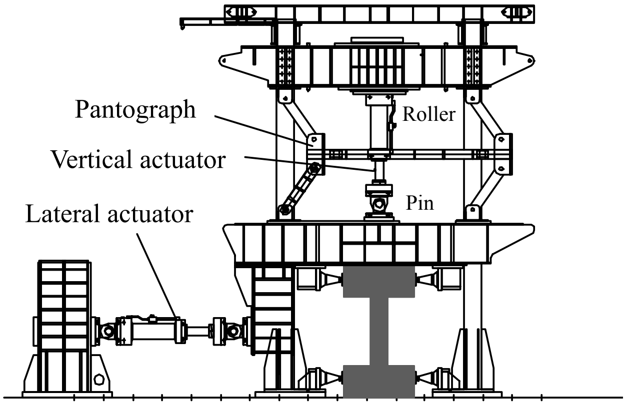

Fig. 2: Test apparatus

3. TEST RESULTS

3.1 General

No.1 through No.5 failed in shear without flexural yielding, while No.6 through No.7 failed in shear after flexural yielding and No.8 failed in flexure after flexural yielding. All specimens finally collapsed. Maximum drift that the specimens have experienced by the step of the collapse is denoted as collapse drift. When drift was large, shear force (force acting on the direction perpendicular to the column axis) a little differed with lateral load. Shear force V was determined by the following equation.

$$V = H\cos R + N\sin R \tag{1}$$

where H: lateral load, R: Drift angle, and N: axial load.

Observed results and computed strength are summarized in Table 4 (IS drift angle is explained in Section 4.1). Damage conditions and drift angle vs. shear relations are shown in Photo 2 and Fig. 3 for selected specimens.

Table 4: Observed results and computed strength

Name	Max. shear (kN)	Shear failure		Collapse		Computed strength			Failure mode (1)
		Drift angle (%)	IS drift angle (%)	Drift angle (%)	IS drift angle (%)	Flexure (kN)	Shear (kN)	Strength ratio	
No.1	234	0.57	0.38	13.4	8.9	241	177	0.73	S
No.2	230	0.58	0.39	5.4	3.6	241	167	0.69	S
No.3	230	0.38	0.25	2.0	1.3	241	162	0.67	S
No.4	261	0.73	0.49	2.0	1.3	276	197	0.71	S
No.5	275	1.3	0.87	2.0	1.3	288	208	0.72	S
No.6	219	5.3	3.6	5.3	3.6	195	168	0.86	FS
No.7	213	2.0	1.3	2.0	1.3	195	159	0.82	FS
No.8	174	17.9	11.9	17.9	11.9	156	150	0.96	F

(1) S：Shear FS：Flexure-Shear F：Flexure

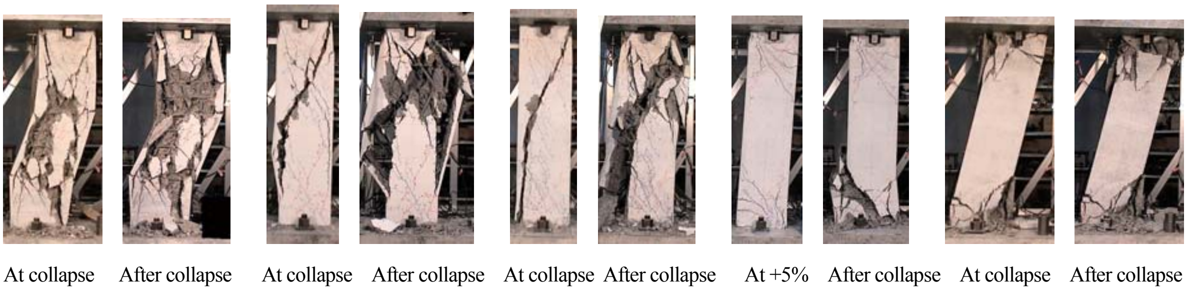

(a) No.1 **(b) No.3** **(c) No.4** **(d) No.6** **(e) No.8**

Photo 2: Damage conditions

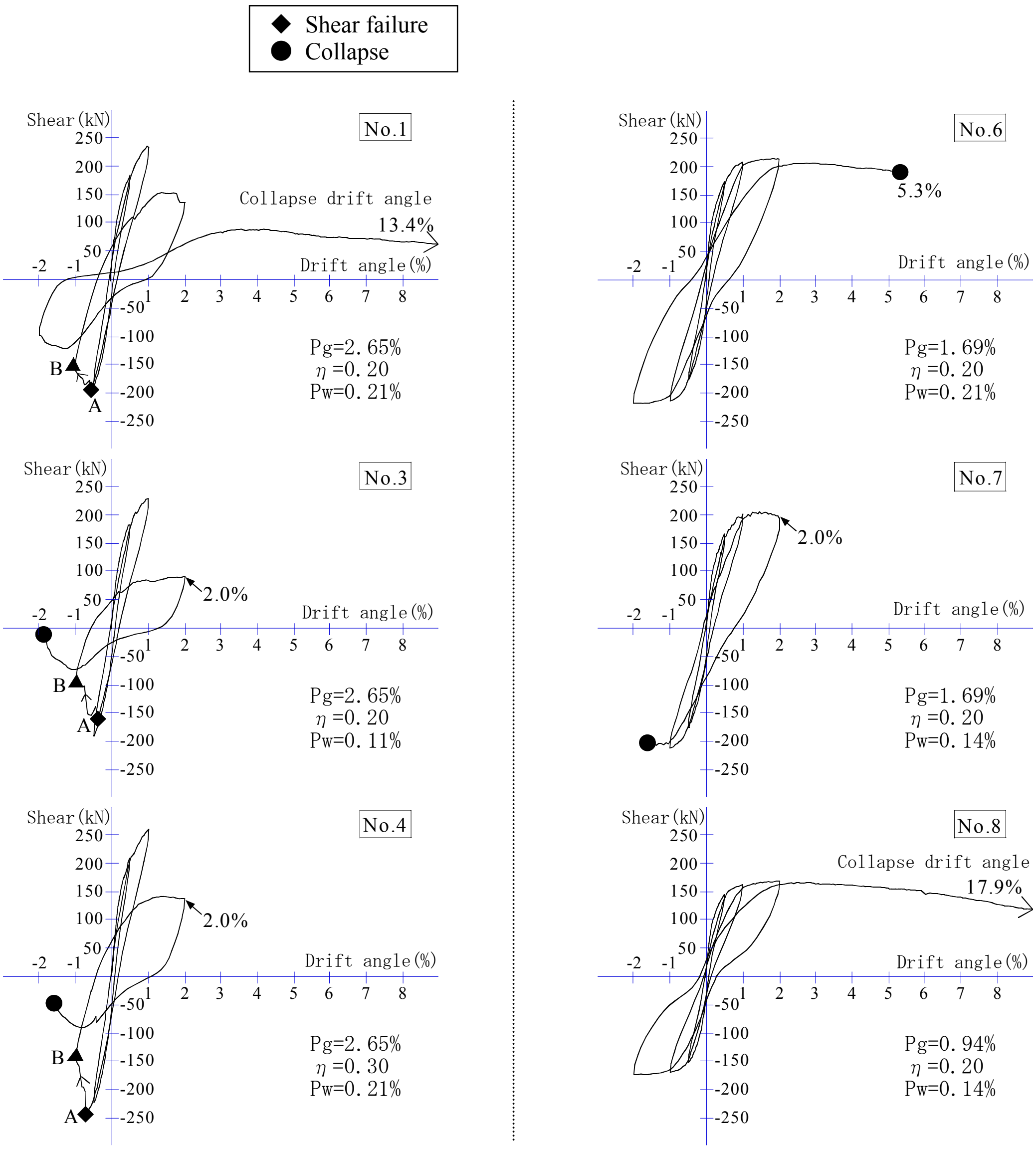

(a) Shear mode **(b) Flexure-Shear mode (No.8: Flexure mode)**

Fig. 3: Drift angle vs. shear force

3.2 Specimens with Shear Mode

No.1, No.3 and No.4 failed in shear at point A in Fig. 3(a) when a shear crack occurred at the column middle portion. At that moment the transverse bars that the shear crack crossed yielded and shear force dropped (point A→point B). However, the collapse did not occur. The shear crack widened during the subsequent loading, and when shear force decreased nearly to zero, the collapse occurred. The buckling of longitudinal bars and the fracture or loosing at the hook of transverse bars were observed at the column middle portion. All specimens with the shear mode exhibited similar procedures to the collapse.

The procedures to the collapse are discussed for No.3 based on measured strains of the longitudinal bars. Fig. 4 shows the locations where strains of longitudinal bars were measured. Strain gauges were attached at the two sides of bars. The strains measured at locations, L1, L2 and L3 are shown in Fig. 5 for the loading aiming at drift angle of –1% where shear failure occurred. The value of strains is an average of those at the two sides. After point A, the strain at L2 that was near the shear crack began to deviate from those at L1 and L3. The stains at L2 measured at the two sides are shown in Fig. 6. The two strains went to the opposite direction after point A throughout the loading aiming at drift angle of –1%. This was because local (flexural) deformation occurred on this bar at L2 due to the shear crack. The widening of the shear crack lead to the increase of the local deformation, resulting in the decrease of compression carrying capacity of this bar. On the other hand, after the point of drift angle of –1%, average strains at L2 were observed to proceed to compression, indicating that the compression carried by this bar increased probably because the contact area of concrete above and below the shear crack decreased as the shear crack widened. The above behavior is schematically depicted in Fig. 7. The locations of longitudinal bars that were confirmed to have had local deformation are shown in Fig. 8. The occurrence of the local deformation was judged whether the strains at the two sides proceeded to the opposite direction. The local deformation occurred on the longitudinal bars at the locations along the shear crack.

3.3. Specimens with Flexure-Shear or Flexure Mode

No.6 and No.7 that first yielded in flexure failed in shear at the hinge region due to the crushing of concrete (compression-shear failure), and the collapse occurred simultaneously. They occurred suddenly without showing any symptom of the collapse. The buckling of longitudinal bars, and the fracture or loosing at the hook of transverse bars were observed at the hinge region. No.8 that yielded in flexure failed in flexure at the hinge region, and the collapse occurred simultaneously. The procedures to the collapse of this specimen was similar to those of No.6 and No.7.

Average strains at the hinge region were measured by displacement transducers. Drift angle vs. average strain relations are shown in Fig. 9 for No.6 at two locations, VER and DIA. Compression strains at VER increased with the increase of drift angle, reaching as much as 0.8% at the collapse, indicating that the damage to concrete had become severe before the collapse. Compression strains at DIA were also large, 0.4% at the collapse, indicating the concrete was subjected to large compression strains due to shear force as well as bending moment. Thus, those specimens with the flexure-shear mode collapsed because of the crushing of concrete at the hinge region.

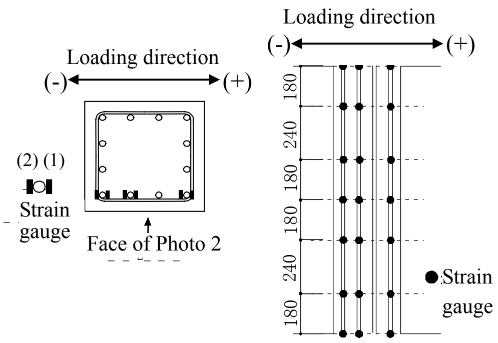

Fig. 4: Strain measurement (Longi. bars)

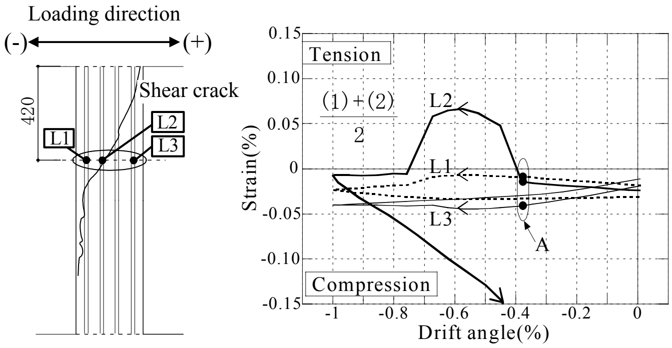

Fig. 5: Drift angle vs. strain (Longi. bars, No.3)

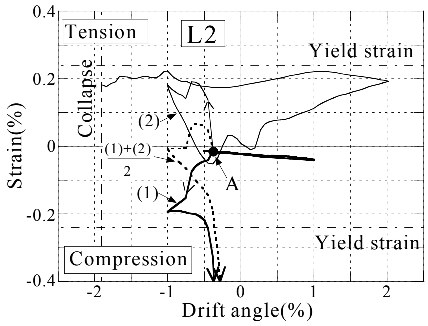

Fig. 6: Drift angle vs. strain (Longi. bar, No.3)

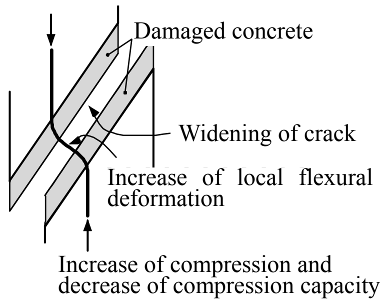

Fig. 7: Behavior of longi. bar near shear crack

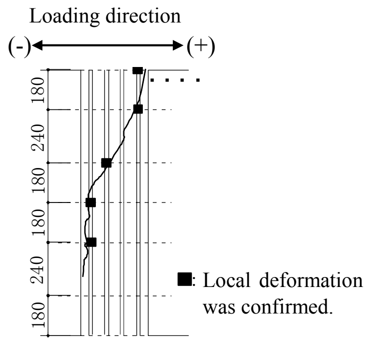

Fig. 8: Location of longi. bars with local deformation (No. 3)

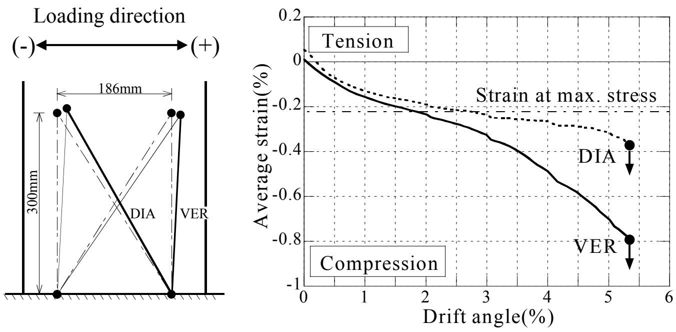

Fig. 9: Drift angle vs. average strain (No.6)

3.4 Effect of Test Variables on Collapse Drift

The specimens with the shear mode and flexure-shear mode (hereafter, including flexure mode for the sake of convenience) differed in the collapse mechanism. The effect of test variables on the collapse drift was studied for each mode. The interaction of test variables are shown in Fig. 10. For the specimens with the shear mode, if p_g and axial load were same, the collapse drift angle increased with the increase of p_w: No.1 (13.4%)＞No.2 (5.4%)＞No.3 (2.0%). And if p_g and p_w were same, it in general increased with the decrease of axial load: No.1 (13.4%)＞No. 4 (2.0%)=No.5 (2.0%). For the specimens with the flexure-shear mode, if p_g and axial load were same, the collapse drift angle was larger for larger p_w: No.6 (5.3%)＞No.7 (2.0%). And if axial load and p_w were same, it was larger for smaller p_g: No.8 (17.9%)＞No.7 (2.0%).

On the other hand, the comparison of the specimens that had a different failure mode because of different p_g and same axial load and p_w, revealed that the collapse drift angle was larger for the shear mode than for the flexure-shear mode: No.1 (13.4%)＞No.6 (5.3%) and No.2 (5.4%)＞No.7 (2.0%). It is interesting to note these results are opposite to the general recognition that specimens with the shear mode are inferior in deformability to those with the flexure-shear mode. This is discussed again in Chapter 5.

4. COLLAPSE DRIFT OF SPECIMENS WITH SHEAR MODE

4.1 Combined Effect of Longitudinal Reinforcement and Axial Load on Collapse Drift

For the specimens with the shear mode, as drift increased or a shear crack widened, longitudinal bars attracted more axial compression near the shear crack while the compression strength of them decreased. It suggests that the longitudinal bars have a significant role on the collapse. Hence, a ratio of axial load to initial compression strength of the longitudinal bars, η_s (bar stress ratio) was introduced.

$$\eta_s = N/(A_s \cdot \sigma_y) \tag{2}$$

where N: axial load, A_s: total area of longitudinal bars, and σ_y: yield stress of longitudinal bars.

Five specimens with the shear mode tested this time and other ten with the same mode tested earlier were studied. The totally fifteen specimens were different in the column clear height (h_0=600mm, 900mm and 1200mm). Therefore, same drift angle does not mean same drift. In addition, from the practical viewpoint it would be convenient if drift angle is expressed in terms of interstory (IS) drift angle of full-scale buildings. Collapse drift angle was translated to collapse IS drift angle, and η_s vs. collapse IS drift angle relations were discussed.

The way to translate drift angle into IS drift angle was as follows. A full-scale building with particular geometric properties, as shown in Fig. 11, was assumed. The specimens were deemed to be half-scale models of the columns in this building. Let H_0 be story height. Then collapse IS drift angle R_{st} is obtained from drift angle R.

$$R_{ST} = (h_0 / H_0) \cdot R \tag{3}$$

Major results of the past tests including R_{st} are tabulated in Table 5.

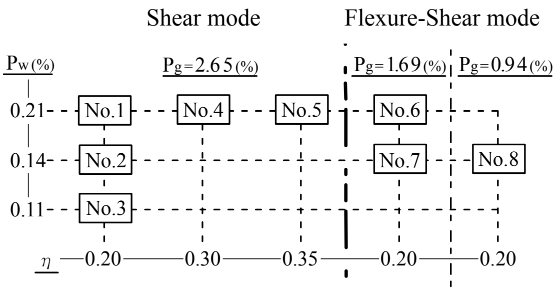

Fig. 10: Interaction of test variables

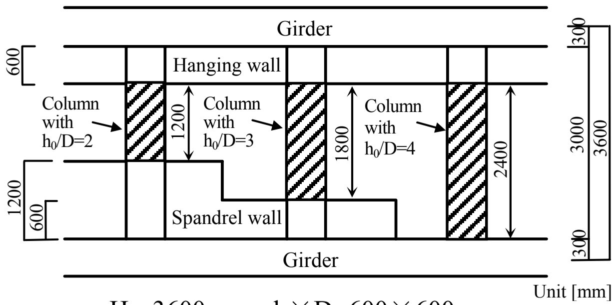

H_0=3600mm, b×D=600×600mm

Fig. 11: Assumed full-scale building

Table 5: Results of past tests

Name	h_0 (mm)	b×D (mm)	h_0/D	p_g (%)	η	p_w (%)	Strength ratio	Shear failure		Collapse	
								Drift angle (%)	IS drift angle (%)	Drift angle (%)	IS drift angle (%)
N18M	900	300 × 300	3	2.65	0.18	0.21	0.65	0.80	0.40	10.3	5.2
N18C								0.93	0.46	20.6	10.3
N27M					0.27		0.62	0.78	0.39	4.7	2.4
N27C								0.54	0.27	3.0	1.5
2M	600	300 × 300	2	2.65	0.19	0.21	0.52	0.66	0.22	11.2	3.7
2C								0.27	0.09	7.8	2.6
3M					0.29		0.49	0.60	0.20	5.6	1.9
3C								0.72	0.24	5.3	1.8
2M13				1.69	0.19		0.66	0.43	0.14	4.1	1.4
2C13								0.47	0.15	3.0	1.0

The relation between η_s and collapse IS drift angle are shown in Fig. 12. The range of test variables were as follows: h_0/D=2～4, p_g=1.69%～2.65%, η=0.18～0.35 and p_w=0.11%～0.21%. No.2 and No.3 alone were 0.11% and 0.14% in p_w. For the remaining thirteen specimens with p_w of 0.21%, the collapse IS drift angle tended to increase as η_s decreased, although plots were widely scattered. This suggests that if p_w is same, the collapse IS drift angle may be evaluated using the bar stress ratio η_s that includes the effect of p_g and axial load. As stated earlier, the results of No.1, No.2 and No.3 that were different in p_w and same in η_s (0.58) showed that as p_w increased, the collapse ID drift angle increased. In consideration that the result of No.3 that is minimum in p_w (0.11%) is 1.3%, it can be said if p_w is more than 0.1% and η_s is less than 0.6, the collapse IS drift angle of 1% is secured.

The results of C2 and 2C13 that are identical except for p_g indicates that as p_g is more or η_s is less, the collapse IS drift angle is larger.

4.2 Existing Equation That Predicts Collapse Drift Angle

Moehle et al. proposed the equation to predict the collapse drift angle using shear-friction model. This equation was applied to the above fifteen specimens. A free body of a column upper portion subjected to shear force and axial load is shown in Fig 13, where V=0, V_d=0 and P_s=0 are assumed. Note that the compression carried by longitudinal bars were assumed zero. Observed and computed collapse drift angles are compared in Fig. 14. The agreement was good in case of large values of η_s ($\eta_s > 0.6$). However, in case of small values of η_s ($\eta_s \leqq 0.6$) the computed values were considerably smaller than the observed ones. Let us compare the results of 2C and 2C13. For 2C that had a small value of η_s, the computed result underestimated the observed one, while for 2C13 the agreement was good. It may be due to that this model ignores the effect of longitudinal bars on the compression carrying capacity. The collapse drift angles computed for 2C by assuming P_s=0 and $P_s=0.2\, a_s \sigma_y$ are compared in Fig. 15. By considering the effect of longitudinal bars on the compression carrying capacity, the computed value became larger. The equation may be improved if this effect is appropriately included.

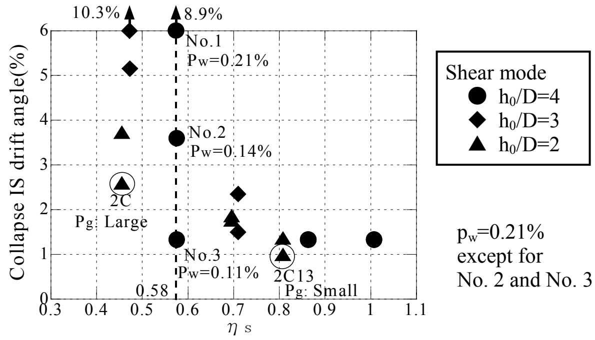

Fig. 12: η_s vs. collapse IS drift angle

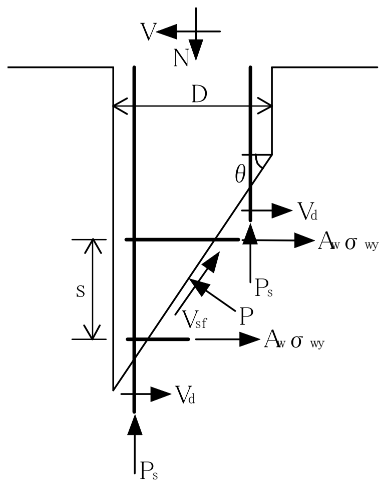

Fig. 13: Free body after shear failure

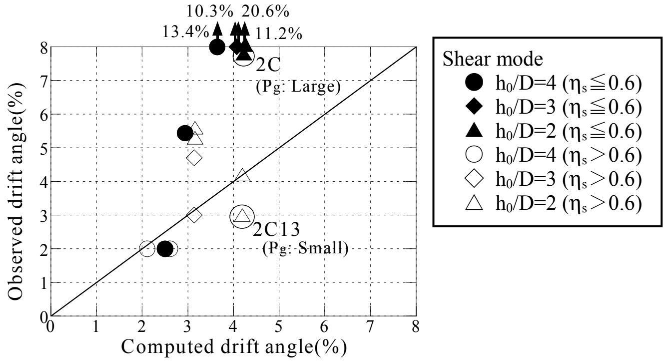

Fig. 14: Comparison of collapse drift angle

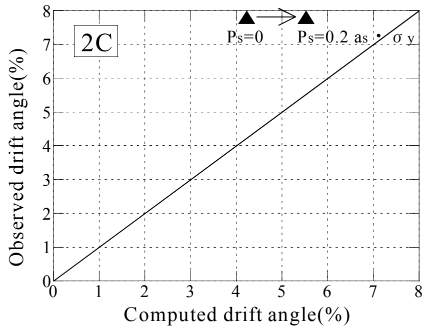

Fig. 15: Change of computed collapse drift angle

5. RELATIONS BETWEEN STRENGTH RATIO AND COLLAPSE IS DRIFT ANGLE

As an index to assess column deformability, a ratio of computed shear strength to computed flexural strength, strength ratio, is often used. The relations between strength ratio and collapse IS drift angle were studied for all specimens including three that yielded in flexure, are shown in Fig. 16.

For the specimens with the shear mode, the results were against the expectation that as the strength ratio increased, the collapse IS drift angle increased. It was mainly because some specimens with large strength ratios showed small values (less than 3%). Most of them were specimens the bar stress ratios of which were large ($\eta_s > 0.6$), in other words, p_g was small and/or axial load was large. This implies that the effect of p_g and axial load on the collapse, though included in the strength ratio, is for the above cases more than the extent considered in this ratio. On the other hand, the specimens with the flexure-shear mode met the expectation.

It is interesting to note that there is a big gap in the IS collapse drift angles of No.1 that is largest in the strength ratio among the shear specimens and No. 7 that is smallest among the flexure-shear specimens. The latter value is about one sixth of the former one. Not only this result is opposed to the general recognition that as the strength ratio increases, deformability increases, but also the difference is extremely large. The problem lies in No.7 that is rather high (0.82) in the strength ratio but very low in the collapse IS drift angle. It is urgent to study the border region of failure modes where the strength ratio is around 0.75 to 0.80.

The relations between strength ratio and IS drift angle at shear failure (flexure failure for No.8) are shown in Fig. 17. The translation of drift angle into IS drift angle was done by the way shown in Section 4.1. For all specimens, as the strength ratio increased, the IS drift angle at shear failure tended to increase. This suggests the strength ratio may be a good index to express the IS drift angle at shear failure.

It is likely that for the specimens with the shear mode a clear trend between strength ratio and IS collapse drift angle was not observed because the shear failure and collapse did not occur at the same time, while for the specimens with the flexure-shear mode a clear trend between them was observed because they occurred at the same time.

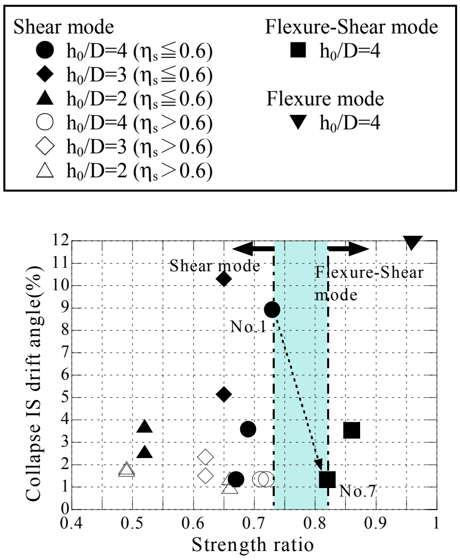

Fig. 16: Strength ratio vs. collapse IS drift angle

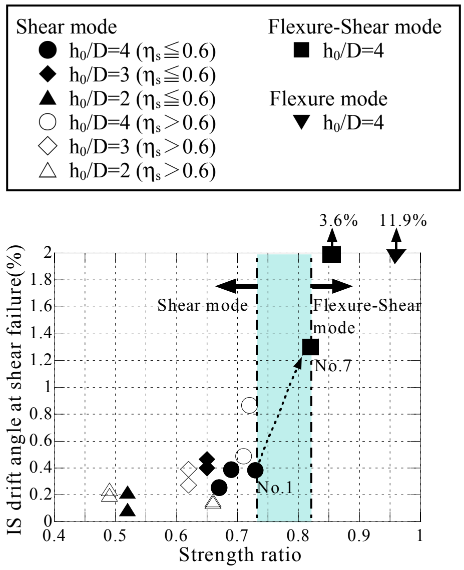

Fig. 17: Strength ratio vs. IS drift angle at shear failure

6. CONCLUSIONS

The major findings from this test and the past tests are as follows. The range of test variables are as follows: h_0/D=2～4, p_g=0.94%～2.65%, η=0.18～0.35 and p_w=0.11%～0.21%.

(1) Procedures to collapse

The specimens with the shear mode fails in shear at the column middle portion. However, the collapse does not occur at that time. During the subsequent loading, when the shear crack widens and shear force decreases nearly to zero, the collapse occurs. The collapse is considered to relate with the increase of axial load carried by the longitudinal bars and the decrease of compression strength of them. On the other hand, for the specimens with the flexure-shear mode the shear failure and collapse occur at the same time at the hinge region, suddenly without showing any symptom of collapse. The collapse is considered to relate with the crushing of concrete.

(2) Relations between η_s and collapse IS drift angle

For the specimens with the shear mode, there is a correlation between bar stress ratio η_s and collapse IS drift angle, indicating this drift angle may be assessed using η_s that includes the effect of p_g and axial load. And if p_w is more than 0.1% and η_s is less than 0.6, the collapse IS drift angle of 1% is secured.

(3) Relations between strength ratio and collapse IS drift angle

For the specimens with the shear mode, the results are against the expectation that as the strength ratio increases, the collapse drift increases, while the specimens with the flexure-shear mode meets this expectation. This is believed to be due to the difference in the collapse mechanism of them. It is interesting to note that there is a big gap in the collapse IS drift angles of the specimen that is largest in the strength ratio among the shear specimens and the specimen that is smallest among the flexure-shear specimens. The latter value is about one sixth of the former one. Not only the result is opposed to the general recognition that as the strength ratio increases, deformability increases, but also the difference is extremely large. It is urgent to study the border region of failure modes where the strength ratio is around 0.75 to 0.80.

(4) Equation based on shear-friction model to predict collapse drift angle

For the specimens with the shear mode, the equation based on shear-friction model gives good approximation in case of large values of η_s ($\eta_s > 0.6$). However, it underestimates the observed collapse drift in case of small values of η_s ($\eta_s \leqq 0.6$). It may be because the equation ignores the effect of longitudinal bars on the compression carrying capacity, suggesting the possibility of improving the equation if this effect is appropriately included.

REFERENCES

Moehle, J. P., Elwood, K. J., and Sezen, H. (2001). Gravity Load Collapse of Building Frames during Earthquakes. ACI SP-197. Behavior and Design of Concrete Structures for Seismic Performance. American Concrete Institute.

Nakamura, T. and Yoshimura, M. (2002). Gravity Load Collapse of Reinforced Concrete Columns with Brittle Failure Modes. Journal of Asian Architecture and Building Engineering. Architectural Institute of Japan. Vol.1. No.1: 21-27.

Nakamura, T. and Yoshimura, M. (2003). Axial Collapse of R/C Short Columns. Proceedings of the fib Symposium - Concrete Structures in Seismic Regions -: 228-229.

KEYWORDS

collapse drift, shear failure, flexure-shear failure, strength ratio, axial load

PREDICTING THE SEISMIC PERFORMANCE OF A RC BUILDING IN THE CENTRAL U.S.

Mary Beth D. HUESTE[1] and Jong-Wha BAI[2]

ABSTRACT

The predicted seismic performance of a reinforced concrete frame building in the Central United States was investigated. The case study building is a five-story, reinforced concrete office building designed based on the code requirements used in this region during the mid-1980s. The structure was analyzed using nonlinear time history analysis with synthetic ground motion records for probabilities of exceedance of 2% and 10% in fifty years for St. Louis, Missouri and Memphis, Tennessee. In addition, two analytical approaches for nonlinear response analysis are compared. FEMA 356 criteria were used to predict the seismic performance of the case study building. The predicted responses for the St. Louis motions and the 10% in 50 years Memphis motion are within the FEMA 356 Basic Safety Objective (BSO) limits based on global level criteria (drift). The predicted drift response meets the BSO for the 2% in 50 years Memphis event. However, the corresponding member response (plastic rotation) is not within the limits of the BSO.

1. INTRODUCTION

Earthquakes are of concern to cities in the Central United States (U.S.) because of the history of seismic activity around the New Madrid Seismic Zone (NMSZ). Three major earthquakes took place during the winter of 1811-1812 with body-wave magnitudes of 7.35, 7.2, and 7.5. The epicentral locations for these earthquakes are near New Madrid, Missouri and are the center of the NMSZ. This study focuses on predicting the expected seismic performance of a reinforced concrete (RC) building in the Central U.S. characteristic of office buildings constructed in that area during the mid-1980s. Nonlinear analysis was used to predict the seismic response of the prototype RC building for two locations: St. Louis, Missouri and Memphis, Tennessee. For the initial assessment, two nonlinear analysis tools were used: DRAIN-2DM, which uses a macro model approach and ZEUS-NL, which uses a fiber model approach. Global response parameters from the two models were compared. The *Prestandard and Commentary for the Seismic Rehabilitation of Buildings (FEMA 356)* (ASCE 2000) performance criteria were used to assess the seismic performance of the case study building using the ZEUS-NL response analysis.

[1] *Department of Civil Engineering, MS 3136, Texas A&M University, College Station, Texas 77843-3136*
E-mail: mhueste@tamu.edu
[2] *Department of Civil Engineering, MS 3136, Texas A&M University, College Station, Texas 77843-3136*
E-mail: jongwhabai@tamu.edu

2. PERFORMANCE CRITERIA

FEMA 356 provides analytical procedures and criteria for the performance-based evaluation of existing buildings and for designing seismic rehabilitation alternatives. Performance *levels* describe limitations on the maximum damage sustained during a ground motion, while performance *objectives* define the target performance level to be achieved for a particular intensity of ground motion. Structural performance levels in FEMA 356 include Immediate Occupancy (IO), Life Safety (LS), and Collapse Prevention (CP). Structures at the CP are expected to remain standing, but with little margin against collapse. Structures at LS may have sustained significant damage, but still provide an appreciable margin against collapse. Structures at IO should have only minor damage. In FEMA 356, the *Basic Safety Objective (BSO)* is defined as LS performance for the Basic Safety Earthquake 1 (BSE-1) earthquake hazard level and CP performance for the BSE-2 earthquake hazard level. BSE-1 is defined as the *smaller* of an event corresponding to 10% probability of exceedance in 50 years (10% in 50 years) and 2/3 of BSE-2, which is the 2% probability of exceedance in 50 years (2% in 50 years) event.

3. DESCRIPTION OF CASE STUDY BUILDING

A case study building was designed according to the codes used in St. Louis, Missouri during the early 1980s, prior to St. Louis' assignment to Seismic Zone 2 of the Building Officials and Code Administrators (BOCA) Basic/National Code (BOCA 1987). Several engineers with design experience in the St. Louis area provided information for use in selecting a prototype structure by responding to questionnaires (Hart 2000). The five-story RC case study building has a moment frame system not specially detailed for ductile behavior. The floor system is composed of a flat slab and perimeter moment resisting frames with spandrel beams. A floor plan is shown in Figure 1 and an elevation view is provided in Figure 2. The load requirements were taken from the ninth edition of the BOCA code (BOCA 1984), in which St. Louis is considered to be in seismic Zone 1. It should be noted that Memphis, Tennessee was also assigned to seismic Zone 1, based on the map given in the 1984 BOCA code. The perimeter frames were designed to resist the full design lateral load based on design practices that were common and generally accepted during the 1980s. The structural member design follows the provisions of the American Concrete Institute (ACI) Building Code Requirements for Reinforced Concrete, ACI

318-83 (ACI Comm. 318 1983). The material properties are a concrete compressive strength of 28 MPa and steel reinforcement yield strength of 410 MPa.

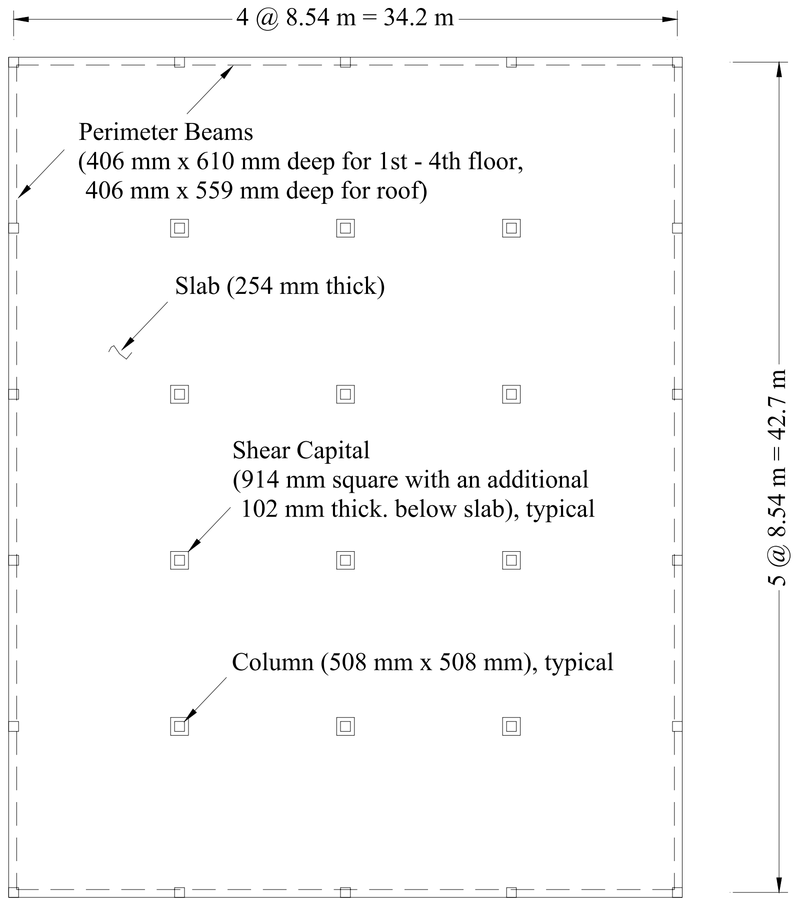

Figure 1. Plan view of case study building

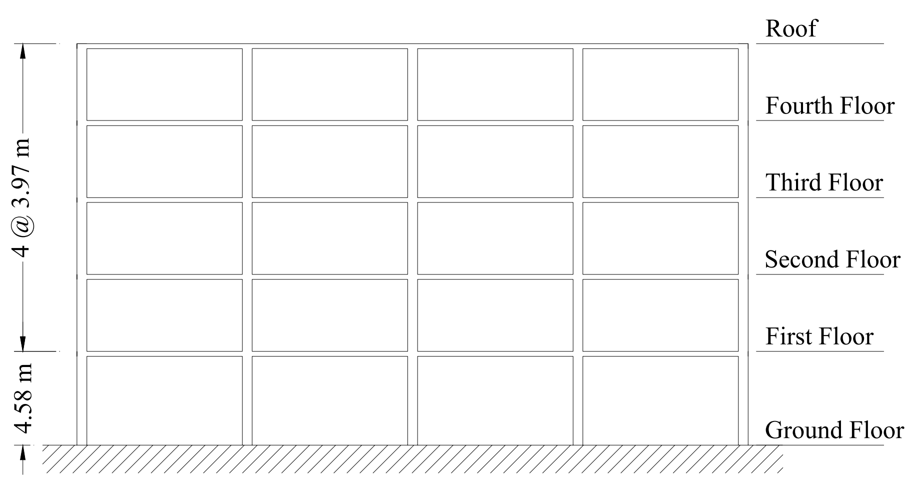

Figure 2. Elevation view of case study building

4. ANALYTICAL MODELS

4.1 DRAIN-2DM

4.1.1 General

DRAIN-2D is a nonlinear structural analysis program developed at the University of California at Berkeley (Kanaan and Powell 1973, Powell 1973). Modifications to the program have been made at the University of Michigan and this version is called DRAIN-2DM (Al-Haddad and Wight 1986, Tang and Goel 1988, Raffaelle and Wight 1992, Soubra et al. 1992, Hueste and Wight 1997). Nonlinearity at the member level is included through a macro modeling approach, where nonlinear rotational springs at the member ends are included in the element description.

4.1.2 Overall Building Model

DRAIN-2DM is restricted to two-dimensional analysis, which is adequate for the symmetric case study building. The model takes advantage of the building's symmetry such that only half of the structure is analyzed. The model consists of one exterior frame and two interior frames, oriented along the short direction of the building, linked with rigid truss elements denoted by dash lines (see Figure 3). Only lateral forces and displacements are transmitted between frames. The seismic dead weight was included in the model by specifying lumped masses at each column joint and applying fixed end forces at the slab and beam member ends. The selected Rayleigh damping proportionality factors give approximately a two percent critical damping ratio.

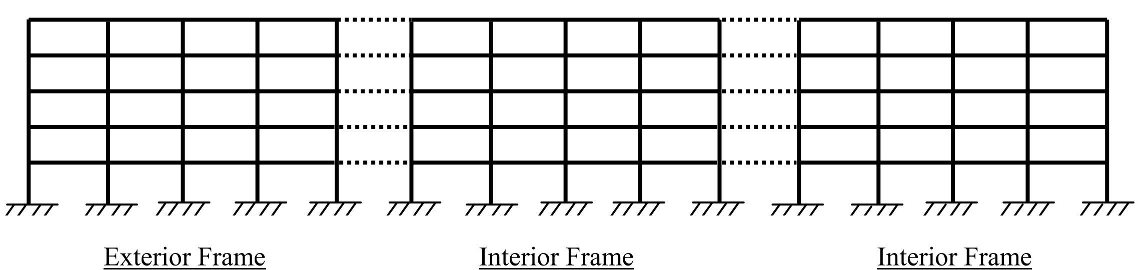

Figure 3. DRAIN-2DM model of case study building

Rigid joints are included in the DRAIN-2DM model, such that inelastic behavior is monitored outside the joint. For the case study building, the horizontal dimension of the rigid zone within each joint was specified to be equal to the column width. The height of the rigid zone was set equal to the spandrel beam depth for joints around the perimeter of the building; and equal to the slab depth, not including the additional thickness due to the shear capital, for interior slab-column joints. DRAIN-2DM monitors the presence of inelastic rotation during the analysis through the use of nonlinear rotational springs, defined to be adjacent to the rigid joint zone.

4.1.3 Modeling of Individual Members

Three element types used to model the column, beam and slab members are summarized in Table 1. The member stiffness was based on cracked section moments of inertia I_{cr}. The values for I_{cr} were computed as a proportion of the gross moment of inertia I_g for the concrete section using the factors given in ACI 318-02 (ACI Comm. 318 2002). The effective flange width for the spandrel beams was based on the ACI 318-02 Chapter 8 provisions for edge beams. For interior slab members, the width was taken as the full distance between centerlines of adjacent panels.

Table 1. Element types and cracked moment of inertia

Member Type	DRAIN-2DM Element	Cracked Moment of Inertia (I_{cr})
Columns	RC Beam-Column Element (Element 2)	0.70 I_g
Beams	RC Beam Element (Element 8)	0.35 I_g
Slabs	RC Slab Element (Element 11)	0.25 I_g

The post-yield stiffness was assumed to be two percent of the initial elastic stiffness. In DRAIN-2DM, a pinching factor of 1.0 represents full hysteretic loops with no pinching. For the perimeter beams the pinching factor was selected as 0.75 based on previous work (Hueste and Wight 1997). A value of 0.30 was used for the unloading stiffness factor based on previous studies (Chien and Wight 1994, Raffaelle and Wight 1992). Strength degradation was not used. The hysteretic parameters used to define the behavior of the nonlinear springs at each slab member end were the same as for the perimeter beams, except that the pinching factor was reduced to 0.50. The yield moment for positive bending at the member ends was reduced compared to the yield moment at midspan because some bottom bars were assumed to be cut off near the supports based on the details for bottom bars given in ACI 318-83. The RC slab element includes a punching shear prediction model. The model defines a limiting rotation at which a punching shear is predicted based on the ratio of the gravity shear to the nominal shear strength (V_g/V_o), along with the unloading behavior when a punch occurs (Hueste and Wight 1999). Relatively low values of V_g/V_o were determined for the case study building (0.29 at the floor levels and 0.39 at the roof level) due to the presence of the shear capitals.

4.2 ZEUS-NL

4.2.1 General

ZEUS-NL is a finite element structural analysis program developed for nonlinear dynamic, conventional and adaptive push-over, and eigenvalue analysis (Elnashai et al. 2002). The program can be used to model two-dimensional and three-dimensional steel, RC and composite structures, taking into account the effects of geometric nonlinearities and material inelasticity. The program uses the fiber element approach to model these nonlinearities, where the cross-sections are divided into fibers monitoring the confined concrete section, the unconfined concrete cover and the steel reinforcement.

4.2.2 Overall Building Model

The ZEUS-NL model is also two-dimensional and follows the same general assumptions used for the DRAIN-2DM model (see Figure 4). Rigid zones were used to define the joint regions. Members were divided such that a Gauss point would monitor the member section just outside the joint region. In order to refine this model, a second node was added near the joint at 91 cm (3 ft.) from each column face. Additional nodes were used along the horizontal members to allow the self-weight to be included as equivalent point loads. The lumped mass element (Lmass) was used to include the mass at the column joints for the dynamic analysis.

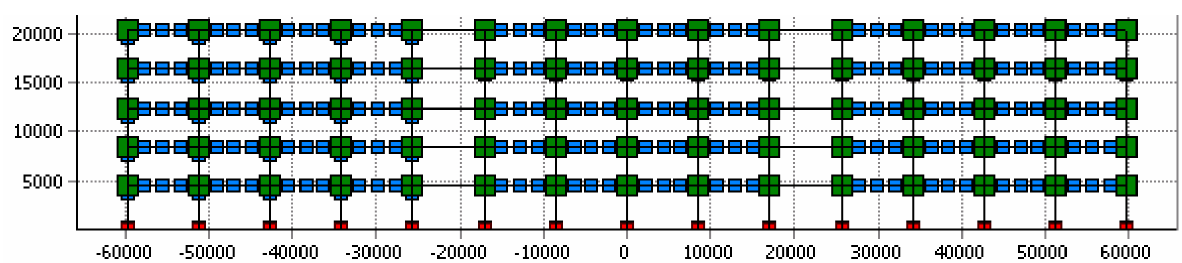

Figure 4. Model of case study building used in ZEUS-NL analysis (units in mm)

4.2.3 Modeling of Individual Members

A cubic elasto-plastic three-dimensional element (cubic) was used for column, beam, slab and rigid connections. The joint element with uncoupled axial, shear and moment actions (joint) was used to model the joints as rigid. It is possible to model bond-slip using the joint element, but this was not included in this analysis. The cross-sections of the column members were described using the RC rectangular section (rcrs), while the cross-sections of the beam and slab members were defined using the RC T-section (rcts). The bilinear elasto-plastic material model with kinematic strain hardening (stl1) was used for the reinforcement and rigid connections, and the uniaxial constant confinement concrete material model (conc2) was used for the concrete.

5. GROUND MOTION RECORDS

The ground motions used for the nonlinear time history analyses are suites of synthetic records developed by Wen and Wu (2000). Each suite contains ten ground motions whose median response (based on a lognormal distribution) corresponds to the specified return rate and location. Return rates of 475 years (10% probability of exceedance in 50 years) and 2475 years (2% probability of exceedance in 50 years) were used for St. Louis, Missouri and Memphis, Tennessee. These ground motions were based on representative soil conditions for each city. The response spectra for the ground motion sets are shown in Figure 5 and details are provided in Tables 2 and 3. To reduce the computation time, the ground motions were shortened for the nonlinear dynamic analysis at the time point when the energy reaches 95% of the total energy imparted by the acceleration record, based on the procedure developed by Trifunac and Brady (1975). The resulting duration of the records ranged between approximately 10 to 60 seconds.

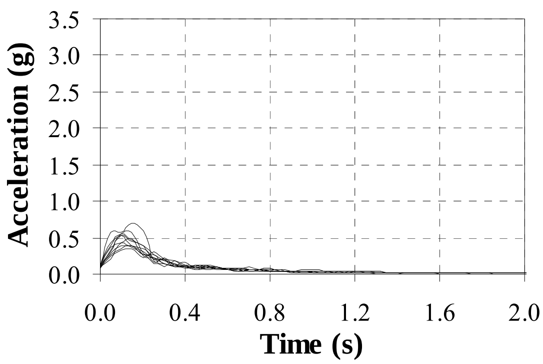

(a) 10% in 50 years for St. Louis motions

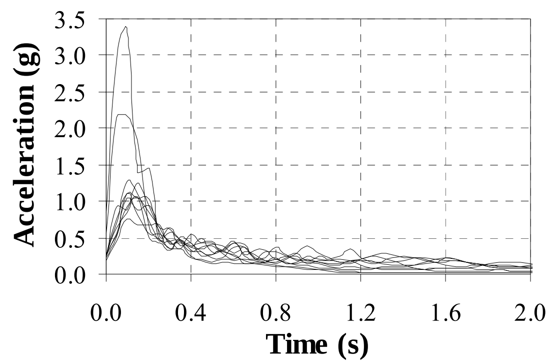

(b) 2% in 50 years for St. Louis motions

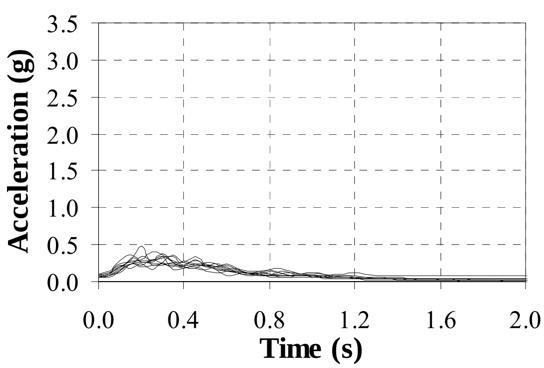

(c) 10% in 50 years for Memphis motions

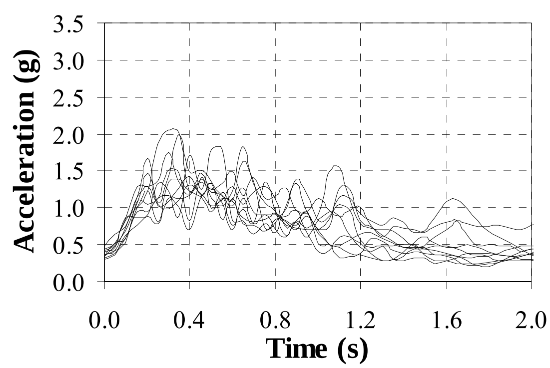

(d) 2% in 50 years for Memphis motions

Figure 5. Response spectra for synthetic ground motion sets (two percent damping)

Table 2. Characteristics of St. Louis synthetic ground motions

10% in 50 years						2% in 50 years					
Record ID	PGA	Duration (s)	Body Wave Magnitude	Focal Depth (km)	Epicentral Distance (km)	Record ID	PGA	Duration (s)	Body Wave Magnitude	Focal Depth (km)	Epicentral Distance (km)
l10_01s	0.13g	25	6.0	2.7	76.4	l02_01s	0.23g	70	8.0	17.4	267.0
l10_02s	0.10g	40	6.9	9.3	201.5	l02_02s	0.25g	70	8.0	9.1	229.5
l10_03s	0.09g	40	7.2	4.4	237.5	l02_03s	0.83g	10	5.4	2.1	28.7
l10_04s	0.11g	25	6.3	9.8	252.2	l02_04s	0.25g	45	7.1	5.5	253.1
l10_05s	0.13g	20	5.5	2.9	123.1	l02_05s	0.19g	55	8.0	17.4	254.3
l10_06s	0.11g	30	6.2	7.7	207.6	l02_06s	0.24g	40	6.8	5.8	224.8
l10_07s	0.10g	40	6.9	1.7	193.7	l02_07s	0.24g	70	8.0	33.9	196.3
l10_08s	0.12g	25	6.2	27.6	174.5	l02_08s	0.24g	35	8.0	9.1	260.7
l10_09s	0.11g	30	6.2	6.5	221.3	l02_09s	0.25g	35	8.0	9.1	280.5
l10_10s	0.08g	40	6.9	2.7	237.2	l02_10s	0.54g	20	5.9	4.4	47.7

Table 3. Characteristics of Memphis synthetic ground motions

10% in 50 years						2% in 50 years					
Record ID	PGA	Duration (s)	Body Wave Magnitude	Focal Depth (km)	Epicentral Distance (km)	Record ID	PGA	Duration (s)	Body Wave Magnitude	Focal Depth (km)	Epicentral Distance (km)
m10_01s	0.06g	41	6.3	5.2	121.0	m02_01s	0.44g	150	8.0	25.6	147.6
m10_02s	0.08g	41	6.4	6.7	57.5	m02_02s	0.33g	150	8.0	33.9	186.1
m10_03s	0.07g	41	6.8	18.1	125.1	m02_03s	0.36g	150	8.0	25.6	163.2
m10_04s	0.07g	41	6.8	2.1	92.4	m02_04s	0.32g	150	8.0	9.1	169.6
m10_05s	0.11g	41	6.2	27.0	107.1	m02_05s	0.48g	150	8.0	9.1	97.6
m10_06s	0.05g	150	6.2	3.2	41.2	m02_06s	0.42g	150	8.0	17.4	117.6
m10_07s	0.07g	41	6.5	11.5	58.8	m02_07s	0.37g	150	8.0	17.4	119.2
m10_08s	0.09g	20.5	6.5	23.9	129.1	m02_08s	0.29g	150	8.0	9.1	145.7
m10_09s	0.09g	20.5	6.3	9.5	166.4	m02_09s	0.34g	150	8.0	9.1	170.5
m10_10s	0.06g	41	6.8	8.7	35.6	m02_10s	0.41g	150	8.0	17.4	187.7

6. ANALYTICAL RESULTS

6.1 Comparison of DRAIN-2DM and ZEUS-NL Analysis

Static nonlinear (push-over) analysis and dynamic analysis were conducted using both the DRAIN-2DM and ZEUS-NL models to compare the overall structural response. While the ZEUS-NL model gave a reasonable prediction of the structural response to monotonically increasing lateral load, the DRAIN-2DM gave some unexpected results. Further investigation is needed for the DRAIN-2DM analysis.

Figures 6 and 7 provide a comparison of the average building drift and base shear as a function of time for the two models. The selected ground motions are those that most closely match the median response for the 2% in 50 years suites for both St. Louis and Memphis, based on the maximum average building drift. For this comparison, the punching shear prediction in DRAIN-2DM was not included. Some differences in the dynamic response can be observed. However, the peak values of the displacement response are similar. The differences are likely due to differences in the element formulation, as well as the approach used in introducing cracked section behavior into the models. ZEUS-NL model updates the model for cracked section behavior under loading, while the DRAIN-2DM requires an initial assumption of the cracked section moment of inertia for individual members. Prior to applying ground motions, the fundamental period for the DRAIN-2DM model was 1.80 seconds, while the fundamental period for the ZEUS-NL model was 1.14 seconds. For verification, the DRAIN-2DM model was modified such that all members were uncracked. The corresponding fundamental period is 1.18 seconds, which is very close to the fundamental period for the undamaged ZEUS-NL model.

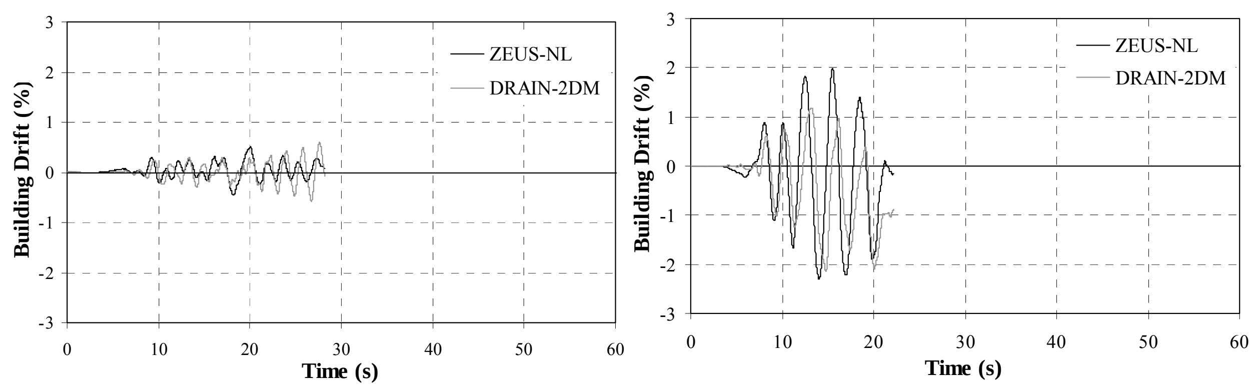

(a) St. Louis (l02_08s) (b) Memphis (m02_10s)

Figure 6. Comparison of building drift for 2% in 50 years motions

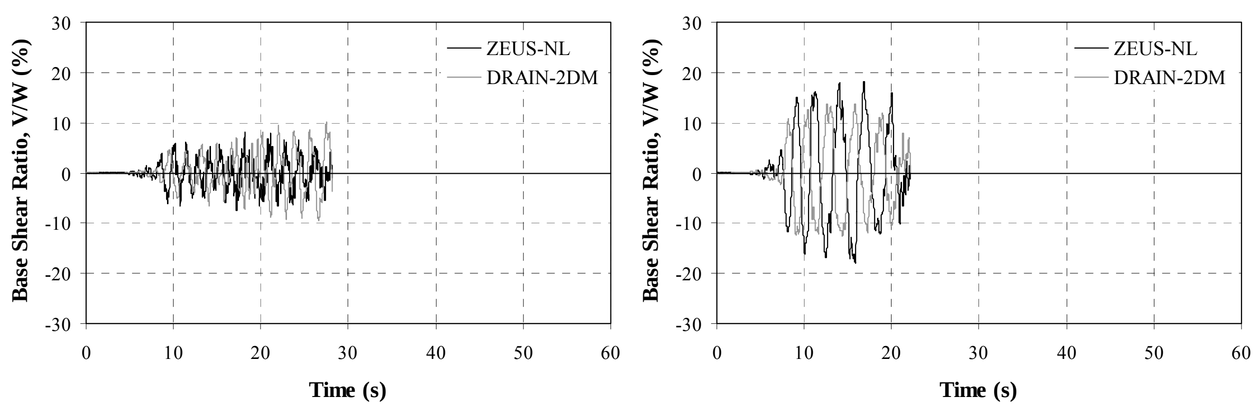

(a) St. Louis (l02_08s) (b) Memphis (m02_10s)

Figure 7. Comparison of base shear for 2% in 50 years motions

6.2 Nonlinear Static Analysis

The push-over analysis conducted for the ZEUS-NL model is summarized in Figure 8. Both an inverted triangular and rectangular load pattern was used for comparison. The interstory drift profiles for both one percent and two percent average building drifts are shown for both load patterns. In addition, results from the subsequent dynamic analysis using the synthetic ground motions are plotted versus the push-over response curves to indicate the maximum base shear and maximum building drift from each dynamic analysis. The maximum global demands from the less intense motions follow the push-over response curves relatively well, while the more significant demands from the Memphis motions are not bounded by the curves.

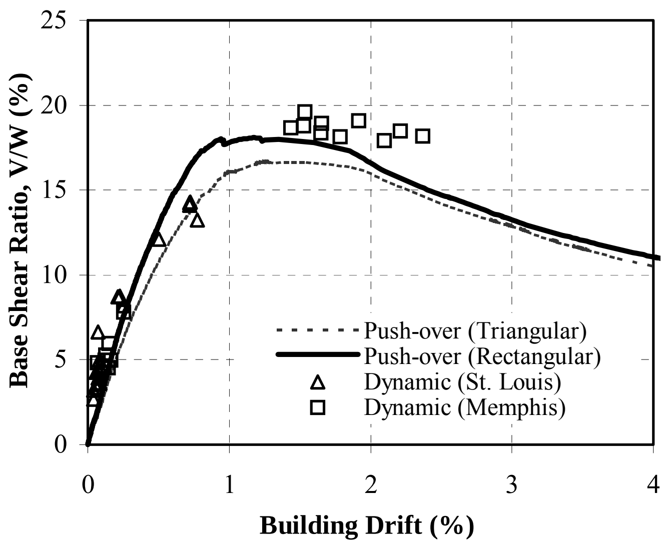

(a) Comparison between static and dynamic analysis

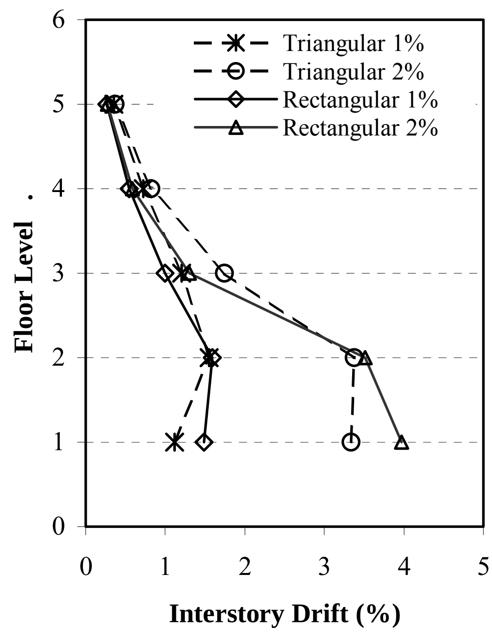

(b) Interstory drift profiles

Figure 8. Push-over analysis results for ZEUS-NL model

6.3 St. Louis, Missouri

The ZEUS-NL model was used to evaluate the response of the case study building for the St. Louis ground motion records. Figure 9 provides maximum interstory drifts for all motions. For an approximate global assessment, FEMA 356 provides limiting drift values for RC frame structures as one, two and four percent for the IO, LS and CP performance levels, respectively.

The median maximum interstory drift values for both suites are below one percent, indicating that the structure is well within the BSO described in FEMA 356, based on the global response.

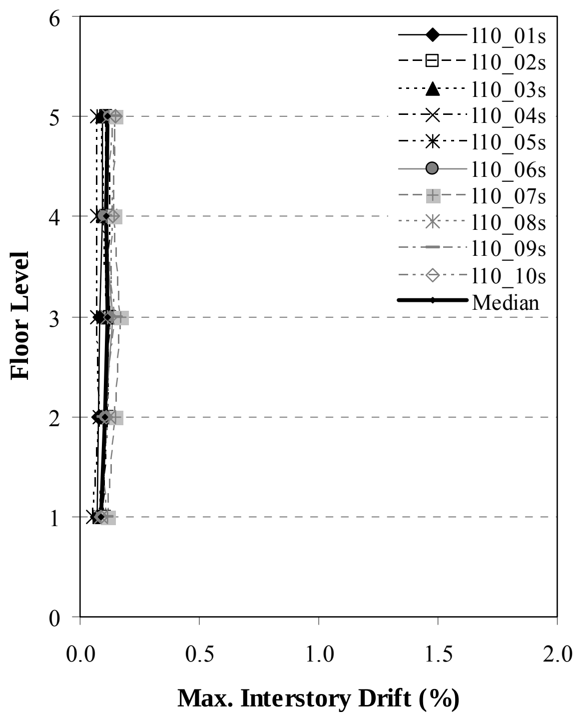

(a) 10% in 50 years

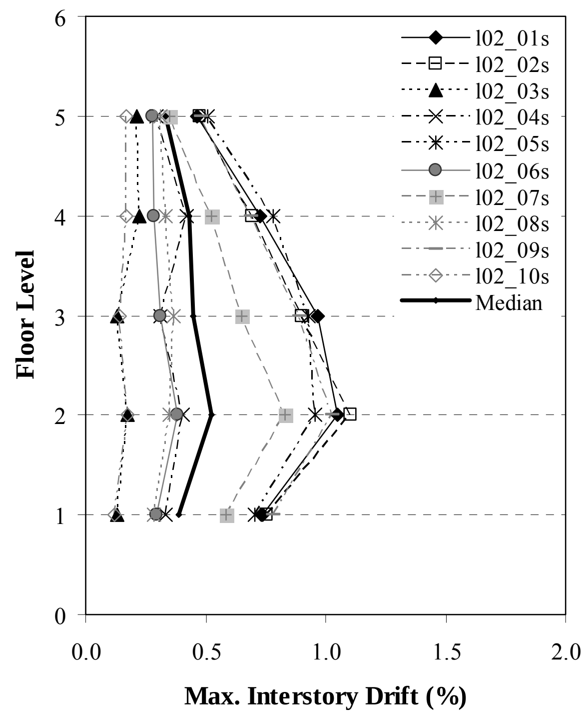

(b) 2% in 50 years

Figure 9. Maximum interstory drift values for St. Louis motions

6.4 Memphis, Tennessee

The maximum interstory drifts from the ZEUS-NL analysis with the Memphis motions are shown in Figure 10. Based on a global level performance evaluation, the structure meets the BSO of LS for the 10% in 50 years event in Memphis. In this case, the median drift values are well below the LS limit of two percent. For the 2% in 50 years event, the median drift values (ranging from 0.9 to 2.9 percent) are well below the CP limit of four percent, indicating that the BSO objective for this event is also met. For the 10% in 50 years event, no plastic rotations occurred and so the BSO of LS for this event was satisfied. The member level performance evaluation for the 2% in 50 years event is summarized in Table 4. In this table, the FEMA 356 criteria are listed vertically in the order of IO, LS and CP. Cases where the BSO is not met are noted with bold font. For the 2% in 50 years event, the BSO of CP is not met because limits for plastic rotation are exceeded in several components, including columns, beams, slabs and joints. Shear failures are not included in the ZEUS-NL analysis. Additional calculations for the 2% in

50 years Memphis event indicate that the median maximum base shear does not exceed the available column shear strength. However, punching shear failures are expected at the first and second floor levels based on the gravity shear ratio and interstory drift demand.

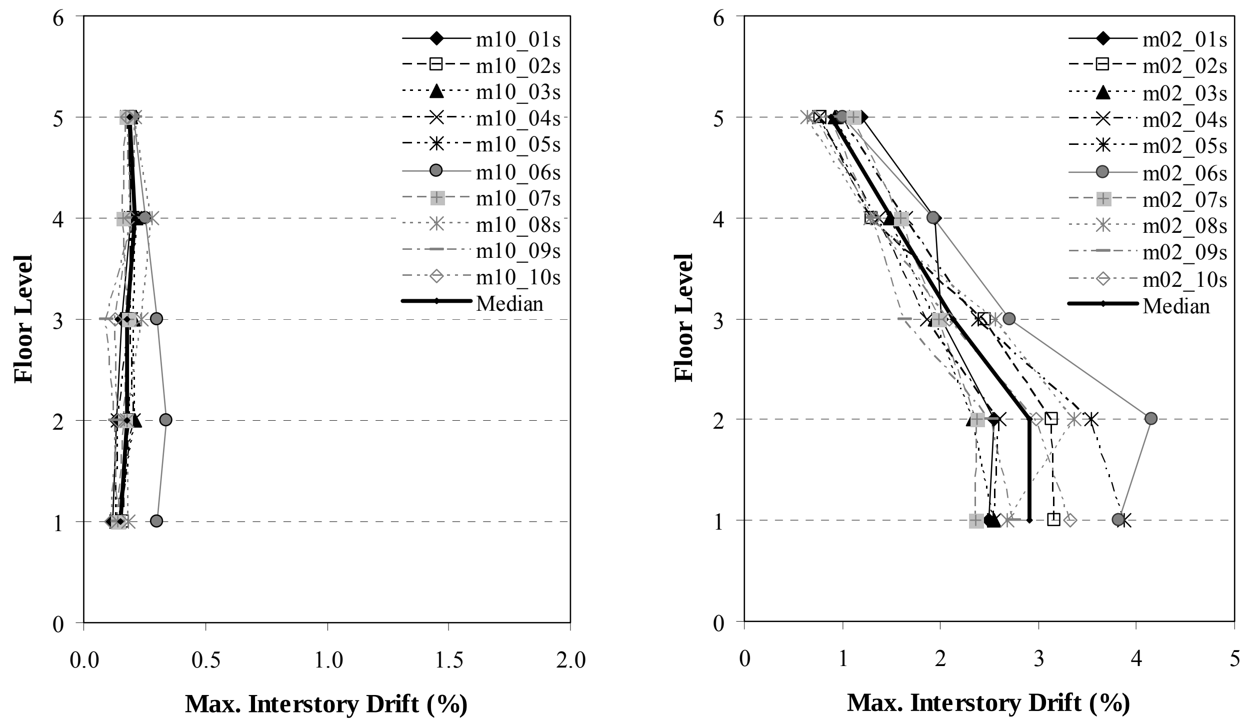

(a) 10% in 50 years

(b) 2% in 50 years

Figure 10. Maximum interstory drift values for Memphis motions

Table 4. Member level evaluation for 2% in 50 years Memphis motions

Story	Median Ground Motion	Beams		Columns		Beam-Column Joints		Slabs and Slab-Column Joints	
		FEMA Limit	Max. Plastic Rotation	FEMA Limit	Max. Plastic Rotation	FEMA Limit	Max. Plastic Rotation	FEMA Limit	Max. Plastic Rotation
		0.00210		0.002		0		0.0055	
1	m02_09s	0.00586	**0.0179**	0.002	**0.0286**	0	**0.0179**	0.0083	**0.0179**
		0.00758		0.003		0		0.0110	
		0.00210		0.002		0		0.0055	
2	m02_10s	0.00586	**0.0168**	0.002	**0.0222**	0	**0.0163**	0.0083	**0.0127**
		0.00758		0.003		0		0.0110	
		0.00210		0.002		0		0.0055	
3	m02_10s	0.00586	**0.0110**	0.002	**0.0175**	0	**0.0110**	0.0083	0.00768
		0.00758		0.003		0		0.0110	
		0.00210		0.002		0		0.0055	
4	m02_03s	0.00586	0.00487	0.002	**0.0112**	0	**0.00732**	0.0083	0
		0.00758		0.003		0		0.0110	
		0.00216		0.002		0		0.0005	
5	m02_09s	0.00594	0	0.002	**0.00507**	0	0	0.0008	0
		0.00783		0.003		0		0.0010	

7. CONCLUSIONS

Nonlinear analyses were conducted for a prototype five-story RC frame building designed for mid-1980s code requirements in the Central U.S. A comparison of the overall dynamic response using a macro model (DRAIN-2DM) and a fiber model (ZEUS-NL) showed similar global drift predictions, however some differences in the response were observed due to the different modeling approaches. The FEMA 356 performance criteria were applied to determine whether the predicted response of the building meets the suggested Basic Safety Objective (BSO). It was found that the predicted response for the St. Louis ground motions was within the BSO limits. For the Memphis ground motions, different outcomes occurred when the global level performance criteria (drift) were used versus the member level criteria (plastic rotation). Based on the drift limits, the predicted building response meets the BSO for both the 10% in 50 years and the 2% in 50 years events. However, an evaluation using the member level limits indicated that the member response is not within the limits of the BSO for the 2% in 50 years event. It must be noted that this evaluation is specific to the characteristics of this structure. Additional studies are needed to characterize the expected seismic performance of vulnerable structures and to develop effective seismic rehabilitation techniques that meet the selected performance objectives.

8. ACKNOWLEDGMENTS

The authors wish to acknowledge the National Science Foundation and the University of Illinois who funded this research through the Mid America Earthquake Center (NSF Grant Number EEC-9701785). The financial support provided by the Civil Engineering Department at Texas A&M University, where this research was conducted, is also appreciated. The authors also wish to express their appreciation to Jason Hart for his contribution in defining the case study building. The opinions expressed in this paper are those of the authors and do not necessarily reflect the views or policies of the sponsors.

9. REFERENCES

ACI Committee 318 (1983). *Building Code Requirements for Reinforced Concrete (ACI 318-83)*. American Concrete Institute, Detroit, MI.

ACI Committee 318 (2002). *Building Code Requirements for Structural Concrete (ACI 318-02)*. American Concrete Institute, Farmington Hills, MI.

ASCE (2000). *NEHRP Prestandard and Commentary on the Guidelines for the Seismic Rehabilitation of Buildings (FEMA Publication 356).* Building Seismic Safety Council, Washington, D.C.

Al-Haddad, M.S. and J.K. Wight (1986). Feasibility and consequences of moving beam plastic hinging zones for earthquake resistant design of R/C buildings. *Report No. UMCE 86-1*, Department of Civil Engineering, University of Michigan, Ann Arbor, July.

Building Officials and Code Administrators International, Inc. (BOCA) (1984). *The BOCA Basic/National Building Code/1984.* Country Club Hills, IL.

Building Officials and Code Administrators International, Inc. (BOCA) (1987). *The BOCA Basic/National Building Code/1987.* Country Club Hills, IL.

Chien, S.H. and J.K.Wight (1994). Testing and analysis of existing slab-column frame buildings and analysis of retrofitting with steel bracing. *Report No. UMCEE 94-31*, Dept. of Civil and Environ. Engineering, The University of Michigan, Ann Arbor, Michigan.

Elnashai, A.S., Papanikolaou, V. and Lee, D.H. (2002). *ZEUS-NL User Manual*. Mid-America Earthquake Center, University of Illinois at Urbana-Champaign.

Hart, J.F. (2000). Analysis of a typical midwestern structure subjected to seismic loads. *University Undergraduate Research Fellow Program Senior Honor Thesis.* Department of Civil Engineering, Texas A&M University, College Station, TX.

Hueste, M.D., and J.K. Wight (1997). Evaluation of a reinforced concrete building damaged during the Northridge earthquake and development of a punching shear failure model for nonlinear analysis. *Report No. UMCEE 97-17*. Dept. of Civil and Envier. Engine., University of Michigan, Ann Arbor, Michigan.

Hueste, M.D. and J.K. Wight (1999). A nonlinear punching shear failure model for interior slab-column connections. ASCE *Journal of Structural Engineering*. Vol. 125, No. 9, Sept., pp. 997-1008.

Kanaan, E.A., and G. H. Powell (1973), DRAIN-2D, a general purpose computer program for inelastic dynamic response of plane structures. *Report No. EERC 73-6*. Univ. of California, Berkeley.

Powell, G.H. (1973). DRAIN-2D, user's guide. *Report No. EERC 73-22*. Univ. of California, Berkeley.

Raffaelle, G.S. and J.K. Wight (1992). R/C eccentric beam-column connections subjected to earthquake-type loading. *Report No. UMCEE 92-18*. Dept. of Civil and Envier. Engine., Univ. of Michigan, Ann Arbor.

Soubra, K.S., J.K. Wight and A.E. Newman (1992). Fiber reinforced concrete joints for precast construction in seismic areas. *Report No. UMCEE 92-2*. Dept. of Civil and Envier. Engine., Univ. of Michigan, Ann Arbor.

Tang, X. and S.C. Goel (1988). DRAIN-2DM technical notes and user's guide. *Research Report UMCE 88-1*. Department of Civil Engineering, The University of Michigan, Ann Arbor, Michigan.

Trifunac, M.D. and A.G. Brady (1975). A study on the duration of strong earthquake ground motion. *Bulletin of the Seismological Society of America*, Vol. 65, No. 3, pp. 581-626.

Wen, Y.K., and C.L. Wu (2000). *Generation of Ground Motions for Mid-America Cities*. Mid-America Earthquake Center, 27 Jan. 2000, http://mae.ce.uiuc.edu/Research/RR-1/Gmotions/Index.html.

10. KEYWORDS

Slab, nonlinear analysis, push-over, performance, seismic, nonductile, frames, reinforced concrete, FEMA 356, DRAIN-2DM, ZEUS-NL

SESSION 3-B: SEISMIC RETROFIT OR STRENGTHENING

Chaired by

♦ M. N. Fardis and Akira Tasai ♦

EFFECTS OF REINFORCING DETAILS ON AXIAL LOAD CAPACITY OF R/C COLUMNS

Daisuke KATO[1] , LI Zhuzhen[2] , Katsuhiro SUGA[2] and Yukiko NAKAMURA[1]

ABSTRACT

Final objective of this study is to prevent pancake type collapse of R/C old buildings during sever earth quake. For this purpose axial load carrying capacity of columns failing in flexure have been studied. In this study the scope was extended to shear failing columns, axial load capacity under residual deformation and effects of reinforcing details. Ten R/C specimens with square sections were tested. Two types of specimens were made with varying only reinforcing details. The hoop of H-series had 135 degrees hook. And the hoop of P-series had 90 degree hook details. Another main variable was loading methods; i.e. monotonic eccentric axial loading, eccentric axial loading under constant lateral drift and normal reversed lateral loading under constant axial load. Conclusions were as follows. i)There was little difference of behavior between specimens with normal reinforcing details and those with poor reinforcing details. ii)Specimens with high axial load, which required cohesion and friction to sustain axial load, lost scheduled axial load far before it's axial deformation reached axial load – axial deformation relation of specimen with centric axial load. On the other hand, Specimens with low axial load, which required only friction to sustain axial load, lost scheduled axial load when it's axial deformation reached axial load – axial deformation relation of specimen with centric axial load. iii)Effectiveness factor of hoop α was introduced and obtained using experimental data. Obtained factors degraded with increasing axial deformation but they should be examined furthermore.

1. INTRODUCTION

Final objective of this study is to prevent pancake type collapse of R/C old buildings during sever earth quake. For this purpose axial load carrying capacity of columns have been studied (Kato (2001)). But in these tests the objectives were only columns failing flexure. On the other hand some studies have been done about columns including shear failing columns and residual axial capacity (Santiago Pujol (2000), J. P. Moehle (1999), Nakamura T. (2002), Kitada T.(1998)). So in this study the scope was extended to shear failing columns, axial load capacity under residual deformation and effects of reinforcing details

1.Department. of Architecture, faculty of Engineering, Niigata University, Niigata, Japan.
Email:dkato@eng.niigata-u.ac.jp
2.Graduate student, Dept. of Architecture, faculty of Engineering, Niigata University

2. OUTLINE OF TEST

2.1 Specimens

In order to understand axial load capacity centric axial loading test is the most basic testing method. But the actual axial load capacity should be discussed using columns subjected to axial load and lateral load reversals. These two cases have studied widely. But in this study eccentric axial loading tests were also done under constant residual deformation.

Figure 1 shows specimens. Table 1 shows properties of specimens. All specimens were rectangular reinforced concrete columns with steel footings at both ends for repeatable use. 180mm square section, longitudinal reinforcement (4-D10 bars) and hoop reinforcement (2D6@70) were commonly used for all specimens. Two types of specimens were made. Only reinforcing details were different. The hoop of H-series had 135 degrees hook. And the hoop of P-series had 90 degree hook details. The hook position was rotated along column's axis. Tables 2(a)(b) show material strength of concrete and steel.

Tables 3(a)(b) show variables of loading method. Left table shows axial loading test series. Axial loading test was composed by preloading meaning reversed lateral loading and main loading meaning monotonic axial loading. Maximum drift angles of preloading were 1/50 or 1/100 rad. And drift angles at loading which means residual lateral drift were also 0, 1/50 or 1/100 rad. Note that specimen H-0 and P-0 without preloading were monotonic centric axial loading specimens which had been done widely enough. On the other hand right hand table shows lateral loading specimens. This series was composed by main loading which means normal reversed lateral loading test under constant axial load and post loading which means monotonic axial loading. Post loading was started after the specimen lost its axial load capacity to sustain scheduled constant axial load.

Table 1 Properties of specimen

<table>
<tr><th rowspan="2">specimen</th><th colspan="2">column size</th><th rowspan="2">main bar</th><th colspan="4">hoop</th></tr>
<tr><th>section</th><th>height</th><th>hoop</th><th>hoop spacing</th><th>hook</th><th>anchorage length</th></tr>
<tr><td>H-series</td><td rowspan="2">180x180mm</td><td rowspan="2">360mm</td><td rowspan="2">4-D10</td><td rowspan="2">2-D10</td><td rowspan="2">70mm</td><td>135 deg</td><td>6d</td></tr>
<tr><td>P-series</td><td>90 deg</td><td>8d</td></tr>
</table>

Table 2 Strength of material (N/mm^2)

(a)steel

steel	yield strength	maximum strength
D10	383	521
D6	316	490

(b)concrete

specimen	concrete strength
H-0,1,2 P-	33.7
H-3,4 P-3,4	35.2

Table 3 Loading method

(a)axial loading test series

specimen	pre loading (reversed lateral loading)	main loading (monotonic axial loading)
	maximum drift angle(rad)	drift angle at loading (rad)
H-0	-	0
H-1	1/50	1/50
H-2	1/50	0
P-0	-	0
P-1	1/50	1/50
P-2	1/100	1/100

(b)lateral loading test series

specimen	main loading (reversed lateral loading)	post loading (monotonic axial loading)
	axial load (kN)	drift angle at loading (rad)
H-3	400	free
H-4	200	free
P-3	400	free
P-4	300	free

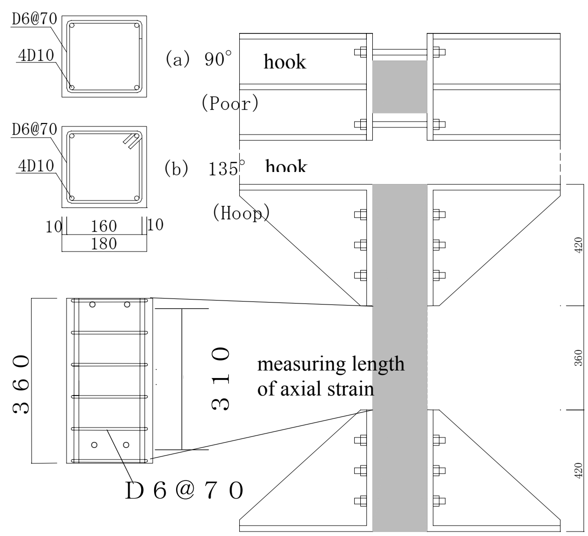

Figure 1 Specimen and reinforcement

2.2 Loading method

Figure 2 shows loading setup. Triangle steel footings were repeatable footings. Note that the confinement from the footing base could be different from that of normal type specimen with H shape type. But as far as failure occurs around the middle part of the specimen the difference can be neglected.

Eccentric axial loading test under constant residual deformation was applied as follows. At first column was subjected to lateral load reversals under constant axial load of 150kN. The lateral load was reversed twice for each drift angle of 1/100rad (H-1,2 P-1,2) and 1/50rad (H-1,2 P-1). After lateral loading axial load was subjected under constant residual deformation, which meant residual deformation.

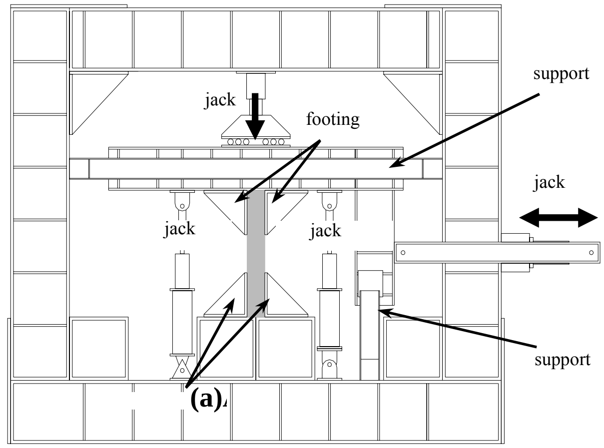

Figure 2 Loading setup

3. TEST RESULTS

3.1 Test result of axial loading test series(H-0,1,2 and P-0,1,2)

Figures 3(a)-(f) shows test result of axial loading test series (H-0,1,2 and P-0,1,2). Top figure shows axial load-axial deformation relationship and bottom figure shows lateral load-axial deformation relationship. Figures (a)(d) show the test results of monotonic centric axial loading test. The variable was reinforcing details. But little difference can be seen between behaviors of these two specimens.

Figure (c) shows the test results of specimen H-2 subjected to preloading which means lateral load reversals up to the drift angle of 1/50 rad. Effect of preloading can be seen comparing to specimen H-0 subjected to monotonic axial loading, i.e. maximum axial load degraded by preloading and little difference can be seen about the behavior after peak point.

Figures (b)(e)(f) show the behavior of Specimens H-1,P-1,2 subjected to both preloading and eccentric axial loading. Effect of eccentric axial loading can be seen comparing to specimen H-0 subjected to monotonic axial loading, i.e. axial deformations at maximum axial load of specimens H-1 were much larger than that of specimen H-0. This was caused by lateral load to maintain constant residual deformation. The bottom figures show this lateral load. And the lateral load was much larger than that of specimen H-0.

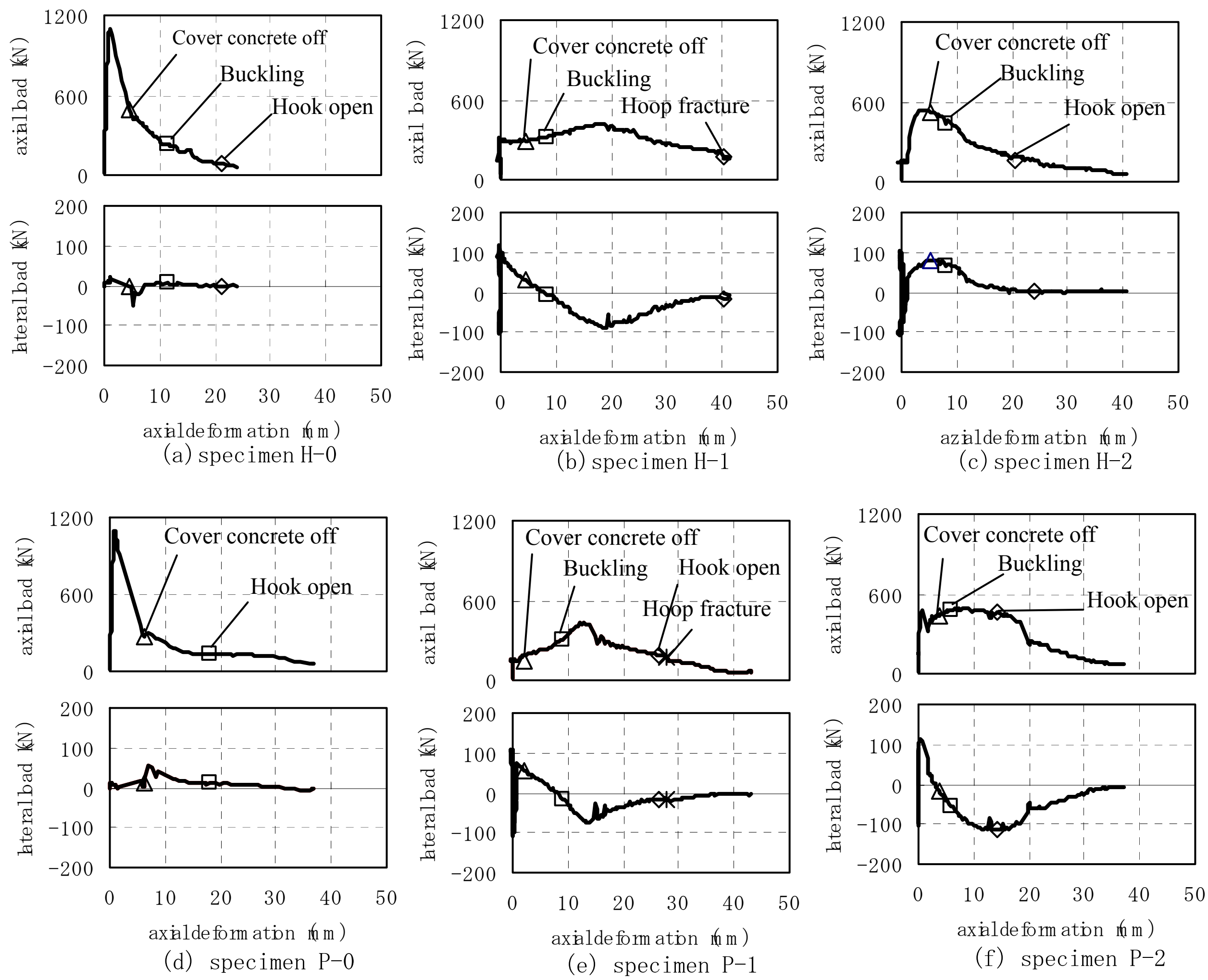

Figure 3 Test results of axial loading test series (H-0,1,2 P-0,1,2)

3.2 Test result of lateral loading test series(H-3,4 and P-3,4)

Figure 4 shows crack patterns and failure mode. Figure (a) shows crack patterns at drift angle 1/100rad and Figure (b) shows failure mode after main loading test (lateral reversed loading). Figures 5(a)-(d) show test results of lateral loading test series (H-3,4 and P-3,4). Left figure shows axial load-axial deformation relationship, middle figure shows lateral load-axial deformation relationship and right figure shows lateral load-lateral deformation relationship.

Figures (a)(c) show the test results of lateral loading series specimens with high axial load. Specimens H-3 and P-3 were subjected to axial load of 400 kN which was large among 4 specimens. And circle marks represent starting points of post loading. In other words the specimens lost their axial load carrying capacities for scheduled axial load at these points. Post loading meaning eccentric axial loading started from this points. But at these cases lateral drifts were not confined. In left figures showing axial load – axial deformation relationship test results of accompanying monotonic axial centric loading specimen are also compared, indicating that axial load-axial deformation relationship of lateral loading specimens converged to that of centric axial loading specimen in the final loading stage. Also specimens H-3 and P-3 with high axial load lost scheduled axial load far before their axial deformation reached axial load – axial deformation relation of specimen with centric axial load.

Figures (b)(d) show the test results of lateral loading series specimens H-4 and P-4 with low axial load comparing to specimens H-3 and P-3. Specimens in these cases lost their scheduled axial load when their axial deformation reached axial load – axial deformation relation of specimens with centric axial load. This is understandable like that the scheduled axial load of these specimens could be sustained by friction of the failure surface only which was supposed to be a same condition as final part of centric axial loading test. In other words scheduled axial load of specimens H-3 and P-3 with high axial load could not be sustained by friction only. They needed cohesion to sustain high axial load. And this is why they lost their axial load capacity early. But this result should be examined further more.

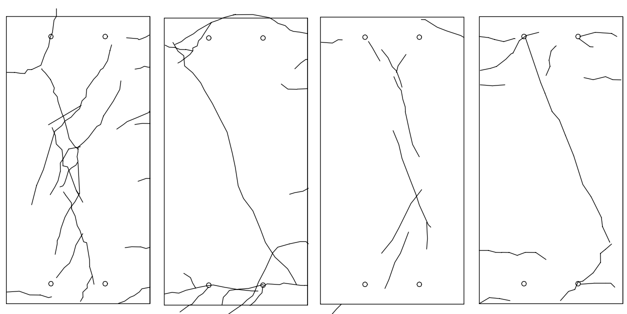

(a)drift angle 1/100rad

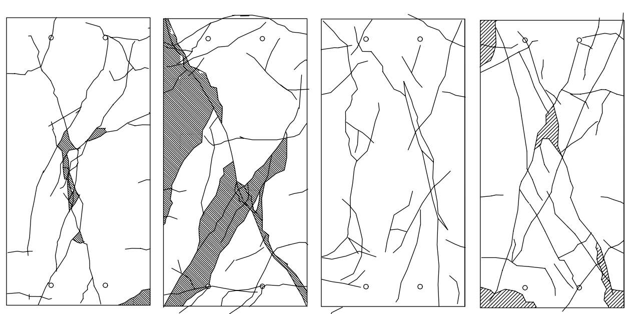

(b)after main loading test (lateral reversed loading)

Figure 4 crack patterns and failure

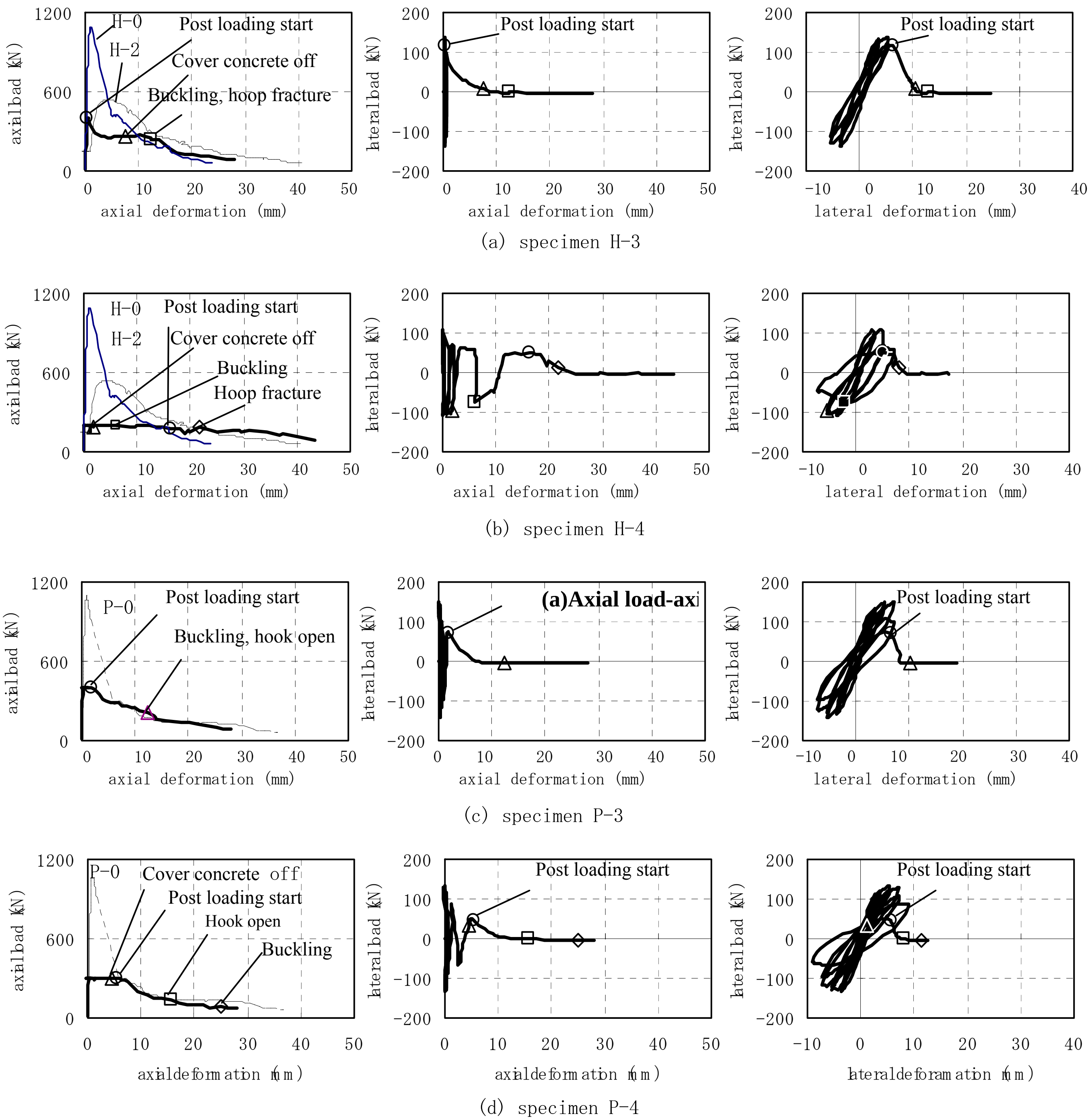

Figure 5 Test results of lateral loading test series (H-3,4 P-3,4)

4. EFFECTS OF REINFORCING DETAILS ON AXIAL LOAD CAPACITY

4.1 Evaluating method

Mohr's stress circle and Mohr-Coulomb's failure criterion are effective to understand the condition after maximum strength (Santiago Pujol (2000), J. P. Moehle (1999)). Trial to understand the effects of hoop reinforcement on axial load capacity using stress circle and failure criterion is shown in this section.

Figure 6 shows basic concept of stress circle and criterion. The original criterion has the value of cohesion C and friction μ. Once the stress circle touches the criterion the criterion degrades gradually and finally reaches origin point and after that keeps this line. The line crossing the origin point is called after slip criterion in this study. Note that the value of C=5.8 and μ=1.7 are used tentatively, which should be discussed furthermore.

In this study two types of failure conditions are considered. Figure 7 shows these two types of failure condition; i.e. (a)failure according to current failure criterion as shown in Fig. 6 and (b)slip failure along existing failure surface with the inclination of θ e which has been developed in the previous loading step.

Figure 8 shows the procedure to obtain failure condition by slip along existing failure surface. For drawing stress circle using experimental data in this procedure there are two problems. Firstly effect of hoop reinforcement which is necessary to draw stress circle degrades according to loading step. So effectiveness factor of hoop α after slip occurred is introduced. And the procedure is as follows; i.e. assuming α, subtracting steel contribution and drawing stress circle. If slip occurs this means the collect value of α.

Second problem to obtain stress circle is the estimation of contribution of longitudinal steel . Figure 9 shows the estimated contribution of longitudinal reinforcement. As shown in the figure buckling is taken in account. The model was already proposed (Kato 1995). The figure indicates that behavior after buckling depends on effectiveness factor of hoop α.

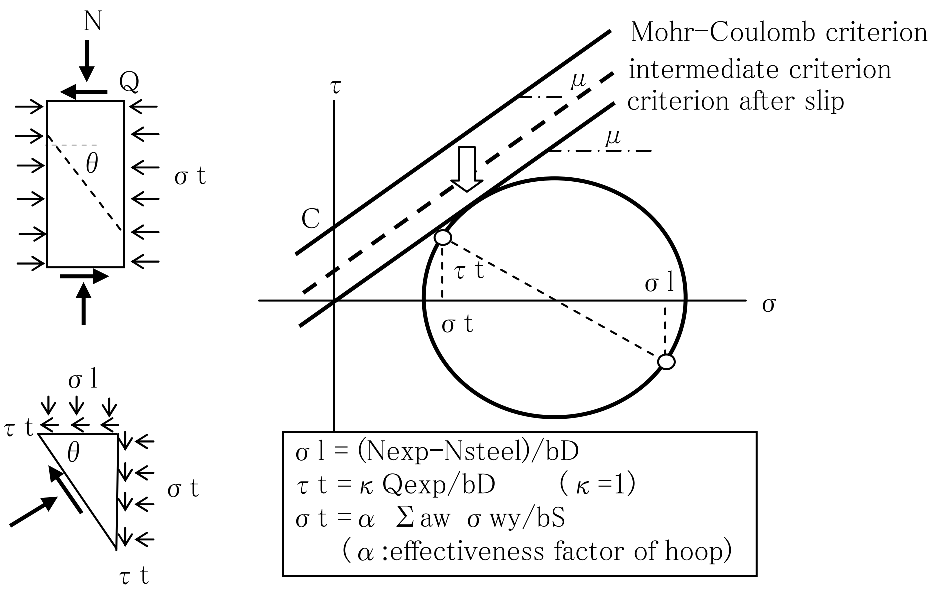

Figure 6 Basic concept of stress condition of concrete and failure criterion

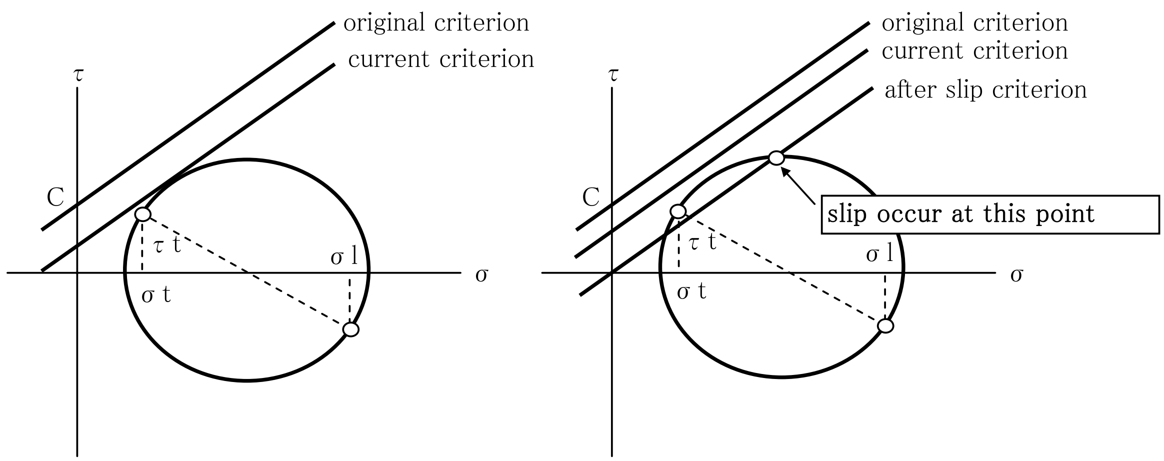

(a)according to current criterion **(b)slip along existing failure surface (inclination is θ e)**

Figure 7 Two types of failure condition

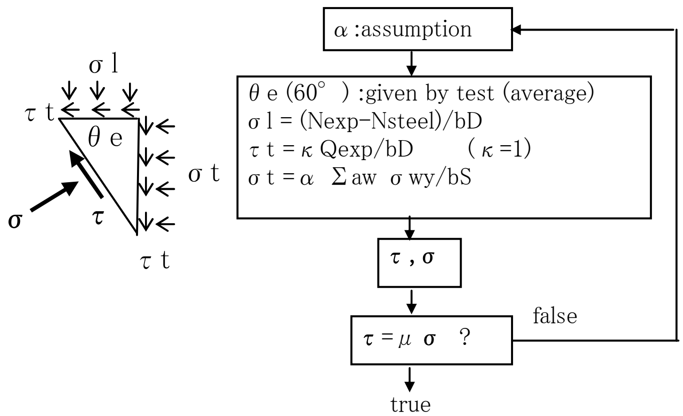

Figure 8 Estimation of effectiveness factor of hoop α from test results (failure type is slip along existing failure surface (inclination is θ e=60°)

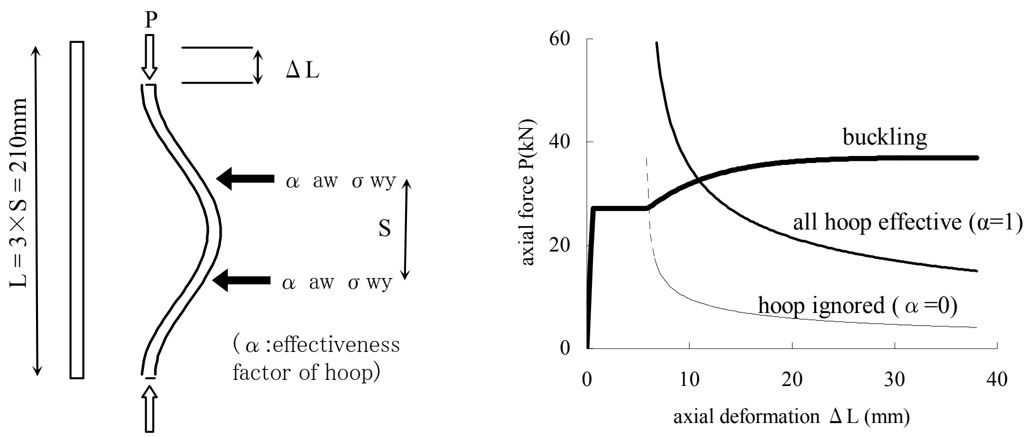

(a)buckling model **(b)axial force – axial deformation relationship**

Figure 9 Estimation of contribution of axial force supported by one longitudinal bar

4.2 Effectiveness factor of hoop

Figures 10(a)(b) show an example of estimated effectiveness factor of hoop α of specimen H-0 with monotonic central axial loading. Figure (a) shows axial load - axial deformation relationship of the specimen. Contributions of longitudinal steels are also shown in the figure. And Figure (b) shows estimated α. Three dashed circles represent before failure, failure according to Mohr-Coulomb criterion and failure according to after slip criterion.

Bottom two figures of Figures 11(a)(b) show estimated effectiveness factor of hoop of all specimens. If the value of α cannot be obtained within the range from 0 to 1, which means slip does not occur, stress circle in this case is assumed to touch the current criterion as shown in Fig. 7(a). In this case cohesion can be obtained assuming α=0. Top figures show estimated cohesion. Horizontal axis of these figures represents axial deformation.

Figures indicate that estimated values degrade according to axial deformation. And circle marks represent starting point of post loading of lateral loading specimens. And specimens H-3 and P-3 with high axial load lost their axial load capacities before they reached after slip criterion. And specimens H-4 and P-4 with low axial load lost their axial load capacity in the after slip criterion range.

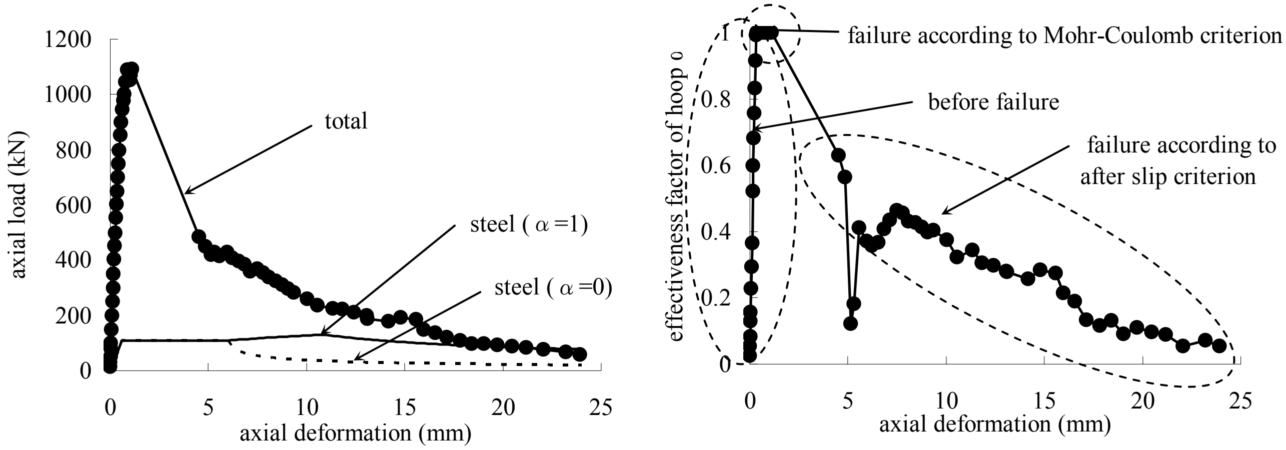

(a)Axial load-axial deformation **(b)Estimated effectiveness factor –axial deformation**

Figure 10 Example of estimated α (specimen H-0)

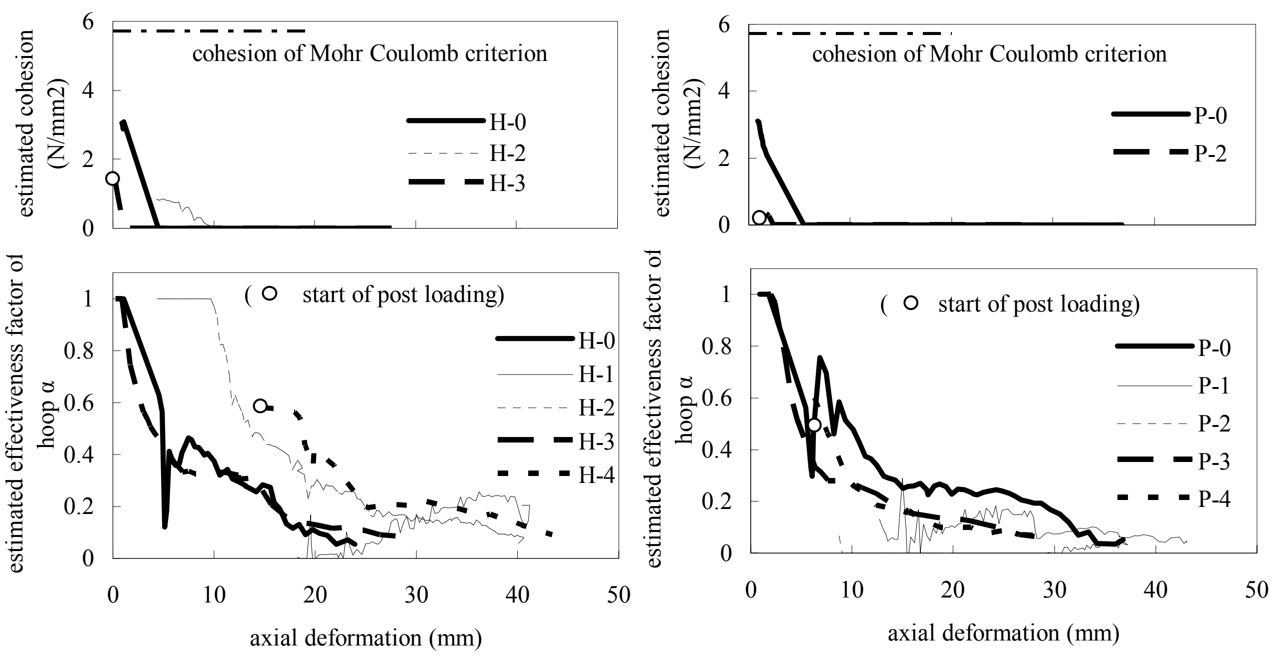

(a)H-series **(b)P-series**

Figure 11 Estimation of effectiveness factor of hoop α and cohesion of specimens after peak points (maximum axial load point(H-0,1,2,P-0,1,2) or starting point of post loading(H-3,4,P-3,4))

5. CONCLUSIONS

(1)There was little difference of behavior between specimens with normal reinforcing details (H-series) and those with poor reinforcing details (P-series).

(2)Maximum axial load degraded by preloading meaning lateral load reversals. But little difference was observed after the peak point.

(3)Axial deformations at maximum axial load of specimens with eccentric loading were much larger than those of other specimens. This is caused by lateral load to maintain constant residual deformation.

(4)Axial load-axial deformation relationship of lateral loading specimens converged to that of centric axial loading specimen in the final loading stage.

(5) Specimens with high axial load, which required cohesion and friction to sustain axial load, lost scheduled axial load far before it’s axial deformation reached axial load - axial deformation relation of specimen with centric axial load. On the other hand, Specimens with low axial load, which required only friction to sustain axial load, lost scheduled axial load when its axial deformation reached axial load - axial deformation relation of specimen with centric axial load.

(6)Effectiveness factor of hoop α was introduced and obtained using experimental data. Obtained factors degraded with increasing axial deformation but they should be examined furthermore.

REFERENCES

Kato,D., Ohnishi, K. (2001)., *Axial load carrying capacity of R/C columns under lateral load reversals, The third U.S.-Japan Workshop on performance-Based Earthquake Engineering Methodology for Reinforced Concrete Building Structures, pp.231-239*

Santiago Pujol, Mete Sozen, Julio Ramirez (2000)., *Transverse reinforcement for columns of RC frames to resist earthquakes, Journal of Structural Engineering, April 2000, pp.461-466*

J. P. Moehle, K. J. Elwood, H. Sezen (1999)., *Shear failure and axial load collapse of existing reinforced concrete columns, The first U.S.-Japan Workshop on performance-Based Earthquake Engineering Methodology for Reinforced Concrete Building Structures, pp.233-247*

Nakamura T., Yoshimura M., Owa S. (2002)., *Axial load carrying capacity of reinforced concrete short columns with shear mode, Journal of structural and construction engineering, AIJ, No.561,pp193-100 (in Japanese)*

Kitada T., Tasai A.(1998)., *Study on residual axial capacity and damage restorability of flexural columns after earthquake, JCI, pp.433-438 (in Japanese)*

Kato, D., Kanaya, J. and Wakatsuki, K.(1995)*, Buckling Strains of Main Bars in Reinforced Concrete Members, Proceedings of the fifth East Asia-Pacific Conference on structural Engineering and Construction, Volume 1, pp.699-704*

SHEAR TRANSFER, CONFINEMENT, BOND, AND LAP SPLICE SEISMIC RETROFIT USING FIBER REINFORCED POLYMER COMPOSITES

Chris P. PANTELIDES

ABSTRACT

Reinforced concrete structures have been built in areas of seismic activity with various code provisions, resulting in performance ranging from collapse to repairable damage for buildings of different design, material strength, reinforcement details, and age. To ensure better performance for a range of existing reinforced concrete structures in seismic regions with substandard structural details, seismic retrofit is an economical solution. To improve the performance of reinforced concrete structures built with substandard details non-ductile failure must be prevented. The paper presents analytical and experimental results in which carbon fiber reinforced polymer composites can be used to improve the performance of reinforced concrete buildings whose components are vulnerable to shear failure, flexural-compression failure, joint reinforcement bond failure, or longitudinal reinforcement lap splice failure. By strengthening the columns and joints of reinforced concrete building frames against such failures, their vertical load carrying capacity can be enhanced thus leading to better performance against collapse of reinforced concrete buildings.

1. INTRODUCTION

The use of fiber reinforced polymer (FRP) composites in seismic retrofit of reinforced concrete (RC) structures has developed in the last 25 years. FRP composites are receiving acceptance because of high-strength to weight ratio, environmental resistance, and ease of application over materials such as structural steel. Although some guidelines for the design of externally bonded FRP systems for strengthening concrete structures exist, such as ACI 440 (2002), seismic retrofit design criteria based on performance-based design are currently under development (Pantelides and Gergely 2002, Moran and Pantelides 2002b); performance-based design approaches for seismic rehabilitation of buildings are in progress (Ruiz and Badillo 2001). Columns and joints in RC frames are the critical elements that have to be strengthened in order to protect against building collapse in damaging earthquakes. Shear failure, confinement, bond or anchorage failure, and lap splice failure must be prevented for satisfactory performance. Experimental and analytical results are presented which show that FRP composites can be used to retrofit columns

---

Department of Civil and Environmental Engineering, University of Utah, Salt Lake City, Utah, USA
Email: chris@civil.utah.edu

and joints against such failures. In addition, such retrofits can result in the enhancement of the vertical load carrying capacity of columns and joints at large deformations, thus leading to better performance of RC buildings in severe earthquakes and gravity load collapse prevention.

2. SHEAR TRANSFER RETROFIT

Shear transfer tests for concrete reinforced internally with steel hoops were used to determine the horizontal design of precast shear connections and develop the shear friction design method (Birkeland and Birkeland 1966, Mast 1968, Mattock and Hawkins 1972). To study shear transfer across a plane in concrete, externally reinforced with FRP composites, a test unit was designed to fail in shear at a known plane, as shown in Figure 1(a), which was ensured by placing reinforcing steel away from the shear plane to eliminate flexural, compression or bearing failure. Figure 1(b) shows the steel reinforcement with a yield stress f_y = 410 MPa, which was not placed at the shear failure plane so it would not influence the results. The average 28-day concrete compressive strength was $f_c^{'}$ = 36 MPa. A carbon FRP composite with an epoxy-resin matrix was used with the following properties: (1) tensile strength f_{fu} = 903 MPa; (2) tensile modulus, E_f = 68 GPa; (3) ultimate tensile strain ε_{fu} = 1.33%; (4) ply thickness t_i = 1.00 mm.

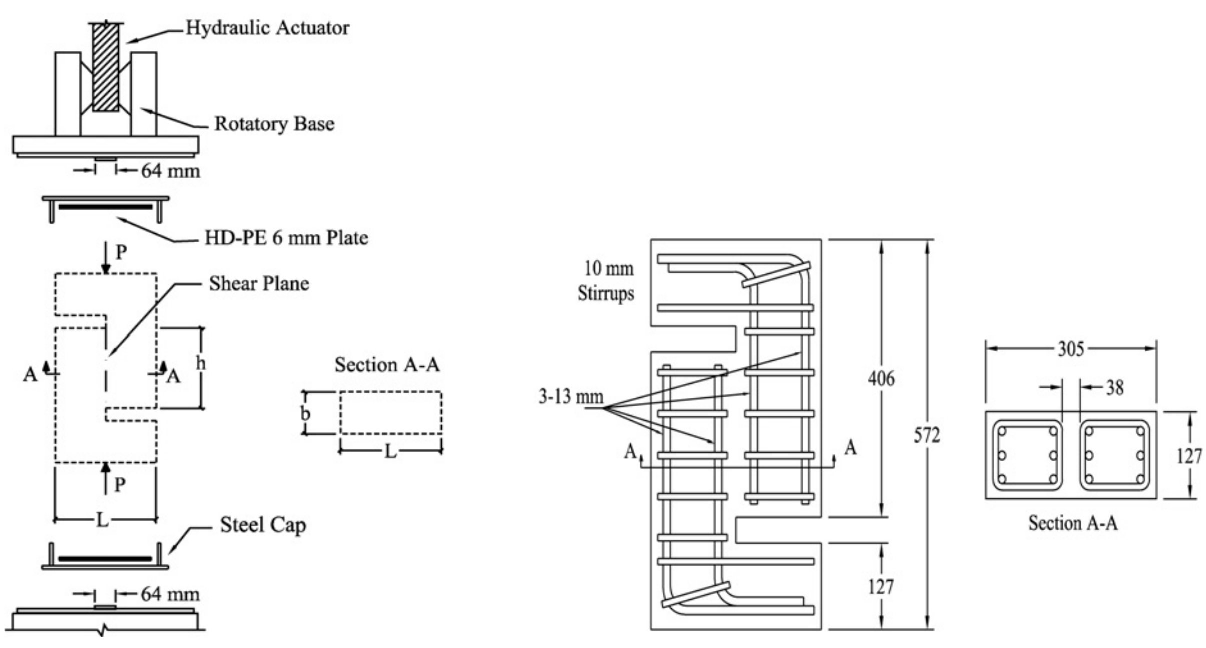

(a) (b)

Figure 1. Shear transfer test unit: (a) setup, (b) reinforcement details

Test units with a two-sided wrapped scheme, as shown in Figure 2(a), were tested for varying carbon FRP reinforcement ratios; as-is units without carbon FRP composite were also tested for comparison. The FRP reinforcement ratio is defined as:

$$\rho_f = \frac{\sum t_i * w_f}{b * h} \tag{1}$$

where t_i = ply thickness, w_f = ply width, b = width of rectangular cross section (127 mm), and h = shear plane height; note that for all units L = 305 mm, as shown in Figure 1. Figure 2(b) shows the unit at failure, which was caused by concrete cohesive failure and peeling of the FRP laminate. This type of failure was observed on both sides of the units. The bond failure mechanism is brittle, and the failure stages were: (1) the imposed shear stress was controlled by concrete alone until the concrete shear capacity was reached; and (2) the additional imposed shear stress was resisted by the carbon FRP composite acting as a clamping force, inducing additional aggregate interlock or shear friction until the bond between laminate and concrete failed.

To determine the concrete shear friction strength and the additional shear friction strength provided by the concrete-carbon FRP interaction, the relation between ultimate shear to concrete compressive strength, $v_u \big/ f_c^{'}$, versus carbon FRP stiffness normalized by the concrete compressive strength, $\rho_f f_{fu} \big/ f_c^{'}$, is calculated and presented in Figure 3; using least squares the following expression is obtained (Saenz and Pantelides 2003):

$$v_u = 0.505\, \rho_f f_{fu} + 0.117\, f_c^{'} \tag{2}$$

The first term in Equation (2) is the shear friction strength contributed by concrete-carbon FRP shear friction interaction, where 0.505 is the shear friction interaction coefficient, and $\rho_f f_{fu}$, is the effective carbon FRP composite clamping stress; the second term is the concrete shear friction strength, where 0.117 is the component for bond and asperity shear as proposed by Mattock (2001), and Kahn and Mitchell (2002). Equation (2) is in agreement with the models by Birkeland and Birkeland (1966), Mattock and Hawkins (1972), Mattock (2001), and Kahn and Mitchell (2002), in which shear transfer in steel reinforced concrete was studied.

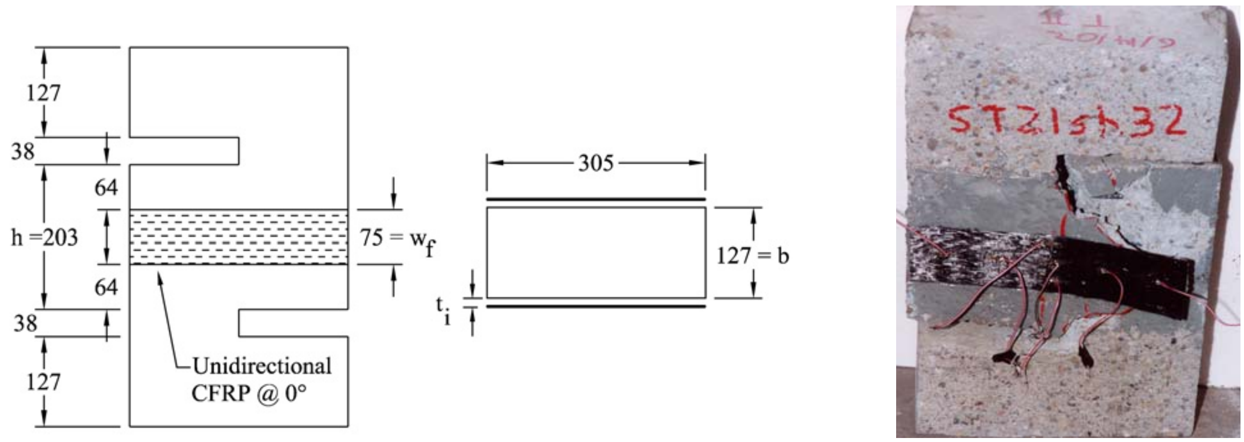

Figure 2: Shear transfer test unit: (a) CFRP composite details, (b) bond failure

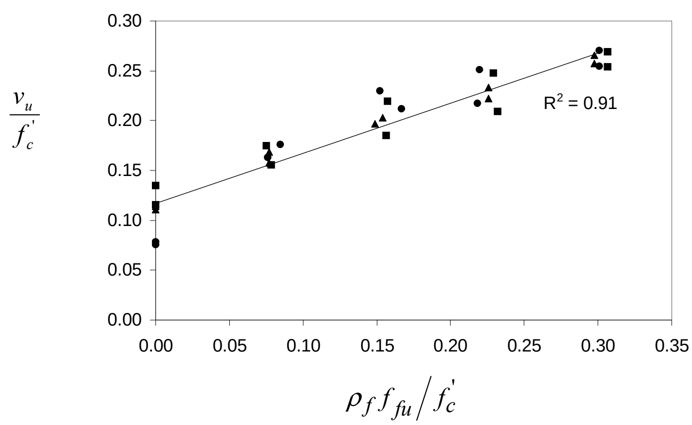

Figure 3. Normalized ultimate shear stress versus normalized CFRP stiffness

The shear friction expression for steel reinforced concrete proposed by Mattock (2001) is:

$$v_u = 0.8\,\rho_s f_y + 0.1 f_c^{'} \tag{3}$$

The first term in Equation (3) is equivalent to the first term in Equation (2); the second term is the component for bond and asperity shear, which is approximately the same as in Equation (2). For externally bonded carbon FRP composite plates, the concrete-carbon FRP shear friction interaction coefficient (0.505) of Equation (2) is lower than that for internal steel reinforcement (0.8) of Equation (3); the bond strength between externally bonded carbon FRP composite to concrete does not increase beyond the effective bond length, so that bond strength cannot increase; this is the difference between internal and external reinforcement, where internal reinforcement can achieve full tensile strength. The shear transfer units reinforced with carbon

FRP composites increased shear transfer capacity by a factor from 1.32 to 3.25 times compared to the as-is concrete units, for a carbon FRP reinforcement ratio ranging from 0.3% to 1.2%. An upper bound for the shear transfer capacity of the units tested with FRP was established as $0.27 f_c^{'}$.

3. CONFINEMENT RETROFIT

Various experimental investigations of RC columns retrofitted by FRP composites have been carried out. Seible et al. (1997) tested circular and rectangular columns with carbon FRP composite retrofits, which exhibited large displacement ductility, while maintaining constant load-capacity without significant cyclic capacity degradation. Several investigators have introduced stress-strain models for concrete confined by FRP jackets. Two models amongst these are those by Spoelstra and Monti (1999), and Xiao and Wu (2000). The Xiao and Wu (2000) model is an elasticity-based bilinear model in which the behavior of the FRP confined concrete is described in terms of the mechanical properties of the concrete core and confining FRP jacket. The Spoelstra and Monti (1999) model, is an iterative equilibrium-based model in which the behavior of the FRP confined concrete is governed by the Mander et al. (1988) model for steel confined concrete and the Pantazopoulou and Mills (1995) constitutive model for concrete. In the Mander et al. (1988) model for steel confined concrete, the increase in peak compressive strength of the confined concrete is expressed in terms of a constant effective confining pressure, and a resultant constant strain ductility ratio that defines the increase in compressive strain relative to the increase in compressive strength of steel confined concrete.

The axial plastic compressive strain, ε_{cp}, and stress, f_{cp}, corresponding to plastic radial strain $\varepsilon_{\theta p}$, are shown in Figure 4. The increase in strain ductility of concrete confined by steel reinforcement is obtained from the strain ductility ratio R, shown in Figure 5(a), proposed by Mander et al. (1988) as:

$$R = \left(\frac{\varepsilon_{cc}}{\varepsilon_{co}} - 1 \right) / \left(\frac{f_{cc}}{f_{co}} - 1 \right) \tag{4}$$

in which f_{co} = unconfined concrete strength, f_{cc} = confined concrete strength, ε_{co} = compressive strain of unconfined concrete at f_{co}, and ε_{cc} = compressive strain of the confined concrete at f_{cc}.

For the case of steel confined concrete, Mander et al. (1988) determined that the strain ductility ratio is constant with R=5.0. For FRP confined concrete, the concept of a variable plastic strain ductility ratio, R_p, is introduced as shown in Figure 5(b), for a given plastic radial strain, $\varepsilon_{\theta p}$, in the FRP jacket, where $\varepsilon_{\theta o} \le \varepsilon_{\theta p} \le \varepsilon_{\theta u}$. The variable plastic strain ductility ratio is defined in terms of the axial plastic compressive strain, ε_{cp}, and stress, f_{cp}, as:

$$R_p = \left(\frac{\varepsilon_{cp}}{\varepsilon_{co}-1}\right) \Big/ \left(\frac{f_{cp}}{f_{co}-1}\right) \tag{5}$$

in which $\varepsilon_{\theta o}$ = radial strain in the FRP jacket corresponding to the compressive strain of the unconfined concrete, and $\varepsilon_{\theta u}$ = ultimate radial strain in the FRP jacket. For a given plastic radial strain, $\varepsilon_{\theta p}$, in the FRP jacket, relationships between the plastic confinement efficiency, k_{cp}, and plastic strain efficiency, $k_{\varepsilon p}$, can be developed as:

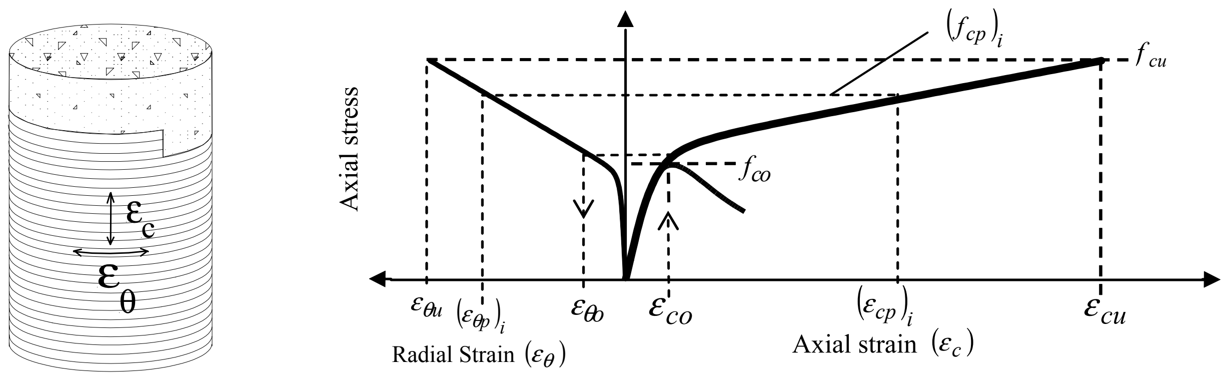

Figure 4. Stress-strain parameters for FRP-confined concrete

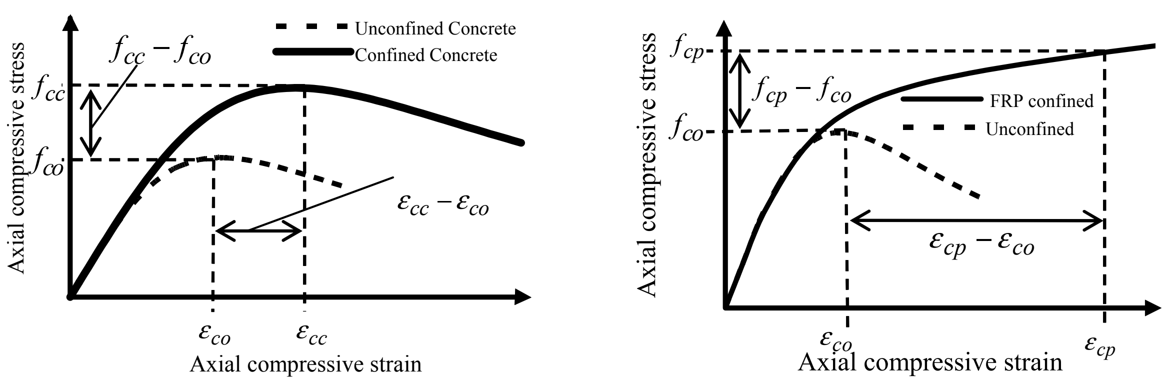

(a) (b)

Figure 5. Strain ductility ratio: (a) steel-confined concrete, (b) FRP-confined concrete

$$k_{cp} = \frac{f_{cp}}{f_{co}} = 1 + k_{1p}k_{re} \; ; \quad k_{\varepsilon p} = \frac{\varepsilon_{cp}}{\varepsilon_{co}} = 1 + k_{2p}k_{re} \; ; \quad k_{re} = K_{je}\varepsilon_{\theta} \; ; \qquad K_{je} = \frac{2t_j E_j}{D_c f_{co}} k_e \tag{6}$$

where t_j = FRP jacket thickness, E_j = FRP tangent hoop modulus of elasticity, D_c = concrete column diameter, and k_e = confinement efficiency of FRP composite jacket that accounts for arching; for circular FRP continuous jackets k_e is equal to 1.0. The coefficients k_{1p} and k_{2p} can be determined experimentally. At high effective confinement ratios, k_{re}, the plastic confinement coefficient, k_{1p}, approaches asymptotically an average value of $(k_1)_{avg}$; from analysis of CFRP jacketed concrete cylinder tests by Xiao and Wu (2000), $(k_1)_{avg} = 4.14$.

From considerations of volumetric strain effectiveness and experimental evidence, the following relationship is obtained for the plastic strain coefficient, k_{2p} (Moran and Pantelides 2002b):

$$k_{2p} = \frac{\Delta_{\varepsilon}}{\varepsilon_{co} K_{je} \mu_p} ; \quad \Delta_{\varepsilon} = \frac{\varepsilon_{\theta p} - k_b \varepsilon_{\theta o}}{\varepsilon_{\theta p}} ; \quad \mu_p = \left| \frac{d\varepsilon_{\theta}}{d\varepsilon_c} \right|_p ; \quad \mu_p = \frac{4.635}{\left(K_{je}\right)^{2/3}} \tag{7}$$

in which $k_b = 2.36$, and μ_p is the asymptotic plastic dilation rate in the range $0.5\ \varepsilon_{\theta u} \leq \varepsilon_{\theta p} \leq \varepsilon_{\theta u}$. In an FRP confined concrete member, compressive failure will occur simultaneously with failure of the FRP jacket. This failure occurs at an ultimate radial FRP jacket strain, $\varepsilon_{\theta u}$ that may be below the rupture strain of FRP composite tensile coupon tests. Premature failure of the FRP jacket can occur as a result of interaction between the axial shortening and radial dilation which induces a biaxial state of stress and strain in the FRP jacket, i.e. axial compression and radial tension, in addition to stress concentrations at the jacket-to-concrete interface that occur as dilation of the FRP confined concrete core progresses. By considering equilibrium and strain compatibility, the stress-strain model of Equation (6) can be expressed at the ultimate radial strain as (Moran and Pantelides 2002a):

$$\varepsilon_{cu} = \varepsilon_{co}\left(1 + \frac{\Delta\theta_u}{\mu_p}\right) \; ; \qquad \Delta\theta_u = \frac{\varepsilon_{\theta u} - k_b \varepsilon_{\theta o}}{\varepsilon_{co}} ; \qquad f_{cu} = f_{co}\left(1 + (k_1)_{avg} K_{je} \varepsilon_{\theta u}\right) \tag{8}$$

A conservative estimate for the ultimate radial strain in the FRP jacket, for carbon FRP ($\varepsilon_{\theta u}$ = 8.5 mm/m), or glass FRP ($\varepsilon_{\theta u}$ = 12.5 mm/m) can be used. For a given FRP thickness, the asymptotic plastic dilation rate, μ_p, can be determined from Equation (7); substitution into Equation (8) gives the ultimate axial compressive strain, ε_{cu}, and the ultimate compressive stress, f_{cu}. It can be shown that the present model is less conservative than strength-based design methods. It is clear that the process can be reversed, as is desirable in performance based design, i.e. for a required ductility, the design ultimate compressive strain can be obtained, and from Equation (8) the required thickness of the FRP composite can be determined. The axial compressive strength of confined columns with FRP composites can be increased by a factor of 2.0 or more, which is significant in gravity load collapse prevention.

4. BOND AND ANCHORAGE RETROFIT

The ductility of structural systems built before current code provisions is limited by bond or anchorage failure of RC elements. Examples include inadequately anchored bottom bars of exterior and interior beam-column building joints, and the longitudinal steel bars terminating prematurely in unconfined bent cap-column joints of bridge bents. Performance-based evaluation of exterior RC building joints has been carried out (Hakuto et al. 2000, Pantelides et al. 2002a, 2002c). In the case of building joints, anchorage of the bottom steel bars, which terminated only 125 mm into the joint and left a 150 mm gap between them, as shown in Figure 6, can be improved by externally bonding a sufficient length and width of FRP strips, as in Figure 7; two layers of FRP were used that were applied in two steps. The capacity of the as-built unit was controlled by the pullout of the discontinuous bottom beam reinforcement, as shown in Figure 6. The FRP composite retrofit scheme was designed to overcome this shortcoming and further increase the ductility of the joint; this was achieved, using FRP composites in addition to those shown in Figure 7; the FRP composite strips in Figure 7 reached high tensile strains, thus reducing the tensile strain demand on the internal steel bars. The retrofit performed very well, by improving joint ductility and reaching a drift ratio of 8%, as shown in Figure 8(b).

Similarly, in bridge T-joints, a U-strap starting at one column face below the bent cap soffit, continuing over the bent cap and ending on the opposite column face, as shown in Figure 9(b), improves anchorage of the column steel terminating in the joint. The RC bridge bent was built in the 1960's and was tested in-situ, as shown in Figure 9(a), after a carbon FRP seismic retrofit was implemented (Pantelides et al. 2002b). The longitudinal column steel in the T-joint was terminated 310 mm below the top of the bent cap, as shown in Figure 9(a); no confining steel

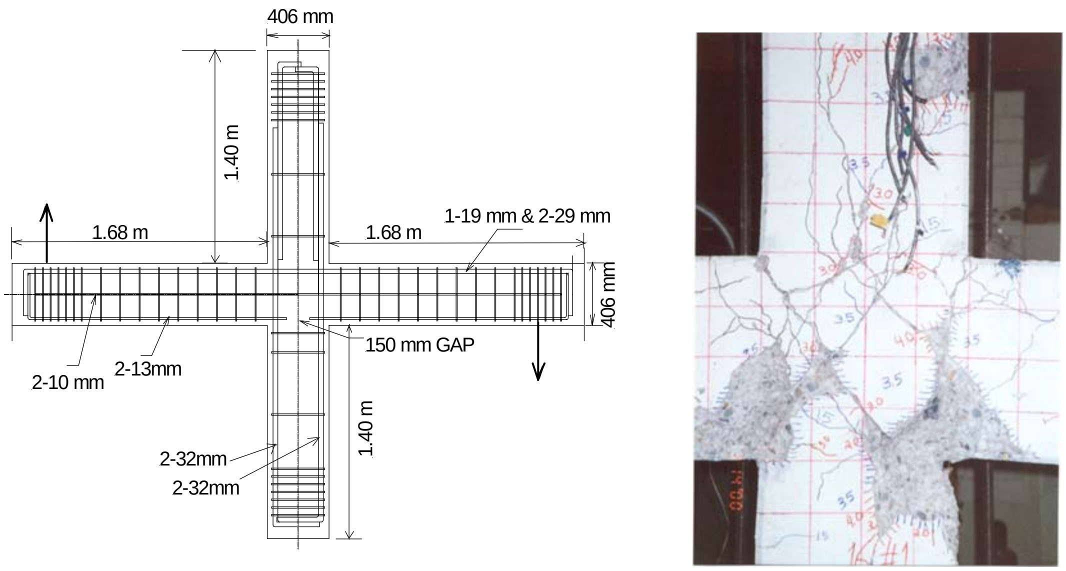

Figure 6. Interior RC building joint with insufficient embedment of the bottom steel bars and bond failure of bottom bars

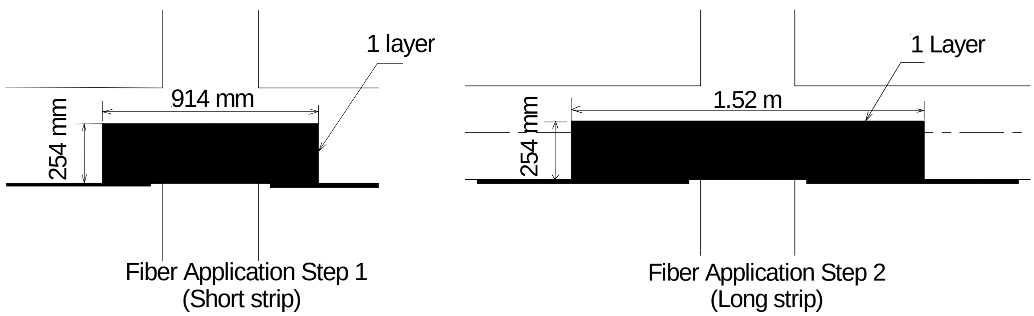

Figure 7. FRP composite retrofit to prevention bond failure of interior RC building joint

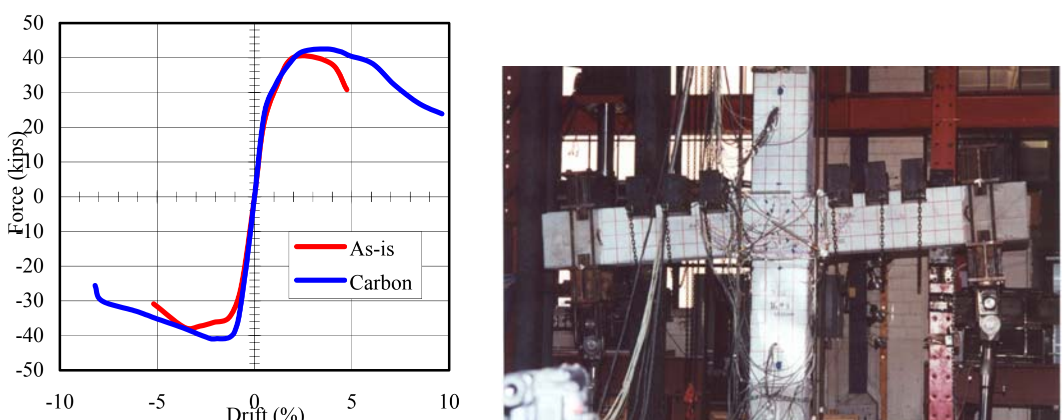

(a) (b)

Figure 8. Building joint performance with FRP composite retrofit: (a) hysteresis envelope comparison with as-built joint, (b) joint at high drift levels

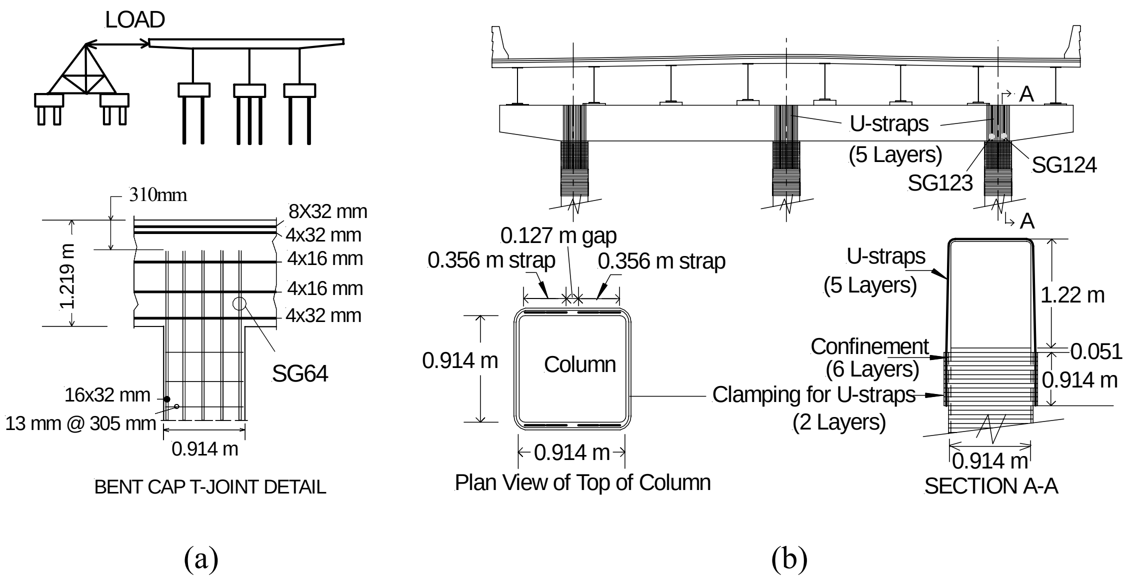

Figure 9. Bridge: (a) Test setup and longitudinal column steel, (b) carbon FRP U-straps

was provided in the joint, which violates current code requirements. The longitudinal steel is vulnerable to loss of anchorage and debonding at low drift ratios; however, the carbon FRP U-straps acted as "external anchorage", and allowed the longitudinal column steel to yield, and remain bonded to the concrete, as shown in Figure 10(a). The carbon FRP U-straps reached their maximum strain at a drift ratio of 4%, as shown in Figure 10(b), and ruptured which then caused the longitudinal steel to debond. The rupture of the carbon FRP U-straps, was the point at which the maximum lateral load capacity of the bridge bent was achieved.

5. LAP SPLICE RETROFIT

Lap splices in the new AASHTO seismic provisions are permitted only within the center half of the column height and the splice length can not be less than 60 bar diameters; in the bridge bent tested, the splice was in the plastic hinge region at the bottom of the column, and the splice length was only 24 bar diameters, as shown in Figure 11(a); in addition, the requirement for spacing of transverse reinforcement in the splice region of 100 mm was violated since the spacing of the ties was 305 mm. The steel ties also violated the AASHTO requirements of a closed tie with 135-degree hooks having a 75 mm extension at each end. The recorded maximum tensile steel strains, at the base of the columns in the splice region, for the retrofitted bent were significantly less than those of a bent tested without FRP composites.

Comparisons between the as-built and retrofitted bent indicate that there was a reduction in the tensile demand applied to the lap splice bars of the retrofitted column due to the additional confinement clamping of the carbon FRP composite 14 layers (14L), as shown in Figure 11(b), which picked up a significant strain thus reducing the demand on the spliced bars. The 14 carbon FRP confinement layers provided additional clamping capacity to the lap splice, they added additional flexural stiffness to the lap splice top region, and caused the plastic hinge to transfer above the lap splice elevation. The condition of the splice, which eventually failed at 5.5% drift, is shown in Figure 12(b), which also shows the rupture of the carbon FRP U-straps at the T-joint of the west column. The condition of the retrofitted bridge at 6.8% drift, at which the lateral load capacity dropped by 47% is shown in Figure 12(a).

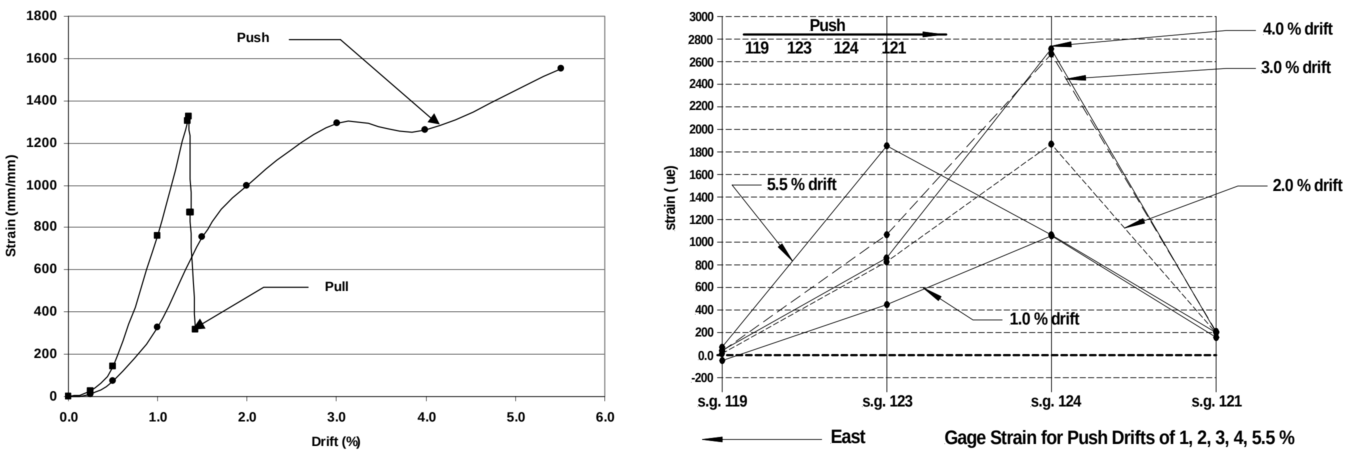

(a) (b)

Figure 10. Strains as function of drift ratio: (a) longitudinal column steel (SG64), (b) carbon FRP U-straps (SG123, SG124)

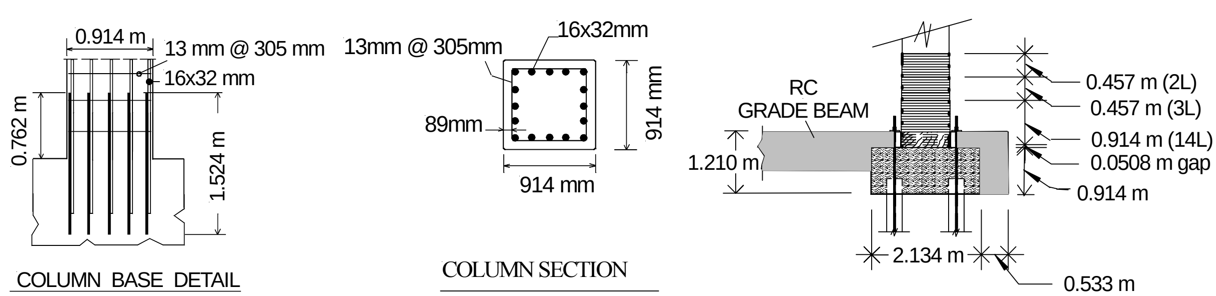

(a) (b)

Figure 11. Lap splice: (a) steel details, (b) carbon FRP U-strap retrofit

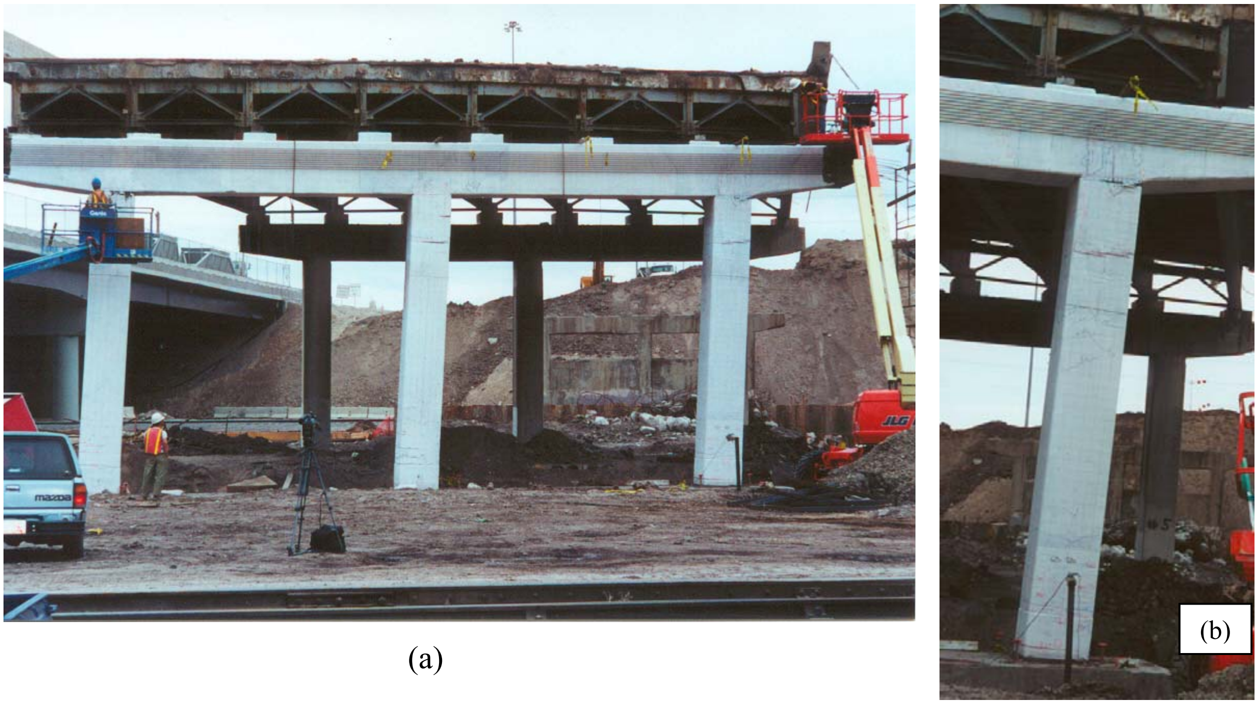

(a) (b)

Figure 12. In-situ bridge test: (a) Ductile performance at 6.8% drift, (b) failure of FRP U-straps and lap splice of column steel bars

6. CONCLUSIONS

Shear transfer units reinforced with CFRP composites increased shear capacity by a factor from 1.32 to 3.25 times compared to the as-is concrete units, with an upper bound for shear capacity of $0.27 f_c^{'}$. An analytical model for representing the compressive behavior of concrete columns confined using FRP composite jackets was developed. The distinguishing feature of the analytical model is that the plastic behavior of the FRP-confined concrete is represented by an experimentally derived variable strain ductility ratio, which defines the increase in plastic axial compressive strain versus the increase in plastic axial compressive strength of the FRP-confined concrete. An expression was obtained for predicting the ultimate compressive strength and strain of FRP-confined concrete based on equilibrium. The model can be used for seismic retrofit design using performance-based criteria for improving the displacement ductility of existing RC columns. Bond of steel reinforcement and anchorage can be improved using FRP composites, as demonstrated here for interior building joints, and bridge T-joints. In addition, FRP composites are effective in clamping lap spliced bars that are not confined at the base of the column.

Using seismic retrofit techniques with FRP composites, it is possible to upgrade the performance of RC building components with non-ductile details. Moreover, confinement along the whole length of the columns could prevent catastrophic collapse due to loss of vertical load carrying capacity, since the axial compressive strength of confined columns with FRP composites can be increased by a factor of 2.0 or more. Future experimental investigations should be aimed at verifying the ability of FRP composites, designed using performance-based design criteria, to seismically retrofit existing or rehabilitate damaged RC building systems for gravity load collapse prevention.

7. ACKNOWLEDGMENTS

This work was supported by the National Science Foundation, the Pacific Earthquake Engineering Research Center, the Federal Highway Administration, the Idaho National Engineering and Environmental Laboratory, and the Utah Department of Transportation. The author would like to acknowledge Professor Lawrence D. Reaveley of the University of Utah, for his assistance in the experimental investigations referenced in this paper and for helpful discussions. Nicolas Saenz, Domingo Moran, Yasuteru Okahashi, Ph.D. candidates, and Jeffrey Duffin, Jon Hansen, Chandra Clyde, and Justin Nadauld, M.Sc., at the University of Utah, contributed to studies referenced in this paper. Any opinions, findings and conclusions or recommendations are those of the author.

8. REFERENCES

American Concrete Institute Committee 440. (2002). *Guide for the design and construction of externally bonded FRP systems for strengthening concrete structures.* Farmington Hills, Michigan.

Birkeland, P. W., and H. W., Birkeland. (1966). Connections in precast concrete construction. *ACI Journal Proceedings*, Vol. 63, No. 3, March, 345-368.

Hakuto, S., R. Park, and H. Tanaka. (2000). Seismic load tests on interior and exterior beam-column joints with substandard reinforcing details. *ACI Structural Journal*, 97(1), 11-25.

Kahn, F. L., and A. D. Mitchell. (2002). Shear friction tests with high-strength concrete. *ACI Structural Journal*, Vol. 99, No. 1, January-February, 98-103.

Mast, R. F. (1968). Auxiliary reinforcement in precast concrete connections. *Journal of Structural Division*, ASCE, Vol. 94, No. ST6, 1485-1504.

Mander, J.B., M.J.N. Priestley, and R. Park. (1988). Theoretical stress-strain model for confined concrete. *Journal of Structural Engineering,* ASCE*,* 114(8), 1804-1826.

Mattock, A.H., and N. M. Hawkins. (1972). Shear transfer in reinforced concrete-recent research. *PCI Journal*, Vol. 17, No. 2, March-April, 55-75.

Mattock, A. H. (2001). Shear friction and high-strength concrete. *ACI Structural Journal*, Vol. 98, No. 1. January-February, 50-59.

Moran, D.A., and C.P. Pantelides. (2002a). Stress-strain model for fiber-reinforced polymer-confined concrete. *Journal of Composites for Construction*, ASCE, 6(4), 233-240.

Moran, D.A., and C.P. Pantelides. (2002b). Variable strain ductility ratio for fiber-reinforced polymer-confined concrete. *Journal of Composites for Construction*, ASCE, 6(4), 224-232.

Pantazopoulou, S. J., and R.H., Mills. (1995). Microstructural aspects of the mechanical response of plain concrete. *ACI Materials Journal,* 92(6), 605-616.

Pantelides, C.P., J. Gergely, and L.D. Reaveley. (2001). In-situ verification of rehabilitation and repair of reinforced concrete bridge bents under simulated seismic loads. *Earthquake Spectra*, Earthquake Engineering Research Institute, 17(3), 507-530.

Pantelides, C.P., and J. Gergely (2002). Carbon-fiber-reinforced polymer seismic retrofit of RC bridge bent: design and in-situ validation. *J. of Composites for Construction*, ASCE, 6(1), 52-60.

Pantelides, C.P., J. Hansen, J. Nadauld, and L.D. Reaveley (2002a). Assessment of reinforced concrete building exterior joints with substandard details." *Report No. PEER-2002/18*, Pacific Earthquake Engineering Center, University of California, Berkeley, 103 pp.

Pantelides, C. P., J.B. Duffin, J. Ward, C. Delahunty, and L.D. Reaveley. (2002b). In-situ tests at South Temple Bridge on Interstate 15. *7th National Conference on Earthquake Engineering, 7NCEE,* Earthquake Engineering Research Institute, Oakland, California, July 21-25, 2002.

Pantelides, C.P., C. Clyde, and L.D., Reaveley. (2002c). Performance-based evaluation of reinforced concrete building exterior joints for seismic excitation. *Earthquake Spectra*, Earthquake Engineering Research Institute, 18(3), 449-480.

Ruiz, S.E., and H., Badillo. (2001). Performance-based design approach for seismic rehabilitation of buildings with displacement-dependent dissipators. *Earthquake Spectra*, Earthquake Engineering Research Institute, 17(3), 531-548.

Saenz, N., and C.P. Pantelides. (2003). Shear transfer for concrete with external carbon FRP strips: I-Experiments. *Journal of Structural Engineering*, ASCE, (under review).

Seible, F., M.J.N., Priestley, G. Hegemier, and D. Innamorato. (1997). Seismic retrofitting of RC columns with continuous carbon fiber jackets. *J. of Composites for Construction,* 1(2), 52-62.

Spoelstra, M.R., and G. Monti. (1999). FRP-confined concrete model. *J. of Composites for Construction,* ASCE, 3(3), 143-150.

Xiao, Y., and H. Wu. (2000). Compressive behavior of concrete confined by carbon fiber composite jackets. *J. Materials Civil Engineering*, ASCE, 12(2), 139-146.

Earthquake Resistant Performance of Reinforced Concrete Frame Strengthened by Multi-Story Steel Brace

KITAYAMA Kazuhiro [*1], KISHIDA Shinji [*2] and SATO Teruyoshi [*3]

ABSTRACT

Earthquake resistant performance in plane R/C frames strengthened by multi-story steel brace was investigated through the tests under cyclic load reversals focusing on the base uplift rotation of the brace and the entire flexural failure at the bottom of the brace caused by tensile yielding ofall longitudinal bars in a R/C edge column beside the brace. Two plane frame specimens with two-story and three-bay were tested placing multi-story steel brace at the central bay. Lateral resistance in base uplift rotation of a multi-story brace decreased gradually after flexural yielding at the end of boundary beams and the bottom of first story bare columns. Lateral strength measured in the specimen agreed well with that computed by taking account of restraining effect of both boundary and foundation beams on uplift rotation. For another specimen failed in entire flexure at the bottom of the brace, controlled by tensile yielding of all longitudinal bars in a R/C edge column beside a brace, lateral resistance diminished abruptly by concrete compressive crushing and fracture of column longitudinal bars at the bottom of both edge columns. Ultimate limit deformations in two specimens were underestimated by the computation considering deformation ability of neighboring beams and isolated multi-story steel brace. The amount of energy dissipation for entire flexural failure at the bottom of a brace was by 50 percent greater than that for base rotation failure. Earthquake resistant performance of strengthened R/C frames which is controlled by the entire flexural failure at the bottom of a multi-story steel brace is superior to that in the failure due to the brace uplift rotation within the range of the drift angle of 2 %.

1. INTRODUCTION

For seismic retrofit of existing reinforced concrete (R/C) buildings, steel braces enclosed by perimeter steel rims are often installed into moment resisting open frames. It is most desirable that the one of diagonal chords of steel braces yields in tension and the other buckles in compression under earthquake excitations. Unfortunately the base of a multi-story steel brace may be uplifted and rotate in some cases prior to the yielding or buckling of steel chords depending primarily on the aspect ratio of the span to the height. In other cases, the strength of a multi-story steel brace is attributed to entire flexural resistance in I-

*1 *Associate Professor, Graduate School of Engineering, Tokyo Metropolitan University, Dr. Eng.*
Email : kitak@ecomp.metro-u.ac.jp

*2 *Research Associate, Graduate School of Engineering, Tokyo Metropolitan University, Dr. Eng.*
Email : skishida@ecomp.metro-u.ac.jp

*3 *Graduate student, Tokyo Metropolitan University*
Email : te-ru@dc5.so-net.ne.jp

shaped section at the bottom of a unit bay consisting of a steel brace and R/C edge columns, which is induced by tensle yielding of all longitudinal bars in a R/C edge column (called as the failure of Type 3) before the full capacity of a steel brace can be developed.

In the paper, earthquake resistant performance of R/C frames strengthened by a multi-story steel brace, which were designed to develop uplift rotation of a base foundation beneath a multi-story steel brace or the failure of Type 3, was studied by static load reversal tests.

2. OUTLINE OF TEST

2.1 SPECIMENS

Reinforcement details and section dimensions are shown in **Fig. 1**. Two plane frame specimens with a quarter scale to actual buildings were tested which had three bays with each 1000 mm span length and two stories with the height of 800 mm, placing a multi-story steel brace at the central bay. Section dimensions of R/C beams and columns and steel brace were common for two spcimens except for the amount of longitudinal reinforcement of R/C edge columns beside a steel brace (denoted as Column 2 and 3 in **Fig. 1**).

The failure type of R/C central bay containing a multi-story steel brace was chosen as a test parameter. Specimen No.1 was designed to develop the rotation of base foundation due to the uplift of a multi-story steel brace. On the other hand, Specimen No.2 was designed to result in entire flexural failure at the bottom of a multi-story steel brace which is caused by both yielding of all longitudinal bars in a R/C tensile edge column and pull-out of anchorage bars connecting between horizontal steel rim of a brace and R/C foundation beam. The amount of longitudinal bars in edge columns beside the brace was reduced in Specimen No.2 comparing with those in Specimen No.1 in order to cause the failure of Type 3. Boundary beams and isolated columns were designed according to the weak-beam strong-column concept.

Cross section of a steel brace was a H-shape with 60 mm width and 60 mm depth, which was built by welding flat plates with 6 mm thickness. Details of connection between R/C member and steel rim are illustrated by **Fig. 2**. Anchorage bars of D10 were welded in a row to perimeter steel rims with the center-to-center spacing of 60 mm. Although non-shrinkage mortar is injected between steel rims and R/C members to unify each other for actual practice, mortar injection was omitted in construction of specimens by casting concrete in the state that steel braces were placed at proper position with reinforcement

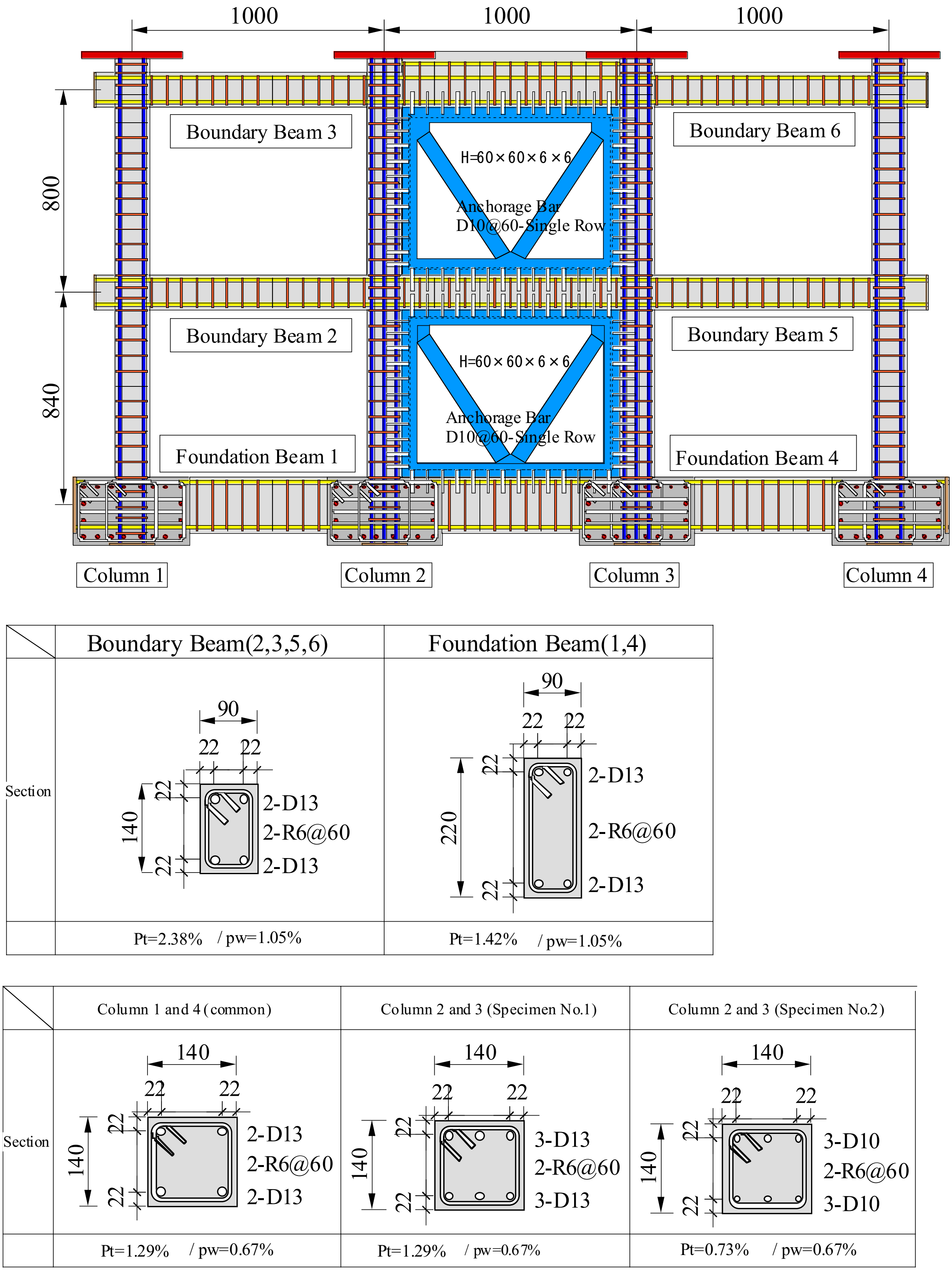

Fig. 1 Reinforcement details and section dimensions

Table 1 Material properties of steel and concrete

(a) Steel

	Bar size	Yield strength MPa	Young's modulus GPa	Yield strain %
Longitudinal bar in edge column	*D13	336.1	180	0.187
	**D10	367.8	185	0.199
Longitudinal bar in bare column	D13	429.1	179	0.239
Beam longitudinal bar	D13	345.6	184	0.188
Anchorage bar	D10	383.2	188	0.204
Shear reinforcing bar	R6	588.7	207	0.284
Steel brace	flat bar	435.3	208	0.209

* : Specimen No.1 , ** : Specimen No.2

(b)Concrete

Specimen	Compressive strength MPa	Strain at compressive strength %	Secant modulus GPa	Tensile strength MPa
No.1	28.9	0.195	30.5	1.97
No.2	30.3	0.216	28.0	2.43

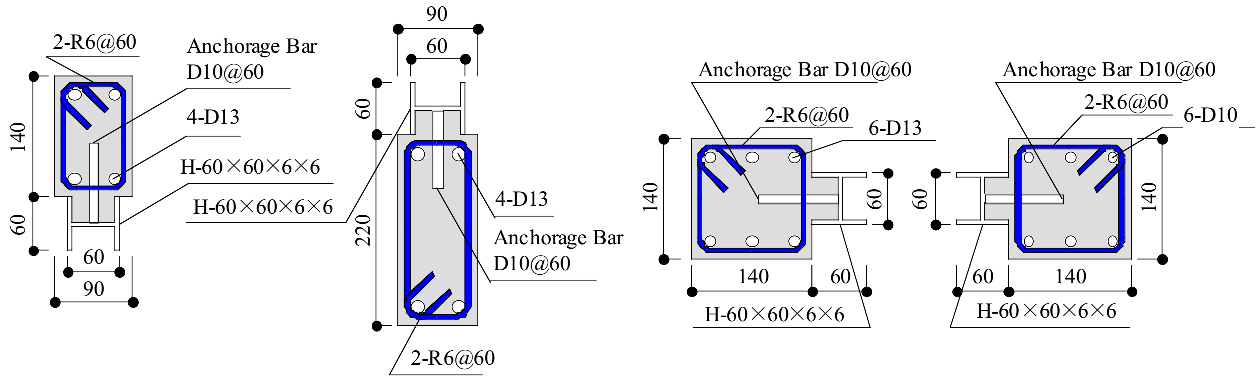

(a) Beam (b) Foundation Beam (c) Column of Specimen No.1 (d) Column of Specimen No.2

Fig. 2 Details of connection between R/C members and steel rim

cages of beams and columns. Concrete was cast in the horizontal position using metal casting form. Material properties of concrete and steel are listed in **Table 1**. Concrete compressive strength was 30 MPa approximately by cylinder tests.

2.2 LOADING METHOD AND INSTRUMENTATION

The loading system is shown in **Fig. 3**. Top lateral force was applied alone at the center of the specimen by two oil jacks. Each column axial load was kept constant, i.e., 40 kN to isolated columns and 80 kN to edge columns beside a steel brace respectively. Four footings of Specimen No.2 were fixed to R/C reaction floor by PC tendons. For Specimen No.1 designed to cause the uplift of a multi-story steel brace, on the other hand, two footings under the steel brace were not connected to the floor, but lateral reaction force was supported through round steel bar inserted between R/C footing subjected to axial compression and steel reaction plate settled on reaction floor. This testing method was accepted by referring to the study carried out by Kato [1].

Specimen was controlled by the drift angle for one cycle of 0.25 %, two cycles of 0.5 %, 1 % and 2 % respectively and one cycle of 4 %. The drift angle is defined as the horizontal

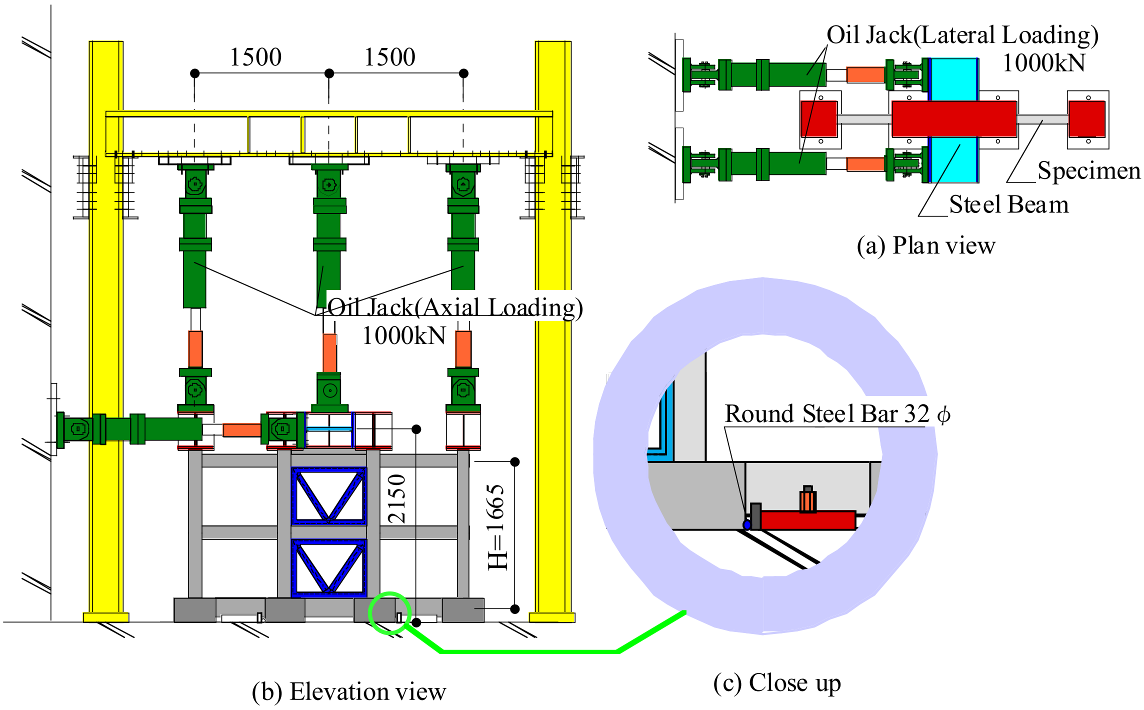

Fig. 3 Loading apparatus

displacement at the center of a top floor beam divided by the height between the center of a foundation beam and a top floor beam, i.e., 1665 mm.

Lateral force and column axial load were measured by load-cells. Horizontal displacement at load applying point and at the center of top and second floor beams, local rotation in a plastic hinge region of beams and columns, and vertical displacement of footings due to uplift of a steel brace were measured by displacement transducers. Strains of beam and column longitudinal bars, vertical and diagonal steel chords of a brace and anchorage bars at the bottom of a first-story steel brace were measured by strain gauges.

3. TEST RESULTS

3.1 PROCESS TO FAILURE AND STORY SHEAR - DRIFT RELATIONS

Crack patterns at the end of test are shown in **Fig. 4** and **Photo. 1**. Story shear force - drift angle relations are shown in **Fig. 5** for cyclic load reversals and **Fig. 6** as an envelope curve in positive loading illustrating successive phenomena occurred in the specimen. Story shear force in this paper is defined as the horizontal force applied by oil jacks corrected for the P-Delta effect resulted from column axial load.

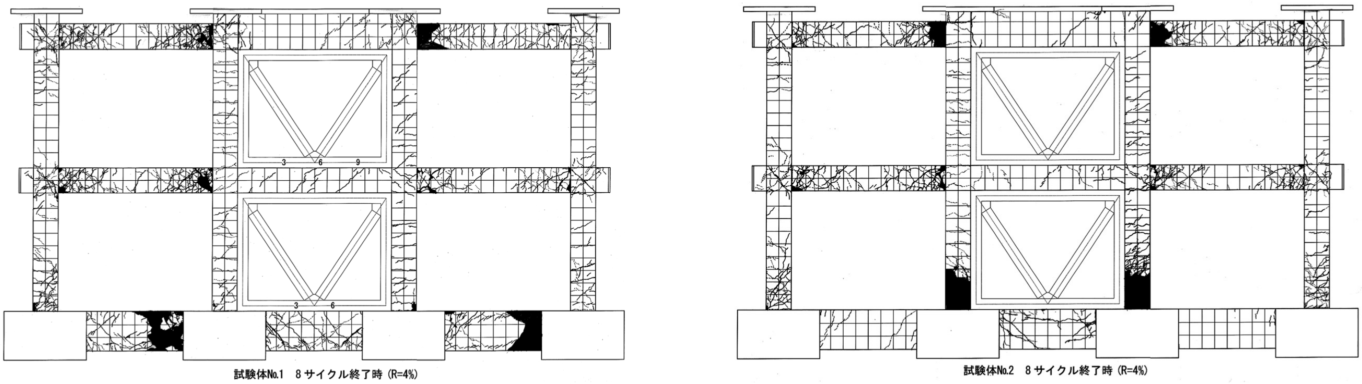

(a) Specimen No.1　　　　(b) Specimen No.2

Fig. 4 Crack patterns at end of test

(a) Specimen No.1　　　　(b) Specimen No.2

Photo. 1 Failure of specimens

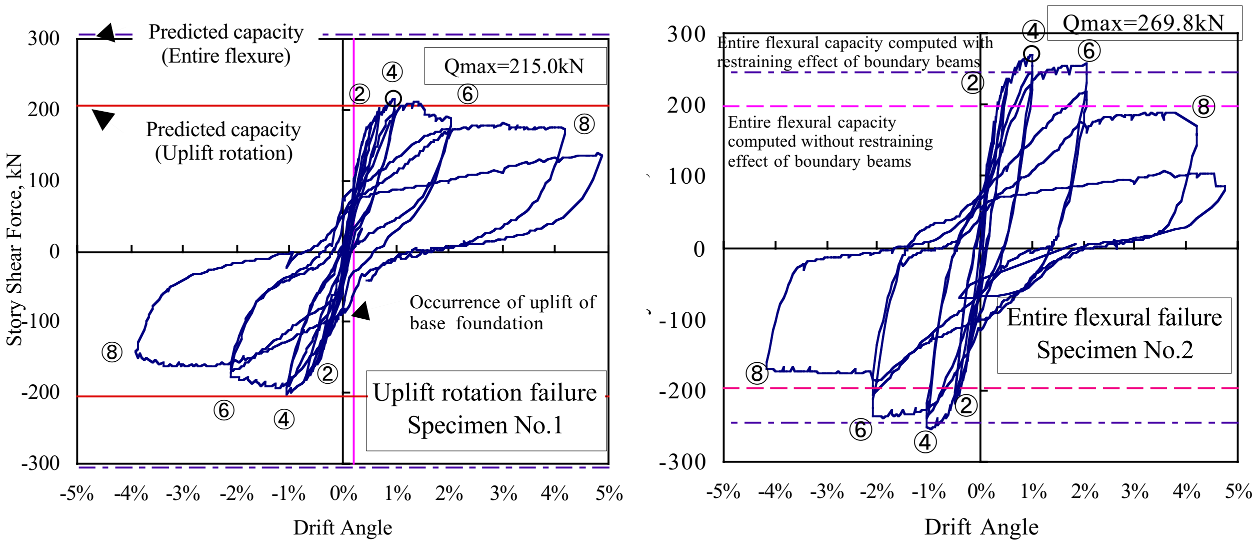

(a) Specimen No.1　　　　(b) Specimen No.2

Fig. 5 Story shear force- drift angle relations

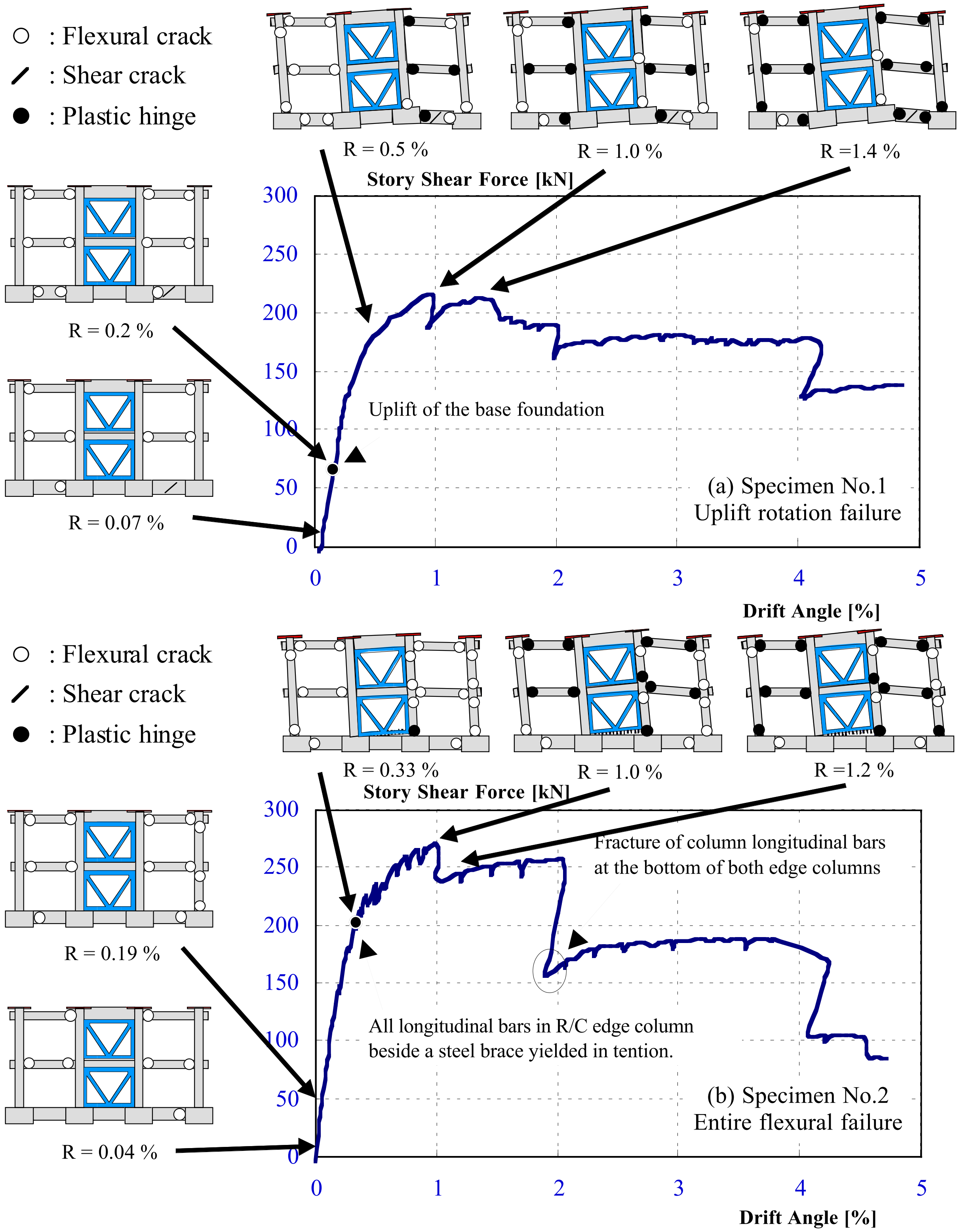

Fig. 6 Envelope curves of story shear force - drift angle relation

(a) Specimen No.1

Uplift of the base foundation under a multi-story steel brace occurred at the drift angle of 0.2 %. Collapse mechanism was formed at the drift angle of 1.4 %, developing flexural yielding at the end of boundary beams and the bottom of first story bare columns. Lateral resistance capacity decayed gradually due to concrete compressive failure at these hinge

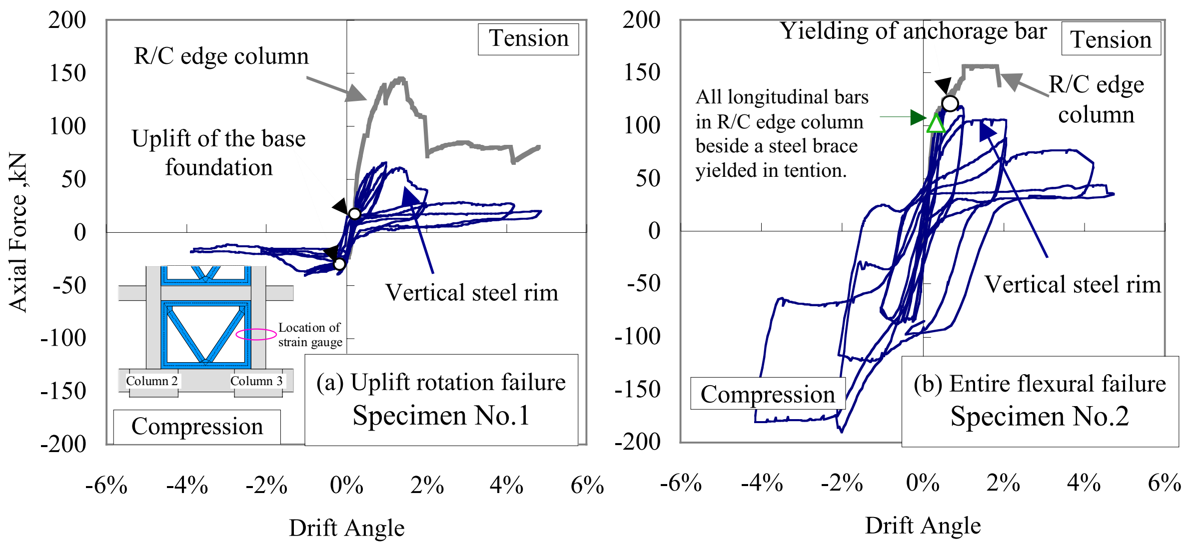

Fig. 7 Axial force acting on vertical steel rim and R/C edge column

regions after attaining the peak strength of 215.0 kN at the drift angle of 1 %. Obvious stiffness degradation caused by both base uplift and concrete crushing at hinge regions was observed after sixth loading cycle at the drift angle of 2 % as shown in **Fig. 5 (a)**. Hysteresis loops showed a little pinching shape comparing with those for Specimen No.2.

(b) Specimen No.2

All longitudinal bars in R/C edge column beside a steel brace yielded in tension at the drift angle of 0.3 %. Lateral force resistance reached the maximum capacity of 269.8 kN at the drift angle of 1 %, forming plastic hinges at all boundary beam ends and cracking horizontally at the gap between horizontal steel rim and R/C foundation beam due to pull-out of anchorage bars. Hereafter lateral resistance diminished abruptly by the concrete crushing and the fracture of column longitudinal bars at the bottom of both edge columns at the drift angle of 2 % in eighth loading cycle. Hysteresis loops showed a stable spindle shape until the drift angle of 2 %.

3.2 AXIAL FORCE ACTING ON VERTICAL STEEL RIM AND R/C EDGE COLUMN

Axial force acting on vertical steel rim of the brace, which was computed from measured strain at the mid-height in a first story brace, is shown in **Fig. 7**. Vertical steel rims did not yield for both specimens. Tensile axial force induced in R/C edge column beside a brace which was computed by measured strain of longitudinal bars at the mid-height of a first-story edge column is also shown in **Fig. 7**. In Specimen No.2, failed in entire flexure at the bottom of a multi-story steel brace, tensile axial force of vertical steel rim increased even after all longitudinal bars yielded at the bottom of R/C edge column, and attained the peak force with the yielding of anchorage bars at the bottom of the brace. The peak tensile force

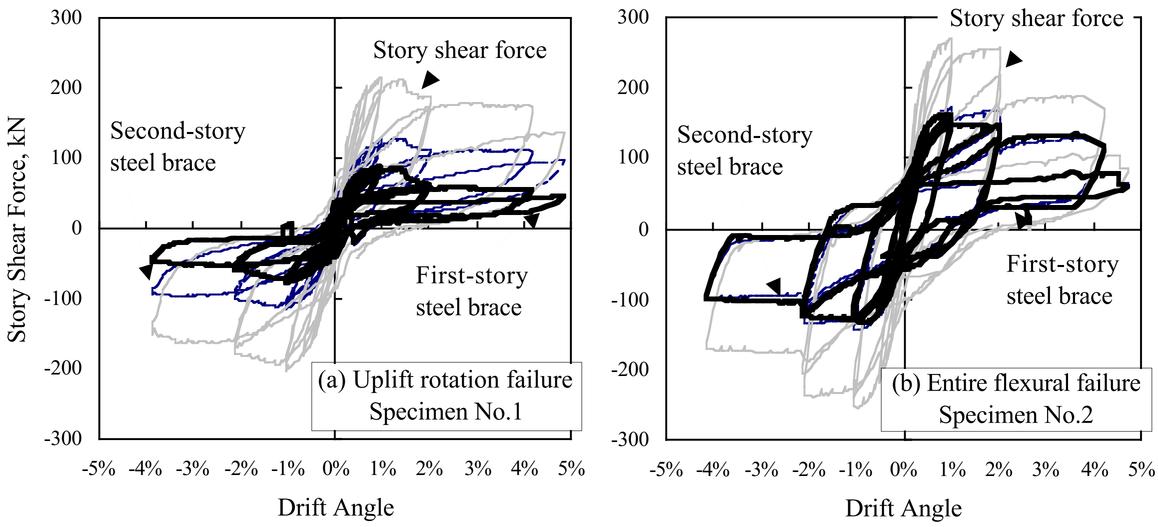

Fig. 8 Horizontal shear force resisted by steel brace

of vertical steel rim was three-quarters times that of axial force in R/C edge column at the drift angle of 1 %. Therefore it is important to take account of the contribution of vertical steel rim to entire flexural resistance at the bottom of a multi-story steel brace in addition to the longitudinal column bars.

3.3 HORIZONTAL SHEAR FORCE RESISTED BY STEEL BRACE

Shear force resisted by a steel brace can be obtained as horizontal component of axial force in diagonal steel chords subjected to tension and compression, which was computed from measured strain at these chords, and is shown in **Fig. 8**. Thick or thin solid lines represent the lateral shear component of first- or second-story steel brace respectively. Lateral resistance of the first-story steel brace in Specimen No.1, failed by uplift rotation of a multi-story steel brace, was by 30 percent smaller than that of the second-story steel brace since lateral force applied at the top of a multi-story steel brace was carried to the ground through neighboring beams and columns escaping from a steel brace. On the contrary, lateral resistance of the first-story steel brace in Specimen No.2, failed in entire flexure at the bottom of a multi-story steel brace, was almost equal to that of the second-story steel brace. The ratio of shear force shared by a first-story steel brace to entire lateral resistance of the specimen was 38 % for Specimen No.1 and 60 % for Specimen No.2.

3.4 TENSILE STRESS OF ANCHORAGE BAR

Tensile stress of anchorage bars connecting the bottom of steel rim of a multi-story steel brace with a foundation beam for Specimen No.2 is shown in **Fig. 9**. Tensile stress of the closest anchorage bar to a R/C edge column reached the yield stress and decreased after the

Table 2 Measured and computed lateral strength of specimens

Specimen	Measured Strength (kN)	Computed Strength (kN)				Ratio of computed to measured strength
		Yielding of diagonal chord in brace	Type 3[*] failure	Type 3[**] failure	Brace base rotation failure	
No.1	215.0	490.1	256.9	305.1	205.1	0.95
No.2	269.8	468.3	198.0	246.2	–	[*] 0.73 [**] 0.91

[*] , [**] : Computed lateral strength of Type 3 failure without or with consideration of restraining effect by boundary beams respectively

drift angle of 0.76 % due to pull-out of the bar caused by the entire flexural resistance. Tensile stress of second and third anchorage bars denoted as A2 and A3 reached peak stress prior to yielding because horizontal crack occurred in the foundation beam, crossing these anchorage bars and pull-out force was reduced.

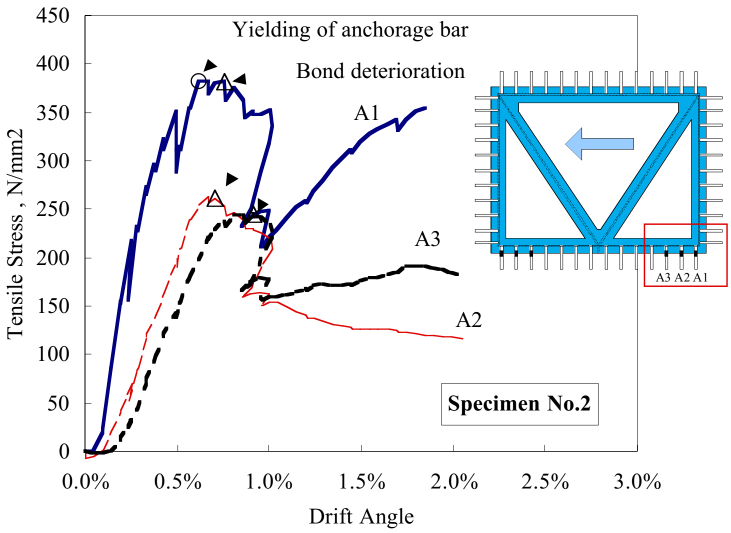

Fig. 9 Tensile stress of anchorage bars

4. DISCUSSIONS

4.1 LATERAL STRENGTH

Lateral strength Q_{max} obtained by the test is compared with the computed strength Q_{cal} by Eq.(1) and listed in **Table 2**.

$$Q_{cal} = Q_{c1} + Q_{c4} + Q_{Bf} \qquad (1)$$

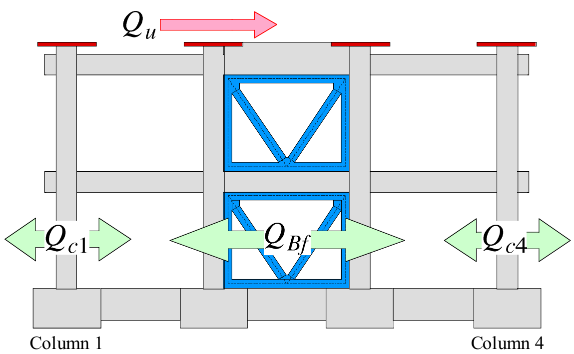

Fig. 10 Lateral resisntance of frame

where Q_{c1} and Q_{c4} : lateral strength of a R/C isolated column (i.e., Column 1 and Column 4 in **Fig. 10**) computed by Eq.(2) since shear strength was greater than flexural strength for both columns.

$$Q_{c1}, Q_{c4} = \frac{2M_{cu}}{h} \qquad (2)$$

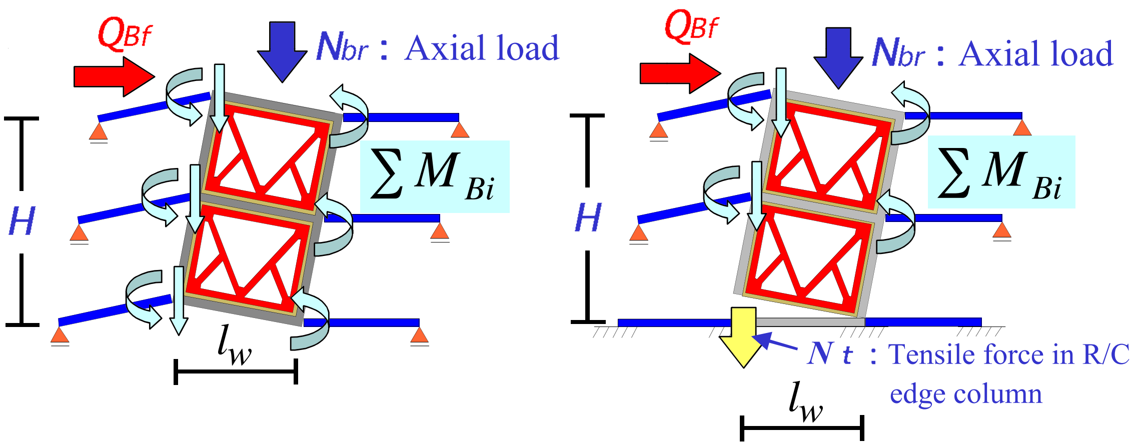

(a) Uplift rotation failure (b) Entire flexural failure

Fig. 11 Lateral shear resistance of R/C unit frame with multi-story steel brace

where h : clear height of the column and M_{cu} : ultimate bending moment at column critical section which can be computed by Eq.(3).

$$M_{cu} = 0.8a_t \cdot \sigma_y \cdot D + 0.5N_{col} \cdot D\left(1 - \frac{N_{col}}{bD \cdot \sigma_B}\right) \qquad (3)$$

where a_t , σ_y : sectional area and yield strength of tensile longitudinal reinforcement in the column, D : column depth, N_{col} : column axial load, b : column width and σ_B : concrete compressive strength.

Q_{Bf} : lateral shear resistance shared by the R/C central bay containing a multi-story steel brace which can be computed by Eq.(4) as illustrated in **Fig. 11**.

For uplift rotation failure,
$$Q_{Bf} = \frac{0.5N_{br} \cdot l_w + \sum_i M_{Bi}}{H} \qquad (4.a)$$

For entire flexural failure (i.e., Type 3),
$$Q_{Bf} = \frac{a_t \cdot \sigma_y \cdot l_w + 0.5N_{br} \cdot l_w + \sum_i M_{Bi}}{H} \qquad (4.b)$$

where a_t , σ_y : sectional area and yield strength of tensile longitudinal reinforcement of edge column beside a steel brace, N_{br} : compressive axial load imposed at the center of a steel brace, l_w : center-to-center distance between R/C edge columns beside a steel brace, $\sum_i M_{Bi}$: sum of the flexural yielding moment of boundary beams framing into a multi-story steel brace, including the restraining moment due to shear force of boundary beams framing into uplift edge column, and H : height between the center of a foundation beam and a top floor beam (1665 mm). It is assumed for Eq.(4) that concentrated roof-level load was applied to the R/C central bay containing a multi-story steel brace.

Lateral strength measured in Specimen No.1 agreed well with that computed by taking account of restraining effect of both boundary and foundation beams on uplift rotation.

For Specimen No.2, predicted lateral strength of 198.0 kN without consideration of restraining effect by boundary beams, i.e., lateral shear strength obtained by extracting the term of $\sum_i M_{Bi}$ from Eq.(4.b), was almost equal to measured resistance when all longitudinal bars yielded in a tensile edge column. In the test lateral resistance increased and attained the peak strength with the formation of beam hinge mechanism. Therefore lateral strength for entire flexural failure at the bottom of a multi-story steel brace was computed by Eq.(4.b) and it was 91 percent of measured lateral strength. It seems that contribution of the vertical steel rim to entire flexural resistance at the bottom of a brace may be considered to the extent that anchorage of a steel brace to R/C foundation beam is effective to carry tensile axial force in vertical steel rim to the foundation.

4.2 CONTRIBUTION TO LATERAL RESISTANCE

Contribution of a multi-story steel brace and isolated R/C columns to lateral resistance of specimens is shown in **Fig. 12**. Shear force resisted by the R/C central bay containing a multi-story steel brace, Q_{Bf}, was computed by the same manner as Eq.(4) using measured strains of longitudinal bars in boundary beams and edge columns for each peak in loading cycles. For Specimen No.2, pull-out resultant force of three anchorage bars at the bottom of a multi-story brace was regarded as effective on entire flexural resistance cooperating with tensile force in a R/C edge column, and was added to right-hand side of Eq.(4.b). Shear resistance of isolated R/C columns, $Q_{c1} + Q_{c4}$, was calculated as follows ;

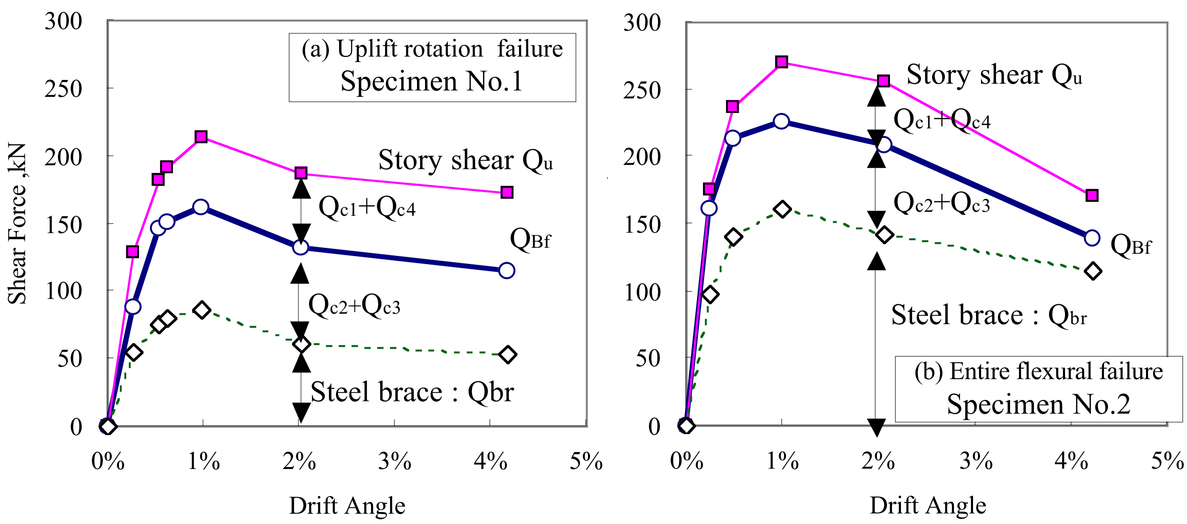

Fig. 12 Contribution to lateral resistance

$$Q_{c1} + Q_{c4} = Q_u - Q_{Bf} \qquad (5)$$

where Q_u : measured story shear force. Lateral shear force, Q_{Br}, shared by diagonal steel chords in the first-story brace, obtained in Chapter 3.3, is also shown in **Fig. 12**.

Shear force resisted by isolated R/C columns, $Q_{c1} + Q_{c4}$, was almost same for both specimens at the drift angle of 2 %, developing flexural yielding capacity of those columns. This means that the computation method for shear force resisted by a central bay, Q_{Bf}, is roughly adequate. The difference between Q_{Bf} and Q_{Br}, which is shown as $Q_{c2} + Q_{c3}$ in **Fig. 12**, indicates shear force shared by two R/C edge columns beside a brace. For Specimen No.2, failed in entire flexure at the bottom of a brace, $Q_{c2} + Q_{c3}$ was greater than $Q_{c1} + Q_{c4}$ because lateral force was carried through punching shear in the edge column subjected to compression.

4.3 DEFORMATION PERFORMANCE

Standard for evaluation of seismic capacity of existing R/C buildings [2] was revised in 2001 in Japan. Deformation ability for a multi-story steel brace which fails by uplift rotation of the base or entire flexural yielding at the bottom of a brace (i.e., Type 3 failure) can be estimated according to this standard. Deformation ability is expressed by the ductility index denoted as F which is a function of the ductility factor as follows ;

$$F = \frac{\sqrt{2R_{mu}/R_y - 1}}{0.75\left(1 + 0.05R_{mu}/R_y\right)} \qquad (6)$$

where R_{mu} : ultimate story drift angle of R/C members and R_y : yielding story drift angle assumed to be 0.67 %.

The F index for a multi-story steel brace with boundary beams is computed by Eq.(7).

$$F = {}_wq \cdot {}_wF + \Sigma\left({}_bq \cdot {}_bF\right) \qquad (7)$$

where, ${}_wF$, ${}_bF$: ductility index for an isolated steel brace and a R/C boundary beam respectively which can be estimated by Eqs.(8) and (9);

for uplift rotation failure, ${}_wF = 3.0$ (8.a)
for entire flexural failure (Type 3), ${}_wF = 2.0$ (8.b)

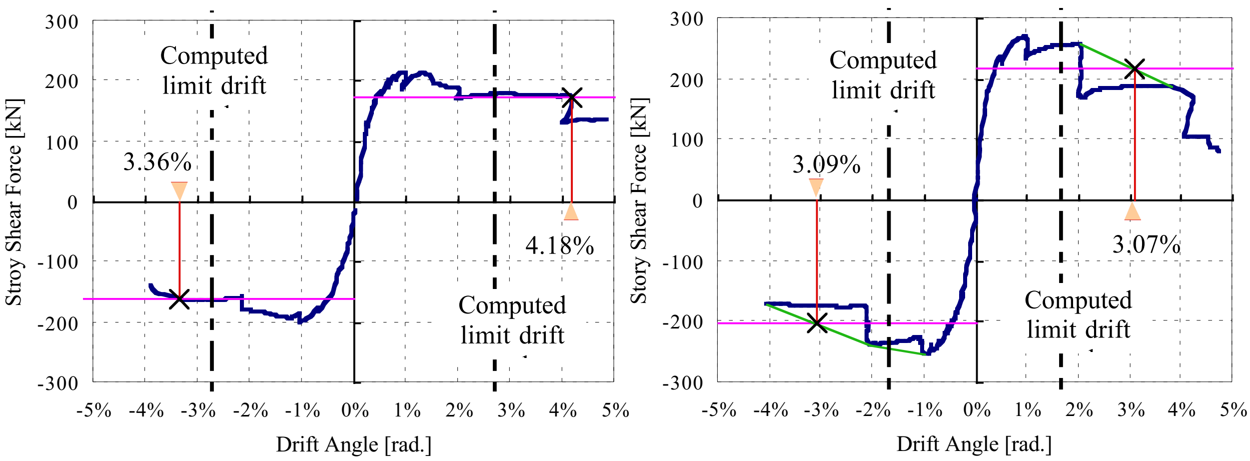

(a) Specimen No.1 (b) Specimen No.2

Fig. 13 Ultimate limit drift angle obtained in test and computation

if ${}_bQ_{su} / {}_bQ_{mu} \le 0.9$, ${}_bF = 1.27$ (9.a)

if ${}_bQ_{su} / {}_bQ_{mu} \ge 1.3$, ${}_bF = 3.5$ (9.b)

if $0.9 \le {}_bQ_{su} / {}_bQ_{mu} \le 1.3$, the ${}_bF$ index shall be computed by the linear interpolation between Eq.(9.a) and Eq.(9.b), where ${}_bQ_{su}$, ${}_bQ_{mu}$: ultimate shear and flexural strength of a boundary beam respectively.

Table 3 Ductility index and ultimate limit drift angle

	R : Limit Drift Angle	Specimen No.1 Positive Loading	Specimen No.1 Negative Loading	Specimen No.2 Positive Loading	Specimen No.2 Negative Loading
Test Result	R	4.18%	3.36%	3.07%	3.09%
	R(average)	3.77%		3.08%	
Computed Result	F index	2.96		2.38	
	R	2.70%		1.68%	

$$ {}_wq = \frac{{}_wM}{{}_wM + \Sigma {}_bM} \quad (10.a) $$

$$ {}_bq = \frac{{}_bM}{{}_wM + \Sigma {}_bM} \quad (10.b) $$

where ${}_wM$: brace contribution to ultimate resisting moment at the height where the lateral strength of a multi-story steel brace was decided and ${}_bM$: ultimate resisting moment of a boundary beam framing into a multi-story steel brace.

The F index taken as explained above was 2.96 for Specimen No.1 and 2.38 for Specimen No.2 as listed in **Table 3**. These values correspond to the drift angle of 2.70 % and 1.68 % respectively, which were converted through Eq.(6).

On the other hand, ultimate limit drift angle was obtained in the test as shown in **Fig. 13** which is defined as the drift angle when the lateral resistance descended to 80 % of peak strength for the envelope curve of the story shear force - drift angle relation. Average ultimate limit drift angle for positive and negative loading directions was 3.8 % for

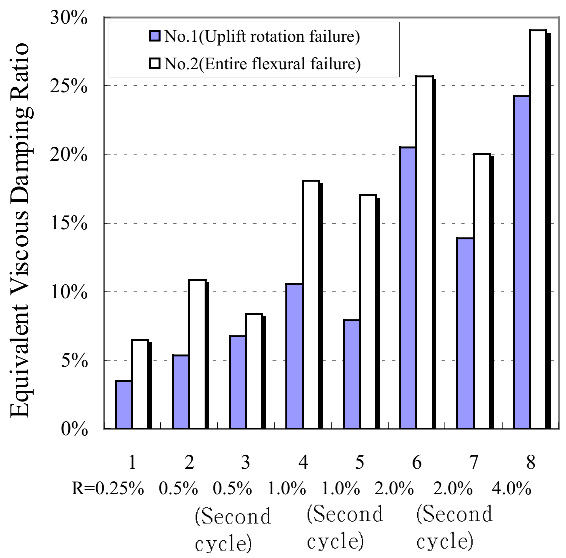

Fig. 14 Equivalent viscous damping ratio

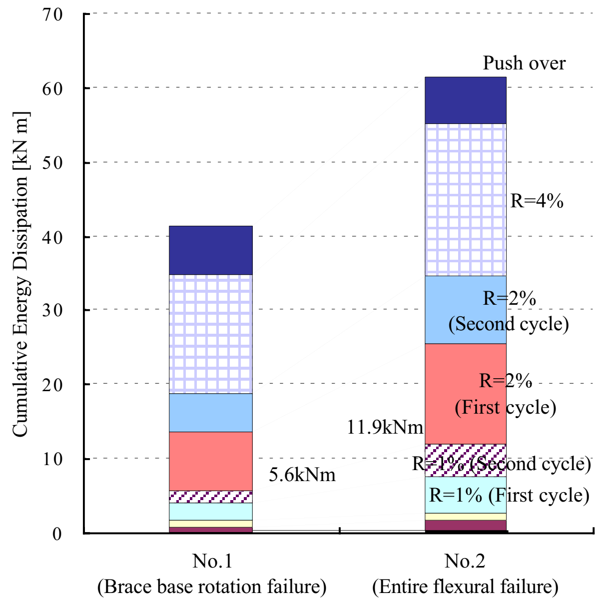

Fig. 15 Cumulative energy dissipation

Specimen No.1 and 3.1 % for Specimen No.2. This indicates that ductility performance in the case of uplift rotation failure of a multi-story steel brace was superior to that for entire flexural failure due to tensile yielding of all longitudinal bars in a R/C edge column as predicted by the F indices. Computed ultimate limit deformations based on the F index for both specimens were conservative comparing with test results. Ultimate limit drift angle for Specimen No.2 can be supposed to be 2 % approximately if the effect of cyclic load reversals on seismic resistant performance is taken into account, because significant lateral resistance degradation occurred after the drift angle of 2 %. Then predicted ultimate limit drift angle of 1.68 % for Specimen No.2 seems to be adequate.

4.4 ENERGY DISSIPATION

The equivalent viscous damping ratio for each loading cycle in story shear force - drift angle relations is shown in **Fig. 14**. The equivalent viscous damping ratio was calculated by normalizing the dissipated energy within half a cycle by the strain energy at peak of an equivalent linearly elastic system. The equivalent viscous damping ratio in Specimen No.1 was smaller than 10 % at the drift angle less than or equal to 1 % and increased rapidly to 20 % at sixth loading cycle with the formation of beam hinge mechanism. The equivalent viscous damping ratio in Specimen No.2 exceeded 10 % even at second loading cycle corresponding to the drift angle of 0.5 % since all longitudinal bars yielded in the R/C edge column beside a steel brace. The equivalent viscous damping ratio in Specimen No.2 was greater than that in Specimen No.1 for all loading cycles. Therefore it is pointed out that the entire flexural failure at the bottom of a multi-story steel brace absorbed more hysteresis energy than the uplift rotation failure.

Cumulative energy dissipation is shown in **Fig. 15**. The amount of cumulative energy dissipation for Specimen No.2 was by 113 percent greater than that for Specimen No.1 at the drift angle of 1 % at which the peak lateral strength was achieved, and by 50 percent greater than that for Specimen No.1 at the last loading stage.

5. CONCLUSIONS

Earthquake resistant performance in plane R/C frames strengthened by a multi-story steel brace was investigated through the tests under cyclic load reversals focusing on the base uplift rotation of the brace and the entire flexural failure at the bottom of the brace caused by tensile yielding of all longitudinal bars in a R/C edge column. The following concluding remarks can be drawn from the present study:

(1) Lateral resistance for the base uplift rotation of a multi-story steel brace decreased gradually after flexural yielding occurred at the end of boundary beams and the bottom of first-story isolated columns at the drift angle of 1.4 %. Lateral strength computed by taking account of restraining effect of both boundary and foundation beams on uplift rotation agreed well with the test result.

(2) For the specimen failed in entire flexure at the bottom of a multi-story steel brace, all longitudinal bars in a R/C edge column subjected to tension beside the brace yielded at the drift angle of 0.3 %. Hysteresis loops showed a spindle shape until the drift angle of 2 %, stably dissipating hysteresis energy. However lateral resistance diminished abruptly by concrete crushing and fracture of column longitudinal bars at the bottom of both edge columns. Lateral strength computed by considering both flexural resistance attributed to tensile force in a R/C edge column and resisting moment of boundary beams same as the case of the base uplift rotation underestimated a little that obtained in the test. Contribution of the vertical steel rim to the entire flexural resistance should be taken into account if anchorage of the bottom of a multi-story steel brace to R/C foundation beam is sufficient to carry tensile axial force in vertical steel rim to the foundation.

(3) Ultimate limit deformations in two specimens estimated by considering respective deformation ability of boundary beams and an isolated multi-story steel brace were conservative comparing with test results.

(4) Ductility performance in the brace uplift rotation failure was superior to that in the entire flexural failure due to tensile yielding of all longitudinal bars in a R/C edge column.

(5) The amount of energy dissipation in the entire flexural failure at the bottom of a multi-story steel brace was by 50 percent greater than that in the brace uplift rotation failure.

(6) It is judged that earthquake resistant performance of strengthened R/C frames which is controlled by the entire flexural failure at the bottom of a multi-story steel brace is superior to that in the brace uplift rotation failure within the range of the drift angle of 2 %.

ACKNOWLEDGMENT

The study reported in the paper was sponsored by a Grant-in-aid for Scientific Research of Japan Society for the Promotion of Science (Head researcher : K. Kitayama). The test was executed by Mr. H. Kato, Rui Design Room Co.Ltd, as a part of the master thesis in Tokyo Metropolitan University.

REFERENCES

[1] Kato, D., H. Katsumata and H. Aoyama : Effect of Wall Base Rotation on Behavior of Reinforced Concrete Frame-Wall Buildings, Proceedings of the Eighth World Conference on Earthquake Engineering, San-Francisco, July, 1984.

[2] Japan Building Disaster Prevention Association : Standard for Evaluation of Seismic Capacity of Existing Reinforced Concrete Buildings, revised in 2001, (in Japanese).

SESSION 4-A: STATE OF DESIGN PRACTICE AND DAMAGE ASSESSMENT

Chaired by

♦ Mary Beth Hueste and Tetsuo Kubo ♦

Post-Earthquake Damage Assessment For R/C Buildings

Masaki MAEDA[1]

Dae-eon KANG[2]

Yoshiaki NAKANO[3]

ABSTRACT

In this paper described is the basic concept of the Guideline for Post-earthquake Damage Assessment of RC buildings, revised in 2001, in Japan. This paper discusses the damage rating procedures based on the residual seismic capacity index *R* that is consistent with the Japanese Standard for Seismic Evaluation of Existing RC Buildings, and their validity through calibration with observed damage due to the 1995 Hyogoken-Nambu (Kobe) earthquake and seismic response analyses of SDF systems. It is shown that the intensity of ultimate ground motion for a damaged RC building structure can be evaluated conservatively based on the *R*-index in the Guideline.

1. INTRODUCTION

To restore an earthquake damaged community as quickly as possible, well-prepared reconstruction strategy is most essential. When an earthquake strikes a community and destructive damage to buildings occurs, quick damage inspections are needed to identify which buildings are safe and which are not to aftershocks. However, since such quick inspections are performed within a restricted short period of time, the results may be inevitably coarse. In the next stage following the quick inspections, damage assessment should be more precisely and quantitatively performed, and then technically and economically sound solution should be applied to damaged buildings, if rehabilitation is necessary. To this end, a technical guide that may help engineers find appropriate actions required in a damaged building is needed, and the Guideline for Post-earthquake Damage Evaluation and Rehabilitation (JBPDA 2001a) originally developed in 1991 was revised considering damaging earthquake experience in Japan.

The Guideline describes damage evaluation basis and rehabilitation techniques for three typical structural systems, i.e., reinforced concrete, steel, and wooden buildings. Presented in this

[1] *Department of Architecture and Building Science, Tohoku University, Sendai, Japan*
Email: maeda@struct.archi.tohoku.ac.jp

[2] *Department of Architecture and Building Science, Tohoku University, Sendai, Japan*
Email: kde0898@struct.archi.tohoku.ac.jp

[3] *Institute of Industrial Science, The University of Tokyo, Tokyo, Japan*
Email: iisnak@iis.u-tokyo.ac.jp

paper are outline and basic concept of the Guideline for reinforced concrete buildings. This paper discusses the damage rating procedures based on the residual seismic capacity index that is consistent with the Japanese Standard for Seismic Evaluation of Existing RC Buildings (JBPDA 2001b), and their validity through calibration with observed damage due to the 1995 Hyogoken-Nambu (Kobe) earthquake and seismic response analyses of SDF systems.

2. OUTLINE OF DAMAGE EVALUATION GUIDELINE

First, structural damage is surveyed and damage of structural members is classified in the most severely damaged story. The residual seismic capacity ratio index R is then calculated and damage rating of the building structure, i.e., [slight], [minor], [moderate], [severe], and [collapse] is made. Necessary actions are finally determined comparing the intensity of the ground motion at the building site, building damage rating, and required seismic capacity against a future earthquake.

2.1 Damage Classification of Structural Members

Damage of columns and shear walls is classified based on the damage definition shown in **Table 1**. As was reported in the past earthquake in Japan, typical damage is generally found in vertical members, and the Guideline is essentially designed to identify and classify damage in columns and walls rather than in beams. Columns and walls are classified in one of five categories I through V as defined in **Table 1**. **Figure 1** schematically illustrates the load carrying capacity, load-deflection curve, and member damage class.

Table 1: Damage Class For RC Structural Members

Damage Class	Observed Damage on Structural Members
I	Visible narrow cracks are found (Crack width is less than 0.2 mm)
II	Visible clear cracks on concrete surface (Crack width is about 0.2 - 1 mm)
III	Local crush of covering concrete Remarkable wide cracks (Crack width is about 1 - 2 mm)
IV	Remarkable crush of covering concrete with exposed reinforcing bars Spalling off of covering concrete (Crack width is more than 2 mm)
V	Buckling of reinforcing bars Cracks in core concrete Visible vertical and /or lateral deformation in columns and/or walls Visible settlement and/or inclination of the building

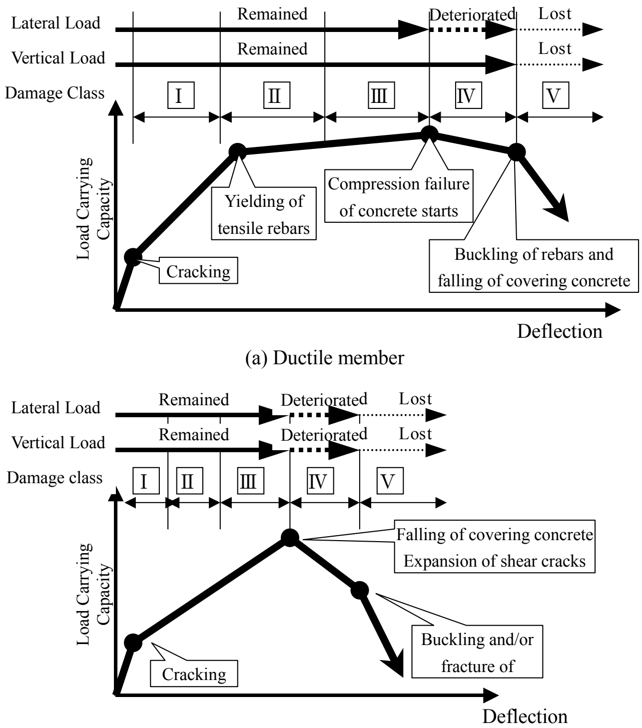

(a) Ductile member

(b) Brittle member

Figure 1: Lateral Load – Deflection Relationships and Damage Class

2.2 Residual Seismic Capacity Ratio Index *R*

A residual seismic capacity index *R*, which corresponds to building damage, is defined by as the ratio of seismic capacity after damage to that before an earthquake (i.e., the ratio of the residual capacity to the original capacity).

$$R = \frac{{}_D Is}{Is} \times 100 \qquad (1)$$

where, *Is*: seismic capacity index of structure before earthquake damage

${}_D Is$: seismic capacity index of structure considering deteriorated member strength

Is-index can be calculated based on the Standard for Seismic Evaluation (JBPDA, 2001b), which is most widely applied to evaluate seismic capacity of existing buildings in Japan. The basic concept of the Standard to calculate *Is*–index appears in APPENDIX. The Guideline recommends to calculate ${}_D Is$-index for a damaged building in the analogous way for pre-event buildings, considering seismic capacity reduction factor η defined as the ratio of the absorbable hysteretic energy after earthquake to the original absorbable energy of a structural member as illustrated in **Fig. 2**. **Table 2** shows the definition of the reduction factor η in the Guideline.

$$\eta = \frac{E_r}{E_t} \qquad (2)$$

where, E_d : dissipated energy, E_r : residual absorbable energy,

E_t : entire absorbable energy ($E_t = E_d + E_r$).

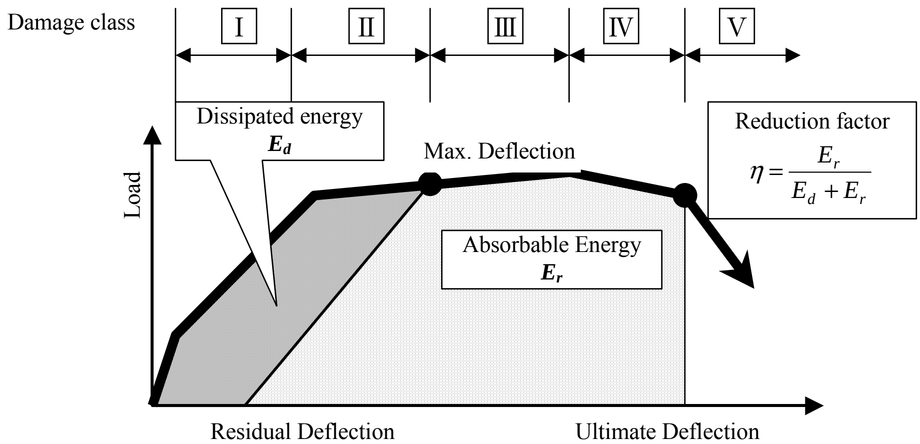

Figure 2: Definition of Seismic Capacity Reduction Factor η

Table 2: Seismic Capacity Reduction Factor η

Damage Class	Ductile Column	Brittle Column	Wall
I	0.95	0.95	
II	0.75	0.6	
III	0.5	0.3	
IV	0.1	0	
V	0	0	

The values in **Table2** were determined based on authors' several experimental results. Comparison between the reduction factor η of the Guideline and experiments are shown in **Fig. 3**. The results four ductile beam specimens (Maeda and Bun-no 2001) and three column specimens (Jung and Maeda 2002) were shown in the figure. The η values in the Guideline generally correspond to the lower bound of the test results. It is noted, however, that available data related to residual capacity is still few, especially for brittle column and wall members, and more efforts should be directed toward clarifying residual performance of damaged members.

${}_{D}Is$-index for a damage building can be calculated from residual member strength reduced by the reduction factor η and the original member ductility, and then residual seismic capacity index R is evaluated.

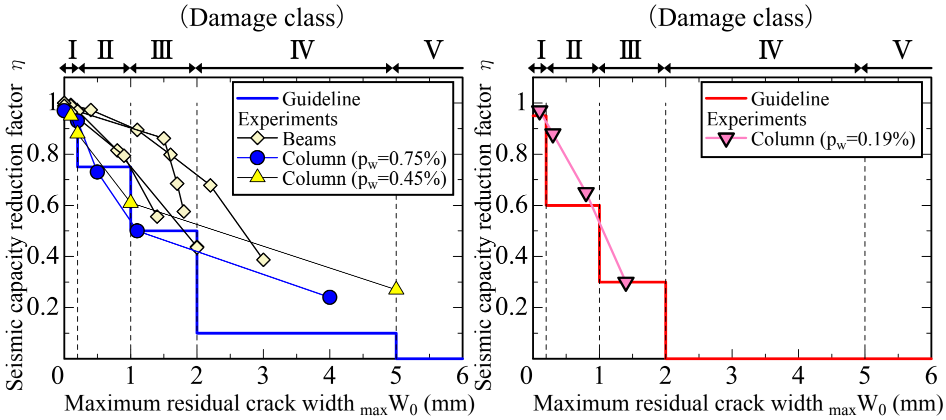

(a) Ductile member **(b) Brittle member**

Figure 3: Comparison of Seismic Capacity Reduction Factor η and Experimental results

2.3 Damage Rating of Building

The residual seismic capacity ratio index *R* can be considered to represent damage sustained by a building. For example, it may represent no damage when *R* =100% (100% capacity is preserved), more serious damage with decrease in *R*, and total collapse when *R* =0% (no residual capacity). To identify the criteria for damage rating, *R* values of 145 RC school buildings that suffered 1995 Kobe Earthquake are compared with observed damage and judgments by experts as shown in **Fig. 4**. The Guideline defines the damage rating criteria shown below.

[slight] $95 \leqq R$ (%)

[minor] $80 \leqq R < 95$ (%)

[moderate] $60 \leqq R < 80$ (%)

[severe] $R < 60$ (%)

[collapse] $R \approx 0$

As can be seen in the figure, no significant difference between damage levels and residual seismic capacity ratio *R* can be found although near the border some opposite results are observed.

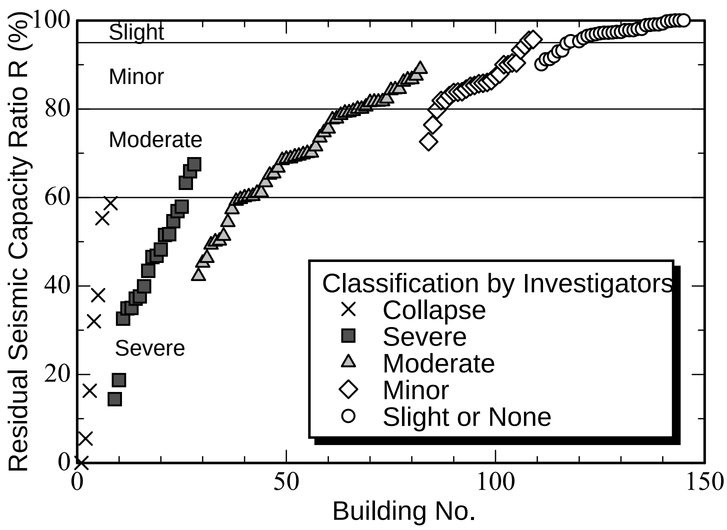

Figure 4: Residual Seismic Capacity Ratio *R* vs. Observed Damage

3 CALIBRATION OF *R* INDEX WITH SEISMIC RESPONSE OF SDF SYSTEMS

3.1 Outline of Analysis

In the Damage Assessment Guideline, the seismic capacity reduction factor η was defined based on absorbable energy in a structural member, which was evaluated from an idealized monotonic load-deflection curve as shown in **Fig. 2** and accordingly the effect of cyclic behavior under seismic vibration was not taken into account. Therefore nonlinear seismic response analyses of a single-degree-of-freedom (SDF) system were carried out and validity of the residual seismic capacity ratio R in the Guideline was investigated through comparison of responses for damage and undamaged SDF systems.

Residual seismic capacity ratio based on seismic response, R_{dyn}, was defined by the ratio of the intensity of ultimate ground motion after damage to that before an earthquake (**Fig. 5**). The ultimate ground motion was defined as a ground motion necessary to induce ultimate limit state in a building and the building would collapse.

$$R_{dyn} = \frac{A_{di}}{A_{d0}} \quad (3)$$

where, A_{d0}: intensity of ultimate ground motion before an earthquake (damage class 0)

A_{di}: intensity of ultimate ground motion after damage (damage class "i")

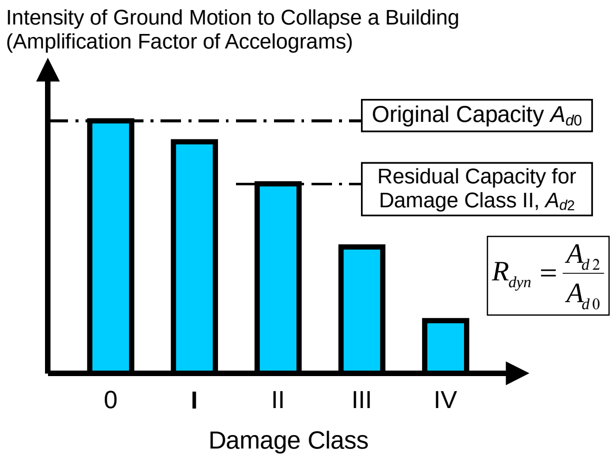

Figure 5: Residual Seismic Capacity Ratio based on Seismic Response R_{dyn}

3.2 Analytical Model

Three models were used to represent the hysteresis rules of the SDF systems; i.e., Takeda model, Takeda-pinching model and resistance-deteriorating model (**Fig. 6.a, b, and c**). Force-deflection properties were chosen common among the models. Yield resistance F_y was chosen to be 0.3 times the gravity load. Cracking resistance F_c was one-third the yielding resistance F_y. Initial stiffness for a series of models was designed so that the elastic vibration periods T were 0.1, 0.2, 0.3, 0.4, 0.5 and 0.6sec. The secant stiffness at the yielding point, K_y, and the post-yielding stiffness, K_u, were 30 and 1 percent of the initial stiffness, respectively.

Three systems with different ultimate ductility μ_{max} were assumed as shown in **Fig. 7** based on authors' column test results (Jung and Maeda 2002). **Figure 7.a** represents a brittle structure of which ultimate deflection is 2 times yielding deflection (μ_{max} =2). **Figure 7.b and c** represent ductile structures with μ_{max} =3 and 5, respectively. The relationship between deflection and damage class was determined in accordance with authors' experimental results as shown in **Fig. 7.** In case of resistance-deteriorating model, the yield resistance F_y was deteriorated as shown in **Fig. 7** after deflection reached to the region of the damage class IV.

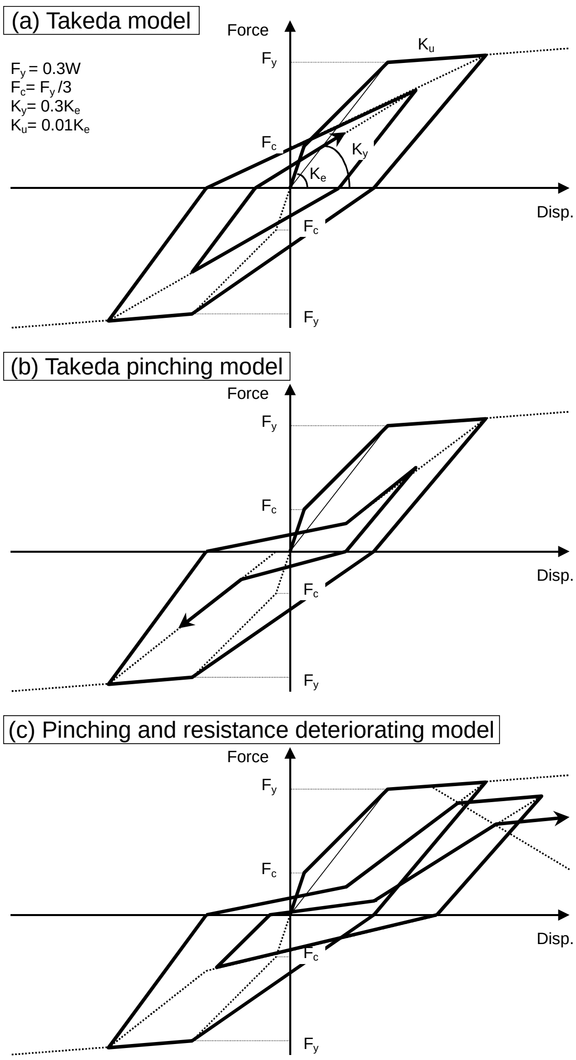

Figure 6: Hysteretic Models

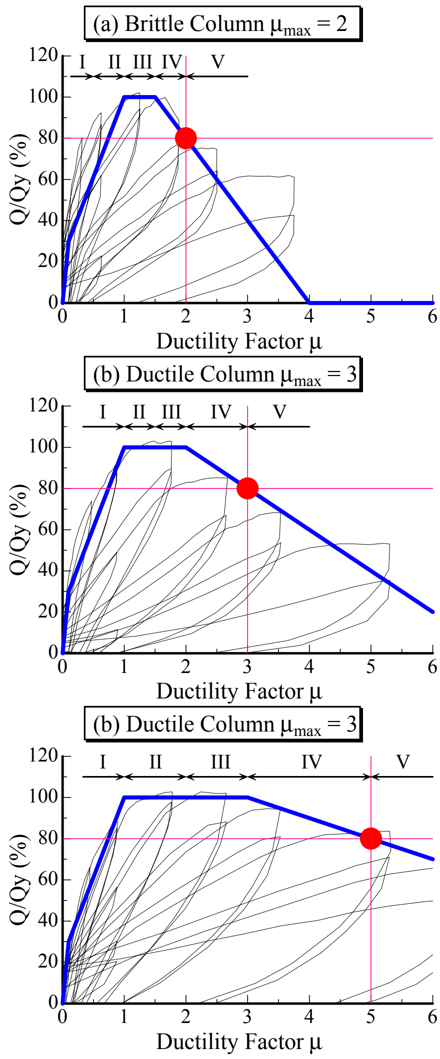

Figure 7: Envelope Curve and Damage Class

3.3 Method of Analyses

Four observed earthquake accelograms were used: the NS component of the 1940 El Centro record (ELC), the NS component of the 1978 Tohoku University (TOH), the NS component of the 1995 JMA Kobe (KOB), and the N30W component of the 1995 Fukiai recode (FKI).

Moreover, two simulated ground motion with same elastic response spectra and different time duration was used. Acceleration time history and acceleration response spectra are shown in **Fig. 8** and **Fig. 9**, respectively. The design acceleration spectrum in the Japanese seismic design provision was used as target spectrum and Jennings-type envelope curve was assumed in order to generate the waves. A simulate wave with short time duration is called Wave-S and with long time duration Wave-L. The equation of motion was solved numerically using Newmark-β method with β = 1/4.

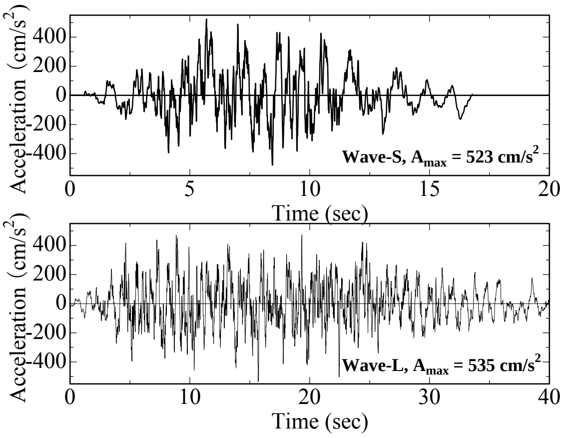

Figure 8: Time History of Simulated Ground Motions

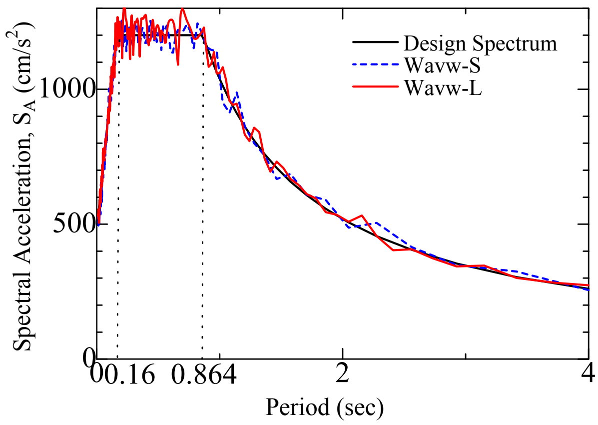

Figure 9: Acceleration Spectrum of Simulated Ground Motions

3.4 Analytical Results

To investigate the relationship between maximum displacement response and intensity of ground motion, parametric analyses were run under the six ground motions with different amplification factors. The results for a system with μ_{max} =3 and T =0.2 sec. under ELC and Wave-S are shown in **Fig. 10**. Thick lines indicate results before damage. Ductility factor μ increases with increase in the amplification factor. The upper bound of amplification factor for damage class IV is assumed to correspond to intensity of ground motion which induce failure of the structure, and is defined as the intensity of ultimate ground motion before damage, A_{d0}. Ultimate amplification factor for damaged structure, A_{di}, was estimated from analytical results for systems damaged by pre-input. For example, first ductility factor μ =2 (damage class III) was induced to a system using amplified ground motion, and then additional ground motion was inputted continuously to find the ultimate amplification factors for damage class III, A_{d3}, by parametric studies (**Fig. 11**). 0 cm/s^2 acceleration was inputted for 5 seconds between the first and second ground motion in order to reduce vibration due to the first input.

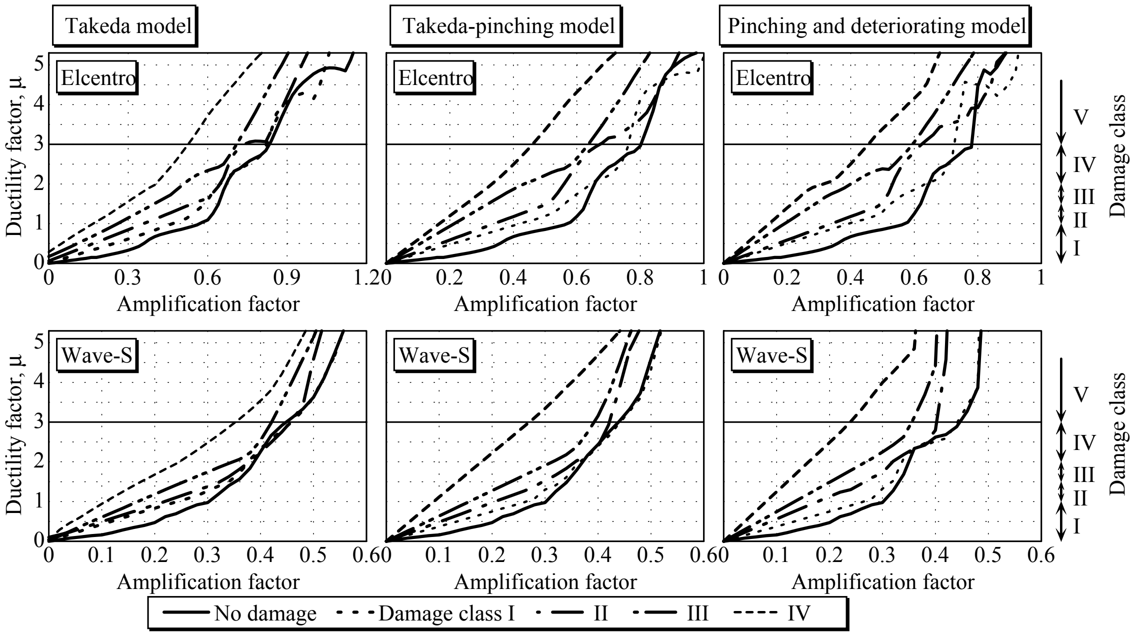

Figure 10: Amplification Factor vs. Max. Ductility Factor

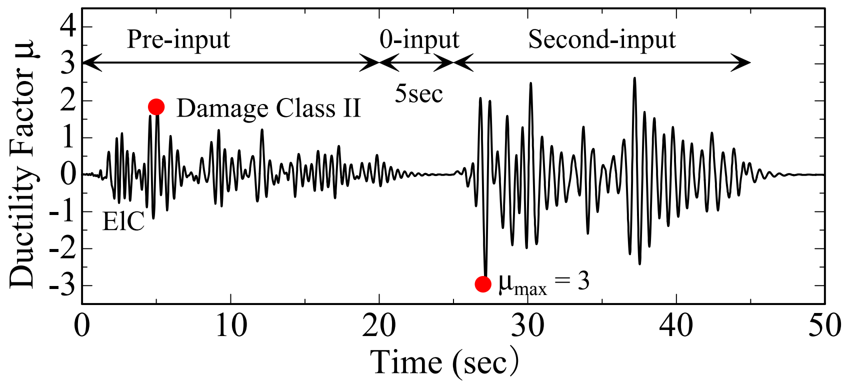

Figure 11: Response Time History for a System Damaged by Pre-input

Differences of the residual seismic capacity ratio index R_{dyn} between the three hysteretic models are compared in **Fig. 12**. It can be seen from the figures that R_{dyn}-index is generally lowest considering both pinching and lateral resistance deterioration (Pinching and resistance-deteriorating model). Although the results only for T=0.2 sec. under TOH and Wave-S were shown in the figures, the general tendency was almost same for the other period T and ground motions. Therefore, in the following discussion, the pinching and resistance-deteriorating model was used.

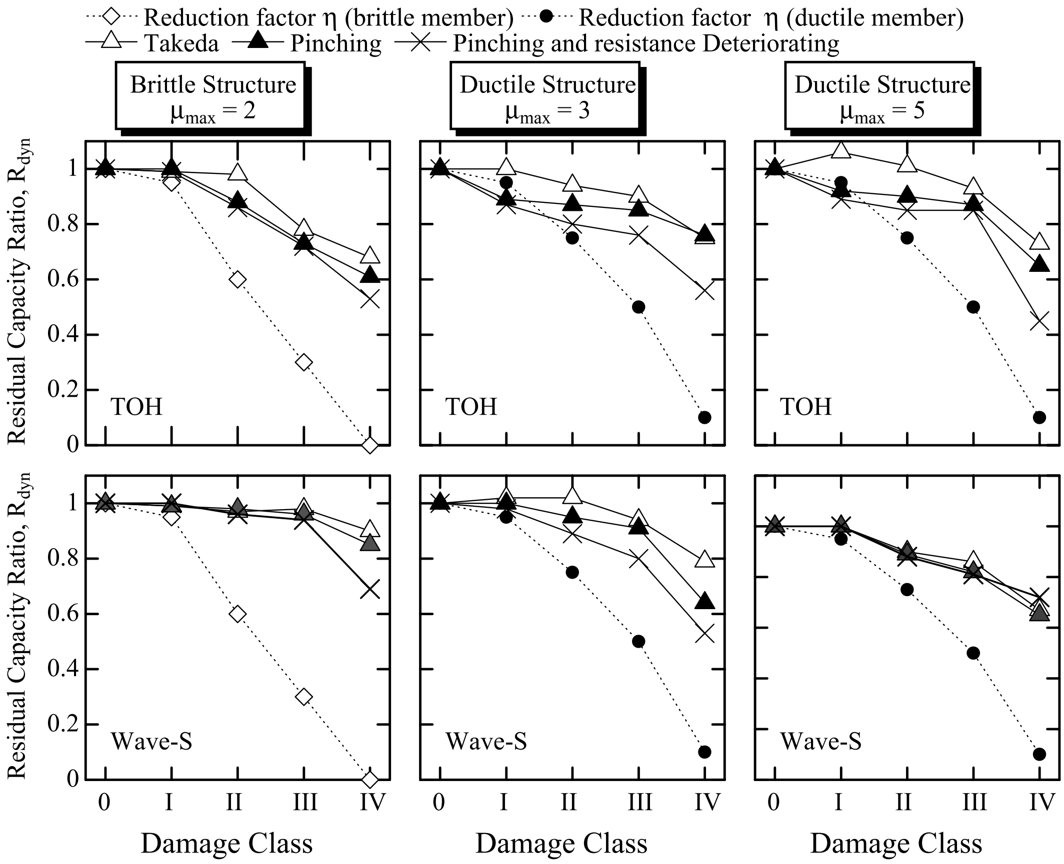

Figure 12: Comparison of R_{dyn} Indices between Three Hysteretic Models

The residual capacity ratio index R_{dyn}, obtained from analyses of systems with different initial period T under the six ground motions, was shown in **Fig. 13**. The reduction factor η in the Guideline (Table 2), which is correspond to the R value for a SDF system, was also shown in the figure. As can be seen from the figure, R_{dyn} values based on analyses are ranging rather widely and R-index in the Guideline generally corresponds to their lower bound, although some of analytical results R_{dyn}–index for damage class I are lower than values in the Guideline. Therefore, The Guideline may give conservative estimation of the intensity of ultimate ground motion for a RC building structure damaged due to earthquake.

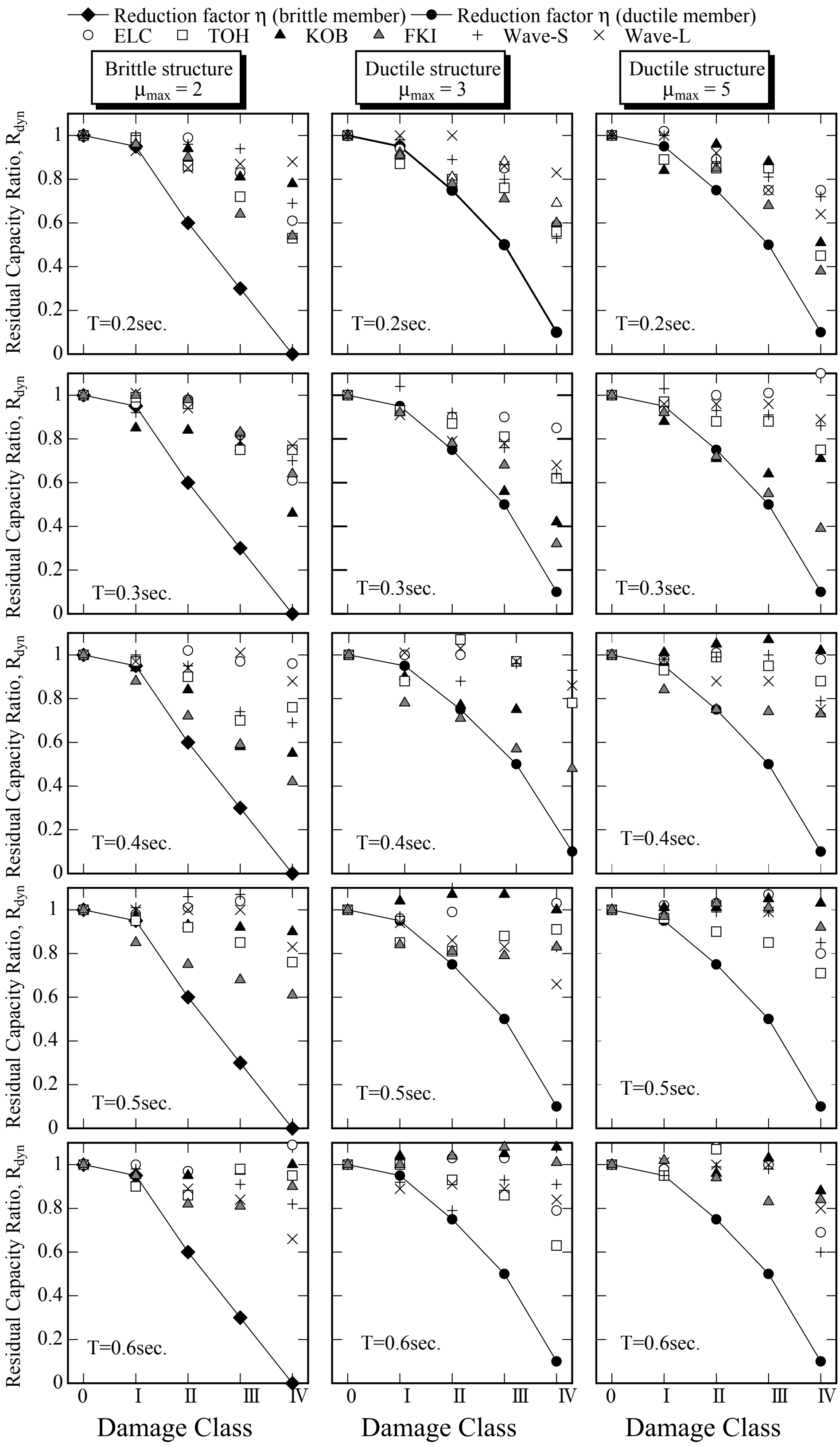

Figure 13: Comparison of Residual Capacity Ratio R_{dyn} with values in the Guideline

4. CONCLUDING REMARKS

In this paper, the basic concept and procedure of new Guideline for post-earthquake damage assessment of RC buildings in Japan were presented. The concept and supporting data of the residual seismic capacity ration R –index, which is assumed to represent post-earthquake damage of a building structure, were discussed. Moreover, the validity of the R –index was examined through calibration with seismic response analyses of SDF systems. As discussed herein, the intensity of ultimate ground motion for a damaged RC building structure can be evaluated conservatively based on the R-index in the Guideline. Much work is, however, necessary to improve the accuracy of the post-earthquake damage evaluation, because available data related to residual seismic capacity are still few.

5. REFERENCES

JBDPA / The Japan Building Disaster Prevention Association (2001a). *Guideline for Post-earthquake Damage Assessment and Rehabilitation of Reinforced Concrete Buildings*. (in Japanese)

JBDPA / The Japan Building Disaster Prevention Association (2001b). *Standard for Seismic Evaluation of Existing Reinforced Concrete Buildings*. (in Japanese)

Jung, M., and Maeda, M. (2002). Estimation of residual seismic performance for R/C building damage due to earthquake (in Japanese). *Journal of structural engineering, Vol. 46B, AIJ*:

Maeda, M., and Bun-no M. (2001). Post-earthquake damage evaluation for R/C buildings based on residual seismic capacity in members (in Japanese). *The 3rd U.S.-Japan Workshop on Performance-based Earthquake Engineering for R/C Building Structures*: 157-170.

6. APPENDIX
BASIC CONCEPT OF JAPANESE STANDARD FOR SEIMIC PERFORMANCE EVALUATION

The Standard consists of three different level procedures; first, second and third level procedures. The first level procedure is simplest but most conservative since only the sectional areas of columns and walls and concrete strength are considered to calculate the strength, and the inelastic deformability is neglected. In the second and third level procedures, ultimate lateral load carrying capacity of vertical members or frames are evaluated using material and sectional properties together with reinforcing details based on the field inspections and structural drawings.

In the Standard, the seismic performance index of a building is expressed by the *Is*-Index for each story and each direction, as shown in Eq. (7)

$$Is = E_0 \times S_D \times T \tag{7}$$

where, E_0: basic structural seismic capacity index calculated from the product of strength index (C), ductility index (F), and story index (ϕ) at each story and each direction when a story or building reaches at the ultimate limit state due to lateral force, i.e., $E_0 = \phi \times C \times F$.

C: index of story lateral strength, calculated from the ultimate story shear in terms of story shear coefficient.

F: index of ductility, calculated from the ultimate deformation capacity normalized by the story drift of 1/250 when a standard size column is assumed to failed in shear. F is dependent on the failure mode of structural member and their sectional properties such as bar arrangement, member proportion, shear-to-flexural-strength ratio etc. F is assumed to vary from 1.27 to 3.2 for ductile column, 1.0 for brittle column and 0.8 for extremely brittle short column.

ϕ: index of story shear distribution during earthquake, estimated by the inverse of design story shear coefficient distribution normalized by base shear coefficient. A simple formula of $\phi = \frac{n+1}{n+i}$ is basically employed for the *i*-th story level of an *n*-storied building by assuming straight mode and uniform mass distribution.

S_D: factor to modify E_0-Index due to stiffness discontinuity along stories, eccentric distribution of stiffness in plan, irregularity and/or complexity of structural configuration, basically ranging from 0.4 to1.0

T: reduction factor to allow for the deterioration of strength and ductility due to age after construction, fire and/or uneven settlement of foundation, ranging from 0.5 to 1.0.

THREE CASE STUDIES IN PERFORMANCE-BASED SEISMIC DESIGN OF REINFORCED CONCRETE BUILDINGS IN THE U.S.

Mason T. WALTERS and Simin NAASEH[1]

ABSTRACT

Three recently constructed examples of performance-based seismic design using reinforced concrete are presented. The examples include two unusual seismic retrofit projects, and a new transportation facility structure. The lateral force-resisting systems used for the respective buildings include reinforced concrete shear walls, ductile reinforced concrete moment frames, and seismic isolation. The structures and their functions are described, and the methods used for their evaluation are discussed. The inter-relationship between project-specific seismic performance goals, design criteria, and the selected structural design strategy is emphasized.

1. INTRODUCTION

The application of performance-based seismic engineering principles is a relatively recent trend in structural engineering practice. Since publication of the concept of project-specific performance goals in the "Vision 2000" appendix of the SEAOC Bluebook, practicing engineers in the U.S. have become familiar with performance-based evaluation and design approaches for buildings by way of numerous recently composed guidelines such as ATC-40 and FEMA 356. Still other performance-based codes and guidelines have been written for transportation-related structures, including buildings, such as those developed by California Department of Transportation (Caltrans) and Bay Area Rapid Transit (BART).

Meanwhile, the first generation of buildings designed using performance-based techniques has been constructed, and much can be learned about practitioners' implementation of such new techniques by studying the implemented structural solutions. Such retrospection may assist in the ongoing effort by researchers and practitioners to improve the quality and applicability of performance-based evaluation and design techniques and guidelines.

---

[1] *Forell/Elsesser Engineers, Inc., San Francisco, CA, USA, E-mail: mason@forell.com, Fax: (415) 837-0800*

The purpose of this paper is to portray the inter-relationship between project-specific seismic performance goals, performance-based design criteria, and the selection of structural design strategy by way of specific, diverse design examples of reinforced concrete building in the San Francisco Bay Area. The selected examples include the seismic retrofit of a university laboratory structure using ductile shear walls, a new multi-level light rail station employing large ductile moment-resisting frame elements, and the seismic isolation of an historic landmark city administration building.

2. CASE STUDY 1: SEISMIC RETROFIT OF A UNIVERSITY LABORATORY

2.1. Building Description

Barker Hall is a 6,800 m^2, seven-story biological research laboratory at the north west corner of the UC Berkeley campus. The building was moderately damaged during the Loma Prieta Earthquake in 1989, and received a seismic rating of "Very Poor" in the course of the University's campus-wide seismic evaluation process in 1997-98. Refer to the photo in Figure 1 for the appearance of the Barker Hall prior to the commencement of the rehabilitation work.

The building is supported by a heavy cast-in-place reinforced concrete pan joist and column structural system. Columns bear on individual spread footings. The basement wall bears on a continuous spread footing. The existing foundations rest on dense sandy clay material with relatively high load bearing capacity. Lateral resistance was originally provided only by several weak core elements within the building and by an unusual and brittle precast/pretensioned concrete cladding panel system, in which the panel tops and sides were doweled to the perimeter beams and columns, but were not positively connected at the base.

Special requirements for the rehabilitation construction included the following:

1. The building would remain at least partially occupied,
2. Neither the spaces nor the functions could be affected by the retrofitting process,
3. The mechanical, electrical, and lab *service* systems, which were extremely condensed, could not be significantly disrupted by the retrofitting process.

Figure 1: Barker Hall Biomedical Research Laboratory at U.C. Berkeley

2.2. Seismic Performance Goals

The seismic performance goal was Life Safety for the 475-year return period event, and Collapse Prevention for the 970-year return period event. (Please refer to article entitled Design Criteria and Seismic Hazard, below).

2.3. Design Criteria and Seismic Hazard

The seismic hazard on the University of California, Berkeley campus has been studied and quantified through probabilistic site hazard analysis. A family of ground motion spectra has been developed for earthquake levels EQ-I (72-yr return period), EQ-II (475-yr return period), and EQ-III (970-yr return period.) The acceleration spectrum for EQ-II (the design-level event) is shown in Figure 2.

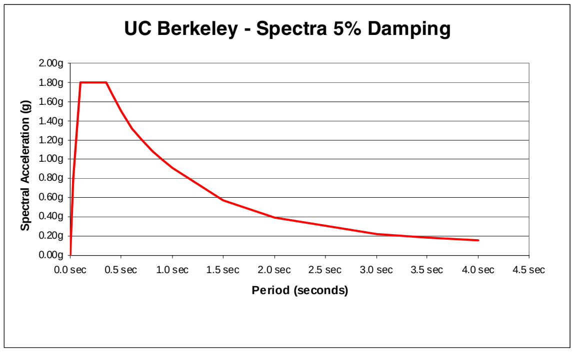

Figure 2: Ground Motion Spectra for the U.C. Berkeley Campus

In addition, Woodward-Clyde developed a suite of time-histories for the EQ-II level event for Barker Hall, which were used primarily evaluate dynamic movements of the foundation, and foundation pressures.

2.4. Design Strategy and Selected Rehabilitation Scheme

F/E developed several possible retrofit schemes, each of which could be constructed largely on the exterior perimeter of the building. Finally, a system of eight shear walls (two per building face) with drilled pier foundations was selected. Refer to Figure 3. Ultimately, the foundation design was changed to a unique continuous post-tensioned concrete grade beam or “belt” system, in lieu of drilled piers and pier caps. The belt beam, which is 1.8m wide and 3.4m deep, bears directly on the soil approximately 3m beneath the existing foundation. This close-in construction of a deep foundation beam required the entire perimeter to be underpinned, but was still less costly than the competing drilled pier foundation. In addition, it was less disturbing to the adjacent animal research facility.

Figure 3: Ductile Concrete Shear Wall Reinforcement

2.5. Analysis Procedures and Results

The shear walls were evaluated using a nonlinear capacity-spectrum pushover analysis. The walls and the foundation system were proportioned to achieve a maximum rooftop lateral displacement of approximately 0.28m in the 475 year event, corresponding to flexural yielding at the wall bases with a defined tensile strain limit (0.10) in the boundary steel and a compressive strain limit in the confined concrete (0.01) of the opposite boundary. Material over-strength was considered for the proportioning of the collectors and foundations.

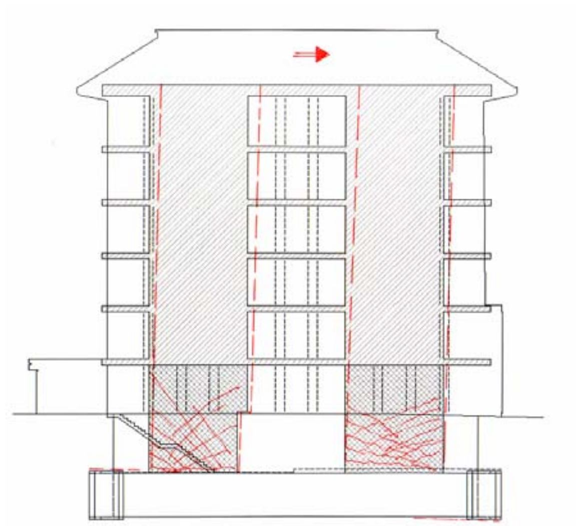

Figure 4: Elevation Showing Flexural Yielding of Walls and Rocking of Foundation

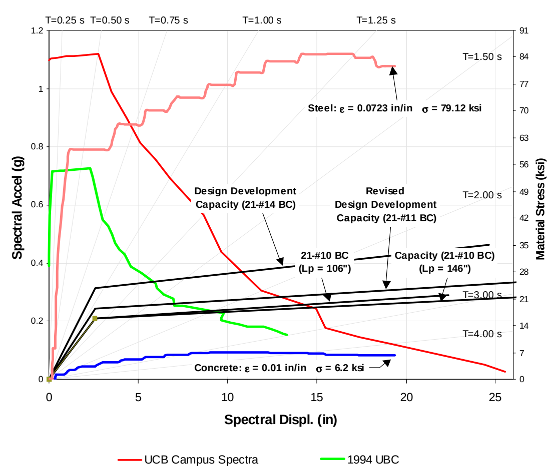

Figure 5: Pushover Demand Capacity Comparison

The rocking of the belt foundation system was evaluated using a SAP 2000 3-d non-linear time-history analysis. This analysis confirmed that the extent of anticipated dynamic uplift of the footings at the corners is small and acceptable, and that the dynamic bearing pressures were within the extreme limits prescribed by the geotechnical engineer.

3. CASE STUDY 2: MULTI-LEVEL LIGHT RAIL STATION

3.1. Project Description

The new San Francisco International Airport "Concourse H" facility is a 270m long by 30m wide, three-level above-grade transit station. It supports two levels of light rail guideways with station platforms, and a pedestrian transit level that links the International Terminal to the airport parking garages. The upper level of light rail is used by the Airport Rapid Transit (ART) trains. The lower level is occupied by Bay Area Rapid Transit (BART). The design of the structure began in 1996 after the U.S. Congress rejected a below-grade design concept. It is estimated that the above-grade scheme saved over $200,000,000 in tunneling-related expenses. However, the above-grade concept entailed numerous technical obstacles, including significant seismic design challenges. Refer to the photo in Figure 6 for a view of the upper level, at the west end of Concourse H.

Figure 6: San Francisco International Airport "Concourse H" Multi-Level Light Rail Station

Concourse H's function is basically to connect the BART line to the airport terminals, and to the airport transit trains. As such, it is structurally tied to the aerial guideways of both BART and ART.

3.2. Seismic Performance Goals

The basic seismic performance goal for Concourse H is to remain functional after a brief shutdown period following the occurrence of a "Maximum Credible" earthquake on the San Andreas Fault, which is situated approximately 4 km east of the site. The airport authority views the function of the transit link as "essential."

3.3. Design Criteria and Seismic Hazard

SFIA and BART required the development of a site-specific response spectrum for the MCE, including consideration of near-fault directional effects. Refer to Figure 7. Furthermore, BART required that the ultimate lateral displacement capacity of the structure be at least 50% greater than the cracked elastic displacement of the structure using the full spectral acceleration. This approach is based on the "equal displacement" approximation developed by Newmark. Refer to Figure 8 for a graphic illustration of this requirement.

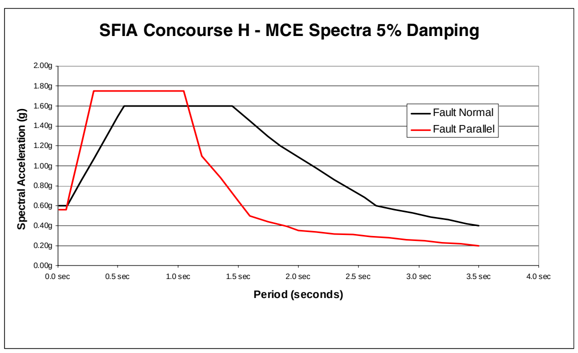

Figure 7: Site-Specific Ground Motion Spectra

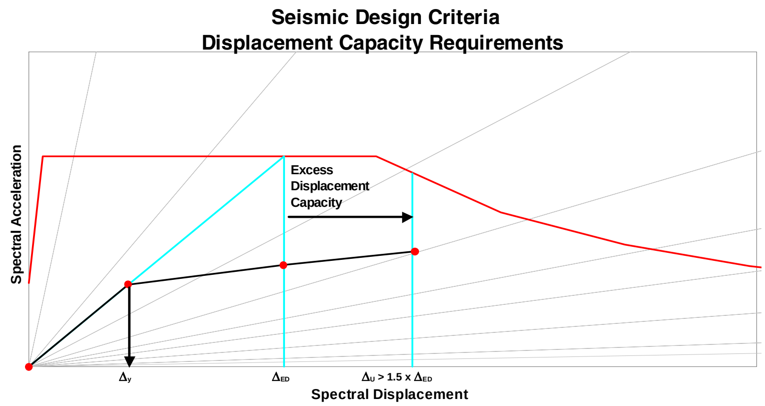

Figure 8: SFIA-BART Lateral Displacement Capacity Requirements

Furthermore, BART required that the crossing of their welded steel tracks from the aerial train guideways to Concourse H remain continuous without joints, but could sustain approximately 0.3 m of slippage without failure.

The design criteria also required that yielding be prevented in beam elements that support train guideways, in order that the guideways could maintain function after a major earthquake.

3.4. Design Strategy and Selected Structural System

The selected strategy requires the 42 main 2.4 m diameter columns to yield in flexure at top and bottom. The upper structure, which houses the train systems, will be prevented from yielding by strong longitudinal and transverse guideway girders. Refer to Figure 9 for a view of a typical transverse support bent.

The girder-column joints were designed in accordance with Caltrans requirements, which are based on large-scale tests of double-deck freeway structures. Refer to Figure 10 for a plan detail of the required joint reinforcement.

In order to prevent damage or loss of support to the connection between the incoming aerial guideway structures and Concourse H, and to maintain BART rail continuity, a connection was required that would limit the longitudinal rail slippage to 0.3 m, and prevent the guideways from pounding or pulling away from their supports. Large passive hydraulic dampers (400 t) were used for this connection. Refer to Figure 11.

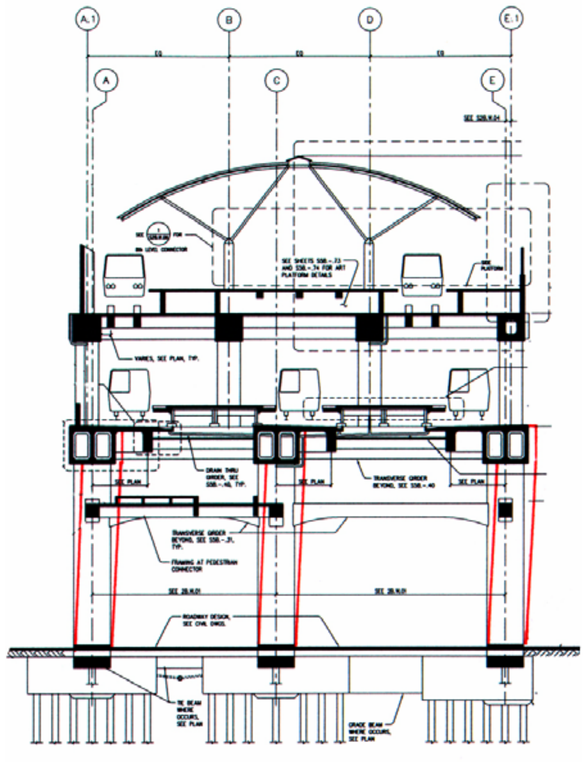

Figure 9: Cross-Section

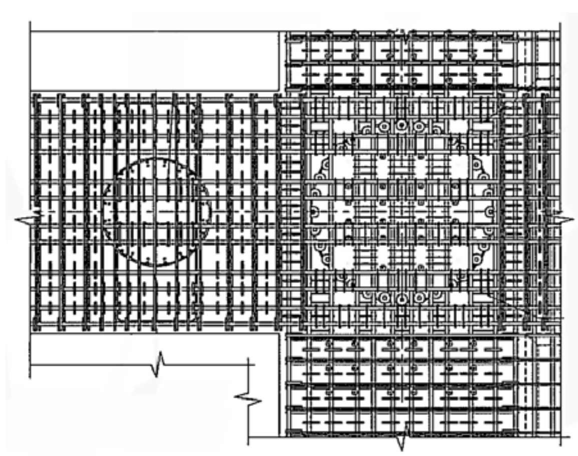

Figure 10: Girder-Column Joint Reinforcement Details

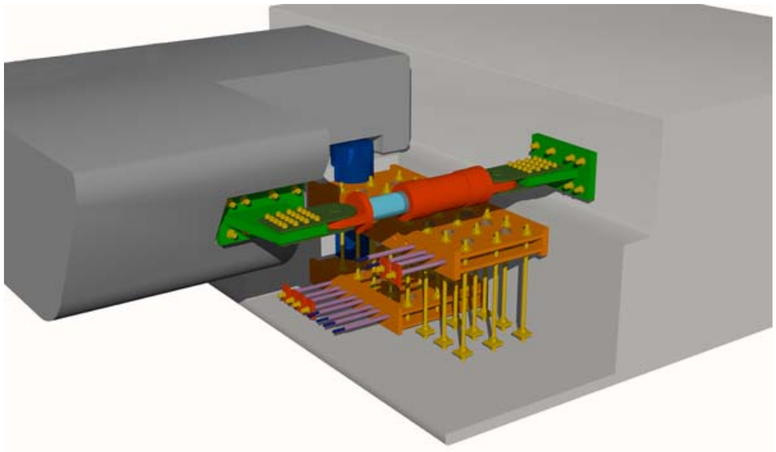

Figure 11: Passive Damper Connection at Station-Guideway Interface

3.5. Analysis Procedures and Results

The lateral force-displacement "pushover" response was evaluated using DRAIN 2D. The maximum resultant horizontal displacement at the BART level was calculated to be approximately 0.5 m, with no yielding occurring in the upper level. The seismic base shear corresponding to the maximum displacement is approximately 0.5g.

4. CASE STUDY 3: SEISMIC ISOLATION OF AN HISTORIC CITY ADMINISTRATION BUILDING

4.1. Building Description

The Martin Luther King, Jr. Civic Center Building is a designated city landmark, and the cornerstone of Berkeley's Civic Center Historic District (Figure 12). The 1930's building was a 5 story non-ductile concrete building with limited seismic capacity. The goal of seismic upgrading of the building was to meet the City's stringent seismic performance criteria while respecting the budget constraints, and the intent to have minimal intrusion to the building's historic fabric.

Figure 12: Martin Luther King, Jr. – Berkeley Civic Center Building

4.2. Seismic Performance Goals

Although the building is not officially designated as an essential facility, the city administration stipulated that the building should be occupiable within two weeks following a 475-year event, and two months following a 970-year event.

4.3. Design Criteria and Seismic Hazard

Site-specific response spectra were developed by Geomatrix for the 475-year events. Refer to Figure 13 for a comparison of these spectra with those from the adjacent U.C. Berkeley campus. A suite of three compatible time history records was developed for use in the dynamic evaluation. These records included velocity pulse input to simulate the possible "fling" caused by the nearby Hayward Fault.

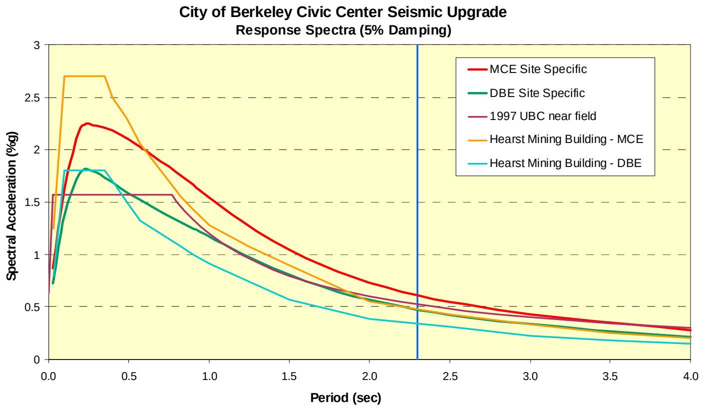

Figure 13: Site-Specific Ground Motion Spectra

4.4. Design Strategy and Selected Rehabilitation Scheme

The selected strategy of seismic isolation was accompanied by the addition of reinforced concrete shear walls in the superstructure to minimize the lateral deformation demands in the existing concrete structure, and to correspondingly maximize the superstructure stiffness. The walls are designed to be capable of resisting 100% of the lateral load, as well as to remain essentially elastic during the 475-year earthquake. Refer to Figure 14.

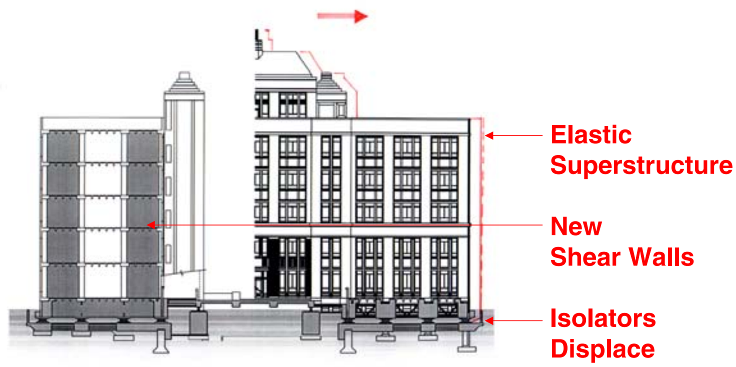

Figure 14: Building Cross-Section

4.5. Analysis Procedures and Results

The seismically isolated structure was modeled using the computer program SAP2000, using nonlinear hysteretic spring elements to represent the isolators and elastic elements to represent the cracked concrete structure above. The calculated peak dynamic lateral displacement at the tops of the isolators is approximately 0.7 m for the 970-year event.

5. CONCLUSIONS

The introduction of performance-based design methods into earthquake engineering practice has improved engineers' conceptualization of the effects of earthquakes on reinforced concrete structures, which has resulted in improved effectiveness in the design of structures to satisfy performance expectations. These techniques are appropriate for application to both new and existing structures, and for both conventional and advanced seismic protection methods. However, the effective application of performance-based methods depend on the accuracy of engineers' understanding and modeling of how building structures behave up to the point of collapse. Consequently, the following topics relating to reinforced concrete should be explored further to provide practical, but not overly conservative, evaluation and design techniques to the practicing engineer:

- How to practically model the effects of cyclic degradation in capacity evaluations

- How to practically and realistically estimate collapse displacement (and failure deformations) of R/C structures.

- How to practically account for the effects of earthquake duration.

- How to reliably estimate extent of r/c hinge zones in different member types, given that current methods imply significant possible variation.

REFERENCES

FEMA 356: Prestandard and Commentary for the Seismic Rehabilitation of Existing Buildings (2000). Federal Emergency Management Agency, Washington, D.C.

Miranda, E. and V. V. Bertero. (1994). Evaluation of Strength Reduction Factors for Earthquake-Resistant Design, *Earthquake Spectra*, vol. 10, no. 2, Oakland, CA.

KEYWORDS

Seismic evaluation, rehabilitation, passive damper, seismic isolation, pushover analysis

SESSION 4-B: PERFORMANCE OF CONNECTIONS OR JOINTS

Chaired by

♦ Marc Eberhard and Daisuke Kato ♦

RECENT CODE DEVELOPMENTS IN PERFORMANCE-BASED DESIGN OF PRECAST SYSTEMS

Michael E. KREGER[1]

ABSTRACT

In the past, precast seismic-resistant building systems were typically subject to severe design penalties unless designed to satisfy design provisions for cast-in-place concrete building systems. The resulting systems typically behave essentially like equivalent cast-in-place reinforced concrete buildings. Recent codes continue to permit the design of systems that mimic cast-in-place construction, but some provide for the design of seismic-resistant building systems that utilize the unique properties of interconnected precast elements. A provisional standard, ACI T1.1-01, was produced by the American Concrete Institute to facilitate development of special precast moment frame systems for use in seismic-resistant design. An overview of that document is presented.

1. BACKGROUND

Current building codes, such as the Uniform Building Code (International Conference of Building Officials 1997) and the ACI Building Code (ACI Committee 318 2002), contain provisions for seismic-resistant design of reinforced concrete building systems. Precast lateral-force-resisting systems can be designed, using either of these codes, to behave like equivalent cast-in-place reinforced concrete systems. This requires satisfying all the applicable provisions for reinforced concrete design as well as additional provisions required of only precast concrete systems.

For design of a precast lateral-force-resisting system that does not satisfy these requirements, such as one that utilizes the "*unique properties of a system composed of interconnected precast elements*," only vague guidance is provided in the Uniform Building Code (International Conference of Building Officials 1997). Section 1921.2.1.6 of the Uniform Building Code (UBC) classifies such a system as an "*undefined structural system*." As such, the code further requires, in Section 1629.9.2, that the overstrength and global ductility factor, *R*, used in the design of the system be substantiated by test data and analyses. The UBC requires that the dynamic response characteristics, lateral force resistance, overstrength and strain hardening or

[1] *Department of Civil Engineering, University of Texas at Austin, Austin, Texas, U.S.A.*
Email: kreger@uts.cc.utexas.edu

softening, strength and stiffness degradation, energy dissipation characteristics, system ductility, and redundancy of the system be addressed in the process of establishing a value for *R*.

Until publication of the 2002 edition, the ACI Building Code was equally vague, stating in Section 21.2.1.5 of Chapter 21 that "*A reinforced concrete structural system not satisfying the requirements of this chapter shall be permitted if it is demonstrated by experimental evidence and analysis that the proposed system will have strength and toughness equal to or exceeding those provided by a comparable monolithic reinforced concrete structure satisfying this chapter*." (ACI Committee 318 1999) A recent ACI publication, "Acceptance Criteria for Moment Frames Based on Structural Testing (T1.1-01) and Commentary (T1.1R-01)," (ACI Innovation Task Group 1 and Collaborators 2001), which is referenced in Section 21.6.3 of the 2002 ACI Building Code, is the subject of the remaining portion of this paper, and is intended to satisfy Section 21.2.1.5 of the Building Code and, in part, Section 1629.9.2 of the UBC for frame systems.

2. OVERVIEW OF ACI T1.1-01

2.1 Purpose of T1.1-01

ACI T1.1-01 was developed by Innovation Task Group 1 to define minimum acceptance criteria for new reinforced concrete frame systems intended for use in regions of high seismic risk. Acceptance of new frame systems is based on analysis of experimental data collected during testing of representative beam-column connection modules and appropriate comparisons with the acceptance criteria. The new frame systems, which are designed using capacity-design techniques resulting in strong column-weak beam behavior, are intended to exhibit response that is at least equivalent to response of monolithic frames designed to satisfy Sections 21.2 through 21.5 of ACI 318-99. A secondary purpose of ACI T1.1-01 is to provide validation of the design procedure used to proportion the test modules.

2.2 Acceptance Testing Program

Prior to fabrication of test modules, a design procedure is developed for the prototype frame for which acceptance is sought. The procedure, which is used to proportion the test modules, must account for concrete cracking, deformation of members and connections, and the effects of reversed cyclic loads.

Test modules are required to represent each typical configuration of beam-to-column connection in the prototype frame, and have a scale (at least 1/3 full scale) sufficient to represent the complexities and behavior of actual materials and load-transfer mechanisms in the prototype frame system. The nearest contraflexure points in the beams and columns framing into the beam-column joint define the minimum extent of the test modules.

Test modules are subjected to a sequence of displacement-controlled reversed cyclic loads that include an initial cycle to a drift ratio in the essentially linear-elastic range of response, with subsequent cycles to drift ratios between 1-1/4 and 1-1/2 times the previous maximum drift ratio. Each load cycle to a specified drift ratio is repeated three times, and testing continues until the drift ratio reaches or exceeds 0.035.

The drift ratio versus column shear force response must be recorded at a sufficient frequency to effectively describe the continuous response of each test module. In addition, photographs are required to document the condition of test modules at the end of each sequence of load cycles to a specified drift ratio. The ACI T1.1-01 document also specifies minimum requirements for reporting results of an acceptance-testing program.

The measured lateral resistance versus drift ratio response for each test module is evaluated based on the acceptance criteria described in the following subsection.

2.3 Acceptance Criteria

An example of measured lateral force versus drift ratio response for a test module is illustrated in Figures 1 and 2 to aid in understanding the acceptance criteria specified in ACI T1.1-01. A test module is deemed to have demonstrated acceptable behavior if the following criteria are satisfied for both directions of response to applied load.

1. A test module must attain a maximum lateral resistance that equals or exceeds the resistance, E_n, (determined using nominal geometric properties and material strengths, a strain compatibility-based analysis, and strength reduction factor, φ, of 1.0) before the drift ratio exceeds the value consistent with the allowable story drift specified in the

International Building Code (International Code Council 1998) (see Fig. 1). This acceptance criterion, which is intended to provide adequate initial stiffness for the candidate frame system, is indicated by the resistance E_n and drift ratio B in Fig. 1.

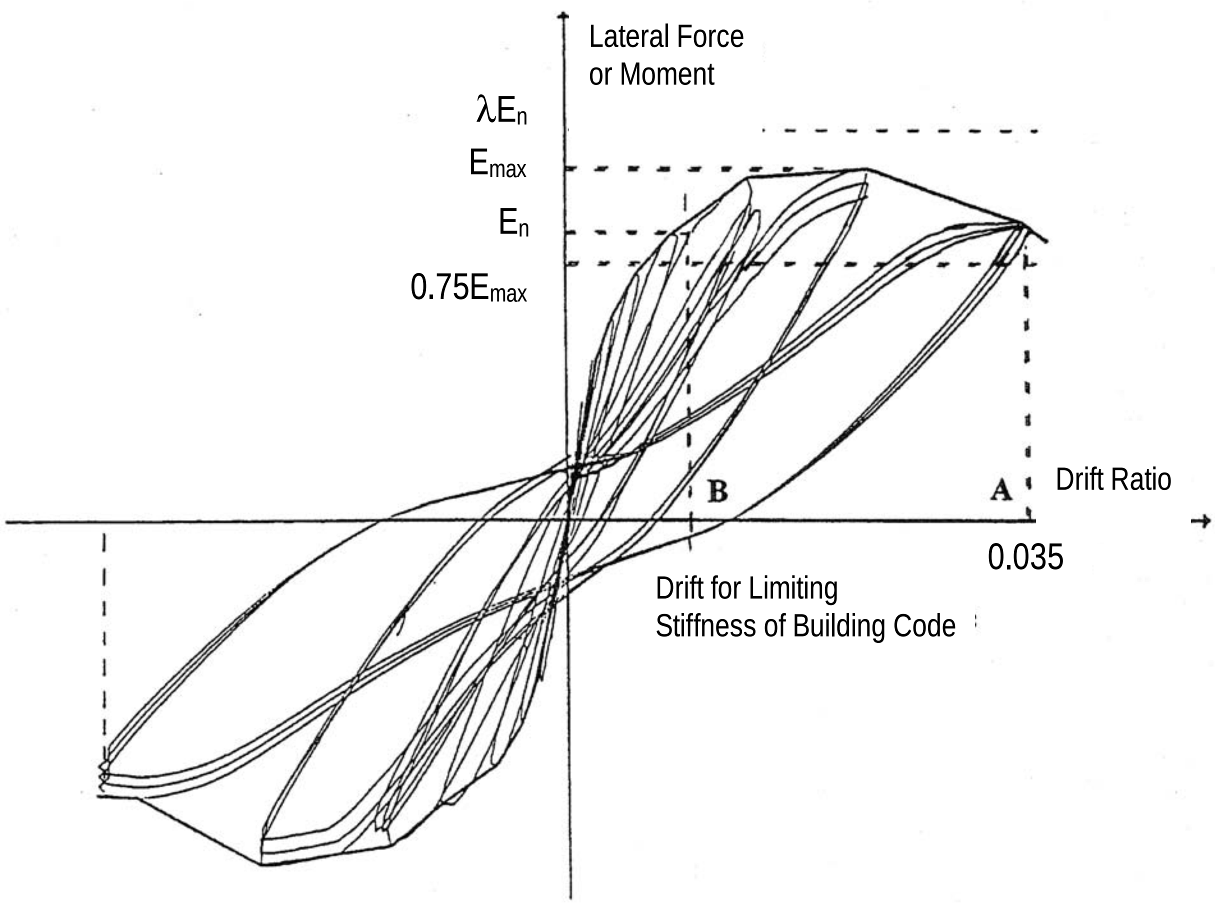

Figure 1 Quantities used in evaluating acceptance criteria
(ACI Innovation Task Group 1 and Collaborators 2001).

2. The maximum lateral resistance, E_{max}, attained by a test module cannot exceed λE_n, where λ is the specified overstrength factor for the column incorporated in the test module (see Fig. 1). This criterion is intended to result in weak beam/strong column behavior in the frame system and provide some margin against column yielding.
3. During the third cycle at a drift ratio for which acceptance is sought (but not less than a drift ratio of 0.035), the peak resistance of the test module must be $0.75E_{max}$ or higher (see Fig. 1), the relative energy dissipation ratio, β (illustrated and defined in Fig. 2), must be 1/8 or higher, and the secant stiffness based on the response at drift ratios of –0.0035 and

+0.0035 must be at least five percent of the stiffness for the initial drift ratio (Fig. 3). These acceptance criteria for high cyclic drift ratios are intended to limit the amount of strength degradation, and thus enhance toughness, to provide the system with adequate hysteretic damping, and to preclude large displacements under small lateral forces following a major earthquake.

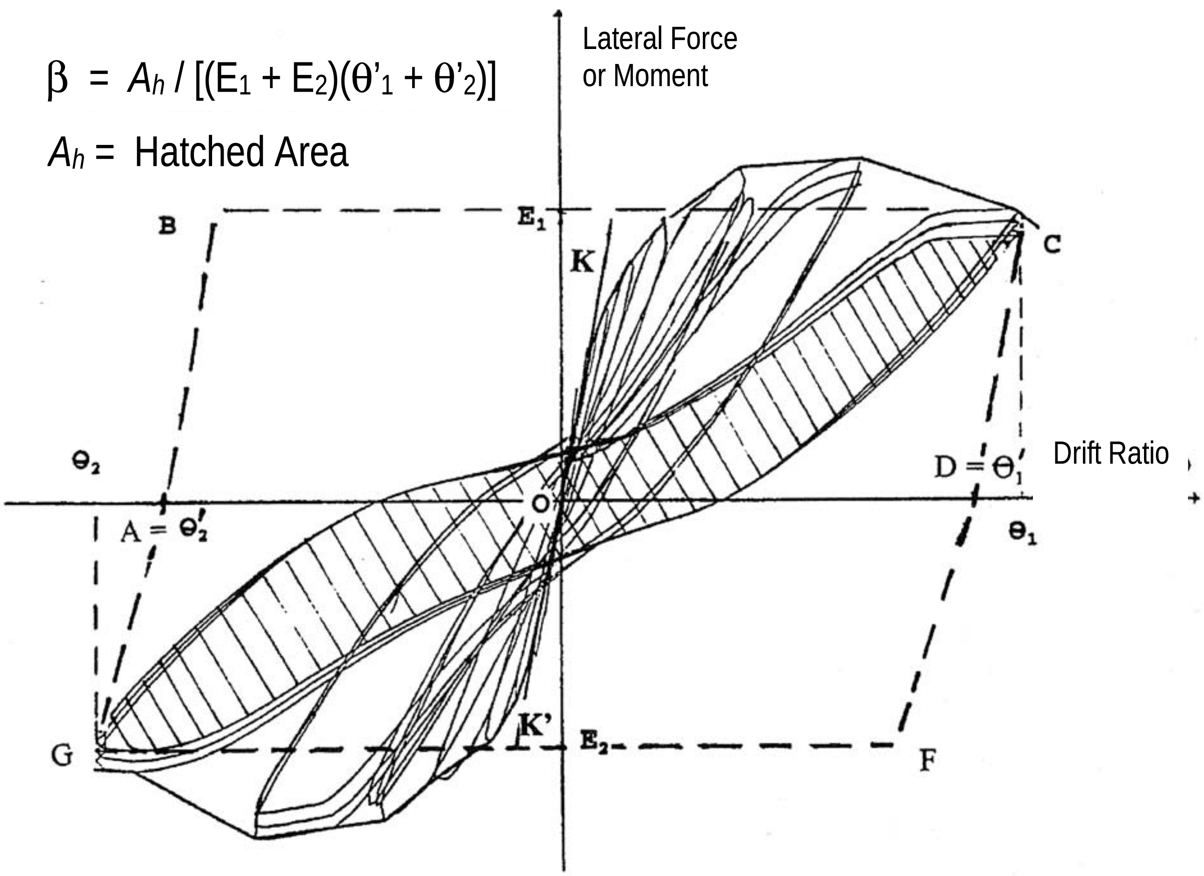

R2.4—Relative energy dissipation ratio.

Figure 2 Relative energy dissipation ratio
(ACI Innovation Task Group 1 and Collaborators 2001).

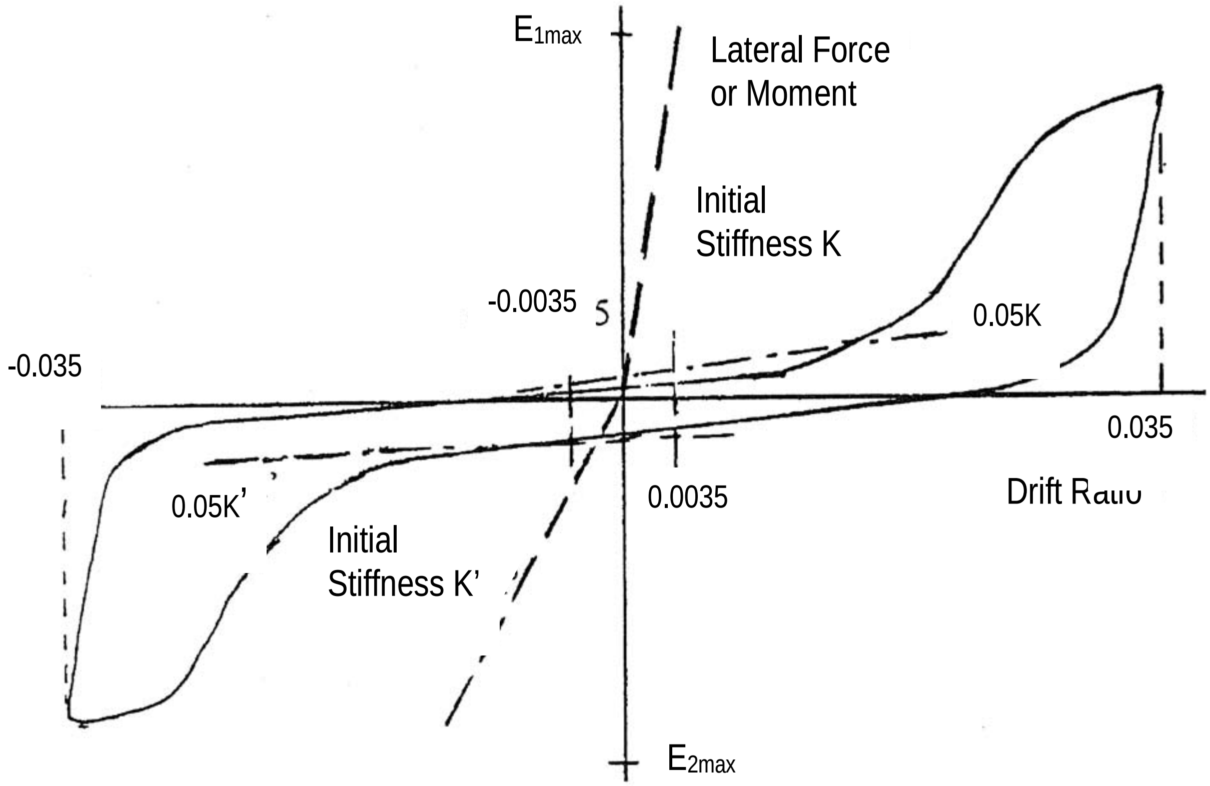

Figure 3 Minimum acceptable stiffness
(ACI Innovation Task Group 1 and Collaborators 2001).

3. FUTURE DEVELOPMENTS

ACI T1.1-01 was developed to address acceptance testing for moment frames. Provisions in current design codes provide little guidance for the design of precast structural wall systems that are not intended to mimic the behavior of cast-in-place special reinforced concrete structural walls. The American Concrete Institute recently formed Innovation Task Group 5 to develop a provisional standard containing acceptance criteria for special structural walls based on validation testing.

4. REFERENCES

ACI Committee 318. (1999). *Building Code Requirements for Structural Concrete (ACI 318-99) and Commentary (ACI 318R-99)*. Farmington Hills, Michigan: American Concrete Institute.

ACI Committee 318. (2002). *Building Code Requirements for Structural Concrete (ACI 318-02) and Commentary (ACI 318R-02)*. Farmington Hills, Michigan: American Concrete Institute.

ACI Innovation Task Group 1 and Collaborators. (2001). *Acceptance Criteria for Moment Frames Based on Structural Testing (T1.1-01) and Commentary (T1.1-01)*. Farmington Hills, Michigan: American Concrete Institute.

International Code Council. (1998). 2000 International Building Code. Falls Church, Virginia.

International Conference of Building Officials. (1997). *Uniform Building Code*. Whittier, California.

NEW MODEL FOR JOINT SHEAR FAILURE OF R/C KNEE JOINTS

Hitoshi Shiohara[1], Yongwoo Shin[2]

ABSTRACT

A new theory for joint shear failure of reinforced concrete beam-column joint is applied to knee joints. The theory considers four diagonal flexural critical sections in beam-column joints associating with joint shear deformation observed in tests, called J-mode deformation. The equilibrium equations are used to derive relations of forces such as column shear, beam shear, column and axial force, to the magnitude of stress resultants in steel and concrete on the flexural critical sections. The result are combined with failure criteria for material such as, concrete, steel and bond stress, to derive joint shear capacities. This paper focuses on demonstration of the theory with numerical calculation applied to knee joints. Calculated results are compared with current equations in design recommendations in the US and Japan. It is revealed that the theory is universally applicable to beam-column joints with different geometries such as interior, exterior and knee joints.

1. INTRODUCTION

Current seismic design of moment resisting frames demands to preclude premature failure of monolithic RC beam-column joints before ductile beam hinges are formed. However no theories or models are used in practice for the design of RC beam-column joints. A quarter century ago, truss and strut model are proposed by Paulay et al. (Pauley 1978). Since then, a lot of mathematical model are proposed and investigated. But there still exists a big challenge for the models not to be solved. The challenge common for all of the existing models is that the models give no explanation why the joint shear capacity of beam-column joint is drastically changes reflecting the geometry of beam-column joint; interior, exterior or knee joints. This is an obviously crucially weak point and the reliability of the models.

This study attempts to offer a simple, comprehensive and unified theory in which joint shear failure for all types of beam-column joints with different geometries is intrinsically incorporated. This theory require no empirical geometrical factors accounting the difference in strength for

1. *Associate Professor, Department of Architecture, Graduate School of Engineering, The University of Tokyo, Tokyo, 113-8656 Japan Email: shiohara@arch.t.u-tokyo.ac.jp*
2. *Graduate Student, Department of Architecture, Graduate School of Engineering, The University of Tokyo, Tokyo, 113-8656 Japan Email: shin@rcs.arch.t.u-tokyo.ac.jp*

geometry of beam-column joints. The new theory now covers interior, exterior and knee joints. Models for interior and exterior beam-column joints was originally proposed based on the re-examination of existing test data by the author in the references (Shiohara 2001, 2002a). This paper explains application of this theory in particular to the knee joint with numerical demonstration. The theories based on mathematical model are useful as a tool for engineers to understand the behavior of beam-column joint as well as for performance based design. They enable engineers (a) to invent a new beam-column joint outperform conventional design, (b) to invent rational methods for retrofitting of existing beam-column joint vulnerable to seismic disaster, (c) to develop rational guidelines for design of special beam-column joint, such as prestressed joint, joint with special detail, which is recognized as out of scope of the empirical equations for joint shear capacity and to (d) to predict the extent of damage and location.

In particular knee joint is known to be sensitive to the anchorage detail and confining detail in joints among different geometry of beam-column joint. So the mathematical model is more important for the development of rational method reflecting variety of anchorage and joint confining details.

2. GEOMETRICAL FACTORS IN NOMINAL JOINT SHEAR CAPACITY

Recent design recommendations, such as ACI 352 (ACI 2002) and the AIJ design guidelines (AIJ 1999) provide upper limit for joint shear stress input based on empirical equations. The recommendations recognize that the joint shear capacity is significantly affected for different geometry.

Table 1: Comparison of geometrical factors for joint shear design in US and Japan

loading direction	a. 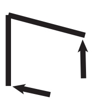	b. 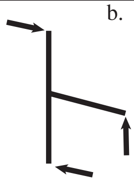	c. 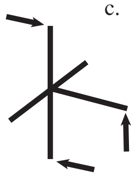	d. 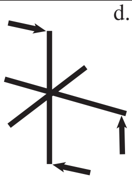	e. 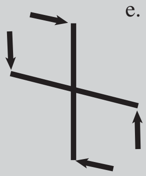	f. 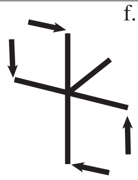	g. 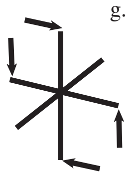
ACI 352 type I (2002)	$\gamma = 12$ 0.6	$\gamma = 15$ 0.75	$\gamma = 20$ 1.0	$\gamma = 24$ 1.33	$\gamma = 20$ 1.0	$\gamma = 20$ 1.0	$\gamma = 24$ 1.33
AIJ Guidelines (1999)	$k = 0.4$ $\phi = 0.85$ 0.40	$k = 0.7$ $\phi = 0.85$ 0.70	$k = 0.7$ $\phi = 1.0$ 0.82	$k = 0.7$ $\phi = 1.0$ 0.82	$k = 1.0$ $\phi = 0.85$ 1.0	$k = 1.0$ $\phi = 0.85$ 1.0	$k = 1.0$ $\phi = 1.0$ 1.18

The nominal shear capacity of beam-column joint in ACI 352 is $0.083\gamma\sqrt{f'_c}A_j$ (in MPa) , where γ is given as $\gamma = 20$ for joints confined on two opposite faces, while $\gamma = 12$ corner (knee) joints, where A_j is the effective horizontal area of beam-column joint. The nominal joint shear capacity of knee joint is 60 percent of one for interior beam-column joint. AIJ Guidelines (AIJ 1999) adopts the equations $\kappa\phi \times 0.8 f'^{0.7}_c A_j$ (in MPa) for nominal joint shear capacity, where factors κ is for accounting the number of framing member into joint in loading direction, $\kappa = 1.0$ for crucial shape, $\kappa = 0.4$ for knee joint, while ϕ is a factor accounting for the effect of transverse beams, and $\phi = 1.0$ for joint with two opposite transverse beams and $\phi = 0.85$ for the others. Hence the nominal joint shear capacity of knee joint is 40 percent of one for interior beam-column joint. Table 1 compares geometrical factors for US and Japan. The nominal joint shear strength of knee joint is much different in the two countries. The joint strength in AIJ guidelines for knee joint is based on experiments in Japan. The commentary of the AIJ guidelines explains that the equations estimate lower bound of test results. However the scattering of test data is large and sometimes estimated values are much smaller than test result, whereas, the equation gives non-constructive shear strength for knee joint with poor detail. As the effect of the anchorage and confining detail is not well known, intensive experiment have been carried out in Japan recently.

3. A THEORY OF BEAM-COLUMN JOINT

A simple mathematical model for interior beam-column joints was proposed for the first time by the author in 2001 (Shiohara 2001). The model considers flexural critical sections associated with deformation modes, called J-mode and B-mode (Shiohara 2002a) as shown in Fig. 1(a). The basic idea of the critical section is same to the classical flexural theory where local curvature cause moment resistance by a pair of force resultants of tension and compression, whereas Bernoulli-Eular assumption of plain sections remain plain is not used, because bond-slip has significant effect for the behavior of RC beam-column joints.

The first category of critical section is called B(beam)-mode. B-mode considers critical sections along column face. The increase of local curvature at B-mode critical section associate with beam end rotation.

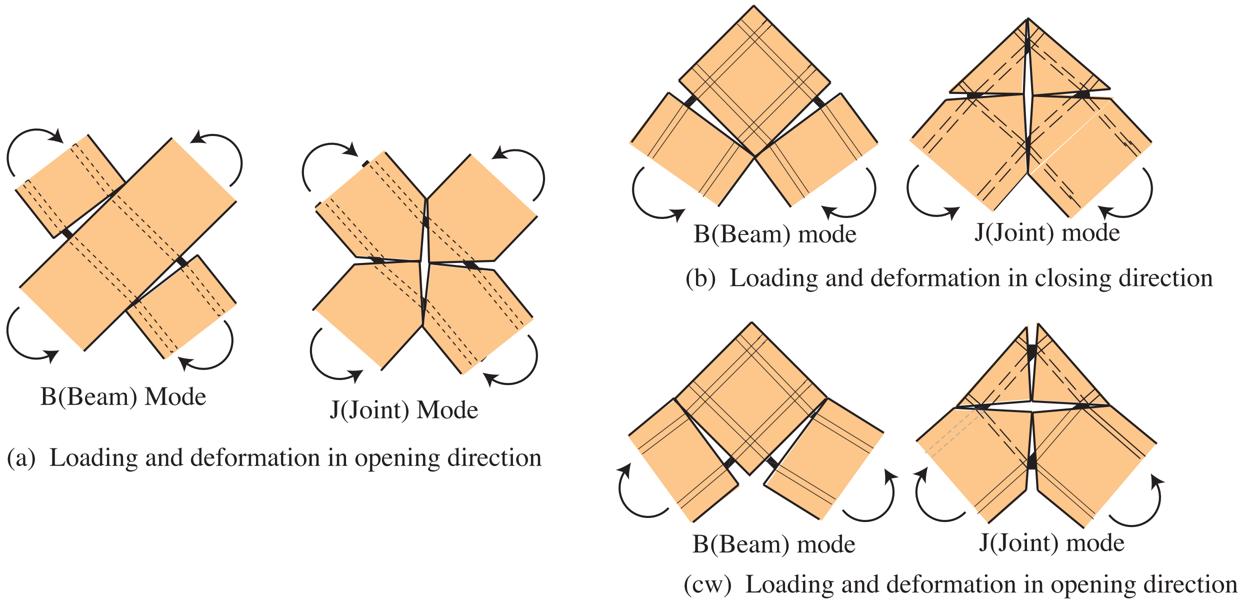

Figure 1: Two types of deformation modes for interior beam-column joint and knee joints

The second category of critical section is called J(joint)-mode. J-mode considers four coupled critical sections on two diagonal lines. The increase of local curvature at J-mode critical sections associate with joint shear deformation. If local curvature due to J-mode increase excessively, concrete crush and cover concrete of joint spall off adjacent to the crossing point of diagonal cracks. The typical failure pattern observed in real tests endorses this view of joint shear failure. Joint shear deformation increase due to opening of diagonal crack. These behavior is what really happens in the tests of beam-column joint failed in shear failure mode.

By considering the equilibrium equations, the relations between forces and stresses can be established. The stress resultants can not exceed their material strength and bond strength. Considering the equilibrium equations and restrictive conditions of material and bond strength, the maximum joint shear strength is derived as an force at optimal state when some of material strength and/or bond strength are reached.

In general the joint shear strength of J-mode and B-mode are calculated independently and give different values. The relation of the strengths have close relation to the deformation modes. If the J-mode strength is smaller than that of B-mode, then J-mode deformation become dominant mode and vice versa. The influence of the bond capacity to the two failure modes for interior beam-column joints were discussed in detail in the reference (Shiohara 2002a). The application of this theory to the exterior beam-column joint was discussed in the reference (Shiohara 2002b). They reported that the predicted joint shear capacity by this theory shows good correlation both for interior and exterior beam-column joints.

These two category of critical section is also applicable to knee joints as shown in Fig. 1(b) and (c). So the this theory is applied to knee joint in this paper.

4. ANALYSIS OF RC KNEE JOINTS BY THE NEW THEORY

4.1 Geometry and notations for RC Knee Joint

Figure 2 shows the geometry of the knee joint considered in this paper. To reduce complexity of the solution, assumptions are made that the substructure are symmetric and the depth of beam and column are same. Thus the shape of the joint panel is square of joint depth D. The thickness of beam, column and joint and panel were common and assumed to be t. The distance between the center of the joint to the contra flexural points in the beam or column is L. External load are applied at the contra flexural points in the direction of straight line connecting the two contra flexural points. As a result, column shear Q and column axial force N (=Q) acts on the contra flexural points on the column.

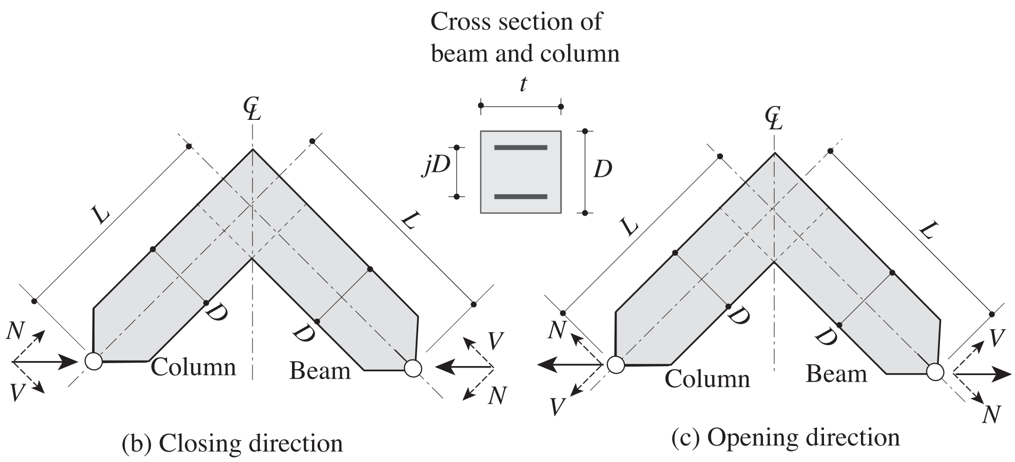

Figure 2: knee joint subassembledge and definition of loading direction

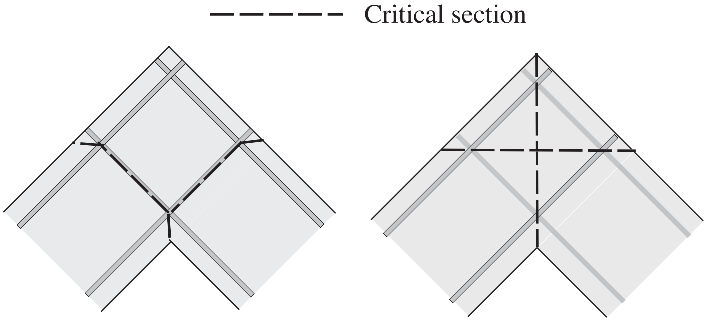

(a) Critical sections for B-mode (b) Critical sections for J-mode

Figure 3: Critical sections

4.2 Notations for internal forces

Critical sections of B-mode and J-mode for flexural resistance in a knee joint are shown in Figs. 3(a) and 3(b). To describe the equilibrium condition, the internal forces need to be given notations. So Figs. 4(a) and 4(b) show the notations necessary to define the set of internal forces at the critical sections for the J-mode of knee joints subject to loading in closing direction and opening direction respectively. The notations T_1, T_2, T_3, T_4 represent the resultant tensile forces in longitudinal bars, while C_1 C_2 and C_3 represent the resultant compressive forces on the concrete boundaries when it subjects to closing force, and C_4 C_5 and C_6 represent the resultant compressive forces in concrete when it subjects to load in opening direction. The values of C_1 and C_2 equal to the x component of compressive resultant in concrete. So the direction of concrete principle stress is normal to the critical section. The forces T_2, T_3 are common variables for both B-mode and J-mode. All of the compressive stress in concrete on the critical section is assumed to be normal to the critical section and their distribution are assumed to be modeled as stress blocks with compressive stress of σ_c. The notation T_5 represents the resultant force in joint shear reinforcements distributed in beam-column joint, which confine the joint core. In this paper, horizontal and vertical resultant forces are assumed to be same for the sake of simplicity. The distance of tensile and compressive longitudinal bars is assumed to be jD. The unit of all the forces are $Dt\sigma_c$, while the unit of length is D. General case where knee joint is non symmetric is more general but complicate. So it is not treated here. But same principle may be applicable.

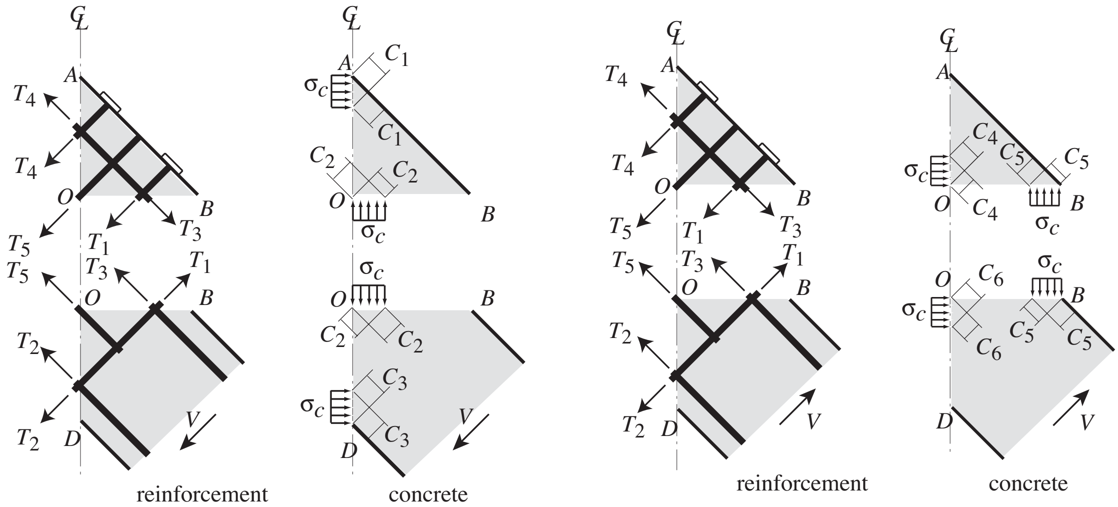

(a) loading in closing direction

(b) loading in opening direction

Figure 4: Notations for stresses defining J-mode

4.3 Strength for J-mode

Equilibrium Equations

There are three equilibrium equations for each free body in principle. By considering the symmetry of the free body, six equilibrium equations is necessary to define the equilibrium of a knee joint. However number of independent equilibrium equations is five for each case (1) under closing moment shown in Fig. 4(a), and (2) under opening moment shown in Fig. 4(b). In the case under closing moment, the independent equilibrium equations are from Eqns. (1) to (5).

$$-T_2 - T_3 + C_2 + C_3 - T_5 - V = 0 \tag{1}$$

$$-T_1 - T_4 + C_1 + C_2 - T_5 = 0 \tag{2}$$

$$T_1 - T_2 - C_2 + C_3 - V = 0 \tag{3}$$

$$\frac{jD}{2}(2T_4 - T_1 - T_3) + C_2^2 - C_1(1 - C_1) = 0 \tag{4}$$

$$\frac{jD}{2}(T_1 - 2T_2 + T_3) - C_2^2 + C_3(1 - C_3) - LV = 0 \tag{5}$$

In the case under opening moment, equilibrium equations are Eqns. (6) to (10).

$$-T_2 - T_3 + C_5 + C_6 - T_5 + V = 0 \tag{6}$$

$$-T_1 - T_4 + C_4 + C_5 - T_5 = 0 \tag{7}$$

$$T_1 - T_2 - C_5 + C_6 + V = 0 \tag{8}$$

$$\frac{jD}{2}(2T_4 - T_1 - T_3) - C_4^2 + C_5(1 - C_5) = 0 \tag{9}$$

$$\frac{jD}{2}(T_1 - 2T_2 + T_3) + C_6^2 - C_5(1 - C_5) + LV = 0 \tag{10}$$

By solving the simultaneous equations of the equilibrium, relation is derived for shear in beam (or column) and stress in reinforcing bar at critical section.

Closing Directional Loading

In a case under closing moments, the value of T_1, T_2;the resultant forces in compressive longitudinal bar are assumed to be zero. As a result, five unknown variables V, T_4, C_1, C_2, C_3 are obtained as a function of T_3 by solving the simultaneous equations from (1) to (5).

Opening directional Loading

In a case under opening moments, the value of C_4, C_5;the resultant forces in concrete are assumed to be zero. As a result, five unknown variables V, T_4, T_1,T_3,C_6 are obtained as a function of T_2 by solving the simultaneous equations from (6) to (10).

In both cases, the force T_5, effective of confinement due to horizontal and vertical joint reinforcement are assumed to be equal to the yield stress.

Example solutions for J model equilibrium equations

Numerical solution of the equilibrium equations for J-mode is shown for example in Fig. 5 for closing direction and opening direction respectively. The value shown in Fig. 5 is calculated

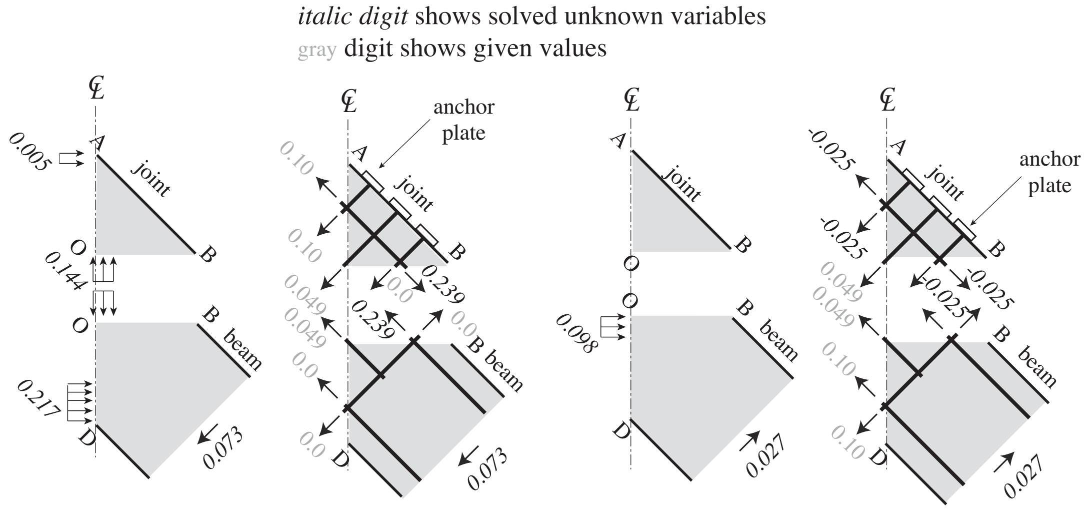

(a) Under closing directional loading ($T_4 = 0.10$)

(b) Under opening directional loading ($T_2 = 0.10$)

Figure 5: Sample solution satisfying the equilibrium equations

stresses at the stage, T_3 (under closing forces) or T_4 (under opening forces) is equal to 0.235. Concrete compressive stress at stress block is assumed to be 85 percent of the compressive concrete strength.

Table 2: Parameters of knee joint

L : distance from center of joint to contra-flexural point in mm	1000	σ_B : concrete compressive strength in MPa	25.6
t : thickness of joint (=thickness of joint) in mm	300	p_w : transverse reinforcement ratio in joint in horizontal direction %	0.3
D : column depth (=beam depth) in mm	300	f_y : yield point of transverse reinforcement MPa	367
j : ratio of the distance between tension and compression reinforcement to the D	0.8	σ_c/σ_B : strength reduction factor	0.85

4.4 Strength for B-mode

Once the stress resultant for J-mode is calculated, T_2 and T_3; the stress in longitudinal bars at critical section of B-mode are already obtained. So the calculated value of T_2, T_3 and N (=Q); axial

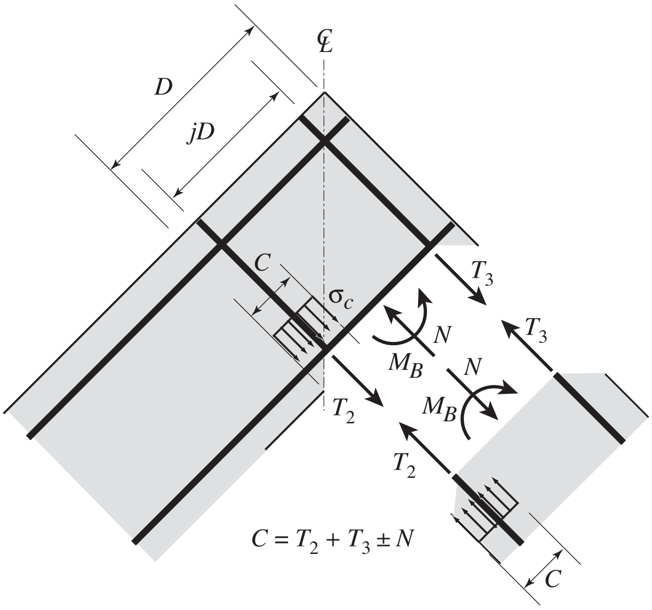

Figure 6: Notations for internal forces on critical sections of B-modes

force in beam are substituted to Eqn. (11) for calculating the strength of B-mode. The equilibrium at the critical section of B-mode is shown in Fig. 6. The resisting moment M_B at critical section are obtained from the equilibrium of axial force by Eqn. (11). The first term in Eqn (11) is moment due to the forces in longitudinal reinforcing bars while the second term is due to the resistance of concrete. In this equation, '±' means'+' for case under closing forces and '-' for under opening forces. All the value of forces are normalized by $Dt\sigma_c$ as a unit. Values of lengths are normalized by D as a unit.

$$M_B = \pm\frac{T_3 - T_2}{2}jD + \frac{(T_2 + T_3 \pm N)}{2}\left(1 - \frac{T_2 + T_3 \pm N}{tD\sigma_c}\right) \tag{11}$$

The column shear (= beam shear) is calculated by substituting the value of M_B with the Eqn (12).

$$V_B = \frac{M_B}{L - jD/2} \tag{12}$$

5. PREDICTIONS OF STRENGTH AND FAILURE MODES OF KNEE JOINTS

The principles and assumptions to obtain the strength of J-mode and B-mode are explained in the previous sections. The method for prediction of the strength and failure modes are describe for knee joints by showing examples.

5.1 Joint Shear Capacity

Sometimes joint shear is defined as horizontal joint shear force at mid-height of the joint. The value of ($T_3\ Dt\sigma_c$) is equal to the joint shear. However existing test data are not based on the measured stress in longitudinal bars but the beam shear and assumed length for moment lever arm at a beam end. So in this paper, joint shear stress τ is calculated from the beam shear V using the equation (13). (13)

$$\tau = \frac{V}{tD}\left(\frac{L - jD/2}{jD} - 1\right) \tag{14}$$

In this equation, length of moment lever arm is assumed to be constant value of *jD*.

Relationship of force in longitudinal bars T_2, T_3 or T_4 and joint shear τ is calculated and shown in Figs. 7 and 8 for the knee joint with parameters described in Table 1. Joint shear stress τ/σ_B is calculated by from the value τ calculated with Eqn. (13).

Strength of knee joint under closing moments

Figure 7 shows the theoretical B-mode strength and J-mode strength for the knee joint under closing moment. B-mode strength almost linearly increases proportional to the tensile force T_3. J-mode strength is smaller at the stage of low joint shear level. But the slope of J-mode strength decrease and the order of B-mode strength and J-mode strength is reversed at the point at which the line of J-mode strength and B-mode strength cross over, at which the value of T_3 is 0.123. From this fact, it is predicted that B-mode deformation will be dominant, if yielding of beam bars precede to this crossing point. However if beam is longitudinally reinforced heavier than that value at the crossing point, J-mode deformation will dominant before the longitudinal bars yield. It is interpreted that joint shear failure happens even yielding of beam (or column) longitudinal bars occur. In this case, the joint shear strength is function of the amount of longitudinal reinforce-

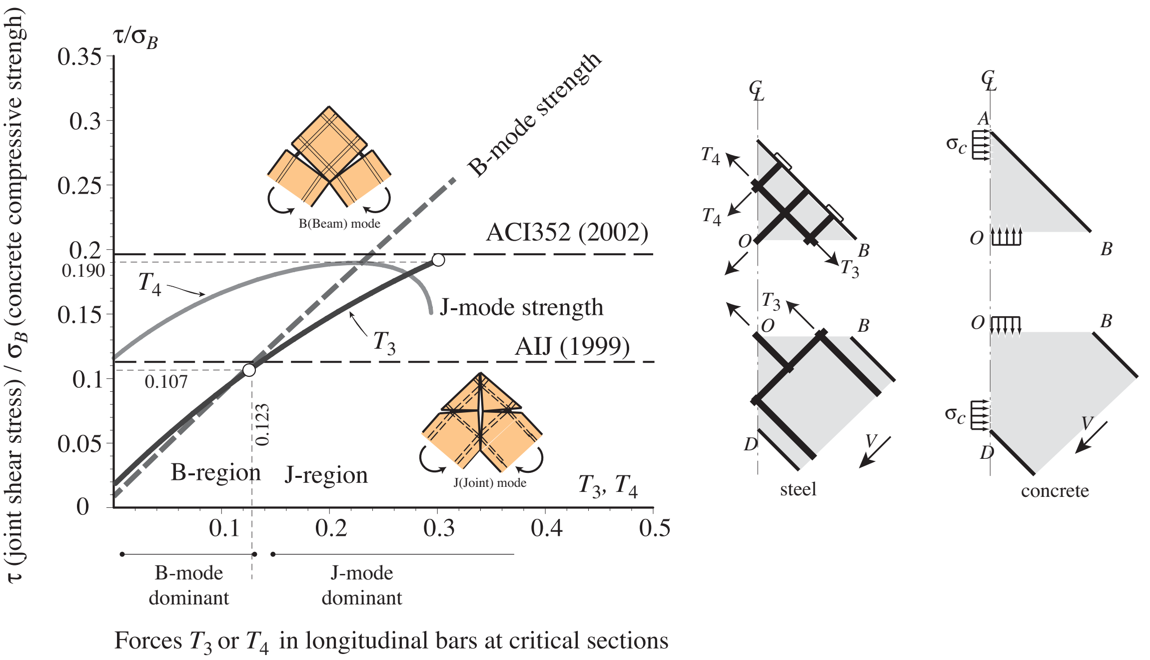

Figure 7: Theoretical prediction of knee joint behavior under closing moment

ment and on the line of J-mode strength. If the longitudinal bars in the beam or the column are infinitely strong, knee joint will reach to the upper bound of the J-mode strength; 19% of concrete compressive strength. This is theoretical maximum joint shear derived from this theory, which is close to the value given by ACI352 for type I joints. It is two times larger than that given by AIJ Guidelines.

For the design of knee joint, it is recommended to avoid damage in knee joint, by keeping the tensile reinforcement in beam or column, such that the value of T_3 should be less than 0.123 by choosing the amount of bars and yield strength.

Strength of knee joint under opening moment

Figure 8 shows the theoretical B-mode and J-mode strength of the knee joint under opening moments. B-mode strength and J-mode strength show similar relation obtained for joint under closing moment. On the contrary to that, level of joint shear stress is quite smaller than that under closing moments. The order of the B-mode and J-mode inverses at earlier stage of 0.111 for T_2 Value than the case under closing moment. Theoretical maximum joint shear for this case is

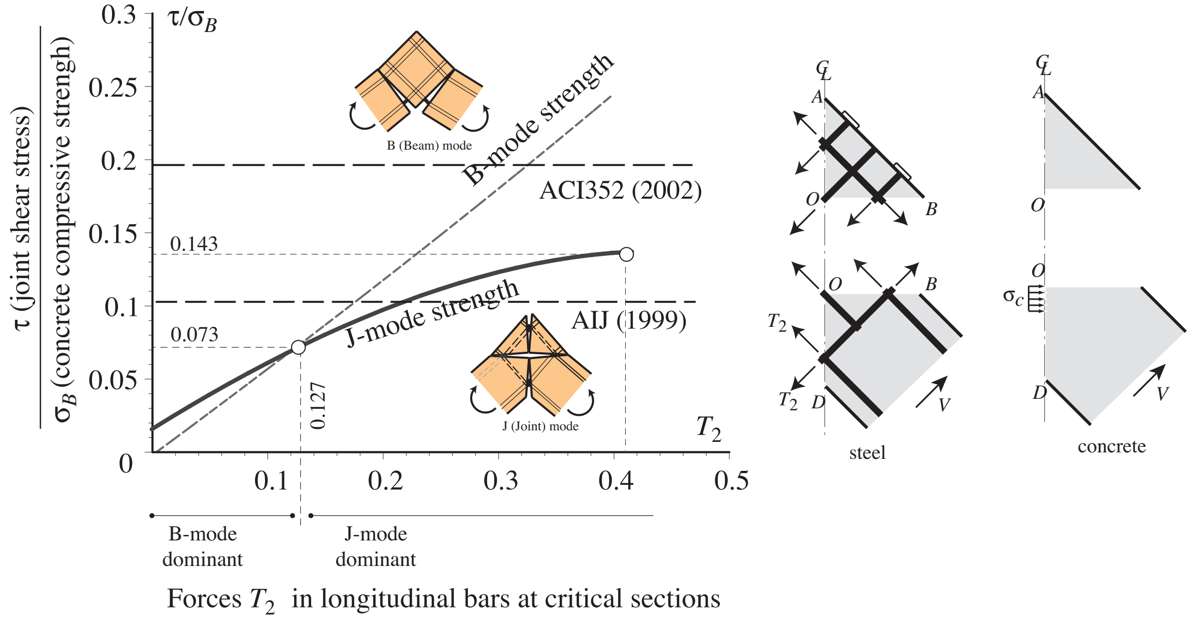

Figure 8: Theoretical prediction of knee joint behavior under closing moment

14.3% of concrete compressive strength. It is around 75% of the strength under closing moment. This value is smaller than that specified in ACI352 and larger than that by AIJ Guidelines. It is recommended by this theory that the longitudinal reinforcement in beams or column should be designed so that the value of T_2 need to be less than 0.127 if damage in knee joint is need to be minimized.

5.2 Joint Shear Failure Accompanied by Yielding of Longitudinal Bars

This theory gives reasonable explanation to the observed behavior in experimental results reported by researchers before, e. g. (Cui et al 2003). They reported that some of joint shear failure of knee joint occur after longitudinal bars yield, while the strength is much lower than that predicted by flexural theory of beam and its yielding moment. Number of knee joint specimen exhibiting joint shear failure is large but number of specimens without yielding of longitudinal bars among them are very limited.

5.3 Loading Direction

By comparison of the Figs 7 and 8, it is obvious that the joint shear capacity is not identical if the direction of loading reversed. This is also recognized by the tests (Cui et al 2003). This theory also predicts joint shear strength under opening moment is smaller than that under closing moment in general. The difference in the strength is not mentioned in the latest recommendations such as ACI352 nor AIJ Guidelines. It is recommended to investigate this issue by re-examination of test and model for knee joint.

5.4 The Other Parameters

There are more parameters influential to the behavior of knee joints such as anchorage detail and confining detail. However, due to the shortage of space in this paper, the parametric study is not described here. This theory for knee joint is just easily extended to the case with finite anchorage strength, with more joint shear reinforcement etc.. The effect of such parameters is going to be easily incorporated to further study.

6. CONCLUSIONS

It is demonstrated in this paper that the new theory for beam-column joint is successfully applied to the knee joint. It can explain the reason why the geometrical parameter affect joint shear strength of reinforced concrete beam-column joint. It is necessary to verify the model by the comparison with test results as a future study.

7. REFERENCES

American Concrete Institute (ACI). (2002). "Recommendations for Design of Beam-Column Connections in Monolithic Reinforced Concrete Structures." ACI352R-02, Farmington Hills, Michigan.

Architectural Institute of Japan (AIJ), (1999). "Design Guideline for Earthquake Resistant Reinforced Concrete buildings Based on Inelastic Displacement Concept." Tokyo, Japan. (in Japanese)

Cui Jianyu, Fujii S., Nishiyama N. and Watanabe F. (2003) "Modeling of Load-resistant Mechanism on Corner Joints." Journal of Structure and Construction, AIJ, No. 567, May, 2003, pp. 101-109. (in Japanese)

Paulay, T., Park, R., and Priestley, M. J. N., (1978). "Reinforced Concrete Beam-Column Joints Under Seismic Actions." Journal of ACI, 75 (11), 585-593.

Shiohara, H., (2001). "New Model for Shear Failure of RC Interior Beam-Column Connections." Journal of Structural Engineering, ASCE, Vol. 127, No. 2, February 2001, 152-160.

Shiohara, H., (2002a). "Effects of Interaction between Joint Shear and Anchorage Force within R/C beam-column Joints on their Strength and Failure Modes, Proceedings of the Seventh U.S. National Conference on Earthquake Engineering (7NCEE), July 21-25, 2002, Boston, Massachusetts.

Shiohara, H., (2002b). "New Model for Joint Shear Failure of R/C Exterior Beam-column Joints." Proceedings of US-Japan Workshop on Performance Based Earthquake Resistant Engineering of RC Structures, Toba, October 2002.

USE OF EXPERIMENTAL EVIDENCE TO DEFINE PERFORMANCE LIMIT STATES FOR RCS FRAME CONNECTIONS

Gustavo J. PARRA-MONTESINOS[1], James K. WIGHT[2] and Xuemei LIANG[3]

ABSTRACT

A correlation between joint deformations and damage is established, based on experimental results, in order to propose target shear distortion levels for use in performance-based design of hybrid RCS connections. Shear distortions of 0.5% were found to correspond to an immediate occupancy performance level, while a shear distortion of 1.2% is proposed as the value where connections reach their ultimate strength with a damage corresponding to a collapse prevention performance level. In order to avoid excessive drifts and joint damage due to large connection distortions, the use of strength factors calibrated at a shear distortion of 0.5% are recommended for use in connection design. The design method proposed in this investigation uses a deformation-based capacity design philosophy, where the maximum joint shear force demand when adjacent beams reach their ultimate capacity is kept lower than the joint strength at the target shear distortion. Four beam-column-slab subassemblies were tested in order to evaluate the effectiveness of the proposed design method for controlling joint distortions and damage. Comparisons of predicted versus observed joint distortion response and damage suggest that the deformation-based capacity design procedure is effective for achieving the desired joint target performance state.

1. INTRODUCTION

Beam-column connections in reinforced concrete (RC) and hybrid reinforced concrete column-steel beam (RCS) frame structures have been traditionally designed using strength-based procedures. In general, the shear strength of RC connections is specified as a function of $\sqrt{f'_c}$ (ACI Building Code 2002), with strength factors primarily determined based on experimental evidence. Similarly, the strength of the concrete panel specified in the ASCE design guidelines for RCS connections (ASCE 1994) is also a function of $\sqrt{f'_c}$, while the strength of the steel web panel is estimated as in steel beam-column connections. Currently, no explicit provisions are given in either the ACI Committee 352 design recommendations for RC connections (ACI 2002) or the ACI Building Code (2002) regarding expected shear distortions and damage based on applied shear and reinforcement detailing. The situation is similar for RCS joints, although the

[1] *Assistant Professor, Department of Civil and Environmental Engineering, University of Michigan. Email: gjpm@umich.edu*
[2] *Professor, Department of Civil and Environmental Engineering, University of Michigan. Email: jwight@umich.edu*
[3] *Structural Engineer, S.K. Ghosh Associates Inc., Northbrook, Il.*

adequacy of the strength equations in the ASCE guidelines was evaluated at joint distortions of 1.0% in interior subassemblies. Thus, even though well detailed RC and RCS connections have been shown to behave satisfactorily under load reversals (Meinheit and Jirsa 1981; Durrani and Wight 1982; Ehsani and Wight 1982; Kanno 1993; Parra and Wight 2000), beam-column connections subjected to high shear stresses could undergo excessive distortions that may significantly affect structural performance.

During the last fifteen years, the role of connection distortions as a key parameter in beam-column connection design has been recognized by several researchers (for example Pantazopoulou and Bonacci 1992; Bonnaci and Wight 1996; Parra and Wight 2001; 2002; Parra et al. 2003). In the research conducted by Pantazopoulou and Bonacci, equilibrium, compatibility and constitutive relations for concrete and steel were used in order to model the behavior of beam-column joints of seismic-resistant frames. From this investigation, recommendations were given in order to estimate the shear stress corresponding to yielding of the joint hoops because of the significant joint deterioration at larger distortions. Bonacci and Wight also proposed a displacement-based design procedure for RC frames that explicitly accounts for the contribution of joint distortions to frame drift. In that procedure, the connections are designed to remain elastic, based on the joint model developed by Pantazopoulou and Bonacci (1992).

More recently, Parra and Wight (2001; 2002) developed a simple joint model in order to predict the shear force versus shear distortion envelope response of RC and hybrid RCS connections subjected to load reversals. In that model, the state of strain in the connection was defined through the ratio between principal tensile and compression strains, which was assumed to increase linearly with joint shear distortions. Design equations were proposed for predetermined levels of shear distortion that would allow designers to control the amount of damage sustained by a connection during an earthquake. The important role played by connection distortions in RC frames has also been recognized in the prestandards for the seismic rehabilitation of structures (FEMA 356) developed by ASCE (2000). In that document, joint modeling parameters are given for RC connections, based on the level of applied shear, axial load, and reinforcement detailing. In addition, shear distortion limits are proposed for immediate occupancy, life safety and collapse prevention performance states.

In this paper, the joint model proposed by Parra and Wight for hybrid RCS connections is used to implement a deformation-based capacity design procedure and its accuracy is evaluated through experimental results obtained from reversed cyclic load tests of beam-column subassemblies. A correlation between joint damage and shear distortion is established in order to select target distortions for various performance levels. The ability of the proposed model and corresponding design procedure to maintain joint distortions within acceptable limits is evaluated based on experimental results.

2. STRENGTH AND DISTORTIONS IN RCS CONNECTIONS

It has been generally accepted that the shear strength of RCS connections is provided by a steel web panel, an inner diagonal concrete strut, and an outer diagonal strut (Fig. 1). The steel web panel behavior is similar to that in steel frame structures. The inner diagonal strut is activated through bearing of the concrete against the steel beam flanges and Face Bearing Plates (FBPs) at the front and back column faces (Fig. 2a). The outer diagonal strut is activated through the use of shear keys, such as steel columns that are typically used for erection purposes (Figs. 2a and 2b), or steel band plates wrapping around the RC column just above and below the steel beam (Fig. 2b). Detailed information on the transfer of forces in RCS connections can be found elsewhere (ASCE 1994; Parra and Wight 2001). In order to provide confinement to the connection, overlapping U-shaped stirrups (Fig. 2a) or steel band plates (Fig. 2b) are used. Experimental results (Parra and Wight 2000) have shown that there is no need for joint stirrups when steel band plates are used, and thus transverse beams can frame directly into the column (Fig. 2b).

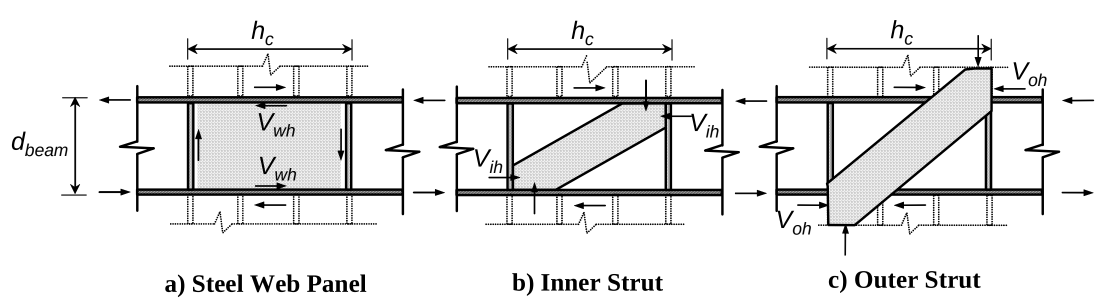

Fig. 1 - Strength Mechanisms in RCS Joints

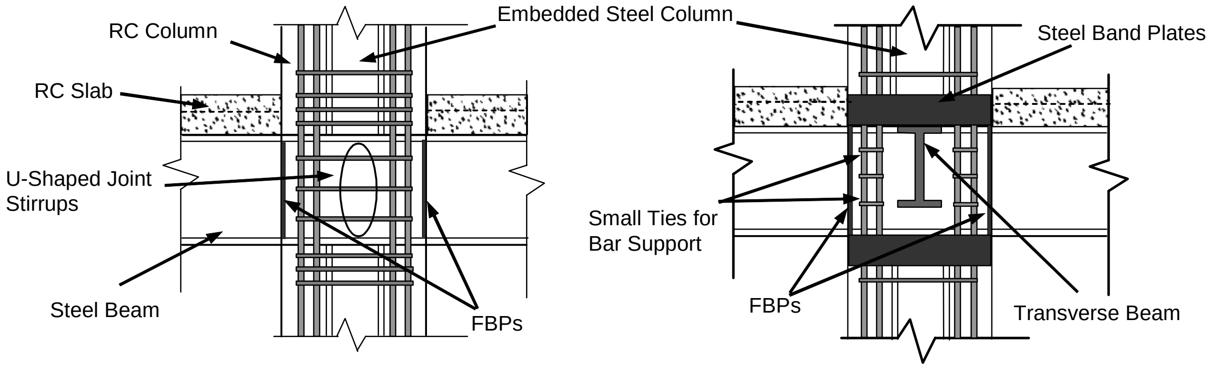

a) Joint with U-Shaped Stirrups **b) Joint with Steel Band Plates**

Fig. 2 - Typical RCS Joint Details

In terms of distortions, RCS connections deform in shear as in steel or RC beam-column connections (Fig. 3a). However, an additional source of flexibility is present in RCS joints, due to high bearing stresses between the beam flanges and the surrounding concrete. These bearing stresses may lead to local concrete crushing and the opening of a gap adjacent to the beam flanges that allow a rigid body rotation of the steel beam inside the connection region (Fig. 3b). Thus, the total joint distortion in RCS connections is the summation of the joint shear distortion and beam bearing distortion. Fig. 4 shows a typical normalized shear force (applied shear ÷ ultimate strength) versus distortion (shear and bearing) envelope curves for RCS connections (Parra and Wight 2001). Based on the distortions that occur in RCS joints, two failure modes have been identified: a panel shear failure, and a bearing failure (ASCE 1994). Bearing failures have been shown (Kanno 1993) to be less stable than shear failures, and thus RCS connections should be designed such that their bearing strength is larger than their shear strength.

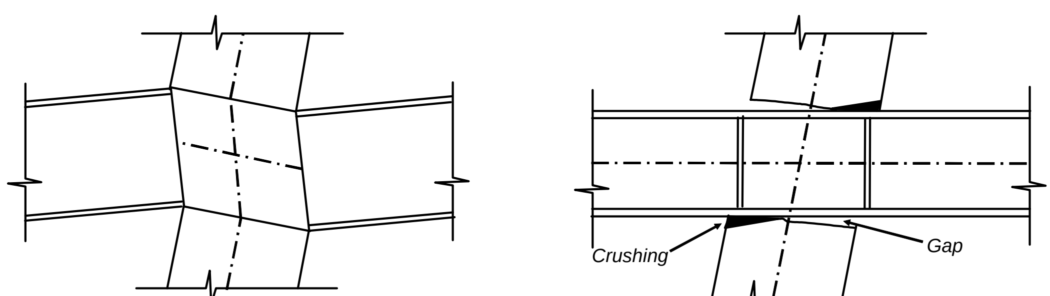

a) Shear Distortion **b) Bearing Distortion**

Fig. 3 - Distortions in RCS Joints

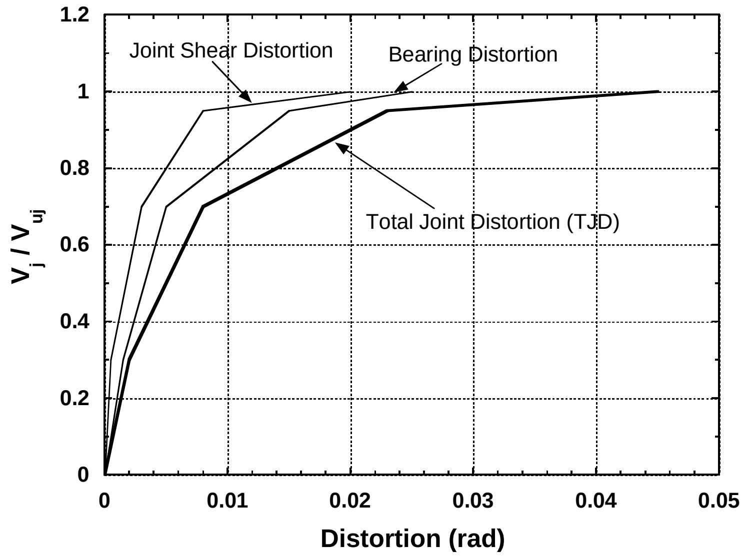

Fig. 4 - Typical Joint Shear Force versus Distortion Response

3. DESIGN OF RCS CONNECTIONS

Design equations for RCS connections in the U.S. were first developed by an ASCE task group (ASCE 1994), based on results from research conducted at the University of Texas during the late 1980s (Sheikh et al. 1987; Deierlein et al 1988). These guidelines adopted a strength-based approach, where the design equations for the steel and concrete panels are similar to those used in steel and RC connections. Comparison of predicted and experimental results from tests of interior RCS beam-column subassemblies suggested that the ASCE design equations are safe when calibrated at total joint distortions of 1.0%. More recently, Parra and Wight (2001) conducted a series of tests on exterior beam-column subassemblies. When comparing the measured joints strengths with the predictions from the ASCE guidelines, it was observed that the shear capacity of exterior RCS joints could be significantly overestimated. In addition, total joint distortions in excess of 3.0%, accompanied by severe damage, could be expected in RCS joints subjected to shear stresses close to the connection capacity. Thus, a deformation-based capacity design procedure, based on shear distortions, was proposed by the writers (Parra et al. 2003) in order to design RCS connections such that their shear distortions would not exceed a predefined deformation and performance level.

The discussion above implies that acceptable levels of shear distortion in RCS connections must be defined. For this purpose, damage observed in tests of RCS connections at different deformation levels can be evaluated to select appropriate performance states for various earthquake intensities. Fig. 5 shows a lateral load versus joint shear distortion response for an exterior RCS connection designed following a strength-based approach (Parra and Wight 2000), and Figs. 6a and b show the joint damage at 0.5% and 1.5% shear distortion, respectively. As can be observed in Fig. 5, the hybrid connection behaved in a stable manner up to a shear distortion of about 0.75%. When larger deformation demands were imposed to the subassembly, a substantial loss of shear stiffness occurred, leading to a peak shear distortion of approximately 1.5%. From Fig. 6a, it can be observed that a shear distortion of 0.5% would correspond to moderate joint damage, which could be comparable to an immediate occupancy performance level. However, significant damage can be expected at shear distortions of 1.5% (Fig. 6b), characterized by extensive steel web panel yielding and diagonal crack widths exceeding 5 mm. This damage state would correspond to a collapse prevention performance level.

In the proposed design procedure, the horizontal shear strength of the steel web panel V_{wh}, inner diagonal strut V_{ih}, and outer diagonal strut V_{oh} can be estimated using Eqs. (1) thru (3), respectively, as follows,

$$V_{wh} = k_w \frac{f_y}{\sqrt{3}} t_w \, h_c \tag{1}$$

$$V_{ih} = k_i \; f'_c \, (1.13 - 0.033 \; f'_c \;) \, h_c \, (b_f \; - t_w \,) \tag{2}$$

$$V_{oh} = k_o \; f'_c \, (1.13 - 0.033 \, f'_c \;) \, h_c \, b_o \tag{3}$$

where f_y and t_w are the yield strength and thickness of the steel web panel, h_c is the column depth, f'_c is the concrete compressive strength (in ksi), and b_f and b_o are the beam flange width and outer panel width, respectively. The width of the outer diagonal strut can be determined based on the shear key used (i.e. steel column or steel band plates), as suggested by Parra and Wight (2001). Three strength factors k_w, k_i and k_o are used to evaluate the strength of the steel and concrete components and depend on the target shear distortion level and connection type, i.e. interior versus exterior.

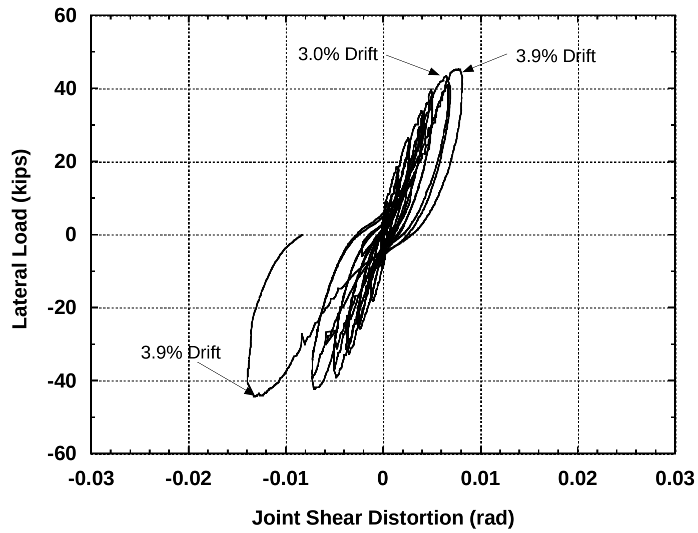

Fig. 5 - Load versus Joint Shear Distortion Response of RCS Connection Designed Following a Strength-Based Approach

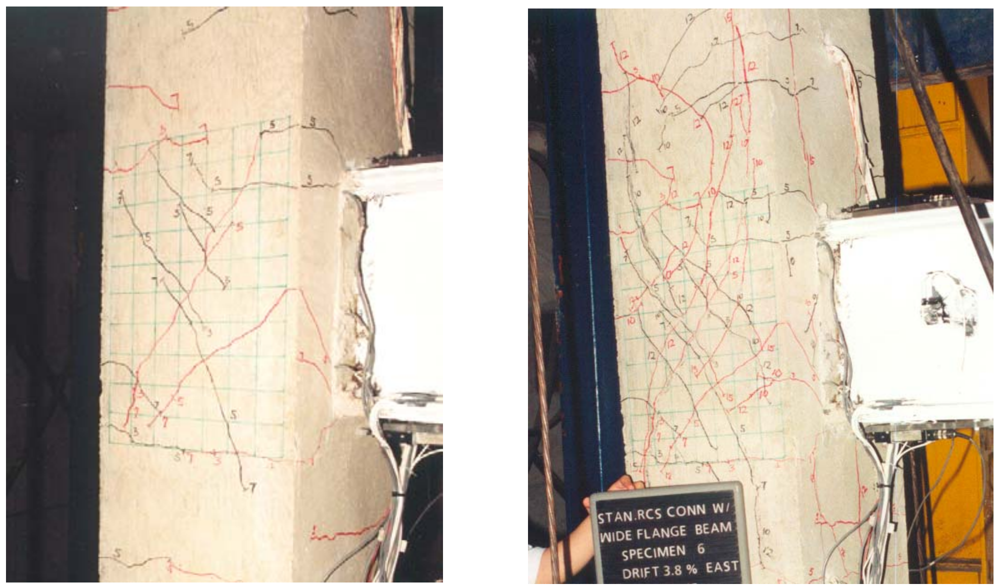

a) 0.5% Shear Distortion **b) 1.5% Shear Distortion**

Fig. 6 - Joint Damage at 0.5% and 1.5% Shear Distortion

Because yielding in the middle region of the steel web panel starts at low distortion levels and spreads rapidly towards the column faces, most of the steel web panel depth is effective in resisting the applied shear at reasonable levels of shear distortion (≥0.5%). Parra and Wight (2001) recommended k_w = 0.9 and 0.8 for interior and exterior RCS joints, respectively, based on experimental results.

The factors k_i and k_o can be determined from the model developed by Parra and Wight (2001), which allows the determination of the shear force versus shear distortion envelope curve for RCS joints. Based on the observed correlation between joint shear distortion and damage, values for the strength factors corresponding to shear distortions of 0.5% and 1.2% were developed and are shown in Table 1.

When designing RCS frame systems following a strong column-weak beam philosophy, most of the inelastic deformations are expected to concentrate at the beam ends and at the column bases. In connections of RCS frame systems, the behavior will be affected by the peak demand imposed by the adjoining members, which can be estimated as,

$$(V_{jh})_{max} = \frac{\Sigma(M_u)_{beam}}{d_{beam} - t_f} - (V_u)_{col} \tag{4}$$

where V_{jh} is the horizontal joint shear force demand, $\Sigma(M_u)_{beam}$ is the summation of the ultimate moment capacities of the composite beams in one plane framing into the connection, d_{beam} and t_f are the steel beam depth and flange thickness, respectively, and $(V_u)_{col}$ is the column shear force when the beams reach their ultimate moment strength. When determining the ultimate beam moment strength, material overstrength and strain hardening of the steel should be considered.

For a moderate to large earthquake (i.e. 10% probability of exceedance in 50 years) that imposes limited inelastic rotations at the beam ends, the joint shear force demand would be in between those corresponding to beam yield moment and ultimate moment capacities. However, for a rare event (i.e. 2% probability of exceedance in 50 years), the maximum shear force demand in the connections will approach that determined using Eq. (4). Referring to Fig. 4, it is clear that a good estimation of the joint shear force demand/capacity ratio is essential for predicting the peak distortion expected during an earthquake event. Moreover, for shear force demands that exceed approximately 70% of the connection capacity, small changes in force lead to large differences in joint distortions, which makes it difficult to accurately predict connection performance. Thus, in a realistic scenario, a structural engineer might only select one target performance level that will be satisfied at the maximum joint shear demand (beams reaching their ultimate moment capacity). Based on the damage observed in RCS connections at various shear distortion levels, and given the difficulties involved in connection repairs, a target shear distortion of 0.5% is recommended for design. Some inelastic joint deformations are expected at this shear distortion level and the expected total joint distortion would be approximately 1.0%, which is considered a substantial joint deformation.

Table 1 – Strength Factors for Immediate Occupancy and Collapse Prevention Performance States

			Joint Detail			
			Standard		Steel Band Plates	
Target Shear Distortion	**Performance Level**	**k Factor**	**Interior**	**Exterior**	**Interior**	**Exterior**
0.5%	**Immediate Occupancy**	k_i	0.25	0.17	0.32	0.24
		k_o	0.14	0.10	0.17	0.12
1.2%	**Collapse Prevention**	k_i	0.32	0.21	0.40	0.29
		k_o	0.17	0.11	0.22	0.15

4. APPLICATION OF DEFORMATION-BASED CAPACITY DESIGN PROCEDURE FOR RCS CONNECTIONS

4.1 Experimental Program

In order to evaluate the effectiveness of the proposed model for controlling joint distortions and damage during a seismic event, four RCS beam-column-slab subassemblies, two interior and two exterior, were tested under reversed cyclic loading. Two simple joint details were used, consisting of face bearing plates, steel columns, and either overlapping U-shaped stirrups or steel band plates for joint confinement (Figs. 2a and b). The connections in the interior test specimens were designed such that the maximum shear distortion would be limited to 0.5% when the composite beams reach their ultimate moment capacity. Thus, only moderate joint damage would be expected when large inelastic rotation demands are imposed on the beams. For moderate beam rotation demands, the hybrid joint should behave in the elastic range with only minor damage, characterized by a few hairline diagonal cracks.

Because the RC column and steel beam sections used in the interior specimens were also used in the exterior specimens (only one beam framing into the column), lower joint shear distortions would be expected due to a decrease in the joint shear force demand. Thus, the results presented in this paper will focus on the behavior of the two interior specimens where larger demands were imposed on the connections. A sketch of the test setup is shown in Fig. 7. All test specimens were subjected to twenty reversed cyclic displacement cycles with drifts ranging from 0.5% to 5.0%. A small axial load corresponding to approximately 5% of the column axial capacity was applied to the RC columns.

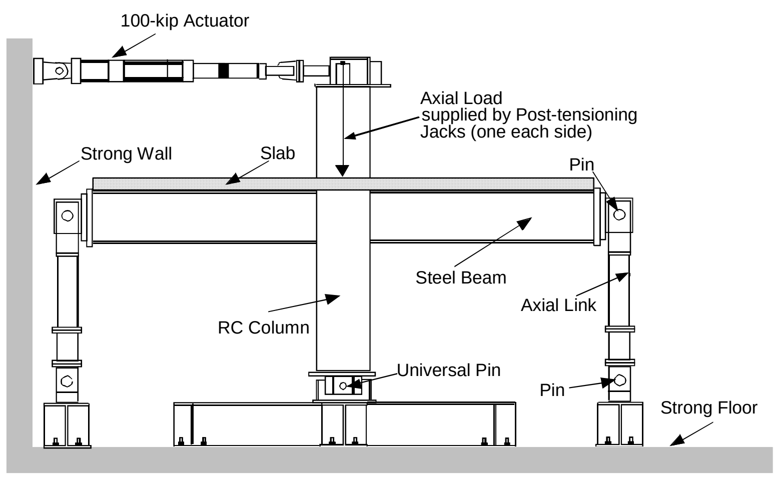

Fig. 7 - Test Setup

4.2 Experimental Results

4.2.1 Cracking Pattern and Load versus Displacement Response

Because of test setup deformations, the actual drifts achieved during the tests were slightly lower than the intended displacements. The drift values reported in this section refer to the actual drifts. First diagonal cracking in the joint region of Specimens 1 and 2 occurred at approximately 0.5% story drift. For Specimen 2, which had transverse beams in the orthogonal direction, diagonal cracks originated from the tips of the bottom flange of the transverse beams. Flexural cracks across the width of the concrete slabs were also observed at 0.5% drift. Specimens 1 and 2 behaved in the cracked-elastic range up to 1.0% drift. For larger drift levels, beam yielding started to occur, and at 2.0% drift, after significant beam yielding had taken place, local buckling was observed in the beam flanges and web. The peak load for Specimens 1 and 2 was reached during the first cycle at 3.0% drift. During the second cycle to this drift level, flange local buckling became severe, leading to a drop in the lateral strength of the subassemblies. New diagonal cracks continued to form in the joint region up to the point when the peak load was reached, but most of the joint cracking occurred before 2.5% story drift. The joint region in Specimens 1 and 2 sustained only moderate damage at the end of the tests, as intended (Fig. 8a).

Slight pinching can be observed in the load vs. displacement response (Fig. 8b) for cycles below 2.5% drift because of joint diagonal cracking and beam rigid body rotations within the joints. At larger displacement cycles, during which large beam plastic deformations occurred, full hysteresis loops were observed. Both specimens exhibited stable responses, retaining more than 75% of their peak strength at the end of the tests.

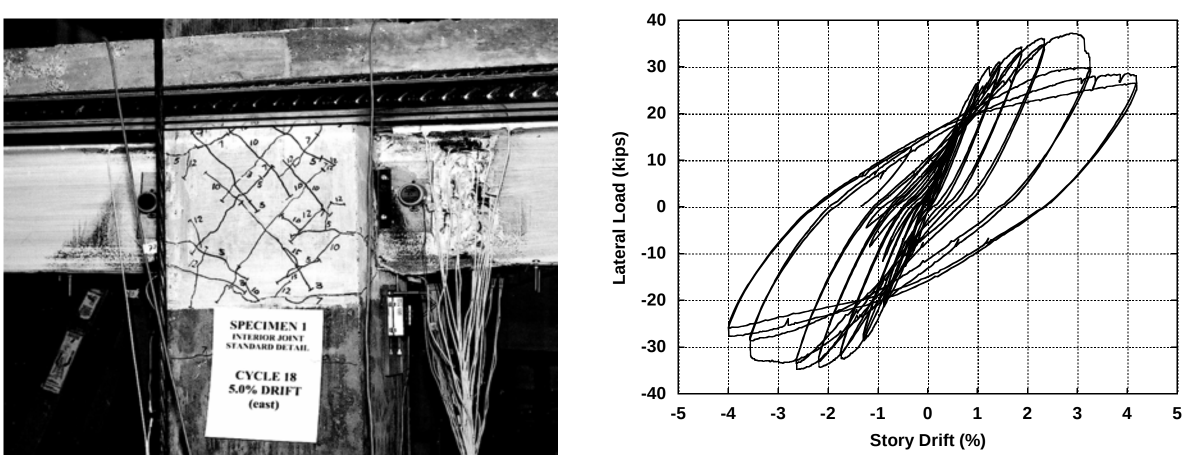

a) Cracking Pattern

b) Load versus Displacement Response

Fig. 8 - Cracking Pattern and Hysteresis Response of Specimen 1

4.2.2 Predicted versus Measured Joint Distortions

The lateral load versus joint shear distortion envelope responses for Specimens 1 and 2 are shown in Fig. 9a. The predicted lateral load versus joint shear distortion curves are also shown for comparison purposes. As can be observed, the predicted behavior represented a good estimate of the connection response. In addition, the peak joint shear distortion was approximately 0.5% for Specimens 1 and 2, which indicates that the deformation-based capacity design procedure was effective in controlling joint shear distortions. With respect to joint damage, it is clear from the cracking pattern shown in Fig. 8a that only moderate damage occurred at a shear deformation of 0.5%, a damage state that could be correlated with an immediate occupancy performance level.

With regard to total distortions, Fig. 9b shows the experimental lateral load versus shear, bearing and total joint distortion envelope for Specimen 2. As can be observed, a maximum total joint distortion of about 1.1% was measured in the test, which is very close to the target total distortion of 1.0%. Even though bearing distortions were larger than shear distortions, joint damage is better correlated to shear distortions, given that the joint bearing strength is larger than the shear strength. It should be noted that even though connection shear deformations are intended to remain below 0.5%, some inelastic response is expected, and thus the proposed target deformation is not too conservative. In addition, the expected total joint distortion (shear + bearing) of 1.0% roughly contributes to 1.0% drift in the subassembly, which the writers consider appropriate for connections.

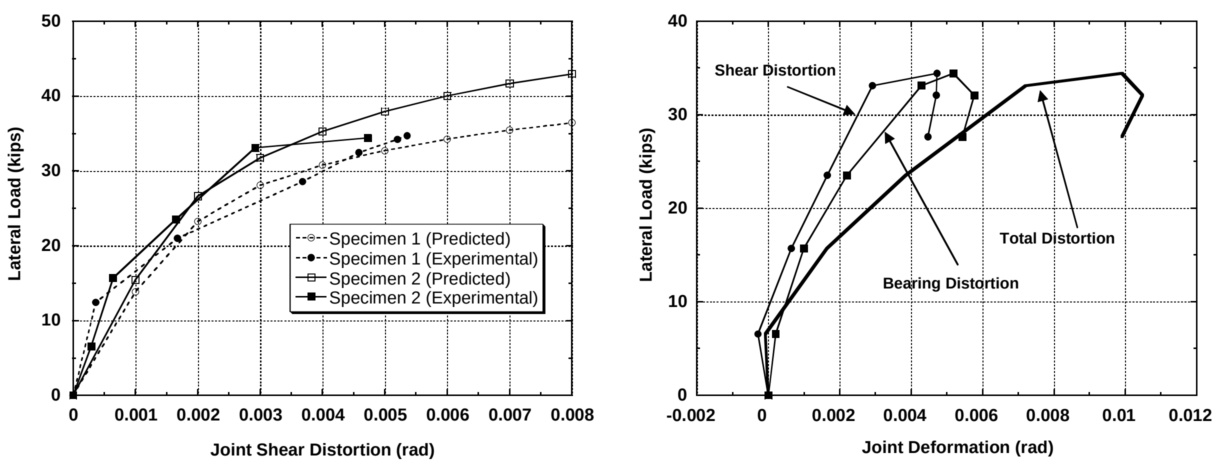

a) Predicted vs. Measured Shear Distortion **b) Measured Total Joint Distortion (Spec 2)**

Fig. 9 - Predicted and Measured Joint Distortions

Through experimental results, it has been demonstrated that the deformation-based capacity design procedure for RCS connections can be effectively used for achieving target deformations and performance states. Thus, designers can limit connection damage and drifts due to joint distortions for earthquakes of various intensities.

5. SUMMARY AND CONCLUSIONS

The use of a deformation-based capacity design procedure for RCS connections is recommended to limit joint damage and the contribution from joint distortions to frame drift. Based on experimental evidence, a design target shear distortion of 0.5% is proposed, which would lead to moderate joint damage and a corresponding immediate occupancy performance state. Because of bearing deformations that also take place in RCS connections, the expected total joint distortion and corresponding contribution to story drift is estimated as 1.0%. Through results from the tests of several beam-column-slab subassemblies under large displacement reversals it was shown that the proposed deformation-based joint design procedure is effective in controlling joint damage and distortions.

6. REFERENCES

ACI Committee 318. (2002). *Building Code Requirements for Structural Concrete*. Report No. ACI 318-02, American Concrete Institute, Farmington Hills, Michigan.

ACI-ASCE Committee 352. (2002). *Recommendations for Design of Beam-Column Joints in Monolithic Reinforced Concrete Structures*. Report ACI 352R-02, American Concrete Institute, Farmington Hills, MI.

ASCE Task Committee on Design Criteria for Composite Structures in Steel and Concrete. (1994). Guidelines for design of joints between steel beams and reinforced concrete columns. *Journal of Structural Engineering*, ASCE, 120(8), pp. 2330-2357.

ASCE. (2000). *Prestandard and Commentary for the Seismic Rehabilitation of Buildings*. FEMA 356.

Bonacci, J.F., and Wight, J.K. (1996). Displacement-based assessment of beam-column joint designs. *Mete A. Sozen Symposium: A Tribute from His Students*, ACI Special Publication 162, pp. 117-138.

Deierlein, G.G., J.A. Yura, and J.O. Jirsa. (1988). *Design of Moment Connections for Composite Framed Structures*. PMFSEL Report No. 88-1, University of Texas at Austin, Austin, Texas.

Durrani, A.J., and J. K. Wight. (1982). *Experimental and Analytical Study of Internal Beam to Column Connections Subjected to Reversed Cyclic Loading*. Report No. UMEE 82R3, Dept. of Civil and Environmental Engineering, University of Michigan, Ann Arbor, MI.

Ehsani, M.R., and J.K. Wight. (1982). *Behavior of External Reinforced Concrete Beam to Column Connections Subjected to Earthquake Type Loading*. Report No. UMEE 82R5, Dept. of Civil and Environmental Engineering, University of Michigan, Ann Arbor, MI.

Kanno, R. (1993). *Strength, Deformation, and Seismic Resistance of Joints Between Steel Beams and Reinforced Concrete Columns*. Ph.D. Thesis, Cornell University, Ithaca, NY.

Meinheit, D.F., and Jirsa, J.O. (1981). Shear strength of R/C beam-column connections. *Journal of the Structural Division*, ASCE, 107(ST 11), pp. 2227-2244.

Pantazopoulou, S., and Bonacci, J. (1992). Consideration of questions about beam-column joints. *ACI Structural Journal*, 89(1), pp. 27-36.

Parra-Montesinos, G., and Wight, J.K. (2000). Seismic response of exterior RC column-to-steel beam connections. *Journal of Structural Engineering*, ASCE, 126(10), pp. 1113-1121.

Parra-Montesinos, G., and Wight, J.K. (2001). Modeling shear behavior of hybrid RCS beam-column connections. *Journal of Structural Engineering*, ASCE, 127(1), pp. 3-11.

Parra-Montesinos, G., and Wight, J.K. (2002). Prediction of strength and shear distortion in R/C beam-column joints. *S. M. Uzumeri Symposium: Behavior and Design of Concrete Structures for Seismic Performance*, ACI Special Publication 197, pp. 191-214.

Parra-Montesinos, G., Liang, X., and Wight, J.K. (2003). Towards deformation-based capacity design of RCS beam-column connections. *Engineering Structures*, 25(5), pp. 681-690.

Sheikh, T.M., J.A. Yura, and J.O. Jirsa. (1987). *Moment Connections Between Steel Beams and Concrete Columns*. PMFSEL Report No. 87-4, University of Texas at Austin, Austin, Texas.

PLENARY SESSION 2: METHODS OF TESTING AND DISCUSSION ON FUTURE COLLABORATION

Chaired by

♦ James Wight and Sunsuke Sugano ♦

DYNAMIC TEST AND ANALYSIS OF REINFORCED CONCRETE WALL ELEMENTS

Toshimi KABEYASAWA[1],

Tomoya MATUI[2], Atsushi KATO[3], Hiroshi KURAMOTO[4] and Ichiro NAGASHIMA[5]

ABSTRACT

A dynamic experiment of two reinforced concrete walls was carried out as a preliminary test towards three-dimensional full-scale testing at E-defense. The two specimens were identical and 1/3 scale model of a plane shear wall with boundary columns representing lower two stories in a six-story wall-frame building. Upper stories were modeled with mass of steel weight over concrete stab. Only the height to the center of the mass from the base was changed between the two specimens to simulate the effect on the collapse mechanism, because the effective height of dynamic lateral loads may change to the change in distribution. The two specimens were subjected to the same series of earthquake motions, the intensity of which were amplified gradually, until up to failure. The first specimen Wall-A with the lower mass height failed in shear after flexural yielding as was expected from the calculated shear strength which was close to the flexural strength. The second specimen Wall-B, the calculated shear strength of which is apparently higher than the flexural strength, also failed in shear under the smaller input motion level. From the analysis on the hysteretic energy dissipation, this is estimated to caused by many cyclic responses due to longer period in Wall-B so that the total input energy was accumulated, although the maximum deformation amplitudes were not much larger than those of Wall-A.

1. INTRODUCTION

A dynamic experiment of two reinforced concrete wall elements representing lower two stories of medium-rise wall-frame building was carried out. This experiment was planned as a preliminary test towards three-dimensional full-scale testing at E-defense, the world largest 3-D earthquake simulator under construction in Miki city, Hyogo-ken. The aims of this study are to obtain dynamic restoring force characteristics or hysteresis characteristics, to compare dynamic behavior with static one, and to develop and verify the wall member model for nonlinear dynamic analysis.

---

[1] *Earthquake Research Institute, The University of Tokyo*
Email: kabe@eri.u-tokyo.ac.jp
[2] *Graduate student, Department of Architecture, The University of Tokyo*
Email:matsui@eri.u-tokyo.ac.jp
[3] *National research Institute for Earth science and Disaster prevention*
Email:kato@bosai.go.jp
[4] *Associate professor, Toyohashi University of Technology, Toyohashi, Japan*
Email: kura@tutrp.tut.ac.jp
[5] *Technical Research Center, Taisei Corporation, Japan*
Email: ichiro.nagashima@sakura.taisei.co.jp

Also as the preliminary test towards the full-scale test, technical methods for dynamic tests are to be verified and developed, such as control of base acceleration, measurement and recording of acceleration, displacement, force and strains. The test was carried out in June and July, 2002 on the large-size shaking table of NIED in Tukuba. In this paper, the method and the result of the test are outlined.

2. TEST METHOD

2.1 Specimen

Two simple shear wall elements (Wall-A and Wall-B) shown in Fig.1 were tested. The two specimens were identical and 1/3 scale model of a plane shear wall with boundary columns representing lower two stories in a six-story wall-frame building. The dynamic loading direction is in-plane direction only and out-of-plane deformations are under restraint by the support of the steel frames on both sides as shown Fig.2. The special roller devices were inserted between the specimen and the frames. Sectional dimensions and reinforcement details are shown in Table 1. The size of the wall panel in a story is 800mm height, 1600mm wide, and 80mm thickness. As the vertical and horizontal reinforcement, D6 bars are placed at the spacing of 100mm, the shear reinforcement ratio (ps) of which is 0.004. The steel mass of 442kN with concrete block was loaded on the specimen to give equivalent effect of gravity and lateral loads in the proto-type structure. The equivalent height of lateral loads may change due to the wall-frame interaction and the effect of higher modes of response. To simulate the effects of the shear force level at the flexural yielding on the collapse mechanism, only the height to the center of the mass from the base was changed between the two specimens: 2750mm for Wall-A and 3500mm for Wall-B. Shear span ratios to the total depth of the wall are 1.38 for Wall-A and 1.75 for Wall-B. The ratios were selected so that the calculated shear strength is almost equal to the shear at the flexural yielding for Wall-A, whereas the shear strength is higher for Wall-B.

Nominal strength of used concrete is 21N/mm^2 (target strength is 27N/mm^2 on test. Material property of concrete on test is shown Table2. Maximum size of coarse aggregate is 13mm. Construction joint was ravage on the day after installation. Material property of reinforcement is shown Table3. Nominal strength of reinforcement is SD295A for D6 and D10, SD390 forD13 and SD345 for D25.

Table 1 Section details of member (unit: mm)

		1F	2F
Column	B×D	200×200	
	Main bar	12-D13(pg=3.8%)	
	Hoop	2-D6@60 (pw=0.53%)	2-D6@50 (pw=0.64%)
	Sub hoop	2-D6@120 (pw=0.27%)	—
Beam	B×D	150×200	200×500 (included 300 in top stab)
	Main bar	4-D10(pt=0.54%)	
	Hoop	2-D6@100(pw=0.42%)	
Wall	Thickness	80	
	Vertical bar	D6@100(ps=0.4%)	2-D6@100(ps=0.8%) (top 400mm) D6@100(ps=0.4%)
	Horizontal bar	D6@100(ps=0.4%)	

Table 2 Material properties of concrete

Specimen		Age (days)	σ_B (N/mm^2)	ε (μ)	Ec (kN/mm^2)	ν	σ_t (N/mm^2)
Specimen A (Shear failure type) on 6/24	1st story wall	40	26.4	1770	24.4	0.19	2.62
	2nd story wall	32	30.0	1861	25.4	0.19	2.69
	Base stab	47	28.4		—	—	2.44
	Top stab	25	29.3		—	—	2.28
Specimen B (Bending failure type) on 7/2	1st story wall	48	25.2	1811	24.8	0.18	2.47
	2nd story wall	40	29.6	1828	26.2	0.19	2.48
	Base stab	55	26.4		—	—	2.36
	Top stab	33	29.0		—	—	2.46

σ_B : cylinder strength, ε : strain at σ_B, Ec : σ_B/3 secant modulus, ν : Poisson ratio、 σ_t : tension strength

Table 3 Material properties of steels

		σ_y (N/mm^2)	ε_y (μ)	E_s (kN/mm^2)	σ_t (N/mm^2)	Elongation (%)
D6 (SD295A)	Wall, Hoop of column and beam	377	1952	196	493	29.4
D10 (SD295A)	Main bar of beam	366	2018	181	503	28.0
D13 (SD390)	Main bar of column	434	2538	186	605	22.8

σ_y : yielding strength, ε_y : yielding strain, E_s : Young's modulus, σ_t : tension strength

2.2 Similitude Law

In order to satisfy axial stress equivalent to the first-story shear wall of the six-story proto-type structure, the additional weight on the specimen was required so that steel weight was added on top weight make 442kN, as a result target similitude low was nearly satisfied. The duration time of the base motions was scaled by $1/\sqrt{3}$. Input acceleration acting specimen corresponds to the effect to the structure of an original design, applying similitude law of time.

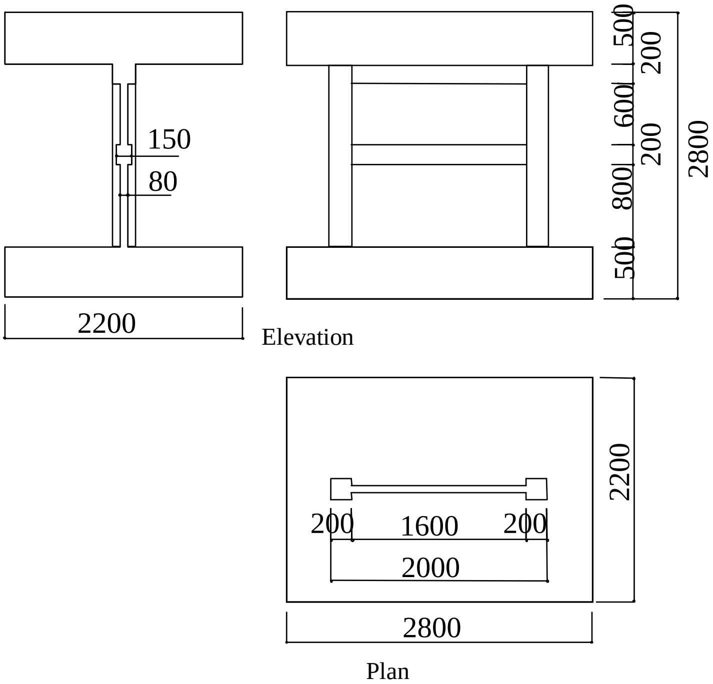

Fig. 1 Plan and elevation of the specimen

Fig. 2 Test Set-up

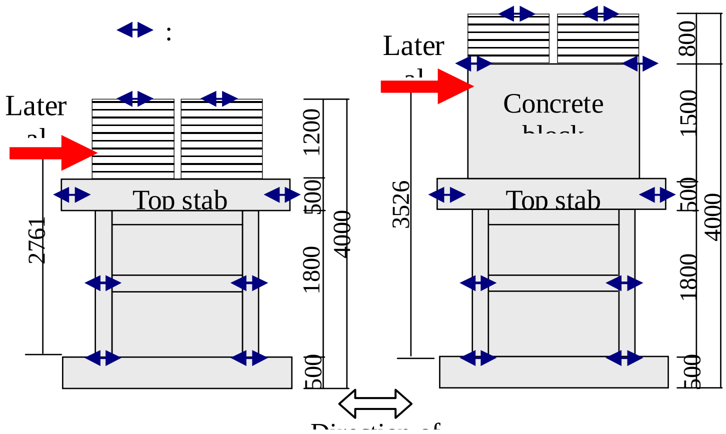

Fig. 3 Location of acceleration meters

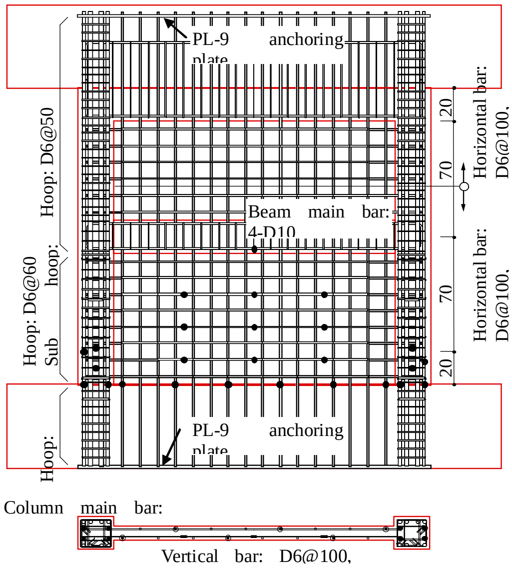

Fig. 4 Location of strain gauges

2.3 Measurement Method

30 components of accelerations were measured, such as base motion direction on top weight, 3-direction on top stab, beam of first-story and foundation stab, as shown in Fig. 3. Displacements were measured lateral displacement on top stab and perimeter column, axial displacements of perimeter column divided into fore parts, displacements of wall with displacement transducers. Strains of reinforcement were measured main position of reinforcement of column, beam and wall with strain gauges, as shown in Fig. 4. The original sampling rate of measuring was 2000Hz. The data were converted into those of 200Hz for analysis with higher mode filtering.

2.4 Input Base Motions

The two specimens were subjected to the series of recorded motions with selected five levels as shown in Table 4: TOH, Miyagi-ken Oki earthquake recorded at Tohoku university in 1978, ELC, Imperial Valley earthquake recorded at EL Centro in 1940, JMA, Hyogo-ken-Nambu earthquake recorded at Japan Meteorological Agency in 1995, CHI, Chile earthquake in 1985, TAK, Hyogo-ken Nanbu earthquake recorded at Takatori station. The level of base motions were determined on the basis of preliminary analysis results in terms of equivalent maximum velocity to the proto-type scale, in order to obtain the responses in elastic, nearly yield point and up to ultimate state after yield point, the two specimens were subjected to the same series of base motions. Before and after the input of base motions, a white noise motion with small level was input to observe the change of the natural frequency of the damaged specimens.

Table 4 Base motion input plan

Maximum target velocity	Earthquake data	Ratio to the prototype	Maximum acceleration of prototype	Maximum velocity of prototype	Maximum acceleration input of specimen	Maximum velocity input of specimen	duration
(kine)			(gal)	(kine)	(gal)	(kine)	(sec)
25	TOH	0.6	258.2	40.9	154.9	14.4	26.6
37	ELC	1.1	341.7	34.8	375.9	21.4	31.0
50	JMA	0.6	820.6	85.4	492.4	28.9	34.6
75	JMA	0.9	820.6	85.4	738.5	43.3	34.6
60	CHI	0.9	884.4	70.6	796.0	34.6	57.7
100	JMA	1.2	820.6	85.4	984.7	57.7	34.6
50	CHI	0.7	884.4	70.6	619.1	28.9	57.7
125	TAK	1.0	605.5	124.2	605.5	72.2	23.1
70	CHI	1.0	884.4	70.6	884.4	40.4	57.7

3. TEST RESULTS

3.1 Damage Process of Specimens

Cracks observed after each test run, measured strains of reinforcements and natural frequency calculated from the acceleration records at the base and top beam are summarized in Table 5. Natural frequency of specimens before damaged was 10.25Hz for Wall-A and 8.06Hz for Wall-B. Observed cracks in the specimens was shown Fig. 5 for Wall-A after CHI50 and for Wall-B after CHI60, where the number after the earthquake name denotes maximum equivalent target velocity of the run to the proto-type full-scale). The crack patterns of the two specimens were different: On Wall-A the shear crack occurred 45 degrees, whereas on Wall-B the flexural share crack occurred at the base. At the ultimate state of Wall-A, the shear cracks in the center of the first-story wall panel opened widely and the wall panel crushed in the diagonal compression, followed by the crushing of the boundary columns. As for Wall-B, the corner of the wall panel and the boundary column crushed almost simultaneously. Although the ultimate collapse modes were different as above, the level of the ultimate deformation at the failure, that is the deformability, were not so much different: the deformability of Wall-B was not much improved. Both specimens failed in a brittle failure mode after flexural yielding.

Table 5 Damage process of specimen

Input wave	Damage and natural frequency(Hz)	
	Wall-A	Wall-B
white noise	10.25	8.06
TOH25	No damage.	No damage.
white noise	10.25	8.06
ELC37	No damage.	No damage.
white noise	10.01	7.81
JMA50	No damage.	Flexural shear cracks Vertical bars yielding(5). Horizontal bar yielding(1).
white noise	10.01	7.57
JMA75	Shear cracks, Vertical bar yielding Horizontal bar yielding (2).	Cracks(Max0.3mm) Horizontal bars(3) Column main bars yielding(all)
white noise	9.52	3.66
CIH60	Cracks propagate	Spalling-off of panel and column concrete, Cracks(Max 0.7mm)
white noise	9.52	2.20
JMA100	Shear cracks (Max 0.5mm) All main bars yielding	Crushing of panel and column base and collapse
white noise	2.44	—
CHI50	Spalling-off of panel concrete Cracks (Max 0.7mm)	—
white noise	2.2	
TAK125	Cracks propagate	
white noise	2.2	
CHI70	Crushing of panel and crushing of wall and collapse	

Table 6 Observed maximum overturning moment and calculated flexural strength

Specimen	Observed maximum overturning moment	calculated flexural strength	Observed/Calculated
Wall-A	2064(kN・m)	1760(kN・m)	1.17
Wall-B	2237(kN・m)	1760(kN・m)	1.27

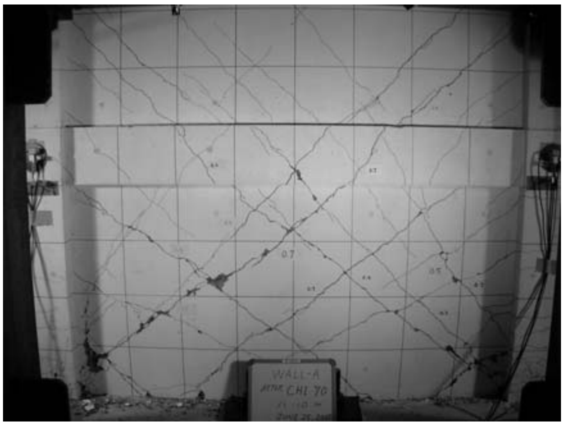

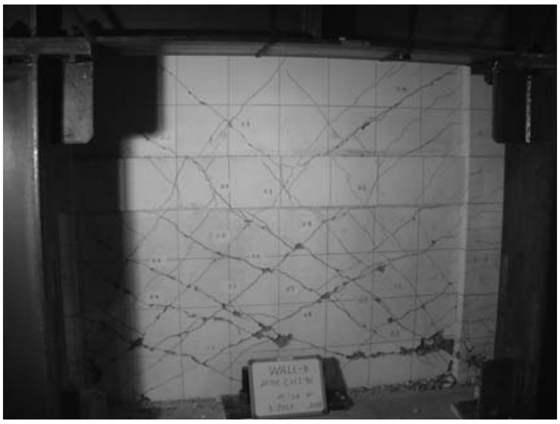

(a) Wall-A (after CHI50) (b) Wall-B (after CHI60)

Fig.5 Crack pattern developed in specimens

3.2 Maximum Strength

Figure 6 shows the relations between the calculated shear strength versus the equivalent height of mass (height of the center of lateral inertia force). The shear strength of the specimen is based on the AIJ design guidelines[AIJ, 1997], where the shear strength is calculated in relation to the target design deformability. The deflection angle of the target deformability R_u is taken as 1/200 and the shear reinforcement ratio as ps=0.006 considering the effect of reinforcement of beam. The result of material test of Table2, Table3 were used for material property(Fc=26.4N/mm^2). The shear force of the test was obtained by multiplying acceleration distribution measured on top stab and weight by mass distribution. Shear force on flexural strength ${}_{w}Q_{mu}$, which were calculated as flexural theory, which is also shown in the figure.

The observed maximum shear force of Wall-A was 730kN at JMA100, whereas the maximum shear force of Wall-B was 578kN at JMA75. The maximum shear force of Wall-B was by about 79% lower than as that of Wall-A, exactly inversely proportional to the equivalent height of the mass(2750/3500=0.786). However, the shear forces are much higher than the shear force at the calculated flexural strength ${}_{w}Q_{mu}$. Although the increase of the strength can be strain rate, this amount of increase is also observed in the static test as well, which is due to the strain hardening of the steel. Flexural strength calculated from the overturning moment in the test were shown in Table 6. The ratio of the maximum overturning moments in the test to the calculation is 1.17 for Wall-A, while 1.27 for Wall-B, which is higher than in case of Wall-A. This difference might be due to the mass distribution.

By comparing the test with the calculation, the measured shear in the Wall-A is higher than the calculated, whereas the calculated shear strength of Wall-B is almost the same as that from the test. The effect of rotational inertia of top stab and weight could be one of reason for the observed shear strength increment in the test. Therefore, the relations between the rotational moment and the shear force in the test were investigated as shown in Fig. 7, the ratio of which, i.e., the slope of the straight lines, represent the equivalent height.

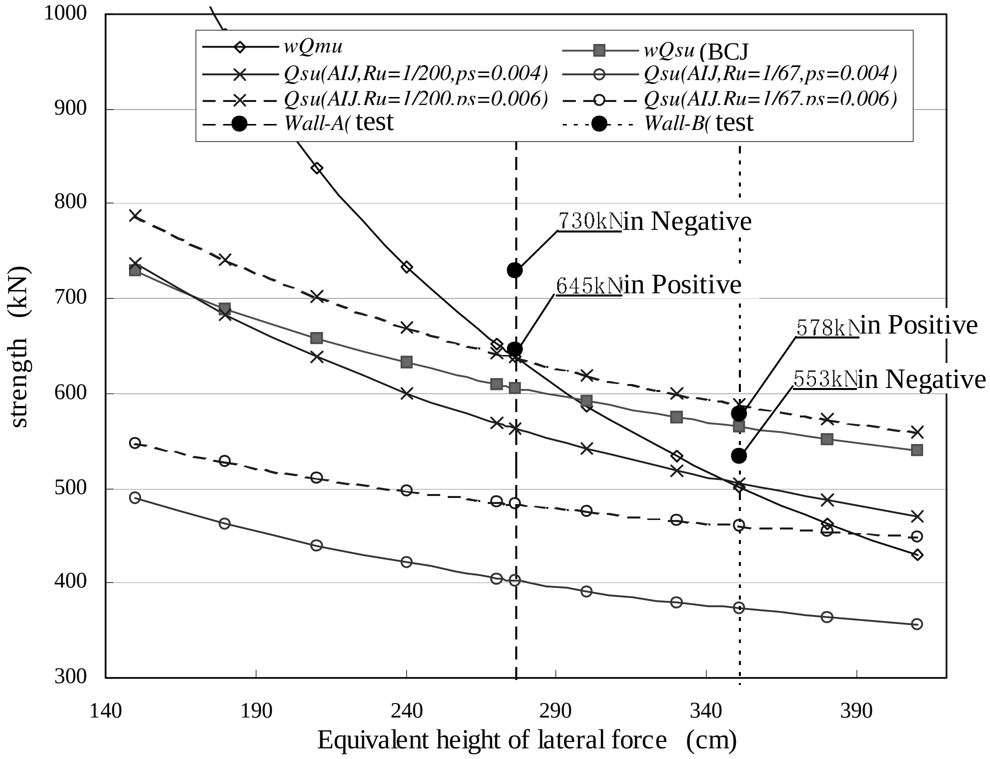

Fig. 6 Calculated flexural and shear strengths and observed maximum strengths

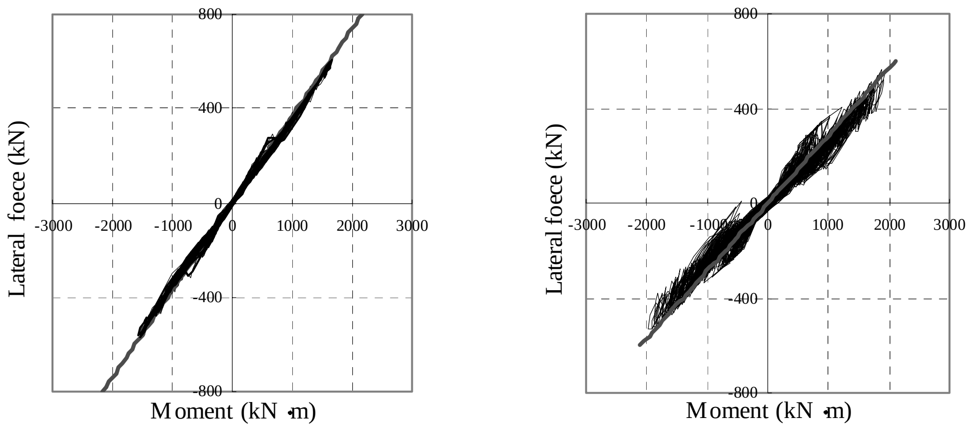

(a) Wall-A **(b) Wall-B**

Fig. 7 Relations between base moment and shear forces acting on the specimens

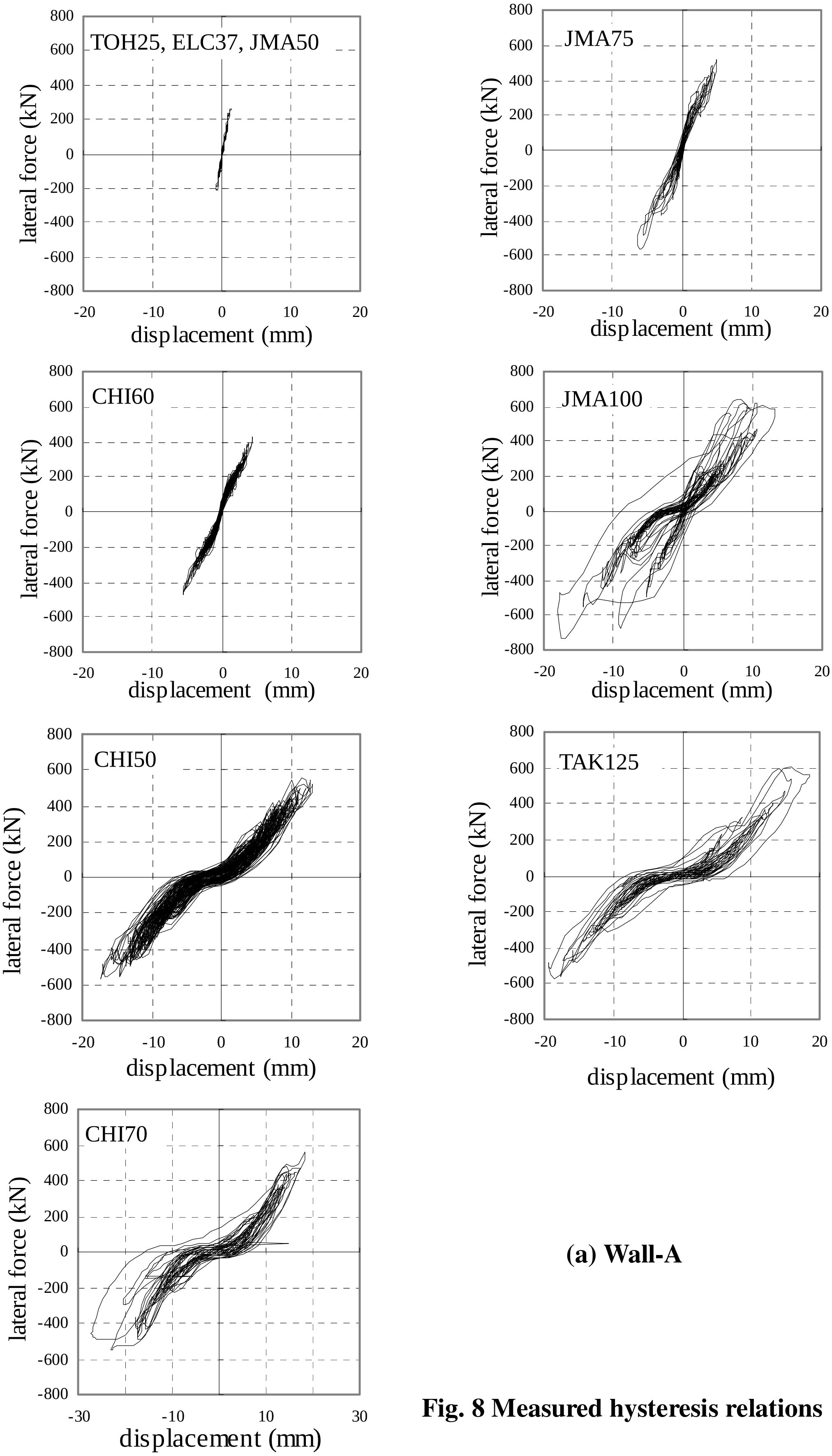

(a) Wall-A

Fig. 8 Measured hysteresis relations

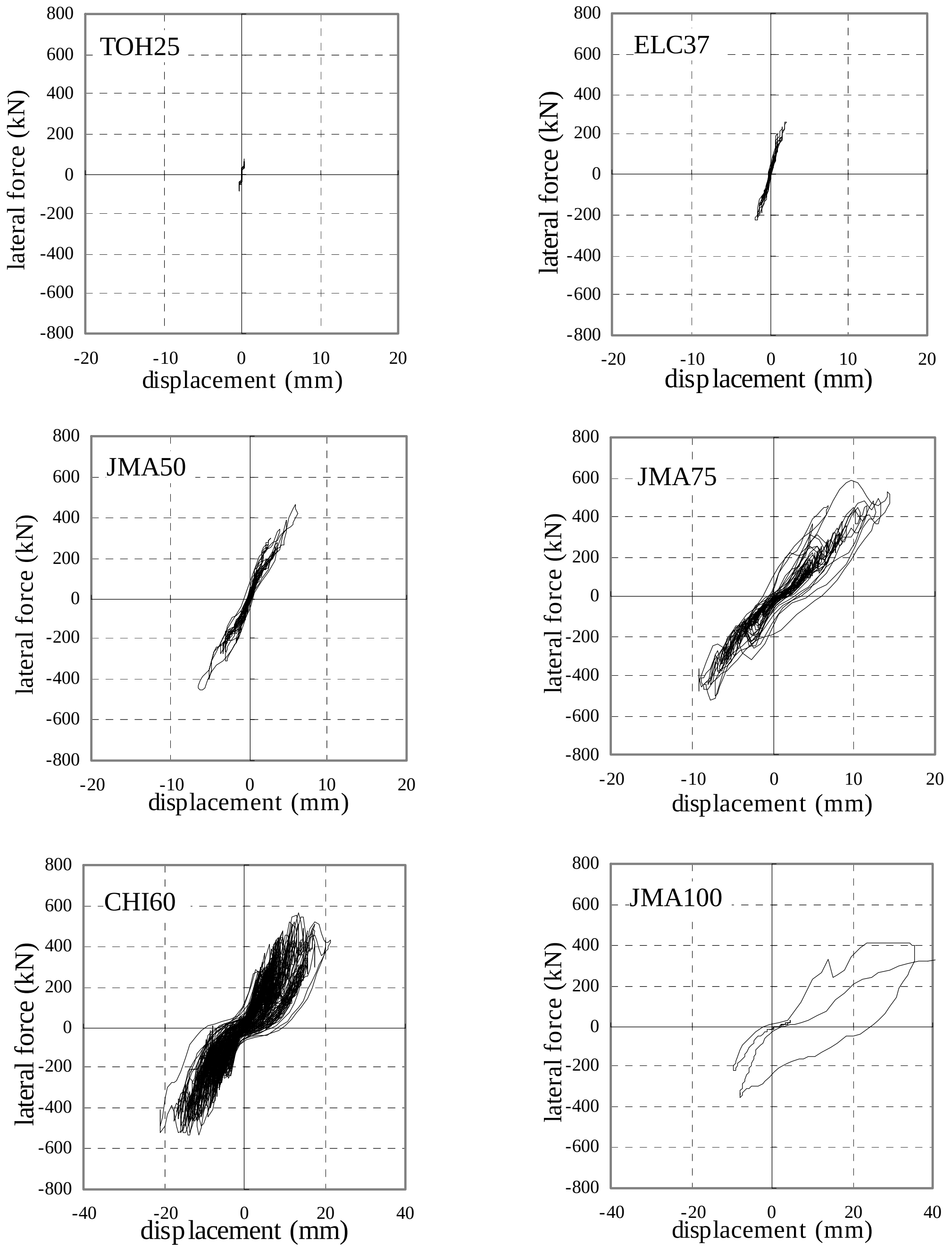

(b) Wall-B

Fig. 8 Measured hysteresis relations

The ratios observed in Wall-A corresponds to the straight line, while the response of Wall-B in JMA75, CHI60 shows that the equivalent height of mass is fluctuating due to the second mode rotation of the mass. However, this effect is not large enough at the maximum response of shear. Further investigation is needed.

3.3 Relation of Lateral Force-Horizontal Displacement

Relations of lateral inertia force and horizontal displacement at top stab (height is 200cm) of specimens are shown in Fig. 8. Wall-A was in elastic range under TOH25, ELC37. Under JMA50 the specimen reached nearly yielding and apparent stiffness degradation was observed under JMA75. Wall-B was also in elastic stage under TOH25 and ELC37, although the stiffness degradation was observed under JMA50. Both specimens showed pinching hysteresis where energy absorption capacity was not high and residual displacement was small. Lateral force of Wall-A attained the maximum shear of 645kN at the deflection angle of R=1/248 in positive direction, and 730kN(R=1/121) in the next negative direction. After that, hysteresis curve changed to an obvious pinching type with degradation of stiffness and strength. Pinching but relatively stable hysteresis relations were observed for Wall-A until collapse under CHI70. Lateral force of Wall-B attained 533kN at the deflection angle of R=1/248 in negative direction, and the maximum of 578kN (R=1/208) in the next positive-direction. Wall-B collapsed under JMA100. Deflection angles at the maximum lateral forces were around 1/250 which were not so different between the two specimens. After the lateral force reached the maximum under the input of CHI60, strength decay was observed in Wall-A. Although the deformation progressed gradually with cyclic load reversals, the deflection angle of both specimens did not exceed much more than 1/100. Although the level of the base motion of Wall-B was different from that of Wall-A, the hysteretic energy of Wall-B was larger than that of Wall-A.

3.4 Cumulative Energy Dissipation

Cumulative energy in each run dissipated by the inelastic hysteretic energy with viscous damping energy is shown in Fig. 9 and Fig. 10. Figure 9(a) shows the hysteretic and damping energy calculated from displacements measured by displacement transducers while Figure 9(b) shows the hysteretic and damping energy calculated from displacements integrated from measured floor accelerations. Figure 10 shows the energy dissipated by the deformation components decomposed into the flexural and the shear deformations. The flexural deformation is obtained by the curvature distribution, which is calculated from the axial deformations of both boundary columns divided into four segments along the height. The shear deformation is defined as the residual deformation to the total deformation. The restoring force, the shear force in the wall, is estimated from the absolute accelerations measured at the top of the wall and at the top of the steel weight as in the hysteretic relations of Fig. 8. Therefore, the calculated energy includes not only the hysteretic energy but also the viscous damping energy. To estimate the displacement response from the measured accelerations with adequate accuracy, a method of filtering is applied based on the past research[2]. The accelerations were filtered through Butterworth 4th filtering function. Each component from TOH25 to CHI50 of Wall-A, from TOH25 to JMA100 is shown in the figure. It was verified that the input and dissipated energy was almost identical. The difference is due to the errors of measurement and calculation. It should be noted that although the input energy is different in each run between the two specimens mainly because of effective natural frequency, the cumulative dissipated energy by the total deformation up to the collapse was almost identical between the Wall-A and Wall-B. It should be investigated further whether this result is incidental or not. The dissipated energy up to JMA100 from the first run of Wall-B was about four times as large as that of Wall-A. The effect of input motion of CHI60 after Wall-B reached maximum shear force was large. As for the flexural and shear deformation, the ratios in each input wave were almost the same, and the shear deformation occupied most of the deformation of walls. However, Wall-B demonstrated larger energy dissipation capacity under CHI60 with long duration, and as a result the total cumulative energy of Wall-B could attain as much as that Wall-A until collapse.

E_H: Total cumulative hysteretic and damping energy from response accelerations
E_I: Total cumulative hysteretic and damping energy from input base accelerations

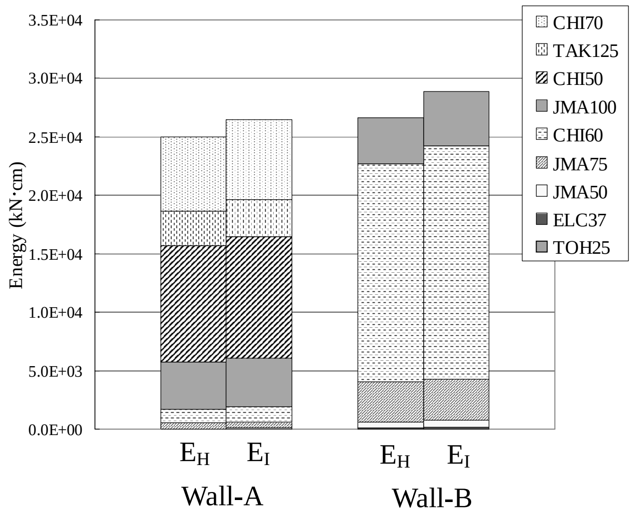

(a) Calculated from displacements measured by displacement transducers

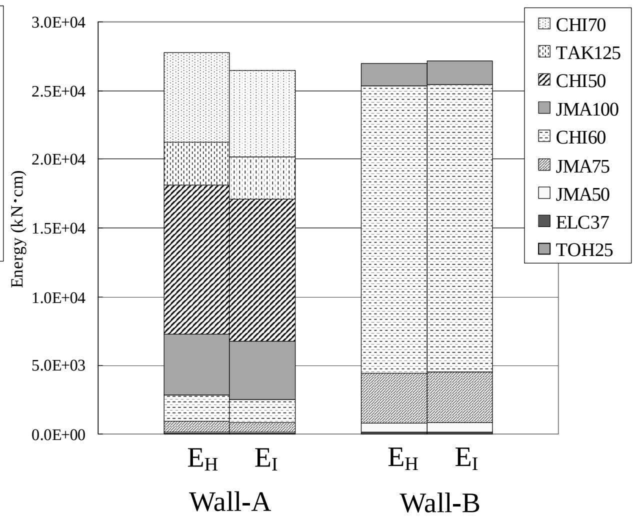

(b) Calculated from displacements integrated from horizontal accelerations

Fig. 9 Cumulative hysteretic and damping energy dissipation

E_{HB}: Cumulative hysteretic and damping energy by bending deformations
E_{HS}: Cumulative hysteretic and damping energy by shear deformations

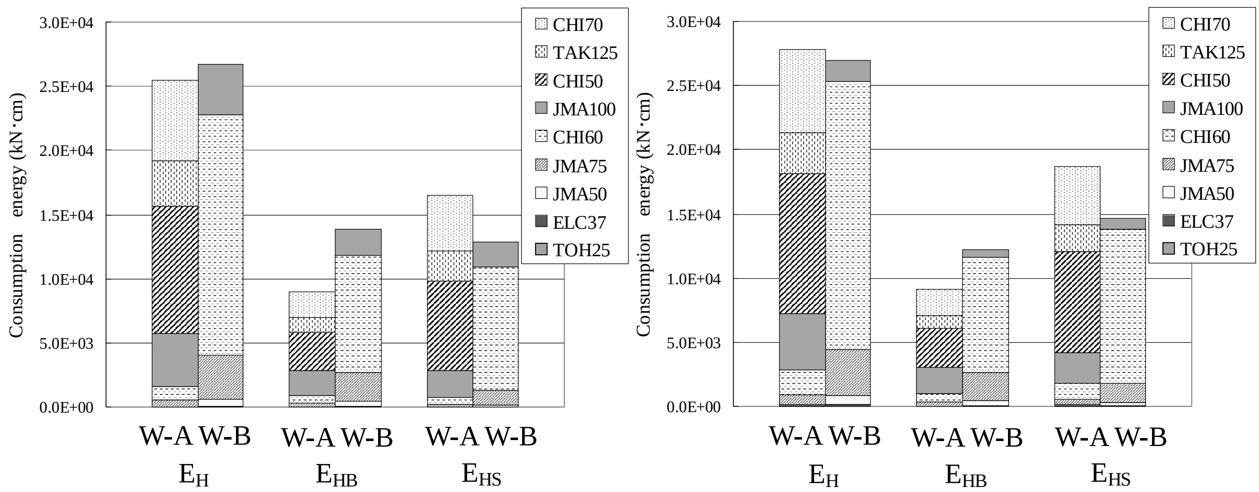

(a) Calculated from displacements measured by displacement transducers

(b) Calculated from displacements integrated from horizontal and vertical accelerations

Fig. 10 Cumulative energy dissipation by flexural and shear deformations

4. CONCLUSION

Two identical reinforced concrete wall elements, Wall-A and Wall-B, were tested on the shaking table, where only the equivalent height of the inertia force was varied. The following can be drawn from the earthquake simulation tests.

(1) Both specimens failed in shear after flexural yielding. The failure mode was different: Wall-A in higher shear at flexural yielding failed in panel first, whereas Wall-B in low shear failed more in the boundary column. The deformability of Wall-B was not larger than expected from the design guidelines based on static tests.

(2) Maximum shear force of Wall-B was about 80% as lower as that of Wall-A corresponding to the equivalent height of the mass. The observed flexural strength was generally higher than the calculated one, mainly due to the effect of strain hardening. The flexural strength in terms of base overturning moment was higher in Wall-B.

(3) The maximum shear of Wall-A was higher than the calculated shear strength, while that of Wall-B is almost equal.

(4) Both specimens showed pinching hysteresis relations with low dissipating energy especially in large amplitudes of responses dominated by shear behavior.

(5) Ultimate deformability defined at 80% strength decay from the maximum strength was larger in Wall-A than the calculated by AIJ guidelines, while the deformability of Wall-B was smaller than the calculated. This may be due to many cyclic load reversals under CHI60 than in past static loading tests.

(6) Wall-B demonstrated large energy dissipation capacity under CHI60 with long duration time, and as a result Wall-B could attain almost the same cumulative energy dissipation as that of Wall-A until collapse.

ACKNOWLEDGEMENT

The study was carried out as a part of "National research project on mitigation of major disaster in major city/ Theme II Improvement of seismic performance of structures using E-defense/ Reinforced concrete structures (DaiDaiToku/RC project)" of MEXT. The test carried out in June and July 2002 on the large-size shaking table of NIED in Tukuba. In the dynamic test, support and cooperative works of Makiko Ohi, SongTao Zhuang, Kim Jin-Gon, graduate students, Univ. of Tokyo, Tomohusa Akita, Toyohashi Univ. of technology, and Hideyoshi Watanabe, Sadayuki Ishizaki, Taisei Corporation are gratefully acknowledged.

REFERENCES

[1] AIJ, "Design Guidelines for Earthquake Resistant Reinforced Concrete Building's Based on Inelastic Displacement Concept", AIJ, 1997(draft) and 1999.

[2] Songtao Zhuang, Toshimi Kabeyasawa, YooSok Kim, et al., "Shaking table test on piloties-type structures with eccentricity, Part 4 Monitoring of response drifts with seismograms (in Japanese)," Proceedings of AIJ annual convention, 2002.

Keywords: Reinforced concrete, Shear wall, Dynamic test, Shaking table, Shear strength, Deformability

EXPERIMENTAL METHODS TO ADVANCE PERFORMANCE-BASED ENGINEERING

Catherine French[1]

ABSTRACT

This paper describes examples of how experimental research can be used to facilitate Performance-based engineering. In addition, limitations and challenges in model idealization and loading are described. New opportunities to overcome some of these limitations are provided through the National Science Foundation (NSF) George E. Brown, Jr., Network for Earthquake Engineering Simulation (NEES) program and through the development of new test methods such as effective force testing (EFT) which will further facilitate the advancement of PBE.

1. INTRODUCTION

Experimental tests on structural subassemblages can lead to the advancement of performance-based engineering (PBE) concepts through development of new structural systems and retrofitting schemes, as well as, in the development of mathematical models of critical structural components. The numerical models can be incorporated in nonlinear numerical analyses to investigate the overall response of complete structural systems incorporating similar details and subjected to a variety of ground motions.

Test structures typically represent key portions of structural systems, such as beam-column joints. In developing and testing subassemblages, simplifications are made which may result in the omission of elements (e.g., slabs or soil-structure interaction) or load components (e.g., axial or bi-directional lateral loads) that can have a significant impact on the structural response. The National Science Foundation (NSF) George E. Brown, Jr., Network for Earthquake Engineering Simulation (NEES) may provide a means to overcome some of the experimental limitations by enabling tests on large-scale subassemblages, as well as integrated studies including effects of soil-structure interaction.

The development of new large-scale dynamic test methods, such as effective force testing, may be used to experimentally investigate the impact of velocity dependent devices (i.e., active and

[1] *Department of Civil Engineering, University of Minnesota, Minneapolis, MN, USA*
Email: cfrench@umn.edu

passive dampers) on improving structural performance through limiting deformations and damage.

The potential for better characterization of the behavior of structural systems through advanced experimental facilities and new testing methodologies will lead to the development of more reliable performance-based engineering methodologies.

2.0 LIMITATIONS DUE TO IDEALIZATIONS OF SUBASSEMBLAGES

The simplification of structural systems into physical models can limit observations learned from subassemblage response. An example is the idealization of structural subassemblages as planar beam-column joints (Figure 1(a)). Prior to the early 1980's, much of the subassemblage research ignored the contribution of the floor slab to the structural response. Tests on the full-scale seven-story reinforced concrete frame wall structure conducted at the Building Research Institute (BRI) in Tsukuba, Japan (JTCC, 1988) in the early 1980's demonstrated that the slab has a significant impact on the structural response by providing increased tensile reinforcement to the beam when bending in negative curvature (i.e., the top of the slab in tension). Thus, neglecting the slab contribution can lead to underestimations of the beam flexural strength in plastic hinge regions (at the face of beam-column connections), which can have a significant impact on the anticipated beam shear demands, total base shear demands, and progression of plastic hinge formation between the beam and column elements in the structural system. Since the mid-1980's, more and more tests have been conducted on complete beam-column-slab subassemblages (Figure 1(b)) (French et al., 1989; Kurose, 1988; Shahrooz et al., 1987).

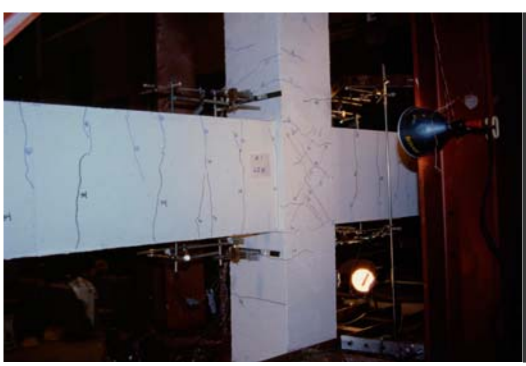

(a) Beam-column **(b) Beam-column-slab**

Figure 1 Subassemblage configurations

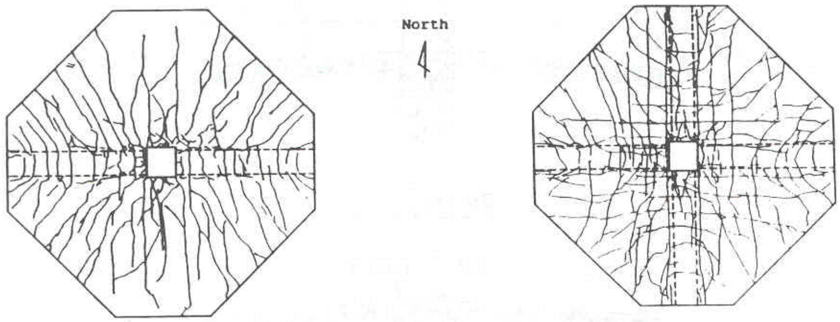

(a) Isolated beam-column-slab unidirectional loading

(b) Isolated beam-column-slab bi-directional loading

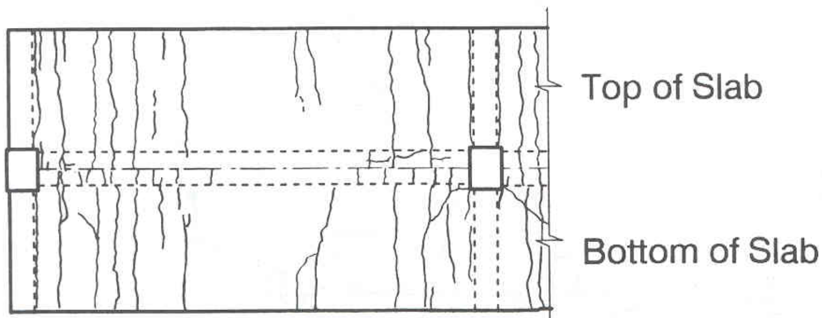

(c) Beam-column-slab in indeterminate system

Figure 2 Effect of boundary conditions and loading direction (French and Moehle, 1991)

Simplifications can also be made in testing physical models. For example, in tests of isolated beam-column and beam-column-slab subassemblages, the location of the inflection points are typically created by physical hinges idealized at the midspan of the beams and the midheight of the columns. In reality, due to the unsymmetric reinforcement in the top and bottom of the beam, especially with the slab reinforcement acting as additional tension reinforcement to the beams and higher mode effects on the columns, the location of the inflection points can change dramatically. In addition, subassemblage loading is typically simplified as unidirectional reversed cyclic loading. As evident in Figure 2, the boundary conditions and loading direction have a significant influence on the observed crack patterns. The effect of boundary conditions can be observed by comparing the isolated beam-column-slab response of Figure 2(a) (where the actuators were attached at the beam ends leaving the slab ends free) to the indeterminate beam-column-slab response exhibited by Figure 2(c) where the cracks developed normal to the loading direction. The effect of loading direction can be observed by comparing the responses exhibited in Figures 2(a) and (b) which show the crack patterns resulting from unidirectional and bi-directional loading. Damage due to bi-directional loading can have a significant impact on loading in the orthogonal direction by reducing the stiffness of the structural system including the torsional stiffness of the orthogonal elements.

Multi-directional experimentation of subassemblages has been limited in the past due to the lack of experimental capabilities. In cases where it has been used, it has been typically limited to application of lateral load in “cloverleaf” patterns (Kurose, 1988) due to difficulties in simultaneous control of multiple actuators.

3.0 OPPORTUNITIES FOR EXPERIMENTAL ADVANCES WITH NEES

The George E. Brown, Jr. Network for Earthquake Engineering Simulation (NEES) is an integrated network of experimental facilities that may alleviate some of the limitations experienced in past subassemblage tests. The network includes testing facilities that can accommodate large-scale subassemblages subjected to complicated multi-directional load histories. An example is the Multi-Axial Subassemblage Testing (MAST) system at the University of Minnesota shown in Figure 3, which features 6-degree-of-freedom (DOF) control technology to apply deformations and loading in a straightforward and reproducible manner, including the capability for mixed-mode control. The primary loading element for the MAST system is a rigid steel crosshead attached to eight large-capacity actuators that react against an L-shaped strong wall-strong floor system.

Figure 3 Rendering of MAST Laboratory and testing system

Applications of the MAST system are broad. The mixed-mode control features can be used to specify a lateral displacement history in the horizontal plane while maintaining a constant gravity load or varying axial load on the subassemblage to simulate overturning load effects. In addition, with 6-DOF control, moments can be controlled about orthogonal axes to simulate specified moment-to-shear ratios that would correspond to assumed lateral load distributions on the structural subassemblage. Rotation or moment about the vertical axis can be controlled to eliminate or simulate limited torsional effects on the test structure.

Complex structural subassemblages such as nonrectangular walls which are required to resist lateral forces and limit damage to nonstructural elements by limiting deformations in the two primary directions of the structure are ideally suited for testing in the MAST system. Such research can advance PBE of nonrectangular walls. The research upon which current displacement-based design principles were based was conducted on unidirectional tests of nonrectangular wall systems (Wallace, 1994; Moehle, 1992). The effects of multi-directional loading might be expected to have a significant influence on the response as the tips of the flanges may become damaged due to loading in the orthogonal direction (i.e., orthogonal to the web).

Figure 4 features eleven of the sixteen NEES equipment sites which offer a broad range of resources in five categories including large-scale structural testing facilities (e.g., MAST), shake tables, geotechnical centrifuges, field equipment sites and a tsunami wave tank. The web-based telepresence features of NEES will facilitate integrated tests among multiple collaborators at multiple facilities. It will be possible to integrate the simulation and testing of multiple structural subassemblages tested simultaneously at a number of equipment sites. The networked sites will also facilitate integration of soil-structure interaction effects in the experiments, which can further facilitate the development of PBE.

Another key feature of NEES is the development and maintenance of a national curated searchable data repository that will contain a complete archive of the visual, sensor, and simulation data that may assist practitioners in the implementation of PBE design principles. Past experimental results can be used to validate new numerical models for structural systems.

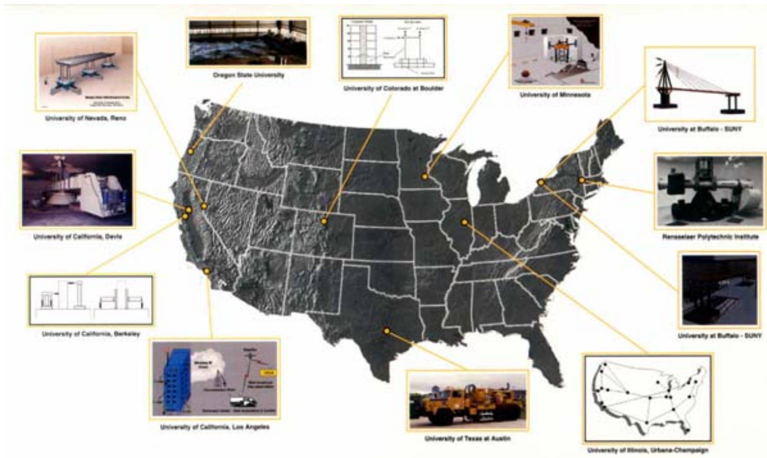

Figure 4 Description and geographical distribution of NEES Phase I Equipment Sites (Website: http://www.nees.org)

4.0 EFFECTIVE FORCE TESTING (EFT) TO INVESTIGATE DAMPING DEVICES

Velocity-dependent devices, such as dampers, can be used to improve the response and limit damage in structural systems to further facilitate PBE objectives. To investigate the behavior of such systems, real-time dynamic testing is necessary for assessing the behavior of structures employing velocity dependent devices under seismic loadings. A shake table is often used to simulate the dynamic effects of earthquakes on structural models. However, shake table capacity limitations typically require reduced scale models. At smaller scales, structural details such as connections cannot be represented realistically, and energy dissipation of structural control devices may not be demonstrated accurately.

Effective force testing (EFT) is a dynamic testing procedure under development at the University of Minnesota that can be used to apply real-time earthquake loads to large-scale structures (Dimig et al., 1999; Shield et al., 2001). In an EFT test (shown in Figure 5 compared to a shake table test), the test structure is anchored to a stationary base, and dynamic forces are applied by hydraulic actuators to the center of each story mass of the structure. The force to be imposed, P_{eff} (effective force), is the product of the structural mass and the ground acceleration record, and thus is independent of the structural properties and their changes during the test. Motions measured relative to the ground are equivalent to the response that the structure would develop relative to a moving base as in a shake table test or an earthquake event.

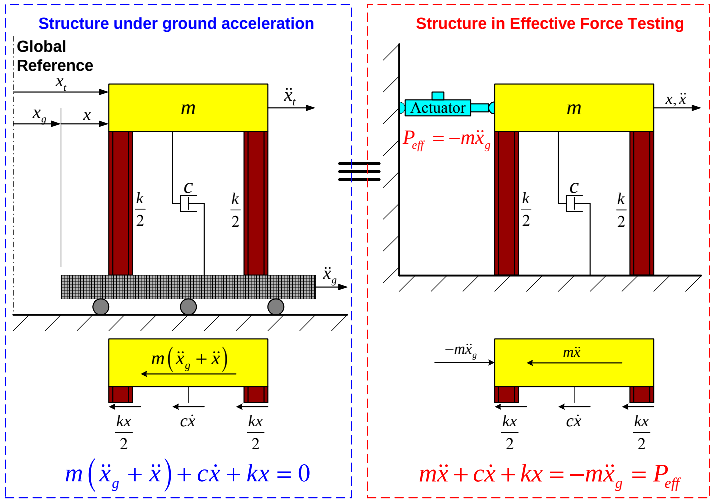

Figure 5 Comparison of Shake Table (or ground excitation) System to Effective Force Testing

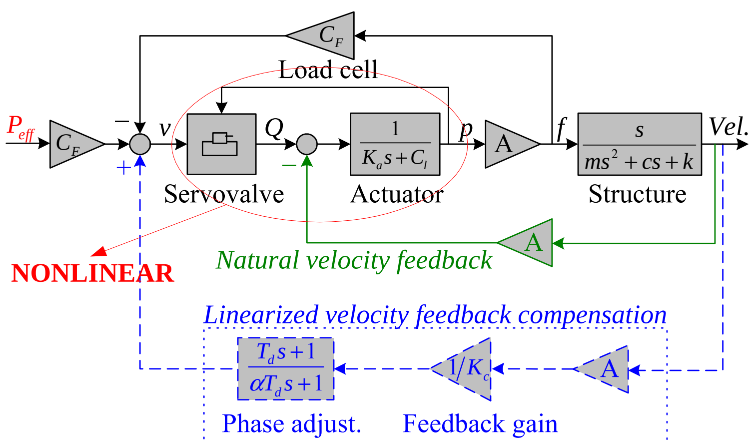

Figure 6 Model of Force-Controlled Testing System Incorporating Linearized Velocity Feedback Correction

The direct implementation of EFT is not feasible because of the natural velocity feedback phenomena, which impairs the ability of the actuator to apply forces near the resonant frequency of the test structure. A schematic of the EFT test system is shown in the block diagram of Figure 6 including a velocity feedback correction loop (dashed line in Figure 6) required to negate the effect of the natural velocity feedback phenomena. The implementation requires the measurement of the velocity of the piston or test structure to which it is attached. This information is then used to determine the increased flow required in the actuator to compensate for the velocity feedback phenomena by determining a modified command signal to account for these effects. As noted in the figure, because the velocity feedback is compensated at the command signal to the servovalve, information regarding modeling of the actuator servovalve must be incorporated into the feedback correction loop. The initial velocity feedback compensation shown in Figure 6 was incorporated assuming that the servovalve characteristics could be linearized. Figures 7 and 8 illustrate the direct implementation of the EFT method and the implementation including the velocity feedback compensation loop, respectively. The figures illustrate the force and displacement histories for a single-degree-of-freedom (SDOF) system and the Fast Fourier Transform (FFT) of the force. The limited ability of the actuator to apply forces near the resonant frequency of the test structure is evident in the FFT of the force in Figure 7, and the success of the velocity feedback correction implementation is evident in Figure 8. This implementation, using a linear model of the servovalve for the velocity feedback correction, was shown to be successful as long as the hydraulic oil flow demands were not high (Figure 8). The effects of two major types of nonlinearities of the servo-system, *nonlinear flow property* of the servovalve and *load pressure influence* on the actuator performance, have been identified. Advanced velocity feedback compensation schemes featuring nonlinear velocity feedback compensation indicate promising performance of the EFT method in situations of high flow demands when the nonlinearities become significant (Zhao, 2003).

5.0 SUMMARY

Experimental tests have led to advances in PBE through improved understanding of structural behavior. Further advances may be made with an enhanced and integrated network of testing facilities such as that developed through the NSF George E. Brown, Jr. NEES program. These systems will enable multi-directional testing of large-scale structural subassemblages and integrated experiments combining multiple subassemblage tests and soil-structure interaction. This will facilitate investigation of more representative structural subassemblages including complex load histories. In addition, the development of new real-time testing techniques such as effective force testing (EFT) can be used to evaluate velocity dependent devices such as dampers that can be incorporated into structural systems to further mitigate damage incurred due to seismic effects.

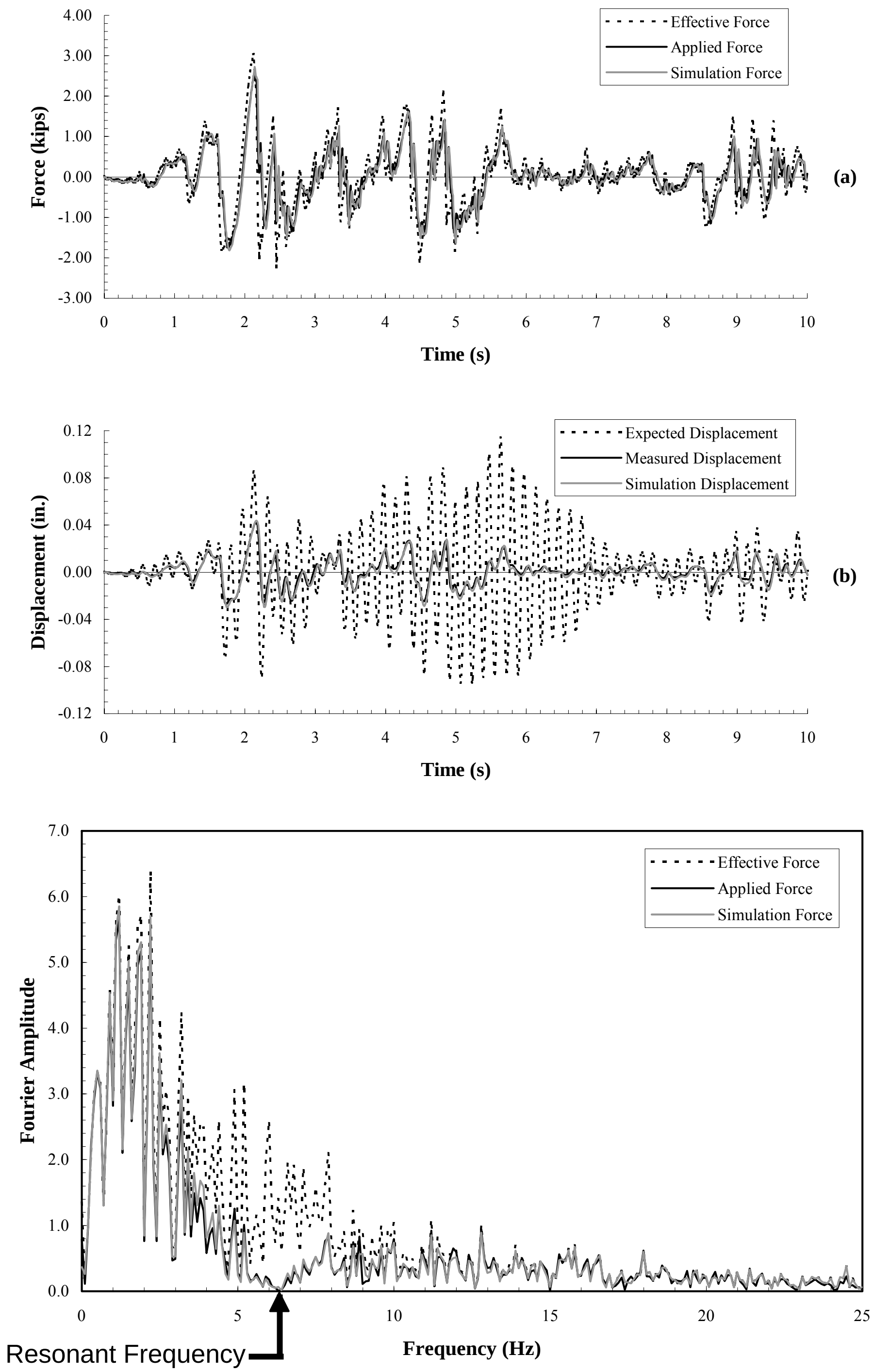

Figure 7 Comparison of the expected, measured, and simulation response for Elcn10 ground motion (0.17g) [Timm, 1999]

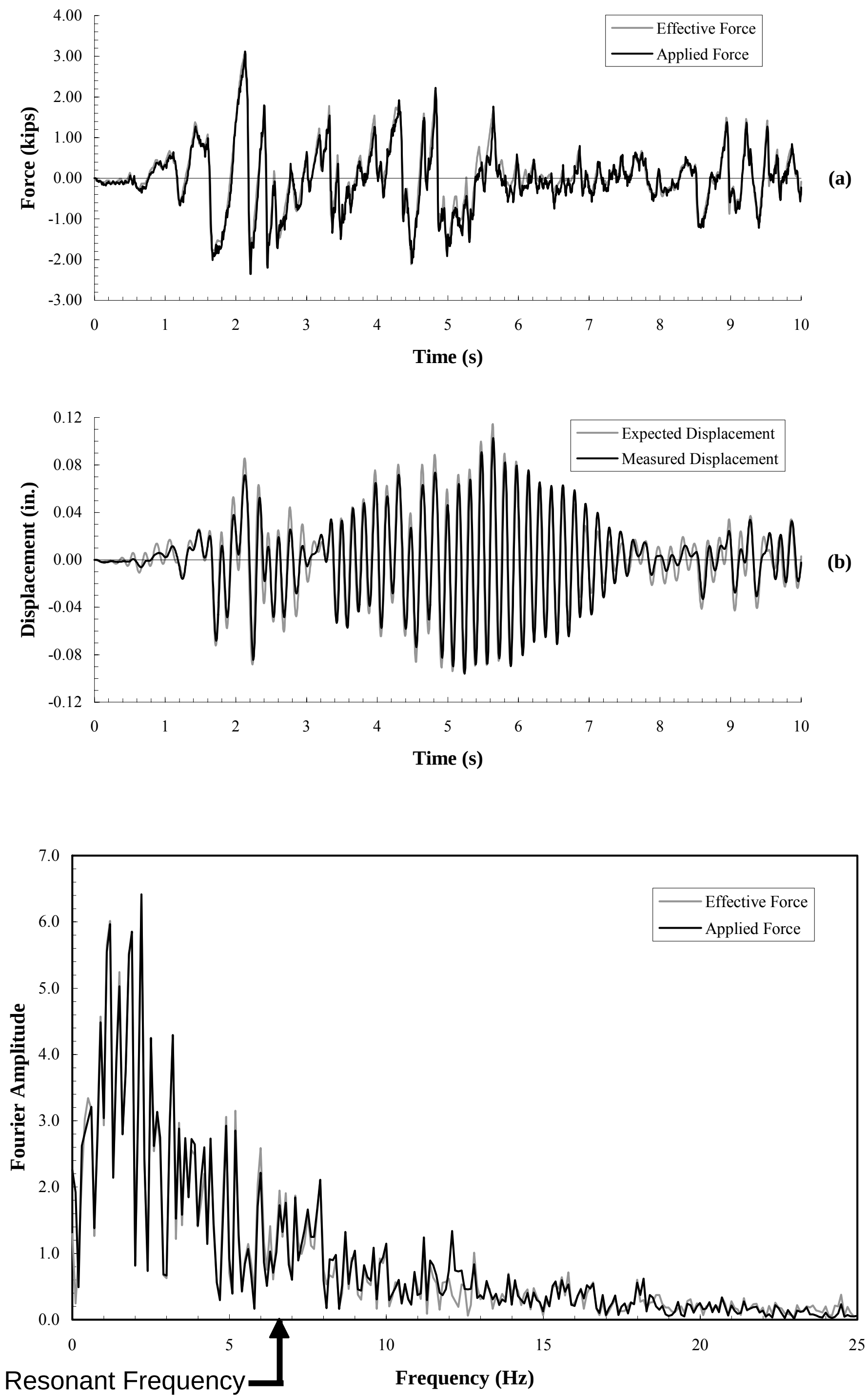

Figure 8 Comparison of the expected, measured, and simulation response for Elcn10 ground motion (0.17g) with velocity feedback compensation

6.0 REFERENCES

Dimig, J., C. Shield, C. French, F. Bailey, and A. Clark. (1999). Effective Force Testing: A Method of Seismic Simulation for Structural Testing. *Journal of Structural Engineering*, ASCE, 125(9): 1028-1037.

French, C. W. and A. Boroojerdi. (1989). “Contribution of R/C Floor Slabs in Resisting Lateral Loads. *Journal of Structural Engineering*, 115(1): 1-18.

French, C. W. and J. P. Moehle. (1991). Effect of Floor Slab on Behavior of Slab-Beam-Column Connections. *ACI SP-123: Design of Beam-Column Joints for Seismic Resistance*, American Concrete Institute. 225-258.

Joint Technical Coordinating Committee (JTCC). (1988). U.S. – Japan Research: Seismic Design Implications. *Journal of Structural. Engineering*, ASCE, 114(9): 2000-2016.

Kurose, Y., G. Guimaraes, Z. Liu, M. Kreger, and J. Jirsa. (1988). Study of Reinforced Concrete Beam-Column Slab Joints under Uniaxial and Biaxial Loading. *PMFSEL Report No. 88-2*, Phil Ferguson Structural Engineering Laboratory, University of Texas at Austin. 146 pp.

Moehle, J. P. (1992). Displacement-Based Design of RC Structures Subjected to Earthquakes. *Earthquake Spectra*, EERI, 8(3): 403-428.

Shahrooz, B. M. and J. P. Moehle. (1987). Experimental Study of Seismic Response of RC Setback Buildings. Report No. UCB/EERC-87/16, Earthquake Engineering Research Center, University of California at Berkeley. 347 pp.

Shield, C.K., C. W. French, and J. Timm. (2001). Development and Implementation of the Effective Force Testing Method for Seismic Simulation of Large-Scale Structures. *Philosophical Trans. of the Royal Society: Special Issue on Dynamic Testing of Structures*, 359: 1911-1929.

Timm, J. (1999). Natural velocity feedback correction for effective force testing. Master’s Thesis, Civil Engineering, University of Minnesota, Twin Cities.

Wallace, J. W. (1994). New Methodology for Seismic Design of RC Shear Walls. *Journal of Structural Engineering*, ASCE, 120(3): 863-884.

Website: http://www.nees.org

Zhao, J. (2003). Development of EFT for Nonlinear SDOF Systems. Doctoral Dissertation, Civil Engineering, University of Minnesota, Twin Cities.

KEYWORDS: performance-based engineering, experiment, test methods, subassemblage tests, boundary conditions, multi-directional testing, effective force testing

PLENARY SESSION 3: SUMMARY REPORTS AND RESOLUTIONS

Chaired by

♦ Jack Moehle and Toshimi Kabeyasawa ♦

RESOLUTIONS

Recent urban earthquakes have caused significant economic losses, injuries, and fatalities in both the U.S. and Japan. This was evident during the 1994 Northridge (Los Angeles) and the 1995 Hyogo-ken Nambu (Kobe) earthquakes. These and other recent earthquakes in the U.S. and Japan (Seattle and Miyagi, respectively), as well as in Turkey, Taiwan, and, Algeria have demonstrated the need for effective and practical methods for evaluating and rehabilitating existing hazardous buildings and for designing new buildings for more reliable and improved performance.

Although great progress has previously been made in engineering earthquake-resistant structures, the suggested frameworks for performance-based earthquake engineering will accelerate progress by focusing efforts and bridging gaps. This will lead to future earthquake engineering with increasing emphasis on quantitative measures of performance over qualitative measures, precision over approximation, reliability over uncertainty, and intelligent engineering and life-cycle cost design over minimum capital cost design.

The papers presented at the First, Second, Third, Fourth, and Fifth U.S.-Japan Workshops on Performance-Based Earthquake Engineering Methodology for Reinforced Concrete Building Structures demonstrate progress being made in performance-based earthquake engineering. In the Fifth Workshop, presentations in the plenary sessions included a brief history of earthquake engineering, the need for verification of advanced analytical techniques, seismic hazard analysis, and practical applications of performance-based engineering. Two working group sessions covered the most recent research findings related to analysis and performance assessment in support of performance-based design. Discussions of the presented papers enhanced understanding and advanced the state of the art in performance-based earthquake engineering. Important outcomes of the workshop include

(a) Better understanding of the present state of knowledge and practice of performance-based earthquake engineering, especially future research needs;

(b) Detailed understanding of seismic demands, especially statistical or energy-based seismic demand estimation, and progressive collapse analysis for performance-based earthquake engineering of reinforced concrete buildings;

(c) Detailed understanding about the seismic capacities of structures and structural members, especially reinforced concrete columns and beam-column joints, and about the dynamic behavior of structures to collapse;

(d) Better understanding of the practical applications of performance-based design and of innovative retrofitting methods; and

(e) Identification of common areas of concern, areas of needed advances, and future research projects that might benefit from collaboration, such as the NEES project in the U.S. and the DaiDaiToku project using E-Defense in Japan.

The topic of performance-based earthquake engineering is a particularly effective one for workshop discussion because it brings together and promotes a common focus of experts in ground motion, analysis, and design, and because the workshop format is not constrained by prescriptive code requirements that vary from one country to another. Understanding of the work of individuals with different expertise was achieved in ways that would not be possible without meeting in this format.

The workshop was a successful continuation of progress made for more than two decades of cooperative U.S.-Japan research in earthquake engineering. The success at this workshop suggests that the two countries will benefit from continued cooperation. The reasons for continued cooperation are that

(a) the two countries have a shared need to develop improved methods for seismic design and evaluation;

(b) in both countries there is a need for integrated analytical and experimental approaches, which is promoted in this meeting format; and

(c) each side brings unique data, experience, knowledge, and facilities, the sharing of which benefits all.

Discussions of issues in performance-based earthquake engineering are best accomplished through face-to-face meetings of extended duration such as occur in a workshop format.

Therefore, the following recommendations are offered:

(1) Because of the rapid rate at which new information and applications are being achieved, the importance of advances to Japan and the U.S., and the success of the First through Fifth Workshops, the participants recommend that the Sixth U.S.-Japan Workshop on Performance-Based Seismic Engineering Methodology for Reinforced Concrete Building

Structures be organized by the U.S. side next year. Consideration should also be given to convening or participating in a major international conference or workshop on the theme subject around one year later, for example, at the 13WCEE in Vancouver, Canada.

(2) At future workshops, several topics for focused discussion should be considered. A reduced number of these should be the focus of the Sixth Workshop:

(a) simplified and rigorous methods for predicting seismic demands;

(b) simplified and rigorous methods for predicting seismic capacities;

(c) design methodology to bring these together; and

(d) knowledge-based rapid post-earthquake response.

(a) simplified and rigorous methods for predicting seismic demands

(i) identification of severe earthquakes

(ii) continuation of the topic of inelastic displacement demands for SDOF and MDOF systems

(iii) practical application of advanced analysis methods

(iv) use of probabilistic bases for PBEE incorporating uncertainty and variability

(v) performance of strength-degrading structures

(vi) seismic demands including life-cycle loss and fatality estimation

(b) simplified and rigorous methods for predicting seismic capacities

(i) definitions and measures of performance

(ii) modeling of damage and definition of reparability

(iii) hysteretic energy dissipation of members

(iv) deformations at loss of lateral and gravity load capacity of members

(v) continuation of the topic of residual gravity load capacity of members

(vi) damage models including cumulative and cyclic effects

(vii) exchange of database on test results

(viii) behavior of nonstructural component

(c) design methodology to bring these together

(i) validation of performance-based earthquake engineering methods

(ii) assessment of system performance needed to be carried out based on component performance

(iii) evaluation of moderate damage for assessment of damage repair cost

(iv) development of performance-derived design criteria

(d) knowledge-based rapid post-earthquake response

(i) development and verification of sensor and monitoring system

(ii) residual performance assessment of damaged structures

(iii) development and verification of retrofit technology

(3) At the Sixth Workshop, the following format should be considered:

(a) A focus on two to four topics, emphasizing presentation of papers on those topics coupled with special theme sessions to examine topics in greater detail and

(b) Participation of researchers, professional engineers, representatives of code-writing organizations, representatives of national organizations responsible for construction, and leading international participants.

(4) Cooperative activities between individual participants from the U.S. and Japan are encouraged to address problems of mutual concern. Efforts should be undertaken to facilitate exchange of personnel, including students, faculty, and professional researchers and practitioners, as well as of information on technical issues and applications. Funding agencies are encouraged to support these activities.

PEER REPORTS

PEER reports are available from the National Information Service for Earthquake Engineering (NISEE). To order PEER reports, please contact the Pacific Earthquake Engineering Research Center, 1301 South 46th Street, Richmond, California 94804-4698. Tel.: (510) 231-9468; Fax: (510) 231-9461.

PEER 2003/13	*Effects of Connection Hysteretic Degradation on the Seismic Behavior of Steel Moment-Resisting Frames.* Janise E. Rodgers and Stephen A. Mahin. March 2004.
PEER 2003/11	*The Fifth U.S.-Japan Workshop on Performance-Based Earthquake Engineering Methodology for Reinforced Concrete Building Structures.* February 2004.
PEER 2003/10	*A Beam-Column Joint Model for Simulating the Earthquake Response of Reinforced Concrete Frames.* Laura N. Lowes, Nilanjan Mitra, and Arash Altoontash. February 2004.
PEER 2003/08	*A Technical Framework for Probability-Based Demand and Capacity Factor Design (DCFD) Seismic Formats*. Fatemeh Jalayer and C. Allin Cornell. November 2003.
PEER 2003/06	*Performance of Circular Reinforced Concrete Bridge Columns under Bidirectional Earthquake Loading*. Mahmoud M. Hachem, Stephen A. Mahin, and Jack P. Moehle. February 2003.
PEER 2003/05	*Response Assessment for Building-Specific Loss Estimation.* Eduardo Miranda and Hesameddin Aslani. September 2003.
PEER 2003/04	*Experimental Assessment of Columns with Short Lap Splices Subjected to Cyclic Loads*. Murat Melek, John W. Wallace, and Joel Conte. April 2003.
PEER 2003/03	*Probabilistic Response Assessment for Building-Specific Loss Estimation.* Eduardo Miranda and Hesameddin Aslani. September 2003.
PEER 2003/02	*Software Framework for Collaborative Development of Nonlinear Dynamic Analysis Program.* Jun Peng and Kincho H. Law. September 2003.
PEER 2003/01	*Shake Table Tests and Analytical Studies on the Gravity Load Collapse of Reinforced Concrete Frames.* Kenneth John Elwood and Jack P. Moehle. November 2003
PEER 2002/24	*Performance of Beam to Column Bridge Joints Subjected to a Large Velocity Pulse.* Natalie Gibson, André Filiatrault, and Scott A. Ashford. April 2002.
PEER 2002/23	*Effects of Large Velocity Pulses on Reinforced Concrete Bridge Columns.* Greg L. Orozco and Scott A. Ashford. April 2002.
PEER 2002/22	*Characterization of Large Velocity Pulses for Laboratory Testing.* Kenneth E. Cox and Scott A. Ashford. April 2002.
PEER 2002/21	*Fourth U.S.-Japan Workshop on Performance-Based Earthquake Engineering Methodology for Reinforced Concrete Building Structures*. December 2002.
PEER 2002/20	*Barriers to Adoption and Implementation of PBEE Innovations.* Peter J. May. August 2002.

PEER 2002/19 *Economic-Engineered Integrated Models for Earthquakes: Socioeconomic Impacts.* Peter Gordon, James E. Moore II, and Harry W. Richardson. July 2002.

PEER 2002/18 *Assessment of Reinforced Concrete Building Exterior Joints with Substandard Details.* Chris P. Pantelides, Jon Hansen, Justin Nadauld, and Lawrence D. Reaveley. May 2002.

PEER 2002/17 *Structural Characterization and Seismic Response Analysis of a Highway Overcrossing Equipped with Elastomeric Bearings and Fluid Dampers: A Case Study.* Nicos Makris and Jian Zhang. November 2002.

PEER 2002/16 *Estimation of Uncertainty in Geotechnical Properties for Performance-Based Earthquake Engineering.* Allen L. Jones, Steven L. Kramer, and Pedro Arduino. December 2002.

PEER 2002/15 *Seismic Behavior of Bridge Columns Subjected to Various Loading Patterns.* Asadollah Esmaeily-Gh. and Yan Xiao. December 2002.

PEER 2002/14 *Inelastic Seismic Response of Extended Pile Shaft Supported Bridge Structures.* T.C. Hutchinson, R.W. Boulanger, Y.H. Chai, and I.M. Idriss. December 2002.

PEER 2002/13 *Probabilistic Models and Fragility Estimates for Bridge Components and Systems.* Paolo Gardoni, Armen Der Kiureghian, and Khalid M. Mosalam. June 2002.

PEER 2002/12 *Effects of Fault Dip and Slip Rake on Near-Source Ground Motions: Why Chi-Chi Was a Relatively Mild M7.6 Earthquake.* Brad T. Aagaard, John F. Hall, and Thomas H. Heaton. December 2002.

PEER 2002/11 *Analytical and Experimental Study of Fiber-Reinforced Strip Isolators*. James M. Kelly and Shakhzod M. Takhirov. September 2002.

PEER 2002/10 *Centrifuge Modeling of Settlement and Lateral Spreading with Comparisons to Numerical Analyses***.** Sivapalan Gajan and Bruce L. Kutter. January 2003.

PEER 2002/09 *Documentation and Analysis of Field Case Histories of Seismic Compression during the 1994 Northridge, California, Earthquake.* Jonathan P. Stewart, Patrick M. Smith, Daniel H. Whang, and Jonathan D. Bray. October 2002.

PEER 2002/08 *Component Testing, Stability Analysis and Characterization of Buckling-Restrained Unbonded Braces™.* Cameron Black, Nicos Makris, and Ian Aiken. September 2002.

PEER 2002/07 *Seismic Performance of Pile-Wharf Connections.* Charles W. Roeder, Robert Graff, Jennifer Soderstrom, and Jun Han Yoo. December 2001.

PEER 2002/06 *The Use of Benefit-Cost Analysis for Evaluation of Performance-Based Earthquake Engineering Decisions*. Richard O. Zerbe and Anthony Falit-Baiamonte. September 2001.

PEER 2002/05 *Guidelines, Specifications, and Seismic Performance Characterization of Nonstructural Building Components and Equipment*. André Filiatrault, Constantin Christopoulos, and Christopher Stearns. September 2001.

PEER 2002/04 *Consortium of Organizations for Strong-Motion Observation Systems and the Pacific Earthquake Engineering Research Center Lifelines Program: Invited Workshop on Archiving and Web Dissemination of Geotechnical Data, 4–5 October 2001*. September 2002.

PEER 2002/03 *Investigation of Sensitivity of Building Loss Estimates to Major Uncertain Variables for the Van Nuys Testbed.* Keith A. Porter, James L. Beck, and Rustem V. Shaikhutdinov. August 2002.

PEER 2002/02 *The Third U.S.-Japan Workshop on Performance-Based Earthquake Engineering Methodology for Reinforced Concrete Building Structures*. July 2002.

PEER 2002/01 *Nonstructural Loss Estimation: The UC Berkeley Case Study. Mary C. Comerio and John C. Stallmeyer.* December 2001.

PEER 2001/16 *Statistics of SDF-System Estimate of Roof Displacement for Pushover Analysis of Buildings.* Anil K. Chopra, Rakesh K. Goel, and Chatpan Chintanapakdee. December 2001.

PEER 2001/15 *Damage to Bridges during the 2001 Nisqually Earthquake.* R. Tyler Ranf, Marc O. Eberhard, and Michael P. Berry. November 2001.

PEER 2001/14 *Rocking Response of Equipment Anchored to a Base Foundation.* Nicos Makris and Cameron J. Black. September 2001.

PEER 2001/13 *Modeling Soil Liquefaction Hazards for Performance-Based Earthquake Engineering.* Steven L. Kramer and Ahmed-W. Elgamal. February 2001.

PEER 2001/12 *Development of Geotechnical Capabilities in OpenSees.* Boris Jeremic. September 2001.

PEER 2001/11 *Analytical and Experimental Study of Fiber-Reinforced Elastomeric Isolators*. James M. Kelly and Shakhzod M. Takhirov. September 2001.

PEER 2001/10 *Amplification Factors for Spectral Acceleration in Active Regions.* Jonathan P. Stewart, Andrew H. Liu, Yoojoong Choi, and Mehmet B. Baturay. December 2001.

PEER 2001/09 *Ground Motion Evaluation Procedures for Performance-Based Design.* Jonathan P. Stewart, Shyh-Jeng Chiou, Jonathan D. Bray, Robert W. Graves, Paul G. Somerville, and Norman A. Abrahamson. September 2001.

PEER 2001/08 *Experimental and Computational Evaluation of Reinforced Concrete Bridge Beam-Column Connections for Seismic Performance*. Clay J. Naito, Jack P. Moehle, and Khalid M. Mosalam. November 2001.

PEER 2001/07 *The Rocking Spectrum and the Shortcomings of Design Guidelines.* Nicos Makris and Dimitrios Konstantinidis. August 2001.

PEER 2001/06 *Development of an Electrical Substation Equipment Performance Database for Evaluation of Equipment Fragilities*. Thalia Agnanos. April 1999.

PEER 2001/05 *Stiffness Analysis of Fiber-Reinforced Elastomeric Isolators.* Hsiang-Chuan Tsai and James M. Kelly. May 2001.

PEER 2001/04 *Organizational and Societal Considerations for Performance-Based Earthquake Engineering.* Peter J. May. April 2001.

PEER 2001/03 *A Modal Pushover Analysis Procedure to Estimate Seismic Demands for Buildings: Theory and Preliminary Evaluation.* Anil K. Chopra and Rakesh K. Goel. January 2001.

PEER 2001/02 *Seismic Response Analysis of Highway Overcrossings Including Soil-Structure Interaction.* Jian Zhang and Nicos Makris. March 2001.

PEER 2001/01 *Experimental Study of Large Seismic Steel Beam-to-Column Connections.* Egor P. Popov and Shakhzod M. Takhirov. November 2000.

PEER 2000/10 *The Second U.S.-Japan Workshop on Performance-Based Earthquake Engineering Methodology for Reinforced Concrete Building Structures.* March 2000.

PEER 2000/09 *Structural Engineering Reconnaissance of the August 17, 1999 Earthquake: Kocaeli (Izmit), Turkey.* Halil Sezen, Kenneth J. Elwood, Andrew S. Whittaker, Khalid Mosalam, John J. Wallace, and John F. Stanton. December 2000.

PEER 2000/08 *Behavior of Reinforced Concrete Bridge Columns Having Varying Aspect Ratios and Varying Lengths of Confinement.* Anthony J. Calderone, Dawn E. Lehman, and Jack P. Moehle. January 2001.

PEER 2000/07 *Cover-Plate and Flange-Plate Reinforced Steel Moment-Resisting Connections.* Taejin Kim, Andrew S. Whittaker, Amir S. Gilani, Vitelmo V. Bertero, and Shakhzod M. Takhirov. September 2000.

PEER 2000/06 *Seismic Evaluation and Analysis of 230-kV Disconnect Switches.* Amir S. J. Gilani, Andrew S. Whittaker, Gregory L. Fenves, Chun-Hao Chen, Henry Ho, and Eric Fujisaki. July 2000.

PEER 2000/05 *Performance-Based Evaluation of Exterior Reinforced Concrete Building Joints for Seismic Excitation.* Chandra Clyde, Chris P. Pantelides, and Lawrence D. Reaveley. July 2000.

PEER 2000/04 *An Evaluation of Seismic Energy Demand: An Attenuation Approach.* Chung-Che Chou and Chia-Ming Uang. July 1999.

PEER 2000/03 *Framing Earthquake Retrofitting Decisions: The Case of Hillside Homes in Los Angeles.* Detlof von Winterfeldt, Nels Roselund, and Alicia Kitsuse. March 2000.

PEER 2000/02 *U.S.-Japan Workshop on the Effects of Near-Field Earthquake Shaking.* Andrew Whittaker, ed. July 2000.

PEER 2000/01 *Further Studies on Seismic Interaction in Interconnected Electrical Substation Equipment.* Armen Der Kiureghian, Kee-Jeung Hong, and Jerome L. Sackman. November 1999.

PEER 1999/14 *Seismic Evaluation and Retrofit of 230-kV Porcelain Transformer Bushings*. Amir S. Gilani, Andrew S. Whittaker, Gregory L. Fenves, and Eric Fujisaki. December 1999.

PEER 1999/13 *Building Vulnerability Studies: Modeling and Evaluation of Tilt-up and Steel Reinforced Concrete Buildings.* John W. Wallace, Jonathan P. Stewart, and Andrew S. Whittaker, editors. December 1999.

PEER 1999/12 *Rehabilitation of Nonductile RC Frame Building Using Encasement Plates and Energy-Dissipating Devices.* Mehrdad Sasani, Vitelmo V. Bertero, James C. Anderson. December 1999.

PEER 1999/11 *Performance Evaluation Database for Concrete Bridge Components and Systems under Simulated Seismic Loads.* Yael D. Hose and Frieder Seible. November 1999.

PEER 1999/10 *U.S.-Japan Workshop on Performance-Based Earthquake Engineering Methodology for Reinforced Concrete Building Structures.* December 1999.

PEER 1999/09 *Performance Improvement of Long Period Building Structures Subjected to Severe Pulse-Type Ground Motions*. James C. Anderson, Vitelmo V. Bertero, and Raul Bertero. October 1999.

PEER 1999/08 *Envelopes for Seismic Response Vectors.* Charles Menun and Armen Der Kiureghian. July 1999.

PEER 1999/07 *Documentation of Strengths and Weaknesses of Current Computer Analysis Methods for Seismic Performance of Reinforced Concrete Members.* William F. Cofer. November 1999.

PEER 1999/06 *Rocking Response and Overturning of Anchored Equipment under Seismic Excitations.* Nicos Makris and Jian Zhang. November 1999.

PEER 1999/05 *Seismic Evaluation of 550 kV Porcelain Transformer Bushings.* Amir S. Gilani, Andrew S. Whittaker, Gregory L. Fenves, and Eric Fujisaki. October 1999.

PEER 1999/04 *Adoption and Enforcement of Earthquake Risk-Reduction Measures.* Peter J. May, Raymond J. Burby, T. Jens Feeley, and Robert Wood.

PEER 1999/03 *Task 3 Characterization of Site Response General Site Categories*. Adrian Rodriguez-Marek, Jonathan D. Bray, and Norman Abrahamson. February 1999.

PEER 1999/02 *Capacity-Demand-Diagram Methods for Estimating Seismic Deformation of Inelastic Structures: SDF Systems*. Anil K. Chopra and Rakesh Goel. April 1999.

PEER 1999/01 *Interaction in Interconnected Electrical Substation Equipment Subjected to Earthquake Ground Motions.* Armen Der Kiureghian, Jerome L. Sackman, and Kee-Jeung Hong. February 1999.

PEER 1998/08 *Behavior and Failure Analysis of a Multiple-Frame Highway Bridge in the 1994 Northridge Earthquake.* Gregory L. Fenves and Michael Ellery. December 1998.

PEER 1998/07 *Empirical Evaluation of Inertial Soil-Structure Interaction Effects.* Jonathan P. Stewart, Raymond B. Seed, and Gregory L. Fenves. November 1998.

PEER 1998/06 *Effect of Damping Mechanisms on the Response of Seismic Isolated Structures.* Nicos Makris and Shih-Po Chang. November 1998.

PEER 1998/05 *Rocking Response and Overturning of Equipment under Horizontal Pulse-Type Motions.* Nicos Makris and Yiannis Roussos. October 1998.

PEER 1998/04 *Pacific Earthquake Engineering Research Invitational Workshop Proceedings, May 14–15, 1998: Defining the Links between Planning, Policy Analysis, Economics and Earthquake Engineering.* Mary Comerio and Peter Gordon. September 1998.

PEER 1998/03 *Repair/Upgrade Procedures for Welded Beam to Column Connections.* James C. Anderson and Xiaojing Duan. May 1998.

PEER 1998/02 *Seismic Evaluation of 196 kV Porcelain Transformer Bushings.* Amir S. Gilani, Juan W. Chavez, Gregory L. Fenves, and Andrew S. Whittaker. May 1998.

PEER 1998/01 *Seismic Performance of Well-Confined Concrete Bridge Columns.* Dawn E. Lehman and Jack P. Moehle. December 2000.